
# Electronic structure calculations of spin-coupled iron-sulfur clusters

Barði Benediktsson

Faculty of Physical Sciences
University of Iceland

# Electronic structure calculations of spin-coupled iron-sulfur clusters

Barði Benediktsson

Dissertation submitted in partial fulfillment of a
*Philosophiae Doctor* degree in Chemistry

Advisor
Ragnar Björnsson

Supervisor
Hannes Jónsson

PhD Committee
Asmus Ougaard Dohn
Tobias Krämer

Opponents
Adam Kubas
Dimitrios A. Pantazis

Faculty of Physical Sciences
School of Engineering and Natural Sciences
University of Iceland
Reykjavik, 22.06.2022

Electronic structure calculations of spin-coupled iron-sulfur clusters

Dissertation submitted in partial fulfillment of a *Philosophiae Doctor* degree in Chemistry



Faculty of Physical Sciences
School of Engineering and Natural Sciences
University of Iceland
Dunhagi 5
107, Reykjavik
Iceland

Telephone: 525-4000

Bibliographic information:
Barði Benediktsson, , *Electronic structure calculations of spin-coupled iron-sulfur clusters* , PhD dissertation, Faculty of Physical Sciences, University of Iceland, 217 pp.

ISBN 978-9935-9630-4-8

Printing: Háskólaprent
Reykjavik, Iceland, 22.06.2022

# Abstract

Iron-sulfur clusters are integral to the biochemistry of living organisms and a lot of effort has been devoted to research their structure and function. However, describing these polynuclear iron-sulfur clusters with computational chemistry poses a challenge due to their complicated open-shell electronic structure and the fact they are embedded within a protein. Many electronic structure methods (*e.g.* DFT) struggle with describing correctly the phenomena encountered in these clusters, such as their spin coupling. The overarching goal is to model these systems (QM or QM/MM), in particular the cofactors of the nitrogenase enzymes, and understand their electronic structure within the language of DFT. Firstly, the resting state of the iron-vanadium cofactor as it appears in the 1.35 Å resolution X-ray structure is found to be best described as $[VFe_7S_8C(CO_3)]^{2-}$. Secondly, a test set of 11 dimeric spin-coupled Fe or Mo clusters and a test set of 5 dimeric Fe closed shell clusters are introduced and are demonstrated to behave differently w.r.t. density functional choice. Thirdly, the calculated nuclear resonance vibrational spectra (NRVS) of iron-sulfur proteins modelled by QM/MM is shown to be sensitive to functional choice and model size. NRVS is additionally a promising method in the study of nitrogenase and calculations suggest that a combined experimental-computational approach could help characterize the isolable states in the catalytic cycle of nitrogenase.

# Útdráttur

Prótein sem innihalda járn-brennisteins hjálparþætti gegna mikilvægu hlutverki í lífverum og mikil rannsóknarvinna hefur farið í að skilja hvernig þessi prótein virka. Reikniefnafræðilega er þó ekki einfalt að lýsa þessum hjálparþáttum vegna þess hve flókin rafeindabygging þeirra er, sem og vegna áhrifa frá próteinumhverfinu. Þéttnifellafræði (DFT) á erfitt með að lýsa rétt rafeindabyggingu þessa hjálparþátta vegna fyrirbæra eins og spunavíxlerkun. Markmið rannsóknanna sem lýst er í þessu verkefni er að kortleggja hve vel mismunandi þéttnifelli (DF) lýsa þessum kerfum, svo og skilja undirliggjandi rafeindabyggingu þeirra ásamt því að lýsa umhverfisáhrifum út frá fjölskala reiknilíkönum (QM/MM). Þessa þekkingu má síðan nota til að lýsa betur hjálparþáttum nítrógenasa ensímanna sem eru oft taldir vera meðal flóknustu málm hjálparþáttum sem finna má í próteinum. Niðurstöðum verkefnisins má skipta í þrennt. Í fyrsta lagi var fjölskalareiknilíkan af vanadíum-járn hjálparþætti vanadíum nítrógenasa borið saman við kristalbyggingu ensímsins og fundið að hjálparþættinum er best lýst sem $[VFe_7S_8C(CO_3)]^{2-}$ klasa. Í öðru lagi voru tvö sameindasöfn útbúin þar sem eitt innihélt 11 spunakúplaða tvíjárns-komplexa og annað 5 tvíjárns-komplexa með allar rafeindir paraðar og sýnt fram á að mismunandi þéttnifelli lýsa þeim misvel. Í þriðja lagi voru kjarntitringshermiróf (NRVS) af járn-brennisteins hjálparþáttum reiknuð með fjölskalareiknilíkönum þar sem áhrif vals á þéttnifellis, fjölda atóma lýst með skammtafræði og fjölda atóma í reikningum á annarri afleiðu orkunnar var rannsakað. Niðurstöður benda til að lífrænir tenglar frá próteininu séu næmari fyrir þessum þáttum en ólífrænir tenglar og að NRVS-tilraunir ásamt reikningum ætti að vera góð aðferð til að greina ástönd sem hægt er að einangra í hvarfgangi nítrógenasa.

*Dedicated to my wonderful family*

# Table of Contents

# List of Original Articles

I **Quantum Mechanics/Molecular Mechanics Study of Resting-State Vanadium Nitrogenase: Molecular and Electronic Structure of the Iron–Vanadium Cofactor**

**B. Benediktsson**, R. Bjornsson

Inorganic Chemistry **59**, 11514-11527, 2020.

II **Analysis of the Geometric and Electronic Structure of Spin-Coupled Iron–Sulfur Dimers with Broken-Symmetry DFT: Implications for FeMoco.**

**B. Benediktsson**, R. Bjornsson

Journal of Chemical Theory and Computation **18**, 1437-1457, 2022.

III **Environmental Effects in Theoretical Calculations of $^{57}$Fe Nuclear Resonance Vibrational Spectra: From Molecular Complexes to Complex Metalloproteins.**

**B. Benediktsson**, R. Bjornsson

In manuscript.

*Articles not included in this thesis and briefly discussed*

IV **A Model for Dinitrogen Binding in the $E_4$ State of Nitrogenase**

A. Th. Thorhallsson, **B. Benediktsson**, R. Bjornsson

Chemical Science **10**, 11110-11124, 2019.

# Abbreviations

| | |
|---|---|
| ADP | Adenosine diphosphate |
| ATP | Adenosine triphosphate |
| BS | Broken Symmetry |
| BO | Born-Oppenheimer |
| CASSCF | Complete active space self-consistent field |
| CPCM | Conductor-like Polarizable Continuum Model |
| DF | Density Functional |
| DFT | Density Functional Theory |
| DMRG-CASSCF | Density Matrix Renormalization Group Complete Active Space Self-Consistent Field |
| ECP | Effective Core Potential |
| ENDOR | Electron-Nuclear Double Resonance |
| EPR | Electron Paramagnetic Resonance |
| FeMoco | Iron-Molybdenum cofactor |
| FeMoD11 | Iron and Molybdenum Dimers 11 |
| FeCSD5 | Iron Closed Shell Dimers 5 |
| FeVco | Iron-Vanadium cofactor |
| GGA | General Gradient Approximation |
| GTO | Gaussian-Type Orbitals |
| HERFD-XAS | High Energy Resolution Fluorescence Detected X-ray Absorption Spectroscopy |
| HF | Hartree-Fock |
| IR | Infrared |
| KS-DFT | Kohn-Sham Density Functional Theory |
| LCAO | Linear Combination of Atomic Orbitals |
| LDA | Local Density Approximation |
| LT | Lowe-Thorneley |
| MAD | Mean Absolute Deviation |
| MD | Mean Deviation |
| MM | Molecular Mechanics |
| MRCC | Multireference Coupled Cluster |
| NFS | Nuclear Forward Scattering |

| | |
|---|---|
| NIS | Nuclear Inelastic Scattering |
| NRIXS | Nuclear Resonant Inelastic Scattering |
| NRVS | Nuclear Resonance Vibrational Spectroscopy |
| Pi | Inorganic phosphate |
| QM | Quantum Mechanics |
| QM/MM | Quantum Mechanics/Molecular Mechanics |
| RMSD | Root-Mean-Square Deviation |
| RR | Resonance Raman |
| SCF | Self-Consistent Field |
| SHE | Standard Hydrogen Electrode |
| SIE | Self-Interaction Error |
| SpReAD | Spatially Resolved Anomalous Dispersion |
| STO | Slater-type orbitals |
| TIP3P | Transferable Intermolecular Potential 3P |
| UCO | Unconstrained Corresponding Orbitals |
| XAS | X-ray Absorption Spectroscopy |
| XES | X-ray Emission Spectroscopy |
| XMCD | X-ray Magnetic Circular Dichroism |
| WFT | Wave Function Theory |

## Acknowledgments

On the date which this thesis will be defended (hopefully, since I am writing this in advance), it has been exactly 2800 days – or 7 years and 8 months – since I sent an email to Ragnar regarding a possible B.Sc. project about creating a QM/MM model of Mo-nitrogenase. At that time I had no idea this email would turn out to become one of the most important emails I have ever written in my life. The B.Sc. project turned then into a M.Sc project and then into a Ph.D. project. At the beginning I was wholly underprepared for the challenges of computational chemistry but thanks to the guidance and assistance of Ragnar I feel like I have managed to rise up to the challanges and become the scientist I am today. Thank you, Ragnar.

I have many fond memories with the current and former members of Ragnar's group and I am thankful for having been a part of it. The countless discussions and culinary explorations with Albert have been enjoyable (and tasty). The multiple discussions, scientific or not, with Nico have been educational and (usually) fun. Furthermore, for a very long time, or approximately 3 and 1/2 years, I was the sole member of the outpost of Bjornsson group in Iceland, but that is no longer the case and I have Heiðar to thank for that. It is a shame that we couldn't discuss more in person about nitrogenase Yunjie Pang, but I do cherish the culinary adventure to try hot pot during my time in Mülheim. Thank you everyone.

My supervisor, Hannes, has been helpful throughout my studies. As long as he is not occupied in a meeting it has been so easy to knock on his door and discuss whatever topic is on my mind. Also, thanks to his both direct and indirect support, I haven't felt as academically isolated as one could imagine due to the fact that my advisor and I live in different countries.

I want to thank Tobias Krämer and Asmus Ougaard Dohn for being on my Ph.D. committee and my opponents Adam Kubas and Dimitrios Pantazis for reading my thesis and coming all the way to Iceland for the Ph.D. defense.

In the ugliest building on the university campus – namely, VR-III – are located the most beautiful people that I have ever had the joy to work with. I don't think there is enough space on two pages to write all the things that we have done that I am grateful for, but for the unenlightened reader about VR-III activities, they include everything from mundane little things such as coffee breaks to the wild excursions into the wilderness of Iceland. To current and former members of the VR-III gang (Harsha, Villi, Kristbjörg, Björn, Alejandro, Benni, Mohammad, Elli, Aleksei, Andre, Yorick, Kateryna, Ming, Heman, Clara, Amrita, Rohit, Narges, Swetha, Robert, and Maicol), I want to say thank you, it has been a blast (if I

forgot your name then I am really sorry and will personally print out this page and add your name here _____).

My family has been very supportive of my choice to be in school since I started kindergarten in 1995 but this has not always been an easy journey and they have supported me at every point. I am grateful for having the greatest parents, sisters, and nephew(s) in the whole world!

Life would be boring without friends, so to you (Steinar, Stella, Steini, Einar, Aron, Sunna, Kjartan, Ármann, Jóhann, Atli, Dagur, and everyone else), thank you for making life considerably more joyful and tolerating my complaints. I would also like to give special thanks to the wonderful Ksyusha.

The University of Iceland has been kind to me and I want to give thanks go to the friendly and helpful staff located in Tæknigarður, and especially to Þura, who has always been ready to help with anything with the shortest notice.

I am thankful for the University of Iceland for the academic environment and for the teacher's assistant grant. Furthermore, this PhD project was partially made possible with a grant from the Icelandic Research Fund.

# 1 Introduction

Chemistry occurs everywhere around us. Plants absorb carbon dioxide from the air and convert it into sugars, muscles use chemical energy to perform physical actions, nutrients become more accessible when a potato is cooked, and the batteries in our devices are made from the same lithium which in another form is a mood stabilizer. These are but a few examples of the plethora of chemical phenomena that chemistry deals with. In fact, some describe chemistry as the central science since it connects other fields of science, a thought that is often credited to the first philosopher of science, the Frenchman Auguste Comte, who lived in the $19^{th}$ century France. This is a thought (or an opinion) that the author shares with Auguste Comte. On the other hand, the author does not go as far to agree with everything that the respected philosopher said, such as:

*"Every attempt to employ mathematical methods in the study of chemical questions must be considered profoundly irrational and contrary to the spirit of chemistry.... if mathematical analysis should ever hold a prominent place in chemistry – an aberration which is happily almost impossible – it would occasion a rapid and widespread degeneration of that science." –Auguste Comte*

This statement sounds probably somewhat amusing to the ears of a modern chemist but it does nonetheless capture what the people's idea of chemistry was at that time period in history. Chemistry was a discipline that had partially originated from alchemy, a pseudoscience which in the western world was devoted to the futile endeavor of converting cheaper metals, such as lead, into gold.

Chemistry has changed a lot since the days of Auguste Comte. Modern chemistry embraces math and physics and recognizes their importance to describe and predict chemical phenomena. Furthermore, math is an essential tool in computational chemistry, a field where the line between theoretical physics and chemistry becomes blurred.

Computational chemistry is a relatively young discipline within chemistry and provides a way to study chemical phenomena without ever setting a foot into a research laboratory. One of its many applications include the use

of quantum mechanics (QM) to describe events that happen in chemistry, like a chemical reaction between two hydrogen atoms to form a molecule of dihydrogen. In order to model this chemical reaction, it is necessary to model the nuclei and electrons with many body wavefunction theory which requires a solution to the famous Schrödinger equation. Solving the Schrödinger equation analytically is impossible (for all but one electron atoms) but doing so numerically is achievable. Even with this being the case, modelling nuclei and electrons is computationally expensive. Instead, one can revisit classical molecular mechanics (MM) which is computationally cheap but cannot (typically) desribe chemical reactions. MM is useful to describe other chemical phenomena, like the behavior of a protein dissolved in water. One may in fact choose to use both for a large system, *i.e* QM to describe a small part of the system accurately and MM to describe the rest of the system approximately. A metalloprotein dissolved in water is an example of such a system.

Metalloproteins, like the name suggests, are proteins that contain metal atoms. One type of metalloproteins are the iron-sulfur proteins, a large group of proteins that play an important role in living organisms. These proteins are used for electron transfer processes or to catalyze reactions that are difficult, or near impossible, to do so from proteins constructed from amino acid residues alone.[1] One such important iron-sulfur enzyme is found in diazotrophs, a term used for a type of bacteria and archaea that can utilize the relatively inert dinitrogen in the atmosphere and incorporate it into their biomolecules by catalyzing the reaction of dinitrogen to ammonia.[2] This enzyme is nitrogenase, an enzyme (or rather three enzymes, as discussed in chapter 3) that contains three iron-sulfur clusters with one of the clusters being at the core of the active site of the enzyme. The best known one is the molybdenum nitrogenase, named so due to the iron-molybdenum cofactor (FeMoco, Figure 1.1).[3]

This cofactor is a remarkable feat of evolution as it is an active catalyst for $N_2$ reduction at ambient temperature and pressure.[4] The human solution of activating and reducing dinitrogen is the Haber-Bosch process, an incredibly efficient but energy consuming process that needs high temperature and pressure as well as a source of dihydrogen (which is usually derived from fossil fuels). The Haber-Bosch process is furthermore responsible for approximately 2 % of all human made $CO_2$ emissions. [5] Therefore, it would be beneficial to take inspiration from life and design a more environmental friendly catalyst to synthesize ammonia.

This brings the discussion back to computational chemistry. It is possible to gain insight into chemical reactions and electronic structure of catalysts

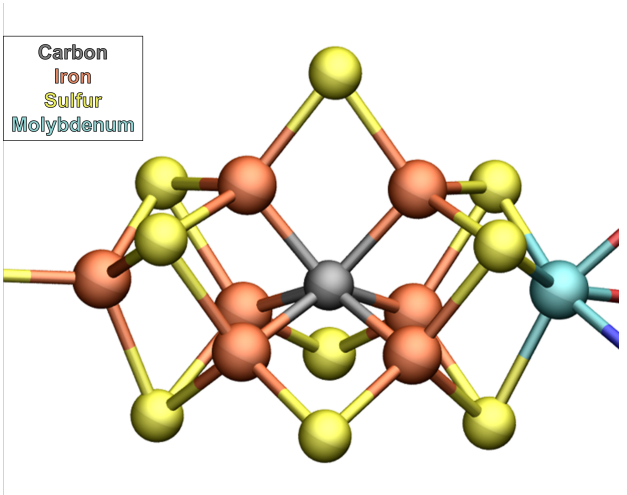


Figure 1.1: The iron-molybdenum cofactor of nitrogenase.

from theoretical calculations. Sometimes it is a straightforward process but in the case of iron-sulfur chemistry, especially where more than one iron is present, it can be somewhat difficult. What one has to consider is how well the method of choice describes the many unpaired electrons in the system: The covalency of the iron-sulfide bonds, the superexchange between two or more iron centers through bridging ligands, the direct exchange through direct 3d-3d overlap between two or more iron centers, 3d-xp overlap between iron and ligands, ferromagnetic or antiferromagnetic coupling, delocalized electrons in an effectively singly occupied orbital, and multireference character of the wavefunction due to multiple low in energy electronic states.[6, 7]

The overarching story in this thesis is to further our understanding of Fe-S chemistry in order to model the catalytically active site of the nitrogenase enzymes more accurately. By careful modelling it should be possible to calculate properties of the cofactors that can then be compared to experimental data. The discussion will begin with reviewing the theoretical background behind the work in this thesis (chapter 2), then move on to characterizing the resting state of the iron-vanadium cofactor of vanadium nitrogenase (chapter 3), continuing into analysis of the electronic structure of iron-sulfur dimers and what density functionals are appropriate to describe such chemistry from geometrical perspective (chapter 4), how to accurately predict nuclear resonance vibrational spectra of iron-sulfur cofactors within a protein or molecular crystal (chapter 5), and finally a quick summary will be given about the author's part of an article describing the $E_4$ state

(the state that binds dinitrogen) of nitrogenase (chapter 6).

# 2 Theoretical Background

## 2.1 Electronic structure Theory

### 2.1.1 Wavefunction theory

In order to model chemical reactions, one needs to be able to describe the interaction between electrons and nuclei. In quantum mechanics, these systems are described by a wavefunction and one needs to use operators to extract information about these systems. The non-relativistic Schrödinger equation[8, 9] describes such a system with the wavefunction $\Psi$ with respect to time as:

$$i\hbar\frac{\partial\Psi(r,t)}{\partial t} = \hat{H}\Psi(r,t) \tag{2.1}$$

with the Hamilton operator ($\hat{H}$) as:

$$\hat{H} = -\frac{\hbar^2}{2m}\frac{\partial^2}{\partial r^2} + V(r,t) \tag{2.2}$$

where $\hbar$ is the reduced Planck's constant, $m$ is the mass of the particle, $r$ is a spatial coordinate, $t$ is time, and $V(r,t)$ is the potential energy.

The wavefunction is an eigenfunction of the Hamiltonian and the energy of the system is an eigenvalue of the Hamiltonian. The Schrödinger equation can be written in a time-independent manner as:

$$\hat{H}\psi = E\psi. \tag{2.3}$$

For the case of an atomic or molecular system, the Hamiltonian operator can be written in terms of sum of operators for the kinetic and potential energy:

$$\hat{H} = \hat{T}_{ele} + \hat{T}_{nuc} + \hat{V}_{nuc,ele} + \hat{V}_{ele,ele} + \hat{V}_{nuc,nuc} \tag{2.4}$$

where $\hat{T}_{nuc}$ and $\hat{T}_{ele}$ are the operators for the kinetic energy of the nuclei and electrons, respectively, whereas $\hat{V}_{ele,ele}$ and $\hat{V}_{nuc,nuc}$ are the operators for the potential energy of electron-electron and nuclei-nuclei repulsion, respectively, and $\hat{V}_{ele,nuc}$ is the operator for the potential energy of electron-nuclei attraction.

Written in full, the Hamiltonian operator for a system of $N$-electrons and $M$-nuclei is:

$$\hat{H} = -\sum_{i}^{N} \frac{\hbar^2}{2m_e}\nabla_i^2 - \sum_{k}^{M} \frac{\hbar^2}{2m_k}\nabla_k^2 - \sum_{i}^{N}\sum_{k}^{M} \frac{e^2 Z_k}{4\pi\epsilon_0 r_{ik}} + \sum_{i<j}^{N} \frac{e^2}{4\pi\epsilon_0 r_{ij}} + \sum_{k<l}^{M} \frac{e^2 Z_k Z_l}{4\pi\epsilon_0 r_{kl}} \tag{2.5}$$

where $i$ and $j$ are the indices of the electrons whereas $k$ and $l$ are the indices of the nuclei, with $Z_k$ being the charge of the k-th nuclei, $m_k$ mass of the k-th nuclei, $m_e$ the mass of an electron, $e$ the charge of an electron, $4\pi\epsilon_0$ the permittivity of free space, and the $\nabla$ is the Laplacian operator in cartesian coordinates:

$$\nabla^2 = \frac{\partial^2}{\partial x^2} + \frac{\partial^2}{\partial y^2} + \frac{\partial^2}{\partial z^2}. \tag{2.6}$$

Since electrons move much faster than the nuclei, it is possible to make the approximation that the nuclei are stationary with respect to the electrons. This is known as the Born-Oppenheimer (BO) approximation,[10] in which the second term in Equation 2.5 is ignored and classical energy potential for the fifth term is introduced in equations 2.4 and 2.5. Therefore, the Schrödinger equation within the BO approximation can be written as:

$$(\hat{H}_{ele} + V_{nuc,nuc})\psi_{ele} = E_{ele}\psi_{ele} \tag{2.7}$$

$$\hat{H}_{ele} = -\sum_{i}^{N} \frac{\hbar^2}{2m_e}\nabla_i^2 + \sum_{i}^{N}\sum_{k}^{M} \frac{e^2 Z_k}{4\pi\epsilon_0 r_{ik}} + \sum_{i<j}^{N} \frac{e^2}{4\pi\epsilon_0 r_{ij}} \tag{2.8}$$

$$V_{NN} = \sum_{k<l}^{N} \frac{Z_k Z_l}{r_{kl}}. \tag{2.9}$$

Even with the BO approximation, the Schrödinger equation is still analytically unsolvable. This stems from the fourth term in equation 2.4 which deals with the electron-electron repulsion. It is an example of a many body problem, since if one electron moves it would cause a spontaneous change in other electrons at the same time, which would in turn interact with the electron that just moved. However, the Schrödinger equation is solvable numerically thanks to the variational principle:[11]

$$E_{trial} = \frac{\langle \Phi_{trial} | \Phi_{trial} \rangle}{\langle \Phi_{trial} | \hat{H} | \Phi_{trial} \rangle} \geq E_0 \tag{2.10}$$

where $\Phi_{trial}$ is a trial wavefunction, $E_{trial}$ is the energy of the trial wavefunction, and $E_0$ is the real energy of the system. What the variational principle states is that the energy of any well-behaved trial wavefunction is always going to be higher than the energy of the true energy for the system. This means that it is possible to guess a wavefunction and evaluate its energy iteratively. The energy will always be higher (or equal) to the true energy of the ground state and can therefore be used as a guide to find the correct wavefunction of the system.

### 2.1.2 Hartree-Fock theory

The Hartree-Fock (HF) approximation is a method to deal with chemical systems. It is based on making an $n$-electron wavefunction from an $n$-number of single electron wavefunctions, where the electron-electron repulsion term is approximated as an electron experiencing other electrons as a mean field.[9] Before discussing HF theory and how to construct a wavefunction, it is practical to address three topics. Firstly, relativity is neither accounted for in Hartree-Fock theory nor in the Schrödinger equation, which means that electron spin does not appear in the derivation of HF and therefore is added in an ad-hoc manner (as well as other relativistic effects). Secondly, the Pauli exclusion principle states that no two electrons can have exactly the same quantum numbers. Thirdly, the wavefunction must be antisymmetric. Using a Slater determinant to construct the wavefunction, these three criteria can be satisfied.

The wavefunction of an $n$-electron system is the Slater determinant of $n$-number of one-electron functions that are constructed from a spatial orbital and a spin function ($\alpha$ or $\beta$ spin), generally termed as spin-orbitals ($\phi(x)$). An $n$-electron wavefunction as a Slater determinant is:

$$\psi_{SD} = \frac{1}{\sqrt{N!}} \begin{vmatrix} \phi_1(x_1) & \phi_2(x_1) & \cdots & \phi_n(x_1) \\ \phi_1(x_2) & \phi_2(x_2) & \cdots & \phi_n(x_2) \\ \vdots & \vdots & \ddots & \vdots \\ \phi_1(x_n) & \phi_2(x_n) & \cdots & \phi_n(x_n) \end{vmatrix} \tag{2.11}$$

As can be seen in equation 2.11, the wavefunction $\Psi_{SD}$ is constructed from single electron spin-orbitals and therefore the issue of electron-electron

interaction still remains. As briefly mentioned earlier, in HF theory this is solved by creating a mean field such that the electrons experience an average electron repulsion from all the other electrons. The HF equation for the energy of a system is:

$$E_{HF} = \langle \psi_{SD} | \hat{H}_{elec} | \psi_{SD} \rangle + V_{NN}. \tag{2.12}$$

Now it is clear how one can construct a trial wavefunction that satisfies the previously mentioned conditions and how to calculate its energy. By varying the spin-orbitals of the Slater determinant wavefunction, one can iteratively guess the form of the wavefunction by varying the spin-orbitals and evaluate the energy of the wavefunction until it cannot be lowered further. This is accomplished by solving the HF equations:

$$\hat{f}\Phi_i = \epsilon_i \phi_i \tag{2.13}$$

for each i-th electron, where $\epsilon$ are the eigenvalues to the Fock operator $\hat{f}$, which operates on single electrons:

$$\hat{f}_i = \hat{h}_i + \sum_{i}^{N_{ele}/2} (\hat{J}_i - \hat{K}_i) \tag{2.14}$$

where $\hat{h}_i$ is the single electron Hamiltonian, $\hat{J}_j$ is the Coulomb operator, $\hat{K}_j$ is the exchange operator, and j is the number of electrons (therefore the number of spin-orbitals are number of electrons divided by two, $N_{ele}/2$). The energy of the system is converged to the lowest possible value by solving the HF equation through a self-consistent field (SCF). When the energy stops decreasing by a certain value, then the trial wavefunction is converged.

The energy of the wavefunction is therefore:

$$E_{HF} = \sum_{i}^{N_{ele}} \hat{h}_i + \frac{1}{2} \sum_{i,j}^{N_{ele}} (\hat{J}_{ij} - \hat{K}_{ij}) + V_{nuc} \tag{2.15}$$

where the 1-electron, Coulomb, and exchange integrals are written as $\hat{h}_i$, $\hat{J}_{ij}$, and $\hat{K}_{ij}$, respectively.

Since the electron-electron repulsion is accounted for as a mean field, the wavefunction cannot be exact except for a single electron system such as hydrogen. The difference between the exact energy of the system and the HF energy is defined as the correlation energy:

$$E_{corr} = E_{exact} - E_{HF} \tag{2.16}$$

There are multiple ways to account for this correlation term which is the topic of post-HF methods. Methods include Møller-Plesset pertubation theory and coupled-cluster theory, which will not be discussed further.[9]

### 2.1.3 Basis sets

Most commonly employed computational methods in quantum chemistry use linear combination of atomic orbitals (LCAO) in order to generate molecular orbitals. These orbitals are then iteratively modified in such a way that the overall energy of the system decreases until it converges to the lowest energy possible. For an $n$-atom system, where the basis functions are centered on the atoms:

$$\phi_i = \sum_n c_{ni}\chi_n \tag{2.17}$$

where $\phi_i$ is the $i$-th molecular orbital, $c_{ni}$ is a coefficient, and $\chi_n$ is a basis function. In modern computational quantum chemistry software, the HF (and DFT) equations are solved numerically and the basis functions take the form of either Slater-type orbitals (STO), which are based on an $e^{-\alpha r}$ function, or Gaussian-type orbitals (GTO), which are based on an $e^{-\alpha r^2}$ function. The $\alpha$ is a constant that controls diffuseness and $r$ is the distance from the nuclei. The STOs have properties that are closer to the 1-electron hydrogen orbitals but, GTOs are more commonly used since they are computationally more efficient to use, since the derivative of a GTO is another GTO. In a Cartesian coordinate system, a GTO is:

$$\chi^{GTO}_{\zeta,l_x,l_y,l_z}(x,y,z) = Nx^{l_x}y^{l_y}z^{l_z}e^{-\zeta r^2} \tag{2.18}$$

where $N$ is a normalization constant and $l_x, l_y$, and $l_z$ determine the type of orbital ($e.g$ $l_x + l_y + l_z = 1$ is a p-orbital).

It is possible to take more than one GTO and make a linear combination of GTOs in order to approximate the behavior of STOs:

$$\phi^{GTO}_i = \sum_j d_{ij}\chi^{GTO}_j \tag{2.19}$$

where $\chi^{GTO}_i$ is a linear combination of GTOs, $d_{ij}$ is a contraction coefficient, and $\phi^{GTO}_j$ is the original GTO (primitive Gaussian). To recap; the molecular orbital is constructed from contracted Gaussians that are in turn made from primitive Gaussians.

A basis set is a set of basis functions and they come in various flavors and sizes. It is essential that a basis set is large enough that it is accurate

for calculations, yet small enough so that it is computationally viable to use. Minimal basis sets contain usually only one basis function for each molecular orbital. For a first-row element, there would be only one function (1s), whereas for a second-row element, the basis functions would be five (1s, 2s, $2p_x$, $2p_y$, $2p_z$). This kind of a basis set would be termed single-$\zeta$ (SZ). When increasing the basis set size, additional functions are added to each orbital, where doubling the amount of basis functions will yield a double-$\zeta$ (DZ) basis set, tripling a triple-$\zeta$ (TZ) basis set, and so forth. Taking an element in the second row as an example, a SZ basis set has one function for each orbital (five in total), a DZ basis set has two functions for orbital (ten in total), and a TZ basis set has three functions for each orbital (fifteen in total).

For atoms such in the second or third row transition metals, then it is the valence electrons that are generally of interest. In such a case to reduce the computational cost it is possible to describe the core orbitals by a single function (SZ) whereas the valence electrons are described by more basis functions (*i.e* TZ) . These kind of basis sets are termed split-valence basis sets. Alternatively, it is possible to replace every core electron with an effective core potential (ECP).

Two other factors to consider are polarization and diffuseness. Polarized basis functions are in the form of additional basis functions with higher angular quantum number than the highest valence orbitals are introduced. By introducing these additional basis functions, complex bonding can be described in a better way, *e.g* a hydrogen-fluoride bond. Diffuse basis functions on the other hand are useful to describe the parts of orbitals that are far from the nuclei and are important when describing anions.

### 2.1.4 Density functional theory

Instead of describing a system through a wavefunction, density functional theory (DFT) postulates that it is possible to obtain the energy of a system in its ground state through the electron density alone *via* a density functional, bypassing altogether the need for a wavefunction. Hohenberg and Kohn proved in 1964 that such a functional does in fact exist and that it follows the variational principle.[12] The form of this functional, *i.e.* its mathematical formulation, is though unknown. One year later in 1965, Kohn and Sham hypothesized that the density of a system of non-interacting fermions (electrons in the case of atoms and molecules) has the same density as a system of interacting fermions.[13]

There have been attempts at finding the correct form of the "one and only" functional, but none successful. This is the reason why multiple

density functionals (DFs) exist nowadays which approximate this DF.

A Kohn-Sham density functional contains some of the same components as the Schrödinger equation:

$$E(\rho(r)) = T_{ele}(\rho(r)) + V_{nuc,nuc} + V_{ele,ele}(\rho(r)) + V_{nuc,ele}(\rho(r)) \quad (2.20)$$

where $\rho(r)$ is the electron density at a spatial coordinate $r$, $T_{ele}$ is the electron kinetic energy functional, $V_{nuc,nuc}$ is the nuclear-nuclear repulsion functional, $V_{ele,ele}$ is the electron-electron repulsion functional, and $V_{nuc,ele}$ is the nuclear-electron attraction functional. In a SCF procedure, $V_{nuc,nuc}$ is a constant and will not be included in further formulations. Some effort has gone into deriving $T_{ele}$ from the electron density alone with Thomas and Fermi spending considerable effort to do so.[14, 15] In KS-DFT, the $T_{ele}$ is derived by using orbitals, similarly as in HF.[13] There is a practical aspect to use orbitals, since it is known from HF how to construct them, and it is relatively straightforward to derive the electron density:

$$\rho_{KS}(r) = \sum_n \int |\phi_n|^2 ds \quad (2.21)$$

here, $|\phi_n|^2$ is the orbital probability function, whereas $ds$ indicates that the function is integrated over the coordinate of each spin-orbital.

Now, within KS formalism (assuming $\rho_{KS}(r) = \rho(r)$), the total energy of a system becomes:

$$E(\rho(r)) = T_{KS}(\rho(r)) + V_{nuc,ele}(\rho(r)) + J(\rho(r)) + E_{xc}(\rho(r)) \quad (2.22)$$

where $T_{KS}$ is the KS kinetic energy functional and $V_{ele,ele}(\rho(r))$ has been split up into two, the Coulomb interaction between electrons $J(\rho(r))$, and the exchange-correlation functional $E_{xc}(\rho(r))$. It is possible to derive the first, second, and third term in equation 2.22 as:

$$T_{KS}(\rho(r)) = -\sum_n \frac{1}{2} \langle \phi_n | \nabla^2 | \phi_n \rangle \quad (2.23)$$

$$V_{nuc,ele}(\rho(r)) = -\sum_k Z_k \int \frac{\rho(r)}{r_k} dr \quad (2.24)$$

$$J(\rho(r)) = \frac{1}{2} \int \int \frac{\rho(r_1)\rho(r_2)}{r_{12}} dr_1 dr_2. \quad (2.25)$$

The fourth term in equation 2.22 is the problematic one and cannot be derived exactly. It is the term that is responsible accounting for electron

correlation (instantaneous electron-electron repulsion), electron exchange, and the error (if any) that arises from assuming that a density of non-interacting electrons is the same as the density of electrons that do interact. This term, $E_{xc}(\rho(r))$, is the reason why DFs come in various flavours.

It is possible to split the $E_{xc}(\rho(r))$ functional into two parts, one being the exchange functional and the other the correlation functional. Discovering the true form of these functionals has warranted a lot of research but as of today, the true form remains unknown. One way to deal with exchange and correlation is to derive it from the uniform electron gas, where it is assumed that the electrons are distributed equally throughout space, which is known as the local density approximation (LDA).[9] This approximation works for systems where electrons are distributed equally, but in the case of molecules, it is a rather poor approximation since electron density varies greatly. Assuming for the non-uniformity of the electron density in molecules, the general gradient approximation (GGA) incorporates the gradient of the density into the functional.[9] An example of this is the Becke88 exchange functional,[16] which is then paired with a correlation functional, such as the Perdew86 correlation functional.[17] This a combination for the popular GGA density functional BP86.

There is one issue with how the exchange functional behaves in KS DFT. The Coulomb interaction where the electron interacts with itself is not cancelled out like in HF theory. This error is termed the self-interacting error (SIE) and it is possible to correct for it somewhat by introducing HF exchange as originally proposed by Becke [18] (there is also some research being performed into correcting the SIE without introducing HF exchange). Functionals that contain HF exchange are termed hybrid DFs.

So far, the discussion has been focused on systems that have all electrons paired (closed shell systems), and calculations on such systems with DFs are termed restricted KS-DFT. Not all chemical systems are closed shell and many do in fact contain unpaired electrons, *i.e.* electrons that are alone in a spin orbital. In order to deal with such systems, unrestricted KS-DFT is needed where the $\alpha$ and $\beta$ electrons are described separately.

### Broken Symmetry Density Functional Theory

It is common that molecular systems that contain transition metal(s) (especially the first-row transition metals) contain unpaired electron and have an overall spin of $S > 0$. It is also a possibility that a molecular system which has more than one transition metal contains transition metals that have a local spin greater than zero, yet the overall spin of the molecule is zero. Let's assume two spin centers, A and B, where each spin center

contains a single unpaired electron. The two electrons can have the same spin (*e.g.* two electrons with $\alpha$ spin) so that the overall spin is $S = 1$ in a ferromagnetic coupling, or the electrons can have opposite spin (*e.g.* one electron with $\alpha$ spin and one with $\beta$ spin), resulting in an overall spin of $S = 0$ in an antiferromagnetic coupling.

Theoretically, describing a ferromagnetically coupling system is simpler and can be done with a single determinant wavefunction, unless the system exhibits a strong multireference character. On the other hand, theoretically it is not sufficient to describe an antiferromagnetically coupling system with a single determinant wavefunction, and a multireference wavefunction is needed. In practice, single determinant wavefunctions have proven useful to study antiferromagnetic systems. In order to do so, the spatial spin symmetry is broken, and the spin is localized on each of the spin centers. This methodology is referred to as broken-symmetry (BS), and it is worth noting that the BS wavefunctions are not eigenfunctions of the total spin operator, $\hat{S}^2$.[9]

A way to describe the correct spin-states of spin coupled systems is the phenomenological Heisenberg Hamiltonian.[6] For two spin centers, atom A and B:

$$\hat{H}_{spin} = -2J_{AB}\hat{S}_A\hat{S}_B \tag{2.26}$$

where $J_{AB}$ is the exchange-interaction constant that describes the energy between the spin states. Although BS-DFT states are not eigenfunctions of the total spin operator, it is possible to derive $J$ for the Heisenberg Hamiltonian. It is though not straightforward for iron-sulfur systems and its applicability is questionable for such systems. This is due to the Heisenberg Hamiltonian double exchange (electron exchange between two ions non-equal oxidation state) model underestimating the number of states due to many Fe $\rightarrow$ Fe 3d transitions being absent.[19]

Let's consider a (BS) state of a system, *e.g.* a [2Fe-2S] cluster with an overall spin of $S = 0$ where the iron centers are antiferromagnetically coupled and the oxidation state of each iron is $Fe^{3+}$. Within the quantum chemistry program ORCA [20] (which is used extensively throughout this thesis), this BS state can be generated in two ways. One way is to use the "BrokenSym" option where essentially a ferromagnetic (high spin) state is found, the orbitals are localized and the wavefunction reconverged to the antiferromagnetic broken symmetry (low spin) state. The second way is to use the "FlipSpin" option, where the spin density itself is used. The wavefunction is converged to the ferromagnetic state and the $\alpha$ spin block of the density is replaced with $\beta$ spin block on the atom(s) which the user

has defined and then converged to the antiferromagnetic BS state.

Within this thesis, a pure spin state is labelled as $S$ whereas for a BS state, $M_S$ is used.

## 2.2 Molecular mechanics

It is computationally expensive to use quantum mechanics to describe chemical systems through either WFT or DFT and prohibitively expensive for large biochemical systems such as proteins, deoxyribonucleic acids, or lipid membranes. A way to bypass this limitation (to some extent) is to use classical mechanics to describe molecules, commonly termed as molecular mechanics (MM). In MM, electrons and nuclei are described as a single entity, *i.e* atoms. This means that within MM modelling, chemical reactions are not possible (with some exceptions, such as reactive forcefields).[9]

In MM, the total energy of a system is the sum of covalent and non-covalent interactions and can be expressed as:[9]

$$E_{tot} = \sum_{bonds} k_d(d-d_0)^2 + \sum_{Angles} k_\theta(\theta-\theta_0)^2 + \sum_{Dihedrals} k_\phi(1+cos(n\phi+\delta)) + \sum_{vanderWaals} 4\epsilon_{AB}(\frac{\sigma_{AB}}{r_{AB}})^{12} - \frac{\sigma_{AB}}{r_{AB}})^6 + \sum_{Electrostatic} \frac{1}{4\pi\epsilon_0}\frac{q_A q_B}{r_{AB}} \tag{2.27}$$

where $k_d$, $k_{theta}$, and $k_\phi$ are the bond, angle, and dihedral force constants, respectively, $d_0$ and $\theta_0$ are the equilibrium bond length and angle, $\phi$ is the dihedral angle, $\delta$ is a periodic constant, $\epsilon_{AB}$ is the lowest point in a Lennard-Jones potential, $r_{AB}$ is the distance between two interacting particles, $q_A$ and $q_B$ are the partial charges of two interacting particles $A$ and $B$. The first three terms describe covalent interactions whereas the two last terms describe non-covalent interactions such as electrostatic interaction (*via* the Coulomb equation) and van der Waals interactions (*via* Lennard-Jones equation).

All the constants in equation 2.27 need to be derived in one way or another, since MM is not an *ab initio* method. One way to do so is to fit these parameters to experimental data or to derive these parameters from high theory calculations. Furthermore, these parameters are not element specific. Let's take a carbon atom in a ethane molecule and compare it to a carbon atom in a bicarbonate molecule. From chemical intuition alone, it is straightforward to see that these two carbon atoms have very different properties. In MM, the two carbon atoms would have different

atom type. There are multiple atom types where each atom type has its own constants and a collection of those is called a forcefield. The issue about these parameters is that there doesn't exist a universal consensus on what is the best constant for an atom type and therefore multiple forcefields exist. Usually, they are designed for a particular type of molecules, such as DNA, lipids, proteins, solvents and *etc.*

Discussing solvents brings up the topic of water. Since systems of biological interest contain considerable amount of water molecules, it is important how it is described. An example of a water model is the transferable intermolecular potential 3p (TIP3P) water model.[21] The water molecule contains three points where there are forcefield parameters present. Furthermore, the water molecule is rigid, meaning that the forcefield parameters only contain intermolecular interactions on its three atoms.

## 2.3 Quantum Mechanics/Molecular Mechanics

When studying large systems that has a smaller region of interest, *e.g.* the cofactor of an enzyme, it is necessary to model the reaction center with QM since MM cannot describe chemical reactions, but QM is too expensive to describe every residue in the enzyme. Quantum-mechanics/molecular-mechanics (QM/MM) is a method to deal with these kind of systems. The reaction center is described with QM whereas the rest of the enzyme is described with MM. The energy of the QM region is just the energy of the SCF (and any additional corrections) whereas the energy of the MM region is calculated from a forcefield. The overall energy of the system is not just the sum of these two terms since the QM region and MM region interact with each other. It is necessary to account for the QM/MM interaction and in general there are two ways to do so.

The first option is the subtractive scheme,[22] where MM energy of the whole system is calculated and the QM energy of the QM region, then the MM energy of the QM region is subtracted from the total energy:

$$E_{QM/MM} = E_{QM} + E_{MM} - E_{MM}^{QM} \tag{2.28}$$

where $E_{QM/MM}$ is the total QM/MM energy, $E_{QM}$ is the QM energy, $E_{MM}$ is the MM energy, and $E_{MM}^{QM}$ is the MM energy of the QM region.

Although it is a relatively simple method conceptually, it is somewhat troublesome in practice. The subtractive scheme QM/MM method requires that forcefield parameters exist for the whole system, which is not always the case, and new ones need to be made. Developing new forcefield parameters can furthermore be time consuming and therefore not always an attractive

option. Additionally, the electron density of the QM region is not polarized by the MM charges.

The second option is the additive scheme,[22] where the total energy of the system is the QM energy, MM energy, and the QM-MM interaction energy (this scheme is used throughout this work). The total QM/MM energy of a system is:

$$E_{QM/MM} = E_{QM} + E_{MM} + E_{QM-MM} \tag{2.29}$$

where the $E_{QM-MM}$ is the sum of electrostatic, van der Waals, and bonded interactions between the regions. The $E_{QM-MM}$ term is comprised of:

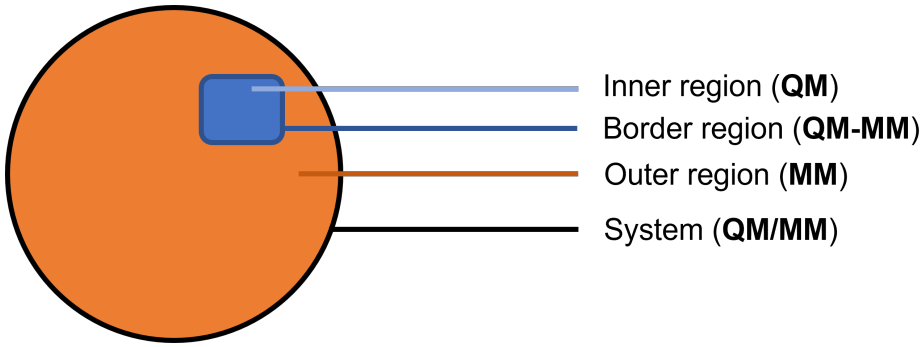


Figure 2.1: How the system is defined within QM/MM. At the center is the QM region, then there is the border region which deals with covalent QM-MM interaction, then the MM region

$$E_{QM-MM} = E^{elstat}_{QM-MM} + E^{vdW}_{QM-MM} + E^{bonded}_{QM-MM} \tag{2.30}$$

where the first term describes the Coloumb interaction between the QM and MM region, the second term describes van der Waals (vdW) interactions between the QM and MM region, and the third term deals with the QM-MM boundary region.

The electrostatic interaction (Coulomb interaction) between the QM region and the MM region is typically described in one of three ways.[22] The first method is mechanical embedding, where all interacting particles are described as pointcharges, including the QM atoms which effectively get pointcharges. There are drawbacks to this method. The QM electron density is not polarized by the pointcharges surrounding the QM region, the pointcharges of the QM atoms may need to be updated, and the pointcharges have to fit the forcefield that describes the MM region.

The second way is electrostatic embedding, where the pointcharges of the MM region can polarize the QM region. One way to do so is to include

the pointcharges as a single electron terms in the Hamiltonian, which then becomes (in atomic units):

$$\hat{H}^{el}_{QM-MM} = -\sum_{i}^{ele}\sum_{M}\frac{q_M}{|\mathbf{r_i} - \mathbf{R_M}|} + \sum_{Q}\sum_{M}\frac{q_M Z_Q}{|\mathbf{R_Q} - \mathbf{R_M}|} \tag{2.31}$$

where the $q_M$ is the charge of a pointcharge in the MM region ($M$ subscript denotes MM atoms), $Z_Q$ is the nuclear charge of QM atoms ($Q$ subscript denotes QM atoms), $\mathbf{R_M}$ is the spatial coordinate of an MM pointcharge, and $\mathbf{R_Q}$ is the spatial coordinate of a QM atom nucleus. The first term in equation 2.31 describes the Coulombic interaction of the electrons in the QM region with the pointcharges in the MM region whereas the second term describes the Coulombic interaction of nuclear charges in the QM region with the pointcharges of the MM region. Within electrostatic embedding, the pointcharges of the atoms in the MM region interact directly with the electron density of the QM region which is arguably a better description of the Coulomb interaction than generating MM pointcharges for the atoms in the QM region. This creates though an issue at the boundary of the QM and MM region, since the MM pointcharges close to the boundary can over polarize the QM electronc density. Furthermore, these MM pointcharges are not necessarily a faithful representation of the charge present, but rather designed parameters for a MM simulation. Although there are drawbacks, electrostatic embedding is the most popular scheme used today.

The third way is polarized embedding, which is arguably the most theoretically rigorous way to perform QM/MM calculations.[23] In polarized embedding, the MM region can polarize the electron density of the QM region which in turn polarizes the MM region. Since the polarized force field changes with change in the QM electron density, then the changes to the polarized force field needs to be calculated iteratively. One way to do so is to iterate the polarizable force field parameters for each step of the SCF, until both converge. One such method is induced point dipoles (there are other ways to create polarized force fields but will not be discussed here), which is a method that treats polarizability by giving each atom a point charge and a point dipole. A calculation is converged when the attraction between all atoms is maximized and the repulsion is minimized.

The van der Waals interaction between the QM region and the MM region is typically described by a Lennard-Jones (LJ) potential. This is a practical solution and LJ parameters from the force field must exist for the atoms in the MM and QM region, which is not always the case. Furthermore, it is possible that the nature of the atoms in the QM region can change

due to chemical reactions and the LJ parameter for the atom would not strictly be correct anymore. Changing the LJ parameters to account for this change would be troublesome since it would mean that the potential energy surface (PES) is no longer the same. It is quite possible that the LJ interactions between the QM and MM region becomes problematic but the easy solution to this is just to increase the QM region.[22]

If the QM region is not bonded to the MM region, then no special precaution has to be taken at the QM-MM border (the QM-MM boundary term). In biomolecules such as enzymes, this is most of the time not the case and the QM-MM boundary term cannot be dismissed. In practice it is said that a bond is "cut" when a covalent bond which goes through the boundary between the QM region and the MM region is dealt with. When cutting, it is important to cut a relatively insignificant bond, preferably a covalent C-C bond within the same charge group, which will cause the least amount of disruption to the QM region. Furthermore, the cut bond creates a vacancy on the atoms where the bond was cut and there is a chance of overpolarization at the border. From the QM region perspective, one of the three following methods are generally used to saturate the vacant position on a QM atom.

The first and most common method is to introduce a so-called link atom, which is generally a hydrogen atom, and is used to saturate the free vacancy present on the QM atom. The QM/MM calculation is performed in such a way that the link atom is part of the QM calculation whereas the bond between the QM and MM region is described *via* a forcefield. Introducing a new atom to the QM region increases the number of degrees of freedom of a system and the link atom is especially vulnerable to overpolarization, due to being in an unusual proximity to point charges. The issue of additional numbers of freedom can be dealt with by constraining the link atom and QM atom bond whereas the issue of overpolarization can be dealt with by shifting the point charges and distributing them over the molecule (there exist other methods such as deleting or smearing pointcharges but they will not be discussed further).[24] Another option is to use special boundary atoms that are part of both the QM and the MM region. Yet another option is to use frozen localized orbitals to cap the vacancy present.

## 2.4 Electronic structure analysis

The energy of a system which is being studied is used to guide and converge the wavefunction. The energy by itself is incredibly useful but one may want to analyze the resulting wavefunction or electron density in more traditional

terms of chemistry, such as atoms connected by bonds. There are three common ways to do so. Firstly, to partition the wavefunction based on the basis functions. Secondly, to derive information from the electrostatic potential. Thirdly, to partition the electron density into domains based around the atomic nuclei.[9]

### 2.4.1 Population analysis

The electron density $\rho$ at coordinate $\mathbf{r}$ in a molecular orbital $\phi$ is

$$\rho(\mathbf{r}) = \phi_i^2(\mathbf{r}) \tag{2.32}$$

and the total number of electrons in a molecule is obtained by integrating over all of the electronic density which is derived from occupied orbitals

$$N_{ele} = \sum_{i}^{N_{occ}} \int \rho(\mathbf{r}) d\mathbf{r} \tag{2.33}$$

where $N_{ele}$ is the number of electrons and $N_{occ}$ is the number of occupied orbitals.

Mulliken population analysis can be used when the density is constructed from atom centered basis functions and writing the molecular orbitals as linear combinations of basis functions:[9, 25]

$$N_{ele} = \sum_{i}^{N_{occ}} \sum_{\alpha\beta}^{M_{basis}} c_{\alpha i} c_{\beta i} \int \chi_{\alpha i} \chi_{\beta i} d\mathbf{r} \tag{2.34}$$

By introducing an occupation number, $n$, which can be 0, 1, or 2 for each molecular orbital, equation 2.34 can be rewritten as:

$$\begin{aligned} N_{ele} &= \sum_{i}^{N_{occ}} \sum_{\alpha\beta}^{M_{basis}} n_i c_{\alpha i} c_{\beta i} \int \chi_{\alpha i} \chi_{\beta i} d\mathbf{r} \\ &= \sum_{\alpha i \beta i}^{M^{basis}} D_{\alpha i \beta i} S_{\alpha i \beta i} \end{aligned} \tag{2.35}$$

where the sum of the coefficients $\chi_{\alpha i}$ and $\chi_{\beta i}$ and the occupation numbers $n$ is the density matrix $D_{\alpha i \beta i}$ whereas the multiplication of $\chi_{\alpha i}$ and $\chi_{\beta i}$ is the overlap matrix $S_{\alpha i \beta i}$.

In Mulliken population analysis, the inner product of elements $D \odot S$ is used to distribute the electrons into atomic contributions. The diagonal

element is the number of $\alpha$ electrons whereas the off-diagonal element is the number of $\alpha$ and $\beta$ electrons. The contributed atomic orbitals with a certain atom can be summed up to yield the number of electrons associated with the atom. Furthermore, for a chemical bond between two atoms, the partitioning of charge is considered to be equal between two atoms. The population of Mulliken charge on an atom A is defined as:

$$\rho_A = \sum_{\alpha \in A}^{M_{basis}} D_{\alpha i \beta i} S_{\alpha i \beta i} \tag{2.36}$$

And the overall charge for an atom A is therefore the charge of the nuclei minus the number of electrons:

$$Q_A = Z_A - \rho A \tag{2.37}$$

The issue with basis function population analysis like Mulliken is that more than two electrons may reside in a MO due to the diagonal matrix element being larger than two as well as negative orbital occupancy due to off-diagonal elements being negative. Since it is also purely based on basis functions, an electron will always be designated to the atom that has the basis function whereas chemical "intuition" might be to put the electron on the more electronegative atom. Furthermore, this means that Mulliken charges show great basis set dependency.

A better option may be to base a population analysis on some physical properties of the wavefunction such as the electron density. The electron density is integrated for specific spatial volume around a nucleus to obtain the number of electrons that reside within an atomic basin (specific volume) $\Omega$ is:

$$N_A = \int_{\Omega} \rho(r) d\mathbf{r} \tag{2.38}$$

and the charge for an atom A would be the number of electrons subtracted from the nuclear charge.

$$Q_A = Z_A - N_A \tag{2.39}$$

A weight function can be introduced which determines fractionally how much an electron belongs to atom A, and is defined as:

$$w_A(\mathbf{r}) = \frac{\rho_A^{ad}(\mathbf{r})}{\rho_{pd}(\mathbf{r})} \tag{2.40}$$

and the number of electrons is then:

$$N_A = \int w_A(\mathbf{r})\rho(r)d\mathbf{r} \tag{2.41}$$

The integration is relatively straightforward but it requires some definition as to what an atomic basin should look like. One such scheme is the Hirshfeld population analysis which is based on using the atomic electronic densities for partitioning of the molecular electronic densities.[26] The starting point is the promolecular density, which is simply the sum over the atomic densities of the atoms in the molecule

$$\rho_{pd}(\mathbf{r}) = \sum_{A}^{M_{Atoms}} \rho_A^{ad}(\mathbf{r}) \tag{2.42}$$

where $\rho_{pd}$ is the promolecular density and $\rho_A^{ad}$ is the atomic density.

Hirshfeld charges are arguably physically more realistic than Mulliken charges since they are dependent on the electron density but not directly on the basis functions, which is also a practical argument in favor for their use.

### 2.4.2 Bond orders

Bond orders are an attempt to make a complicated electron structure into something that resembles a Lewis structure. Typically, if a bond order between two atoms is 1, it indicates a single covalent bond, if it is 2, it indicates a double bond and so forth. One method to calculate bond orders is the Mayer bond order (MBO).[9, 27] For atoms A and B, the MBO is defined as:

$$\delta^{MBO}(A,B) = \sum_{\mu\in}\sum_{\lambda\in}(DS)_{\mu\lambda}(DS)_{\lambda\mu} + (RS)_{\mu\lambda}(RS)_{\lambda\mu} \tag{2.43}$$

where $\delta^{MBO}(A,B)$ is the MBO for atoms A and B, $D$ is the electron density matrix, R is the spin-density matrix, and $S$ is the overlap matrix. The MBO is a Mulliken population like method since it is based on basis sets rather than the electron density itself and is therefore quite sensitive to basis set size and how diffuse it is.

# 3 The Electronic Structure of the Iron-Vanadium Cofactor

The main body of this work has already been published in Article I.[28] Computational details and QM/MM model preparation can be found in Appendix A.

## 3.1 Nitrogenase

The nitrogenase enzymes are the only biological systems known to man that are capable of the difficult process of reducing dinitrogen to ammonia.[4] Three nitrogenase enzymes are known and are named after the presence or absence of a non-iron metal ion at the catalytic active site of the enzyme. These enzymes are the Molybdenum nitrogenase (Mo-nitrogenase), the Vanadium nitrogenase (V-nitrogenase), and the Iron-only nitrogenase (Fe-nitrogenase).[3] Of the three nitrogenase enzymes, the Mo-nitrogenase has received the most attention due to being catalytically more active than the other two variants and generally the enzyme of choice for bacteria. One may ask then why the two less active enzymes exist, since the Mo-nitrogenase is the most active one. One possible explanation is in a scenario of a Mo-deficient environment, then there are backup enzymes available to fix nitrogen.[29] Another possible explanation is that they are evolutionary related and all the genes have been retained.[3] Whatever the case is, in *Azotobacter vinelandii* all the necessary genes are in place and all three nitrogenase enzymes can be expressed.[30]

Although V-nitrogenase is not as active as the Mo-nitrogenase, it is nonetheless just as (if not more) interesting due to its different reaction capabilities.[31] It can reduce carbon monoxide, perform alkyl coupling reactions, and is more reactive than its Molybdenum counterpart at low temperatures.[32]

The three nitrogenase enzymes are believed to catalyze the reaction of dinitrogen in a similar way, with two molecules of ammonia and one molecule of dihydrogen formed for each molecule of dinitrogen reacted according to the following stoichiometry:[4]

$$N_2 + 8\,e^- + 8\,H^+ + 16\,MgATP \longrightarrow 2\,NH_3 + H_2 + 16\,MgADP + 16\,Pi$$

Why the enzyme "wastes" energy to form dihydrogen is not immediately obvious and puzzled researchers for a long time. Furthermore – perhaps to add to the confusion – then nitrogenase is also a rather good hydrogenase in the absence of other substrates than protons.[4, 33, 34] Nowadays, there is a near-consensus that this previously mentioned molecule of dihydrogen is formed from two metal hydrides that are ligated to the catalytic active site of nitrogenase in a reductive elimination at one point in the catalytic cycle. Originally this was demonstrated for Mo-nitrogenase,[35] then Fe-only nitrogenase,[36] and more recently for V-nitrogenase.[37]

The three enzymes show great structural homology and although only X-ray structures of Mo-nitrogenase and V-nitrogenase exist, the genes that encode all the three nitrogenase enzymes are known, which makes it possible to compare their amino acid residue sequence.[3, 38] The Mo-nitrogenase is comprised of the molybdenum-iron protein (MoFe protein), an $\alpha_2\beta_2$ heterotetramer which is encoded by the *nifD* and *nifK* genes, and the iron protein (Fe protein), an $\alpha_2$ homodimer encoded by the *nifH* gene. The V-nitrogenase is similarly comprised of the vanadium-iron protein (VFe protein), an $\alpha_2\beta_2\gamma_2$ heterohexamer encoded by the *vnfD*, *vnfK*, and *vnfG* genes with its own Fe protein encoded by the *vnfH* gene. The Fe-nitrogenase is believed to be more similar to V-nitrogenase, with genes that encode the iron-iron protein (FeFe-protein), *anfD*, and *anfK*, being highly similar to their VFe counterpart. The same applies to the Fe-nitrogenase specific Fe-protein, encoded by the *anfH* gene. Actually, the Fe-proteins of the nitrogenase enzymes are soe similar that the MoFe, VFe, and FeFe proteins can use them interchangeably.[3]

Although the VFe protein is an $\alpha_2\beta_2\gamma_2$ heterohexamer, the $\alpha_2\beta_2$ part is structurally similar to the MoFe protein, as can be seen in Figure 3.1.

The catalytically active site of the three nitrogenase enzymes all contain a complex metallocofactor.[3] In the case of Mo-nitrogenase it is the iron-molybdenum cofactor (FeMoco), a $[MoFe_7S_9C]$-homocitrate cluster which features a peculiar hexavalent central carbide (formally $C^{4-}$)[39–41], six trivalent sulfides, three bivalent sulfides (generally referred to as the bridging sulfides), seven tetrahedral iron ions in formal oxidation states of Fe(II), Fe(2.5), or Fe(III), and an octahedral molybdenum ion ligated to homocitrate.[40] FeMoco is bound to the MoFe protein through $\alpha - 275^{Cys}$, ligated to Fe1 on "one end" of the cofactor, and $\alpha - 442^{His}$, ligated to Mo on the "other end" of the cofactor.[40]

The FeMoco counterpart of V-nitrogenase is the iron-vanadium cofactor

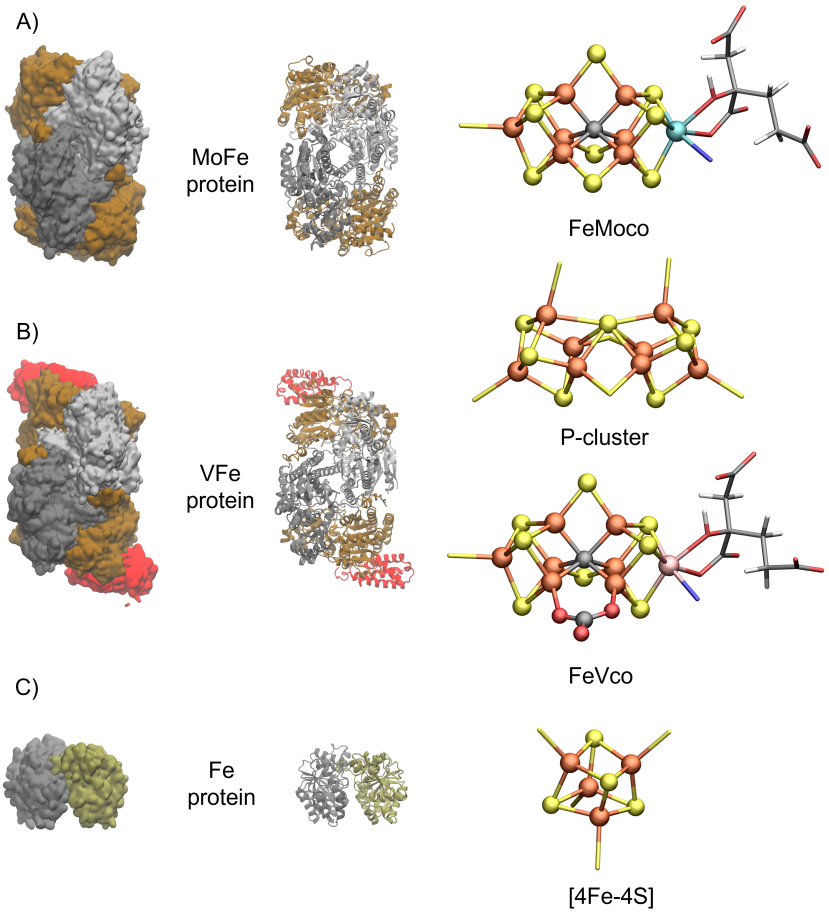


Figure 3.1: The structural similarity between the MoFe protein and the VFe protein where A) shows the MoFe protein and FeMoco, whereas B) shows the VFe protein of V-nitrogenase, and C) the Fe protein of Mo-nitrogenase and its [4Fe-4S] cluster. The P-cluster is found in both the VFe and MoFe protein. The color code (for the cofactors) is cyan is Mo, pink is V, orange is Fe, yellow is S, gray is C, red is O, and blue is N. The inorganic part of the cofactors are ball and stick whereas the organic ligands is visualized as sticks.

(FeVco). It is structurally very similar to FeMoco where the main difference is that one of the bridging sulfides has been replaced with a four-atom ligand, which the authors speculated to be a nitrate or carbonate based on the X-ray structure. Similarly to FeMoco, it is a $[VFe_7S_8(CO_3)C]$-homocitrate cluster which is ligated to the protein matrix through $\alpha - 257^{Cys}$ on the Fe1 and $\alpha - 423^{His}$ on V.[42]

What is known of the electronic structure of these cofactors comes from spectroscopy and theoretical electronic structure calculations of the cofactors. From electron paramagnetic resonance (EPR), it is known that FeMoco in its resting state has an overall spin of $S = {}^3/_2$.[43] The overall charge of the cluster is $[MoFe_7S_9C]^-$ and the oxidation state of the irons are 3Fe(II) and 4Fe(III) as understood from Mössbauer spectroscopy,[44] spatially resolved anomalous dispersion (SpReAD) spectroscopy,[45] and theoretical models.[46] The molybdenum is a Mo(III) ion and has a peculiar electron structure which is interpreted as a non-Hund state from results of X-ray emission spectroscopy (XES), DFT, and X-ray magnetic circular dichroism (XMCD) spectroscopy.[47, 48]

FeVco is more troublesome with respect to overall spin of the cofactor. V-nitrogenase also exhibits a $S = {}^3/_2$ signal which has been for a long time attributed to FeVco in its resting state,[49] but there is recent evidence that FeVco is either in a diamagnetic or an integer spin state in its resting state.[50] In the case of the overall charge of FeVco, there is evidence from high energy resolution fluorescence detected X-ray absorption spectroscopy (HERFD-XAS), X-ray emission spectroscopy (XES), and DFT that the irons of FeVco are more reduced in its resting state than for the resting state of FeMoco.[51] The local oxidation state of the vanadium ion is V(III), as understood from XAS.[52, 53]

The whole catalytic cycle of Mo-nitrogenase takes eight steps and it is necessary for FeMoco to acquire 3-4 electron and protons (which are stored on the cofactor as hydrides or protons) before it can bind and reduce dinitrogen.[4, 37] It has proven challenging to study the reaction intermediates of the reaction for the $E_1$-$E_4$ states, since the nitrogenase enzymes (being also good hydrogenases) can release dihydrogen and relax to a previous $E_{n-2}$ state, making it hard to trap reaction intermediates.[4]. When it comes to the whole enzymatic catalytic cycle of dinitrogen reduction, a lot more is known about Mo-nitrogenase than V-nitrogenase (and even less for Fe-nitrogenase). In Figure 3.2 is the Lowe-Thorneley (LT) scheme for Mo-nitrogenase,[54, 55] adapted from.[3] The LT-scheme describes eight different states for the catalytic cycle from enzyme kinetics studies. In the LT-scheme, states are termed $E_n$ where n indicates how many electrons and

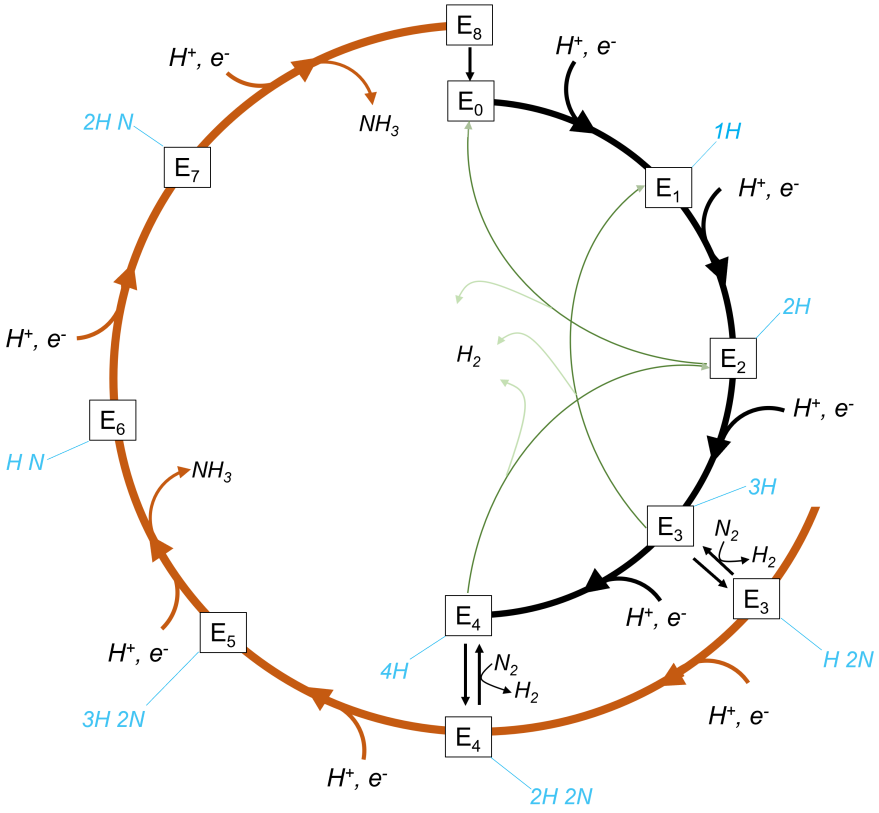


Figure 3.2: A Thorneley–Lowe scheme of the reaction cycle for the nitrogenase enzymes, based on the Mo-nitrogenase. In each step of the reaction cycle, a proton and an electron are added to the cofactor. When three or four protons and electrons have accumulated on the cofactor, *i.e.* at the $E_3$ or $E_4$ state, dinitrogen can bind to the cofactor with a release of dihydrogen from reductive elimination of two hydrides. The cofactor reduces dinitrogen to two molecules of ammonia by continued flux of electrons and protons. The cofactor can relax from $E_n$ ($n > 2$) states to lower states by releasing molecular hydrogen.[4, 54]

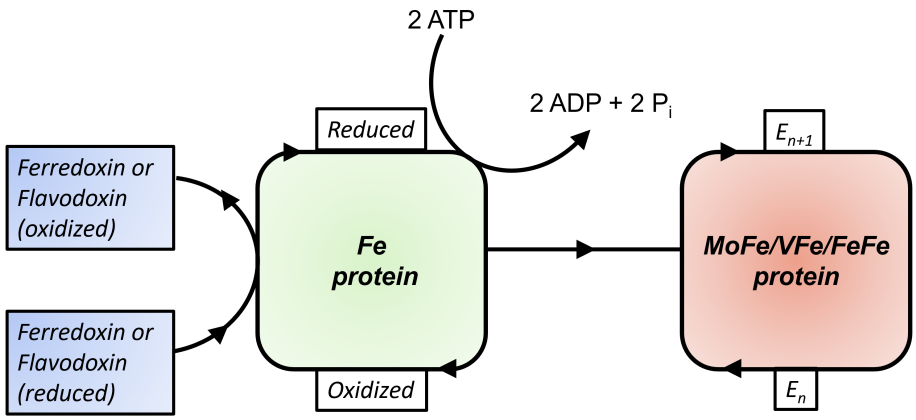


Figure 3.3: A simplified scheme demonstrating how electrons are transferred from an electron carrier (ferredoxin or flavodoxin), through the Fe-protein to the MoFe/VFe/FeFe protein. This process repeats itself between each state in the catalytic cycle.

protons have been transported to the cofactor. The electrons are donated from the Fe-protein and shuttled through the P-cluster to FeXco (X = Mo, V, Fe), see Figure 3.3, where the dissociation of the Fe-protein is the rate limiting step.[4, 56]

The catalytic cycle of V-nitrogenase differs to some extent to the one of Mo-nitrogenase, but how much is not really known. What is known is that V-nitrogenase and Mo-nitrogenase don't have exactly the same reactive properties. V-nitrogenase binds CO in the resting state and can catalyze CO and $CO_2$[57–59] and a proposed reaction intermediate has been crystallized and its X-ray structure analyzed,[60] which has not been possible for Mo-nitrogenase. The proposed reaction intermediate structure has though been challenged by computational models and an OH ligand has been proposed instead.[61, 62]

## 3.2 Motivation and article summary

As previously stated, V-nitrogenase has received considerable less attention than its Molybdenum counterpart and relatively fewer computational studies have been undertaken.[51, 61, 63–68] and the main reason is simple and a technical one. It is only 2017 when an X-ray structure of the VFe protein became available.[42]

With an X-ray structure available and fewer computational studies

undertaken, it makes FeVco a ripe subject to study. Before a catalytic cycle can be suggested from calculations, as has been done for Mo-nitrogenase, a good computational description of the resting state FeVco is needed. Therefore, it is important to characterize FeVco as it appears in the X-ray structure before a catalytic cycle can be suggested. The question that we wanted to answer by QM/MM modelling of the VFe protein were:

1. The molecular structure of FeVco is not clear. The 4-atom bridging ligand is most likely either a carbonate or a nitrate ligand. Can we discriminate between these two options with QM/MM modelling?

2. There is no EPR data available for the crystals that were used to solve the X-ray structure of the VFe protein. Therefore, the spin state of FeVco as it appears in the X-ray structure is not known. Is it possible to shed light on the spin and overall charge with QM/MM modelling?

3. How comparable are the electronic structures of FeMoco and FeVco? Is there something inherent in the electronic structure that could explain the difference in reactivity?

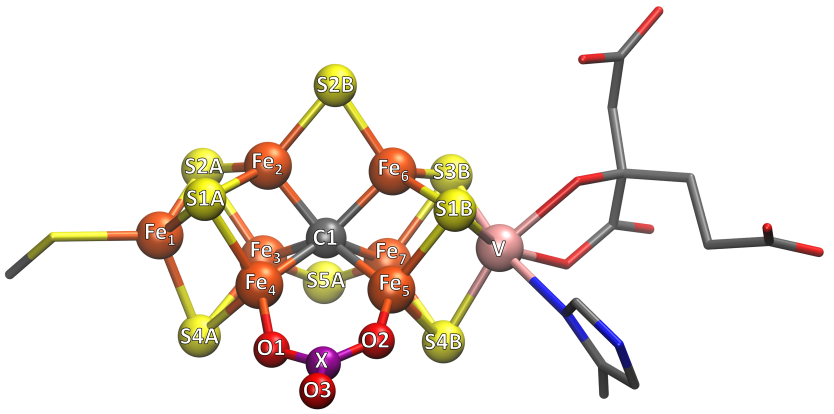


Figure 3.4: The iron-vanadium cofactor (FeVco) with atom labelling. The 4-atom bridging ligand with an atom denoted as X, was originally proposed as carbonate although a nitrate could not be ruled out.

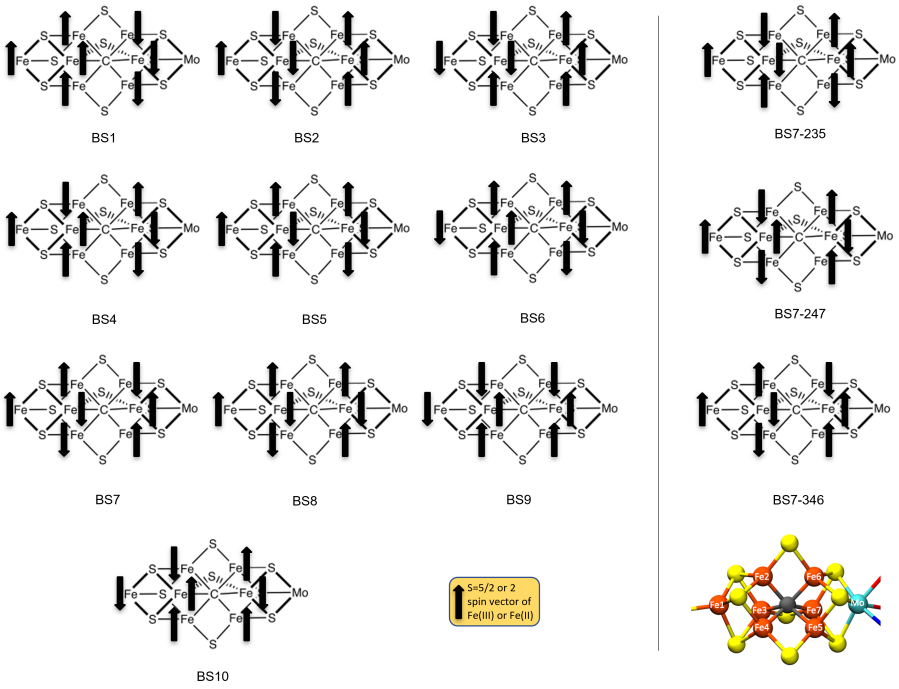


Figure 3.5: To the left: the original 10 BS determinants as described by Noodleman for FeMoco with a total spin of $M_S = {}^3/_2$. He assumed a threefold symmetry through Fe1, the central carbide, and Mo. The favored BS determinant is the one which maximizes antiferromagnetic coupling between the metal ions in FeMoco, which is BS7. To the right: in reality, one cannot assume a threefold symmetry since the protein matrix and the terminal ligands on Mo break it. In the case of the BS7 determinant, there are three different determinants (BS7-235, BS7-247, and BS7-346).

### 3.2.1 Broken symmetry determinants of FeVco

Within the language of BS-DFT, every iron in FeMoco or FeVco has a local $\alpha$ or $\beta$ spin. There are 35 ways to orient the spins so the overall spin matches the experimentally determined value, *i.e* S = $^3/_2$ (in BS-DFT, $M_S$ = $^3/_2$).[69, 70] The 35 BS determinants for FeMoco are shown in Figure 4.1. Throughout this discussion, the BS determinants will be labelled as BSn-xyz (*e.g* BS7-235) where the n is a number from the original Noodleman labelling and xyz indicate iron ions with a majority $\beta$ spin, as opposed to other iron ions with a majority $\alpha$ spins.

For FeMoco, the three BS7 (BS7-235, BS7-247, and BS7-346) are energetically favored in the resting state. It is not clear from the outset which BS determinant is favored for FeVco as it may depend on the redox state, the vanadium ion, and the 4-atom bridging ligand. Therefore, all the 35 different BS determinants need to be tested for each possible model. These models are $[\mathbf{V}\text{-}CO_3]^{0,1-,2-}$ and $[\mathbf{V}\text{-}NO_3]^{1+,0,1-}$ (**V** indicates FeVco and $XO_3$ the unknown bridging ligand, either $CO_3^{2-}$ or $NO_3^-$) where the overall spin can be $M_S$ = 0, 1, 2 for integer spin states or $M_S$ = $^3/_2$, $^1/_2$ for non-integer spin states (we decided to include $M_S$ = $^1/_2$ for completeness although there is no experimental evidence for such a state). Therefore, there are fourteen different models in all that need to be tested. In order to save computation time, single point calculations of the X-ray geometry of FeVco with the protein matrix (simulated as forcefield pointcharges) were performed without geometry optimization.

The results are tabulated in Table 3.1. The first thing to notice is that no matter the redox state and the nature of the 4-atom bridging ligand, the BS7-235 determinant is favoured. It is also consistently the BS determinant which is the lowest in energy for a favored spin state. Furthemore, in a non-integer spin state – no matter the redox state – the overall spin of $M_S$ = $^3/_2$ is preferred, which is consistent with experiment. It is though worth noting that the energy difference between $M_S$ = $^3/_2$ and $M_S$ = $^1/_2$ is 11.08 kcal/mol for $[\mathbf{V}\text{-}CO_3]^{2-}$, 3.27 kcal/mol for $[\mathbf{V}\text{-}CO_3]^0$, 2.76 kcal/mol for $[\mathbf{V}\text{-}NO_3]^-$, and 2.51 kcal/mol for $[\mathbf{V}\text{-}NO_3]^-$.

As energetics for FeMoco have been demonstrated to be highly functional dependent,[71] we contemplated the possibility that this preferrence for BS7-235 which is observed could be due to functional sensitivity of the BS determinants. Therefore TPSS (a 0% HF version of TPSSh) and B3LYP (a 20% HF hybrid) were used to shed light on this conundrum. Using $[\mathbf{V}\text{-}CO_3]^{2-}$ as the model of choice, TPSS still retains this preference for BS7-235. Interestingly though, the second and third lowest in energy BS determinants are now the BS7-247 and BS7-346, being 5.03 kcal/mol and

Table 3.1: Energetically favored BS determinants within each redox state.

| Model | Charge | Spin | $1^{st}$ BS | $2^{nd}$ BS | $3^{rd}$ BS |
|---|---|---|---|---|---|
| [**V**-$CO_3$] | 2- | $^3/_2$ | BS7-235 (0) | BS8-237 (+ 7.58) | BS7-247 (+ 7.83) |
| | | $^1/_2$ | BS8-236 (+ 11.08) | BS7-235 (+ 12.29) | BS10-147 (+ 13.64) |
| | 1- | 2 | BS7-235 (+ 1.51) | BS7-346 (+ 8.67) | BS7-247 (+ 8.84) |
| | | 1 | BS7-235 (0) | BS10-147 (+ 7.73) | BS10-146 (+ 8.12) |
| | | 0 | BS10-147 (+ 11.83) | BS5-256 (+ 11.83) | BS10-146 (+ 8.12) |
| | 0 | $^3/_2$ | BS7-235 (0) | BS6-167 (+ 6.09) | BS2-234 (+ 6.19) |
| | | $^1/_2$ | BS7-235 (+ 3.27) | BS10-147 (+ 4.95) | BS10-146 (+ 5.06) |
| [**V**-$NO_3$] | 1- | $^3/_2$ | BS7-235 (0) | BS7-346 (+ 3.30) | BS7-247 (+ 4.09) |
| | | $^1/_2$ | BS7-235 (+ 2.76) | BS10-147 (+ 8.68) | BS10-127 (+ 9.02) |
| | 0 | 2 | BS7-346 (+ 8.42) | BS6-167 (+ 8.42) | BS4-356 (+ 9.99) |
| | | 1 | BS7-235 (0) | BS10-147 (+ 6.10) | BS10-146 (+ 6.38) |
| | | 0 | BS10-147 (+ 9.99) | BS8-236 (+ 9.99) | BS5-256 (+ 9.99) |
| | +1 | $^3/_2$ | BS7-235 (0) | BS6-167 (+ 6.50) | BS2-234 (+ 8.20) |
| | | $^1/_2$ | BS7-235 (+ 2.51) | BS10-146 (+ 4.22) | BS10-147 (+4.70) |

5.17 kcal/mol higher in energy, respectively. This is still though a far cry from what is observed in FeMoco where the energy difference between the three BS7 determinants is just approximately 1 kcal/mol. The B3LYP results on the other hand are in line with TPSSh, the BS7-235 is favored, with BS8-237 and BS7-247 being 7.88 kcal/mol and 8.60 kcal/mol higher in energy, respectively.

Furthermore, as the protocol here is QM/MM based with the protein explicitly described, there is a possibility that this preference for BS7-235 could be the result of electrostatic interactions from the MoFe protein. Using the continuum solvation model CPCM with a dielectric constant of $\epsilon = 4$, there is still a clear preference for the BS7-235 determinant for the $[\mathbf{V}\text{-}CO_3]^{2-}$ model. The second and third lowest in energy BS determinants are the BS8-236 and BS7-346 determinants, which are 7.96 kcal/mol and 9.28 kcal/mol higher in energy, respectively.

It is not obvious as to what causes this preference for the BS7-235 determinant, but it seems to be the combined effect of vanadium, the 4-atom bridging ligand, and the protein. That the BS7-235 determinant is favored is an important result, since if one BS determinant is preferred over all other determinants, it has a large implication for the following discussion. No matter the overall charge, the nature of the 4-atom bridging ligand, the protein matrix, and functional, the BS7-235 determinant will always be favored. Therefore it is concluded that it is not necessary to investigate which of the 35 BS determinants is lowest in energy during geometrical optimizations, which saves a lot of computation time.

### 3.2.2 Overall charge, spin, and molecular structure of FeVco

There is a strong preference for the BS7-235 determinant and therefore other BS determinants were not explored. The models that we considered to be plausible were $[\mathbf{V}\text{-}CO_3]^{2-,1-,0}$ and $[\mathbf{V}\text{-}NO_3]^{1-,0,1+}$ where for non-integer spin states only $M_S = {}^3/_2$ spin was considered but for integer spin states, both $M_S = 1$ and $M_S = 2$ were considered. By comparison of computed Fe-Fe distances (which are generally best resolved in an X-ray structure due to having the greatest electron density), it was possible to discriminate between these six options. Looking at Figure 3.6 which compares the possible models, it can be seen that the $Fe_4$–$Fe_5$ distance is both sensitive to ligand choice and overall charge. For all models with a nitrate ligand, the deviation in the $Fe_4$–$Fe_5$ distance of the models from the X-ray structure is equal or greater than 0.13 Å, therefore making nitrate an unlikely candidate. Furthermore, the $Fe_2$–$Fe_3$ and $Fe_6$–$Fe_7$ distances are sensitive to the overall oxidation state, and the lengthening observed for this metal-metal distance

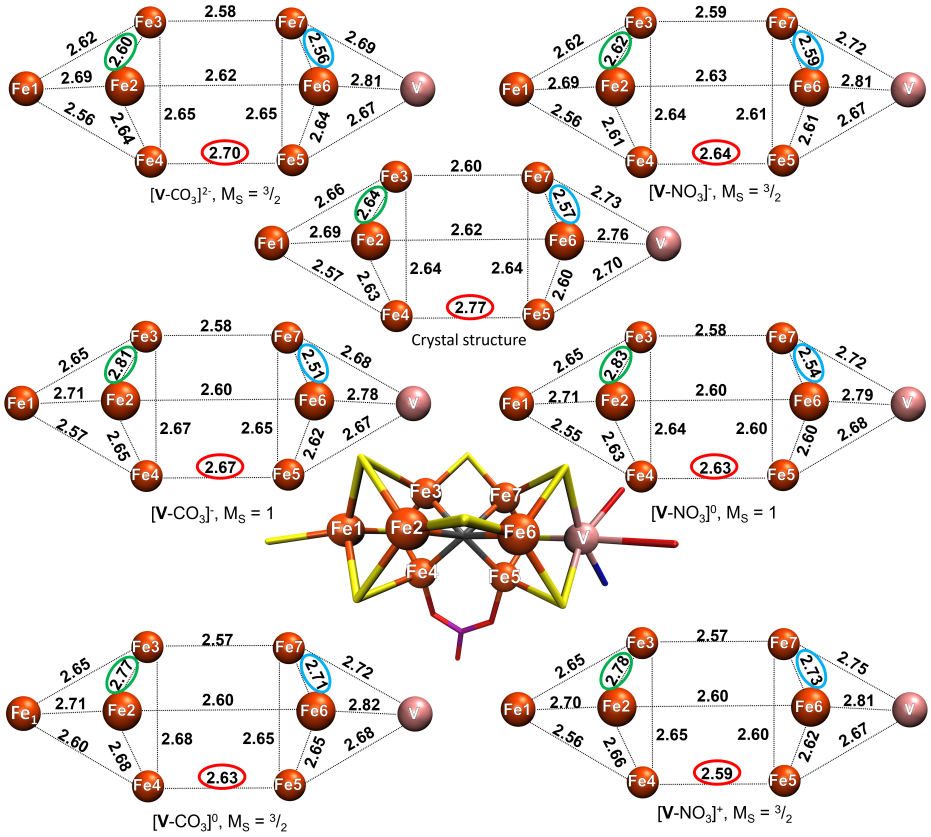


Figure 3.6: Metal-metal distances of the six QM/MM models (QM region: 181 atoms) calculated using the BS7-235 solution compared to the X-ray structure. The colored ellipsoids indicate

when FeVco is oxidized is approximately 0.2 Å. Overall, this makes one model more likely than the others as a likely candidate for the resting state FeVco (or at least how it appears in the X-ray structure), namely $[\mathbf{V}\text{-}CO_3]^{2-}$.

### 3.2.3 Electronic structure of FeVco

The electronic structure of both FeMoco and FeVco as understood from IAOIBOs is presented in Figure 3.7. The overall electronic structure is similar, with delocalized electrons being located between the same metal pairs in both FeMoco and FeVco for the BS7-235 determinant. There are differences, firstly the electron is somewhat more localized on $Fe_4$ in FeVco when compared to FeMoco, secondly the $Fe_5$ is Fe(III) in FeMoco but Fe(II)

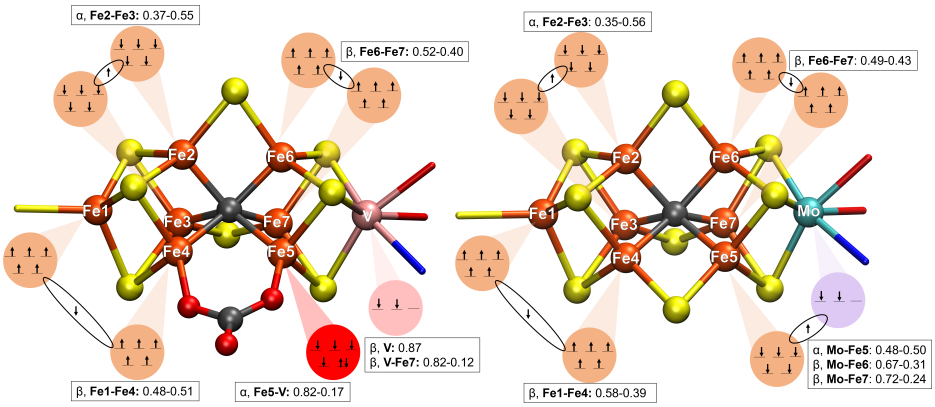


Figure 3.7: The electronic structure FeVco and FeMoco as understood from IAOIBOs for the BS7-235 determinant. Left: IAOIBOs from a QM/MM calculation with a QM region of 181 QM atoms. Right: IAOIBOs from a QM/MM calculation with a QM region of 254 QM atoms. The values in the boxes are the population of the localized orbitals which indicate how much a minority spin electron is delocalized between metals.

in FeVco, and thirdly the vanadium ion is in $3d^2$ configuration whereas the molybdenum ion is in a non-Hund state and has a $4d^3$ configuration.

### 3.2.4 Conclusion

From a detailed comparison of the metal-metal distances of optimized geometries to the X-ray structure, the most favorable model is $[VFe_7S_8(CO_3)C]^{2-}$ with an overall spin of $M_S = {}^3/_2$ and the true electron structure best approximated by the BS7-235 determinant. Furthermore, the electronic structure of FeMoco and FeVco are similar where FeVco is more reduced than FeMoco, which fits with X-ray experiments. This could in part explain why the catalytic properties of V-nitrogenase differs from that of Mo-nitrogenase, since it is capable of binding CO in the resting state.

At this point it is though worth noting again that there is new spectroscopic evidence from EPR experiments that FeVco is in an integer state or diamagnetic in the resting state.[50] This means that the resting state of FeVco is $[\mathbf{V}\text{-}CO_3]^{2-}$ with an overall spin of S = 0,1,2. Although this does not fit with the findings from QM/MM modeling then it is not known whether the X-ray structure is of the resting state and no EPR measurements are available.

As a final note, although and integer spin resting state does not agree with the best model, it was impossible to discern between $[VFe_7S_8(CO_3)C]^{2-}$ or

$[VFe_7S_8(CO_3)C]^-$ from RMSD values alone.

# 4 The Geometric and Electronic Structure of Spin-Coupled Iron-Sulfur Dimers

The main body of this work has already been published in Article II.[72]

## 4.1 Iron sulfur clusters

Iron-sulfur systems can be found in various places in nature with the most abundant iron-sulfur system being Pyrite, or more informally "Fools gold", a $FeS_2$ mineral with iron in ferrous form.[73] Outside of geology, biological iron-sulfur clusters are common and necessary for bacteria, eukaryotes, and archaea to thrive. It is estimated that approximately 5 % of all proteins in *Escherichia coli* contain an iron-sulfur cluster that serve various functions, such as electron transport, redox catalysis, non-redox catalysis, and even gene regulation.[74] Simple $Fe^{3+,2+}$, [2Fe-2S], and [3Fe-4S] clusters are usually used as one electron transporters whereas larger and more complex clusters, such as [4Fe-4S], serve a wider range of chemical function. The most complex iron-sulfur clusters are though indubitably the cofactors of the nitrogenase enzymes, namely FeMoco, FeVco, FeFeco, and the P-cluster. Furthermore, redox potentials of iron-sulfur clusters can be fine tuned with the protein matrix and they can vary from positive values of up to + 400 to negative values of - 600mV against the standard hydrogen electrode (SHE).[75, 76]

The molecular structure of iron-sulfur dimers, and some iron-sulfur clusters of higher nuclearity in proteins, have been known from the beginning of the 1970s with synthetic chemists synthesizing model compounds to study the iron-sulfur cores of these proteins.[77]. The usefulness of synthetic analogues is at least twofold. Firstly, model compounds can be characterized spectroscopically more easily due to higher effective concentration and without the protein scaffold. Secondly, the synthetic analogues can exhibit catalytic activity, making them attractive catalysts. A recent example where model chemistry, along with spectroscopy and computational chemistry, proved helpful to demonstrate that the molybdenum of FeMoco is in a

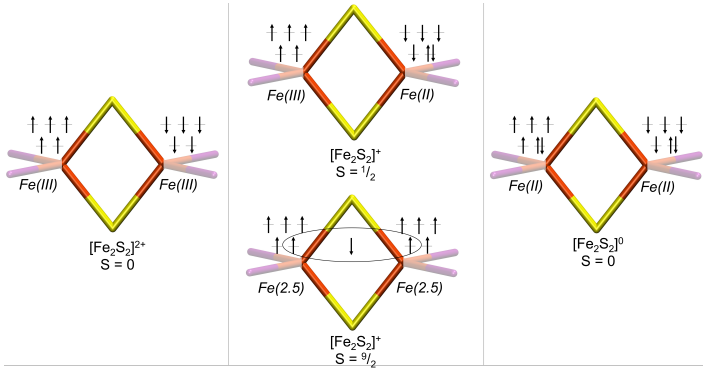


Figure 4.1: Schematic orbital representation for the three redox states observed in iron-sulfur dimers from a BS-DFT picture. Orange is iron, yellow is sulfur, and purple is a terminal ligand.

non-Hund state.[48]

Modelling polynuclear iron-sulfur clusters with computational methods is a theoretically challenging task. These systems exhibit a complex electronic structure where the irons are in a high spin configuration. An iron-sulfur dimer can be thought of as two spin centers that couple either ferromagnetically (*e.g.* two iron ions where each iron has a local $\alpha$ spin of S = $^5/_2$ as in Figure 4.1) or antiferromagnetically (*e.g.* two iron ions where one iron has a local $\alpha$ spin of S = $^5/_2$ and the other a local $\beta$ spin of S = $^5/_2$ as in Figure 4.1). A single determinant method is theoretically sufficient to describe the overall spin density of the ferromagnetic a system, whereas it is not the case for systems composed of two spin centers that couple antiferromagnetically to a ground state of S = 0. In order to treat the antiferromagnetically coupled state with a single determinant method such as DFT, the spin symmetry is broken, *i.e* broken symmetry (BS). In BS-DFT, the alpha spin is localized on one spin center and the beta spin on the other, causing unrealistic spin polarization but yielding the overall spin of $M_S = 0$ (whereas there should be no spin density in such a system). Here, S is used to designate the true spin state whereas $M_S$ is used for a BS spin state.

The coupling constant between the ferromagnetic and antiferromagnetic state cannot be extracted directly from the energy of a BS wavefunction. One way to calculate the coupling constant is to converge the wavefunction of both the ferromagnetic and antiferromagnetic BS determinants and use the Yamaguchi[78, 79] or the Noodleman equations[80–82] approximate spin projection schemes to correct for the spin contamination that comes with BS calculations in the form of *e.g.* Heisenberg–Dirac–van Vleck Hamiltonian.

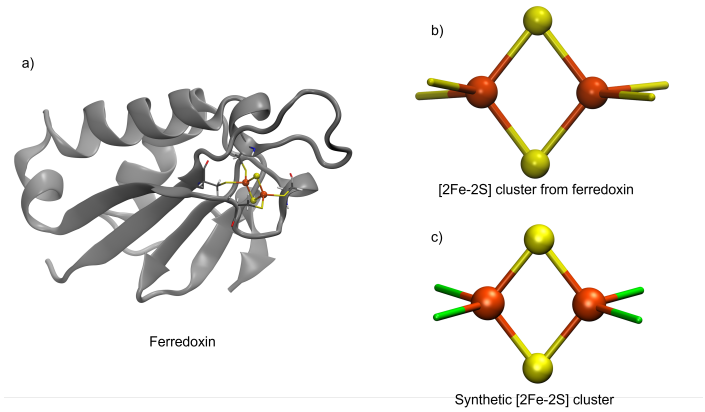


Figure 4.2: The [2Fe-2S] core of Ferredoxin from *Aquifex aeolicus* compared to one of the first synthesized inorganic analog by Holm and coworkers

It is worth noting that correcting for the spin contamination in this way is not straightforward due to functional dependence.[83]

Arguably, a more rigorous approach would be to use spin-adapted multireference wavefunction theory, which uses a linear combination of determinants and can reproduce the correct spin state, to model these systems. Such methods include the complete active space self-consistent field (CASSCF), density matrix renormalization group complete active space self-consistent field (DMRG-CASSCF), full configuration-interaction Monte Carlo, and multireference coupled cluster (MRCC). In practice, these computational methods remain out of reach due to their computational cost and BS-DFT is the method of choice. Furthermore, BS-DFT has proven quite useful to study spin-coupled systems and have proved to be a valuable method to model antiferromagnetically coupled systems where more theoretically rigorous methods remain out of reach (see *e.g.* [84–86]).

## 4.2 Benchmarking studies

There are many benchmarking studies that have been made of computational methods, especially DFT, for reaction energies and more. In general, they are biased towards main group chemistry and focus on energies, with Grimme's general main-group thermochemistry, kinetics, and noncovalent interactions GMTKN55[87] test set being a recent popular example. It was found that the best functionals were in the form of double hybrids (*e.g* DSD-BLYP-D3(BJ) [88]). Some other recommended functionals were the range-separated hybrid functionals ωB97D-V [89] and ωB97X-D3,[90] the

global-hybrid functional PW6B95-D3(BJ),[91] the meta-GGA functional SCAN-D3(BJ),[92] and the GGAs revPBE0-D3(BJ) [93] and B97-D3(BJ) [94] (all included a dispersion correction). While undoubtedly useful to discern between functionals in the zoo that is DFA, accuracy for modelling metal complexes was not a topic.

Bühl and coworkers have benchmarked DF geometries against gas phase data for closed-shell metal complexes [95–97]. They reported that the hybrid DF TPPSh reproduces accurately the geometries of 3d transition metals whereas PBE0 is a better choice for the 4d and 5d transition metals. More recently, Grimme and coworkers have studied DFA for closed shell organometallic complexes with respect to reaction energies where high level theory (DLPNO-CCSD(T)/CBS(def2-TZVPP/def2-QZVPP)) is used to assess the quality of the results of lower level of theory methods. Firstly, results were reported for closed shell complexes [98] where the double-hybrid functional PWPB95-D3(BJ) was found the overall best functional, with $\omega$B97V being the best (ranged seperated) hybrid functional, followed by the hybrid functional PBE0-D3(BJ), whereas SCAN-D3(BJ) and TPSS-D3(BJ) were the best non-hybrid functionals. Secondly, for open shell complexes (notably there were not any iron complexes included in the benchmark due their complicated electronic structure),[99] Grimme and coworkers reported that the best functional was again the double-hybrid functional the PWPB95-D4, with TPSS0-D3(BJ) and TPSSh-D3(BJ) proving to be the best hybrid functionals, and r$^2$SCAN-D3(BJ) the best meta-GGA.

Moving to iron-sulfur chemistry specifically, Szilagyi and coworkers studied spin coupled iron-sulfur dimers and found that B5HFP (a 5% hybrid of BP86) yielded accurate spin densities[100] and Fe-S covalency.[101] In case for other spectroscopic properties, Noodleman and co-workers showed that in order to obtain computed accurate Mössbauer $^{57}$Fe spectra for spin-coupled iron-sulfur systems, good geometries are essential and recommended the following functionals: OLYP, OPBE, PW91, and BP86.[102] Ryde and coworkers recently investigated the accuracy of various computational methods on calculating the relative redox potentials of various iron-sulfur proteins and found that TPSS with double-$\zeta$ basis set (a larger triple-$\zeta$ basis set yielded worse results) and a large QM region (300 atoms) within a continuum solvation model gave the best relative redox potentials.[103] For nitrogenase, Dance recently called into question the use of B3LYP [104], and Ryde and Cao demonstrated that energies obtained from DFT on FeMoco vary wildly with DF choice.[71]

## 4.3 Motivation and article summary

The motivation for studying spin-coupled iron-sulfur dimers comes from the results of the article "A model for dinitrogen binding in the E4 state of nitrogenase",[105] which is discussed to some extent in Chapter 6. To summarize, the geometry of FeMoco was found to be sensitive to the functional choice and it was shown that it stemmed from how different DF described the electronic structure differently.

FeMoco is a notoriously difficult system to study due to its complicated electron structure and it does not help that it is buried in a protein. As mentioned previously, results vary greatly with the choice of DF and research groups generally have their favorite DF of choice and argue for its use such as TPSS for Ryde and coworkers,[106], TPSSh for Bjornsson and coworkers,[105] B3LYP for Siegbahn and coworkers,[107] BP86 for Raugei and coworkers,[108] PBE for Dance,[109] and M06-2X for Adamo and coworkers.[110]

Because of the complexity of FeMoco, studying simpler model systems that are not lodged inside a protein is an attractive option. These model systems exist and one can imagine that FeMoco is constructed from multiple iron-sulfur, iron-carbon, and molybdenum-sulfur dimers, similarly as is shown in Figure 4.3. There is no lack of these dimers and they have been characterized thoroughly *via* multiple spectroscopic methods, as well as X-ray crystallography, making them an excellent choice as model systems. The focus is on geometrical parameters as they are readily available from experiments whereas reaction energies are not. Larger clusters as $MoFe_3S_4$ and $Fe_4S_4$ could also serve as a model systems, but they have a more complicated electronic structure, which makes them a less attractive option.[6, 111]

Two test sets were created. The iron-molybdenum spin-coupled dimers (FeMoD11) that contains 11 M-R (M=Fe,Mo and R=S,C,O) spin coupled clusters that have similar electronic structure properties as FeMoco and the iron closed-shell dimers (FeCSD5) that contains 5 closed shell Fe-R (R=S,SH,C,H) as a control group. The questions that were set to be answered were:

1. What are the effects of basis set size, relativity approximation, continuum, and DF on the geometry of the spin coupled dimers?

2. The metal-ligand bond length and metal-metal distance are functional dependent for FeMoco. Is this the case for the model complexes and can we understand why this is the case from analyzing their electronic structure?

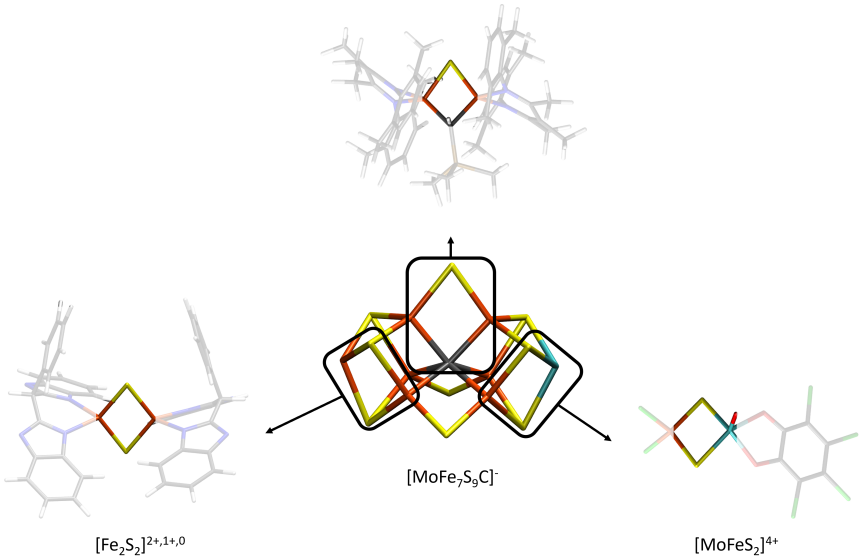


Figure 4.3: It is possible to imagine that FeMoco is constructed from multiple [2Fe-2S], [MoFe-2S], and [2Fe-CS] subunits

### 4.3.1 The FeMoD11 and FeCSD5 test sets

The choice of complexes for a test set should represent the dimeric fragments that one can imagine FeMoco is composed of (see Figure 4.3). These are: Dimers that exist in more than one redox state, have a diamond-like core, and have an available high resolution X-ray structure (preferably with an R-factor lesser than 7 %). The result is the FeMoD11 test set (see Figure 4.4), a test set of eleven dimers comprised of clusters with varying terminal ligands and core cluster, where there are four $[Fe_2S_2]^{2+}$, two $[Fe_2S_2]^{+}$, one $[Fe_2S_2]^{0}$, one $[Fe_2S(CHR)]^{2+}$, two $[MoFeS_2]^{4+}$, and one $[Fe_2(OH)_3]^{2+}$ (not a Fe-S system, but included since it is a rare case of ferromagnetic coupling in an iron-iron dimer).[112] Overall, the Fe-Fe distance is in the range of 2.508 to 2.748 Å. The type of the bridging ligand has the greatest effect (**6** and **9** have the shortest Fe-Fe distance, 2.508 and 2.603 Å, respectively), but oxidation state of iron, and bulkiness of the terminal ligands has an effect as well. It is also a possibility that the counterions and overall charge have an effect too, but that was out of scope for this study. In contrast to FeMoD11, the FeCSD5 test set (see Figure 4.4) includes purely closed shell dimers, that do not exhibit spin coupling with irons in a $Fe^{2+,1+,0}$ oxidation states. With the exception of one dimer (**D1**) with Fe-Fe distance of 3.192 Å, the Fe-Fe distance ranges from 2.505 to 2.589 Å, with the

shortest Fe-Fe distances being observed in complexes with a formal Fe-Fe bond (hydrogenase model complexes **4** and **5**, with Fe-Fe distance of 2.505 and 2.509 Å, respectively). All of these complexes except **9** have an R value lower than 7% for their X-ray structure.

### 4.3.2 The effect of basis sets, relativistic effects, and implicit solvation on the geometry

In order to explore the effects of basis set errors, relativistic effects, and the electrostatic continuum as a replacement for the crystal matrix, **7** was used as a model system due to its relatively simple structure. Three types of basis set families, two of which are commonly used in studies of cofactors of the nitrogenase enzymes, were tested. These were the all-electron def2-Ahlrichs basis set family,[113] the Los Alamos core potentials [114] for iron and molybdenum with the Pople style 6-31G* basis set [115, 116] for other atoms, and the Stuttgart-Dresden core potential[117, 118] for iron with the Pople style 6-31G* basis set for other atoms which were compared against the Ahlrichs quadruple-$\zeta$ relativistically recontracted ZORA-def2-QZVPP basis set using the ZORA relativistic Hamiltonian.[119, 120]

The results reveal that the basis set error is highly systematic and the basis set error is practically converged at the triple-$\zeta$ level with ZORA-def2-TZVP ($\Delta$Fe-Fe = +0.002 Å). The use of core potentials for irons cannot be recommended, with LANLX/6-31G* yielding a geometry with large error in the Fe-Fe distance ($\Delta$Fe-Fe = 0.084 - 0.098 Å) and a small improvement with SDD/6-31G* basis set ($\Delta$Fe-Fe = +0.079 Å). The inclusion of a scalar relativistic Hamiltonian is somewhat important and the difference between geometries obtained at the ZORA-def2-QZVPP basis set level with or without the ZORA approximation is $\Delta$Fe-Fe = 0.014 Å. In the case of a polarizable continuum, it is found that changes to the geometry with varying dielectric constant is near negligible, as long as it is more than 10, with the difference in Fe-Fe distance between $\epsilon = 10$ and $\epsilon = \infty$ being $\Delta$Fe-Fe = 0.003 Å. Therefore it was deemed justified to use ZORA-def2-TZVP as a basis set, the ZORA Hamiltonian, and CPCM with $\epsilon = \infty$ to study functional dependence for all complexes shown in Figure 4.4.

### 4.3.3 DFT functional dependence of the geometry

Sixteen functionals were tested: BP86 (GGA) [16, 17], PBE (GGA) [121], PBE0 (25% HF) [121, 122], TPSS (mGGA) [123], TPSSh (mGGA 10% HF) [123, 124], BLYP (GGA) [16, 125], B3LYP (GGA 20% HF) [16, 18, 125], B3LYP* (GGA 15% HF) [126, 127], BHLYP (GGA 50% HF) [128],

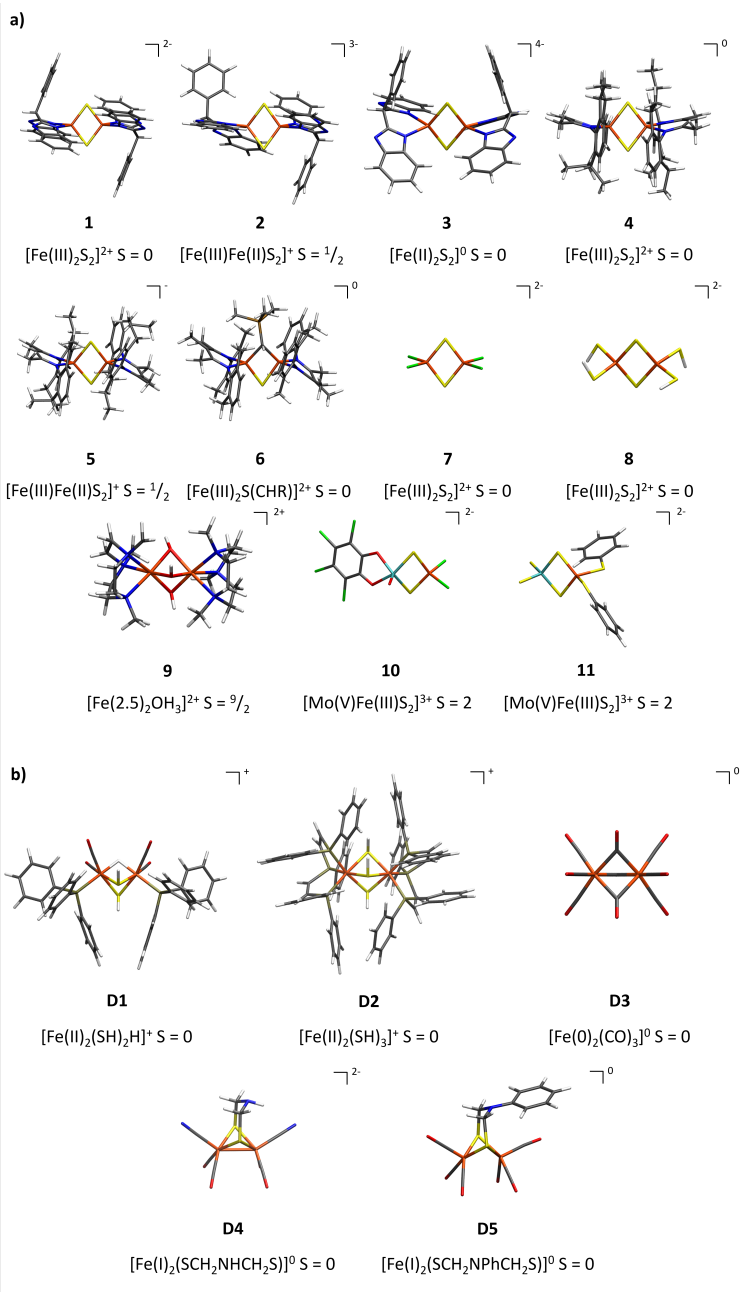


Figure 4.4: a) The eleven complexes that FeMoD11 consists of, with six [2Fe-2S], two [MoFe-2S], one [2Fe-CS], and one [2Fe-3OH] dimers that constitute the FeMod11 test set of mainly iron-sulfur antiferromagnetically coupled dimers. b) The five closed shell dimers that constitute the FeCSD5 test set.

B97-D3 (GGA) [94], r$^2$SCAN (mGGA) [129], M06 (mGGA, 27% HF) [130], M06-2X (mGGA 54% HF) [130], CAM-B3LYP (range-separated GGA) [131], $\omega$B97M-D3BJ (range-separated GGA) [132, 133], and $\omega$B97X-D3BJ (range-separated GGA) [133, 134]. For the FeMoD11 test set, the nonhybrid functionals were found to greatly underestimate the Fe-Fe distance (MD M-Fe < -0.030 Å) as well as the Fe-S bond lengths, with the exceptions of B97-D3 (MD M-Fe = -0.015 Å) and r$^2$SCAN (MD M-Fe = -0.003 Å). Hybrid functionals with HF% $\geq$ 20 on the other hand are found to greatly overestimate the Fe-Fe distance (MD M-Fe > +0.030 Å) and the Fe-S bond lengths. The TPSSh (MD M-Fe = - 0.025 Å) and B3LYP (MD M-Fe = 0.014 Å) hybrid functionals are found yield the best geometries in their class whereas of the range-separated hybrids, only $\omega$B97X-D3BJ (MD M-Fe = 0.003 Å) only moderately overestimates the M-Fe distances on average.

In the case of the FeCSD5 test set, there is no observable trend. All functionals underestimate the Fe-Fe distance, except B97-D3 and BLYP. Interestingly, $\omega$B97X-D3BJ underestimates the Fe-Fe distance the most and performs the worst of the functionals tested for FeCSD5, whereas it was one of the best for FeMoD11.

The trend observed for the functionals for the FeMoD11 test set are almost the same for FeMoco (see Figure 4.5). Comparing **7** with FeMoco, then it is clear that non-hybrid functionals undestimate the M-Fe distances and hybrid functionals with HF % > 10 overestimating the M-Fe distances. Increased Fe-S bond lengths cause increased Fe-Fe distance. Therefore, the dimers prove to be good model systems to study certain trends in the electronic structure of FeMoco even though they have considerably simpler molecular structures.

Considering only the mean absolute deviation (MAD) for the test sets and FeMoco, the four best functionals are r$^2$SCAN, TPSSh, B97-D3, and B3LYP*.

### 4.3.4 The relationship between the Fe-S covalency and Fe-Fe distance

As was shown in Figure 4.5, FeMoco and the complexes of FeMoD11 have similar trends when it comes to Fe-S and Fe-Fe lengths. This can be understood and the reason is twofold.

Firstly, it is a geometric effect. Since the Fe-S bond lengths are being elongated then the Fe-Fe distance will increase as well. However, this effect is limited as can be seen when optimizing the geometry of **7** with different functionals, while constraining the Fe-S bond lengths to crystallographical values. It is observed that the Fe-Fe distance changes – albeit not as much

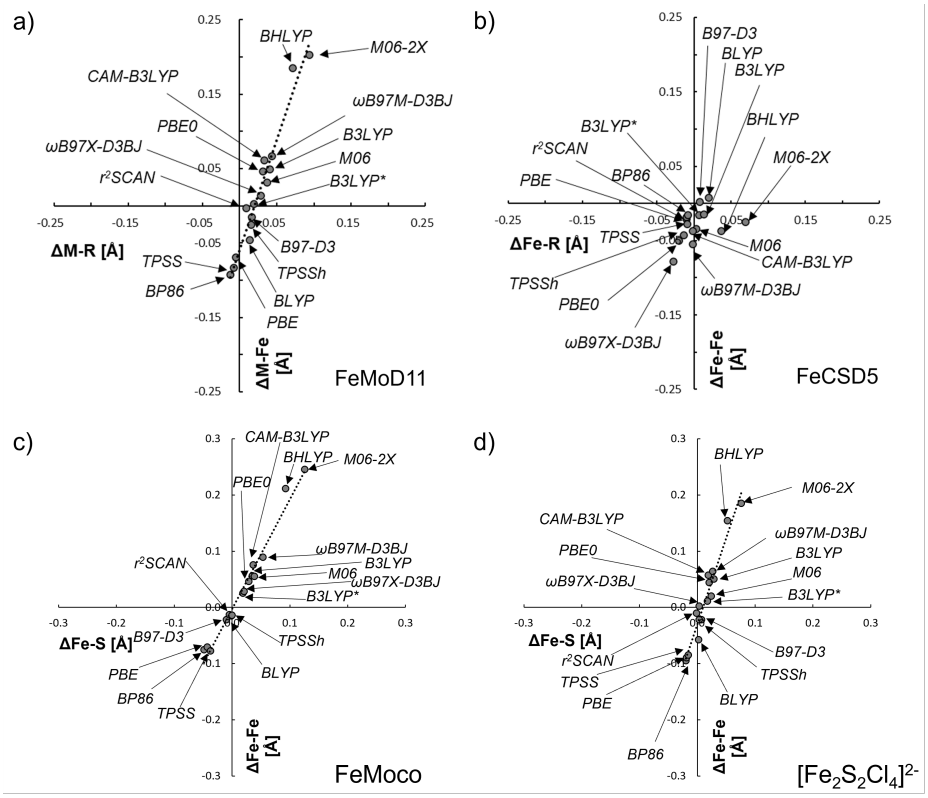


Figure 4.5: (a) Mean deviation (in Å) in the metal-metal distance, ΔM-Fe, vs the mean deviation in the metal-bridging ligand bond length, ΔM-R, for FeMoD11 and for (b) FeCSD5. (c) Mean deviation in Å in the Fe-Fe distance (ΔFe-Fe) vs mean Fe-S distance (ΔFe-S) of optimized structures in comparison to the X-ray structure (for FeMoco, PDB: 3U7Q, and for (d) **7**, CSD: EAPFTM01) with the functionals tested. For (a), M = Fe, Mo and R = C, O, S, whereas for (b), R = C, S, and for (c) the FeMoco data comes from a 244 QM atom QM/MM model.

as in non-constrained optimization – indicating that the difference in the Fe-Fe distance is also influenced by other effects.

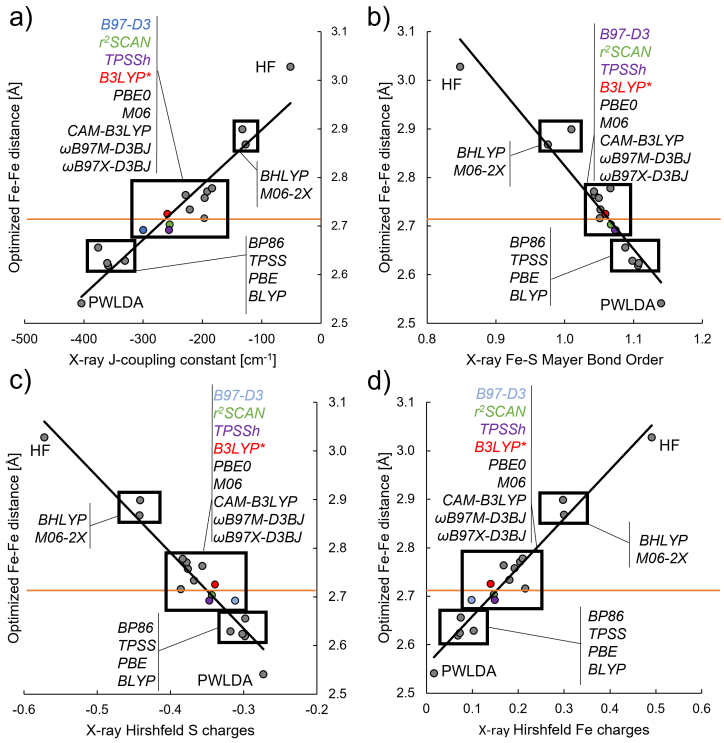


Figure 4.6: Correlation plots of the optimized Fe-Fe distance (y-axis) of **7** vs various parameters avaluated on the X-ray structure (x-axis): J-coupling, Fe-S Mayer bond order, Hirshfeld S charge, or Hirshfeld Fe charge. (a) J-coupling constant evaluated in $cm^{-1}$ according to the Yamaguchi equations, (b) the calculated Fe-S Mayer bond order, (c) average Hirshfeld charge on the sulfides, and (d) average Hirshfeld charges on the irons

Secondly, it is known that in polynuclear Fe-S systems superexchange plays an important role in the interaction between two antiferromagnetically coupled irons. The Fe-Fe distance dependence on the functional choice which is observed here is a direct consequence of this. Functionals with a small amount of HF % overestimate the covalency of the Fe-S bond and that results in stronger antiferromagnetic coupling through superexchange yielding a short Fe-Fe distance. Similarly, in functionals with too high HF %, this effect is underestimated, resulting in too long Fe-Fe distance.

Without optimizing the structure (*i.e.* single point calculation), the J-coupling constant, Fe-S Mayer bond order, and Hirshfeld charges show

a linear trend with decreasing HF %, which can be correlated with the optimized Fe-Fe distance from an optimized structure. Furthermore, by analyzing magnetic orbitals (unconstrained corresponding orbitals (UCO), not shown), it is clear that the antiferromagnetic coupling decreased as the HF % is increased, as well as there seems to be direct overlap between the two irons with some non-hybrid functionals, like BP86.

### 4.3.5 Conclusion

The molecular structure, *i.e* the metal-ligand and metal-metal distances, of FeMoco is observed to behave in the same manner as the dimers of FeMoD11 test set (open shell), but not as the dimers of FeCSD5 test set (closed shell). The metal-metal distance is found to be influenced both by the elongation of the metal-ligand bond and superexchange, both of which depend on the functional. Furthermore, by analyzing the electronic structure that is obtained by varying DFs for the $[Fe_2S_2Cl_4]^{2-}$ cluster, it can be understood that the geometry is closely related to the electronic structure and is method dependent. Non-hybrid DFs describe the Fe-S bond too covalently, which in turn promotes a strong Fe-Fe interaction through superexchange (and short Fe-Fe distance), whereas hybrids with HF% $>$ 20 describe the Fe-S bond as too ionic, which results in a weaker Fe-Fe interaction (and long Fe-Fe distance). The functionals that are found to yield the best geometries for FeMoco, the FeMoD11 test set, and the FeCSD5 test set are r$^2$SCAN, TPSSh, B97-D3, and B3LYP*.

# 5 Calculating Nuclear Resonance Vibrational Spectra of Iron-Sulfur Clusters

Article III is not published but a manuscript is included on p. 165.

## 5.1 Nuclear resonance vibrational spectroscopy

Vibrational spectroscopy is a useful tool to gain information about the molecular and structure of a molecule of interest. A vibrational mode and its energy (vibrational frequency) can be used to identify the presence of a chemical group in a sample as well as being an indicator of the strength of a chemical bond.[135] The two most common vibrational spectroscopy methods are infrared spectroscopy (IR) and Raman spectroscopy. In IR, a beam of electromagnetic radiation (400 - 4000 $cm^{-1}$) is used to excite a molecule of interest from the ground vibrational state into excited vibrational state(s). In order for these transitions to happen, there needs to be an overall change in the dipole moment and if there is no change, the excitation doesn't happen. In Raman spectroscopy, the molecule of interest is not excited directly into excited vibrational states, but rather the energy of an incident beam of electromagnetic radiation excites an electron into a virtual orbital as well as excited vibrational state. When the molecule relaxes from an excited vibrational state to the ground state, it releases a photon which wavelength is longer (less energy) than the incident electromagnetic beam. The energy difference between the incoming electromagnetic beam and the released photon is equal to the energy of a vibrational excitation. In resonance Raman (RR) spectroscopy, the incident beam of electromagnetic radiation is tuned so it matches the excitation energy of an electronic transition of a functional group of interest, but functions otherwise like regular Raman spectroscopy. Unlike IR spectroscopy, where a change in the dipole moment of the molecule needs to happen for a mode to be IR active, the selection rules for Raman spectroscopy are somewhat more complicated but there needs to be an overall change in polarizability of the molecule, *i.e.* different electron distribution between the vibrational ground state and

excited state.[135]

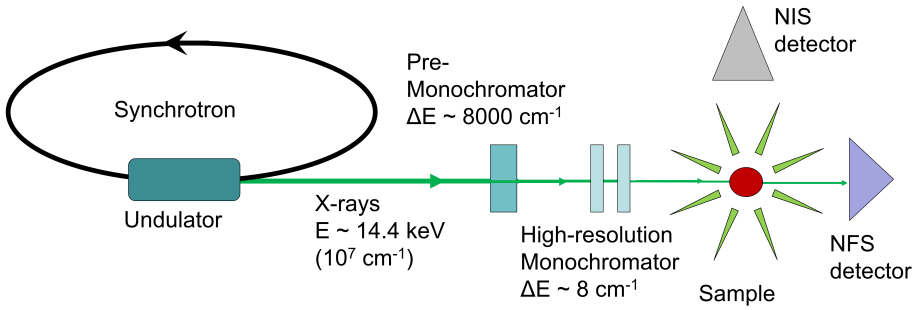


Figure 5.1: Experimental setup for a Nuclear Resonance Vibrational Spectroscopy (NRVS) experiment. In the case of $^{57}$Fe enriched sample, 14.4 keV x-rays from synchrotron are fine tuned through slits and directed at the sample. Nuclear forward scattering (NFS) yields information on hyperfine interactions (similar to conventional Mössbauer) whereas nuclear inelastic scattering (NIS) yields information on vibrational modes that include the $^{57}$Fe atom.

Both IR and Raman spectroscopy suffer from not being selective enough when one is interested in vibrational modes of a certain region for molecules of high molecular weight, such as the cofactor of an enzyme (IR is still useful for C≡O stretches and the excitation energy of RR can sometimes be fine tuned for cofactors). Nuclear resonance vibrational spectroscopy (NRVS) is a method that is both selective and bypasses the selection rules of IR and RR spectroscopy and yields rich vibrational information about the environment of a Mössbauer active nucleus. The best example of a Mössbauer active nucleus is the $^{57}$Fe isotope of iron, which can be used to label the cofactors of the nitrogenase enzymes which would yield vibrational information only about these cofactors.[136]

NRVS, sometimes also termed nuclear inelastic scattering (NIS) or nuclear resonant inelastic X-ray scattering (NRIXS), is a relatively young spectroscopy method that requires synchrotron radiation. It is a technique that uses the Mössbauer absorption of a nucleus which in iron sulfur proteins is the $^{57}$Fe isotope of iron (Mössbauer active isotope). In a NRVS experiment (see Figure 5.1) of an iron-sulfur protein (*e.g.* Rubredoxin), the protein sample is either crystallized or in a frozen solution. The incident beam (14.4125 keV for $^{57}$Fe) excites the nuclei as well as vibrational states. When the nuclei relaxes from its excited state, it emits a photon and the energy of it can only be equal to the energy required to excite the nuclei in addition to the energy of the discrete vibrational modes it was previously excited. In this way, NRVS provides the entire set of vibrational modes

involving the $^{57}$Fe isotope and the intensity of the measured signal (and whether the vibrational mode is active) is dependent only on the magnitude of the partial movement of iron in the vibrational mode. This makes it an atom specific vibrational spectroscopy which is incredibly useful when working with metalloproteins, since vibrational modes of the protein matrix that are not connected to the iron are not observed.[136]

The calculation of an NRVS spectrum is relatively straightforward, since the vibrational modes and their frequencies can be obtained from calculating the Hessian, which is performed here numerically (by displacing the atoms one-by-one).[9] The calculated vibrational frequencies are purely harmonic and are not corrected for anharmonicity, which is expected to have an effect.[137] The calculated intensity is obtained through the iron mode composition factor $e^2_{Fe,a}$:

$$e^2_{Fe,a} = \frac{m_{Fe} r^2_{Fe}}{\sum_j m_j r^2_{j\alpha}} \tag{5.1}$$

where $\alpha$ is an eigenvector, $m_j$ is the mass of atom $j$, and $r^2_{j\alpha}$ is its mean square motion.[138]

Although NRVS is a relatively recently developed spectroscopy method, it has already been used to study many chemical systems with success. Additionally, these studies often include DFT calculations to assist in the interpretation of the experimental vibrational spectra since the measured NRVS spectrum can sometimes be difficult to interpret. NRVS has been particularly useful in the study of porphyrins and studies often include analysis from DFT calculations to complement the experimentally measured spectra.[139–144] NRVS has additionally been applied to study the active site on an oxygen reduction reaction catalyst.[145] and demonstrate the existence of a hydride bridge in [Ni-Fe]-hydrogenase.[146]

For iron-sulfur systems outside of proteins, NRVS has been used to measure the vibrational frequencies of mononuclear and binuclear iron complexes in molecular crystals.[147] In biology, NRVS has been used to measure the vibrational frequencies of the Fe ion of rubredoxin,[148] the [2Fe-2S] cluster of ferredoxin,[149] the [4Fe-4S] cluster of Mo-nitrogenase's Fe-protein,[150] and the cofactors of Mo-nitrogenase's MoFe-protein.[151, 152] Furthermore, NRVS has been used to demonstrate the presence of ligands such as a hydride in [Fe-Fe]-hydrogenase [153] and [Ni-Fe]-hydrogenase[146] or a sulfur species bound to iron in the $O_2$ stable state in [Fe-Fe]-hydrogenase.[154]

Although computational chemistry methods (mainly DFT) have been used to assist in interpretation of NRVS spectra, it is not clear what the optimal computational protocol is for a cofactor buried within a protein.

Furthermore, DFT has seen success in deciphering vibrational spectra and been systematically investigated for high energy vibrational modes (1000 - 3000 $cm^{-1}$) while fewer systematic studies have been devoted to the low energy vibrational modes.

## 5.2 Motivation and article summary

NRVS is a potentially excellent method to study and characterize the many unknown redox states of nitrogenase that can be isolated. However, since the cofactors of nitrogenase are comprised of multiple iron ions and buried within the protein, it is not obvious how well these NRVS spectra can be calculated. The choice of DF, the number of QM atoms included in a calculation (amino acid residues), and the number of atoms included in the calculation of the Hessian has gained limited attention. Furthermore, the QM region and Hessian region (*i.e.* numbers of atom in the calculation of a partial Hessian) do not need to be equally large and the partial Hessian can be calculated of 41 atoms where only 17 of them are described with QM and the rest of the atoms are described by a forcefield. This is computationally efficient, since computing the second derivative of a forcefield is computationally cheaper than doing so with QM. To the knowledge of the author, only one QM/MM study has explored systematically what is needed to obtain a good NRVS spectrum for a metalloprotein. There, it was concluded that small QM/MM models already yield a good calculated NRVS spectrum but a large QM/MM model is needed to capture the asymmetry of the vibrational modes of iron.[155]

FeMoco is a more complicated system in terms of molecular and electronic structure than *e.g.* the Fe center of rubredoxin and has many vibrational modes with an iron character and it is not immediately obvious how well the vibrational modes can be calculated and smaller model systems with fewer vibrational modes should be easier to understand and cheaper to calculate. Therefore a series of simpler iron-sulfur proteins were initially studied in this work as well as molecular crystals.

The research questions were:

1. How sensitive are the vibrational modes to the choice of DF?
2. How important is it to model the protein or crystal environment when calculating the vibrational modes?
3. How many atoms in the QM region or Hessian region (number of atoms included in the calculation of the Hessian) are needed to calculate the vibrational frequencies of the iron-sulfur cluster accurately?

These are vital questions that need to be answered in order to determine whether computed NRVS spectra have predictive power or can help in understanding a measured NRVS spectrum of an interesting state of nitrogenase (*e.g.* a protonated and reduced FeMoco in its catalytic cycle).

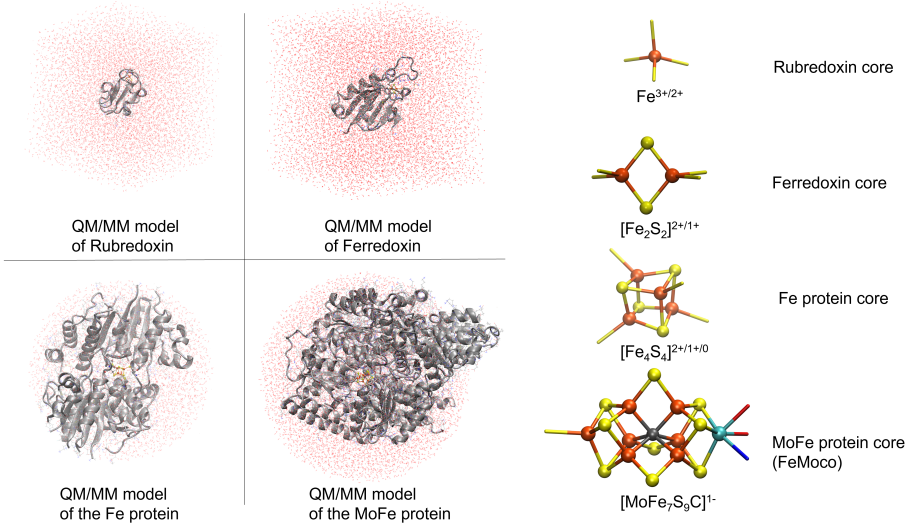


Figure 5.2: The QM/MM models of the systems studied where the size of the systems on the figure is not to scale. On the left hand side: Top left is the *Pyrococcus furiosus*'s rubredoxin, in the top right is the *Aquifex aeolicus's* ferredoxin, in the bottom left is the *Azotobacter vinelandii*'s iron-protein, and in the bottom right is the *Azotobacter vinelandii*'s molybdenum-iron protein. On the right hand side: Top is the $Fe^{3+/2+}$ core of Rubredoxin, the second from top is the $[2Fe\text{-}2S]^{2+/1+}$ core of Ferredoxin, the third from top is the $[4Fe\text{-}4S]^{2+/1+/0}$ core of the Fe protein, and the fourth from the top is FeMoco of the MoFe protein.

### 5.2.1 Choice of systems

The criteria for a system to be studied were relatively simple: A high-resolution X-ray structure and a measured NRVS spectrum must exist for the system. The molecular crystal systems chosen were $[FeCl_4][NEt_4]$, $[FeCl_4][P(C_6H_5)_4]$, and $[Fe_2S_2Cl_4][NEt_4]_2$.[147] The first iron-sulfur protein and the simplest is *Pyrococcus furiosus* Rubredoxin ($Fe^{3+/2+}$ core).[148] The second system is the dimeric iron-sulfur system of *Aquifex aeolicus* ferredoxin ($[2Fe\text{-}2S]^{2+/1+}$ core).[149] The third system is the tetrameric iron-sulfur cubane ($[4Fe\text{-}4S]^{2+/1+/0}$ core) of *Azotobacter vinelandii*'s iron-protein.[150] The fourth system is the FeMoco of *Azotobacter vinelandii*'s molybdenum-iron protein.[151]

The QM/MM models of the proteins were prepared in an analogous way as has been previously described for the MoFe and the VFe QM/MM model.[28, 46] The 0.59 Å X-ray structure (PDB ID: 5NW3) was used for rubredoxin (unpublished data), the 1.5 Å X-ray structure (PDB ID: 1M2A) was used for ferredoxin,[156] and the 1.13 Å X-ray structure (PDB ID: 6N4L) was used for the Fe-protein.[157]

The QM/MM models of the iron-sulfur clusters were prepared with Molcrys[158] and the models are spherical in shape with a radius of 30 Å from the central molecule. The pointcharges (here, CHELPG5 is used as the charge model[159]) are initially calculated from a molecule in vacuum, but the carges are then iterated until converged within the molecular crystal. The parameters for the van der Waals interactions are taken from the UFF.[160] Once the charges are converged, then the central molecule of interest is optimized until the geometry is converged and then the Hessian is calculated. The initial structures were derived from the available X-ray structures for $[Fe_2S_2Cl_4][NEt_4]_2$ (CCSD ID: EAFESD),[161] $[FeCl_4][NEt_4]$ (CCSD ID: TABPIV03),[162], and (CCSD ID: QQQAYM01)[163] as a starting structure.

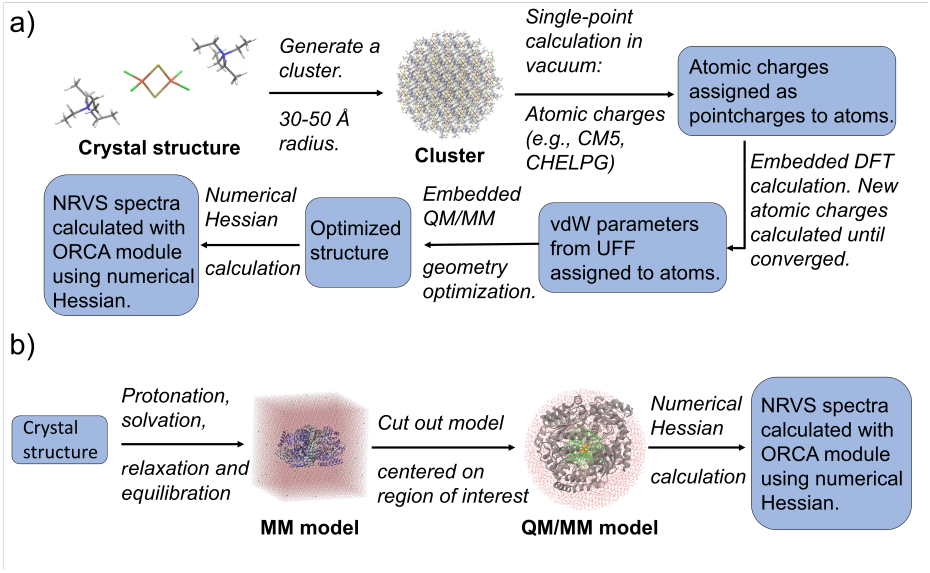


Figure 5.3: The protocol to calculate NRVS spectra of a) molecular crystals and b) proteins.

### 5.2.2 Functional dependence

Sixteen functionals were tested: BP86 (GGA) [16, 17], PBE (GGA) [121], PBE0 (25% HF) [121, 122], TPSS (mGGA) [123], TPSSh (mGGA 10% HF) [123, 124], BLYP (GGA) [16, 125], B3LYP (GGA 20% HF) [16, 18, 125], B3LYP* (GGA 15% HF) [126, 127], BHLYP (GGA 50% HF) [128], B97-D3 (GGA) [94], r$^2$SCAN (mGGA) [129], M06 (mGGA, 27% HF) [130], M06-2X (mGGA 54% HF) [130], CAM-B3LYP (GGA range separated) [131], $\omega$B97M-D3BJ (range separated GGA) [132, 133], and $\omega$B97X-D3BJ (range separated GGA) [133, 134].

As can be seen in Table 5.1, the calculated vibrational frequencies vary for each system with different functionals. In the case of the $Fe^{3+}$ core of rubredoxin and focusing only on the Fe-S stretches ($A_1$ and $T_2$ modes, assuming $T_d$ symmetry), then out of the sixteen functionals tested, non-hybrid functionals have a MAD of 4 to 10 $cm^{-1}$ (excluding r$^2$SCAN), whereas r$^2$SCAN and hybrid functionals with HF% $< 26\%$ have a MAD of 14 to 24 $cm^{-1}$. Hybrid functionals with HF% $> 26\%$ as well as ranged-separated hybrids have a MAD of 27 to 38 $cm^{-1}$. All functionals overestimate the vibrational frequencies.

For the $[2Fe\text{-}2S]^{2+}$ core of Ferredoxin, non-hybrid functionals (except BLYP) systematically underestimate the vibrational frequencies and have a MAD in the range of 14 to 30 $cm^{-1}$. Hybrid functionals with HF% $> 26\%$ either overestimate or underestimate the vibrational modes and have MAD in the range of 7 to 10 $cm^{-1}$. Furthermore, the range separated hybrid functionals perform much better, with MADs being in the range of 7 to 11 $cm^{-1}$.

A $[Fe_2S_2Cl_4]^{2-}$ cluster was studied using CPCM and compared to an experimental NRVS spectrum to assess the functional dependency of the calculated vibrational frequencies. Non-hybrid functionals fare somewhat better than for Ferredoxin, with a MAD of 13-23 $cm^{-1}$. The hybrid functionals TPSSh, PBE0, and M06 have MADs of 5-11 $cm^{-1}$ with B3LYP and B3LYP* performing worse, with MADs of 22 and 30, respectively. The range separated hybrid functionals yield MADs of 7-11 $cm^{-1}$ whereas BHLYP and M06-2X overestimate the calculated vibrational frequencies by 30 and 34 $cm^{-1}$, respectively.

To summarize the results from Table 5.1. It seems there isn't a single functional that performs "perfectly" for the three systems. The reason for this could be that non-hybrids describe better the bonds of iron to organic sulfurs (cysteinate) whereas hybrids describe better iron bonded to inorganic sulfurs (bridging sulfurs in the case of Ferredoxin). This needs to be explored further, as it is possible that the protein in the crystallized

Table 5.1: Mean absolute deviation of vibrational frequencies in $cm^{-1}$ for vibrational modes of rubredoxin (the four $T_d$ modes) and vibrational modes above 280 $cm^{-1}$ of ferredoxin and the $[Fe_2S_2Cl_4]^{2-}$ complex with CPCM.

| Functional | $FeSR_4^-$ | $Fe_2S_2SR_4{}^{2-}$ | $[Fe_2S_2Cl_4]^{2-}$ |
|---|---|---|---|
| BP86 | 8 | 30 | 23 |
| PBE | 6 | 29 | 22 |
| TPSS | 10 | 24 | 14 |
| BLYP | 4 | 27 | 17 |
| B97-D3 | 5 | 18 | 23 |
| $r^2$SCAN | 15 | 14 | 13 |
| TPSSh | 16 | 7 | 11 |
| B3LYP* | 14 | 8 | 30 |
| B3LYP | 16 | 8 | 22 |
| PBE0 | 24 | 10 | 13 |
| M06 | 24 | 10 | 5 |
| M06-2X | 29 | | 34 |
| BHLYP | 34 | 16 | 30 |
| CAM-B3LYP | 27 | 7 | 11 |
| $\omega$B97M-D3BJ | 27 | 10 | 10 |
| $\omega$B97X-D3BJ | 38 | 11 | 7 |

state is a poor representation of the protein in an NRVS experiment, and NRVS calculations of molecular crystals with the functionals should paint a clearer picture. For now though, either r$^2$SCAN or TPSSh seems like a good choice of a functional to calculate the NRVS spectrum of iron-sulfur systems, since the MADs are somewhat similar for all the systems studied. Furthermore, there is good experience with using TPSSh in the group, so the functional choice is also practical decision.

### 5.2.3 QM Region and Hessian Region Convergence

#### Molecular crystals

Three molecular systems, the single iron complexes $[FeCl_4][NEt_4]$ and $[FeCl_4][P(C_6H_5)_4]$ and the diiron complex $[Fe_2S_2Cl_4][NEt_4]_2$, were studied as both high quality NRVS spectrum and X-ray structure exist for all of them.

Starting with $FeCl_4$, then the experimental and calculated NRVS spectra for both salts of the $FeCl_4$ complex can be seen in Figure 5.4. The experimental spectra of the two salts differ due to the presence of different counterion ($P(C_6H_5)_4^+$ or $NEt_4$), and this is not captured in a calculation that does not describe the crystal environment explicitly. By QM/MM modelling, the calculated vibrational frequencies are shifted to higher energies which fit better with experimentally determined values. For the $[FeCl_4][P(C_6H_5)_4]$ salt, the split in the vibrational modes that is seen at 120 - 150 cm$^{-1}$ is reproduced with QM/MM but not within CPCM or vacuum. There is arguably a minor improvement observed by including the counterion in the QM region, but by adding the counterion to the Hessian region, something that resembles lattice modes are observed at 100 cm$^{-1}$.

The experimental $[Fe_2S_2Cl_4][NEt_4]_2$ NRVS spectrum contains a few prominent features. Two peaks at higher energies than 400 cm$^{-1}$, three discernable peaks between 300 and 400 cm$^{-1}$, and peaks at lower energies than 300 cm$^{-1}$. The calculated NRVS spectra for $Fe_2S_2Cl_4^{2-}$ in vacuum or with CPCM give reasonable values for the vibrational frequencies at higher energies than 400 cm$^{-1}$, but not as well for the rest of the spectrum. By introducing the crystal environment as QM/MM there is an improvement in the overall fit of the calculated spectrum, and further improvement is observed when a counterion is introduced into the QM and Hessian region. The difference in the calculated value for the highest in energy vibrational mode and experimental is 0 cm$^{-1}$ and the second highest 3 cm$^{-1}$. Not as good fit is observed for other peaks, where the difference ranges from 3 - 12 cm$^{-1}$.

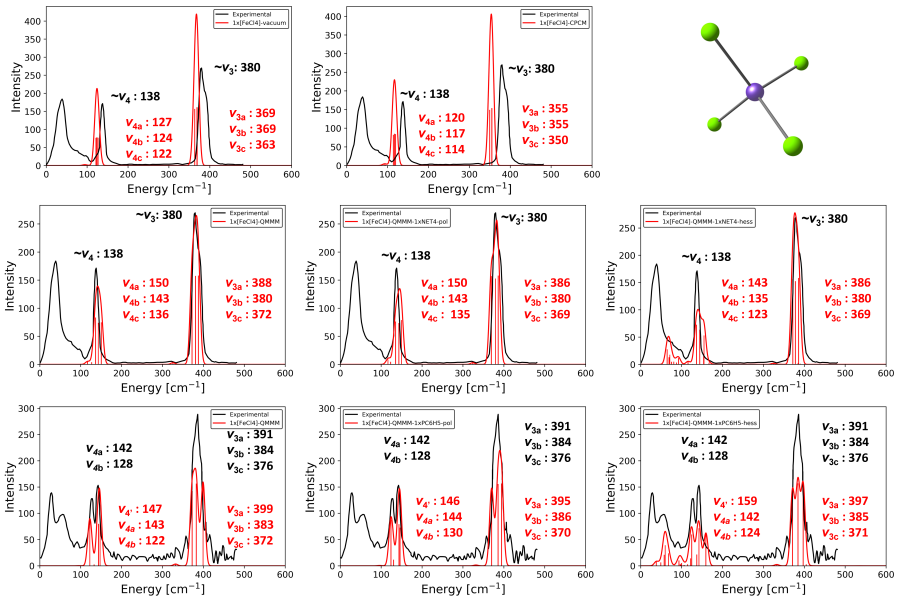


Figure 5.4: A comparison of calculated and experimental NRVS spectra. Top: Experimental (black) NRVS spectrum of $[FeCl_4][Net_4]$ compared to a computed spectrum of $FeCl_4^-$ (red) in either vacuum (to the left) or CPCM (to the right). Middle: Experimental spectrum of $[FeCl_4][NEt_4]$ (black) compared to calculated NRVS spectrum (red) using QM/MM with only $FeCl_4^-$ in the QM region and Hessian region (to the left), then with a single $NEt_4^+$ included in the QM region (in the middle), then with a single $NEt_4^+$ included in the QM and Hessian region (to the right). Bottom: Experimental spectrum of $[[FeCl_4][PC_6H_5]$ (black) compared to calculated NRCS spectrum (red) using QM/MM with only $FeCl_4^-$ in the QM region and Hessian region (to the left), then with a single $PC_6H_5^+$ in the QM region (in the middle), then with a single $PC_6H_5^+$ in the QM region and Hessian region (in the middle).

## Fe-S proteins

For rubredoxin, three different region sizes were designed and can be seen in Figure 5.5 alongside the computed NRVS spectra. The smallest region is comprised of 17 atoms, the medium region is 41 atoms, and the largest region is 120 atoms. Even with the smallest QM region and Hessian region the calculated spectrum is good but it is systematically improved as more atoms are either added to the QM region or Hessian region (or both). Furthermore, when Rubredoxin is reduced the redox shift in the computed spectra is captured.

In the case of the [2Fe-2S] core of ferredoxin, similar trends are seen. The computed NRVS spectra are improved when more of the protein matrix is included in the calculation of the Hessian. There are though two caveats.

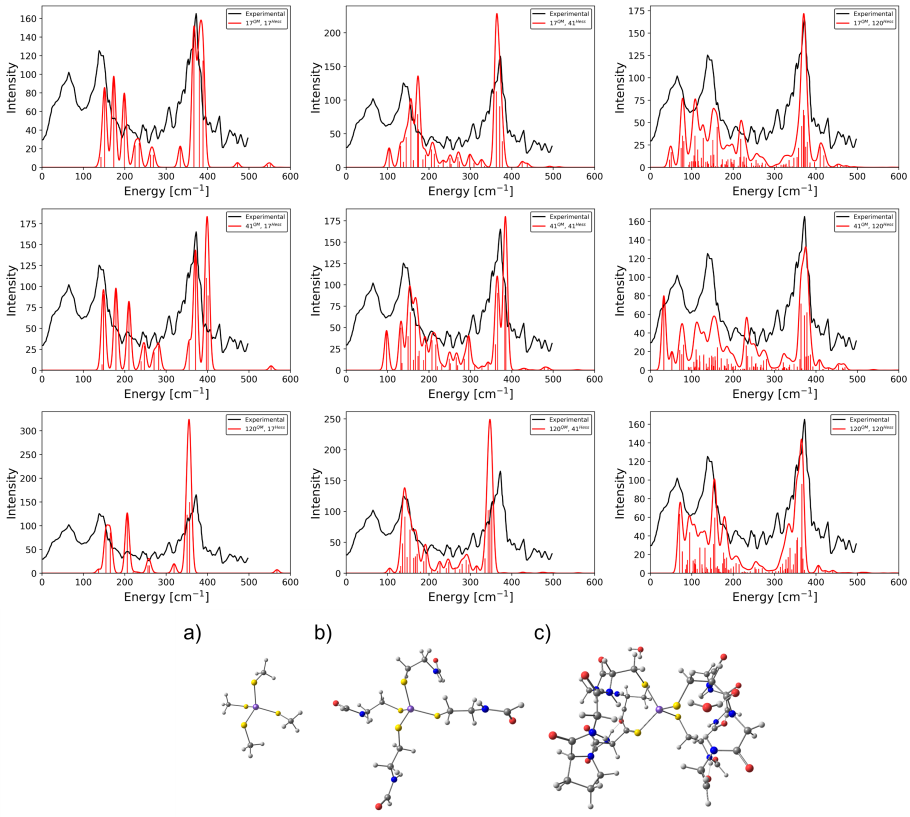


Figure 5.5: Computed spectra for Rubredoxin. The upper part shows the computed NRVS spectra when varying the number of atoms in the QM region and/or Hessian region. The lower part shows the corresponding atoms included in their respective model size, where a) is 17 atoms, b) is 41 atoms, and c) is 120 atoms.

Firstly, the vibrational modes that include the inorganic sulfides are less sensitive to the model size and reasonable values for vibrational frequencies are already obtained with few atoms in the QM region or few atoms in the Hessian region. Secondly, the more atoms that are included in the Hessian region, the more coupling between vibrational modes is observed and it becomes increasingly difficult to interpret the vibrational modes that correspond to a peak. Furthermore, when Ferredoxin is reduced the redox shift in the computed spectra is captured.

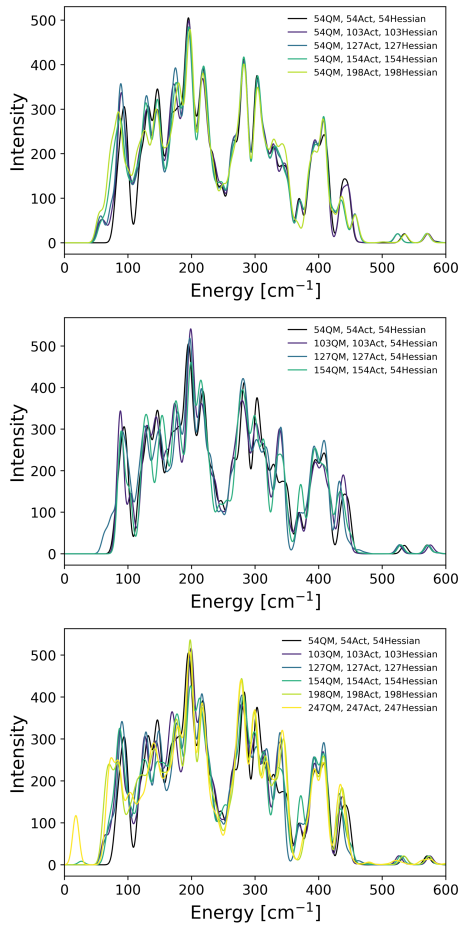


Figure 5.6: Calculated NRVS spectra for FeMoco where the graph at the top shows convergence w.r.t. number of Hessian atoms with constant number of QM atoms, the middle figure shows convergence w.r.t. to number of atoms in the QM region, whereas the bottom figure shows convergence w.r.t. changing both the number of atoms in the QM region and Hessian region. Act indicates how many atoms were included in the optimization before the calculation of the Hessian

In the case of FeMoco, the vibrational modes are relatively insensitive to the QM region size and the Hessian region size as can be seen in Figure 5.6. Starting with just increasing the amount of atoms in the Hessian region, yet keeping the amount of QM atoms constant, there is subtle difference between the computed spectra with the largest difference observed for the peak at 420 cm$^{-1}$ which splits into two. Increasing just the number of atoms in the QM region, similar thing is observed, but the peak observed at 420 cm$^{-1}$ shifts to higher or lower energies. Increasing both the amount

of QM atoms and Hessian atoms simultaneously, there is some difference in intensity observed but the overall shape of the computed spectrum remains the same.

Additionally, NRVS is sensitive to the protonation or reduction of FeMoco. When a bridging sulfide is protonated in FeMoco, then a drop in intensity is observed for the peak that comes from a bridging sulfide vibrational mode.

### 5.2.4 Conclusion

The calculated NRVS spectra of the complexes and cofactors studied are shown to be sensitive to environmental factors, the choice of DF, and size of the QM and Hessian region.

In the case of the vibrational modes of molecular crystals, calculated NRVS spectra can be vastly improved by accounting for the crystal environment via QM/MM modelling as the vibrational modes are observed to be mainly sensitive to the crystal environment. Including a counterion in either or both the QM and Hessian region yields minimum improvements.

In the case of vibrational modes of proteins, then calculated vibrational modes that include iron ions that are not connected directly to the protein backbone are less sensitive to the number of QM atoms and/or number of atoms in the Hessian region. Therefore it can be justified to use smaller QM regions and Hessian regions when the vibrational modes of interest are those of atoms or groups that are not connected directly to the protein matrix, *e.g.* the bridging sulfides of the cofactors of the nitrogenase enzymes. On the other hand, describing the protein environment explicitly instead of implicitly seems to be important to obtain better estimates for the vibrational frequencies.

NRVS calculations on the QM/MM level should therefore be able to assist in deciphering experimental NRVS spectra as well as holding a predictive power.

So far the issue of anharmonicity has not been addressed. The calculated spectra aleady fit experiments quite satisfactory but the results can be misleading since anharmonicity of the vibrational modes at for vibrational modes at low energies could shift the vibrational frequencies considerably. An investigation into how much anharmonicity will effect computed spectra is a basis for a further study on how accurately it is possible to calculate NRVS spectra.

The BS-DFT approximation also affects the quality of the calculated NRVS spectra and it has been demonstrated that extended broken symmetry can yield better vibrational spectra.[164] This is something that could be

investigated further.

# 6 The Functional Sensitivity of the Iron-Molybdenum Cofactor

## 6.1 Summary for article: A model for dinitrogen binding in the $E_4$ state of nitrogenase

The following discussion is for the article: A model for dinitrogen binding in the $E_4$ state of nitrogenase. A. T. Thorhallsson, **B. Benediktsson**, and R. Bjornsson. Chemical science 10, 11110–11124 (2019)

The $E_4$ state in the LT cycle of Mo-nitrogenase is the most probable state where dinitrogen is bound and activated.[4] The exact characteristics of this state is though not exactly known, but experimental evidence from electron paramagnetic resonance (EPR) and electron-nuclear double resonance (ENDOR) spectroscopy point towards the pre-dinitrogen bound $E_4$ state includes two hydrides that bridge two iron ions. [35] A recent X-ray structure of the V-nitrogenase with a missing bridging sulfide on FeVco and a bridging N (or O) containing ligand inspired a catalytic cycle where one of the bridging sulfides is missing, [60] although that this has been challenged by computational models where this is instead suggested to be an X-ray structure of a side reaction with an OH ligand. [61, 67] Furthermore, many computational studies have been undertaken to elucidate the catalytic cycle of the nitrogenase enzymes, including how the $E_4$ state looks like before and after dinitrogen binding.[104–106, 108, 110, 165, 166] The results from these computational studies vary, but they have all a single thing in common: Every research group uses its own computational protocol. This is especially troublesome since energies obtained from calculations have been shown to be extremely method dependent for nitrogenase, especially to the choice of a density functional.[71]

The article deals with characterizing the aforementioned $E_4$ state by comparing energetically 15 plausible pre-dinitrogen bound $E_4$ state models and then calculate the binding energy of dinitrogen of the most favourable models. The models which were found to be energetically favoured were FeMoco with protonated sulfides S2B and S5A and two bridging hydrides between Fe2 and Fe6 with the S2B being a terminal ligand for either Fe2 or Fe6. Furthermore, when dinitrogen binds, dihydrogen is released in a

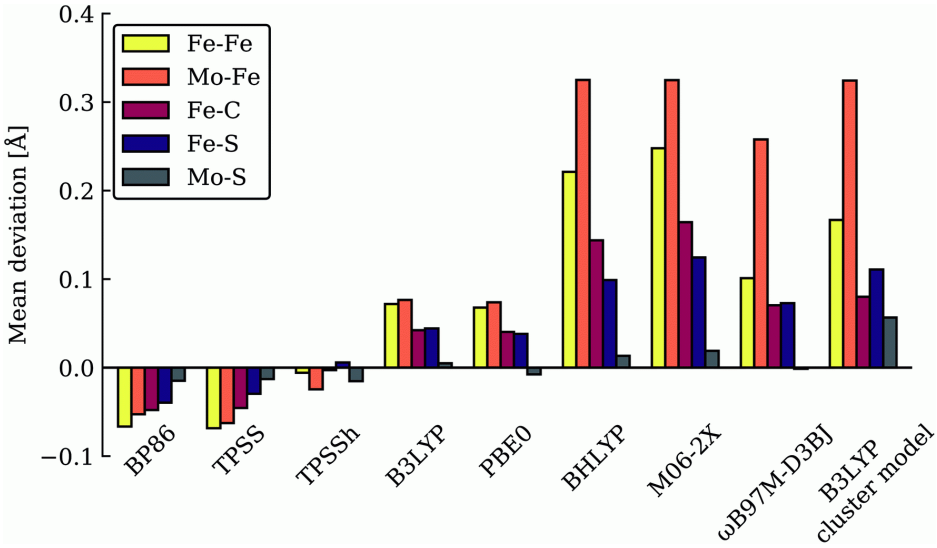


Figure 6.1: Mean deviations of Fe-Fe, Mo-Fe, Fe-C, Fe-S, and Mo-S distances of resting state FeMoco (relative to X-ray structure), calculated with various functionals using the same QM/MM protocol. Also shown is a B3LYP cluster model from Siegbahn.

reductive elimination reaction and the dinitrogen is doubly protonated in an overall exothermic reaction.

My contribution to this article lies within section C of the article, "Computational protocol dependence" as well as the sections "$E_0$ geometric comparison" and "Electronic structure of the resting state $E_0$ with different functionals" in the electronic supplementary information. Cao and Ryde have previously discussed the functional dependency of calculated energies,[71] but in this section the functional dependency of the geometry and electronic structure is explored. It is demonstrated that for a 54 QM atom QM/MM model of FeMoco that both the geometry and the electronic structure is heavily dependent on the functional choice. Non-hybrid functionals are found to underestimate Fe-S bond lengths and metal-metal distances, whereas when the HF% of a hybrid functional is increased, the Fe-S bonds and metal-metal distance increase. This is interpreted as the Fe-S bonds are too covalent in non-hybrid DFs and too ionic in hybrid DFs with HF % $>$ 15 as understood from the drastic changes of the spin population on the metals. It was furthermore found that the 10% hybrid meta-GGA functional TPSSh reproduced the X-ray geometry best, and concluded that since molecular structure is dependent on the electronic structure, then TPSSh should be describing the electron structure better than other functionals considered, giving credibility to the calculations

presented within this study.

# 7 Overview

Some of the issues of modelling iron-sulfur clusters, in or outside of proteins, using single-reference methods, have been tackled in this work. The geometry, electronic structure, and vibrational modes of these spin-coupled clusters are shown to be greatly sensitive to the density functional choice where the amount of exact exchange in hybrids seems to play the largest part. Furthermore, by analyzing how covalently a density functional describes the Fe-S bond *via* MBOs, coupling constant, UCOs, and Hirshfeld charges, it becomes clear that it is primarily due to the strength of interactions between metal centers that effects the distance between them.

By using QM/MM methodology, the protein (or molecular crystal environment) is included in the description of the iron-sulfur systems, which means that important electrostatic effects are accounted for. For the cofactors of nitrogenase this is an important addition since the geometry is considerable worse if a continuum solvation model is used instead to approximate the protein. By using an X-ray structure as a starting point and using available information from spectroscopy, a great deal can be learned from modelling which can be used to discern between possibilites such as oxidation state and a nature of a ligand.

The article "Quantum Mechanics/Molecular Mechanics Study of Resting-State Vanadium Nitrogenase: Molecular and Electronic Structure of the Iron–Vanadium Cofactor" was published in Inorganic Chemistry. It deals with the resting state of FeVco as it appears in the 1.35 Å X-ray structure. Before, there were unanswered questions to the overall charge, the identity of a 4-atom bridging ligand between two irons, and the local electron structure. It was demonstrated that a particular BS state is preferred (BS7-235), the 4-atom bridging ligand is a carbonate ($CO_3^{2-}$), and the overall charge of the cofactor is 2- assuming a $M_S = {}^3/_2$ spin state (recent article calls this result into question, since it is likely that the resting state is in a spin integer state [50]). Furthermore, the electronic structure of FeVco was compared to FeMoco through IAOIBOs and it was found that the irons in FeVco were more reduced compared to FeMoco and the heterometal-iron interactions were stronger in FeMoco than in FeVco.

The article "Analysis of the Geometric and Electronic Structure of Spin-Coupled Iron–Sulfur Dimers with Broken-Symmetry DFT: Implications for

FeMoco" was published in Journal of Chemical Theory and Computation. It deals mainly with iron-sulfur spin coupled dimers and how to accurately model them. A test set of spin-coupled iron-sulfur systems (FeMoD11) is compared with a test set of non-spin-coupled iron-ligand dimers (FeCSD5). It is demonstrated that geometry and the electron structure of the FeMoD11 systems behave completely different to FeCSD w.r.t. functionals. The Fe-Fe distance is dependent on the Fe-S bond length, which is in turn dependent on the capabilities of a functional to describe the bond properly. This is furthermore explained from the viewpoint of the electronic structure (Hirshfeld charges, Mayer bond orders, magnetic orbitals). The results are important for computational studies of the cofactors of the nitrogenase enzymes. FeMoco is shown to exhibit the same change in geometry w.r.t. functional choice as the model systems, which indicates that the change observed in the electronic structure of the model complexes w.r.t. a functional is the same for FeMoco.

The manuscript for "Environmental effects in theoretical calculations of $^{57}$Fe nuclear resonance vibrational spectra: from molecular complexes to complex metalloproteins" is under preparation and the journal of choice for submission is Journal of Chemical Theory and Computation. It deals with how to accurately calculate NRVS spectra of iron-sulfur systems. QM/MM methods are used and the accuracy of modelling is tested. The number of atoms described with QM, the number of atoms included in a calculation of the partial Hessian, and functional dependency is explored. Results include that vibrational modes of organic ligands (amino acids) connected to the protein matrix are more sensitive to the model size than inorganic ligands (*i.e.* sulfides). Furthermore, for redox active complexes the shifts observed in experimental spectra fit with computed ones and indicates that computations should have both predictive and explanatory power for NRVS expiremnts performed in the future for the nitrogenase enzymes. The manuscript for "Environmental effects in theoretical calculations of $^{57}$Fe nuclear resonance vibrational spectra: from molecular complexes to complex metalloproteins" is under preparation and the journal of choice for submission is Journal of Chemical Theory and Computation. It deals with how to accurately calculate NRVS spectra of iron-sulfur systems. QM/MM methods are used and the accuracy of modelling is tested. The number of atoms described with QM, the number of atoms included in a calculation of the partial Hessian, and functional dependency is explored. Results indicate that vibrational modes involving iron and organic ligands (amino acids) connected to the protein are more sensitive to the model size than vibrational modes involving iron and inorganic ligands (*i.e.* sulfides).

Furthermore, for redox active complexes the shifts observed in experimental spectra fit with computed ones and indicates that computations should have both predictive and explanatory power for NRVS experiments performed in the future for the nitrogenase enzymes.

The next step in this project is to use the acquired knowledge of how-to model these systems to explain experimental results, predict what will be obtained from experiment, and to understand the catalytic cycle of the nitrogenase enzymes.

# 8 Articles

# Article I

## Quantum Mechanics/Molecular Mechanics Study of Resting-State Vanadium Nitrogenase: Molecular and Electronic Structure of the Iron–Vanadium Cofactor

B. Benediktsson, R. Bjornsson

Inorganic Chemistry **59**, 11514-11527, 2020.

Inorganic Chemistry

pubs.acs.org/IC Article

# Quantum Mechanics/Molecular Mechanics Study of Resting-State Vanadium Nitrogenase: Molecular and Electronic Structure of the Iron−Vanadium Cofactor

Bardi Benediktsson and Ragnar Bjornsson*

Cite This: *Inorg. Chem.* 2020, 59, 11514−11527 Read Online

ACCESS | Metrics & More | Article Recommendations | Supporting Information

**ABSTRACT:** The nitrogenase enzymes are responsible for all biological nitrogen reduction. How this is accomplished at the atomic level, however, has still not been established. The molybdenum-dependent nitrogenase has been extensively studied and is the most active catalyst for dinitrogen reduction of the nitrogenase enzymes. The vanadium-dependent form, on the other hand, displays different reactivity, being capable of CO and $CO_2$ reduction to hydrocarbons. Only recently did a crystal structure of the VFe protein of vanadium nitrogenase become available, paving the way for detailed theoretical studies of the iron−vanadium cofactor (FeVco) within the protein matrix. The crystal structure revealed a bridging 4-atom ligand between two Fe atoms, proposed to be either a $CO_3^{2-}$ or $NO_3^-$ ligand. Using a quantum mechanics/molecular mechanics model of the VFe protein, starting from the 1.35 Å crystal structure, we have systematically explored multiple computational models for FeVco, considering either a $CO_3^{2-}$ or $NO_3^-$ ligand, three different redox states, and multiple broken-symmetry states. We find that only a $[VFe_7S_8C(CO_3)]^{2-}$ model for FeVco reproduces the crystal structure of FeVco well, as seen in a comparison of the Fe−Fe and V−Fe distances in the computed models. Furthermore, a broken-symmetry solution with Fe2, Fe3, and Fe5 spin-down (BS7-235) is energetically preferred. The electronic structure of the $[VFe_7S_8C(CO_3)]^{2-}$ BS7-235 model is compared to our $[MoFe_7S_9C]^-$ BS7-235 model of FeMoco via localized orbital analysis and is discussed in terms of local oxidation states and different degrees of delocalization. As previously found from Fe X-ray absorption spectroscopy studies, the Fe part of FeVco is reduced compared to FeMoco, and the calculations reveal Fe5 as locally ferrous. This suggests resting-state FeVco to be analogous to an unprotonated $E_1$ state of FeMoco. Furthermore, V−Fe interactions in FeVco are not as strong compared to Mo−Fe interactions in FeMoco. These clear differences in the electronic structures of otherwise similar cofactors suggest an explanation for distinct differences in reactivity.

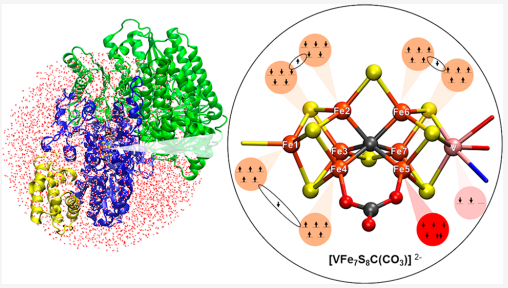




## INTRODUCTION

Nitrogenases are nature's solution to the difficult problem of converting atmospheric nitrogen into a bioavailable form.[1,2] These enzymes catalyze the reaction of dinitrogen to two molecules of ammonia in an adenosine triphosphate (ATP)-dependent process according to the stoichiometry

$$N_2 + 8H^+ + 8e^- + 16MgATP \rightarrow 2NH_3 + H_2 + 16MgADP + 16P_i$$

as recently established for all three types of nitrogenase.[3] For each molecule of reacted dinitrogen, a molecule of dihydrogen is produced. This obligatory dihydrogen formation was hypothesized early on[4,5] as being related to a catalytically active state that included hydrides. Now it is well established that the reductive elimination of two hydrides to form dihydrogen is a part of the mechanism.[6]

Three different types of nitrogenase enzymes exist: molybdenum nitrogenase (Mo-nitrogenase),[7,8] vanadium nitrogenase (V-nitrogenase)[9−11] and iron-only nitrogenase (Fe-nitrogenase),[12,13] which differ in their catalytic activity. Mo-nitrogenase is the most active at ambient temperature[14] and is preferably expressed by organisms. It is also the nitrogenase that has been most extensively studied. V-nitrogenase, on the other hand, has received less attention because of difficulties in expressing it, as it is only produced in Mo-deficient conditions.[10,15] While V-nitrogenase is less active under ambient conditions than Mo-nitrogenase, at cooler

Received: May 4, 2020
Published: August 5, 2020

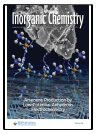




https://dx.doi.org/10.1021/acs.inorgchem.0c01320
*Inorg. Chem.* 2020, 59, 11514−11527

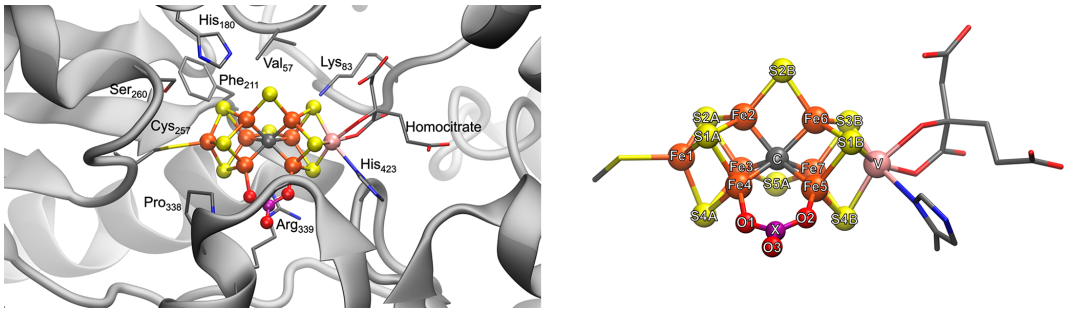


**Figure 1.** Left: FeVco within the protein matrix as it appears in the PBD5N6Y X-ray structure.[27] Right: FeVco with atoms labeled. The 4-atom bridging ligand (shown as $XO_3$) that is proposed to be either carbonate or nitrate.[27]

temperatures, V-nitrogenase is more active than Mo-nitrogenase.[15] In recent years, V-nitrogenase has gained more attention because of its capability of binding CO in its resting state,[16] reducing CO to hydrocarbons,[17] and even reducing $CO_2$ to CO.[18] Little is known about the third type of nitrogenase, the iron-only nitrogenase. It is even less active than V-nitrogenase and seems to be only expressed in Mo- and V-deficient conditions.[19,20]

Mo-nitrogenase consists of the molybdenum−iron protein (MoFe protein), an $\alpha_2\beta_2$ heterotetramer, and the iron protein (Fe protein), which is a $\delta_2$ homodimer. The MoFe protein contains a catalytically active site, the iron−molybdenum cofactor (FeMoco) a [$MoFe_7S_9C$-homocitrate] cluster, and the P-cluster an [$Fe_8S_7$] cluster.[21] In the dithionite reduced state (resting state), FeMoco exhibits an $S = {}^3/_2$ spin state, as revealed via electron paramagnetic resonance (EPR) spectroscopy, whereas the P-cluster is EPR-silent (in an integer spin state).[1,22−24] The Fe protein is a reductase containing an [$Fe_4S_4$] cluster, which shuttles electrons to FeMoco through the P-cluster in an event driven by the hydrolysis of ATP.[25]

Like Mo-nitrogenase, V-nitrogenase is a heteromultimeric protein complex comprised of the vanadium−iron protein (VFe protein) and the Fe protein. The Fe protein of V-nitrogenase shows high similarity to the Fe protein of Mo-nitrogenase, as recently revealed by crystallography.[26] However, the VFe protein, as it appears in the 1.35 Å resolution X-ray structure (PDB 5NY6),[27] is an $\alpha_2\beta_2\gamma_2$ heterohexamer, containing two more peptide chains than the MoFe protein. The role of these additional chains is currently not clear. The VFe protein contains an iron−vanadium cofactor (FeVco) and a P-cluster, with the latter being more or less structurally identical with its MoFe counterpart but with different redox behavior.[28] While the P-cluster of the MoFe protein is EPR-silent in a dithionite solution, there have been reports on $S = {}^1/_2$[29] and ${}^5/_2$[30] EPR signals in similar VFe dithionite preparations, which have usually been attributed to a singly oxidized VFe P-cluster, suggesting that a VFe P-cluster is more easily oxidized than a MoFe one.[28,30]

FeMoco of the MoFe protein is now well characterized via high-resolution crystallography and spectroscopy. The cofactor resembles two fused iron−sulfur cubanes ([$MoFe_3S_3$] and [$Fe_4S_3$]) but with seven Fe ions, nine sulfides, a Mo ion, and a central carbide. It contains a Mo-bound homocitrate ligand and is bound to the protein via a cysteine residue (to one of its Fe atoms) and a histidine residue (to the Mo atom). The overall oxidation state of FeMoco, and the local oxidation state of individual metals, has been a subject of debate. In recent years, the literature has converged on a $[MoFe_7S_9C]^-$ resting state via analysis of the $^{57}$Fe Mössbauer isomer shifts,[31,32] Spatially resolved anomalous dispersion (SpReAD) refinement of the MoFe protein[33] and a computational study by us[34] [we found that quantum mechanics/molecular mechanics (QM/MM)-optimized structures only favored this charge state when compared to the 1.0 Å crystal structure of the MoFe protein (PDB 3U7Q)].[35] A Mo(III) oxidation state was discovered in FeMoco via Mo X-ray absorption spectroscopy (XAS) and X-ray magnetic circular dichroism experiments and theoretical calculations.[36−38] A 3Fe(II)4Fe(III) oxidation state is suggested by SpReAD[33] and Se XAS[39] experiments, while theoretical calculations suggest more delocalization of electrons.[32,34]

Through multiple spectroscopic studies, FeVco was found to be structurally similar to FeMoco, with a proposed $VFe_7$ metal core[40−43] and also featuring a central carbide, as evidenced by Fe X-ray emission spectroscopy.[44] While the first crystal structure of the VFe protein confirmed the overall similar nature of FeVco compared to FeMoco, the crystal structure surprisingly revealed a 4-atom bridging ligand between two Fe atoms ($Fe_4$ and $Fe_5$) instead of a bridging sulfide. The electron density map suggested that either a nitrate ($NO_3^-$) or a carbonate ($CO_3^{2-}$) is present (Figure 1),[27] and this same ligand also appears in another crystal structure of the VFe protein.[45] While spectroscopic confirmation of the carbonate/nitrate ligand is lacking for the VFe protein in solution, it will be assumed for the purposes of this study that the carbonate/nitrate ligand, as revealed by the X-ray structure, is an integral part of FeVco that is always present.

FeVco, like FeMoco, appears to have a noninteger spin of $S = {}^3/_2$ in a dithionite solution (in its resting state),[29,46] analogous to synthetic $[VFe_3S_4]^{2+}$ cubanes synthesized by Holm and co-workers.[47,48] This assignment is complicated, however, by the occurrence of multiple $S = {}^3/_2$ EPR signals with different rhombicities as well as additional $S = {}^1/_2$ and ${}^5/_2$ signals. Although these are plausibly attributed to one-electron-oxidized P-clusters, some debate remains about the origin of these signals.[28]

In the synthetic V-cubanes, the V atom is in a V(III) oxidation state and the Fe atoms in Fe(2.5) and Fe(II) oxidation states according to $^{57}$Fe Mössbauer studies.[48] From V XAS, comparing FeVco and a $[VFe_3S_4]^{2+}$ cubane, the V ion of FeVco was also found to be in a V(III) oxidation state.[40,41] A V(III) oxidation state results in a $d^2$ configuration, in


https://dx.doi.org/10.1021/acs.inorgchem.0c01320
Inorg. Chem. 2020, 59, 11514−11527

contrast to the $d^3$ configuration for Mo(III) in FeMoco and $[MoFe_3S_4]^{3+}$ cubanes.[36,49] A joint Fe high-energy-resolution fluorescence detection (HERFD)-XAS and density functional theory (DFT) study comparing $[MoFe_3S_4]^{3+}/[VFe_3S_4]^{2+}$ cubanes and MoFe/VFe proteins suggests a more reduced Fe part in FeVco compared to FeMoco.[50]

In our previous theoretical studies[34,51] of FeMoco in the MoFe protein, we demonstrated that the geometric structure of FeMoco is well described by our computational protocol by comparison to the 1.0 Å X-ray structure of the MoFe protein. Our protocol accounts for the protein environment via a systematically improvable QM/MM model and describes the electronic structure via broken-symmetry DFT (BS-DFT) calculations using the TPSSh exchange-correlation functional, which we have found to describe the complex electronic structure of the cofactor better than other functionals.[51] Furthermore, we have shown that the calculated structures are highly sensitive to the redox state of the cofactor and that the charge state of FeMoco could be unambiguously determined by the structural comparison. The analysis furthermore indicated a specific electronic state (BS determinant) to be in better agreement with the experimental structure than the other low-lying states.[34]

In comparison to FeMoco, few computational studies have focused on FeVco,[44,50,52−55] and to the best of our knowledge, only a single study[55] from our own group has presented calculations on FeVco that included the new 4-atom ligand (carbonate or nitrate). Our previous study presented calculations on a nonresting ligand-bound state and focused primarily on the assignment of a light-atom ligand (NH or OH) bridging $Fe_2$ and $Fe_6$ of FeVco in a recent crystal structure.[45] Our QM/MM calculations found a structure with an OH ligand to be more consistent with the crystal structure than an NH ligand. The results were not as clear-cut, however, for the identity of the 4-atom ligand bridging $Fe_4$ and $Fe_5$, with calculated structures slightly favoring carbonate over nitrate.

In this study, we present QM/MM calculations of FeVco in the VFe protein in its resting state. The aim is to characterize the electronic structure of the cofactor and compare it to the resting state FeMoco in the MoFe protein. Thus, we seek to critically examine, via comparison to the recent crystal structure,[27] whether the calculations are more consistent with a carbonate or a nitrate ligand and whether the Fe redox state of the cofactor is more reduced or oxidized than that in FeMoco. We also set out to understand the differences in the electronic structures between both cofactors that are known to give rise to different reactivities.

## COMPUTATIONAL DETAILS

**MM Model Preparation.** The VFe protein was first modeled classically using the 1.35 Å X-ray structure of the VFe protein from *Azotobacter vinelandii* as a starting point.[27] The protocol is similar to that of our previous model for the MoFe protein.[34] All molecules and residues present in the crystal structure were included, and no attempt was made to model missing residues. *GROMACS*, version 5.1.4,[56−58] was used to prepare the MM model and add missing H atoms. The VFe protein is an $\alpha_2\beta_2\gamma_2$ heterohexamer (it contains two VnfDKG trimers), and the protonation state of titrable residues was determined in a single $\alpha\beta\gamma$ trimer by visual inspection of the hydrogen-bonding patterns [see the Supporting Information (SI) for specific assignments]. It is assumed here that the protonation state of the titrable residues is the same in both $\alpha\beta\gamma$ subunits. The CHARMM36 protein force field[59] was used in all MM and QM/MM calculations (see the SI for details on force-field parameters for inorganic residues). The protein was solvated in a cubic periodic box and as the overall charge of the protein was 62 -, the charge was neutralized by adding 62 Na ions ions, giving a total system size of 531080 atoms. The MM model was then simulated in the *NVT* ensemble at 300 K for 5 ns. Further details on the MM setup are given in the SI.

**QM/MM Preparation and Calculations.** A spherical QM/MM model (Figure 2) was generated from a snapshot from the MM molecular dynamics trajectory). All residues from a single $\alpha\beta\gamma$ trimer (VnfDKG) and all residues from the second $\beta$ monomer (VnfK) of the VFe protein are in the QM/MM model (chains A−C and E, as labeled in PDB 5N6Y),[27] i.e., an $\alpha\beta_2\gamma$ heterotetramer. Additionally, all water molecules and other crystallographically determined ions within ~42 Å of the carbide of a single FeVco unit, as well as 35 Na ions, are included to keep the system charge-neutral. See the SI for further information. The QM/MM model size is 32562 atoms. An alternative QM/MM model consisting of the full protein was also prepared, as detailed in the SI and discussed in the Results and Discussion section.

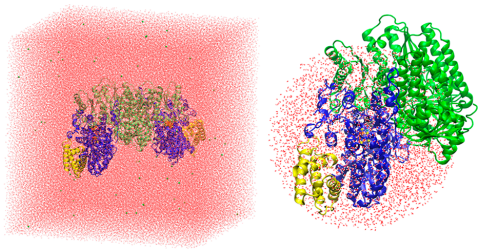

**Figure 2.** Left: 531080-atom MM model. Right: 32562-atom QM/MM model.

*Chemshell*, version 3.7,[60,61] was used for all QM/MM calculations using *ORCA*, version 4.1.0[62,63] (unless otherwise stated), as the QM code within an electrostatic embedding QM/MM coupling scheme. Broken-symmetry solutions of FeVco were found with the spin-flipping procedure, as implemented in *ORCA* from a high-spin ferromagnetic state ($M_S = {}^{35}/_2$, ${}^{34}/_2$, or ${}^{33}/_2$, depending on the redox state).

Link atoms were used to terminate the QM/MM border using a charge shift scheme, as implemented in *Chemshell*.[60] For the QM calculations, we used the same methodology as that in previous studies,[34,51,55] the TPSSh hybrid density functional[64,65] with a relativistically recontracted def2 Ahlrichs basis set[66,67] with a triple-$\zeta$ ZORA-def2-TZVP for V, Fe, S, carbide, and the $XO_3$ ligand, whereas a double-$\zeta$ ZORA-def2-SVP was used for other atoms.[67] The RIJCOSX approximation[68,69] was used with the default grid setting to speed up the Coulomb and exchange integrals. The D3BJ dispersion correction[70,71] and ZORA relativistic approximation[72,73] were also used. The MM calculations used the CHARMM36 force field within the *DL_POLY* program,[74] as implemented in *Chemshell*, and QM/MM geometry optimizations were performed with *DL-FIND*.[75]

The QM/MM optimizations used an active region of 1038 atoms (except where otherwise stated), with all other atoms of the model frozen. Three QM regions were used, with the smallest region being 57 atoms, the intermediate region being 83 atoms, and the largest region being 181 atoms (link atoms are not included in the atom count); see Figures S1−S3. Single-point QM/MM calculations on the crystal structure geometry were calculated using *ORCA* with the MM point charges included. The *VMD* program[76] was used to render the figures of molecular structures in this Article and to calculate RMSDs of the structures. Polarized QM energies (i.e., QM energies polarized by the MM point charges) are primarily discussed instead of total QM/MM energies.


https://dx.doi.org/10.1021/acs.inorgchem.0c01320
*Inorg. Chem.* 2020, 59, 11514−11527

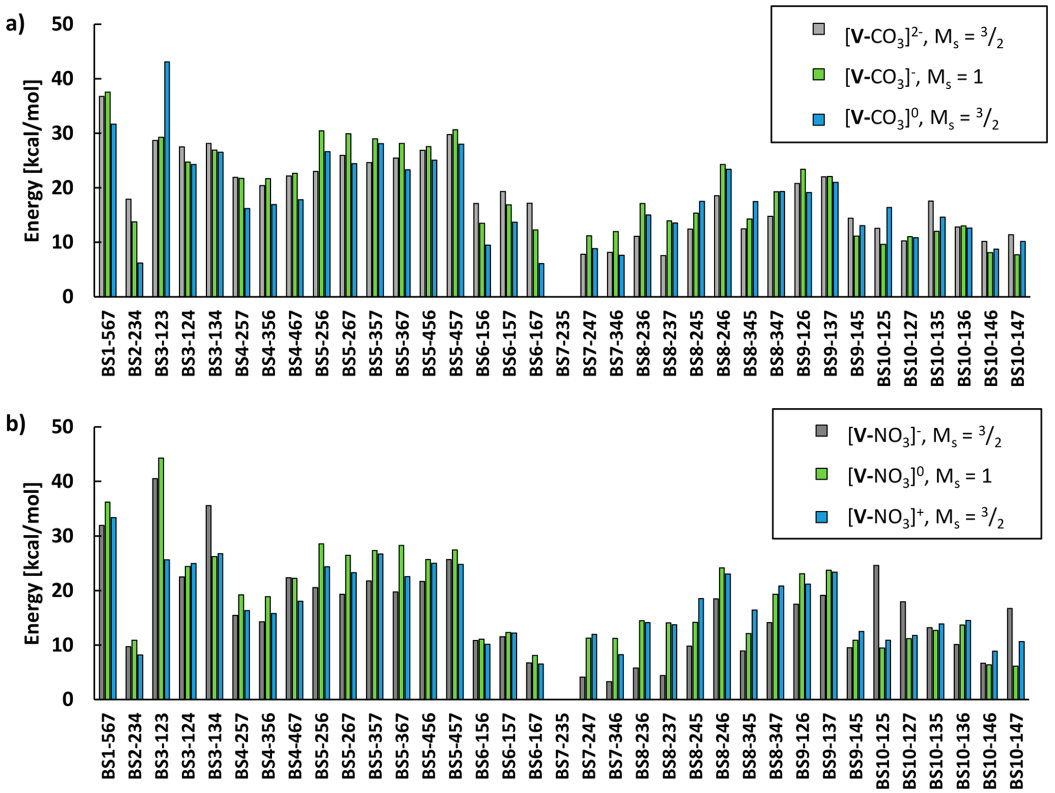


**Figure 3.** Relative energies (polarized QM energies) of all 35 broken-symmetry solutions of FeVco. All calculations were performed on the crystal structure geometry of the cofactor, with MM point charges included.[27] In all cases, the BS7-235 state was found to be favored, and all energies are therefore relative to the BS7-235 solution for each redox state and ligand model. (a) Relative energies for carbonate models. (b) Relative energies if nitrate is the 4-atom ligand. The QM-region size in the QM/MM model is 57 atoms.

## RESULTS AND DISCUSSION

A computational model of the resting state FeVco depends on the identity of the 4-atom ligand, redox state, total spin state ($M_S$ value in BS-DFT), and actual spin-coupling configuration (an electronic or a broken-symmetry state in BS-DFT). We are describing the spin coupling of this complicated system via BS-DFT, which unfortunately is not capable of describing pure spin states. Nonetheless, for the related FeMoco system, BS-DFT has been rather successful for describing its various geometric and spectroscopic properties,[32,44,50,77] and the landscape of broken-symmetry solutions has been extensively explored in multiple studies.[53,78,79] This, however, is not the case for FeVco since the discovery of the 4-atom ligand. We will thus start our discussion by exploring the broken-symmetry landscape of FeVco via single-point calculations on the X-ray crystal structure for various models (section 1), before moving on to QM/MM geometry optimizations for the most plausible broken-symmetry states compared to the crystal structure (section 2). We note that the X-ray structure of the VFe protein has a resolution of 1.35 Å[27] compared to the X-ray structure of the MoFe protein with 1.0 Å resolution.[35] As will be shown, the lower resolution is still sufficient for distinguishing between different cofactor models. The electronic structure of the final FeVco model is then analyzed in detail and compared to the more studied FeMoco (section 3). Finally, we discuss the problem of redox stability of FeVco in these calculations (section 4)

**1. Broken-Symmetry Solutions of FeVco (Using the X-ray Structure).** Noodleman and co-workers originally proposed 10 different BS solutions for FeMoco,[79] assuming 3-fold symmetry of the cofactor. For FeMoco and FeVco, this symmetry is broken, both by the ligation on Mo/V and by the protein environment. In recent studies that account for the protein environment,[51,80−82] it has become common to consider all 35 BS ways of flipping the Fe ions in FeMoco, and as shown in our QM/MM study on FeMoco,[34] spin-isomeric solutions (i.e., solutions equivalent under 3-fold symmetry) give important geometric differences. In the case of FeVco, the new 4-atom bridging ligand further breaks the symmetry, and hence it becomes necessary to consider all possible broken-symmetry solutions. We label the broken-symmetry solutions according to the Noodleman classification[79] but also according to which Fe ions are spin-down, e.g., "BS7-235" (BS7 class according to Noodleman), and where $Fe_2$, $Fe_3$, and $Fe_5$ (crystal-structure numbering) are spin-down. Because the V ion is part of the spin coupling in the cluster, it could also be considered part of the spin-flipping problem. In practice, we have found (similar to FeMoco) that the V ion


https://dx.doi.org/10.1021/acs.inorgchem.0c01320
Inorg. Chem. 2020, 59, 11514−11527

will always flip to its lowest configuration on its own (see the SI for more information).

Because the charge, ligand, and metal oxidation states of FeVco in the X-ray structure are not completely clear, we will consider three different redox states for each carbonate and nitrate ligand model: $[VFe_7S_8C(CO_3)]^{0,1-,2-}$ and $[VFe_7S_8C(NO_3)]^{1-,0,1+}$. We note that an Fe XAS study showed that FeVco (in the VFe protein) in its $S = {}^3/_2$ resting state likely contains a more reduced Fe part compared to FeMoco.[50] While the protein crystals in the X-ray crystallography study were not subject to an EPR investigation, the dithionite conditions employed in crystallization of the protein should result in crystallized resting state (i.e., the $S = {}^3/_2$ state). We considered two redox states compatible with $S = {}^3/_2$ ($[VFe_7S_8C(CO_3)]^{0,2-}$ and $[VFe_7S_8C(NO_3)]^{1-,1+}$) and one integer-spin redox state ($[VFe_7S_8C(CO_3)]^-$ and $[VFe_7S_8C(NO_3)]^0$) for comparison. All models with different redox states, different ligands, and different total spins ($M_S$ in BS-DFT) and their energies are tabulated in Table S1.

The electronic energies of the 35 broken-symmetry solutions (single-point QM/MM energies on the X-ray structure; QM region of 57 atoms) for each model are shown in Figure 3. For simplicity, only the lowest-energy total spin states ($M_S$), where the lowest-energy BS solution is found, are shown (see Figures S4–S18 and Table S1 for data on other spin states). In the following discussion, we use the abbreviation $[\mathbf{V}\text{-}XO_3]^n$, where **V** indicates the $VFe_7S_8C$ part of the cofactor, X is either C or N in the 4-atom ligand, and $n$ indicates the total charge.

In the case of $[\mathbf{V}\text{-}CO_3]^0$, the $M_S = {}^3/_2$ BS7-235 solution is favored, while $M_S = {}^1/_2$ BS7-235 (+3.27 kcal/mol), BS10-147 (+4.95 kcal/mol), and BS10-146 (+5.06 kcal/mol) are the second, third, and fourth lowest in energy, respectively. The BS solution that is the second lowest for $M_S = {}^3/_2$ is BS6-167 (+6.09 kcal/mol), whereas the BS7-346 (+7.63 kcal/mol) and BS7-247 (+8.30 kcal/mol) with $M_S = {}^3/_2$ are even higher in energy.

For the integer-spin redox state $[\mathbf{V}\text{-}CO_3]^-$, BS7-235 with $M_S = 1$ is favored, followed closely by $M_S = 2$ BS7-235 (+1.51 kcal/mol; Figure S5), $M_S = 2$ BS7-346 (+8.67 kcal/mol; Figure S5), and $M_S = 2$ BS7-247 (+9.37 kcal/mol; Figure S5). For $[\mathbf{V}\text{-}CO_3]^{2-}$, BS7-235 with $M_S = {}^3/_2$ is favored, followed by BS8-237 (+7.58 kcal/mol), BS7-247 (+7.83 kcal/mol), and BS7-346 (+8.18 kcal/mol). The $M_S = {}^1/_2$ BS8-236 (+11.08 kcal/mol) is the lowest $M_S = {}^1/_2$ solution.

Exchanging the $CO_3$ ligand for a $NO_3$ ligand results in some changes to the energy landscape. The BS7-235 solution with $M_S = {}^3/_2$ is still preferred for $[\mathbf{V}\text{-}NO_3]^+$, followed by $M_S = {}^1/_2$ solutions BS7-235 (+2.51 kcal/mol), BS10-146 (+4.22 kcal/mol), and BS10-147 (+4.70 kcal/mol), whereas the BS6-167 (+6.50 kcal/mol) solution with $M_S = {}^3/_2$ is the fifth lowest in energy.

For $[\mathbf{V}\text{-}NO_3]^0$, the $M_S = 1$ BS7-235 is favored, with $M_S = 1$ BS10-147 (+6.10 kcal/mol) being the second lowest in energy, whereas $M_S = 1$ BS10-146 (+6.38 kcal/mol) and $M_S = 1$ BS6-167 (8.10 kcal/mol) are the third and fourth lowest in energy, respectively.

For $[\mathbf{V}\text{-}NO_3]^-$, $M_S = {}^3/_2$ BS7-235 is the lowest in energy, with BS7-346 (+3.30 kcal/mol) being second lowest, whereas BS7-247 (+4.09 kcal/mol) and BS8-237 (+4.41 kcal/mol) are the third and fourth lowest in energy, respectively.

Overall, the BS7-235 broken-symmetry solution is always favored, regardless of whether a $CO_3$ or a $NO_3$ ligand is considered or what the redox state is. Unlike FeMoco, the other spin-isomeric BS7 solutions (BS7-247 and BS7-346) are usually higher in energy for FeVco than other non-BS7 solutions. For FeMoco ($[MoFe_7S_9C]^-$; $M_S = {}^3/_2$), the BS7 class of solutions is the lowest in energy[34,79] and energetically indistinguishable but does result in distinct geometric differences. As discussed in our previous study,[34] the FeMoco BS7-235 solution yields a calculated structure in very good agreement with the geometry of the crystal structure (and captures trends in the metal–metal distances not seen for the other BS solutions) but is not quite the lowest in energy (being 0.7 kcal/mol higher in energy than BS7-346).

The functional dependence of these single-point energy calculations was explored by redoing the calculations on $[\mathbf{V}\text{-}CO_3]^{2-}$ with the nonhybrid TPSS functional and the 20% Hartree–Fock (HF) exchange hybrid B3LYP functional (Figure S19); BS7-235 was still always preferred. Calculations were also performed without an explicit protein environment using a continuum solvation model (CPCM with a dielectric constant of 4) instead of QM/MM (Figure S20), but the preference for BS7-235 was retained.

Mulliken spin populations of the different $[VFe_7S_8CXO_3]^n$ models are tabulated in Tables S4–S17. We note that if the self-consistent field did not converge to the specific BS solution attempted but rather another one, then no attempt was made to force convergence.

**2. QM/MM-Optimized Models.** As discussed, the BS7-235 solution is overall favored by a few kilocalories per mole for all redox states and ligands considered. When considering the other BS7 solutions, this preference for BS7-235, compared to BS7-346 and BS7-247, seems to be an effect exerted by both V and $XO_3$, which stabilize this particular BS solution (see "the BS7 solutions" chapter in the SI). Because of this strong preference, we will only discuss the BS7-235 solution from now on. QM/MM geometry optimizations were performed for the BS7-235 solution for each ligand and each redox state considered: $[\mathbf{V}\text{-}CO_3]^{0,1-,2-}$ and $[\mathbf{V}\text{-}NO_3]^{1+,0,1-}$. For the noninteger spin redox states, we only considered a $M_S = {}^3/_2$ spin state due to the strong preference for this spin state (and due to the experimental spin state being $S = {}^3/_2$), as previously discussed, while for $[\mathbf{V}\text{-}CO_3]^-$, both $M_S = 1$ and 2 spin states were considered (because of the small energy gap between these states).

The root-mean-square deviations (RMSDs) of the optimized cofactors (the $[VFe_7S_8C(XO_3)]$ part) with respect to both cofactors in the crystal structure are shown in Table 1 for two different QM regions. This RMSD definition is used throughout the Article.

For a small 57-atom QM region, the optimized $[\mathbf{V}\text{-}CO_3]^{2-}$ model yields a structure that is in best agreement with the X-ray structure, based on the RMSDs. The $M_S = 1$ $[\mathbf{V}\text{-}CO_3]^-$ model, however, gives an RMSD value of only 0.003 Å higher. Other models give larger deviations and appear at first glance less likely. The $M_S = 2$ $[\mathbf{V}\text{-}CO_3]^-$ model is interestingly in worst agreement with the crystal structure, despite the previous single-point calculations showing the $M_S = 1$ and 2 states as close in energy (1.51 kcal/mol in favor of $M_S = 1$). Once optimized, the energy difference between the two $M_S$ states increases to 8.60 kcal/mol for the 57-atom QM-region QM/MM model and further increases to 13.08 kcal/mol for the 181-atom QM-region QM/MM model.

As the QM-region size is increased from 57 to 181 atoms, the spread in the RMSD values for the models becomes smaller. $[\mathbf{V}\text{-}CO_3]^{2-}$ and $[\mathbf{V}\text{-}CO_3]^-$ now yield equally good


https://dx.doi.org/10.1021/acs.inorgchem.0c01320
Inorg. Chem. 2020, 59, 11514–11527

**Table 1. RMSDs[b] (in Å) of Different QM/MM-Optimized Geometries Compared to the Experimentally Determined X-ray Structure[a,27]**

| structure and spin | 57-atom QM region | 181-atom QM region |
|---|---|---|
| $[V\text{-}CO_3]^{2-}$, $M_S = {}^3/_2$ | 0.082 | 0.079 |
| $[V\text{-}CO_3]^{-}$, $M_S = 1$ | 0.085 | 0.079 |
| $[V\text{-}CO_3]^{-}$, $M_S = 2$ | 0.111 | 0.104 |
| $[V\text{-}CO_3]$, $M_S = {}^3/_2$ | 0.104 | 0.091 |
| $[V\text{-}NO_3]^{-}$, $M_S = {}^3/_2$ | 0.095 | 0.085 |
| $[V\text{-}NO_3]$, $M_S = 1$ | 0.095 | 0.082 |
| $[V\text{-}NO_3]^{+}$, $M_S = {}^3/_2$ | 0.093 | 0.088 |

[a]The BS7-235 solution is used for all calculations. [b]The RMSD is defined as the deviation of the $[VFe_7S_8C(XO_3)]$ part with respect to both cofactors in the X-ray structure.

structures, and $[V\text{-}NO_3]^0$ is only 0.003 Å worse. The simple RMSD metric thus appears to not be beneficial in distinguishing between different FeVco models. However, if instead we focus on comparing individual metal−metal distances of the optimized structures to the X-ray structure (presented in Figure 4 and Table 2), a clear distinction between models becomes apparent.

We note in this context that there is little variation in the metal−metal distances of FeMoco in X-ray structures of the MoFe protein of differing resolution, as is shown in Table S26. In the comparison of a 1.0-Å-resolution X-ray structure (PDB 3U7Q) to a 1.43-Å-resolution X-ray structure (PDB 4TKU),[83] there is a maximum of 0.04 Å difference in the metal−metal distance, whereas the mean absolute deviation is only 0.01 Å. We therefore consider the 1.35 Å resolution of the VFe protein

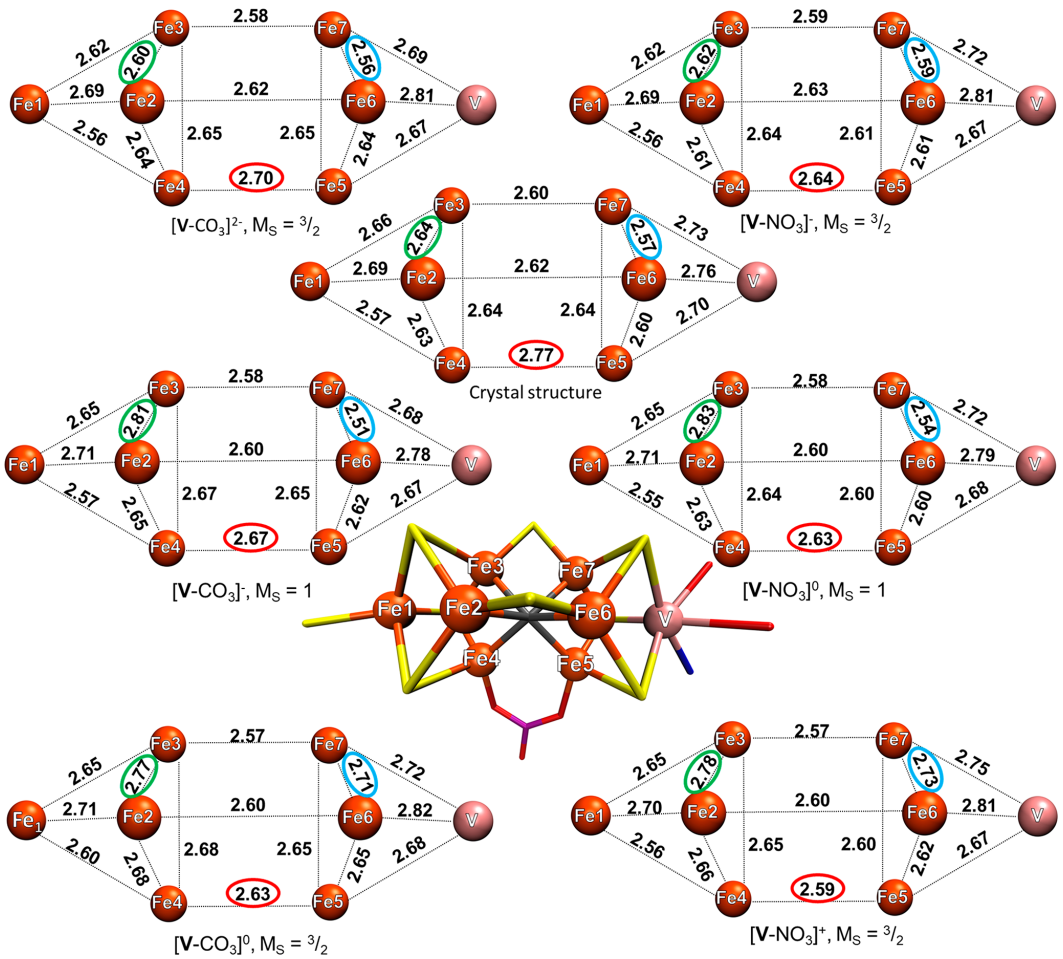


**Figure 4.** Metal−metal distances of six QM/MM models (QM region: 181 atoms) calculated using the BS7-235 solution compared to the X-ray structure. The green and blue ellipsoids highlight the $Fe_2$−$Fe_3$ and $Fe_6$−$Fe_7$ distances that are strongly affected by the redox state. The red ellipsoid highlights the change in the $Fe_4$−$Fe_5$ distance with the bridging $XO_3$ ligand. The metal−metal distances of the crystal structure are the average of the two cofactors found in the 5N6Y crystal structure. All distances are in angstroms.


https://dx.doi.org/10.1021/acs.inorgchem.0c01320
Inorg. Chem. 2020, 59, 11514−11527

Table 2. Various Bond Lengths (Å), Atom−Atom Distances (Å), and a Dihedral Angle (deg) of the Two Instances of FeVco in the PBD 5N6Y Crystal Structure and Values from Relaxed QM/MM (181 QM-Region Atoms) Structures

| model | crystal A | crystal B | $[V\text{-}CO_3]^{2-}$ | $[V\text{-}CO_3]^{-}$ | $[V\text{-}CO_3]$ | $[V\text{-}NO_3]^{-}$ | $[V\text{-}NO_3]$ | $[V\text{-}NO_3]^{+}$ |
|---|---|---|---|---|---|---|---|---|
| spin ($M_S$) | N/A | N/A | $^3/_2$ | 1 | $^3/_2$ | $^3/_2$ | 1 | $^3/_2$ |
| BS | N/A | N/A | BS7-235 | BS7-235 | BS7-235 | BS7-235 | BS7-235 | BS7-235 |
| $Fe_1-Fe_2$ | 2.71 | 2.68 | 2.69 | 2.71 | 2.71 | 2.69 | 2.71 | 2.70 |
| $Fe_1-Fe_3$ | 2.66 | 2.65 | 2.63 | 2.65 | 2.65 | 2.62 | 2.65 | 2.65 |
| $Fe_1-Fe_4$ | 2.58 | 2.57 | 2.58 | 2.57 | 2.60 | 2.56 | 2.55 | 2.56 |
| $V-Fe_5$ | 2.70 | 2.69 | 2.67 | 2.67 | 2.68 | 2.67 | 2.68 | 2.67 |
| $V-Fe_6$ | 2.77 | 2.75 | 2.81 | 2.78 | 2.82 | 2.81 | 2.79 | 2.81 |
| $V-Fe_7$ | 2.73 | 2.74 | 2.69 | 2.68 | 2.72 | 2.72 | 2.72 | 2.75 |
| $Fe_2-Fe_3$ | 2.63 | 2.65 | 2.60 | 2.81 | 2.77 | 2.62 | 2.83 | 2.78 |
| $Fe_2-Fe_4$ | 2.62 | 2.63 | 2.64 | 2.65 | 2.68 | 2.61 | 2.63 | 2.66 |
| $Fe_3-Fe_4$ | 2.63 | 2.64 | 2.65 | 2.67 | 2.68 | 2.64 | 2.64 | 2.65 |
| $Fe_5-Fe_6$ | 2.60 | 2.60 | 2.64 | 2.62 | 2.65 | 2.61 | 2.60 | 2.62 |
| $Fe_5-Fe_7$ | 2.63 | 2.64 | 2.65 | 2.65 | 2.65 | 2.61 | 2.60 | 2.60 |
| $Fe_6-Fe_7$ | 2.57 | 2.57 | 2.56 | 2.51 | 2.71 | 2.59 | 2.54 | 2.73 |
| $V-Fe_1$ | 7.11 | 7.09 | 7.05 | 7.00 | 7.00 | 7.04 | 7.01 | 6.99 |
| $C-Fe_1$ | 3.48 | 3.49 | 3.47 | 3.39 | 3.44 | 3.45 | 3.38 | 3.42 |
| C−V | 3.63 | 3.60 | 3.59 | 3.61 | 3.57 | 3.59 | 3.63 | 3.57 |
| $Fe_2-Fe_6$ | 2.61 | 2.63 | 2.62 | 2.60 | 2.60 | 2.63 | 2.60 | 2.60 |
| $Fe_3-Fe_7$ | 2.60 | 2.60 | 2.58 | 2.58 | 2.57 | 2.59 | 2.58 | 2.57 |
| $Fe_4-Fe_5$ | 2.76 | 2.78 | 2.70 | 2.67 | 2.63 | 2.64 | 2.63 | 2.59 |
| $Fe_4-O1_{XO3}$ | 1.97 | 1.93 | 1.96 | 1.93 | 1.90 | 2.05 | 2.04 | 2.01 |
| $Fe_5-O2_{XO3}$ | 1.93 | 1.94 | 1.97 | 1.94 | 1.91 | 2.05 | 2.02 | 2.00 |
| $\angle Fe_4-O1_{XO3}\text{-}O2_{XO3}\text{-}Fe_5$ | −11.30 | −10.93 | −13.85 | −14.42 | −15.09 | −11.15 | −10.76 | −10.74 |
| $V-O_{alcohol}$ | 2.17 | 2.17 | 2.16 | 2.14 | 2.12 | 2.15 | 2.12 | 2.07 |
| $V-O_{carboxy}$ | 2.12 | 2.10 | 2.08 | 2.05 | 2.03 | 2.06 | 2.03 | 2.02 |
| $V-N_{His423}$ | 2.30 | 2.31 | 2.21 | 2.21 | 2.20 | 2.21 | 2.21 | 2.21 |
| $Fe_1-S_{Cys257}$ | 2.29 | 2.32 | 2.29 | 2.27 | 2.25 | 2.28 | 2.26 | 2.25 |
| $Fe_2-S2B$ | 2.21 | 2.23 | 2.21 | 2.17 | 2.17 | 2.19 | 2.16 | 2.16 |
| $Fe_6-S2B$ | 2.17 | 2.21 | 2.19 | 2.17 | 2.15 | 2.17 | 2.17 | 2.14 |
| $Fe_3-S5A$ | 2.23 | 2.23 | 2.20 | 2.17 | 2.16 | 2.19 | 2.16 | 2.15 |
| $Fe_7-S5A$ | 2.27 | 2.25 | 2.21 | 2.19 | 2.17 | 2.20 | 2.18 | 2.15 |

sufficient for our comparison of computed models to X-ray geometries.

Considering first the X-ray structure, a comparison of distances involving $Fe_1$ and $Fe_2$, $Fe_3$, and $Fe_4$, respectively (in the $Fe_4S_3C$ cubane part of FeVco), reveals $Fe_1-Fe_4$ as the shortest (2.57 Å), $Fe_1-Fe_3$ in the middle (2.66 Å), and $Fe_1-Fe_2$ as the longest (2.69 Å). All computed models also show this trend, revealing an asymmetry in the Fe−Fe interactions. Turning our attention to the $Fe_2-Fe_3$ distance next, for $[V\text{-}CO_3]^-$ and $[V\text{-}NO_3]^0$, the $Fe_2-Fe_3$ distance is significantly overestimated compared to the experiment by 0.17 and 0.19 Å, respectively. The same applies for the $[V\text{-}CO_3]^0$ and $[V\text{-}NO_3]^+$ models, where the same distance is overestimated by 0.13 and 0.14 Å, respectively, whereas the more reduced $[V\text{-}CO_3]^{2-}$ and $[V\text{-}NO_3]^-$ models underestimate it by only 0.04 and 0.02 Å, respectively. Hence, a clear sensitivity of the cofactor geometry with respect to the redox state is revealed.

In the $VFe_3S_3C$ cubane, the X-ray structure reveals the trend of $Fe_5-Fe_7$ being longer (2.64 Å) than the $Fe_5-Fe_6$ (2.60 Å) and $Fe_6-Fe_7$ (2.57 Å) distances. This trend is not captured at all for the more oxidized models, $[V\text{-}CO_3]^0$ and $[V\text{-}NO_3]^+$, which instead show $Fe_6-Fe_7$ as the longest distance. The carbonate models $[V\text{-}CO_3]^-$ and $[V\text{-}CO_3]^{2-}$ capture the trend reasonably well and the nitrate models less well.

These redox-dependent structural changes for the $Fe_2-Fe_3$ and $Fe_6-Fe_7$ pairs are particularly significant and can be understood. The $[V\text{-}CO_3]^{2-}$ and $[V\text{-}NO_3]^-$ models are in good agreement with the X-ray structure for these distances. For $Fe_2-Fe_3$, the deviations are only 0.04 and 0.02 Å, respectively, but when an electron is removed, the distance increases by 0.21 Å for both the $[V\text{-}CO_3]^-$ and the $[V\text{-}NO_3]^0$ models.

Similarly, the $Fe_6-Fe_7$ distance is affected as the cluster is further oxidized. Upon going from the $[V\text{-}CO_3]^-$ and $[V\text{-}NO_3]^0$ models to the more oxidized models $[V\text{-}CO_3]^0$ and $[V\text{-}NO_3]^+$, this distance is increased by ∼0.2 Å. Clearly, these redox-dependent structural changes correspond to the removal of electrons at specific parts of FeVco and, as discussed later, correlate well with the presence or absence of the mixed-valence delocalized electrons of FeVco.

As for the $V-Fe_5$, $V-Fe_6$, and $V-Fe_7$ distances in the crystal structure, the $V-Fe_5$ distance is the shortest (2.70 Å), $V-Fe_7$ is in the middle (2.73 Å) and $V-Fe_6$ is the longest (2.76 Å). All models capture this trend, but the models do not capture the absolute values well.

Overall, only the $[V\text{-}CO_3]^{2-}$ model reproduces both the metal−metal distances well enough as well as captures all of the observed trends within the cofactor. On the basis of the specific redox-dependent structural changes, the more oxidized $[V\text{-}CO_3]^{1-,0}$ and $[V\text{-}NO_3]^{0,1+}$ models can all be safely ruled out. Additionally, the 0.13 Å shorter $Fe_4-Fe_5$ distance in $[V\text{-}NO_3]^-$ makes this model an unlikely candidate. Therefore, we conclude that the model that best reproduces the crystal structure is $[V\text{-}CO_3]^{2-}$.


https://dx.doi.org/10.1021/acs.inorgchem.0c01320
Inorg. Chem. 2020, 59, 11514−11527

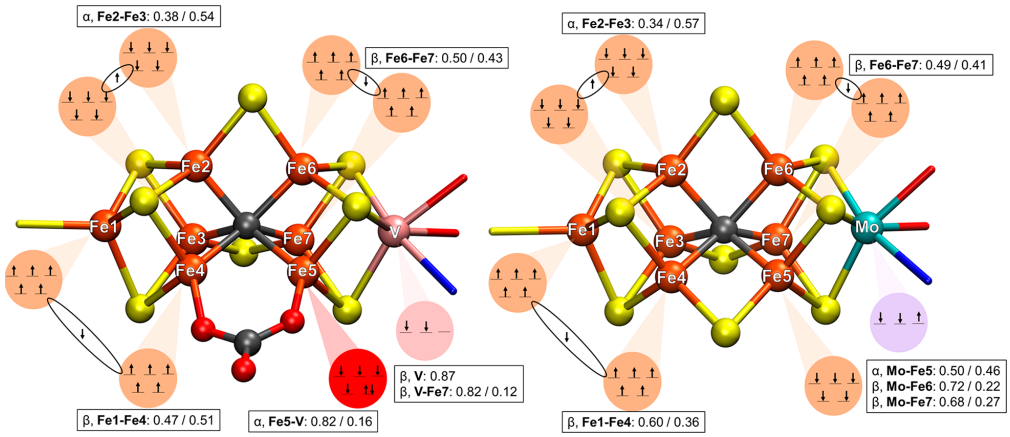


**Figure 5.** Proposed electronic structure as interpreted from IAOIBO localized orbitals of the BS7-235 broken-symmetry determinant for both FeVco and FeMoco computational models. Left: $[V\text{-}CO_3]^{2-}$ 181-atom-QM-region-optimized QM/MM model. Right: 254-atom-QM-region-optimized QM/MM model of FeMoco (from a previous study).[34] The values in the boxes give the population of the localized orbitals (see Figures S21–23 for the localized orbitals) that indicate the magnitude of delocalization of the minority spin electrons between atoms as well as delocalization between the heterometal (Mo/V) and Fe ions.

**3. Electronic Structure of the $E_0$ State of FeVco in Comparison to the $E_0$ State of FeMoco.** Until now, we have not discussed the electronic structure of FeVco in any detail. The electronic structure of iron–sulfur cofactors is complicated[84–86] with FeMoco and FeVco probably being the most complicated examples. Because of the many unpaired electrons, spin coupling, strong covalency, mixed-valence spin delocalization, unusual ligand environment (interstitial carbide), and metal–metal bonding interactions, the electronic structure of these clusters is truly exotic, presenting a true challenge to current quantum chemistry approaches. While the ability of the single-determinant BS-DFT strategy to describe these complex systems should be continuously scrutinized, the good agreement previously obtained for the structure of FeMoco[34,55] and now for the $[V\text{-}CO_3]^{2-}$ model of FeVco compared to the high-resolution X-ray structure, especially in reproducing trends in metal–metal distances, suggests that we are describing at least aspects of the complicated electronic structure correctly. A simple analysis of the spin density via atomic spin populations of the cofactors is typically not very informative. However, as our previous work on FeMoco[32,34,36] has revealed, utilizing localized orbital analysis of the broken-symmetry determinant allows one to gain detailed insight into the cofactor, and approximate oxidation state assignments are possible despite extensive spin delocalization. As discussed in our QM/MM study of FeMoco, the approximate oxidation state assignments from localized orbital analysis could be correlated well with both the experimental and calculated metal–metal distances. We now present a localized orbital analysis of FeVco and compare it to a localized orbital analysis of FeMoco utilizing the intrinsic atomic orbital–intrinsic bond orbital (IAOIBO) method.[87] While previous work by us used Pipek–Mezey localization,[88] the use of better-behaved IAO charges should reduce possible artifacts in the localization procedure arising from maximizing the atomic charge (with the basis set dependence of Mulliken charges being the major issue) of each orbital.

Figure 5 shows our interpretation of the BS7-235 electronic state of $[V\text{-}CO_3]^{2-}$ (181-atom QM/MM model) and the BS7-235 electronic state of FeMoco (247-atom QM/MM model from a previous study by us[34]) based on assignment of the IAOIBO localized orbitals to specific atoms. Isosurfaces of the localized orbitals themselves are shown in Figures S21–S23.

The Fe ions in FeMoco/FeVco are all high-spin Fe(III) or Fe(II). Assigning the five majority-spin electrons (either $\alpha$ or $\beta$ depending on the spin coupling) on each Fe ion is unambiguous because they are always well-localized, and the only difficulty is in assigning the minority-spin electrons.

The minority-spin electrons can either localize on a specific Fe ion [making it localized Fe(II)] or alternatively delocalize between two Fe ions (if the majority spins of both ions are parallel) to create a mixed-valence Fe(2.5)–Fe(2.5) pair. However, depending on competing interactions in the cofactor or the effect of the protein environment, one also observes partial delocalization, which is, furthermore, sensitive to the theory level.

Starting with $Fe_1$ in FeVco and FeMoco, five $\alpha$ electrons are easily assigned via the localized orbital analysis. Additionally, there is a $\beta$ electron delocalized between $Fe_1$ and $Fe_4$ for both cofactors. In FeMoco, the electron is only partially delocalized ($Fe_1$–$Fe_4$: 0.60/0.36), whereas in FeVco, the analogous $\beta$ electron is more delocalized with even slightly more $Fe_4$ character than $Fe_1$ ($Fe_1$–$Fe_4$: 0.47/0.51). For FeMoco, the $Fe_1$–$Fe_2$, $Fe_1$–$Fe_3$, and $Fe_1$–$Fe_4$ distances are more or less equal (~2.66 Å) in the PBD 3U7Q X-ray structure,[35] whereas for FeVco, we observe distinctly different distances. $Fe_1$–$Fe_4$ (X-ray: 2.57 Å) is the shortest distance, $Fe_1$–$Fe_3$ (X-ray: 2.66 Å) is in the middle, and $Fe_1$–$Fe_2$ (X-ray: 2.69 Å) is the longest. This difference between FeMoco and FeVco can be rationalized as being due to the $Fe_1$–$Fe_4$ $\beta$ electron being more delocalized in FeVco than in FeMoco, resulting in stronger Fe–Fe bonding and a shorter $Fe_1$–$Fe_4$ distance in FeVco than in FeMoco. We speculate that the carbonate ligand, bound to $Fe_4$, is behind this increased delocalization of


https://dx.doi.org/10.1021/acs.inorgchem.0c01320
Inorg. Chem. 2020, 59, 11514–11527

the $\beta$ electron, possibly by increased back-bonding between $Fe_4$ and the carbonate.

The minority-spin $\beta$ electron between $Fe_6$ and $Fe_7$ is almost equally delocalized in FeMoco ($Fe_6$–$Fe_7$: 0.49/0.41) as in FeVco ($Fe_6$–$Fe_7$: 0.50/0.43). When the experimental $Fe_6$–$Fe_7$ distances in both cofactors are compared, they are very similar, but FeVco has a 0.03 Å shorter $Fe_6$–$Fe_7$ distance (X-ray: 2.57 Å) compared to FeMoco (X-ray: 2.60 Å).

The minority-spin $\alpha$ electron between $Fe_2$ and $Fe_3$ is somewhat more localized on $Fe_3$ in FeMoco ($Fe_2$–$Fe_3$: 0.34/0.57) than in FeVco ($Fe_2$–$Fe_3$: 0.38–0.54), but classifying $Fe_2$–$Fe_3$ as a Fe(2.5)–Fe(2.5) delocalized pair still seems appropriate. However, the distance between $Fe_2$ and $Fe_3$ in both FeVco (X-ray: 2.64 Å) and FeMoco (X-ray: 2.65 Å) is longer or about equal to those in $Fe_2$–$Fe_4$ and $Fe_3$–$Fe_4$ in the $Fe_2$–$Fe_3$–$Fe_4$ triangle, which is seemingly in disagreement with the assignment of $Fe_2$–$Fe_3$ being a mixed-valent pair but $Fe_2$–$Fe_4$ and $Fe_3$–$Fe_4$ not. We note, however, that calculations of both cofactors are still in good agreement with the respective X-ray structures.

The localized orbital analysis allows us to rationalize the redox-dependent structural changes shown in Figure 4 for the $[\mathbf{V}\text{-}CO_3]^{2-}$, $[\mathbf{V}\text{-}CO_3]^{-}$, and $[\mathbf{V}\text{-}CO_3]^{0}$ models. As electrons are removed from $[\mathbf{V}\text{-}CO_3]^{2-}$, we get first a 0.21 Å elongation of the $Fe_2$–$Fe_3$ distance in $[\mathbf{V}\text{-}CO_3]^{-}$, and this is followed by a 0.20 Å elongation of $Fe_6$–$Fe_7$ in $[\mathbf{V}\text{-}CO_3]^{0}$. These changes obviously correspond to removal of the minority-spin delocalized electrons between these two pairs of Fe ions. A localized orbital analysis of the $[\mathbf{V}\text{-}CO_3]^{-}$ and $[\mathbf{V}\text{-}CO_3]^{0}$ models confirms this interpretation (Figures S22 and S23). Interestingly, the minority-spin on $Fe_5$ remains in these models. This suggests that the delocalized electrons in FeVco occupy higher energy levels than the localized electron on $Fe_5$.

Analyzing the heterometal orbitals, we see first that the oxidation state assignment of V in FeVco appears to be unambiguous based on the presence of two strongly localized $\beta$-spin electrons (and no appreciable V–Fe delocalization) to give a V(III) $3d^2$ assignment. This is in contrast to Mo in FeMoco, where an unusual Mo(III) $4d^3$ configuration is observed with an appreciable Mo–Fe delocalization. As previously discussed, the Mo(III) $4d^3$ configuration is a highly unusual one, breaking Hund's rule, and has been referred to as a "non-Hund" configuration.[34,36,50] Furthermore, the 4d electrons of Mo are not as localized compared to the 3d electrons of V, with slightly more pronounced Fe character of the $\beta$ orbital; Mo–$Fe_6$, 0.72/0.22; Mo–$Fe_7$, 0.68/0.27. The $\alpha$ electron on Mo in FeMoco is even more delocalized (Mo–$Fe_5$: 0.50/0.46), which is suggestive of Mo–Fe bonding. The electronic structure of Mo in FeMoco is thus more ambiguous from the localized orbital analysis than that of V in FeVco. We note that V K-edge XAS of the VFe protein supports the V(III) assignment in FeVco,[41] and Mo K- and L-edge XAS supports the Mo(III) assignment.[36,37] More recently, experimental support for the unusual non-Hund configuration at Mo comes from Mo L-edge X-ray magnetic circular dichroism spectroscopy of a related $[MoFe_3S_4]$ model cubane that shares the unusual electronic structure of FeMoco.[38]

In the X-ray structure of FeMoco (PDB 3U7Q), the Mo–$Fe_5$ distance (X-ray: 2.73 Å) is longer than the Mo–$Fe_6$ (X-ray: 2.67 Å) and Mo–$Fe_7$ (X-ray: 2.68 Å) distances. In our 247-atom QM-region QM/MM model of FeMoco, the calculated Mo–$Fe_5$ distance is also longer (2.71 Å) than the Mo–$Fe_6$ and Mo–$Fe_7$ distances (2.65 and 2.62 Å, respectively). Although the $\alpha$ electron of Mo is somewhat more delocalized than the $\beta$ electrons of Mo, in our computed model, the Mo–$Fe_5$ distance ends up being the longest of the three. This may be related to the higher effective charge at $Fe_5$ [being assigned as Fe(III) rather than $Fe_6$/$Fe_7$ (assigned as Fe(2.5)–Fe(2.5)] or possibly the overall ferromagnetic alignment of $Fe_5$ and Mo.

While V in FeVco lacks a third d electron, an additional localized $\alpha$ electron is instead present on $Fe_5$ ($Fe_5$–V: 0.82/0.16), making it of primarily localized Fe(II) character. In the PBD 5N6Y crystal structure, the V–$Fe_5$ distance (X-ray: 2.70 Å) is shorter than the V–$Fe_6$ (X-ray: 2.76 Å) and V–$Fe_7$ (X-ray: 2.73 Å) distances, in contrast to the analogous Mo–Fe distances in FeMoco. In our 181-atom QM-region QM/MM model of FeVco, the V–$Fe_5$ distance is also shorter (2.67 Å) than the V–$Fe_6$ and V–$Fe_7$ distances (2.81 and 2.69 Å, respectively).

The Mayer bond order (MBO)[89] is a useful metric for the magnitude of bonding between two atoms. The absolute values of MBO between the metals in FeVco and FeMoco are tabulated in Table S20. In the 247-atom QM-region QM/MM model of FeMoco and 181-atom QM-region QM/MM model of FeVco, we observe similar and relatively low MBO values between Fe atoms that do not have a delocalized minority-spin electron (values ranging from 0.21 to 0.31).

Fe atoms that are ferromagnetically aligned and have a delocalized minority-spin electron, on the other hand, show higher MBO values (ranging from 0.41 to 0.47), indicating more bonding character between these Fe atoms compared to Fe interactions with no delocalized electrons.

The MBOs for the heterometal and Fe interaction in FeVco and FeMoco paint a starkly different picture between the two cofactors. The MBOs for V–$Fe_5$ (0.37), V–$Fe_6$ (0.18), and V–$Fe_7$ (0.30) are much lower than the MBOs for Mo–$Fe_5$ (0.47), Mo–$Fe_6$ (0.45), and Mo–$Fe_7$ (0.49), indicating that Mo in FeMoco interacts more strongly with the Fe atoms of FeMoco than V in FeVco.

This difference in interaction between the heterometal and Fe ions in the cofactor is intriguing because the average Mo–Fe distance in FeMoco is shorter than the average V–Fe distance in FeVco. This difference between the average Mo–Fe and V–Fe distances is seemingly in contradiction because one would expect Mo, a larger ion than V, to have longer Mo–Fe distances than the V–Fe distances. In the 1.0-Å-resolution X-ray structure of the MoFe protein (PDB 3U7Q),[35] the average Mo–Fe distance is 2.69 Å, whereas it is 2.70 Å according to extended X-ray absorption fine structure (EXAFS).[90] In comparison, the average V–Fe distance in the 1.35-Å-resolution X-ray structure of the VFe protein (PDB 5N6Y) is 2.73 Å, whereas it is 2.76 Å as interpreted from EXAFS.[40] In our models of FeMoco and FeVco, we underestimate these distances. The average Mo–Fe distance is 2.66 Å (underestimation of 0.03 or 0.04 Å) and the average V–Fe distance is 2.72 Å (underestimation of 0.01 or 0.04 Å). However, the average M–Fe (M = Mo, V) distance agrees with the EXAFS data, where the increase in the average M–Fe (M = Mo, V) distance between Mo–Fe and V–Fe is 0.06 Å, which we capture exactly in our computed models. This difference between EXAFS and the crystal structure for V–Fe may be attributed to the lower-resolution crystal structure (1.35 Å for VFe).


https://dx.doi.org/10.1021/acs.inorgchem.0c01320
Inorg. Chem. 2020, 59, 11514–11527

The delocalization or bonding interactions that we observe between the Mo ion and the Fe ions but less so between the V ion and the Fe ions in our computed models are a likely explanation for the difference between the Mo−Fe and V−Fe distances. It seems likely that this effect is at least partially due to more diffuse 4d orbitals of Mo, resulting in larger overlap between Mo and Fe orbitals than V and Fe orbitals.

These differences in the electronic structure between the two cofactors, which are subsequently reflected in the molecular structure, are likely one of the contributing factors to the difference of the catalytic activity between the two cofactors. Aside from differences in the catalytic activity, another important difference between the two cofactors is that FeVco is capable of binding CO in its resting state, whereas FeMoco can only do so under turnover conditions.[91] One hypothesis is that the more ferrous iron environment in FeVco aids CO binding to an Fe ion in the resting state, something not possible in FeMoco. In fact, the resting state FeVco can be interpreted as being analogous to an unprotonated $E_1$ state in FeMoco, and it has been proposed in a recent joint EXAFS−QM/MM study that the $MoFe_3S_3$ subcubane of FeMoco receives the added electron when reduced to the $E_1$ state,[92] which is analogous to the reduced $VFe_3S_3$ subcubane of our resting state FeVco model.

**4. Stability of the $[VFe_7S_8(CO_3)]^{2-}$ Redox State.** The previously discussed results, in our view, clearly establish the resting state structure of FeVco as containing a bound $CO_3$ ligand and a redox state consistent with $[VFe_7S_8(CO_3)]^{2-}$ and a formal oxidation state distribution as $V(III)Fe(II)_4Fe(III)_3$. Furthermore, the calculated electronic state according to a BS-DFT description is $M_S = {}^3/_2$ (which is consistent with the experimental $S = {}^3/_2$ spin state) and having a lowest-energy BS7-235 solution with spin delocalization, as indicated in Figure 5. Only this specific ligand ($CO_3$), this specific redox state ($[\mathbf{V}\text{-}CO_3]^{2-}$), and this specific alignment of spins (BS7-235) can account for the specific geometric properties of FeVco seen in the experimental X-ray structure.

Until now, we have, however, not discussed a problem that arises from this more negative charge of the resting state FeVco ($[VFe_7S_8(CO_3)]^{2-}$) compared to the resting state FeMoco ($[MoFe_7S_9]^{-}$), namely, that of unbound electrons. The QM/MM model discussed (calculated using a 181-atom QM region and the TPSSh functional) results in 12 $\alpha$ and 11 $\beta$ electrons residing in orbitals with positive orbital energies (Figures S25−S27). Positive orbital energies are unphysical in this context because they suggest that spontaneous detachment of the electrons from the cofactor should occur. While unbound electrons are sometimes an indication of an inflexible basis set, because of the large polarized triple-$\zeta$ basis set used here, this is unlikely to be the case. We considered three possible reasons for the presence of unbound electrons in the $[\mathbf{V}\text{-}CO_3]^{2-}$ computational model: (i) the cofactor is, unlike FeMoco, protonated in the resting state, (ii) the unbound electrons arise because of the DFT self-interaction error (SIE), and (iii) the cofactor is insufficiently stabilized by the QM/MM model.

*i. Protonated Cofactor.* A QM/MM model (58-atom QM region) with an additional proton on the longer carboxylate arm of the homocitrate ligand was found to result in a reduction in the number of unbound electrons to 2 $\alpha$ and 3 $\beta$ electrons (with a subsequent increase in the RMSD to 0.095 Å compared to 0.080 Å for an unprotonated model). Models with protonated belt sulfides S2B or S5A (Table S25) were found to have no unbound electrons. However, the protonation of a belt sulfide was accompanied by a 0.10−0.13 Å elongation of the Fe−S2B/S5A distances, a difference that would likely be resolved in the crystal structure if it were present. Additionally, the RMSD was considerably worse than the unprotonated model (0.106 and 0.121 Å for S2B and S5A protonation, respectively, compared to 0.080 Å for an unprotonated model). Thus, we consider a protonated resting state FeVco model unlikely.

*ii. Self-Interaction Error.* The unbound electrons could arise because of the approximate nature of the density functional used. Approximate density functionals do not show the correct long-range asymptotic behavior of the potential and suffer from SIEs.[93−96] While hybrid density functionals reduce the SIE via the inclusion of exact HF exchange and range-separated hybrids can enforce the correct long-range behavior, the low amount employed in most popular hybrid functionals used for transition-metal chemistry (typically 0−25%) is usually not sufficient to resolve the issues. As revealed in Figure S28, while increasing the global HF exchange in the standard hybrid DFT form results in a decrease of unbound electrons of FeVco, this is not a realistic strategy for describing FeVco because the quality of the geometry deteriorates significantly, as revealed by the strong increase in RMSD with respect to the crystal structure. The 50−70% HF exchange required to remove unbound electrons results in an unacceptable RMSD (>0.20 Å), suggesting that the electronic structure is very poorly described with those functionals. This problem of high HF exchange functionals deteriorating the electronic structure of nitrogenase cofactors has been noted previously by us and others for FeMoco.[51,97]

*iii. Environmental Effects.* Because the spherical QM/MM model does not account for mutual polarization between the QM and MM regions and does not contain the whole VFe protein, we considered the possibility of protein polarization or longer-range bulk electrostatics playing a role in stabilizing the cofactor.

The protein and solvent environment clearly play a role in describing the cofactor, as can be seen by considering a simple 59-atom cluster model of the cofactor in a vacuum; this results in a very unstable cofactor with 195 unbound electrons. Such a vacuum model, furthermore, gives a poor geometric structure (RMSD of 0.166 Å). Using a simple continuum solvation model, COSMO[98] with a dielectric constant of 4, the electronic structure is stabilized considerably, yet 13 unbound electrons remain. A different continuum model, CPCM (using a Gaussian charge scheme and a scaled vdW cavity[99,100]), however, stabilizes the electronic structure, resulting in no unbound electrons. These results thus clearly reveal a sensitivity of the computational model to bulk electrostatics and polarization effects. These continuum model calculations, however, clearly result in cofactor structures inferior to the QM/MM models, as can be judged by the relatively high RMSDs of the cofactor geometries (Table 3), being not much better than the vacuum-optimized geometry.

The lack of protein polarization by the MM environment in the QM/MM models could only be partially explored in this study via a systematic increase of the QM-region size in the calculations. Upon going from a 57-atom QM-region model to a 181-atom model, the number of unbound electrons is only reduced from 29 to 23. Longer-range polarization effects affecting the electronic structure stability can presently not be ruled out and could be explored using even larger QM regions or via polarizable QM/MM methods.


https://dx.doi.org/10.1021/acs.inorgchem.0c01320
Inorg. Chem. 2020, 59, 11514−11527

**Table 3. Unbound Electrons and RMSD (with Respect to the X-ray Geometry) in Cluster and QM/MM Models of FeVco**

| | system size (atoms) | QM-region size (atoms) | charge (QM region) | unbound electrons | RMSD[c] (Å) |
|---|---|---|---|---|---|
| vacuum[b] | 59 | 59 | −6 | 195 | 0.166 |
| COSMO[b] | 59 | 59 | −6 | 13 | 0.140 |
| CPCM[a,b] | 59 | 59 | −6 | 0 | 0.141 |
| QM/MM | 32562 | 57 | −6 | 29 | 0.082 |
| QM/MM | 32562 | 83 | −3 | 32 | 0.085 |
| QM/MM | 32562 | 181 | −3 | 23 | 0.079 |
| QM/MM | 47516 | 57 | −6 | 62 | 0.084 |
| QM/MM | 531080 | 57 | −6 | 0 | 0.085 |
| QM/MM | 47516 | 181 | −3 | 70 | 0.080 |
| QM/MM | 531080 | 181 | −3 | 0 | 0.079 |

[a]Using a Gaussian charge scheme and a scaled van der Waals surface.[100] [b]An additional two protons are added to cap residues $423^{His}$ and $257^{Cys}$. [c]The RMSD is defined as the deviation of the $[VFe_7S_8C(XO_3)]$ part with respect to both cofactors in the crystal structure.

The effect of long-range bulk electrostatics was explored in more detail by the creation of an additional QM/MM setup. Instead of a spherical model (Figure 2, right), centered on the cofactor of half of the hexameric protein, a new QM/MM model consisting of the whole VFe protein was cut from the periodic MM-box model (Figure 2, left) of the whole solvated VFe protein. A 3 Å solvation shell and all $Na^+$ ions were additionally included in the model, resulting in an overall neutral model of 47516 atoms. This model (Figure S29), consisting of the whole protein, is slightly larger than the spherical model of half of the protein. Interestingly, however, this larger model that avoids cutting protein chains and includes the whole protein and all $Na^+$ ions (as MM point charges) actually results in an increase in unbound electrons to 62 (for a 57-atom QM region). This unfavorable result, nonetheless, suggests a strong sensitivity to the bulk electrostatic environment through the presence and/or distribution of MM point charges. When the size of the MM point-charge environment was increased even further, a model where all 531080 atoms (additional water molecules) of the solvated protein box (Figure 2, left) were included in the electrostatic embedding was calculated. Remarkably, this results in complete stabilization of all electrons. QM/MM geometry optimizations at this level of theory further revealed almost negligible structural changes compared to the 47516-atom model, demonstrating that these unphysical unbound electrons do not affect the local structure of the cofactor. Calculations with an even larger 181-atom QM region with the extended MM region resulted in a very similar geometry and no unbound electrons.

The problem of unbound electrons in computational models of FeVco thus appears primarily to be a question of insufficient solvent bulk electrostatic effects. Fortunately, insufficient account of this bulk effect has little consequence for the quality of the cofactor geometry (Table 3) or the spin-density distribution (see the Mulliken spin populations in Table S26). Clearly, however, a proper account of solvent bulk electrostatics needs to be carefully considered in future calculations of the redox properties of these cofactors.

## CONCLUSION

We have performed, to our knowledge, the first extensive computational study on the resting state FeVco of V-nitrogenase from *A. vinelandii* using a QM/MM model starting from the 1.35-Å-resolution X-ray structure (PDB 5N6Y). We systematically explored 35 different broken-symmetry solutions for all plausible oxidation states of FeVco, using either nitrate or carbonate as a possible 4-atom bridging ligand, and found that the BS7-235 solution (with Fe atoms labeled 2, 3, and 5 being spin-down) is energetically favored in all cases. Through a careful comparison of the QM/MM-optimized structures to the X-ray structure by analysis of the Fe−Fe and V−Fe distances, we find that only the $[VFe_7S_8C(CO_3)]^{2-}$ model is in good agreement with the X-ray structure. Analysis of the electronic structure of $[VFe_7S_8C(CO_3)]^{2-}$ via the localized orbitals reveals a reduced $VFe_3$ subcubane compared to the $MoFe_3$ subcubane in FeMoco. This is in good agreement with a previous Fe K-edge XAS study of MoFe and VFe proteins[50] and, interestingly, suggests that the Fe electronic structure of the resting state FeVco is analogous to the $E_1$ state of FeMoco, recently characterized by a joint Fe/Mo EXAFS and QM/MM study.[92] The additional electron in the $VFe_3$ subcubane is localized on $Fe_5$, making it locally ferrous, in contrast to the ferric $Fe_5$ in the analogous computational model of FeMoco (as interpreted from the BS7-235 solution). The oxidation state of V is found to be V(III), in agreement with experimental V K-edge XAS studies,[41] and the V(III) ion is found to have less bonding interactions with Fe ions than Mo(III) in FeMoco.

These electronic structure differences between FeVco and FeMoco are proposed as a likely reason for the experimentally observed differences in the reactivity and catalytic activity.

Finally, we discussed the stability of the electronic structure of the FeVco model with respect to unbound electrons. It is found that the more reduced FeVco model (compared to FeMoco) is highly sensitive to solvent bulk electrostatic effects and that a large number of explicit solvent molecules are required to stabilize the highest electron energy levels of the cofactor.

## ASSOCIATED CONTENT

### Supporting Information

The Supporting Information is available free of charge at https://pubs.acs.org/doi/10.1021/acs.inorgchem.0c01320.

Additional data on computational details, broken-symmetry energies, Mulliken spin populations, figures of localized orbitals, and electron structure as well as optimized geometries (PDF)

## AUTHOR INFORMATION


### Corresponding Author

**Ragnar Bjornsson** − *Science Institute, University of Iceland, 107 Reykjavik, Iceland; Max-Planck Institute for Chemical Energy Conversion, 45470 Mülheim an der Ruhr, Germany;* orcid.org/0000-0003-2167-8374; Email: ragnar.bjornsson@cec.mpg.de

### Author

**Bardi Benediktsson** − *Science Institute, University of Iceland, 107 Reykjavik, Iceland*

Complete contact information is available at: https://pubs.acs.org/10.1021/acs.inorgchem.0c01320

### Author Contributions

The manuscript was written through contributions of all authors.

### Funding

R.B. acknowledges support from the Icelandic Research Fund (Grants 141218051 and 162880051) and University of Iceland Research Fund. Open Access funding was provided by the Max Planck Society.

### Notes

The authors declare no competing financial interest.

## ■ ACKNOWLEDGMENTS

The computations were performed on resources provided by the Icelandic High Performance Computing Centre at University of Iceland.

## ■ REFERENCES

(1) Burgess, B. K.; Lowe, D. J. Mechanism of Molybdenum Nitrogenase. *Chem. Rev.* **1996**, *96* (7), 2983−3012.
(2) Howard, J. B.; Rees, D. C. Structural Basis of Biological Nitrogen Fixation. *Chem. Rev.* **1996**, *96* (7), 2965−2982.
(3) Harris, D. F.; Lukoyanov, D. A.; Kallas, H.; Trncik, C.; Yang, Z. Y.; Compton, P.; Kelleher, N.; Einsle, O.; Dean, D. R.; Hoffman, B. M.; Seefeldt, L. C. Mo-, V-, and Fe-Nitrogenases Use a Universal Eight-Electron Reductive-Elimination Mechanism to Achieve N2 Reduction. *Biochemistry* **2019**, *58* (30), 3293−3301.
(4) Chatt, J.; Dilworth, J. R.; Richards, R. L. Recent Advances in the Chemistry of Nitrogen Fixation. *Chem. Rev.* **1978**, *78* (6), 589−625.
(5) Burgess, B. K.; Wherland, S.; Newton, W. E.; Stiefel, E. I. Nitrogenase Reactivity: Insight into the Nitrogen-Fixing Process through Hydrogen-Inhibition and HD-Forming Reactions. *Biochemistry* **1981**, *20* (18), 5140−5146.
(6) Lukoyanov, D.; Khadka, N.; Yang, Z. Y.; Dean, D. R.; Seefeldt, L. C.; Hoffman, B. M. Reductive Elimination of H2 Activates Nitrogenase to Reduce the NN Triple Bond: Characterization of the E4(4H) Janus Intermediate in Wild-Type Enzyme. *J. Am. Chem. Soc.* **2016**, *138* (33), 10674−10683.
(7) Bulen, W. A.; LeComte, J. R. The Nitrogenase System from Azotobacter: Two-Enzyme Requirement for N2 Reduction, ATP-Dependent H2 Evolution, and ATP Hydrolysis. *Proc. Natl. Acad. Sci. U. S. A.* **1966**, *56* (3), 979−986.
(8) Hoffman, B. M.; Lukoyanov, D.; Yang, Z. Y.; Dean, D. R.; Seefeldt, L. C. Mechanism of Nitrogen Fixation by Nitrogenase: The next Stage. *Chem. Rev.* **2014**, *114* (8), 4041−4062.
(9) Hales, B. J.; Case, E. E.; Morningstar, J. E.; Dzeda, M. F.; Mauterer, L. A. Isolation of a New Vanadium-Containing Nitrogenase from Azotobacter Vinelandii. *Biochemistry* **1986**, *25* (23), 7251−7255.
(10) Eady, R. R.; Robson, R. L.; Richardson, T. H.; Miller, R. W.; Hawkins, M. The Vanadium Nitrogenase of Azotobacter Chroococcum. Purification and Properties of the VFe Protein. *Biochem. J.* **1987**, *244* (1), 197−207.
(11) Sickerman, N. S.; Hu, Y.; Ribbe, M. W. Nitrogenases. *Methods Mol. Biol.* **2019**, *1876*, 3−24.
(12) Chisnell, J. R.; Premakumar, R.; Bishop, P. E. Purification of a Second Alternative Nitrogenase from a NifHDK Deletion Strain of Azotobacter Vinelandii. *J. Bacteriol.* **1988**, *170* (1), 27−33.
(13) Jasniewski, A. J.; Lee, C. C.; Ribbe, M. W.; Hu, Y. Reactivity, Mechanism, and Assembly of the Alternative Nitrogenases. *Chem. Rev.* **2020**, *120* (12), 5107−5157.
(14) Burgess, B. K. The Iron-Molybdenum Cofactor of Nitrogenase. *Chem. Rev.* **1990**, *90* (8), 1377−1406.
(15) Miller, R. W.; Eady, R. R. Molybdenum and Vanadium Nitrogenases of Azotobacter Chroococcum. Low Temperature Favours N2 Reduction by Vanadium Nitrogenase. *Biochem. J.* **1988**, *256* (2), 429−432.
(16) Lee, C. C.; Fay, A. W.; Weng, T.-C.; Krest, C. M.; Hedman, B.; Hodgson, K. O.; Hu, Y.; Ribbe, M. W. Uncoupling Binding of Substrate CO from Turnover by Vanadium Nitrogenase. *Proc. Natl. Acad. Sci. U. S. A.* **2015**, *112* (45), 13845.
(17) Lee, C. C.; Hu, Y.; Ribbe, M. W. Vanadium Nitrogenase Reduces CO. *Science* **2010**, *329* (5992), 642−642.
(18) Sickerman, N. S.; Hu, Y.; Ribbe, M. W. Activation of CO2 by Vanadium Nitrogenase. *Chem. - Asian J.* **2017**, *12* (16), 1985−1996.
(19) Schneider, K.; Gollan, U.; Dröttboom, M.; Selsemeier-Voigt, S.; Müller, A. Comparative Biochemical Characterization of the Iron-Only Nitrogenase and the Molybdenum Nitrogenase from Rhodobacter Capsulatus. *Eur. J. Biochem.* **1997**, *244* (3), 789−800.
(20) Seefeldt, L. C.; Yang, Z.-Y.; Lukoyanov, D. A.; Harris, D. F.; Dean, D. R.; Raugei, S.; Hoffman, B. M. Reduction of Substrates by Nitrogenases. *Chem. Rev.* **2020**, *120*, 5082.
(21) Kim, J.; Woo, D.; Rees, D. C. X-Ray Crystal Structure of the Nitrogenase Molybdenum-Iron Protein from Clostridium Pasteurianum at 3.0-.ANG. Resolution. *Biochemistry* **1993**, *32* (28), 7104−7115.
(22) Davis, L. C.; Shah, V. K.; Brill, W. J.; Orme-Johnson, W. H. Nitrogenase II. Changes in the EPR Signal of Component I (Iron-Molybdenum Protein) of Azotobacter Vinelandii Nitrogenase during Repression and Derepression. *Biochim. Biophys. Acta, Bioenerg.* **1972**, *256* (2), 512−523.
(23) Rawlings, J.; Shah, V. K.; Chisnell, J. R.; Brill, W. J.; Zimmermann, R.; Münck, E.; Orme-Johnson, W. H. Novel Metal Cluster in the Iron-Molybdenum Cofactor of Nitrogenase. Spectroscopic Evidence. *J. Biol. Chem.* **1978**, *253*, 1001−1004.
(24) Münck, E.; Rhodes, H.; Orme-Johnson, W. H.; Davis, L. C.; Brill, W. J.; Shah, V. K. Nitrogenase. VIII. Mössbauer and EPR Spectroscopy. The MoFe Protein Component from Azotobacter Vinelandii OP. *Biochim. Biophys. Acta, Protein Struct.* **1975**, *400* (1), 32−53.
(25) Jasniewski, A. J.; Sickerman, N. S.; Hu, Y.; Ribbe, M. W. The Fe Protein: An Unsung Hero of Nitrogenase. *Inorganics* **2018**, *6* (1), 25.
(26) Rohde, M.; Trncik, C.; Sippel, D.; Gerhardt, S.; Einsle, O. Crystal Structure of VnfH, the Iron Protein Component of Vanadium Nitrogenase. *JBIC, J. Biol. Inorg. Chem.* **2018**, *23*, 1049.
(27) Sippel, D.; Einsle, O. The Structure of Vanadium Nitrogenase Reveals an Unusual Bridging Ligand. *Nat. Chem. Biol.* **2017**, *13* (9), 956−960.
(28) Van Stappen, C.; Decamps, L.; Cutsail, G. E.; Bjornsson, R.; Henthorn, J. T.; Birrell, J. A.; DeBeer, S. The Spectroscopy of Nitrogenases. *Chem. Rev.* **2020**, *120*, 5005.
(29) Morningstar, J. E.; Hales, B. J. Electron Paramagnetic Resonance Study of the Vanadium-Iron Protein of Nitrogenase from Azotobacter Vinelandii. *J. Am. Chem. Soc.* **1987**, *109* (22), 6854−6855.
(30) Lee, C. C.; Hu, Y.; Ribbe, M. W. Unique Features of the Nitrogenase VFe Protein from Azotobacter Vinelandii. *Proc. Natl. Acad. Sci. U. S. A.* **2009**, *106* (23), 9209−9214.
(31) Yoo, S. J.; Angove, H. C.; Papaefthymiou, V.; Burgess, B. K.; Münck, E. Mossbauer Study of the MoFe Protein of Nitrogenase from Azotobacter Vinelandii Using Selective57Fe Enrichment of the M-Centers. *J. Am. Chem. Soc.* **2000**, *122* (20), 4926−4936.
(32) Bjornsson, R.; Neese, F.; DeBeer, S. Revisiting the Mössbauer Isomer Shifts of the FeMoco Cluster of Nitrogenase and the Cofactor Charge. *Inorg. Chem.* **2017**, *56* (3), 1470−1477.
(33) Spatzal, T.; Schlesier, J.; Burger, E.-M.; Sippel, D.; Zhang, L.; Andrade, S. L. A.; Rees, D. C.; Einsle, O. Nitrogenase FeMoco Investigated by Spatially Resolved Anomalous Dispersion Refinement. *Nat. Commun.* **2016**, *7*, 1−7.
(34) Benediktsson, B.; Bjornsson, R. QM/MM Study of the Nitrogenase MoFe Protein Resting State: Broken-Symmetry States, Protonation States, and QM Region Convergence in the FeMoco Active Site. *Inorg. Chem.* **2017**, *56* (21), 13417−13429.
(35) Spatzal, T.; Aksoyoglu, M.; Zhang, L.; Andrade, S. L.; Schleicher, E.; Weber, S.; Rees, D. C.; Einsle, O. Evidence for Interstitial Carbon in Nitrogenase FeMo Cofactor. *Science* **2011**, *334* (6058), 940.

(36) Bjornsson, R.; Lima, F. A.; Spatzal, T.; Weyhermüller, T.; Glatzel, P.; Bill, E.; Einsle, O.; Neese, F.; DeBeer, S. Identification of a Spin-Coupled Mo(III) in the Nitrogenase Iron−Molybdenum Cofactor. *Chem. Sci.* **2014**, *5* (8), 3096−3103.
(37) Bjornsson, R.; Delgado-Jaime, M. U.; Lima, F. A.; Sippel, D.; Schlesier, J.; Weyhermüller, T.; Einsle, O.; Neese, F.; De Beer, S. Molybdenum L-Edge XAS Spectra of MoFe Nitrogenase. *Z. Anorg. Allg. Chem.* **2015**, *641* (1), 65−71.
(38) Kowalska, J.; Henthorn, J.; Van Stappen, C.; Trncik, C.; Einsle, O.; Keavney, D.; DeBeer, S. X-Ray Magnetic Circular Dichroism Spectroscopy Applied to Nitrogenase and Related Models: Experimental Evidence for a Spin-Coupled Mo(III). *Angew. Chem., Int. Ed.* **2019**, *58*, 9373.
(39) Henthorn, J. T.; Arias, R. J.; Koroidov, S.; Kroll, T.; Sokaras, D.; Bergmann, U.; Rees, D. C.; DeBeer, S. Localized Electronic Structure of Nitrogenase FeMoco Revealed by Selenium K-Edge High Resolution X-Ray Absorption Spectroscopy. *J. Am. Chem. Soc.* **2019**, *141* (34), 13676−13688.
(40) George, G. N.; Coyle, C. L.; Hales, B. J.; Cramer, S. P. X-Ray Absorption of Azotobacter Vinelandii Vanadium Nitrogenase. *J. Am. Chem. Soc.* **1988**, *110* (12), 4057−4059.
(41) Arber, J. M.; Dobson, B. R.; Eady, R. R.; Stevens, P.; Hasnain, S. S.; Garner, C. D.; Smith, B. E. Vanadium K-Edge X-Ray Absorption Spectroscopy of the VFe Protein of the Vanadium Nitrogenase of Azotobacter Chroococcum. *Nature* **1987**, *325* (6102), 372−374.
(42) Harvey, I.; Arber, J. M.; Eady, R. R.; Smith, B. E.; Garner, C. D.; Hasnain, S. S. Iron K-Edge X-Ray-Absorption Spectroscopy of the Iron-Vanadium Cofactor of the Vanadium Nitrogenase from Azotobacter Chroococcum. *Biochem. J.* **1990**, *266* (3), 929−931.
(43) Ravi, N.; Moore, V.; Lloyd, S. G.; Hales, B. J.; Huynh, B. H. Mössbauer Characterization of the Metal Clusters in Azotobacter Vinelandii Nitrogenase VFe Protein. *J. Biol. Chem.* **1994**, *269* (33), 20920−20924.
(44) Rees, J. A.; Bjornsson, R.; Schlesier, J.; Sippel, D.; Einsle, O.; DeBeer, S. The Fe-V Cofactor of Vanadium Nitrogenase Contains an Interstitial Carbon Atom. *Angew. Chem., Int. Ed.* **2015**, *54* (45), 13249−13252.
(45) Sippel, D.; Rohde, M.; Netzer, J.; Trncik, C.; Gies, J.; Grunau, K.; Djurdjevic, I.; Decamps, L.; Andrade, S. L. A.; Einsle, O. A Bound Reaction Intermediate Sheds Light on the Mechanism of Nitrogenase. *Science (Washington, DC, U. S.)* **2018**, *359* (6383), 1484−1489.
(46) Eady, R. R. Current Status of Structure Function Relationships of Vanadium Nitrogenase. *Coord. Chem. Rev.* **2003**, *237* (1−2), 23−30.
(47) Kovacs, J. A.; Holm, R. H. Assembly of Vanadium-Iron-Sulfur Cubane Clusters from Mononuclear and Linear Trinuclear Reactants. *J. Am. Chem. Soc.* **1986**, *108* (2), 340−341.
(48) Carney, M. J.; Kovacs, J. A.; Zhang, Y. P.; Papaefthymiou, G. C.; Spartalian, K.; Frankel, R. B.; Holm, R. H. Comparative Electronic Properties of Vanadium-Iron-Sulfur and Molybdenum-Iron-Sulfur Clusters Containing Isoelectronic Cubane-Type [VFe3S4]2+ and [MoFe3S4]3+ Cores. *Inorg. Chem.* **1987**, *26* (5), 719−724.
(49) Thorhallsson, A. T.; Bjornsson, R. Computational Mechanistic Study of [MoFe 3 S 4 ] Cubanes for Catalytic Reduction of Nitrogenase Substrates. *Inorg. Chem.* **2019**, *58* (3), 1886−1894.
(50) Rees, J. A.; Bjornsson, R.; Kowalska, J. K.; Lima, F. A.; Schlesier, J.; Sippel, D.; Weyhermüller, T.; Einsle, O.; Kovacs, J. A.; DeBeer, S. Comparative Electronic Structures of Nitrogenase FeMoco and FeVco. *Dalt. Trans.* **2017**, *46* (8), 2445−2455.
(51) Thorhallsson, A. T.; Benediktsson, B.; Bjornsson, R. A Model for Dinitrogen Binding in the E 4 State of Nitrogenase. *Chem. Sci.* **2019**, *10* (48), 11110−11124.
(52) Dance, I. How Does Vanadium Nitrogenase Reduce CO to Hydrocarbons? *Dalt. Trans.* **2011**, *40* (20), 5516.
(53) Lovell, T.; Torres, R. A.; Han, W. G.; Liu, T.; Case, D. A.; Noodleman, L. Metal Substitution in the Active Site of Nitrogenase $MFe_7S_9$ (M = $Mo^{4+}$, $V^{3+}$, $Fe^{3+}$). *Inorg. Chem.* **2002**, *41* (22), 5744−5753.
(54) Varley, J. B.; Nørskov, J. K. First-Principles Calculations of Fischer−Tropsch Processes Catalyzed by Nitrogenase Enzymes. *ChemCatChem* **2013**, *5* (3), 732−736.
(55) Benediktsson, B.; Thorhallsson, A. T.; Bjornsson, R. QM/MM Calculations Reveal a Bridging Hydroxo Group in a Vanadium Nitrogenase Crystal Structure. *Chem. Commun.* **2018**, *54* (53), 7310−7313.
(56) Hess, B.; Kutzner, C.; Van Der Spoel, D.; Lindahl, E. GRGMACS 4: Algorithms for Highly Efficient, Load-Balanced, and Scalable Molecular Simulation. *J. Chem. Theory Comput.* **2008**, *4* (3), 435−447.
(57) Pronk, S.; Pall, S.; Schulz, R.; Larsson, P.; Bjelkmar, P.; Apostolov, R.; Shirts, M. R.; Smith, J. C.; Kasson, P. M.; van der Spoel, D.; Hess, B.; Lindahl, E. GROMACS 4.5: A High-Throughput and Highly Parallel Open Source Molecular Simulation Toolkit. *Bioinformatics* **2013**, *29* (7), 845−854.
(58) Abraham, M. J.; Murtola, T.; Schulz, R.; Páll, S.; Smith, J. C.; Hess, B.; Lindahl, E. Gromacs: High Performance Molecular Simulations through Multi-Level Parallelism from Laptops to Supercomputers. *SoftwareX* **2015**, *1−2*, 19−25.
(59) Best, R. B.; Zhu, X.; Shim, J.; Lopes, P. E. M.; Mittal, J.; Feig, M.; MacKerell, A. D. Optimization of the Additive CHARMM All-Atom Protein Force Field Targeting Improved Sampling of the Backbone Phi, Psi and Side-Chain Chi(1) and Chi(2) Dihedral Angles. *J. Chem. Theory Comput.* **2012**, *8* (9), 3257−3273.
(60) Sherwood, P.; De Vries, A. H.; Guest, M. F.; Schreckenbach, G.; Catlow, C. R. A.; French, S. A.; Sokol, A. A.; Bromley, S. T.; Thiel, W.; Turner, A. J.; Billeter, S.; Terstegen, F.; Thiel, S.; Kendrick, J.; Rogers, S. C.; Casci, J.; Watson, M.; King, F.; Karlsen, E.; Sjøvoll, M.; Fahmi, A.; Schäfer, A.; Lennartz, C. QUASI: A General Purpose Implementation of the QM/MM Approach and Its Application to Problems in Catalysis. *J. Mol. Struct.: THEOCHEM* **2003**, *632*, 1−28.
(61) Metz, S.; Kästner, J.; Sokol, A. A.; Keal, T. W.; Sherwood, P. ChemShell-a Modular Software Package for QM/MM Simulations. *Wiley Interdiscip. Rev.: Comput. Mol. Sci.* **2014**, *4* (2), 101−110.
(62) Neese, F. The ORCA Program System. *Wiley Interdiscip. Rev.: Comput. Mol. Sci.* **2012**, *2* (1), 73−78.
(63) Neese, F. Software Update: The ORCA Program System. *Wiley Interdiscip. Rev.: Comput. Mol. Sci.* **2018**, *8* (1), 4−9.
(64) Tao, J.; Perdew, J. P.; Staroverov, V. N.; Scuseria, G. E. Climbing the Density Functional Ladder : Nonempirical Meta-Generalized Gradient Approximation Designed for Molecules and Solids. *Phys. Rev. Lett.* **2003**, *91*, 146401.
(65) Staroverov, V. N.; Scuseria, G. E.; Tao, J.; Perdew, J. P. Comparative Assessment of a New Nonempirical Density Functional: Molecules and Hydrogen-Bonded Complexes. *J. Chem. Phys.* **2003**, *119*, 12129.
(66) Weigend, F.; Ahlrichs, R. Balanced Basis Sets of Split Valence, Triple Zeta Valence and Quadruple Zeta Valence Quality for H to Rn: Design and Assessment of Accuracy. *Phys. Chem. Chem. Phys.* **2005**, *7* (18), 3297.
(67) Pantazis, D. A.; Chen, X.-Y.; Landis, C. R.; Neese, F. All-Electron Scalar Relativistic Basis Sets for Third-Row Transition Metal Atoms. *J. Chem. Theory Comput.* **2008**, *4* (6), 908−919.
(68) Neese, F.; Wennmohs, F.; Hansen, A.; Becker, U. Efficient, Approximate and Parallel Hartree-Fock and Hybrid DFT Calculations. A "chain-of-Spheres" Algorithm for the Hartree-Fock Exchange. *Chem. Phys.* **2009**, *356* (1−3), 98−109.
(69) Izsák, R.; Neese, F. An Overlap Fitted Chain of Spheres Exchange Method. *J. Chem. Phys.* **2011**, *135* (14), 144105.
(70) Grimme, S.; Antony, J.; Ehrlich, S.; Krieg, H. A Consistent and Accurate Ab Initio Parametrization of Density Functional Dispersion Correction (DFT-D) for the 94 Elements H-Pu. *J. Chem. Phys.* **2010**, *132* (15), 154104.
(71) Grimme, S.; Ehrlich, S.; Goerigk, L. Effect of the Damping Function in Dispersion Corrected Density Functional Theory. *J. Comput. Chem.* **2011**, *32* (7), 1456−1465.


https://dx.doi.org/10.1021/acs.inorgchem.0c01320
*Inorg. Chem.* 2020, 59, 11514−11527

(72) van Lenthe, E.; van Leeuwen, R.; Baerends, E. J.; Snijders, J. G. Relativistic Regular Two-Component Hamiltonians. *Int. J. Quantum Chem.* **1996**, *57* (3), 281−293.
(73) van Wüllen, C. Molecular Density Functional Calculations in the Regular Relativistic Approximation: Method, Application to Coinage Metal Diatomics, Hydrides, Fluorides and Chlorides, and Comparison with First-Order Relativistic Calculations. *J. Chem. Phys.* **1998**, *109* (2), 392−399.
(74) Smith, W.; Forester, T. R. DL_POLY_2.0: A General-Purpose Parallel Molecular Dynamics Simulation Package. *J. Mol. Graphics* **1996**, *14* (3), 136−141.
(75) Kästner, J.; Carr, J. M.; Keal, T. W.; Thiel, W.; Wander, A.; Sherwood, P. DL-FIND: An Open-Source Geometry Optimizer for Atomistic Simulations*. *J. Phys. Chem. A* **2009**, *113* (43), 11856−11865.
(76) Humphrey, W.; Dalke, A.; Schulten, K. VMD: Visual Molecular Dynamics. *J. Mol. Graphics* **1996**, *14* (1), 33−38.
(77) Rao, L.; Xu, X.; Adamo, C. Theoretical Investigation on the Role of the Central Carbon Atom and Close Protein Environment on the Nitrogen Reduction in Mo Nitrogenase. *ACS Catal.* **2016**, *6* (3), 1567−1577.
(78) Lovell, T.; Li, J.; Case, D. A.; Noodleman, L. FeMo Cofactor of Nitrogenase: Energetics and Local Interactions in the Protein Environment. *JBIC, J. Biol. Inorg. Chem.* **2002**, *7* (7−8), 735−749.
(79) Lovell, T.; Li, J.; Liu, T.; Case, D. A.; Noodleman, L. FeMo Cofactor of Nitrogenase: A Density Functional Study of States $M^N$, $M^{OX}$, $M^R$, and $M^I$. *J. Am. Chem. Soc.* **2001**, *123* (49), 12392−12410.
(80) Cao, L.; Ryde, U. Influence of the Protein and DFT Method on the Broken-Symmetry and Spin States in Nitrogenase. *Int. J. Quantum Chem.* **2018**, *118* (15), e25627.
(81) Cao, L.; Caldararu, O.; Ryde, U. Protonation and Reduction of the FeMo Cluster in Nitrogenase Studied by Quantum Mechanics/Molecular Mechanics (QM/MM) Calculations. *J. Chem. Theory Comput.* **2018**, *14*, 6653.
(82) Cao, L.; Ryde, U. What Is the Structure of the $E_4$ Intermediate in Nitrogenase ? *J. Chem. Theory Comput.* **2020**, *16*, 1936.
(83) Spatzal, T.; Perez, K. A.; Einsle, O.; Howard, J. B.; Rees, D. C. Ligand Binding to the FeMo-Cofactor: Structures of Co-Bound and Reactivated Nitrogenase. *Science* **2014**, *345* (6204), 1620−1623.
(84) Noodleman, L.; Case, D. A.; Aizman, A. Broken Symmetry Analysis of Spin Coupling in Iron-Sulfur Clusters. *J. Am. Chem. Soc.* **1988**, *110* (4), 1001−1005.
(85) Noodleman, L.; Peng, C. Y.; Case, D. A.; Mouesca, J. M. Orbital Interactions, Electron Delocalization and Spin Coupling in Iron-Sulfur Clusters. *Coord. Chem. Rev.* **1995**, *144*, 199−244.
(86) Sharma, S.; Sivalingam, K.; Neese, F.; Chan, G. K. L. Low-Energy Spectrum of Iron-Sulfur Clusters Directly from Many-Particle Quantum Mechanics. *Nat. Chem.* **2014**, *6* (10), 927−933.
(87) Knizia, G. Intrinsic Atomic Orbitals: An Unbiased Bridge between Quantum Theory and Chemical Concepts. *J. Chem. Theory Comput.* **2013**, *9* (11), 4834−4843.
(88) Pipek, J.; Mezey, P. G. A Fast Intrinsic Localization Procedure Applicable for Ab Initio and Semiempirical Linear Combination of Atomic Orbital Wave Functions. *J. Chem. Phys.* **1989**, *90* (9), 4916−4926.
(89) Bridgeman, A. J.; Cavigliasso, G.; Ireland, L. R.; Rothery, J. The Mayer Bond Order as a Tool in Inorganic Chemistry. *J. Chem. Soc. Dalt. Trans.* **2001**, *14*, 2095−2108.
(90) Liu, H. I.; Hodgson, K. O.; Filipponi, A.; Gavini, N.; Burgess, B. K.; Hedman, B.; Di Cicco, A.; Natoli, C. R. EXAFS Studies of FeMo-Cofactor and MoFe Protein: Direct Evidence for the Long-Range Mo-Fe-Fe Interaction and Cyanide Binding to the Mo in FeMo-Cofactor. *J. Am. Chem. Soc.* **1994**, *116* (6), 2418−2423.
(91) Cameron, L. M.; Hales, B. J. Investigation of CO Binding and Release from Mo-Nitrogenase during Catalytic Turnover. *Biochemistry* **1998**, *37* (26), 9449−9456.
(92) Van Stappen, C.; Thorhallsson, A. T.; Decamps, L.; Bjornsson, R.; Debeer, S. Resolving the Structure of the E1 State of Mo Nitrogenase through Mo and Fe K-Edge EXAFS and QM/MM Calculations. *Chem. Sci.* **2019**, *10* (42), 9807−9821.
(93) Cohen, A. J.; Mori-Sánchez, P.; Yang, W. Insights into Current Limitations of Density Functional Theory. *Science (Washington, DC, U. S.)* **2008**, *321* (5890), 792−794.
(94) Cohen, A. J.; Mori-Sánchez, P.; Yang, W. Challenges for Density Functional Theory. *Chem. Rev.* **2012**, *112* (1), 289−320.
(95) Jensen, F. Describing Anions by Density Functional Theory: Fractional Electron Affinity. *J. Chem. Theory Comput.* **2010**, *6* (9), 2726−2735.
(96) Kim, M. C.; Sim, E.; Burke, K. Communication: Avoiding Unbound Anions in Density Functional Calculations. *J. Chem. Phys.* **2011**, *134* (17), 171103.
(97) Cao, L.; Ryde, U. Extremely Large Differences in DFT Energies for Nitrogenase Models. *Phys. Chem. Chem. Phys.* **2019**, *21* (5), 2480−2488.
(98) Barone, V.; Cossi, M. Quantum Calculation of Molecular Energies and Energy Gradients in Solution by a Conductor Solvent Model. *J. Phys. Chem. A* **1998**, *102* (97), 1995−2001.
(99) York, D. M.; Karplus, M. A Smooth Solvation Potential Based on the Conductor-like Screening Model. *J. Phys. Chem. A* **1999**, *103* (50), 11060−11079.
(100) Garcia-Ratés, M.; Neese, F. Effect of the Solute Cavity on the Solvation Energy and Its Derivatives within the Framework of the Gaussian Charge Scheme. *J. Comput. Chem.* **2020**, *41* (9), 922−939.


https://dx.doi.org/10.1021/acs.inorgchem.0c01320
*Inorg. Chem.* 2020, 59, 11514−11527

# Article I: Supplementary information

## Quantum Mechanics/Molecular Mechanics Study of Resting-State Vanadium Nitrogenase: Molecular and Electronic Structure of the Iron–Vanadium Cofactor

B. Benediktsson, R. Bjornsson

Inorganic Chemistry **59**, 11514-11527, 2020.

**Supplementary information for:**

# Quantum Mechanics/Molecular Mechanics Study of Resting-State Vanadium Nitrogenase: Molecular and Electronic Structure of the Iron−Vanadium Cofactor

Bardi Benediktsson[a] and Ragnar Bjornsson[a,b]*

[a]Science Institute, University of Iceland, Dunhagi 3, 107 Reykjavik, Iceland

[b]Max-Planck Institute for Chemical Energy Conversion, Stiftstrasse 34-36, 45470 Mülheim an der Ruhr, Germany.

## Contents



## Computational Details

**Force field parameters.** The CHARMM36 protein force field[1] was used in all MM and QM/MM calculations. As no forcefield parameters are available for FeVco, atomic charges were derived from Hirshfeld population analysis using the $[VFe_7S_8C(CO_3)]^{2-}$ charge configuration and crystal structure geometry for FeVco with relaxed protons (both extended carboxylate arms of FeVco were protonated, making the model 61 QM atoms in total) from a calculation performed with ORCA version 3.0.3 with TPSSh and Ahlrichs def2 triple-ζ basis set on V, Fe and S but def2 double-ζ basis set on other atoms and the protein matrix approximated with COSMO[2] (ε = 4). Same parameters were used for the P-cluster as in a previous study by us.[3] Lennard-Jones parameters were only added to inorganic sulfides (CHARMM atomtype SM used) and not to metals[4]. Forcefield parameters for homocitrate were adapted from those already available for citrate.[5] Water was modelled as TIP3P.[6]

**MM model preparation.**

Protonation state of titrable residues were decided via visual inspection of hydrogen bonds. The residues glutamine, asparagine and histidine were checked whether they were correctly orientated as in crystal structures it is generally not possible to distinguish between carbon and nitrogen. No arginine and lysine residues were deprotonated, and no glutamate was protonated. The aspartate residues $\alpha\text{-}9^{Asp}$, $\beta\text{-}30^{Asp}$ and $\beta\text{-}73^{Asp}$ were protonated. As for histidine protonation state in the protein, the following were protonated on the ε nitrogen: $\alpha\text{-}18^{His}$, $\alpha\text{-}70^{His}$, $\alpha\text{-}81^{His}$, $\alpha\text{-}91^{His}$, $\alpha\text{-}106^{His}$, $\alpha\text{-}120^{His}$, $\alpha\text{-}180^{His}$, $\alpha\text{-}181^{His}$, $\alpha\text{-}234^{His}$, $\alpha\text{-}248^{His}$, $\alpha\text{-}342^{His}$, $\alpha\text{-}416^{His}$, $\alpha\text{-}423^{His}$, $\alpha\text{-}426^{His}$, $\alpha\text{-}453^{His}$, $\beta\text{-}51^{His}$, $\beta\text{-}67^{His}$, $\beta\text{-}158^{His}$, $\beta\text{-}234^{His}$, $\beta\text{-}321^{His}$, $\beta\text{-}379^{His}$, $\beta\text{-}409^{His}$, $\beta\text{-}461^{His}$ and $\gamma\text{-}111^{His}$. The following histidine residues were protonated on the δ nitrogen: $\alpha\text{-}364^{His}$, $\alpha\text{-}448^{His}$, $\beta\text{-}80^{His}$, $\beta\text{-}177^{His}$, $\beta\text{-}334^{His}$, $\beta\text{-}386^{His}$, $\beta\text{-}80^{His}$, $\gamma\text{-}5^{His}$ and $\gamma\text{-}110^{His}$. Only $\beta\text{-}150^{His}$ is found to be doubly. Cysteine residues ligated to metals were modeled as deprotonated

cysteinate residues: α-49$^{Cys}$, α-138$^{Cys}$, α-75$^{Cys}$, α-257$^{Cys}$, β-31$^{His}$, β-56$^{Cys}$ and β-115$^{His}$. The following residues had their functional group flipped: α-120$^{His}$, α-249$^{Gln}$, α-426$^{His}$, β-243$^{His}$, β-260$^{Asn}$, β-267$^{Gln}$, β-361$^{Gln}$, γ-3$^{Gln}$ and γ-46$^{Gln}$

The total charge of the system after protonation by GROMACS is -62 and 62 sodium ions were generated in the solute (by randomly replacing water molecules) to neutralize the charge. The size of the periodic box is 174.97 * 174.97 * 174.97 Å with all angles set at 90°. The total volume of the system after solvation is 5356.17 nm$^3$ and has a density of 1006.33 g/l. The final MM model size is 531 080 atoms.

**MD simulations**

All hydrogen atoms, water molecules and sodium ions of the system were then relaxed (all other atoms were kept constrained) using the steepest descent algorithm. The MM model was simulated within the canonical ensemble, with the same constraints, using the velocity-Verlet algorithm[7,8] and coupled to a 4-chain Nosé-Hoover thermostat[9–12] . The system was heated up from 50 K to 300 K in 500 ps and maintained at 300 K for a total of 5 ns. At 1100 ps a snapshot was extracted.

**QM/MM preparation and calculations.**

A spherical cut-out cluster model was generated from a snapshot from the MD trajectory after 1100 ps (Figure 2 in article). All residues, as labelled in the 5N6Y X-ray structure,[13] from chain A (residues numbered 2 to 474), chain B (residues numbered 12 to 475), chain C (residues numbered from 2 to 113) and chain E (residues numbered 12 to 475) and water molecules within 42 Å of the carbide of FeVco are included. 35 sodium ions are included as well to keep the system charge neutral. In total, we are including all residues from $\alpha\beta_2\gamma$ subunits. The QM/MM model contains 32 562 atoms. An active region of 1038 atoms was used in all QM/MM optimizations except in separate calculations concerning the protonation state of FeVco. As the carboxylate arm of homocitrate reaches the boundary of the defined active region, the active region size was increased to include all residues within 13 Å of the central carbide (as compared to 10 Å for previous calculations) to accommodate for the area around the carboxylate group. All protonated models utilize this active region size. Three different QM regions were used: 57, 83 and 181 atoms, shown in Figure S2-S4.

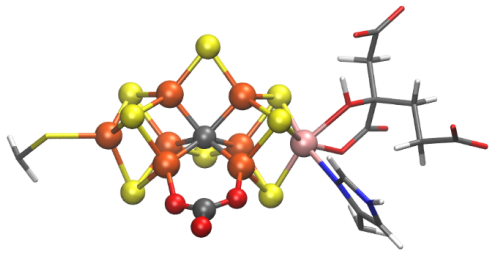

*Figure S 1: 57 QM atom region, [$VFe_7S_8CXO_3$], homocitrate, Cys$^{257}$ and His$^{423}$.*

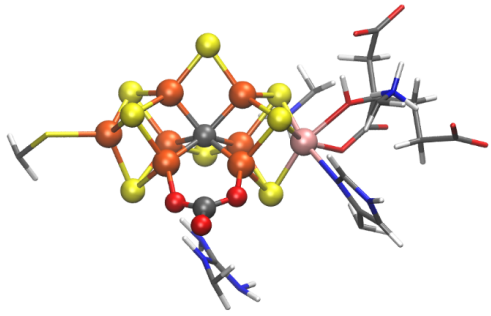

*Figure S 2: 83 QM atom region, [$VFe_7S_8CXO_3$], homocitrate, Cys$^{257}$, His$^{423}$, Arg$^{339}$, Lys$^{83}$ and Lys$^{361}$.*

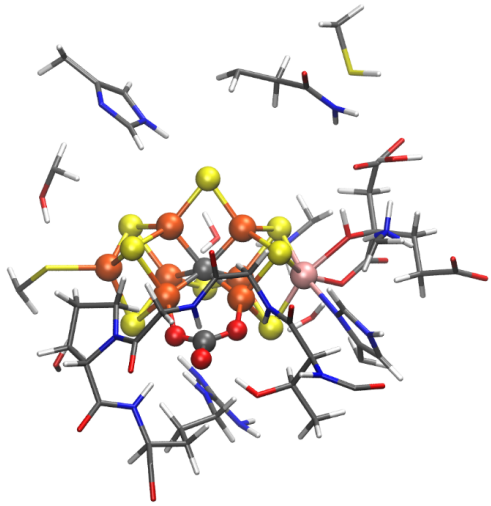

*Figure S 3: 181 QM atom region, [$VFe_7S_8CXO_3$], homocitrate, $Cys^{257}$, $His^{423}$, $Arg^{339*}$, $Lys^{83}$, $Lys^{361}$, $Ser^{260}$, $His^{180}$, $Gln^{176}$, $Cys^{52}$, Thr335, $Gly^{336}$, $Gly^{337}$ and $Pro^{338}$ (* the QM size of $Arg^{339}$ has been increased to include also the whole sidechain and the peptide backbone). Few water molecules have been included as well.*

## References


(1) Best, R. B.; Zhu, X.; Shim, J.; Lopes, P. E. M.; Mittal, J.; Feig, M.; MacKerell, A. D. Optimization of the Additive CHARMM All-Atom Protein Force Field Targeting Improved Sampling of the Backbone Phi, Psi and Side-Chain Chi(1) and Chi(2) Dihedral Angles. *J. Chem. Theory Comput.* **2012**, *8* (9), 3257–3273. https://doi.org/DOI 10.1021/ct3004000x.

(2) Klamt, A.; Schüürmann, G. COSMO: A New Approach to Dielectric Screening in Solvents with Explicit Expressions for the Screening Energy and Its Gradient. *J. Chem. Soc., Perkin Trans. 2* **1993**, No. 5, 799–805. https://doi.org/10.1039/P29930000799.

(3) Benediktsson, B.; Bjornsson, R. QM/MM Study of the Nitrogenase MoFe Protein Resting State: Broken-Symmetry States, Protonation States, and QM Region Convergence in the FeMoco Active Site. *Inorg. Chem.* **2017**, *56* (21), 13417–13429. https://doi.org/10.1021/acs.inorgchem.7b02158.

(4) Chang, C. H.; Kim, K. Density Functional Theory Calculation of Bonding and Charge Parameters for Molecular Dynamics Studies on [FeFe] Hydrogenases. *J. Chem. Theory Comput.* **2009**, *5* (4), 1137–1145. https://doi.org/10.1021/ct800342w.

(5) Wright, L. B.; Rodger, P. M.; Walsh, T. R. Aqueous Citrate: A First-Principles and Force-Field Molecular Dynamics Study. *RSC Adv.* **2013**, *3* (37), 16399. https://doi.org/10.1039/c3ra42437e.

(6) Jorgensen, W. L.; Chandrasekhar, J.; Madura, J. D.; Impey, R. W.; Klein, M. L. Comparison of Simple Potential Functions for Simulating Liquid Water. *J. Chem. Phys.* **1983**, *79* (2), 926–935. https://doi.org/10.1063/1.445869.

(7) Swope, W. C.; Andersen, H. C.; Berens, P. H.; Wilson, K. R. A Computer Simulation Method for the Calculation of Equilibrium Constants for the Formation of Physical Clusters of Molecules: Application to Small Water Clusters. *J. Chem. Phys.* **1982**, *76* (1), 637–649. https://doi.org/10.1063/1.442716.

(8) Verlet, L. Computer “Experiments” on Classical Fluids. I. Thermodynamic Properties of Lennard-Jones Molecules. *Phys. Rev.* **1967**, *159* (1), 98–103.

(9) Nosé, S. A Unified Formulation of the Constant Temperature Molecular Dynamics Methods. *J. Chem. Phys.* **1984**, *81* (1), 511–519. https://doi.org/10.1063/1.447334.

(10) Nosé, S. A Molecular Dynamics Method for Simulations in the Canonical Ensemble. *Mol. Phys.* **1984**, *52* (2), 255–268. https://doi.org/10.1080/00268978400101201.

(11) Hoover, W. G. Canonical Dynamics: Equilibrium Phase-Space Distributions. *Phys Rev A* **1985**, *31* (3), 1695–1697. https://doi.org/10.1103/PhysRevA.31.1695.

(12) Martyna, G. J.; Klein, M. L.; Tuckerman, M. Nosé-Hoover Chains: The Canonical Ensemble via Continuous Dynamics. *J. Chem. Phys.* **1992**, *97* (4), 2635–2643. https://doi.org/10.1063/1.463940.

(13) Sippel, D.; Einsle, O. The Structure of Vanadium Nitrogenase Reveals an Unusual Bridging Ligand. *Nat. Chem. Biol.* **2017**, *13* (9), 956–960. https://doi.org/10.1038/nchembio.2428.

## Single Point Broken Symmetry Solution Comparison

We calculated 35 BS solutions for multiple combinations of ligand ($CO_3$, $NO_3$), redox state and spin state using the X-ray structure. Relative energies of the BS solutions are shown in Figures S5-S18 and Table S1 for each model. Energies are always relative the most stable BS7-235 solution for each model.

Figure S19 shows a BS-state comparison of different density functionals for the [**V**-$CO_3$]$^{2-}$ model and Figure S20 compares QM/MM vs. CPCM results.

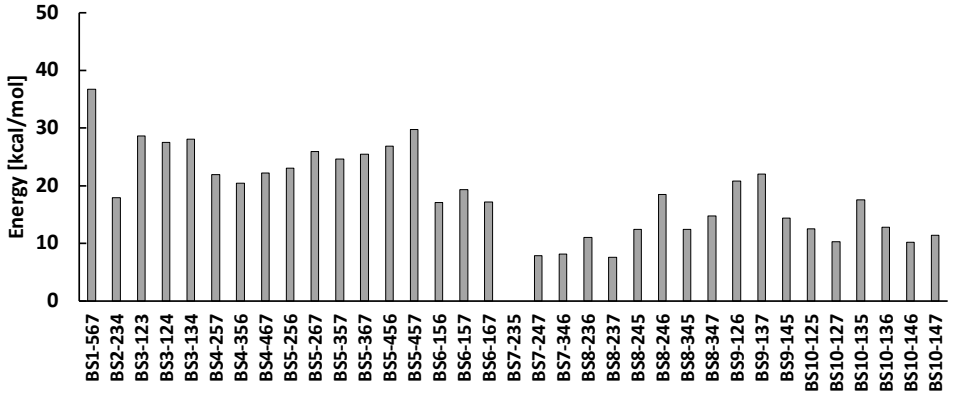


*Figure S 4: The relative energies of the 35 BS solutions for [**V**-$CO_3$]$^{2-}$ and $M_S = {}^3/_2$. Functional: TPSSh. QM-region size: 57 atoms. Energies are relative to the $M_S = {}^3/_2$ BS7-235 solution.*

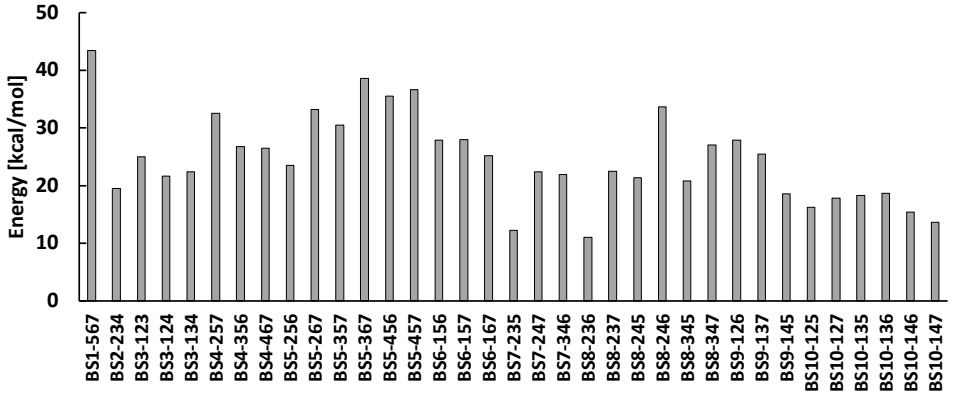


*Figure S 5: The relative energies of the 35 BS solutions for [**V**-$CO_3$]$^{2-}$ and $M_S = {}^1/_2$. Functional: TPSSh. QM-region size: 57 atoms. Energies are relative to the $M_S = {}^3/_2$ BS7-235 solution.*

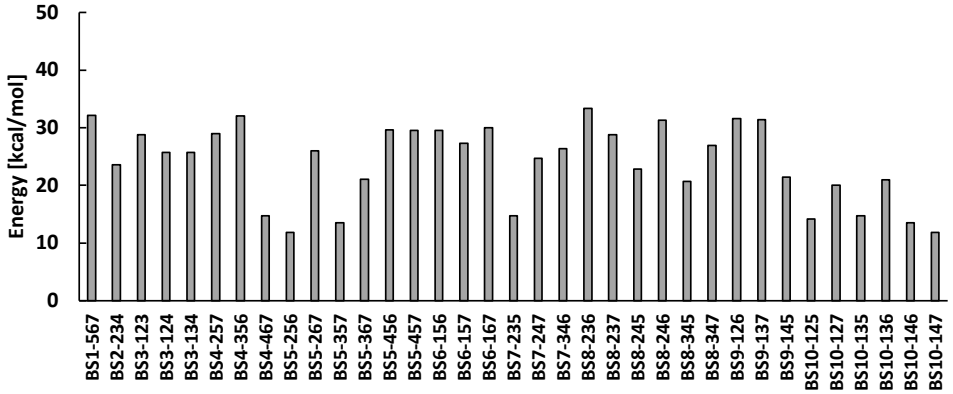


*Figure S 6: The relative energies of the 35 BS solutions for [**V**-$CO_3$]$^-$ and $M_S$ = 0. Functional: TPSSh. QM-region size: 57 atoms. Energies are relative to the $M_S$ = 1 BS7-235 solution.*

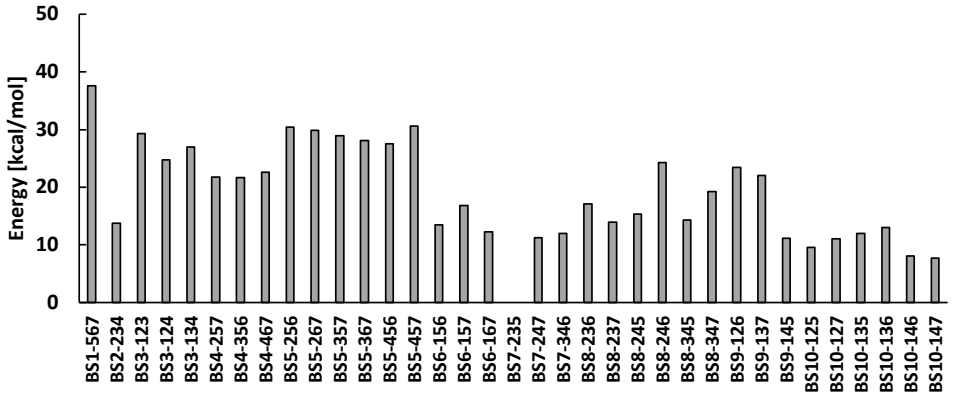


*Figure S 7: The relative energies of the 35 BS solutions for [**V**-$CO_3$]$^-$ and $M_S$ = 1. Functional: TPSSh. QM-region size: 57 atoms. Energies are relative to the $M_S$ = 1 BS7-235 solution.*

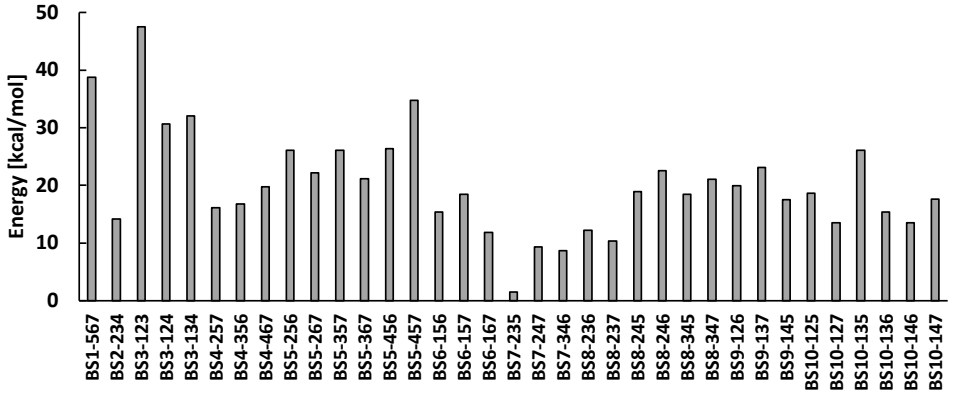


*Figure S 8: The relative energies of the 35 BS solutions for $[V\text{-}CO_3]^0$ and $M_S = 2$. Functional: TPSSh. QM-region size: 57 atoms. Energies are relative to the $M_S = 1$ BS7-235 solution.*

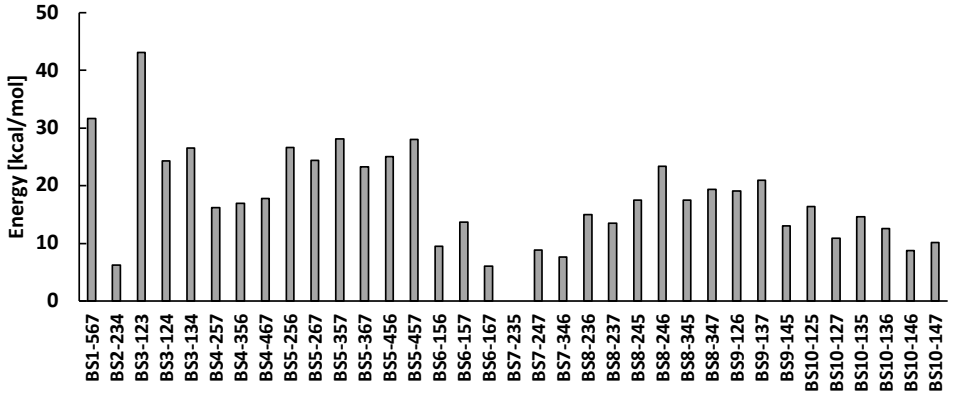


*Figure S 9: The relative energies of the 35 BS solutions for $[V\text{-}CO_3]^0$ and $M_S = {}^3/_2$. Functional: TPSSh. QM-region size: 57 atoms. Energies are relative to the $M_S = {}^3/_2$ BS7-235 solution.*

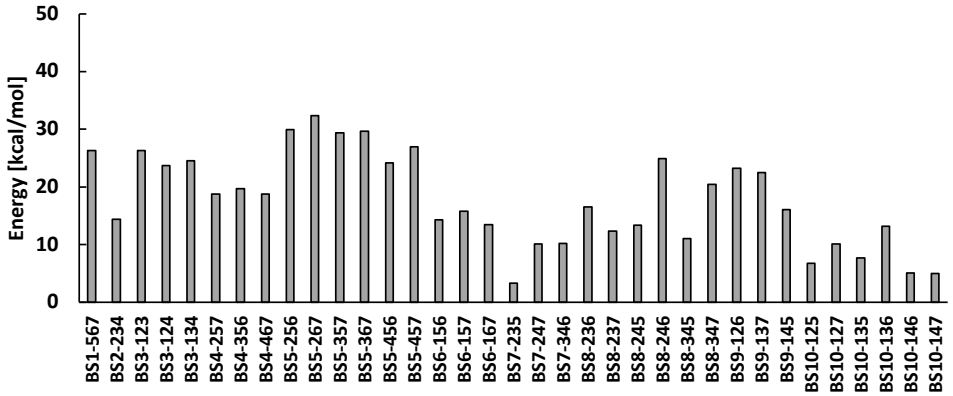


*Figure S 10: The relative energies of the 35 BS solutions for $[V\text{-}CO_3]^0$ and $M_S = {}^1/_2$. Functional: TPSSh. QM-region size: 57 atoms. Energies are relative to the $M_S = {}^3/_2$ BS7-235 solution.*

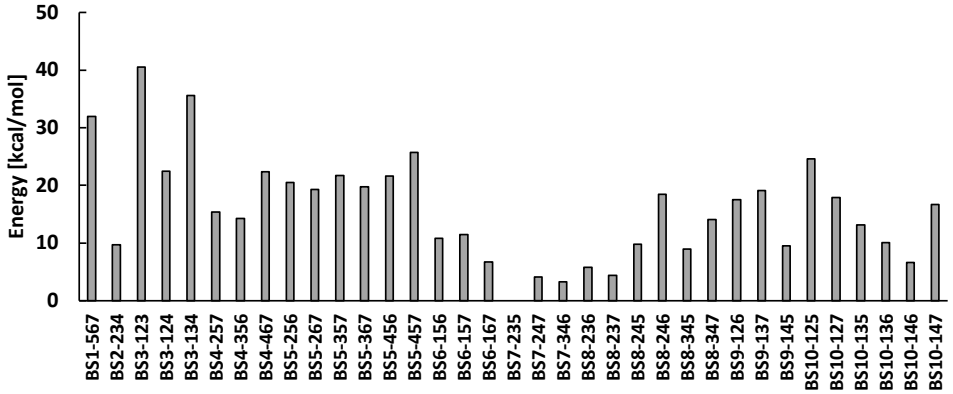


*Figure S 11: The relative energies of the 35 BS solutions for [**V**-$NO_3$]$^-$ and $M_S = {}^3/_2$. Functional: TPSSh. QM-region size: 57 atoms. Energies are relative to the $M_S = {}^3/_2$ BS7-235 solution.*

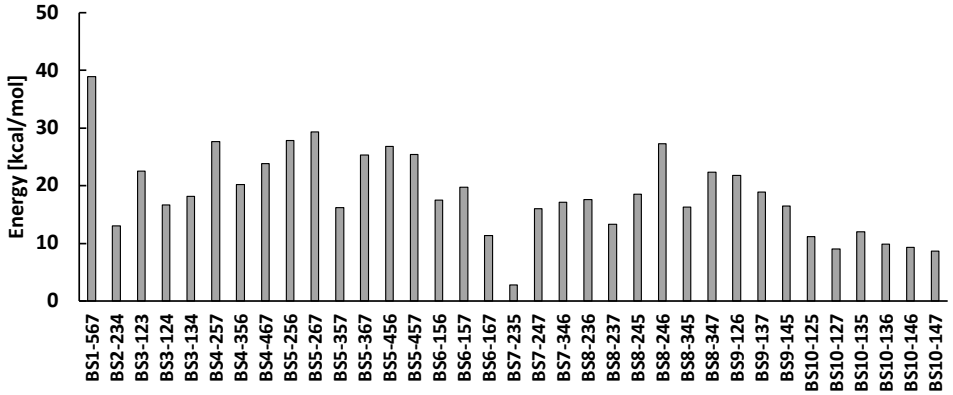


*Figure S 12: Figure S 13: The relative energies of the 35 BS solutions for [**V**-$NO_3$]$^-$ and $M_S = {}^1/_2$. Functional: TPSSh. QM-region size: 57 atoms. Energies are relative to the $M_S = {}^3/_2$ BS7-235 solution.*

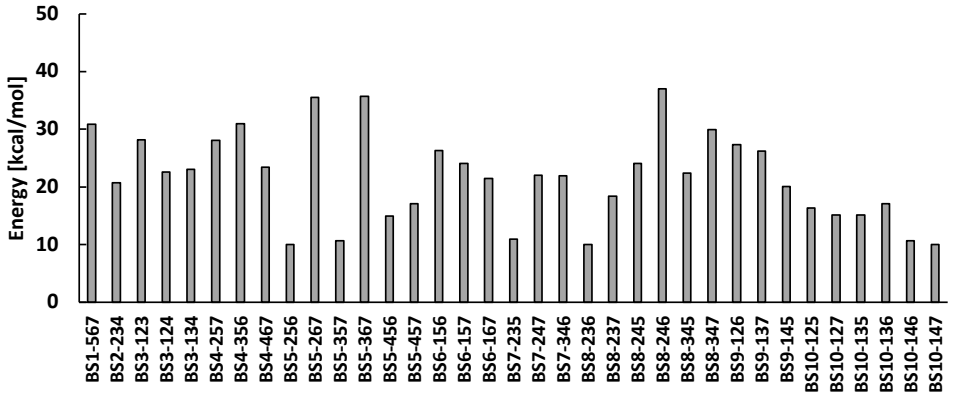


*Figure S 14: The relative energies of the 35 BS solutions for [**V**-$NO_3$]$^0$ and $M_S = 0$. Functional: TPSSh. QM-region size: 57 atoms. Energies are relative to the $M_S = 1$ BS7-235 solution.*

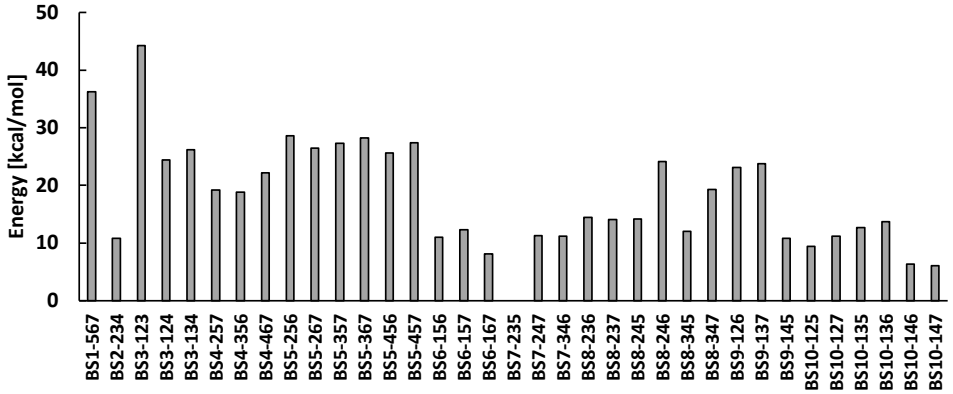


*Figure S 15: The relative energies of the 35 BS solutions for $[V\text{-}NO_3]^0$ and $M_S = 1$. Functional: TPSSh. QM-region size: 57 atoms. Energies are relative to the $M_S = 1$ BS7-235 solution.*

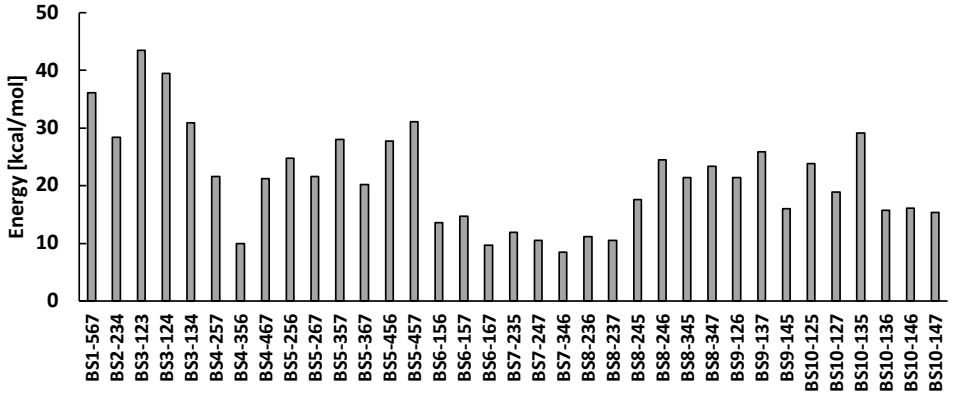


*Figure S 16: The relative energies of the 35 BS solutions for $[V\text{-}NO_3]^0$ and $M_S = 1$. Functional: TPSSh. QM-region size: 57 atoms. Energies are relative to the $M_S = 1$ BS7-235 solution.*

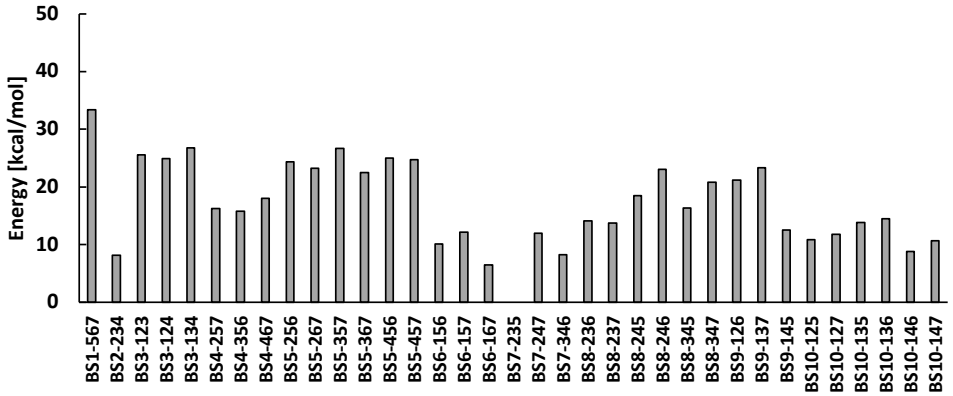


*Figure S 17: The relative energies of the 35 BS solutions for $[V\text{-}NO_3]^+$ and $M_S = {}^3/_2$. Functional: TPSSh. QM-region size: 57 atoms. Energies are relative to the $M_S = {}^3/_2$ BS7-235 solution.*

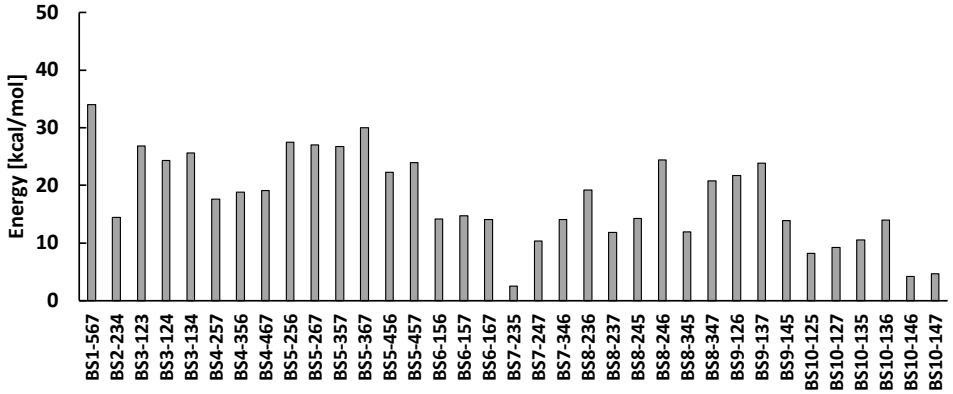


*Figure S 18: The relative energies of the 35 BS solutions for* $[V\text{-}NO_3]^+$ *and* $M_S = {}^1/_2$*. Functional: TPSSh. QM-region size: 57 atoms. Energies are relative to the* $M_S = {}^3/_2$ *BS7-235 solution.*

*Table S 1: Relative QM/MM energies (kcal/mol) of all BS solutions for all FeVco models using the crystal structure geometry. The * indicates the high-spin energy relative to the preferred BS solution. ($M_S$ = 34/2 for [**V**-$CO_3$]$^{2-}$ and [**V**-$NO_3$]$^{-}$, $M_S$ = 35/2 for [**V**-$CO_3$]$^{-}$ and [**V**-$NO_3$]$^{0}$, and $M_S$ = 36/2 for [**V**-$CO_3$]$^{0}$ and [**V**-$NO_3$]$^{+}$).*

| | Carbonate | | | | | | | Nitrate | | | | | | |
|---|---|---|---|---|---|---|---|---|---|---|---|---|---|---|
| | [**V**-$CO_3$]$^{2-}$ $M_S = 3/2$ | [**V**-$CO_3$]$^{2-}$ $M_S = 1/2$ | [**V**-$CO_3$]$^{-}$ $M_S = 0$ | [**V**-$CO_3$]$^{-}$ $M_S = 1$ | [**V**-$CO_3$]$^{-}$ $M_S = 2$ | [**V**-$CO_3$] $M_S = 3/2$ | [**V**-$CO_3$] $M_S = 1/2$ | [**V**-$NO_3$]$^{-}$ $M_S = 3/2$ | [**V**-$NO_3$]$^{-}$ $M_S = 1/2$ | [**V**-$NO_3$] $M_S = 0$ | [**V**-$NO_3$] $M_S = 1$ | [**V**-$NO_3$] $M_S = 2$ | [**V**-$NO_3$]$^{+}$ $M_S = 3/2$ | [**V**-$NO_3$]$^{+}$ $M_S = 1/2$ |
| BS1-567 | 36.77 | 43.47 | 32.16 | 37.57 | 38.74 | 31.68 | 26.30 | 31.94 | 38.92 | 30.83 | 36.20 | 36.10 | 33.37 | 34.00 |
| BS2-234 | 17.90 | 19.47 | 23.62 | 13.75 | 14.15 | 6.19 | 14.36 | 9.71 | 13.06 | 20.69 | 10.86 | 28.37 | 8.20 | 14.47 |
| BS3-123 | 28.68 | 24.98 | 28.77 | 29.26 | 47.47 | 43.10 | 26.35 | 40.52 | 22.56 | 28.22 | 44.29 | 43.47 | 25.60 | 26.82 |
| BS3-124 | 27.49 | 21.62 | 25.70 | 24.69 | 30.64 | 24.29 | 23.67 | 22.48 | 16.63 | 22.62 | 24.42 | 39.49 | 24.92 | 24.31 |
| BS3-134 | 28.12 | 22.37 | 25.76 | 26.94 | 32.06 | 26.52 | 24.57 | 35.55 | 18.14 | 23.02 | 26.21 | 30.95 | 26.75 | 25.60 |
| BS4-257 | 21.91 | 32.56 | 28.98 | 21.72 | 16.18 | 16.20 | 18.75 | 15.41 | 27.64 | 28.10 | 19.21 | 21.60 | 16.30 | 17.66 |
| BS4-356 | 20.40 | 26.75 | 32.01 | 21.69 | 16.74 | 16.90 | 19.70 | 14.23 | 20.18 | 30.94 | 18.85 | 9.99 | 15.79 | 18.81 |
| BS4-467 | 22.18 | 26.52 | 14.75 | 22.64 | 19.81 | 17.78 | 18.74 | 22.34 | 23.82 | 23.42 | 22.22 | 21.23 | 18.05 | 19.10 |
| BS5-256 | 23.01 | 23.54 | 11.83 | 30.43 | 26.10 | 26.62 | 29.95 | 20.51 | 27.87 | 9.99 | 28.57 | 24.73 | 24.33 | 27.50 |
| BS5-267 | 25.94 | 33.23 | 26.04 | 29.89 | 22.17 | 24.43 | 32.35 | 19.31 | 29.36 | 35.53 | 26.44 | 21.55 | 23.28 | 27.06 |
| BS5-357 | 24.60 | 30.45 | 13.49 | 28.97 | 26.13 | 28.08 | 29.34 | 21.72 | 16.21 | 10.68 | 27.32 | 28.06 | 26.69 | 26.78 |
| BS5-367 | 25.47 | 38.61 | 21.09 | 28.12 | 21.15 | 23.29 | 29.63 | 19.76 | 25.28 | 35.69 | 28.24 | 20.17 | 22.51 | 30.03 |
| BS5-456 | 26.86 | 35.49 | 29.62 | 27.57 | 26.33 | 25.05 | 24.16 | 21.64 | 26.78 | 14.99 | 25.66 | 27.72 | 24.98 | 22.30 |
| BS5-457 | 29.78 | 36.61 | 29.51 | 30.65 | 34.77 | 27.98 | 26.93 | 25.68 | 25.44 | 17.14 | 27.42 | 31.07 | 24.78 | 23.98 |
| BS6-156 | 17.12 | 27.90 | 29.55 | 13.49 | 15.38 | 9.47 | 14.32 | 10.81 | 17.54 | 26.35 | 11.04 | 13.63 | 10.11 | 14.15 |
| BS6-157 | 19.30 | 27.99 | 27.32 | 16.87 | 18.42 | 13.70 | 15.80 | 11.50 | 19.76 | 24.03 | 12.30 | 14.74 | 12.19 | 14.75 |
| BS6-167 | 17.16 | 25.21 | 30.00 | 12.27 | 11.83 | 6.09 | 13.45 | 6.72 | 11.34 | 21.43 | 8.10 | 9.67 | 6.50 | 14.06 |
| BS7-235 | 0.00 | 12.29 | 14.75 | 0.00 | 1.51 | 0.00 | 3.27 | 0.00 | 2.76 | 10.90 | 0.00 | 11.95 | 0.00 | 2.51 |
| BS7-247 | 7.83 | 22.41 | 24.67 | 11.20 | 9.37 | 8.84 | 10.09 | 4.09 | 15.97 | 22.03 | 11.27 | 10.49 | 11.94 | 10.38 |
| BS7-346 | 8.18 | 21.98 | 26.40 | 11.99 | 8.67 | 7.63 | 10.16 | 3.30 | 17.13 | 21.90 | 11.24 | 8.42 | 8.25 | 14.13 |
| BS8-236 | 11.08 | 11.08 | 33.39 | 17.10 | 12.24 | 15.02 | 16.51 | 5.77 | 17.63 | 9.99 | 14.46 | 11.16 | 14.11 | 19.19 |
| BS8-237 | 7.58 | 22.47 | 28.79 | 13.95 | 10.32 | 13.52 | 12.31 | 4.41 | 13.27 | 18.42 | 14.05 | 10.55 | 13.74 | 11.86 |
| BS8-245 | 12.42 | 21.39 | 22.79 | 15.33 | 18.92 | 17.51 | 13.38 | 9.77 | 18.52 | 24.07 | 14.13 | 17.62 | 18.51 | 14.24 |
| BS8-246 | 18.52 | 33.68 | 31.33 | 24.29 | 22.59 | 23.40 | 24.90 | 18.46 | 27.25 | 37.00 | 24.13 | 24.46 | 23.02 | 24.44 |
| BS8-345 | 12.48 | 20.86 | 20.74 | 14.27 | 18.47 | 17.46 | 11.01 | 8.92 | 16.29 | 22.41 | 12.08 | 21.44 | 16.39 | 11.97 |
| BS8-347 | 14.77 | 27.08 | 26.96 | 19.29 | 21.03 | 19.32 | 20.40 | 14.09 | 22.33 | 29.98 | 19.29 | 23.33 | 20.80 | 20.75 |
| BS9-126 | 20.77 | 27.93 | 31.55 | 23.41 | 19.91 | 19.12 | 23.24 | 17.50 | 21.80 | 27.36 | 23.09 | 21.41 | 21.16 | 21.74 |
| BS9-137 | 22.00 | 25.48 | 31.42 | 22.06 | 23.16 | 20.98 | 22.52 | 19.09 | 18.92 | 26.23 | 23.72 | 25.84 | 23.34 | 23.91 |
| BS9-145 | 14.40 | 18.56 | 21.41 | 11.16 | 17.53 | 13.04 | 16.05 | 9.52 | 16.51 | 20.06 | 10.85 | 16.04 | 12.50 | 13.88 |
| BS10-125 | 12.56 | 16.21 | 14.20 | 9.60 | 18.64 | 16.38 | 6.74 | 24.61 | 11.18 | 16.38 | 9.45 | 23.81 | 10.86 | 8.24 |
| BS10-127 | 10.28 | 17.80 | 20.04 | 11.06 | 13.56 | 10.84 | 10.12 | 17.93 | 9.02 | 15.16 | 11.17 | 18.93 | 11.77 | 9.22 |
| BS10-135 | 17.56 | 18.32 | 14.71 | 12.02 | 26.06 | 14.63 | 7.66 | 13.20 | 12.02 | 15.10 | 12.69 | 29.17 | 13.85 | 10.53 |
| BS10-136 | 12.79 | 18.64 | 20.94 | 12.98 | 15.42 | 12.59 | 13.22 | 10.09 | 9.85 | 17.14 | 13.67 | 15.69 | 14.51 | 13.98 |
| BS10-146 | 10.18 | 15.44 | 13.49 | 8.12 | 13.53 | 8.75 | 5.06 | 6.64 | 9.32 | 10.68 | 6.38 | 16.10 | 8.84 | 4.22 |
| BS10-147 | 11.38 | 13.64 | 11.83 | 7.73 | 17.65 | 10.18 | 4.95 | 16.70 | 8.68 | 9.99 | 6.10 | 15.39 | 10.63 | 4.70 |
| Hi-Spin* | 132.53 | | | 149.53 | | 160.57 | | 128.07 | | | 147.79 | | 162.17 | |

*Table S 2: Relative QM/MM energies (kcal/mol) of different spin-flip procedures for [**V**-$CO_3$]$^{2-}$, where the spin of V is either flipped after the BS solution is converged or the spin of V is flipped along with the spins of the irons from the high spin solution.. All energies are relative to the BS7-235 solution of the 'normal flip spin' column (which is the same as BS7-235 in the first column, [**V**-$CO_3$]$^{2-}$ and $M_S = {}^3/_2$ in Table S1).*

| | Normal flip spin[a] | V-flip from low spin[b] | V-flip from high spin[c] | Difference between 'V-flip from low spin' and 'normal flip spin' | Difference between 'V-flip from high spin' and 'normal flip spin' |
|---|---|---|---|---|---|
| BS1-567 | 36.77 | 36.77 | 36.77 | 0.00 | 0.00 |
| BS2-234 | 17.90 | 17.85 | 16.48 | -0.05 | -1.41 |
| BS3-123 | 28.68 | 28.68 | 28.68 | 0.00 | 0.00 |
| BS3-124 | 27.49 | 27.48 | 29.05 | 0.00 | 1.57 |
| BS3-134 | 28.12 | 28.12 | 28.12 | 0.00 | 0.00 |
| BS4-257 | 21.91 | 21.91 | 21.91 | 0.00 | 0.00 |
| BS4-356 | 20.40 | 20.40 | 20.40 | 0.00 | 0.00 |
| BS4-467 | 22.18 | 22.18 | 22.18 | 0.00 | 0.00 |
| BS5-256 | 23.01 | 23.01 | 23.01 | 0.00 | 0.00 |
| BS5-267 | 25.94 | 25.94 | 25.94 | 0.00 | 0.00 |
| BS5-357 | 24.60 | 24.60 | 24.60 | 0.00 | 0.00 |
| BS5-367 | 25.47 | 25.47 | 25.47 | 0.00 | 0.00 |
| BS5-456 | 26.86 | 26.86 | 26.86 | 0.00 | 0.00 |
| BS5-457 | 29.78 | 29.78 | 29.71 | 0.00 | -0.07 |
| BS6-156 | 17.12 | 17.12 | 17.12 | 0.00 | 0.00 |
| BS6-157 | 19.30 | 19.30 | 19.30 | 0.00 | 0.00 |
| BS6-167 | 17.16 | 17.16 | 17.16 | 0.00 | 0.00 |
| BS7-235 | 0.00 | 0.00 | 0.00 | 0.00 | 0.00 |
| BS7-247 | 7.83 | 7.83 | 7.83 | 0.00 | 0.00 |
| BS7-346 | 8.18 | 8.18 | 8.18 | 0.00 | 0.00 |
| BS8-236 | 11.08 | 11.08 | 11.08 | 0.00 | 0.00 |
| BS8-237 | 7.58 | 7.58 | 7.58 | 0.00 | 0.00 |
| BS8-245 | 12.42 | 12.42 | 12.42 | 0.00 | 0.00 |
| BS8-246 | 18.52 | 18.52 | 18.52 | 0.00 | 0.00 |
| BS8-345 | 12.48 | 12.48 | 12.48 | 0.00 | 0.00 |
| BS8-347 | 14.77 | 14.77 | 14.77 | 0.00 | 0.00 |
| BS9-126 | 20.77 | 20.77 | 20.77 | 0.00 | 0.00 |
| BS9-137 | 22.00 | 22.00 | 22.00 | 0.00 | 0.00 |
| BS9-145 | 14.40 | 14.40 | 14.40 | 0.00 | 0.00 |
| BS10-125 | 12.56 | 12.56 | 12.56 | 0.00 | 0.00 |
| BS10-127 | 10.28 | 10.28 | 10.28 | 0.00 | 0.00 |
| BS10-135 | 17.56 | 17.56 | 17.56 | 0.00 | 0.00 |
| BS10-136 | 12.79 | 12.79 | 12.79 | 0.00 | 0.00 |
| BS10-146 | 10.18 | 10.18 | 10.18 | 0.00 | 0.00 |
| BS10-147 | 11.38 | 11.38 | 11.38 | 0.00 | 0.00 |

a) Normal flip spin is the same BS solution as acquired with no specific flipping of vanadium

b) V-flip from low spin means that a fully converged BS solution is used as a "high spin" solution and then vanadium is flipped

c) V-flip from high spin means that first a high spin solution is converged and then in the BS step, the vanadium is included in the flip spin procedure.

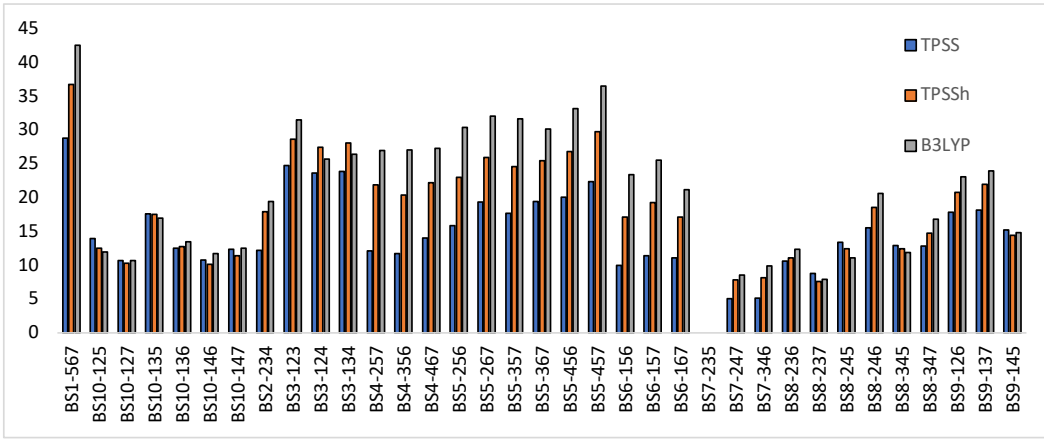


*Figure S 19: Relative QM/MM energies of the 35 BS solutions for the $[V\text{-}CO_3]^{2-}$ model using the X-ray structure with different functionals.*

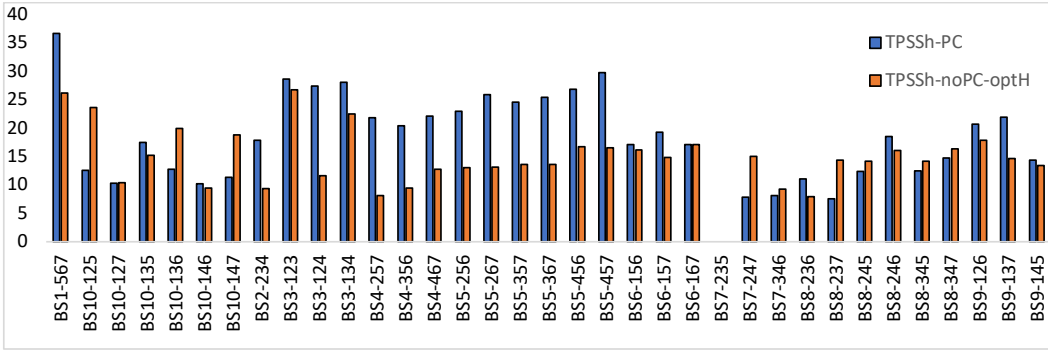


*Figure S 20: Comparison of CPCM-DFT energies and QM/MM energies of the 35 BS solutions for the $[V\text{-}CO_3]^{2-}$ model using the X-ray structure. Functional: TPSSh. Homocitrate was calculated as triply protonated.*

Mulliken spin populations of the 181 QM-atom QM/MM optimized structures

*Table S 3: Mulliken spin population of the QM/MM optimized models. C* is carbide and X is either nitrogen or carbon of the $XO_3$ ligand.*

| Model | [**V**-$CO_3$]$^n$ | | | | | | | | | | [**V**-$NO_3$]$^n$ | | | | | | | | | |
|---|---|---|---|---|---|---|---|---|---|---|---|---|---|---|---|---|---|---|---|---|
| Charge | 2- | 1- | 1- | 1- | 0 | 2- | 1- | 1- | 1- | 0 | 1- | 0 | 0 | 0 | 1+ | 1- | 0 | 0 | 0 | 1+ |
| Spin | $^3/_2$ | 2 | 1 | 0 | $^3/_2$ | $^3/_2$ | 2 | 1 | 0 | $^3/_2$ | $^3/_2$ | 2 | 1 | 0 | $^3/_2$ | $^3/_2$ | 2 | 1 | 0 | $^3/_2$ |
| QM size | 181 | 181 | 181 | 181 | 181 | 57 | 57 | 57 | 57 | 57 | 181 | 181 | 181 | 181 | 181 | 57 | 57 | 57 | 57 | 57 |
| V | -1.62 | 1.00 | -1.58 | -1.59 | -1.52 | -1.65 | 1.02 | -1.61 | -1.61 | -0.65 | -1.69 | -1.66 | -1.67 | -1.62 | -1.56 | -1.73 | 0.85 | -1.69 | -1.65 | -0.84 |
| Fe1 | 3.45 | 3.47 | 3.46 | 3.37 | 3.46 | 3.48 | 3.49 | 3.49 | 2.33 | 3.49 | 3.47 | 3.48 | 3.48 | 3.39 | 3.48 | 3.50 | 3.50 | 3.50 | 3.43 | 3.49 |
| Fe2 | -3.29 | -3.43 | -3.44 | -3.43 | -3.42 | -3.29 | -3.44 | -3.45 | -3.49 | -3.45 | -3.26 | -3.17 | -3.42 | -3.43 | -3.40 | -3.27 | -3.41 | -3.42 | -3.43 | -3.43 |
| Fe3 | -3.27 | -3.44 | -3.45 | -3.45 | -3.42 | -3.29 | -3.48 | -3.48 | -3.47 | -3.46 | -3.25 | -3.17 | -3.43 | -3.44 | -3.39 | -3.27 | -3.45 | -3.45 | -3.47 | -3.42 |
| Fe4 | 3.39 | 3.40 | 3.40 | 2.27 | 3.43 | 3.43 | 3.43 | 3.42 | 3.26 | 3.42 | 3.24 | 3.29 | 3.28 | 2.15 | 3.32 | 3.26 | 3.28 | 3.28 | 2.15 | 3.29 |
| Fe5 | -3.19 | -3.34 | -3.23 | -3.27 | -3.18 | -3.22 | -3.37 | -3.25 | -3.27 | -3.30 | -3.04 | -3.00 | -3.09 | -3.11 | -3.06 | -3.06 | -3.19 | -3.10 | -3.13 | -3.14 |
| Fe6 | 3.29 | 3.29 | 3.15 | 3.06 | 3.39 | 3.28 | 3.30 | 3.18 | 3.19 | 3.19 | 3.27 | 3.44 | 3.13 | 3.05 | 3.36 | 3.27 | 3.28 | 3.15 | 3.06 | 3.17 |
| Fe7 | 3.21 | 2.84 | 3.07 | 2.97 | 3.31 | 3.23 | 2.88 | 3.10 | 3.11 | 3.18 | 3.20 | 3.37 | 3.06 | 2.97 | 3.30 | 3.22 | 2.89 | 3.07 | 2.97 | 3.16 |
| S1A | 0.20 | 0.15 | 0.15 | -0.04 | 0.12 | 0.18 | 0.13 | 0.13 | -0.09 | 0.11 | 0.20 | 0.20 | 0.16 | -0.04 | 0.14 | 0.18 | 0.14 | 0.15 | -0.04 | 0.13 |
| S2A | -0.02 | -0.12 | -0.13 | -0.14 | -0.15 | -0.02 | -0.12 | -0.13 | -0.32 | -0.15 | -0.01 | -0.05 | -0.11 | -0.13 | -0.14 | -0.01 | -0.10 | -0.11 | -0.13 | -0.12 |
| S4A | 0.17 | 0.13 | 0.13 | -0.06 | 0.11 | 0.16 | 0.12 | 0.12 | -0.03 | 0.10 | 0.18 | 0.18 | 0.15 | -0.05 | 0.13 | 0.18 | 0.15 | 0.14 | -0.07 | 0.13 |
| S1B | 0.08 | 0.01 | 0.09 | 0.09 | 0.14 | 0.09 | 0.01 | 0.10 | 0.10 | 0.03 | 0.07 | 0.11 | 0.08 | 0.08 | 0.11 | 0.08 | 0.00 | 0.08 | 0.08 | 0.03 |
| S3B | 0.27 | 0.20 | 0.28 | 0.23 | 0.36 | 0.27 | 0.20 | 0.28 | 0.28 | 0.28 | 0.29 | 0.37 | 0.28 | 0.24 | 0.36 | 0.29 | 0.22 | 0.29 | 0.23 | 0.31 |
| S4B | 0.10 | -0.06 | 0.11 | 0.10 | 0.14 | 0.11 | -0.06 | 0.12 | 0.12 | 0.06 | 0.09 | 0.11 | 0.09 | 0.08 | 0.11 | 0.09 | -0.06 | 0.09 | 0.09 | 0.06 |
| S2B | 0.01 | -0.07 | -0.07 | -0.06 | 0.02 | 0.02 | -0.07 | -0.07 | -0.08 | -0.03 | 0.01 | 0.11 | -0.07 | -0.07 | 0.01 | 0.00 | -0.08 | -0.08 | -0.07 | -0.04 |
| S5A | 0.00 | -0.15 | -0.10 | -0.08 | -0.02 | 0.02 | -0.15 | -0.09 | -0.08 | -0.02 | 0.00 | 0.08 | -0.10 | -0.09 | -0.02 | 0.01 | -0.14 | -0.09 | -0.08 | -0.03 |
| C* | 0.06 | -0.07 | -0.04 | -0.13 | 0.02 | 0.06 | -0.07 | -0.03 | -0.03 | -0.05 | 0.06 | 0.13 | -0.03 | -0.13 | 0.03 | 0.07 | -0.06 | -0.02 | -0.13 | -0.04 |
| X | 0.00 | 0.00 | 0.00 | -0.01 | 0.00 | 0.00 | 0.00 | 0.00 | 0.00 | 0.00 | 0.00 | 0.00 | 0.00 | -0.02 | 0.00 | 0.00 | 0.01 | 0.00 | -0.02 | 0.00 |
| O3 | 0.03 | 0.04 | 0.04 | 0.02 | 0.05 | 0.04 | 0.05 | 0.05 | 0.04 | 0.05 | -0.01 | -0.01 | -0.01 | 0.01 | 0.00 | -0.01 | 0.00 | 0.00 | 0.01 | 0.00 |
| O1 | -0.01 | -0.02 | -0.02 | -0.02 | -0.03 | -0.02 | -0.04 | -0.03 | -0.03 | -0.05 | 0.02 | 0.01 | 0.01 | 0.00 | 0.01 | 0.01 | 0.01 | 0.01 | 0.00 | 0.01 |
| O2 | 0.00 | 0.00 | 0.00 | -0.01 | 0.00 | 0.00 | 0.00 | 0.00 | 0.00 | 0.00 | 0.00 | 0.00 | 0.00 | -0.02 | 0.00 | 0.00 | 0.00 | 0.00 | -0.01 | 0.00 |

Mulliken spin populations of all 35 BS solutions for different FeVco models: Single-point QM/MM calculations using X-ray structure

*Table S 4: Mulliken spin populations of the [**V**-$CO_3$]$^{2-}$ model, $M_S$ = $^3/_2$. Functional: TPSSh*

| No. | *1* | *2* | *3* | *3* | *3* | *4* | *4* | *4* | *5* | *5* | *5* | *5* | *5* | *5* | *6* | *6* | *6* | *7* | *7* | *7* | *8* | *8* | *8* | *8* | *8* | *8* | *9* | *9* | *9* | *10* | *10* | *10* | *10* | *10* | *10* |
|---|---|---|---|---|---|---|---|---|---|---|---|---|---|---|---|---|---|---|---|---|---|---|---|---|---|---|---|---|---|---|---|---|---|---|---|
| Flip | *567* | *234* | *123* | *124* | *134* | *257* | *356* | *467* | *256* | *267* | *357* | *367* | *456* | *457* | *156* | *157* | *167* | *235* | *247* | *346* | *236* | *237* | *245* | *246* | *345* | *347* | *126* | *137* | *145* | *125* | *127* | *135* | *136* | *146* | *147* |
| V | 2.12 | -2.12 | -2.18 | -2.07 | -2.04 | 0.48 | 1.11 | 1.61 | 0.90 | 1.35 | 0.57 | 1.38 | 0.99 | 0.60 | 0.88 | 0.57 | 1.43 | -1.60 | -1.13 | -0.71 | -0.66 | -1.03 | -1.45 | -0.57 | -1.42 | -0.86 | -0.52 | -0.77 | -1.48 | -1.50 | -1.01 | -1.45 | -0.61 | -0.60 | -0.92 |
| Fe1 | 0.81 | 3.46 | -2.34 | -3.38 | -3.37 | 3.31 | 3.32 | 2.15 | 3.28 | 3.20 | 3.31 | 3.29 | 3.15 | 3.23 | -3.45 | -3.45 | -3.48 | 3.44 | 3.37 | 3.34 | 3.40 | 3.41 | 3.36 | 3.34 | 3.34 | 3.32 | -3.32 | -3.33 | -3.39 | -3.32 | -3.32 | -3.35 | -3.35 | -3.41 | -3.40 |
| Fe2 | 3.27 | -3.04 | -3.27 | -3.01 | 3.41 | -3.36 | 2.21 | 3.22 | -3.34 | -3.36 | 2.46 | 2.38 | 3.31 | 2.42 | 3.12 | 3.04 | 3.09 | -3.22 | -3.25 | 3.32 | -3.28 | -3.35 | -3.31 | -3.24 | 3.36 | 3.31 | -3.30 | 3.27 | 3.34 | -3.28 | -3.29 | 3.37 | 3.29 | 3.30 | 3.37 |
| Fe3 | 3.30 | -3.11 | -3.29 | 3.42 | -3.13 | 3.08 | -3.35 | 3.22 | 2.42 | 2.55 | -3.33 | -3.37 | 2.54 | 3.34 | 3.13 | 3.21 | 3.13 | -3.23 | 3.34 | -3.30 | -3.37 | -3.32 | 3.37 | 3.29 | -3.33 | -3.28 | 3.32 | -3.28 | 3.37 | 3.39 | 3.32 | -3.30 | -3.30 | 3.37 | 3.32 |
| Fe4 | 3.32 | -3.23 | 3.41 | -3.28 | -3.23 | 3.13 | 3.29 | -3.44 | 3.38 | 3.26 | 3.38 | 3.28 | -3.43 | -3.41 | 3.20 | 3.21 | 3.20 | 3.43 | -3.36 | -3.35 | 3.39 | 3.41 | -3.38 | -3.47 | -3.35 | -3.44 | 3.42 | 3.45 | -3.32 | 3.44 | 3.45 | 3.47 | 3.47 | -3.34 | -3.34 |
| Fe5 | -3.27 | 3.46 | 3.51 | 3.54 | 3.56 | -3.44 | -3.31 | 3.15 | -3.39 | 3.17 | -3.38 | 3.17 | -3.36 | -3.32 | -3.33 | -3.29 | 3.18 | -3.18 | 3.27 | 3.26 | 3.29 | 3.33 | -3.18 | 3.34 | -3.18 | 3.36 | 3.33 | 3.37 | -3.06 | -3.06 | 3.42 | -3.02 | 3.39 | 3.36 | 3.38 |
| Fe6 | -3.20 | 3.14 | 3.23 | 3.37 | 3.30 | 3.11 | -3.22 | -3.17 | -3.19 | -3.23 | 3.09 | -3.28 | -3.26 | 3.11 | -3.19 | 3.17 | -3.26 | 3.17 | 3.17 | -3.18 | -3.21 | 3.24 | 3.26 | -3.19 | 3.21 | 3.16 | -3.15 | 3.18 | 3.26 | 3.24 | 3.22 | 3.31 | -3.12 | -3.15 | 3.30 |
| Fe7 | -3.28 | 3.24 | 3.28 | 3.36 | 3.45 | -3.28 | 3.12 | -3.23 | 3.06 | -3.33 | -3.21 | -3.28 | 3.07 | -3.27 | 3.13 | -3.21 | -3.31 | 3.22 | -3.14 | 3.20 | 3.24 | -3.15 | 3.26 | 3.16 | 3.30 | -3.14 | 3.22 | -3.10 | 3.33 | 3.33 | -3.09 | 3.28 | 3.22 | 3.29 | -3.11 |
| S1A | 0.31 | 0.00 | -0.04 | -0.41 | -0.03 | -0.01 | 0.26 | -0.05 | 0.10 | 0.04 | 0.28 | 0.24 | 0.09 | 0.05 | 0.02 | 0.01 | 0.00 | 0.18 | -0.13 | 0.15 | 0.14 | 0.12 | -0.16 | -0.17 | 0.15 | 0.10 | -0.11 | 0.19 | -0.10 | -0.09 | -0.11 | 0.17 | 0.17 | -0.12 | -0.14 |
| S2A | 0.27 | 0.02 | -0.27 | -0.05 | -0.08 | 0.05 | -0.01 | 0.20 | 0.07 | 0.07 | 0.08 | 0.05 | 0.26 | 0.28 | -0.02 | -0.01 | 0.00 | -0.06 | 0.17 | 0.13 | -0.11 | -0.11 | 0.14 | 0.15 | 0.12 | 0.13 | -0.11 | -0.12 | 0.13 | -0.11 | -0.11 | -0.15 | -0.14 | 0.11 | 0.11 |
| S4A | 0.27 | -0.03 | -0.03 | -0.03 | -0.38 | 0.36 | 0.03 | -0.01 | 0.25 | 0.22 | 0.08 | 0.05 | 0.05 | 0.11 | 0.04 | 0.05 | 0.03 | 0.15 | 0.15 | -0.14 | 0.09 | 0.13 | 0.14 | 0.09 | -0.15 | -0.16 | 0.17 | -0.10 | -0.09 | 0.17 | 0.17 | -0.10 | -0.12 | -0.11 | -0.10 |
| S1B | -0.25 | 0.29 | 0.31 | 0.30 | 0.30 | -0.01 | -0.24 | -0.08 | -0.25 | -0.08 | -0.02 | -0.09 | -0.26 | 0.00 | -0.25 | 0.01 | -0.08 | 0.08 | 0.23 | -0.01 | -0.01 | 0.26 | 0.09 | 0.01 | 0.07 | 0.24 | 0.00 | 0.25 | 0.11 | 0.10 | 0.26 | 0.10 | 0.01 | 0.01 | 0.25 |
| S3B | -0.32 | 0.25 | 0.27 | 0.31 | 0.32 | 0.00 | -0.05 | -0.27 | -0.04 | -0.29 | 0.01 | -0.29 | -0.07 | -0.01 | -0.04 | 0.01 | -0.31 | 0.26 | 0.04 | -0.02 | 0.00 | 0.06 | 0.29 | -0.03 | 0.28 | 0.03 | 0.01 | 0.07 | 0.30 | 0.30 | 0.06 | 0.30 | 0.01 | 0.00 | 0.07 |
| S4B | -0.29 | 0.30 | 0.33 | 0.32 | 0.33 | -0.26 | -0.02 | -0.10 | -0.03 | -0.10 | -0.24 | -0.09 | -0.02 | -0.25 | 0.00 | -0.24 | -0.10 | 0.10 | 0.01 | 0.23 | 0.24 | 0.01 | 0.08 | 0.23 | 0.10 | 0.02 | 0.24 | 0.01 | 0.12 | 0.11 | 0.03 | 0.12 | 0.25 | 0.25 | 0.02 |
| S2B | -0.03 | 0.06 | 0.03 | 0.24 | 0.50 | 0.04 | -0.19 | -0.06 | -0.46 | -0.47 | 0.21 | -0.21 | -0.07 | 0.23 | -0.09 | 0.40 | -0.12 | 0.03 | 0.03 | -0.05 | -0.45 | 0.01 | 0.03 | -0.45 | 0.46 | 0.44 | -0.45 | 0.42 | 0.46 | 0.03 | 0.03 | 0.49 | -0.02 | -0.04 | 0.48 |
| S5A | 0.01 | 0.02 | -0.02 | 0.46 | 0.17 | -0.15 | -0.07 | -0.01 | 0.14 | -0.19 | -0.41 | -0.44 | 0.15 | -0.01 | 0.36 | -0.04 | -0.08 | -0.01 | 0.03 | -0.03 | -0.04 | -0.38 | 0.42 | 0.38 | 0.00 | -0.38 | 0.39 | -0.38 | 0.43 | 0.44 | 0.03 | -0.02 | -0.04 | 0.41 | 0.03 |
| C* | -0.03 | 0.03 | -0.09 | 0.00 | 0.01 | -0.14 | -0.03 | -0.08 | -0.03 | -0.03 | -0.03 | -0.03 | -0.12 | -0.11 | -0.24 | -0.22 | -0.21 | 0.03 | -0.01 | -0.03 | 0.03 | 0.04 | -0.03 | -0.04 | -0.03 | -0.02 | -0.13 | -0.11 | -0.13 | -0.09 | -0.06 | -0.09 | -0.09 | -0.16 | -0.14 |
| C | 0.00 | 0.00 | 0.01 | 0.00 | 0.00 | 0.00 | 0.00 | 0.00 | 0.00 | 0.01 | 0.00 | 0.01 | -0.01 | -0.01 | 0.00 | 0.00 | 0.01 | 0.00 | 0.00 | 0.00 | 0.01 | 0.01 | -0.01 | 0.00 | -0.01 | 0.00 | 0.01 | 0.01 | -0.01 | 0.00 | 0.01 | 0.00 | 0.01 | 0.00 | 0.00 |
| O3 | 0.03 | -0.04 | 0.06 | -0.02 | -0.01 | 0.02 | 0.03 | -0.05 | 0.03 | 0.04 | 0.04 | 0.05 | -0.06 | -0.06 | 0.03 | 0.03 | 0.05 | 0.04 | -0.04 | -0.04 | 0.06 | 0.05 | -0.06 | -0.06 | -0.06 | -0.05 | 0.06 | 0.07 | -0.05 | 0.05 | 0.06 | 0.05 | 0.07 | -0.04 | -0.04 |
| O1 | -0.03 | 0.04 | 0.06 | 0.05 | 0.05 | -0.05 | -0.03 | 0.02 | -0.04 | 0.04 | -0.04 | 0.04 | -0.05 | -0.05 | -0.04 | -0.04 | 0.04 | -0.02 | 0.03 | 0.03 | 0.05 | 0.05 | -0.04 | 0.03 | -0.04 | 0.03 | 0.04 | 0.04 | -0.03 | -0.02 | 0.04 | -0.02 | 0.05 | 0.03 | 0.03 |
| O2 | 0.00 | 0.00 | 0.03 | 0.00 | 0.01 | -0.01 | 0.00 | 0.00 | 0.00 | 0.02 | 0.00 | 0.02 | -0.03 | -0.02 | 0.00 | -0.01 | 0.02 | 0.00 | 0.00 | 0.00 | 0.02 | 0.02 | -0.02 | 0.00 | -0.02 | 0.00 | 0.02 | 0.02 | -0.02 | 0.00 | 0.02 | 0.00 | 0.03 | 0.00 | 0.00 |

*Table S 5 Mulliken spin populations of the [**V**-$CO_3$]$^{2-}$ model, $M_S$ = $^1/_2$. Functional: TPSSh*

| No. | *1* | *2* | *3* | *3* | *3* | *4* | *4* | *4* | *5* | *5* | *5* | *5* | *5* | *5* | *6* | *6* | *6* | *7* | *7* | *7* | *8* | *8* | *8* | *8* | *8* | *8* | *9* | *9* | *9* | *10* | *10* | *10* | *10* | *10* | *10* |
|---|---|---|---|---|---|---|---|---|---|---|---|---|---|---|---|---|---|---|---|---|---|---|---|---|---|---|---|---|---|---|---|---|---|---|---|
| Flip | *567* | *234* | *123* | *124* | *134* | *257* | *356* | *467* | *256* | *267* | *357* | *367* | *456* | *457* | *156* | *157* | *167* | *235* | *247* | *346* | *236* | *237* | *245* | *246* | *345* | *347* | *126* | *137* | *145* | *125* | *127* | *135* | *136* | *146* | *147* |
| V | 2.09 | -2.15 | -2.12 | -2.12 | -2.12 | 0.33 | 1.09 | 1.60 | 1.06 | 1.50 | 0.58 | 1.42 | 0.86 | 0.54 | 0.88 | 0.60 | 1.66 | -1.55 | -1.09 | -0.75 | -0.66 | -1.34 | -1.41 | -0.53 | -1.37 | -0.89 | -0.70 | -0.99 | -1.55 | -1.49 | -1.14 | -1.48 | -0.76 | -0.67 | -1.04 |
| Fe1 | 0.78 | 3.46 | -3.42 | -3.48 | -3.42 | 2.27 | 3.42 | 0.05 | 3.43 | 3.40 | 3.41 | 1.72 | 2.37 | 2.41 | -3.49 | -3.49 | -3.47 | 3.34 | 2.82 | 1.84 | 3.40 | 3.40 | 3.33 | 3.32 | 3.30 | 3.29 | -3.36 | -3.37 | -3.41 | -3.33 | -3.38 | -3.34 | -3.38 | -3.41 | -3.40 |
| Fe2 | 3.02 | -3.19 | 3.28 | -3.34 | 3.28 | -3.38 | -0.61 | 3.20 | -2.24 | -3.33 | 0.12 | 2.32 | 2.99 | 2.50 | 2.77 | 2.41 | 2.91 | -3.39 | -3.41 | 3.27 | -3.28 | -3.35 | -3.31 | -3.34 | 2.91 | 2.74 | -3.32 | 2.82 | 3.06 | -3.35 | -3.32 | 2.88 | 2.94 | 3.07 | 2.87 |
| Fe3 | 3.04 | -3.32 | -3.32 | 3.33 | -3.32 | 3.08 | -3.22 | 3.25 | -2.91 | -0.29 | -3.32 | -3.36 | 2.52 | 3.01 | 2.57 | 2.95 | 3.01 | -3.46 | 3.20 | -3.31 | -3.37 | -3.35 | 2.95 | 3.22 | -3.34 | -3.31 | 2.89 | -3.35 | 3.17 | 3.12 | 3.11 | -3.36 | -3.36 | 2.85 | 3.14 |
| Fe4 | 3.19 | -3.35 | -3.33 | -3.36 | -3.33 | 3.24 | 3.34 | -3.43 | 3.48 | 3.32 | 3.40 | 3.30 | -3.42 | -3.40 | 3.07 | 3.08 | 2.89 | 3.01 | -3.57 | -3.37 | 3.39 | 3.34 | -3.42 | -3.49 | -3.37 | -3.45 | 3.15 | 3.14 | -3.40 | 3.31 | 3.02 | 3.34 | 2.95 | -3.41 | -3.39 |
| Fe5 | -3.49 | 3.18 | 3.39 | 3.34 | 3.39 | -3.44 | -3.29 | 3.16 | -3.14 | 3.18 | -3.38 | 3.16 | -3.40 | -3.36 | -3.36 | -3.32 | 2.18 | -3.23 | 3.22 | 3.27 | 3.29 | 2.00 | -3.23 | 3.25 | -3.23 | 3.17 | 3.25 | 3.33 | -3.15 | -3.16 | 3.17 | -3.17 | 3.23 | 3.20 | 3.24 |
| Fe6 | -3.34 | 2.91 | 3.08 | 3.15 | 3.08 | 2.69 | -3.16 | -3.18 | -2.56 | -3.17 | 3.14 | -3.26 | -3.28 | 2.90 | -3.21 | 2.76 | -3.31 | 3.05 | 3.13 | -3.18 | -3.21 | 3.15 | 2.98 | -3.27 | 2.67 | 2.67 | -3.17 | 2.99 | 3.01 | 2.98 | 3.05 | 2.99 | -3.14 | -3.21 | 2.98 |
| Fe7 | -3.41 | 2.97 | 3.15 | 3.28 | 3.15 | -3.34 | 3.18 | -3.22 | 3.17 | -3.32 | -3.25 | -3.28 | 2.90 | -3.30 | 2.74 | -3.23 | -3.36 | 3.06 | -3.18 | 3.20 | 3.24 | -3.14 | 2.74 | 1.81 | 3.09 | -3.15 | 2.97 | -3.11 | 3.13 | 2.89 | -3.13 | 3.12 | 3.16 | 3.06 | -3.19 |
| S1A | 0.26 | -0.05 | -0.05 | -0.53 | -0.05 | 0.03 | 0.33 | -0.06 | 0.24 | 0.11 | 0.30 | -0.03 | 0.06 | 0.01 | -0.04 | -0.01 | -0.01 | -0.39 | 0.00 | 0.14 | 0.11 | -0.17 | -0.17 | 0.05 | 0.03 | -0.23 | 0.06 | -0.20 | -0.12 | -0.23 | 0.09 | 0.03 | -0.14 | -0.21 | |
| S2A | 0.19 | -0.03 | -0.14 | -0.16 | -0.14 | 0.03 | 0.05 | 0.19 | 0.08 | 0.07 | 0.05 | -0.09 | 0.04 | 0.03 | -0.04 | -0.03 | -0.04 | -0.20 | 0.06 | 0.03 | -0.11 | -0.13 | 0.06 | 0.13 | 0.05 | 0.04 | -0.20 | -0.22 | 0.06 | -0.21 | -0.13 | -0.23 | -0.16 | 0.02 | 0.03 |
| S4A | 0.26 | -0.03 | -0.45 | -0.04 | -0.45 | 0.21 | 0.08 | 0.01 | 0.18 | 0.26 | 0.10 | 0.00 | 0.01 | 0.09 | 0.02 | 0.00 | 0.02 | -0.01 | -0.01 | -0.27 | 0.09 | 0.13 | 0.07 | 0.07 | -0.16 | -0.16 | 0.06 | -0.21 | -0.16 | 0.11 | 0.04 | -0.12 | -0.22 | -0.20 | -0.11 |
| S1B | -0.31 | 0.23 | 0.28 | 0.25 | 0.28 | -0.09 | -0.22 | -0.08 | -0.15 | -0.07 | -0.04 | -0.09 | -0.25 | -0.02 | -0.23 | -0.03 | -0.20 | 0.07 | 0.22 | -0.01 | -0.01 | 0.10 | 0.07 | -0.01 | 0.05 | 0.16 | 0.00 | 0.23 | 0.05 | 0.08 | 0.19 | 0.04 | 0.00 | 0.00 | 0.20 |
| S3B | -0.33 | 0.24 | 0.28 | 0.31 | 0.28 | -0.09 | -0.02 | -0.27 | 0.00 | -0.28 | 0.01 | -0.29 | -0.09 | -0.04 | -0.08 | -0.03 | -0.33 | 0.23 | 0.04 | -0.01 | 0.00 | 0.08 | 0.17 | -0.01 | 0.18 | 0.02 | -0.05 | 0.02 | 0.25 | 0.21 | 0.05 | 0.24 | 0.01 | -0.06 | -0.01 |
| S4B | -0.33 | 0.27 | 0.27 | 0.30 | 0.27 | -0.26 | -0.02 | -0.10 | -0.01 | -0.10 | -0.23 | -0.09 | -0.03 | -0.24 | -0.04 | -0.22 | -0.20 | 0.08 | 0.01 | 0.24 | 0.24 | 0.03 | 0.07 | 0.14 | 0.09 | 0.01 | 0.22 | 0.02 | 0.08 | 0.06 | 0.02 | 0.10 | 0.21 | 0.20 | 0.02 |
| S2B | -0.18 | -0.06 | 0.41 | 0.00 | 0.41 | -0.07 | -0.29 | -0.04 | -0.22 | -0.46 | 0.26 | -0.18 | -0.13 | 0.23 | -0.14 | 0.23 | -0.13 | -0.02 | -0.01 | -0.02 | -0.45 | 0.00 | -0.02 | -0.48 | 0.22 | 0.20 | -0.45 | 0.35 | 0.37 | 0.00 | 0.01 | 0.36 | -0.10 | -0.08 | 0.35 |
| S5A | -0.14 | -0.13 | -0.01 | 0.41 | -0.01 | -0.07 | -0.01 | 0.01 | 0.03 | -0.21 | -0.42 | -0.42 | 0.18 | -0.07 | 0.18 | -0.08 | -0.09 | -0.09 | -0.07 | -0.02 | -0.04 | -0.36 | 0.19 | 0.28 | -0.05 | -0.40 | 0.29 | -0.38 | 0.36 | 0.32 | -0.03 | -0.04 | -0.04 | 0.30 | 0.00 |
| C* | -0.25 | -0.18 | -0.18 | -0.18 | -0.18 | -0.13 | 0.17 | -0.06 | 0.37 | 0.13 | 0.08 | -0.01 | -0.19 | -0.16 | -0.37 | -0.35 | -0.34 | -0.08 | -0.07 | 0.01 | 0.03 | 0.02 | -0.15 | -0.05 | -0.15 | -0.11 | -0.30 | -0.30 | -0.38 | -0.30 | -0.25 | -0.29 | -0.28 | -0.34 | -0.32 |
| C | 0.00 | 0.00 | 0.00 | 0.00 | 0.00 | 0.00 | 0.00 | 0.00 | 0.00 | 0.01 | 0.00 | 0.01 | -0.01 | -0.01 | 0.00 | 0.00 | 0.01 | 0.00 | 0.00 | 0.00 | 0.01 | 0.01 | -0.01 | 0.00 | -0.01 | 0.00 | 0.02 | 0.02 | -0.01 | 0.00 | 0.01 | 0.00 | 0.01 | 0.00 | 0.00 |
| O3 | 0.02 | -0.05 | -0.03 | -0.03 | -0.03 | 0.03 | 0.03 | -0.04 | 0.04 | 0.05 | 0.04 | 0.05 | -0.06 | -0.06 | 0.03 | 0.03 | 0.03 | 0.02 | -0.06 | -0.04 | 0.06 | 0.05 | -0.07 | -0.06 | -0.06 | -0.05 | 0.04 | 0.04 | -0.05 | 0.05 | 0.04 | 0.05 | 0.03 | -0.04 | -0.04 |
| O1 | -0.04 | 0.02 | 0.04 | 0.03 | 0.04 | -0.04 | -0.03 | 0.02 | -0.02 | 0.04 | -0.03 | 0.04 | -0.05 | -0.05 | -0.04 | -0.04 | 0.01 | -0.03 | 0.02 | 0.03 | 0.05 | 0.03 | -0.04 | 0.03 | -0.04 | 0.02 | 0.04 | 0.05 | -0.03 | -0.02 | 0.04 | -0.02 | 0.04 | 0.03 | 0.03 |
| O2 | -0.01 | 0.00 | 0.00 | 0.00 | 0.00 | 0.00 | 0.00 | 0.00 | 0.00 | 0.02 | 0.00 | 0.02 | -0.03 | -0.02 | -0.01 | -0.01 | 0.01 | 0.00 | -0.01 | 0.00 | 0.02 | 0.01 | -0.02 | 0.00 | -0.02 | 0.00 | 0.02 | 0.02 | -0.02 | 0.00 | 0.02 | 0.00 | 0.02 | 0.00 | 0.00 |

*Table S 6: Mulliken spin populations of the [**V**-$CO_3$]$^-$ model, $M_S$ = 0. Functional: TPSSh*

| BS | 1 | 2 | 3 | 3 | 3 | 4 | 4 | 4 | 5 | 5 | 5 | 5 | 5 | 5 | 6 | 6 | 6 | 7 | 7 | 7 | 8 | 8 | 8 | 8 | 8 | 8 | 9 | 9 | 9 | 10 | 10 | 10 | 10 | 10 | 10 |
|---|---|---|---|---|---|---|---|---|---|---|---|---|---|---|---|---|---|---|---|---|---|---|---|---|---|---|---|---|---|---|---|---|---|---|---|
| Flip | 567 | 234 | 123 | 124 | 134 | 257 | 356 | 467 | 256 | 267 | 357 | 367 | 456 | 457 | 156 | 157 | 167 | 235 | 247 | 346 | 236 | 237 | 245 | 246 | 345 | 347 | 126 | 137 | 145 | 125 | 127 | 135 | 136 | 146 | 147 |
| V | 1.97 | -2.04 | -2.06 | -1.97 | -2.01 | 0.35 | 0.83 | 1.60 | 1.01 | 1.64 | 0.54 | 1.57 | 1.13 | 0.58 | 0.68 | 0.35 | 1.68 | -1.60 | -1.24 | -0.70 | -0.33 | -1.25 | -1.67 | -0.40 | -1.64 | -0.76 | -0.55 | -1.02 | -1.55 | -1.55 | -1.15 | -1.53 | -0.72 | -0.54 | -1.01 |
| Fe1 | -1.41 | 3.48 | -3.59 | -3.54 | -3.55 | 0.33 | 0.35 | -2.64 | 3.45 | -2.68 | 3.45 | 3.43 | 3.28 | 3.32 | -3.50 | -3.50 | -3.49 | 2.64 | 2.61 | 2.41 | 3.41 | 2.35 | 3.29 | 3.45 | 3.25 | 3.48 | -3.61 | -3.34 | -3.43 | -3.35 | -3.43 | -3.37 | -3.43 | -3.45 | -3.45 |
| Fe2 | 3.26 | -3.19 | -3.42 | -3.40 | 3.17 | -3.41 | 3.14 | 3.41 | -2.40 | -2.74 | -3.01 | -1.73 | 3.29 | -1.06 | 2.84 | 1.91 | 2.48 | -3.41 | -3.40 | 2.80 | -3.38 | -3.43 | -3.36 | -3.14 | 2.93 | -0.31 | -3.45 | 1.45 | 3.15 | -3.33 | -3.34 | 2.99 | 2.89 | 3.01 | 2.40 |
| Fe3 | 3.29 | -3.28 | -3.45 | 3.16 | -3.43 | 3.20 | -3.45 | 3.46 | -3.09 | 3.44 | -2.49 | -3.27 | -1.00 | 3.33 | 1.98 | 3.02 | 2.76 | -3.46 | 2.70 | -3.44 | -3.41 | -3.44 | 2.96 | -0.25 | -3.40 | -3.20 | 2.78 | -3.32 | 1.97 | 3.11 | 2.89 | -3.36 | -3.39 | 2.49 | 3.09 |
| Fe4 | 3.31 | -3.35 | 3.37 | -3.44 | -3.40 | 3.29 | 3.27 | -3.12 | 3.45 | 3.48 | 3.46 | 3.40 | -3.43 | -3.38 | 3.14 | 3.13 | 2.97 | 3.12 | -3.59 | -3.57 | 3.28 | 3.16 | -3.53 | -3.41 | -3.49 | -3.38 | 2.96 | 3.32 | -3.41 | 3.27 | 2.81 | 3.30 | 2.75 | -3.46 | -3.45 |
| Fe5 | -3.48 | 3.32 | 3.41 | 3.31 | 3.38 | -3.45 | -3.46 | 3.25 | -3.20 | 3.27 | -3.13 | 3.24 | -3.39 | -3.33 | -3.50 | -3.48 | 2.10 | -3.25 | 3.22 | 3.24 | 1.31 | 3.30 | -3.33 | 3.32 | -3.32 | 3.38 | 3.29 | 3.37 | -3.25 | -3.25 | 3.13 | -3.24 | 3.10 | 3.13 | 3.20 |
| Fe6 | -3.31 | 3.12 | 3.08 | 3.05 | 2.87 | 3.16 | -3.30 | -3.11 | -2.87 | -3.10 | 3.25 | -3.15 | -3.24 | 3.19 | -3.29 | 2.74 | -3.39 | 3.11 | 3.12 | -3.21 | -3.32 | 3.00 | 2.88 | -3.22 | 2.42 | 3.13 | -3.20 | 3.10 | 3.13 | 2.90 | 2.96 | 2.38 | -3.22 | -3.25 | 2.87 |
| Fe7 | -3.38 | 1.22 | 3.17 | 3.06 | 3.14 | -3.33 | 3.12 | -3.12 | 3.20 | -3.18 | -2.88 | -3.22 | 3.10 | -3.25 | 2.73 | -3.32 | -3.44 | 3.12 | -3.14 | 3.11 | 2.85 | -3.16 | 2.46 | 3.14 | 2.99 | -3.16 | 3.01 | -3.20 | 3.19 | 2.36 | -3.18 | 3.05 | 2.99 | 2.88 | -3.20 |
| S1A | 0.32 | -0.08 | -0.19 | -0.56 | -0.10 | -0.08 | 0.26 | 0.14 | 0.21 | 0.11 | 0.15 | 0.19 | 0.08 | 0.04 | 0.01 | 0.02 | 0.00 | -0.14 | -0.39 | -0.13 | 0.07 | -0.13 | -0.19 | -0.08 | 0.03 | 0.06 | -0.35 | 0.00 | -0.15 | -0.13 | -0.28 | 0.10 | -0.02 | -0.15 | -0.21 |
| S2A | 0.36 | -0.03 | -0.56 | -0.16 | -0.18 | -0.04 | -0.06 | 0.35 | 0.03 | 0.06 | 0.04 | 0.01 | 0.19 | 0.20 | -0.01 | 0.00 | -0.01 | -0.35 | -0.05 | -0.07 | -0.16 | -0.33 | 0.05 | 0.13 | 0.03 | 0.15 | -0.30 | -0.21 | -0.01 | -0.16 | -0.14 | -0.19 | -0.16 | -0.04 | -0.03 |
| S4A | 0.29 | -0.06 | -0.20 | -0.08 | -0.50 | 0.30 | -0.07 | 0.11 | 0.11 | 0.31 | 0.19 | 0.12 | 0.04 | 0.12 | 0.05 | 0.04 | 0.05 | -0.11 | -0.06 | -0.36 | 0.06 | -0.10 | 0.04 | 0.05 | -0.18 | -0.09 | -0.05 | -0.15 | -0.16 | 0.10 | -0.02 | -0.12 | -0.26 | -0.19 | -0.11 |
| S1B | -0.33 | 0.31 | 0.31 | 0.26 | 0.29 | 0.01 | -0.29 | -0.10 | -0.19 | -0.09 | 0.01 | -0.09 | -0.27 | 0.00 | -0.27 | -0.04 | -0.23 | 0.10 | 0.24 | -0.01 | -0.03 | 0.25 | 0.11 | -0.01 | 0.08 | 0.25 | -0.02 | 0.27 | 0.08 | 0.10 | 0.19 | 0.06 | -0.03 | -0.01 | 0.19 |
| S3B | -0.34 | 0.19 | 0.25 | 0.29 | 0.26 | 0.01 | -0.04 | -0.25 | -0.02 | -0.27 | 0.05 | -0.29 | -0.08 | -0.01 | -0.08 | -0.03 | -0.36 | 0.25 | 0.07 | -0.02 | -0.04 | 0.09 | 0.15 | -0.03 | 0.16 | 0.04 | -0.06 | 0.05 | 0.28 | 0.13 | 0.05 | 0.14 | -0.01 | -0.05 | 0.02 |
| S4B | -0.35 | 0.18 | 0.34 | 0.31 | 0.30 | -0.27 | -0.02 | -0.10 | -0.02 | -0.13 | -0.16 | -0.09 | -0.04 | -0.24 | -0.05 | -0.25 | -0.25 | 0.10 | 0.03 | 0.23 | 0.05 | 0.04 | 0.09 | 0.23 | 0.12 | 0.01 | 0.23 | 0.02 | 0.11 | 0.09 | -0.01 | 0.12 | 0.18 | 0.16 | 0.02 |
| S2B | -0.12 | 0.04 | -0.06 | -0.08 | 0.33 | 0.02 | -0.13 | 0.05 | -0.24 | -0.27 | 0.08 | -0.29 | -0.04 | 0.30 | -0.19 | 0.19 | -0.15 | -0.05 | -0.06 | -0.10 | -0.51 | -0.10 | -0.04 | -0.44 | 0.17 | 0.32 | -0.52 | 0.24 | 0.43 | 0.02 | 0.02 | 0.25 | -0.10 | -0.08 | 0.24 |
| S5A | -0.05 | -0.18 | -0.12 | 0.28 | -0.10 | -0.07 | -0.07 | 0.12 | -0.01 | 0.08 | -0.17 | -0.42 | 0.27 | 0.02 | 0.16 | -0.12 | -0.10 | -0.12 | -0.05 | -0.15 | -0.15 | -0.42 | 0.15 | 0.27 | -0.09 | -0.37 | 0.30 | -0.38 | 0.24 | 0.23 | -0.03 | -0.03 | -0.06 | 0.17 | 0.01 |
| C* | -0.13 | 0.03 | -0.23 | -0.25 | -0.24 | -0.08 | -0.09 | 0.07 | 0.37 | 0.06 | 0.39 | 0.27 | 0.11 | 0.16 | -0.35 | -0.37 | -0.39 | -0.07 | -0.06 | -0.09 | -0.03 | -0.05 | -0.14 | 0.13 | -0.13 | 0.15 | -0.31 | -0.17 | -0.29 | -0.36 | -0.38 | -0.35 | -0.40 | -0.39 | -0.37 |
| C | 0.00 | 0.00 | 0.01 | 0.00 | 0.00 | 0.00 | 0.00 | 0.00 | 0.00 | 0.01 | 0.00 | 0.01 | -0.01 | -0.01 | 0.00 | 0.00 | 0.01 | 0.00 | 0.00 | 0.00 | 0.00 | 0.01 | -0.01 | 0.00 | -0.01 | 0.00 | 0.01 | 0.01 | -0.01 | 0.00 | 0.01 | 0.00 | 0.01 | 0.00 | 0.00 |
| O3 | 0.03 | -0.05 | 0.08 | -0.05 | -0.05 | 0.04 | 0.03 | -0.03 | 0.05 | 0.08 | 0.05 | 0.06 | -0.07 | -0.08 | 0.03 | 0.03 | 0.04 | 0.03 | -0.07 | -0.07 | 0.05 | 0.05 | -0.09 | -0.06 | -0.08 | -0.05 | 0.04 | 0.06 | -0.06 | 0.05 | 0.02 | 0.05 | 0.02 | -0.05 | -0.05 |
| O1 | -0.05 | 0.04 | 0.06 | 0.04 | 0.04 | -0.05 | -0.05 | 0.03 | -0.03 | 0.05 | -0.03 | 0.04 | -0.05 | -0.06 | -0.06 | -0.05 | 0.01 | -0.03 | 0.03 | 0.03 | 0.02 | 0.05 | -0.05 | 0.04 | -0.04 | 0.05 | 0.05 | 0.06 | -0.04 | -0.03 | 0.05 | -0.03 | 0.05 | 0.03 | 0.03 |
| O2 | -0.01 | 0.00 | 0.03 | 0.00 | 0.00 | -0.01 | -0.01 | 0.00 | 0.00 | 0.03 | 0.00 | 0.03 | -0.03 | -0.03 | -0.01 | -0.01 | 0.01 | 0.00 | -0.01 | -0.01 | 0.02 | 0.02 | -0.03 | 0.00 | -0.03 | 0.00 | 0.03 | 0.03 | -0.03 | 0.00 | 0.02 | 0.00 | 0.02 | 0.00 | 0.00 |

*Table S 7 Mulliken spin populations of the [**V**-$CO_3$]$^-$ model, $M_S$ = 1. Functional: TPSSh*

| BS | 1 | 2 | 3 | 3 | 3 | 4 | 4 | 4 | 5 | 5 | 5 | 5 | 5 | 5 | 6 | 6 | 6 | 7 | 7 | 7 | 8 | 8 | 8 | 8 | 8 | 8 | 9 | 9 | 9 | 10 | 10 | 10 | 10 | 10 | 10 |
|---|---|---|---|---|---|---|---|---|---|---|---|---|---|---|---|---|---|---|---|---|---|---|---|---|---|---|---|---|---|---|---|---|---|---|---|
| Flip | 567 | 234 | 123 | 124 | 134 | 257 | 356 | 467 | 256 | 267 | 357 | 367 | 456 | 457 | 156 | 157 | 167 | 235 | 247 | 346 | 236 | 237 | 245 | 246 | 345 | 347 | 126 | 137 | 145 | 125 | 127 | 135 | 136 | 146 | 147 |
| V | 1.97 | -2.02 | -2.02 | -1.93 | -1.90 | 0.36 | 0.85 | 1.59 | 0.94 | 1.45 | 0.55 | 1.50 | 1.09 | 0.59 | 0.85 | 0.45 | 1.42 | -1.60 | -1.10 | -0.60 | -0.55 | -0.92 | -1.47 | -0.40 | -1.44 | -0.74 | -0.31 | -0.75 | -1.52 | -1.49 | -1.13 | -1.46 | -0.68 | -0.57 | -0.97 |
| Fe1 | 0.96 | 3.47 | -3.43 | -3.52 | -3.53 | 2.42 | 2.52 | 2.08 | 2.46 | 2.37 | 3.38 | 2.56 | 2.43 | 2.41 | -3.50 | -3.50 | -3.49 | 3.44 | 3.33 | 3.27 | 3.42 | 3.43 | 3.37 | 3.32 | 3.34 | 3.29 | -3.35 | -3.36 | -3.43 | -3.35 | -3.40 | -3.37 | -3.39 | -3.44 | -3.43 |
| Fe2 | 3.25 | -3.21 | -3.35 | -3.34 | 3.37 | -3.37 | 3.03 | 3.16 | -3.30 | -3.36 | 0.90 | 2.79 | 3.19 | 2.64 | 2.91 | 2.90 | 2.87 | -3.38 | -3.37 | 3.29 | -3.35 | -3.37 | -3.28 | -3.22 | 3.13 | 2.98 | -3.29 | 3.09 | 3.23 | -3.28 | -3.28 | 3.23 | 3.14 | 3.13 | 3.20 |
| Fe3 | 3.27 | -3.31 | -3.31 | 3.38 | -3.39 | 3.10 | -3.40 | 2.82 | 2.60 | 2.87 | -3.26 | -3.38 | 2.68 | 3.24 | 2.99 | 3.09 | 3.03 | -3.44 | 3.31 | -3.41 | -3.45 | -3.33 | 3.17 | 2.99 | -3.32 | -3.26 | 3.17 | -3.31 | 3.32 | 3.29 | 3.23 | -3.31 | -3.32 | 3.22 | 3.21 |
| Fe4 | 3.25 | -3.36 | 3.46 | -3.36 | -3.31 | 3.26 | 3.21 | -3.46 | 3.34 | 3.17 | 3.46 | 3.06 | -3.41 | -3.37 | 3.21 | 3.21 | 3.02 | 3.43 | -3.56 | -3.53 | 3.30 | 3.26 | -3.38 | -3.47 | -3.35 | -3.44 | 3.42 | 3.43 | -3.37 | 3.43 | 3.40 | 3.44 | 3.39 | -3.39 | -3.37 |
| Fe5 | -3.48 | 3.22 | 3.48 | 3.55 | 3.56 | -3.45 | -3.47 | 3.16 | -3.40 | 3.16 | -3.36 | 3.17 | -3.39 | -3.35 | -3.41 | -3.36 | 3.07 | -3.23 | 3.17 | 3.22 | 3.18 | 3.15 | -3.22 | 3.26 | -3.20 | 3.31 | 3.24 | 3.32 | -3.17 | -3.18 | 3.32 | -3.16 | 3.29 | 3.31 | 3.30 |
| Fe6 | -3.31 | 3.15 | 3.33 | 3.33 | 3.26 | 3.16 | -3.30 | -3.23 | -3.17 | -3.27 | 3.18 | -3.33 | -3.27 | 3.15 | -3.20 | 2.99 | -3.28 | 3.11 | 3.10 | -3.22 | -3.26 | 2.90 | 3.13 | -3.22 | 2.91 | 2.87 | -3.22 | 2.97 | 3.15 | 3.05 | 3.04 | 3.14 | -3.19 | -3.22 | 3.13 |
| Fe7 | -3.38 | 3.25 | 3.39 | 3.32 | 3.40 | -3.33 | 3.11 | -3.31 | 3.05 | -3.37 | -3.16 | -3.30 | 3.07 | -3.29 | 2.95 | -3.24 | -3.34 | 3.10 | -3.18 | 3.08 | 2.94 | -3.18 | 2.92 | 2.83 | 3.20 | -3.17 | 2.87 | -3.17 | 3.24 | 3.14 | -3.14 | 3.14 | 3.12 | 3.16 | -3.17 |
| S1A | 0.30 | -0.09 | -0.10 | -0.52 | -0.05 | 0.03 | 0.17 | -0.03 | 0.10 | 0.02 | 0.19 | 0.05 | 0.08 | 0.03 | 0.01 | 0.04 | 0.02 | 0.14 | -0.24 | 0.05 | 0.08 | 0.07 | -0.17 | -0.17 | 0.07 | 0.05 | -0.12 | 0.16 | -0.16 | -0.08 | -0.12 | 0.15 | 0.12 | -0.15 | -0.14 |
| S2A | 0.27 | -0.07 | -0.50 | -0.15 | -0.17 | 0.02 | -0.02 | 0.02 | -0.04 | 0.02 | 0.05 | 0.01 | 0.02 | 0.01 | 0.01 | 0.01 | -0.01 | -0.17 | 0.14 | 0.09 | -0.16 | -0.14 | 0.10 | 0.06 | 0.10 | 0.04 | -0.16 | -0.18 | 0.11 | -0.13 | -0.12 | -0.15 | -0.15 | 0.08 | 0.09 |
| S4A | 0.27 | -0.05 | -0.06 | -0.04 | -0.47 | 0.22 | 0.00 | -0.03 | 0.03 | 0.08 | 0.13 | 0.03 | 0.02 | 0.09 | 0.06 | 0.04 | 0.06 | 0.10 | 0.08 | -0.22 | 0.06 | 0.06 | 0.09 | 0.06 | -0.17 | -0.16 | 0.15 | -0.10 | -0.11 | 0.15 | 0.12 | -0.09 | -0.11 | -0.12 | -0.10 |
| S1B | -0.33 | 0.25 | 0.33 | 0.33 | 0.31 | 0.00 | -0.29 | -0.10 | -0.27 | -0.11 | 0.00 | -0.12 | -0.29 | 0.00 | -0.27 | -0.01 | -0.11 | 0.10 | 0.23 | -0.02 | -0.03 | 0.18 | 0.10 | 0.00 | 0.10 | 0.19 | -0.02 | 0.22 | 0.09 | 0.09 | 0.22 | 0.09 | 0.02 | 0.02 | 0.23 |
| S3B | -0.34 | 0.33 | 0.34 | 0.32 | 0.32 | 0.01 | -0.05 | -0.31 | -0.05 | -0.32 | 0.05 | -0.33 | -0.08 | 0.00 | -0.07 | 0.00 | -0.33 | 0.26 | 0.05 | -0.03 | -0.02 | 0.06 | 0.21 | -0.04 | 0.22 | 0.03 | -0.07 | 0.01 | 0.28 | 0.25 | 0.06 | 0.26 | 0.00 | -0.03 | 0.04 |
| S4B | -0.35 | 0.30 | 0.35 | 0.34 | 0.35 | -0.27 | -0.02 | -0.12 | -0.03 | -0.13 | -0.24 | -0.11 | -0.03 | -0.27 | -0.03 | -0.25 | -0.12 | 0.11 | 0.01 | 0.22 | 0.19 | 0.00 | 0.11 | 0.16 | 0.12 | 0.02 | 0.18 | 0.00 | 0.11 | 0.11 | 0.05 | 0.10 | 0.21 | 0.21 | 0.03 |
| S2B | -0.11 | -0.01 | 0.08 | 0.10 | 0.50 | 0.03 | -0.17 | -0.06 | -0.47 | -0.51 | 0.17 | -0.18 | -0.06 | 0.28 | -0.12 | 0.34 | -0.17 | -0.05 | -0.08 | -0.04 | -0.49 | -0.08 | 0.03 | -0.46 | 0.27 | 0.24 | -0.48 | 0.38 | 0.43 | 0.03 | 0.01 | 0.41 | -0.08 | -0.06 | 0.40 |
| S5A | -0.06 | -0.08 | 0.07 | 0.47 | 0.02 | -0.09 | -0.07 | -0.08 | 0.17 | -0.14 | -0.39 | -0.48 | 0.18 | 0.01 | 0.28 | -0.06 | -0.12 | -0.12 | 0.04 | -0.15 | -0.18 | -0.42 | 0.23 | 0.14 | -0.02 | -0.40 | 0.32 | -0.41 | 0.41 | 0.37 | 0.01 | -0.02 | -0.05 | 0.36 | 0.02 |
| C* | -0.12 | -0.08 | -0.06 | -0.11 | -0.11 | -0.09 | -0.10 | -0.06 | 0.03 | -0.05 | 0.12 | -0.07 | -0.08 | -0.05 | -0.35 | -0.34 | -0.36 | -0.06 | -0.11 | -0.13 | -0.06 | -0.06 | -0.05 | -0.03 | -0.06 | -0.05 | -0.25 | -0.26 | -0.28 | -0.24 | -0.21 | -0.25 | -0.26 | -0.31 | -0.28 |
| C | 0.00 | 0.00 | 0.01 | 0.00 | 0.00 | 0.00 | 0.00 | 0.00 | 0.00 | 0.01 | 0.00 | 0.01 | -0.01 | -0.01 | 0.00 | 0.00 | 0.01 | 0.00 | 0.00 | 0.00 | 0.00 | 0.01 | 0.01 | -0.01 | 0.00 | -0.01 | 0.00 | 0.01 | -0.01 | 0.00 | 0.01 | 0.00 | 0.01 | 0.00 | 0.00 |
| O3 | 0.03 | -0.05 | 0.08 | -0.03 | -0.03 | 0.03 | 0.02 | -0.06 | 0.04 | 0.04 | 0.05 | 0.04 | -0.07 | -0.07 | 0.04 | 0.04 | 0.05 | 0.05 | -0.08 | -0.08 | 0.06 | 0.06 | -0.08 | -0.07 | -0.07 | -0.06 | 0.08 | 0.08 | -0.06 | 0.07 | 0.08 | 0.07 | 0.08 | -0.05 | -0.05 |
| O1 | -0.05 | 0.03 | 0.07 | 0.06 | 0.06 | -0.05 | -0.05 | 0.03 | -0.04 | 0.04 | -0.04 | 0.04 | -0.06 | -0.06 | -0.05 | -0.05 | 0.04 | -0.03 | 0.02 | 0.03 | 0.05 | 0.04 | -0.05 | 0.03 | -0.04 | 0.04 | 0.04 | 0.05 | -0.04 | -0.03 | 0.05 | -0.03 | 0.05 | 0.04 | 0.04 |
| O2 | -0.01 | 0.00 | 0.04 | 0.01 | 0.01 | -0.01 | -0.01 | 0.00 | 0.00 | 0.02 | 0.00 | 0.02 | -0.03 | -0.03 | -0.01 | -0.01 | 0.02 | 0.00 | -0.01 | -0.01 | 0.02 | 0.02 | -0.03 | 0.00 | -0.03 | 0.00 | 0.03 | 0.03 | -0.03 | 0.00 | 0.03 | 0.00 | 0.03 | 0.00 | 0.00 |

*Table S 8: Mulliken spin populations of the [**V**-$CO_3$]$^-$ model, $M_S$ = 2. Functional: TPSSh*

| BS | 1 | 2 | 3 | 3 | 3 | 4 | 4 | 4 | 5 | 5 | 5 | 5 | 5 | 5 | 6 | 6 | 6 | 7 | 7 | 7 | 8 | 8 | 8 | 8 | 8 | 8 | 9 | 9 | 9 | 10 | 10 | 10 | 10 | 10 | 10 |
|---|---|---|---|---|---|---|---|---|---|---|---|---|---|---|---|---|---|---|---|---|---|---|---|---|---|---|---|---|---|---|---|---|---|---|---|
| Flip | 567 | 234 | 123 | 124 | 134 | 257 | 356 | 467 | 256 | 267 | 357 | 367 | 456 | 457 | 156 | 157 | 167 | 235 | 247 | 346 | 236 | 237 | 245 | 246 | 345 | 347 | 126 | 137 | 145 | 125 | 127 | 135 | 136 | 146 | 147 |
| V | 2.01 | -1.98 | 0.55 | -1.93 | -1.90 | 0.38 | 0.89 | 1.61 | 1.05 | 1.53 | 0.56 | 1.55 | 1.08 | 2.21 | 0.81 | 0.42 | 1.54 | -1.59 | -0.77 | -0.32 | -0.34 | -0.71 | -1.52 | -0.28 | -1.40 | -0.62 | -0.22 | -0.52 | -1.52 | -1.55 | -0.89 | 1.23 | -0.33 | -0.23 | 1.76 |
| Fe1 | 1.19 | 3.47 | -3.37 | -3.32 | -2.58 | 3.52 | 3.51 | 2.37 | 3.46 | 3.39 | 3.47 | 3.42 | 3.40 | 2.39 | -3.44 | -3.46 | -3.49 | 3.46 | 3.39 | 3.36 | 3.47 | 3.47 | 3.60 | 3.38 | 3.36 | 3.37 | -3.28 | -3.31 | -3.40 | -3.23 | -3.29 | -3.37 | -3.37 | -3.44 | -3.43 |
| Fe2 | 3.35 | -3.03 | -3.30 | -2.27 | 3.39 | -3.35 | 3.19 | 3.33 | -3.31 | -3.36 | 2.83 | 2.81 | 3.39 | 2.89 | 3.28 | 3.30 | 3.24 | -3.16 | -3.20 | 3.32 | -3.26 | -3.26 | -3.26 | -3.21 | 3.38 | 3.37 | -3.24 | 3.36 | 3.49 | -3.23 | -3.21 | 3.22 | 3.37 | 3.42 | 3.21 |
| Fe3 | 3.41 | -3.08 | -3.38 | 3.40 | -3.12 | 3.27 | -3.39 | 3.35 | 2.82 | 2.80 | -3.29 | -3.37 | 2.80 | 3.27 | 3.29 | 3.38 | 3.29 | -3.18 | 3.35 | -3.26 | -3.29 | -3.30 | 3.46 | 3.39 | -3.20 | -3.22 | 3.38 | -3.24 | 3.50 | 3.42 | 3.41 | -3.31 | -3.25 | 3.41 | 3.25 |
| Fe4 | 3.49 | -3.23 | 3.49 | -3.33 | -3.26 | 3.32 | 3.33 | -3.45 | 3.38 | 3.33 | 3.43 | 3.34 | -3.40 | -3.37 | 3.41 | 3.42 | 3.44 | 3.45 | -3.33 | -3.33 | 3.44 | 3.45 | -3.32 | -3.41 | -3.31 | -3.38 | 3.51 | 3.55 | -3.29 | 3.57 | 3.48 | 3.44 | 3.50 | -3.32 | -3.38 |
| Fe5 | -3.24 | 3.49 | 3.40 | 3.57 | 3.56 | -3.45 | -3.47 | 3.21 | -3.40 | 3.22 | -3.40 | 3.21 | -3.38 | -3.33 | -3.26 | -3.26 | 3.23 | -3.14 | 3.45 | 3.44 | 3.41 | 3.44 | -3.20 | 3.42 | -3.12 | 3.45 | 3.44 | 3.46 | -3.05 | -3.03 | 3.53 | -3.32 | 3.52 | 3.51 | 3.03 |
| Fe6 | -3.19 | 3.33 | 3.37 | 3.40 | 3.26 | 3.18 | -3.27 | -3.13 | -3.18 | -3.24 | 3.14 | -3.25 | -3.24 | 3.31 | -3.18 | 3.25 | -3.27 | 3.35 | 3.30 | -3.16 | -3.22 | 3.32 | 3.31 | -3.19 | 3.34 | 3.26 | -3.15 | 3.32 | 3.42 | 3.39 | 3.34 | 3.22 | -3.09 | -3.12 | 3.18 |
| Fe7 | -3.27 | 3.41 | 3.19 | 3.36 | 3.44 | -3.30 | 3.13 | -3.14 | 3.09 | -3.28 | -3.20 | -3.29 | 3.08 | -3.30 | 3.22 | -3.18 | -3.29 | 3.39 | -3.13 | 3.32 | 3.32 | -3.17 | 3.29 | 3.29 | 3.42 | -3.13 | 3.32 | -3.10 | 3.44 | 3.44 | -3.05 | 2.98 | 3.38 | 3.39 | -3.28 |
| S1A | 0.35 | -0.04 | -0.04 | -0.25 | -0.05 | 0.04 | 0.49 | 0.00 | 0.12 | 0.07 | 0.32 | 0.32 | 0.15 | 0.03 | 0.08 | 0.10 | 0.08 | 0.17 | -0.14 | 0.14 | 0.17 | 0.13 | -0.05 | -0.16 | 0.16 | 0.12 | -0.04 | 0.23 | -0.06 | -0.04 | -0.05 | 0.15 | 0.20 | -0.09 | -0.14 |
| S2A | 0.25 | 0.00 | -0.51 | -0.03 | -0.05 | 0.12 | 0.08 | 0.25 | 0.15 | 0.12 | 0.17 | 0.13 | 0.29 | 0.08 | 0.05 | 0.07 | 0.02 | -0.08 | 0.16 | 0.12 | -0.10 | -0.11 | 0.23 | 0.20 | 0.13 | 0.19 | -0.07 | -0.08 | 0.20 | -0.06 | -0.06 | -0.15 | -0.11 | 0.15 | 0.10 |
| S4A | 0.34 | -0.06 | -0.05 | -0.06 | -0.21 | 0.46 | 0.02 | 0.01 | 0.28 | 0.28 | 0.10 | 0.04 | 0.09 | 0.08 | 0.07 | 0.08 | 0.10 | 0.14 | 0.14 | -0.15 | 0.09 | 0.14 | 0.23 | 0.11 | -0.15 | -0.14 | 0.21 | -0.05 | -0.05 | 0.21 | 0.20 | -0.09 | -0.09 | -0.10 | -0.09 |
| S1B | -0.26 | 0.32 | 0.26 | 0.34 | 0.31 | 0.01 | -0.29 | -0.10 | -0.27 | -0.09 | 0.00 | -0.12 | -0.29 | -0.03 | -0.26 | 0.02 | -0.10 | 0.12 | 0.29 | -0.01 | 0.00 | 0.28 | 0.11 | 0.00 | 0.12 | 0.26 | 0.00 | 0.27 | 0.15 | 0.14 | 0.30 | 0.04 | 0.02 | 0.01 | 0.12 |
| S3B | -0.34 | 0.35 | 0.27 | 0.33 | 0.33 | 0.02 | -0.04 | -0.27 | -0.04 | -0.30 | 0.04 | -0.31 | -0.08 | -0.01 | -0.04 | 0.02 | -0.33 | 0.34 | 0.04 | -0.01 | 0.00 | 0.06 | 0.32 | -0.01 | 0.33 | 0.06 | 0.01 | 0.07 | 0.35 | 0.34 | 0.08 | 0.18 | 0.02 | 0.00 | 0.01 |
| S4B | -0.30 | 0.34 | 0.17 | 0.33 | 0.35 | -0.27 | -0.03 | -0.10 | -0.04 | -0.13 | -0.26 | -0.11 | -0.03 | -0.34 | 0.01 | -0.25 | -0.12 | 0.14 | 0.01 | 0.27 | 0.26 | 0.02 | 0.11 | 0.25 | 0.13 | 0.01 | 0.25 | 0.01 | 0.15 | 0.14 | 0.04 | -0.05 | 0.27 | 0.26 | -0.14 |
| S2B | 0.04 | 0.14 | 0.11 | 0.23 | 0.48 | 0.03 | -0.15 | 0.01 | -0.48 | -0.50 | 0.27 | -0.19 | 0.01 | 0.32 | -0.02 | 0.45 | -0.06 | 0.14 | 0.12 | -0.09 | -0.47 | 0.11 | 0.02 | -0.47 | 0.52 | 0.49 | -0.44 | 0.48 | 0.53 | 0.13 | 0.13 | 0.40 | 0.00 | -0.02 | 0.40 |
| S5A | 0.10 | 0.10 | -0.02 | 0.47 | 0.09 | -0.08 | -0.07 | 0.07 | 0.18 | -0.14 | -0.42 | -0.46 | 0.16 | 0.00 | 0.41 | 0.06 | 0.02 | 0.09 | -0.01 | 0.06 | 0.03 | -0.40 | 0.50 | 0.42 | 0.12 | -0.39 | 0.44 | -0.37 | 0.49 | 0.50 | 0.08 | -0.08 | 0.06 | 0.47 | -0.02 |
| C* | 0.08 | 0.14 | -0.09 | -0.13 | -0.10 | -0.10 | -0.11 | 0.01 | 0.00 | -0.01 | 0.02 | -0.04 | -0.07 | -0.04 | -0.18 | -0.16 | -0.15 | 0.10 | 0.06 | 0.06 | 0.07 | 0.09 | -0.02 | 0.04 | 0.06 | 0.03 | -0.10 | -0.08 | -0.05 | -0.03 | -0.04 | -0.28 | -0.05 | -0.10 | -0.30 |
| C | 0.00 | 0.00 | 0.01 | 0.00 | 0.00 | 0.00 | 0.00 | 0.00 | 0.00 | 0.01 | 0.00 | 0.01 | -0.01 | -0.01 | 0.00 | 0.00 | 0.01 | 0.00 | 0.00 | 0.00 | 0.01 | 0.01 | -0.01 | 0.00 | -0.01 | 0.00 | 0.01 | 0.01 | -0.01 | 0.00 | 0.01 | 0.00 | 0.01 | 0.00 | 0.00 |
| O3 | 0.05 | -0.04 | 0.08 | -0.03 | -0.02 | 0.03 | 0.03 | -0.07 | 0.05 | 0.06 | 0.05 | 0.06 | -0.07 | -0.07 | 0.06 | 0.05 | 0.08 | 0.05 | -0.04 | -0.05 | 0.06 | 0.06 | -0.07 | -0.05 | -0.07 | -0.04 | 0.09 | 0.10 | -0.06 | 0.08 | 0.08 | 0.07 | 0.09 | -0.04 | -0.05 |
| O1 | -0.03 | 0.05 | 0.06 | 0.06 | 0.06 | -0.05 | -0.05 | 0.03 | -0.04 | 0.05 | -0.05 | 0.05 | -0.06 | -0.06 | -0.03 | -0.03 | 0.04 | -0.03 | 0.05 | 0.05 | 0.06 | 0.06 | -0.04 | 0.05 | -0.04 | 0.05 | 0.06 | 0.06 | -0.04 | -0.03 | 0.07 | -0.04 | 0.07 | 0.05 | 0.02 |
| O2 | 0.00 | 0.01 | 0.03 | 0.01 | 0.01 | -0.01 | -0.01 | 0.00 | 0.00 | 0.03 | 0.00 | 0.03 | -0.03 | -0.03 | 0.00 | 0.00 | 0.03 | 0.00 | 0.01 | 0.01 | 0.03 | 0.03 | -0.03 | 0.00 | -0.03 | 0.01 | 0.03 | 0.03 | -0.03 | 0.00 | 0.03 | 0.00 | 0.03 | 0.01 | 0.00 |

*Table S 9: Mulliken spin populations of the [**V**-$CO_3$]$^0$ model, $M_S$ = $^3/_2$. Functional: TPSSh*

| BS | 1 | 2 | 3 | 3 | 3 | 4 | 4 | 4 | 5 | 5 | 5 | 5 | 5 | 5 | 6 | 6 | 6 | 7 | 7 | 7 | 8 | 8 | 8 | 8 | 8 | 8 | 9 | 9 | 9 | 10 | 10 | 10 | 10 | 10 | 10 |
|---|---|---|---|---|---|---|---|---|---|---|---|---|---|---|---|---|---|---|---|---|---|---|---|---|---|---|---|---|---|---|---|---|---|---|---|
| Flip | 567 | 234 | 123 | 124 | 134 | 257 | 356 | 467 | 256 | 267 | 357 | 367 | 456 | 457 | 156 | 157 | 167 | 235 | 247 | 346 | 236 | 237 | 245 | 246 | 345 | 347 | 126 | 137 | 145 | 125 | 127 | 135 | 136 | 146 | 147 |
| V | 1.85 | -1.84 | 0.73 | -1.81 | -1.79 | 0.22 | 0.82 | 1.55 | 1.82 | 1.54 | 1.79 | 1.54 | 0.49 | 0.03 | 0.66 | 0.28 | 1.42 | -1.53 | -0.63 | -0.13 | -0.05 | -0.34 | -1.42 | -0.26 | -1.35 | -0.65 | -0.06 | -0.44 | -1.48 | -0.05 | -0.76 | -1.46 | -0.29 | -0.13 | -0.51 |
| Fe1 | 1.67 | 3.46 | -3.60 | -2.82 | -2.74 | 3.28 | 3.46 | 2.50 | 2.37 | 2.70 | 2.74 | 2.84 | 3.30 | 3.32 | -3.47 | -3.49 | -3.47 | 3.43 | 3.31 | 3.22 | 3.46 | 3.42 | 3.32 | 3.59 | 3.30 | 3.59 | -3.57 | -3.30 | -3.42 | -3.37 | -3.54 | -2.80 | -3.47 | -3.45 | -3.44 |
| Fe2 | 3.27 | -3.24 | -3.36 | -3.15 | 3.23 | -3.32 | 3.23 | 3.26 | -3.32 | -3.34 | 2.48 | 2.84 | 3.29 | 2.71 | 3.10 | 3.11 | 3.05 | -3.36 | -3.35 | 3.29 | -3.41 | -3.22 | -2.96 | -3.15 | 3.01 | 3.27 | -3.34 | 3.16 | 3.38 | -3.25 | -3.28 | 3.23 | 3.19 | 3.25 | 3.17 |
| Fe3 | 3.35 | -3.31 | -3.47 | 3.26 | -3.22 | 2.68 | -3.37 | 3.29 | 2.72 | 2.89 | -3.33 | -3.37 | 2.78 | 3.35 | 3.13 | 3.30 | 3.22 | -3.42 | 3.31 | -3.39 | -3.44 | -3.25 | 3.07 | 3.33 | -3.12 | -3.19 | 3.30 | -3.21 | 3.44 | 3.25 | 3.32 | -3.17 | -3.28 | 3.18 | 3.35 |
| Fe4 | 3.44 | -3.35 | 3.48 | -3.28 | -3.34 | 3.45 | 2.64 | -3.48 | 3.39 | 3.28 | 3.31 | 3.24 | -3.46 | -3.46 | 3.40 | 3.41 | 3.28 | 3.44 | -3.56 | -3.52 | 3.35 | 3.15 | -3.19 | -3.47 | -3.20 | -3.45 | 3.51 | 3.49 | -3.32 | 3.43 | 3.45 | 3.43 | 3.43 | -3.34 | -3.32 |
| Fe5 | -3.49 | 3.46 | 3.37 | 3.53 | 3.53 | -3.44 | -3.49 | 3.18 | -3.42 | 3.22 | -3.46 | 3.21 | -3.43 | -3.39 | -3.32 | -3.33 | 3.13 | -3.19 | 3.40 | 3.41 | 3.35 | 3.25 | -3.17 | 3.23 | -3.14 | 3.24 | 3.43 | 3.39 | -3.14 | -3.33 | 3.53 | -3.16 | 3.48 | 3.47 | 3.46 |
| Fe6 | -3.31 | 3.29 | 3.29 | 3.23 | 3.10 | 3.21 | -3.29 | -3.31 | -3.16 | -3.21 | 3.19 | -3.22 | -3.26 | 3.21 | -3.17 | 3.04 | -3.27 | 3.32 | 3.26 | -3.20 | -3.31 | 3.09 | 3.23 | -3.24 | 3.10 | 2.71 | -3.18 | 3.16 | 3.33 | 3.06 | 3.30 | 3.14 | -3.15 | -3.18 | 3.24 |
| Fe7 | -3.36 | 3.35 | 3.17 | 3.17 | 3.32 | -3.30 | 3.11 | -3.34 | 3.23 | -3.23 | -3.20 | -3.26 | 3.15 | -3.26 | 3.07 | -3.19 | -3.31 | 3.34 | -3.18 | 3.27 | 3.19 | -3.21 | 3.04 | 2.55 | 3.31 | -3.19 | 3.29 | -3.17 | 3.35 | 3.18 | -3.11 | 3.14 | 3.31 | 3.30 | -3.17 |
| S1A | 0.33 | -0.12 | -0.15 | -0.19 | -0.07 | 0.07 | 0.21 | 0.00 | 0.08 | 0.05 | 0.00 | 0.09 | 0.11 | 0.00 | 0.08 | 0.13 | 0.10 | 0.11 | -0.24 | 0.03 | 0.09 | 0.01 | -0.10 | -0.09 | 0.05 | 0.19 | -0.16 | 0.18 | -0.10 | -0.08 | -0.15 | 0.12 | 0.13 | -0.11 | -0.12 |
| S2A | 0.18 | -0.11 | -0.56 | -0.09 | -0.06 | 0.01 | 0.09 | 0.19 | -0.06 | 0.02 | -0.05 | 0.04 | 0.25 | 0.25 | 0.08 | 0.07 | 0.01 | -0.19 | 0.11 | 0.06 | -0.19 | -0.13 | 0.07 | 0.19 | 0.07 | 0.16 | -0.16 | -0.14 | 0.17 | -0.13 | -0.14 | 0.00 | -0.14 | 0.10 | 0.12 |
| S4A | 0.31 | -0.09 | -0.16 | -0.01 | -0.21 | 0.26 | 0.00 | 0.01 | 0.03 | 0.08 | 0.06 | 0.03 | 0.04 | 0.13 | 0.09 | 0.08 | 0.13 | 0.07 | 0.05 | -0.23 | 0.04 | 0.01 | 0.06 | 0.18 | -0.12 | -0.10 | 0.15 | -0.06 | -0.07 | 0.15 | 0.13 | -0.02 | -0.11 | -0.09 | -0.06 |
| S1B | -0.34 | 0.34 | 0.25 | 0.33 | 0.32 | 0.02 | -0.30 | -0.13 | -0.30 | -0.12 | -0.07 | -0.14 | -0.27 | 0.05 | -0.26 | 0.01 | -0.13 | 0.13 | 0.27 | -0.03 | -0.06 | 0.20 | 0.12 | 0.00 | 0.13 | 0.15 | -0.03 | 0.23 | 0.12 | 0.00 | 0.29 | 0.11 | 0.00 | 0.00 | 0.25 |
| S3B | -0.36 | 0.35 | 0.25 | 0.31 | 0.30 | 0.03 | -0.06 | -0.34 | -0.07 | -0.30 | -0.02 | -0.31 | -0.05 | 0.02 | -0.06 | 0.01 | -0.34 | 0.34 | 0.04 | -0.03 | -0.03 | 0.04 | 0.25 | -0.07 | 0.27 | 0.03 | -0.03 | 0.00 | 0.32 | 0.19 | 0.06 | 0.26 | 0.00 | -0.02 | 0.03 |
| S4B | -0.36 | 0.36 | 0.17 | 0.34 | 0.33 | -0.26 | -0.03 | -0.14 | -0.06 | -0.15 | -0.32 | -0.13 | 0.01 | -0.23 | 0.00 | -0.24 | -0.14 | 0.15 | -0.01 | 0.25 | 0.23 | -0.04 | 0.13 | 0.11 | 0.13 | 0.01 | 0.24 | -0.03 | 0.13 | 0.01 | 0.03 | 0.12 | 0.25 | 0.23 | 0.01 |
| S2B | -0.05 | 0.06 | 0.03 | 0.09 | 0.38 | 0.00 | -0.08 | -0.10 | -0.49 | -0.50 | 0.27 | -0.14 | -0.07 | 0.29 | -0.03 | 0.36 | -0.11 | 0.05 | 0.01 | -0.08 | -0.53 | 0.03 | 0.11 | -0.46 | 0.29 | 0.35 | -0.52 | 0.38 | 0.46 | 0.11 | 0.07 | 0.42 | -0.07 | -0.06 | 0.43 |
| S5A | 0.02 | -0.02 | -0.10 | 0.34 | 0.04 | -0.11 | -0.10 | -0.04 | 0.25 | -0.10 | -0.45 | -0.48 | 0.19 | 0.01 | 0.31 | 0.06 | -0.02 | -0.03 | -0.01 | -0.07 | -0.12 | -0.42 | 0.24 | 0.25 | 0.08 | -0.40 | 0.42 | -0.37 | 0.45 | 0.39 | 0.04 | -0.05 | 0.03 | 0.38 | 0.04 |
| C* | -0.02 | 0.02 | -0.18 | -0.23 | -0.21 | 0.00 | -0.05 | -0.05 | 0.03 | 0.01 | 0.03 | -0.01 | -0.06 | -0.05 | -0.30 | -0.27 | -0.33 | 0.01 | -0.04 | -0.04 | -0.03 | -0.01 | 0.05 | -0.03 | 0.03 | -0.06 | -0.16 | -0.27 | -0.23 | -0.31 | -0.13 | -0.26 | -0.20 | -0.25 | -0.25 |
| C | 0.00 | 0.00 | 0.00 | 0.00 | 0.00 | 0.00 | 0.00 | 0.00 | 0.00 | 0.01 | 0.00 | 0.01 | -0.01 | -0.01 | 0.00 | 0.00 | 0.00 | 0.00 | 0.00 | 0.00 | 0.01 | 0.01 | 0.00 | 0.00 | -0.01 | 0.00 | 0.00 | 0.00 | -0.01 | 0.00 | 0.00 | 0.00 | 0.00 | 0.00 | 0.00 |
| O3 | 0.05 | -0.06 | 0.10 | -0.03 | -0.03 | 0.06 | 0.00 | -0.08 | 0.06 | 0.07 | 0.04 | 0.06 | -0.10 | -0.10 | 0.07 | 0.06 | 0.07 | 0.05 | -0.09 | -0.08 | 0.07 | 0.06 | -0.07 | -0.08 | -0.07 | -0.08 | 0.11 | 0.11 | -0.07 | 0.08 | 0.10 | 0.08 | 0.10 | -0.04 | -0.04 |
| O1 | -0.06 | 0.05 | 0.06 | 0.07 | 0.07 | -0.06 | -0.06 | 0.04 | -0.06 | 0.05 | -0.06 | 0.05 | -0.07 | -0.07 | -0.03 | -0.05 | 0.06 | -0.04 | 0.05 | 0.05 | 0.06 | 0.05 | -0.05 | 0.03 | -0.05 | 0.03 | 0.07 | 0.07 | -0.05 | -0.06 | 0.08 | -0.03 | 0.08 | 0.07 | 0.07 |
| O2 | 0.00 | 0.00 | 0.04 | 0.01 | 0.01 | 0.00 | -0.02 | 0.00 | 0.00 | 0.03 | -0.01 | 0.03 | -0.04 | -0.04 | 0.00 | 0.00 | 0.03 | 0.00 | 0.00 | 0.00 | 0.03 | 0.02 | -0.03 | -0.01 | -0.03 | -0.01 | 0.04 | 0.04 | -0.03 | 0.00 | 0.04 | 0.00 | 0.04 | 0.01 | 0.01 |

*Table S 10: Mulliken spin populations of the [**V**-$CO_3$]$^0$ model, $M_S$ = ½. Functional: TPSSh*

| BS | 1 | 2 | 3 | 3 | 3 | 4 | 4 | 4 | 5 | 5 | 5 | 5 | 5 | 5 | 6 | 6 | 6 | 7 | 7 | 7 | 8 | 8 | 8 | 8 | 8 | 8 | 9 | 9 | 9 | 10 | 10 | 10 | 10 | 10 | 10 |
|---|---|---|---|---|---|---|---|---|---|---|---|---|---|---|---|---|---|---|---|---|---|---|---|---|---|---|---|---|---|---|---|---|---|---|---|
| Flip | 567 | 234 | 123 | 124 | 134 | 257 | 356 | 467 | 256 | 267 | 357 | 367 | 456 | 457 | 156 | 157 | 167 | 235 | 247 | 346 | 236 | 237 | 245 | 246 | 345 | 347 | 126 | 137 | 145 | 125 | 127 | 135 | 136 | 146 | 147 |
| V | 1.84 | -1.89 | -1.87 | -1.82 | -1.79 | 0.26 | 0.83 | 1.56 | 0.59 | 1.38 | 0.19 | 1.43 | 0.61 | 0.06 | 0.68 | 0.30 | 1.41 | -1.60 | -1.81 | -1.78 | -1.81 | -1.86 | -1.70 | -0.21 | -1.65 | -0.69 | -0.10 | -0.69 | -1.49 | -1.55 | -1.78 | -1.53 | -0.73 | -0.30 | -0.86 |
| Fe1 | -1.31 | 3.44 | -3.63 | -3.55 | -3.55 | 1.56 | 2.27 | 1.73 | 2.47 | 2.61 | 2.69 | 2.69 | 2.07 | 2.12 | -3.50 | -3.50 | -3.48 | 3.38 | 3.33 | 3.26 | 3.43 | 3.42 | 3.25 | 2.88 | 3.21 | 3.02 | -3.59 | -3.58 | -3.45 | -3.38 | -3.58 | -3.36 | -3.55 | -3.46 | -3.46 |
| Fe2 | 3.37 | -3.38 | -3.38 | -3.38 | 3.18 | -3.34 | 2.67 | 3.06 | -3.42 | -3.41 | 2.48 | 2.99 | 3.12 | 2.75 | 2.41 | 2.58 | 1.72 | -3.38 | -3.37 | 3.25 | -3.33 | -3.38 | -3.37 | -3.22 | 3.07 | 2.96 | -3.45 | 3.08 | 3.16 | -3.29 | -3.39 | 3.07 | 3.12 | 3.10 | 3.00 |
| Fe3 | 3.44 | -3.46 | -3.45 | 3.17 | -3.46 | 3.12 | -3.39 | 3.03 | 2.62 | 3.07 | -3.45 | -3.47 | 2.79 | 3.18 | 2.96 | 3.02 | 3.18 | -3.43 | 3.25 | -3.41 | -3.44 | -3.37 | 3.08 | 2.91 | -3.41 | -3.34 | 3.20 | -3.47 | 3.33 | 3.18 | 3.25 | -3.31 | -3.44 | 3.11 | 3.16 |
| Fe4 | 3.51 | -3.51 | 3.43 | -3.40 | -3.39 | 3.32 | 3.22 | -3.53 | 3.31 | 2.24 | 3.28 | 2.30 | -3.42 | -3.43 | 3.25 | 3.22 | 3.12 | 3.29 | -3.58 | -3.54 | 3.21 | 3.18 | -3.52 | -3.47 | -3.48 | -3.46 | 3.35 | 3.39 | -3.42 | 3.28 | 3.43 | 3.32 | 3.26 | -3.42 | -3.41 |
| Fe5 | -3.48 | 3.44 | 3.44 | 3.52 | 3.52 | -3.44 | -3.47 | 3.12 | -3.49 | 3.16 | -3.45 | 3.15 | -3.45 | -3.39 | -3.48 | -3.48 | 3.11 | -3.28 | 3.24 | 3.32 | 3.22 | 3.20 | -3.30 | 3.17 | -3.28 | 3.14 | 3.20 | 3.31 | -3.20 | -3.24 | 3.45 | -3.23 | 3.27 | 3.13 | 3.19 |
| Fe6 | -3.31 | 2.97 | 3.29 | 3.24 | 3.06 | 3.17 | -3.33 | -3.36 | -3.32 | -3.38 | 3.11 | -3.37 | -3.29 | 3.19 | -3.26 | 2.90 | -3.28 | 2.93 | 3.11 | -3.29 | -3.31 | 3.03 | 3.09 | -3.28 | 2.93 | 2.82 | -3.24 | 2.92 | 2.85 | 2.98 | 3.18 | 2.96 | -3.19 | -3.25 | 2.92 |
| Fe7 | -3.36 | 3.00 | 3.34 | 3.10 | 3.33 | -3.33 | 3.10 | -3.40 | 3.05 | -3.40 | -3.33 | -3.45 | 3.13 | -3.29 | 2.94 | -3.29 | -3.38 | 2.98 | -3.36 | 3.16 | 3.06 | -3.32 | 2.96 | 2.66 | 3.14 | -3.28 | 2.75 | -3.18 | 3.09 | 3.00 | -3.27 | 3.09 | 3.06 | 2.82 | -3.19 |
| S1A | 0.39 | -0.14 | -0.19 | -0.54 | -0.08 | 0.02 | -0.02 | -0.04 | 0.06 | -0.03 | 0.01 | 0.00 | 0.03 | -0.01 | 0.00 | 0.05 | -0.09 | 0.04 | -0.24 | 0.04 | 0.02 | 0.03 | -0.21 | -0.13 | 0.01 | 0.03 | -0.23 | 0.07 | -0.16 | -0.12 | -0.21 | 0.10 | 0.06 | -0.13 | -0.12 |
| S2A | 0.39 | -0.12 | -0.55 | -0.15 | -0.16 | -0.08 | -0.11 | -0.05 | -0.09 | 0.02 | -0.09 | 0.00 | -0.04 | -0.04 | -0.05 | 0.01 | -0.05 | -0.22 | 0.12 | 0.07 | -0.19 | -0.17 | 0.05 | -0.04 | 0.05 | -0.02 | -0.23 | -0.27 | 0.09 | -0.12 | -0.18 | -0.13 | -0.21 | 0.03 | 0.02 |
| S4A | 0.39 | -0.15 | -0.19 | -0.04 | -0.50 | 0.12 | 0.00 | -0.03 | 0.02 | -0.01 | 0.04 | -0.02 | 0.00 | 0.04 | 0.10 | 0.07 | 0.08 | 0.00 | 0.06 | -0.23 | 0.03 | 0.01 | 0.03 | 0.03 | -0.21 | -0.17 | 0.08 | -0.19 | -0.10 | 0.10 | 0.11 | -0.10 | -0.18 | -0.09 | -0.09 |
| S1B | -0.34 | 0.32 | 0.34 | 0.33 | 0.31 | 0.02 | -0.30 | -0.14 | -0.29 | -0.13 | 0.02 | -0.14 | -0.29 | 0.04 | -0.28 | 0.00 | -0.12 | 0.12 | 0.27 | 0.04 | 0.04 | 0.23 | 0.14 | -0.02 | 0.12 | 0.15 | -0.05 | 0.20 | 0.12 | 0.12 | 0.31 | 0.12 | 0.00 | -0.01 | 0.16 |
| S3B | -0.36 | 0.23 | 0.34 | 0.30 | 0.30 | 0.02 | -0.06 | -0.36 | -0.07 | -0.34 | 0.01 | -0.36 | -0.06 | 0.02 | -0.06 | 0.00 | -0.34 | 0.13 | 0.02 | 0.00 | 0.03 | 0.07 | 0.23 | -0.08 | 0.23 | 0.00 | -0.09 | 0.01 | 0.13 | 0.19 | 0.05 | 0.19 | 0.00 | -0.04 | 0.05 |
| S4B | -0.36 | 0.35 | 0.36 | 0.34 | 0.34 | -0.27 | -0.02 | -0.15 | 0.00 | -0.14 | -0.26 | -0.15 | 0.00 | -0.24 | -0.03 | -0.26 | -0.15 | 0.13 | 0.01 | 0.29 | 0.26 | 0.03 | 0.13 | 0.11 | 0.14 | 0.00 | 0.13 | -0.01 | 0.14 | 0.13 | 0.05 | 0.13 | 0.19 | 0.11 | 0.01 |
| S2B | -0.04 | -0.12 | 0.04 | 0.04 | 0.34 | -0.05 | -0.16 | -0.10 | -0.53 | -0.54 | 0.21 | -0.14 | -0.09 | 0.31 | -0.17 | 0.25 | -0.16 | -0.09 | -0.03 | -0.20 | -0.52 | -0.02 | -0.03 | -0.49 | 0.24 | 0.23 | -0.56 | 0.38 | 0.29 | 0.04 | -0.05 | 0.30 | -0.04 | -0.06 | 0.29 |
| S5A | 0.06 | -0.20 | -0.05 | 0.27 | -0.03 | -0.02 | -0.15 | -0.05 | 0.18 | -0.08 | -0.49 | -0.52 | 0.23 | -0.02 | 0.26 | -0.09 | -0.05 | -0.16 | -0.16 | -0.10 | -0.12 | -0.48 | 0.20 | 0.12 | -0.10 | -0.44 | 0.31 | -0.51 | 0.40 | 0.30 | -0.07 | -0.01 | -0.16 | 0.21 | 0.03 |
| C* | -0.03 | -0.14 | -0.16 | -0.19 | -0.20 | -0.04 | -0.03 | -0.13 | -0.03 | -0.03 | -0.03 | -0.07 | -0.07 | -0.05 | -0.36 | -0.42 | -0.28 | -0.15 | -0.10 | -0.10 | -0.05 | -0.06 | -0.09 | -0.03 | -0.08 | -0.06 | -0.27 | -0.29 | -0.33 | -0.37 | -0.16 | -0.37 | -0.32 | -0.40 | -0.39 |
| C | 0.00 | 0.00 | 0.00 | 0.00 | 0.00 | 0.00 | 0.00 | 0.00 | 0.00 | 0.01 | 0.00 | 0.00 | -0.01 | -0.01 | 0.00 | 0.00 | 0.00 | 0.00 | 0.00 | 0.00 | 0.00 | 0.00 | 0.01 | -0.01 | 0.00 | -0.01 | 0.00 | 0.01 | 0.00 | -0.01 | 0.00 | 0.00 | 0.00 | 0.00 | 0.00 |
| O3 | 0.06 | -0.08 | 0.10 | -0.05 | -0.04 | 0.05 | 0.02 | -0.08 | 0.03 | 0.00 | 0.03 | 0.02 | -0.08 | -0.09 | 0.05 | 0.05 | 0.07 | 0.06 | -0.09 | -0.09 | 0.06 | 0.05 | -0.11 | -0.08 | -0.11 | -0.09 | 0.09 | 0.10 | -0.08 | 0.04 | 0.09 | 0.05 | 0.08 | -0.06 | -0.06 |
| O1 | -0.05 | 0.04 | 0.07 | 0.07 | 0.07 | -0.06 | -0.06 | 0.03 | -0.06 | 0.04 | -0.06 | 0.05 | -0.07 | -0.07 | -0.07 | -0.06 | 0.05 | -0.05 | 0.04 | 0.05 | 0.06 | 0.05 | -0.06 | 0.02 | -0.06 | 0.02 | 0.04 | 0.05 | -0.05 | -0.05 | 0.07 | -0.04 | 0.06 | 0.02 | 0.03 |
| O2 | 0.00 | 0.00 | 0.04 | 0.01 | 0.01 | -0.01 | -0.01 | 0.00 | -0.01 | 0.01 | -0.01 | 0.02 | -0.04 | -0.04 | -0.01 | -0.01 | 0.03 | 0.00 | -0.01 | -0.01 | 0.02 | 0.02 | -0.04 | -0.01 | -0.04 | -0.01 | 0.04 | 0.04 | -0.03 | -0.01 | 0.04 | -0.01 | 0.03 | -0.01 | -0.01 |

*Table S 11: Mulliken spin population of the [**V**-$NO_3$]$^-$, $M_S$ = ³/₂. Functional: TPSSh*

| BS | 1 | 2 | 3 | 3 | 3 | 4 | 4 | 4 | 5 | 5 | 5 | 5 | 5 | 5 | 6 | 6 | 6 | 7 | 7 | 7 | 8 | 8 | 8 | 8 | 8 | 8 | 9 | 9 | 9 | 10 | 10 | 10 | 10 | 10 | 10 |
|---|---|---|---|---|---|---|---|---|---|---|---|---|---|---|---|---|---|---|---|---|---|---|---|---|---|---|---|---|---|---|---|---|---|---|---|
| Flip | 567 | 234 | 123 | 124 | 134 | 257 | 356 | 467 | 256 | 267 | 357 | 367 | 456 | 457 | 156 | 157 | 167 | 235 | 247 | 346 | 236 | 237 | 245 | 246 | 345 | 347 | 126 | 137 | 145 | 125 | 127 | 135 | 136 | 146 | 147 |
| V | 2.00 | -2.02 | 0.56 | -1.98 | 0.44 | 0.51 | 1.00 | 1.65 | 0.75 | 1.47 | 0.40 | 1.41 | 1.02 | 0.56 | 0.85 | 0.49 | 1.49 | -1.67 | -0.89 | -0.44 | -0.48 | -1.01 | -1.45 | -0.39 | -1.54 | -0.68 | -0.23 | -0.63 | -1.40 | 1.16 | 1.73 | -1.55 | -0.37 | -0.38 | 1.88 |
| Fe1 | 1.03 | 3.47 | -3.39 | -3.34 | -3.48 | 3.22 | 3.34 | 2.10 | 3.29 | 3.27 | 3.32 | 3.35 | 2.40 | 2.49 | -3.47 | -3.47 | -3.49 | 3.47 | 3.36 | 3.33 | 3.46 | 3.42 | 3.35 | 3.33 | 3.32 | 3.32 | -3.32 | -3.33 | -3.41 | -3.34 | -3.38 | -3.34 | -3.35 | -3.44 | -3.42 |
| Fe2 | 3.26 | -3.11 | -3.32 | -2.41 | 3.28 | -3.34 | 2.40 | 3.18 | -3.35 | -3.36 | 2.51 | 2.77 | 3.22 | 2.97 | 3.20 | 3.07 | 3.22 | -3.18 | -3.29 | 3.30 | -3.25 | -3.28 | -3.33 | -3.21 | 3.30 | 3.29 | -3.23 | 3.36 | 3.21 | -3.32 | -3.24 | 3.28 | 3.36 | 3.31 | 2.91 |
| Fe3 | 3.33 | -3.20 | -3.39 | 3.36 | -3.35 | 2.53 | -3.37 | 3.04 | 2.53 | 2.74 | -3.33 | -3.38 | 3.01 | 3.22 | 3.20 | 3.29 | 3.27 | -3.21 | 3.33 | -3.35 | -3.36 | -3.25 | 3.31 | 3.26 | -3.40 | -3.32 | 3.36 | -3.25 | 3.35 | 3.21 | 3.30 | -3.30 | -3.29 | 3.37 | 3.13 |
| Fe4 | 3.13 | -3.06 | 3.34 | -3.12 | -3.17 | 3.09 | 3.01 | -3.28 | 3.18 | 3.18 | 3.17 | 3.19 | -3.26 | -3.24 | 3.07 | 3.07 | 3.19 | 3.24 | -3.21 | -3.21 | 3.28 | 3.27 | -3.23 | -3.33 | -3.25 | -3.29 | 3.38 | 3.37 | -3.20 | 3.23 | 3.21 | 3.37 | 3.39 | -3.14 | -3.24 |
| Fe5 | -3.13 | 3.16 | 3.15 | 3.24 | 3.03 | -3.10 | -3.15 | 3.05 | -3.21 | 3.05 | -3.18 | 3.05 | -3.24 | -3.21 | -3.14 | -3.10 | 3.09 | -3.03 | 3.07 | 3.02 | 3.19 | 3.20 | -3.05 | 3.11 | -3.04 | 3.16 | 3.22 | 3.32 | -2.98 | -3.16 | 2.69 | -2.79 | 3.31 | 3.19 | 2.65 |
| Fe6 | -3.23 | 3.22 | 3.32 | 3.30 | 3.22 | 3.19 | -3.25 | -3.16 | -3.22 | -3.21 | 3.11 | -3.23 | -3.30 | 3.14 | -3.21 | 3.19 | -3.27 | 3.15 | 3.22 | -3.20 | -3.22 | 3.29 | 3.17 | -3.19 | 3.15 | 3.21 | -3.15 | 3.30 | 3.12 | 3.04 | 3.04 | 3.21 | -3.12 | -3.17 | 3.23 |
| Fe7 | -3.33 | 3.36 | 3.20 | 3.34 | 3.18 | -3.28 | 3.14 | -3.24 | 3.06 | -3.29 | -3.23 | -3.30 | 3.06 | -3.32 | 3.12 | -3.23 | -3.31 | 3.21 | -3.17 | 3.25 | 3.32 | -3.09 | 3.11 | 3.20 | 3.24 | -3.15 | 3.32 | -3.10 | 3.29 | 2.81 | -3.31 | 3.23 | 3.34 | 3.32 | -3.34 |
| S1A | 0.25 | -0.01 | -0.05 | -0.23 | -0.04 | 0.04 | 0.19 | -0.03 | 0.08 | 0.05 | 0.18 | 0.28 | 0.08 | 0.03 | 0.02 | 0.00 | 0.03 | 0.17 | -0.12 | 0.13 | 0.16 | 0.13 | -0.17 | -0.14 | 0.14 | 0.09 | -0.06 | 0.20 | -0.13 | -0.13 | -0.18 | 0.13 | 0.17 | -0.09 | -0.18 |
| S2A | 0.26 | -0.01 | -0.49 | -0.07 | -0.15 | 0.04 | 0.01 | 0.08 | 0.07 | 0.09 | 0.08 | 0.12 | 0.10 | 0.11 | 0.01 | 0.02 | 0.02 | -0.03 | 0.16 | 0.11 | -0.10 | -0.08 | 0.09 | 0.14 | 0.10 | 0.13 | -0.09 | -0.08 | 0.11 | -0.15 | -0.11 | -0.15 | -0.12 | 0.12 | 0.05 |
| S4A | 0.26 | -0.04 | -0.04 | -0.07 | -0.43 | 0.21 | 0.02 | -0.07 | 0.24 | 0.26 | 0.08 | 0.05 | 0.00 | 0.08 | 0.04 | 0.06 | 0.06 | 0.16 | 0.14 | -0.14 | 0.10 | 0.13 | 0.13 | 0.07 | -0.16 | -0.16 | 0.19 | -0.07 | -0.12 | 0.12 | 0.13 | -0.07 | -0.12 | -0.10 | -0.11 |
| S1B | -0.23 | 0.22 | 0.22 | 0.25 | 0.20 | 0.03 | -0.23 | -0.09 | -0.22 | -0.08 | 0.01 | -0.10 | -0.27 | 0.00 | -0.23 | 0.02 | -0.08 | 0.08 | 0.21 | -0.04 | -0.02 | 0.27 | 0.10 | -0.03 | 0.07 | 0.21 | -0.03 | 0.26 | 0.08 | 0.02 | 0.05 | 0.15 | 0.00 | -0.02 | 0.09 |
| S3B | -0.34 | 0.34 | 0.26 | 0.32 | 0.24 | 0.01 | -0.05 | -0.29 | -0.04 | -0.29 | 0.02 | -0.30 | -0.08 | 0.00 | -0.05 | 0.00 | -0.32 | 0.27 | 0.04 | -0.02 | -0.01 | 0.07 | 0.27 | -0.04 | 0.27 | 0.03 | 0.01 | 0.07 | 0.28 | 0.16 | 0.03 | 0.31 | 0.01 | -0.01 | -0.01 |
| S4B | -0.28 | 0.27 | 0.15 | 0.29 | 0.14 | -0.22 | 0.00 | -0.10 | -0.01 | -0.13 | -0.21 | -0.09 | -0.03 | -0.26 | 0.00 | -0.22 | -0.11 | 0.10 | -0.02 | 0.21 | 0.25 | 0.03 | 0.09 | 0.20 | 0.12 | -0.01 | 0.22 | 0.01 | 0.09 | -0.07 | -0.16 | 0.17 | 0.24 | 0.22 | -0.19 |
| S2B | -0.04 | 0.07 | 0.06 | 0.18 | 0.42 | 0.00 | -0.20 | -0.04 | -0.47 | -0.49 | 0.21 | -0.17 | -0.08 | 0.34 | -0.08 | 0.42 | -0.08 | 0.03 | 0.03 | -0.07 | -0.46 | 0.04 | -0.02 | -0.44 | 0.43 | 0.44 | -0.44 | 0.47 | 0.41 | 0.00 | -0.02 | 0.43 | 0.00 | -0.05 | 0.39 |
| S5A | 0.01 | 0.04 | -0.04 | 0.45 | -0.03 | -0.13 | -0.08 | -0.03 | 0.14 | -0.14 | -0.42 | -0.46 | 0.26 | -0.03 | 0.38 | 0.00 | -0.01 | -0.01 | 0.01 | -0.04 | -0.02 | -0.35 | 0.35 | 0.39 | -0.07 | -0.40 | 0.42 | -0.37 | 0.43 | 0.28 | -0.03 | -0.04 | 0.02 | 0.43 | -0.06 |
| C* | -0.02 | 0.02 | -0.09 | -0.21 | -0.21 | 0.00 | -0.01 | -0.06 | -0.01 | 0.02 | -0.02 | -0.04 | -0.13 | -0.10 | -0.26 | -0.24 | -0.17 | 0.03 | -0.01 | -0.03 | 0.08 | 0.11 | -0.13 | -0.03 | -0.09 | -0.04 | -0.10 | -0.10 | -0.24 | -0.36 | -0.22 | -0.21 | -0.04 | -0.18 | -0.35 |
| N | 0.07 | -0.02 | -0.17 | -0.09 | -0.05 | 0.03 | 0.04 | 0.19 | 0.03 | -0.19 | 0.07 | -0.23 | 0.18 | 0.18 | -0.10 | -0.06 | -0.19 | -0.03 | -0.06 | -0.01 | -0.13 | -0.11 | 0.13 | -0.07 | 0.14 | -0.03 | -0.21 | -0.21 | 0.21 | -0.17 | -0.20 | 0.20 | -0.18 | -0.10 | -0.10 |
| O3 | 0.02 | -0.04 | 0.01 | -0.01 | -0.01 | 0.02 | 0.00 | -0.02 | 0.00 | 0.02 | 0.00 | 0.02 | -0.02 | -0.03 | 0.02 | 0.02 | 0.06 | -0.01 | -0.03 | -0.03 | 0.00 | 0.00 | -0.01 | -0.02 | -0.04 | -0.03 | 0.00 | 0.04 | -0.02 | 0.03 | 0.02 | 0.06 | 0.02 | -0.02 | -0.03 |
| O1 | -0.01 | 0.02 | 0.03 | 0.01 | 0.01 | -0.01 | -0.01 | 0.04 | 0.00 | -0.02 | 0.01 | 0.00 | -0.02 | -0.01 | -0.02 | -0.02 | -0.03 | 0.01 | 0.01 | 0.02 | 0.01 | 0.02 | 0.00 | -0.01 | 0.02 | 0.01 | 0.03 | 0.01 | 0.01 | -0.05 | -0.01 | 0.00 | 0.02 | 0.00 | -0.01 |
| O2 | 0.03 | -0.01 | -0.08 | -0.05 | -0.03 | 0.01 | 0.02 | 0.09 | 0.02 | -0.08 | 0.04 | -0.10 | 0.08 | 0.07 | -0.06 | -0.04 | -0.09 | -0.01 | -0.03 | 0.00 | -0.05 | -0.03 | 0.05 | -0.03 | 0.06 | -0.01 | -0.10 | -0.10 | 0.09 | -0.09 | -0.09 | 0.09 | -0.08 | -0.05 | -0.05 |

*Table S 12: Mulliken spin population of the [**V**-NO$_3$]$^-$, $M_S = {}^1/_2$ Functional: TPSSh*

| BS | 1 | 2 | 3 | 3 | 3 | 4 | 4 | 4 | 5 | 5 | 5 | 5 | 5 | 5 | 6 | 6 | 6 | 7 | 7 | 7 | 8 | 8 | 8 | 8 | 8 | 8 | 9 | 9 | 9 | 10 | 10 | 10 | 10 | 10 | 10 |
|---|---|---|---|---|---|---|---|---|---|---|---|---|---|---|---|---|---|---|---|---|---|---|---|---|---|---|---|---|---|---|---|---|---|---|---|
| Flip | 567 | 234 | 123 | 124 | 134 | 257 | 356 | 467 | 256 | 267 | 357 | 367 | 456 | 457 | 156 | 157 | 167 | 235 | 247 | 346 | 236 | 237 | 245 | 246 | 345 | 347 | 126 | 137 | 145 | 125 | 127 | 135 | 136 | 146 | 147 |
| V | 2.00 | -2.04 | -2.03 | -1.99 | -1.95 | 0.32 | 1.00 | 1.65 | 0.80 | 1.46 | 0.57 | 1.44 | 1.14 | 0.67 | 0.76 | 0.37 | 1.23 | -1.62 | -1.28 | -0.49 | -0.64 | -1.21 | -1.63 | -0.60 | -1.57 | -0.84 | -0.45 | -0.84 | -1.63 | -1.51 | -1.27 | -1.44 | -0.78 | -0.47 | -0.90 |
| Fe1 | 0.95 | 3.45 | -3.41 | -3.51 | -3.51 | 2.26 | 3.46 | -0.61 | 3.42 | 2.28 | 3.47 | 3.41 | 3.28 | 3.35 | -3.50 | -3.49 | -3.49 | 3.40 | 3.30 | 1.82 | 3.43 | 3.43 | 3.31 | 3.33 | 3.24 | 3.26 | -3.39 | -3.37 | -3.47 | -3.34 | -3.41 | -3.38 | -3.41 | -3.44 | -3.43 |
| Fe2 | 3.07 | -3.23 | -3.34 | -3.36 | 3.31 | -3.36 | -0.46 | 3.21 | -3.26 | -3.34 | -3.10 | 0.99 | 3.29 | -0.84 | 2.90 | 2.51 | 2.88 | -3.40 | -3.37 | 3.25 | -3.28 | -3.33 | -3.34 | -3.28 | 2.88 | 2.85 | -3.29 | 3.03 | 2.97 | -3.33 | -3.29 | 3.13 | 3.10 | 3.07 | 2.87 |
| Fe3 | 3.12 | -3.35 | -3.35 | 3.34 | -3.38 | 3.13 | -3.25 | 3.19 | -0.13 | 2.89 | -2.64 | -3.36 | -0.81 | 3.33 | 2.92 | 3.10 | 3.00 | -3.47 | 3.31 | -3.34 | -3.35 | -3.32 | 3.00 | 3.05 | -3.41 | -3.31 | 3.11 | -3.32 | 3.13 | 3.22 | 3.23 | -3.35 | -3.34 | 2.99 | 3.12 |
| Fe4 | 3.17 | -3.27 | 3.32 | -3.20 | -3.14 | 3.01 | 3.07 | -3.16 | 3.20 | 3.08 | 3.40 | 3.13 | -3.28 | -3.22 | 2.95 | 2.91 | 2.90 | 3.13 | -3.50 | -3.21 | 3.27 | 3.26 | -3.32 | -3.42 | -3.28 | -3.35 | 3.27 | 3.20 | -3.27 | 3.25 | 3.25 | 3.13 | 3.16 | -3.27 | -3.19 |
| Fe5 | -3.38 | 3.15 | 3.26 | 3.21 | 3.21 | -3.40 | -3.13 | 3.08 | -3.21 | 2.89 | -2.90 | 3.07 | -3.27 | -3.25 | -3.34 | -3.14 | 2.91 | -3.17 | 2.90 | 3.06 | 1.66 | 2.08 | -3.17 | 3.05 | -3.13 | 3.12 | 3.10 | 3.23 | -3.08 | -3.03 | 3.16 | -3.05 | 3.20 | 3.09 | 3.12 |
| Fe6 | -3.36 | 3.03 | 3.30 | 3.22 | 3.16 | 3.10 | -3.22 | -3.17 | -3.25 | -3.28 | 3.24 | -3.29 | -3.27 | 3.15 | -3.21 | 2.78 | -3.26 | 3.09 | 3.06 | -3.20 | -3.21 | 3.20 | 2.95 | -3.22 | 2.53 | 2.88 | -3.20 | 3.01 | 2.98 | 2.99 | 3.06 | 3.08 | -3.16 | -3.25 | 3.11 |
| Fe7 | -3.42 | 3.05 | 3.36 | 3.28 | 3.24 | -3.33 | 3.19 | -3.22 | 3.12 | -3.39 | -2.38 | -3.29 | 3.09 | -3.29 | 2.92 | -3.26 | -3.33 | 3.09 | -3.15 | 3.26 | 3.26 | -3.16 | 2.53 | 2.68 | 3.10 | -3.18 | 2.99 | -3.15 | 3.07 | 3.01 | -3.13 | 3.14 | 3.15 | 3.13 | -3.21 |
| S1A | 0.26 | -0.06 | -0.09 | -0.48 | -0.05 | -0.03 | 0.28 | -0.01 | 0.12 | 0.00 | 0.17 | 0.14 | 0.16 | 0.10 | -0.02 | -0.02 | 0.01 | 0.07 | -0.23 | 0.00 | 0.16 | 0.11 | -0.17 | -0.17 | 0.05 | 0.02 | -0.17 | 0.10 | -0.21 | -0.13 | -0.18 | 0.09 | 0.07 | -0.14 | -0.18 |
| S2A | 0.17 | -0.06 | -0.48 | -0.17 | -0.17 | 0.03 | 0.05 | 0.12 | 0.09 | 0.02 | 0.01 | 0.07 | 0.19 | 0.21 | 0.00 | -0.01 | -0.01 | -0.19 | 0.13 | 0.01 | -0.12 | -0.12 | 0.04 | 0.09 | 0.03 | 0.04 | -0.17 | -0.19 | 0.04 | -0.15 | -0.13 | -0.15 | -0.14 | 0.04 | 0.04 |
| S4A | 0.26 | -0.06 | -0.05 | -0.05 | -0.45 | 0.23 | 0.07 | 0.03 | 0.25 | 0.11 | 0.22 | 0.07 | 0.03 | 0.13 | 0.02 | 0.01 | 0.04 | 0.04 | 0.06 | -0.27 | 0.09 | 0.14 | 0.05 | 0.05 | -0.16 | -0.16 | 0.10 | -0.14 | -0.16 | 0.12 | 0.12 | -0.17 | -0.17 | -0.18 | -0.11 |
| S1B | -0.31 | 0.24 | 0.29 | 0.24 | 0.25 | -0.02 | -0.21 | -0.09 | -0.22 | -0.14 | 0.02 | -0.11 | -0.25 | -0.01 | -0.26 | 0.00 | -0.09 | 0.08 | 0.21 | -0.04 | 0.00 | 0.12 | 0.09 | 0.01 | 0.05 | 0.17 | -0.02 | 0.23 | 0.07 | 0.08 | 0.20 | 0.07 | 0.02 | -0.03 | 0.19 |
| S3B | -0.34 | 0.25 | 0.33 | 0.32 | 0.30 | 0.00 | -0.03 | -0.28 | -0.04 | -0.32 | 0.07 | -0.31 | -0.09 | -0.02 | -0.06 | -0.03 | -0.32 | 0.25 | 0.07 | -0.02 | 0.02 | 0.10 | 0.16 | -0.04 | 0.18 | 0.04 | -0.05 | 0.02 | 0.25 | 0.23 | 0.07 | 0.25 | 0.00 | -0.05 | 0.01 |
| S4B | -0.34 | 0.27 | 0.31 | 0.28 | 0.27 | -0.26 | -0.01 | -0.10 | -0.02 | -0.16 | -0.06 | -0.09 | -0.02 | -0.25 | -0.02 | -0.20 | -0.12 | 0.09 | -0.01 | 0.22 | 0.14 | 0.03 | 0.09 | 0.11 | 0.12 | -0.01 | 0.19 | 0.01 | 0.07 | 0.08 | 0.04 | 0.10 | 0.22 | 0.18 | 0.00 |
| S2B | -0.18 | -0.05 | 0.05 | 0.01 | 0.45 | 0.01 | -0.20 | 0.00 | -0.47 | -0.50 | 0.04 | -0.23 | -0.06 | 0.30 | -0.13 | 0.24 | -0.15 | -0.03 | -0.09 | -0.03 | -0.45 | 0.03 | -0.03 | -0.47 | 0.18 | 0.22 | -0.48 | 0.37 | 0.36 | 0.02 | 0.01 | 0.40 | -0.08 | -0.09 | 0.36 |
| S5A | -0.11 | -0.14 | 0.01 | 0.43 | -0.03 | -0.09 | -0.01 | 0.04 | 0.18 | -0.13 | -0.14 | -0.45 | 0.26 | 0.00 | 0.26 | -0.04 | -0.12 | -0.10 | 0.05 | -0.03 | -0.02 | -0.38 | 0.17 | 0.14 | -0.08 | -0.41 | 0.31 | -0.40 | 0.35 | 0.34 | 0.01 | -0.01 | -0.04 | 0.33 | -0.02 |
| C* | -0.21 | -0.17 | -0.07 | -0.21 | -0.23 | -0.12 | 0.18 | -0.03 | 0.14 | -0.07 | 0.37 | 0.00 | 0.11 | 0.14 | -0.42 | -0.34 | -0.39 | -0.07 | -0.15 | 0.01 | 0.10 | 0.05 | -0.17 | -0.08 | -0.14 | -0.12 | -0.27 | -0.26 | -0.44 | -0.31 | -0.23 | -0.30 | -0.27 | -0.37 | -0.35 |
| N | -0.18 | -0.18 | -0.17 | -0.10 | -0.06 | -0.28 | 0.00 | 0.18 | 0.07 | -0.26 | 0.23 | -0.27 | 0.24 | 0.22 | -0.28 | -0.08 | -0.30 | -0.25 | -0.29 | -0.06 | -0.21 | -0.20 | 0.16 | -0.25 | 0.16 | -0.25 | -0.27 | -0.24 | 0.12 | -0.21 | -0.25 | -0.21 | -0.25 | -0.18 | -0.12 |
| O3 | 0.02 | -0.07 | 0.00 | -0.02 | -0.01 | 0.01 | 0.01 | -0.03 | 0.01 | 0.00 | 0.07 | 0.03 | -0.02 | -0.06 | 0.03 | 0.02 | 0.02 | 0.03 | -0.10 | -0.03 | -0.01 | -0.01 | -0.03 | -0.09 | -0.04 | -0.08 | 0.05 | 0.05 | 0.00 | 0.03 | 0.02 | 0.04 | 0.06 | -0.05 | -0.03 |
| O1 | -0.06 | 0.02 | 0.04 | 0.01 | 0.01 | -0.08 | -0.02 | 0.04 | 0.00 | 0.02 | -0.02 | -0.01 | -0.02 | 0.01 | -0.08 | -0.03 | 0.02 | -0.07 | 0.01 | 0.01 | 0.05 | 0.03 | 0.01 | 0.03 | 0.02 | 0.02 | 0.01 | 0.00 | 0.00 | -0.05 | 0.02 | -0.06 | -0.01 | 0.01 | 0.01 |
| O2 | -0.10 | -0.09 | -0.08 | -0.06 | -0.03 | -0.14 | 0.00 | 0.10 | 0.04 | -0.13 | 0.12 | -0.13 | 0.12 | 0.11 | -0.15 | -0.04 | -0.15 | -0.13 | -0.15 | -0.03 | -0.11 | -0.10 | 0.06 | -0.13 | 0.07 | -0.12 | -0.14 | -0.12 | 0.04 | -0.11 | -0.12 | -0.12 | -0.13 | -0.09 | -0.06 |

*Table S 13: Mulliken spin population of the [**V**-NO$_3$]$^0$, $M_S = 0$, Functional: TPSSh*

| BS | 1 | 2 | 3 | 3 | 3 | 4 | 4 | 4 | 5 | 5 | 5 | 5 | 5 | 5 | 6 | 6 | 6 | 7 | 7 | 7 | 8 | 8 | 8 | 8 | 8 | 8 | 9 | 9 | 9 | 10 | 10 | 10 | 10 | 10 | 10 |
|---|---|---|---|---|---|---|---|---|---|---|---|---|---|---|---|---|---|---|---|---|---|---|---|---|---|---|---|---|---|---|---|---|---|---|---|
| Flip | 567 | 234 | 123 | 124 | 134 | 257 | 356 | 467 | 256 | 267 | 357 | 367 | 456 | 457 | 156 | 157 | 167 | 235 | 247 | 346 | 236 | 237 | 245 | 246 | 345 | 347 | 126 | 137 | 145 | 125 | 127 | 135 | 136 | 146 | 147 |
| V | 1.97 | -2.04 | -2.06 | -1.97 | -2.01 | 0.35 | 0.83 | 1.60 | 1.01 | 1.64 | 0.54 | 1.57 | 1.13 | 0.58 | 0.68 | 0.35 | 1.68 | -1.60 | -1.24 | -0.70 | -0.33 | -1.25 | -1.67 | -0.40 | -1.64 | -0.76 | -0.55 | -1.02 | -1.55 | -1.55 | -1.15 | -1.53 | -0.72 | -0.54 | -1.01 |
| Fe1 | -1.41 | 3.48 | -3.59 | -3.54 | -3.55 | 0.33 | 0.35 | -2.64 | 3.45 | -2.68 | 3.45 | 3.43 | 3.28 | 3.32 | -3.50 | -3.50 | -3.49 | 2.64 | 2.61 | 2.41 | 3.41 | 2.35 | 3.29 | 3.45 | 3.25 | 3.48 | -3.61 | -3.34 | -3.43 | -3.35 | -3.43 | -3.37 | -3.43 | -3.45 | -3.45 |
| Fe2 | 3.26 | -3.19 | -3.42 | -3.40 | 3.17 | -3.41 | 3.14 | 3.41 | -2.40 | -2.74 | -3.01 | -1.73 | 3.29 | -1.06 | 2.84 | 1.91 | 2.48 | -3.41 | -3.40 | 2.80 | -3.38 | -3.43 | -3.36 | -3.14 | 2.93 | -0.31 | -3.45 | 1.45 | 3.15 | -3.33 | -3.34 | 2.99 | 2.89 | 3.01 | 2.40 |
| Fe3 | 3.29 | -3.28 | -3.45 | 3.16 | -3.43 | 3.20 | -3.45 | 3.46 | -3.09 | 3.44 | -2.49 | -3.27 | -1.00 | 3.33 | 1.98 | 3.02 | 2.76 | -3.46 | 2.70 | -3.44 | -3.41 | -3.44 | 2.96 | -0.25 | -3.40 | -3.20 | 2.78 | -3.32 | 1.97 | 3.11 | 2.89 | -3.36 | -3.39 | 2.49 | 3.09 |
| Fe4 | 3.31 | -3.35 | 3.37 | -3.44 | -3.40 | 3.29 | 3.27 | -3.12 | 3.45 | 3.48 | 3.46 | 3.40 | -3.43 | -3.38 | 3.14 | 3.13 | 2.97 | 3.12 | -3.59 | -3.57 | 3.28 | 3.16 | -3.53 | -3.41 | -3.49 | -3.38 | 2.96 | 3.32 | -3.41 | 3.27 | 2.81 | 3.30 | 2.75 | -3.46 | -3.45 |
| Fe5 | -3.48 | 3.32 | 3.41 | 3.31 | 3.38 | -3.45 | -3.46 | 3.25 | -3.20 | 3.27 | -3.13 | 3.24 | -3.39 | -3.33 | -3.50 | -3.48 | 2.10 | -3.25 | 3.22 | 3.24 | 1.31 | 3.30 | -3.33 | 3.32 | -3.32 | 3.38 | 3.29 | 3.37 | -3.25 | -3.25 | 3.13 | -3.24 | 3.10 | 3.13 | 3.20 |
| Fe6 | -3.31 | 3.12 | 3.08 | 3.05 | 2.87 | 3.16 | -3.30 | -3.11 | -2.87 | -3.10 | 3.25 | -3.15 | -3.24 | 3.19 | -3.29 | 2.74 | -3.39 | 3.11 | 3.12 | -3.21 | -3.32 | 3.00 | 2.88 | -3.22 | 2.42 | 3.13 | -3.20 | 3.10 | 3.13 | 2.90 | 2.96 | 2.38 | -3.22 | -3.25 | 2.87 |
| Fe7 | -3.38 | 1.22 | 3.17 | 3.06 | 3.14 | -3.33 | 3.12 | -3.12 | 3.20 | -3.18 | -2.88 | -3.22 | 3.10 | -3.25 | 2.73 | -3.32 | -3.44 | 3.12 | -3.14 | 3.11 | 2.85 | -3.16 | 2.46 | 3.14 | 2.99 | -3.16 | 3.01 | -3.20 | 3.19 | 2.36 | -3.18 | 3.05 | 2.99 | 2.88 | -3.20 |
| S1A | 0.32 | -0.08 | -0.19 | -0.56 | -0.10 | -0.08 | 0.26 | 0.14 | 0.21 | 0.11 | 0.15 | 0.19 | 0.08 | 0.04 | 0.01 | 0.02 | 0.00 | -0.14 | -0.39 | -0.13 | 0.07 | -0.13 | -0.19 | -0.08 | 0.03 | 0.06 | -0.35 | 0.00 | -0.15 | -0.13 | -0.28 | 0.10 | -0.02 | -0.15 | -0.21 |
| S2A | 0.36 | -0.03 | -0.56 | -0.16 | -0.18 | -0.04 | -0.06 | 0.35 | 0.03 | 0.06 | 0.04 | 0.01 | 0.19 | 0.20 | -0.01 | 0.00 | -0.01 | -0.35 | -0.05 | -0.07 | -0.16 | -0.33 | 0.05 | 0.13 | 0.03 | 0.15 | -0.30 | -0.21 | -0.01 | -0.16 | -0.14 | -0.19 | -0.16 | -0.04 | -0.03 |
| S4A | 0.29 | -0.06 | -0.20 | -0.08 | -0.50 | 0.30 | -0.07 | 0.11 | 0.11 | 0.31 | 0.19 | 0.12 | 0.04 | 0.12 | 0.05 | 0.04 | 0.05 | -0.11 | -0.06 | -0.36 | 0.06 | -0.10 | 0.04 | 0.05 | -0.18 | -0.09 | -0.05 | -0.15 | -0.16 | 0.10 | -0.02 | -0.12 | -0.26 | -0.19 | -0.11 |
| S1B | -0.33 | 0.31 | 0.31 | 0.26 | 0.29 | 0.01 | -0.29 | -0.10 | -0.19 | -0.09 | 0.01 | -0.09 | -0.27 | 0.00 | -0.27 | -0.04 | -0.23 | 0.10 | 0.24 | -0.01 | -0.03 | 0.25 | 0.11 | -0.01 | 0.08 | 0.25 | -0.02 | 0.27 | 0.08 | 0.10 | 0.19 | 0.06 | -0.03 | -0.01 | 0.19 |
| S3B | -0.34 | 0.19 | 0.25 | 0.29 | 0.26 | 0.01 | -0.04 | -0.25 | -0.02 | -0.27 | 0.05 | -0.29 | -0.08 | -0.01 | -0.08 | -0.03 | -0.36 | 0.25 | 0.07 | -0.02 | -0.04 | 0.09 | 0.15 | -0.03 | 0.16 | 0.04 | -0.06 | 0.05 | 0.28 | 0.13 | 0.05 | 0.14 | -0.01 | -0.05 | 0.02 |
| S4B | -0.35 | 0.18 | 0.34 | 0.31 | 0.30 | -0.27 | -0.02 | -0.10 | -0.02 | -0.13 | -0.16 | -0.09 | -0.04 | -0.24 | -0.05 | -0.25 | -0.25 | 0.10 | 0.03 | 0.23 | 0.05 | 0.04 | 0.09 | 0.23 | 0.12 | 0.01 | 0.23 | 0.02 | 0.11 | 0.09 | -0.01 | 0.12 | 0.18 | 0.16 | 0.02 |
| S2B | -0.12 | 0.04 | -0.06 | -0.08 | 0.33 | 0.02 | -0.13 | 0.05 | -0.24 | -0.27 | 0.08 | -0.29 | -0.04 | 0.30 | -0.19 | 0.19 | -0.15 | -0.05 | -0.06 | -0.10 | -0.51 | -0.10 | -0.04 | -0.44 | 0.17 | 0.32 | -0.52 | 0.24 | 0.43 | 0.02 | 0.02 | 0.25 | -0.10 | -0.08 | 0.24 |
| S5A | -0.05 | -0.18 | -0.12 | 0.28 | -0.10 | -0.07 | -0.07 | 0.12 | -0.01 | 0.08 | -0.17 | -0.42 | 0.27 | 0.02 | 0.16 | -0.12 | -0.10 | -0.12 | -0.05 | -0.15 | -0.15 | -0.42 | 0.15 | 0.27 | -0.09 | -0.37 | 0.30 | -0.38 | 0.24 | 0.23 | -0.03 | -0.03 | -0.06 | 0.17 | 0.01 |
| C* | -0.13 | 0.03 | -0.23 | -0.25 | -0.24 | -0.08 | -0.09 | 0.07 | 0.37 | 0.06 | 0.39 | 0.27 | 0.11 | 0.16 | -0.35 | -0.37 | -0.39 | -0.07 | -0.06 | -0.09 | -0.03 | -0.05 | -0.14 | 0.13 | -0.13 | 0.15 | -0.31 | -0.17 | -0.29 | -0.36 | -0.38 | -0.35 | -0.40 | -0.39 | -0.37 |
| N | 0.00 | 0.00 | 0.01 | 0.00 | 0.00 | 0.00 | 0.00 | 0.00 | 0.00 | 0.01 | 0.00 | 0.01 | -0.01 | -0.01 | 0.00 | 0.00 | 0.01 | 0.00 | 0.00 | 0.00 | 0.00 | 0.01 | -0.01 | 0.00 | -0.01 | 0.00 | 0.01 | 0.01 | -0.01 | 0.00 | 0.01 | 0.00 | 0.01 | 0.00 | 0.00 |
| O3 | 0.03 | -0.05 | 0.08 | -0.05 | -0.05 | 0.04 | 0.03 | -0.03 | 0.05 | 0.08 | 0.05 | 0.06 | -0.07 | -0.08 | 0.03 | 0.03 | 0.04 | 0.03 | -0.07 | -0.07 | 0.05 | 0.05 | -0.09 | -0.06 | -0.08 | -0.05 | 0.04 | 0.06 | -0.06 | 0.05 | 0.02 | 0.05 | 0.02 | -0.05 | -0.05 |
| O1 | -0.05 | 0.04 | 0.06 | 0.04 | 0.04 | -0.05 | -0.05 | 0.03 | -0.03 | 0.05 | -0.03 | 0.04 | -0.05 | -0.06 | -0.06 | -0.05 | 0.01 | -0.03 | 0.03 | 0.03 | 0.02 | 0.05 | -0.05 | 0.04 | -0.04 | 0.05 | 0.05 | 0.06 | -0.04 | -0.03 | 0.05 | -0.03 | 0.05 | 0.03 | 0.03 |
| O2 | -0.01 | 0.00 | 0.03 | 0.00 | 0.00 | -0.01 | -0.01 | 0.00 | 0.00 | 0.03 | 0.00 | 0.03 | -0.03 | -0.03 | -0.01 | -0.01 | 0.01 | 0.00 | -0.01 | -0.01 | 0.02 | 0.02 | -0.03 | 0.00 | -0.03 | 0.00 | 0.03 | 0.03 | -0.03 | 0.00 | 0.02 | 0.00 | 0.02 | 0.00 | 0.00 |

*Table S 14: Mulliken spin population of the [**V**-NO$_3$]$^0$, $M_S$ = 1, Functional: TPSSh*

| BS | 1 | 2 | 3 | 3 | 3 | 4 | 4 | 4 | 5 | 5 | 5 | 5 | 5 | 6 | 6 | 6 | 7 | 7 | 7 | 8 | 8 | 8 | 8 | 8 | 8 | 9 | 9 | 9 | 10 | 10 | 10 | 10 | 10 | 10 |
|---|---|---|---|---|---|---|---|---|---|---|---|---|---|---|---|---|---|---|---|---|---|---|---|---|---|---|---|---|---|---|---|---|---|---|
| Flip | 567 | 234 | 123 | 124 | 134 | 257 | 356 | 467 | 256 | 267 | 357 | 367 | 456 | 457 | 156 | 157 | 167 | 235 | 247 | 346 | 236 | 237 | 245 | 246 | 345 | 347 | 126 | 137 | 145 | 125 | 127 | 135 | 136 | 146 | 147 |
| V | 1.89 | -1.87 | 0.71 | -1.81 | -1.81 | 0.16 | 0.63 | 1.63 | 0.67 | 1.56 | 0.26 | 1.47 | 0.90 | 0.35 | 0.48 | 0.10 | 1.44 | -1.66 | -0.72 | -0.21 | -0.37 | -0.83 | -1.55 | -0.15 | -1.53 | -0.45 | 0.06 | -0.54 | -1.61 | -1.53 | -0.85 | -1.50 | -0.29 | -0.25 | -0.74 |
| Fe1 | 1.37 | 3.45 | -3.59 | -3.54 | -3.55 | 2.65 | 2.69 | 1.96 | 2.61 | 1.30 | 3.43 | 3.37 | 2.16 | 2.30 | -3.49 | -3.50 | -3.47 | 3.47 | 3.29 | 3.18 | 3.44 | 3.44 | 3.32 | 3.21 | 3.25 | 3.22 | -3.39 | -3.33 | -3.47 | -3.32 | -3.42 | -3.34 | -3.40 | -3.46 | -3.45 |
| Fe2 | 3.20 | -3.23 | -3.35 | -3.30 | 3.36 | -3.37 | 3.02 | 3.07 | -3.31 | -3.25 | 0.73 | 2.77 | 3.23 | 2.65 | 3.02 | 2.92 | 2.97 | -3.35 | -3.37 | 3.27 | -3.39 | -3.36 | -3.33 | -3.23 | 3.10 | 2.86 | -3.23 | 3.15 | 3.22 | -3.26 | -3.28 | 3.26 | 3.18 | 3.14 | 3.18 |
| Fe3 | 3.29 | -3.35 | -3.46 | 3.36 | -3.37 | 3.15 | -3.41 | 3.06 | 2.65 | 3.27 | -3.24 | -3.41 | 2.76 | 3.26 | 3.03 | 3.17 | 3.16 | -3.43 | 3.29 | -3.40 | -3.48 | -3.32 | 3.19 | 2.80 | -3.39 | -3.30 | 3.20 | -3.26 | 3.31 | 3.33 | 3.32 | -3.30 | -3.31 | 3.21 | 3.19 |
| Fe4 | 3.03 | -3.23 | 3.32 | -3.15 | -3.13 | 3.05 | 2.96 | -3.23 | 3.20 | 3.13 | 3.32 | 2.01 | -3.27 | -3.27 | 3.03 | 3.05 | 2.95 | 3.27 | -3.39 | -3.36 | 3.20 | 3.11 | -3.27 | -3.33 | -3.22 | -3.29 | 3.29 | 3.31 | -3.23 | 3.28 | 3.30 | 3.33 | 3.32 | -3.22 | -3.19 |
| Fe5 | -3.34 | 3.04 | 3.05 | 3.39 | 3.39 | -3.30 | -3.27 | 3.02 | -3.18 | 3.09 | -3.09 | 3.04 | -3.23 | -3.17 | -3.17 | -3.11 | 2.99 | -3.11 | 2.93 | 2.92 | 3.06 | 3.04 | -3.12 | 3.05 | -3.10 | 3.08 | 2.94 | 3.16 | -3.06 | -3.00 | 3.18 | -2.97 | 3.11 | 3.07 | 3.12 |
| Fe6 | -3.32 | 3.19 | 3.23 | 3.32 | 3.24 | 3.17 | -3.30 | -3.29 | -3.19 | -3.12 | 3.21 | -3.21 | -3.31 | 3.18 | -3.21 | 3.04 | -3.27 | 3.09 | 3.10 | -3.24 | -3.30 | 3.00 | 3.16 | -3.24 | 2.88 | 2.99 | -3.22 | 3.09 | 3.14 | 3.05 | 3.13 | 3.10 | -3.22 | -3.25 | 3.17 |
| Fe7 | -3.39 | 3.29 | 3.13 | 3.29 | 3.42 | -3.33 | 3.15 | -3.35 | 3.07 | -3.28 | -3.17 | -3.30 | 3.11 | -3.32 | 3.00 | -3.24 | -3.34 | 3.06 | -3.22 | 3.13 | 3.15 | -3.17 | 2.88 | 3.05 | 3.23 | -3.19 | 3.11 | -3.19 | 3.22 | 3.11 | -3.18 | 3.13 | 3.17 | 3.19 | -3.21 |
| S1A | 0.21 | -0.09 | -0.14 | -0.42 | -0.05 | 0.03 | 0.07 | -0.04 | 0.09 | 0.03 | 0.17 | 0.10 | 0.02 | 0.00 | 0.02 | 0.03 | 0.03 | 0.14 | -0.22 | 0.02 | 0.10 | 0.07 | -0.18 | -0.12 | 0.06 | 0.03 | -0.13 | 0.17 | -0.16 | -0.05 | -0.13 | 0.14 | 0.12 | -0.13 | -0.13 |
| S2A | 0.21 | -0.10 | -0.54 | -0.16 | -0.18 | 0.02 | -0.01 | 0.07 | -0.06 | 0.00 | 0.06 | 0.13 | -0.01 | -0.02 | 0.03 | 0.03 | 0.01 | -0.15 | 0.12 | 0.06 | -0.18 | -0.13 | 0.07 | 0.02 | 0.07 | 0.02 | -0.17 | -0.17 | 0.10 | -0.11 | -0.12 | -0.14 | -0.15 | 0.07 | 0.08 |
| S4A | 0.23 | -0.08 | -0.15 | -0.04 | -0.43 | 0.18 | 0.00 | -0.03 | 0.03 | 0.16 | 0.14 | 0.02 | -0.01 | 0.02 | 0.06 | 0.06 | 0.08 | 0.11 | 0.04 | -0.20 | 0.07 | 0.07 | 0.05 | 0.03 | -0.18 | -0.15 | 0.15 | -0.06 | -0.12 | 0.15 | 0.13 | -0.06 | -0.10 | -0.13 | -0.11 |
| S1B | -0.31 | 0.23 | 0.20 | 0.30 | 0.28 | 0.02 | -0.25 | -0.11 | -0.22 | -0.08 | 0.05 | -0.11 | -0.28 | 0.02 | -0.21 | 0.04 | -0.11 | 0.09 | 0.16 | -0.07 | -0.06 | 0.19 | 0.10 | -0.04 | 0.08 | 0.16 | -0.08 | 0.21 | 0.09 | 0.10 | 0.21 | 0.10 | -0.02 | -0.03 | 0.21 |
| S3B | -0.35 | 0.34 | 0.24 | 0.32 | 0.33 | 0.02 | -0.04 | -0.34 | -0.04 | -0.28 | 0.06 | -0.31 | -0.07 | 0.02 | -0.06 | 0.00 | -0.34 | 0.25 | 0.03 | -0.05 | -0.04 | 0.06 | 0.22 | -0.05 | 0.23 | 0.02 | -0.08 | 0.01 | 0.28 | 0.25 | 0.05 | 0.25 | -0.02 | -0.04 | 0.03 |
| S4B | -0.35 | 0.28 | 0.14 | 0.31 | 0.34 | -0.24 | 0.00 | -0.12 | 0.01 | -0.13 | -0.19 | -0.11 | -0.02 | -0.25 | 0.02 | -0.20 | -0.12 | 0.09 | -0.04 | 0.16 | 0.22 | 0.00 | 0.11 | 0.16 | 0.13 | -0.03 | 0.15 | -0.02 | 0.09 | 0.10 | 0.02 | 0.11 | 0.18 | 0.18 | 0.01 |
| S2B | -0.12 | -0.02 | -0.02 | 0.11 | 0.50 | 0.02 | -0.17 | -0.12 | -0.48 | -0.43 | 0.17 | -0.16 | -0.04 | 0.29 | -0.10 | 0.35 | -0.15 | -0.05 | -0.08 | -0.08 | -0.52 | -0.08 | 0.00 | -0.46 | 0.24 | 0.24 | -0.48 | 0.38 | 0.43 | 0.04 | 0.03 | 0.41 | -0.08 | -0.07 | 0.41 |
| S5A | -0.05 | -0.09 | -0.13 | 0.47 | 0.05 | -0.07 | -0.07 | -0.09 | 0.15 | 0.06 | -0.39 | -0.47 | 0.22 | 0.02 | 0.29 | -0.03 | -0.08 | -0.13 | 0.00 | -0.15 | -0.17 | -0.42 | 0.21 | 0.14 | -0.04 | -0.42 | 0.33 | -0.40 | 0.41 | 0.37 | 0.04 | -0.02 | -0.03 | 0.37 | 0.01 |
| C* | -0.11 | -0.07 | -0.20 | -0.17 | -0.16 | -0.09 | -0.08 | -0.07 | 0.03 | 0.07 | 0.14 | 0.03 | -0.10 | -0.08 | -0.35 | -0.34 | -0.34 | -0.04 | -0.13 | -0.12 | -0.03 | -0.01 | -0.11 | -0.03 | -0.10 | -0.05 | -0.21 | -0.23 | -0.35 | -0.26 | -0.16 | -0.29 | -0.22 | -0.33 | -0.32 |
| N | -0.01 | -0.04 | -0.09 | -0.04 | -0.01 | -0.05 | 0.02 | 0.04 | 0.01 | -0.07 | 0.04 | -0.04 | 0.02 | 0.02 | -0.03 | -0.04 | -0.07 | 0.02 | -0.02 | -0.02 | -0.03 | 0.00 | 0.00 | -0.01 | 0.03 | 0.02 | -0.01 | -0.05 | -0.01 | -0.02 | -0.04 | 0.00 | -0.01 | -0.03 | -0.02 |
| O3 | -0.01 | -0.03 | 0.01 | 0.02 | 0.01 | 0.00 | -0.01 | 0.00 | 0.00 | 0.04 | 0.00 | 0.03 | -0.01 | -0.02 | 0.01 | 0.02 | 0.05 | -0.01 | -0.03 | -0.03 | 0.01 | 0.01 | -0.02 | -0.01 | -0.04 | -0.02 | 0.01 | 0.01 | 0.00 | 0.01 | 0.03 | 0.01 | 0.02 | 0.00 | 0.00 |
| O1 | -0.01 | 0.01 | 0.03 | 0.00 | 0.01 | -0.01 | 0.00 | -0.01 | 0.00 | -0.01 | 0.01 | -0.01 | -0.01 | 0.00 | -0.01 | -0.01 | -0.02 | 0.02 | 0.00 | 0.00 | 0.01 | 0.00 | 0.00 | -0.01 | 0.01 | 0.00 | 0.00 | 0.01 | 0.00 | 0.00 | 0.00 | 0.01 | 0.01 | -0.01 | 0.00 |
| O2 | -0.01 | -0.02 | -0.03 | -0.03 | -0.01 | -0.04 | 0.01 | 0.03 | 0.00 | -0.02 | 0.02 | -0.01 | -0.01 | -0.02 | -0.03 | -0.03 | -0.03 | 0.01 | -0.01 | -0.01 | 0.01 | 0.02 | -0.03 | 0.00 | 0.00 | 0.01 | 0.02 | 0.00 | -0.03 | -0.02 | 0.00 | -0.01 | 0.02 | -0.02 | -0.01 |

*Table S 15: Mulliken spin population of the [**V**-NO$_3$]$^0$, $M_S$ = 2, Functional: TPSSh*

| BS | 1 | 2 | 3 | 3 | 3 | 4 | 4 | 4 | 5 | 5 | 5 | 5 | 5 | 6 | 6 | 6 | 7 | 7 | 7 | 8 | 8 | 8 | 8 | 8 | 8 | 9 | 9 | 9 | 10 | 10 | 10 | 10 | 10 | 10 |
|---|---|---|---|---|---|---|---|---|---|---|---|---|---|---|---|---|---|---|---|---|---|---|---|---|---|---|---|---|---|---|---|---|---|---|
| Flip | 567 | 234 | 123 | 124 | 134 | 257 | 356 | 467 | 256 | 267 | 357 | 367 | 456 | 457 | 156 | 157 | 167 | 235 | 247 | 346 | 236 | 237 | 245 | 246 | 345 | 347 | 126 | 137 | 145 | 125 | 127 | 135 | 136 | 146 | 147 |
| V | 1.87 | 0.53 | 0.70 | 1.01 | -1.80 | 1.77 | 2.32 | 1.65 | 0.81 | 1.55 | 1.83 | 1.59 | 1.90 | 2.02 | 0.69 | 1.98 | 1.51 | -0.08 | -0.54 | -0.13 | 0.02 | -0.38 | -1.44 | -0.05 | 0.13 | 1.24 | -0.04 | -0.27 | -1.64 | 1.78 | 1.90 | 2.05 | -0.21 | 0.77 | 1.84 |
| Fe1 | 1.57 | 3.45 | -2.67 | -3.54 | -2.70 | 2.66 | 3.77 | 2.33 | 3.47 | 3.41 | 3.31 | 3.41 | 2.46 | 2.28 | -3.43 | -3.48 | -3.46 | 3.47 | 3.36 | 3.32 | 3.48 | 3.49 | 3.37 | 3.39 | 3.32 | 3.34 | -3.15 | -3.18 | -3.45 | -3.32 | -3.39 | -3.36 | -3.30 | -3.46 | -3.45 |
| Fe2 | 3.30 | -3.19 | -3.19 | -3.30 | 3.36 | -3.33 | 3.80 | 3.29 | -3.32 | -3.34 | 2.52 | 2.86 | 3.27 | 2.94 | 3.26 | 3.00 | 3.32 | -3.37 | -3.22 | 3.29 | -3.14 | -3.18 | -3.31 | -3.14 | 3.26 | 3.25 | -3.11 | 3.34 | 3.45 | -3.25 | -3.24 | 3.16 | 3.40 | 3.31 | 3.20 |
| Fe3 | 3.39 | -3.34 | -3.31 | 3.37 | -3.07 | 3.18 | 3.73 | 3.32 | 2.87 | 2.84 | -3.35 | -3.35 | 3.09 | 3.29 | 3.29 | 3.26 | 3.40 | -3.43 | 3.33 | -3.32 | -3.20 | -3.24 | 3.40 | 3.35 | -3.40 | -3.30 | 3.40 | -3.10 | 3.49 | 3.30 | 3.33 | -3.31 | -3.23 | 3.39 | 3.21 |
| Fe4 | 3.33 | -3.23 | 3.29 | -3.19 | -3.06 | 3.06 | 3.80 | -3.26 | 3.22 | 3.18 | 3.19 | 3.20 | -3.27 | -3.26 | 3.32 | 3.07 | 3.17 | 3.30 | -3.19 | -3.19 | 3.29 | 3.29 | -3.24 | -3.28 | -3.25 | -3.32 | 3.32 | 3.39 | -3.14 | 3.23 | 3.28 | 3.21 | 3.41 | -3.15 | -3.22 |
| Fe5 | -3.10 | 2.87 | 3.01 | 3.11 | 3.38 | -3.21 | 3.79 | 3.08 | -3.20 | 3.11 | -3.29 | 3.10 | -3.23 | -3.16 | -2.98 | -3.14 | 3.14 | -3.00 | 3.23 | 3.27 | 3.13 | 3.21 | -2.99 | 3.16 | -3.18 | 3.02 | 3.23 | 3.25 | -2.88 | -3.10 | 2.81 | -3.08 | 3.35 | 3.19 | 2.85 |
| Fe6 | -3.20 | 3.28 | 3.16 | 3.37 | 3.24 | 3.24 | 3.61 | -3.09 | -3.20 | -3.20 | 3.13 | -3.22 | -3.31 | 3.26 | -3.17 | 3.19 | -3.23 | 3.17 | 3.30 | -3.15 | -3.21 | 3.28 | 3.36 | -3.22 | 3.09 | 2.92 | -3.14 | 3.28 | 3.39 | 3.14 | 3.18 | 2.76 | -3.09 | -3.14 | 3.27 |
| Fe7 | -3.30 | 3.18 | 3.12 | 3.27 | 3.45 | -3.27 | 3.69 | -3.10 | 3.11 | -3.25 | -3.25 | -3.23 | 3.22 | -3.34 | 3.22 | -3.26 | -3.24 | 3.18 | -3.15 | 3.32 | 3.29 | -3.18 | 3.39 | 3.26 | 3.25 | -3.23 | 3.32 | -3.09 | 3.44 | 2.64 | -3.27 | 3.08 | 3.37 | 3.30 | -3.27 |
| S1A | 0.30 | -0.08 | -0.02 | -0.45 | -0.05 | 0.02 | 0.64 | -0.03 | 0.11 | 0.07 | 0.17 | 0.27 | 0.07 | 0.00 | 0.08 | 0.03 | 0.05 | 0.13 | -0.12 | 0.11 | 0.16 | 0.13 | -0.17 | -0.12 | 0.11 | 0.08 | 0.00 | 0.20 | -0.07 | -0.08 | -0.12 | 0.10 | 0.20 | -0.09 | -0.13 |
| S2A | 0.18 | -0.09 | -0.16 | -0.14 | -0.03 | 0.03 | 0.61 | 0.21 | 0.16 | 0.13 | 0.08 | 0.14 | 0.12 | 0.09 | 0.07 | 0.04 | 0.11 | -0.17 | 0.15 | 0.10 | -0.08 | -0.08 | 0.14 | 0.21 | 0.11 | 0.14 | -0.04 | -0.04 | 0.19 | -0.12 | -0.09 | -0.15 | -0.07 | 0.14 | 0.09 |
| S4A | 0.30 | -0.08 | -0.01 | -0.04 | -0.14 | 0.19 | 0.54 | -0.02 | 0.27 | 0.28 | 0.07 | 0.05 | -0.03 | 0.02 | 0.09 | 0.07 | 0.10 | 0.10 | 0.12 | -0.15 | 0.10 | 0.14 | 0.13 | 0.09 | -0.17 | -0.17 | 0.19 | 0.00 | -0.06 | 0.13 | 0.14 | -0.13 | -0.02 | -0.11 | -0.11 |
| S1B | -0.24 | 0.20 | 0.18 | 0.19 | 0.27 | -0.04 | 0.36 | -0.09 | -0.24 | -0.08 | -0.07 | -0.12 | -0.30 | -0.04 | -0.22 | -0.05 | -0.09 | 0.06 | 0.24 | -0.02 | -0.06 | 0.23 | 0.12 | -0.04 | 0.01 | 0.01 | -0.03 | 0.22 | 0.17 | 0.01 | 0.09 | -0.04 | 0.01 | -0.04 | 0.12 |
| S3B | -0.34 | 0.30 | 0.23 | 0.24 | 0.33 | -0.02 | 0.38 | -0.27 | -0.03 | -0.30 | -0.04 | -0.31 | -0.10 | -0.03 | -0.04 | -0.05 | -0.32 | 0.24 | 0.04 | -0.02 | 0.00 | 0.05 | 0.35 | -0.02 | 0.17 | -0.01 | -0.01 | 0.05 | 0.37 | 0.11 | 0.02 | 0.11 | 0.01 | 0.00 | 0.01 |
| S4B | -0.29 | 0.13 | 0.14 | 0.10 | 0.34 | -0.29 | 0.34 | -0.09 | -0.01 | -0.11 | -0.29 | -0.09 | -0.06 | -0.32 | 0.02 | -0.30 | -0.11 | 0.08 | -0.01 | 0.24 | 0.20 | -0.02 | 0.13 | 0.19 | 0.00 | -0.11 | 0.22 | -0.03 | 0.16 | -0.13 | -0.17 | -0.02 | 0.25 | 0.09 | -0.15 |
| S2B | 0.04 | 0.00 | -0.01 | 0.09 | 0.49 | 0.11 | 0.65 | 0.01 | -0.49 | -0.48 | 0.25 | -0.17 | -0.12 | 0.34 | 0.00 | 0.39 | -0.02 | -0.03 | 0.12 | -0.11 | -0.44 | 0.10 | 0.09 | -0.47 | 0.40 | 0.33 | -0.38 | 0.46 | 0.52 | 0.05 | 0.05 | 0.33 | 0.05 | -0.10 | 0.42 |
| S5A | 0.09 | -0.14 | -0.08 | 0.44 | 0.11 | -0.05 | 0.62 | 0.07 | 0.18 | -0.13 | -0.46 | -0.45 | 0.36 | -0.01 | 0.42 | -0.05 | 0.08 | -0.08 | -0.03 | 0.03 | 0.03 | -0.38 | 0.48 | 0.43 | -0.02 | -0.43 | 0.44 | -0.31 | 0.51 | 0.25 | -0.02 | 0.02 | 0.05 | 0.42 | -0.03 |
| C* | 0.08 | -0.07 | -0.24 | -0.16 | -0.15 | -0.02 | 0.19 | 0.00 | 0.01 | 0.06 | -0.03 | 0.06 | -0.14 | -0.08 | -0.24 | -0.29 | -0.08 | -0.05 | 0.06 | 0.05 | 0.13 | 0.16 | -0.03 | 0.02 | -0.08 | -0.01 | -0.09 | -0.10 | -0.16 | -0.34 | -0.19 | -0.36 | -0.01 | -0.17 | -0.33 |
| N | 0.06 | -0.01 | -0.08 | -0.05 | 0.01 | -0.01 | 0.32 | 0.01 | 0.01 | 0.03 | 0.05 | 0.03 | 0.10 | 0.06 | -0.03 | -0.03 | -0.01 | 0.11 | 0.03 | 0.06 | -0.02 | 0.01 | -0.02 | -0.02 | 0.05 | 0.02 | 0.00 | 0.04 | -0.02 | -0.01 | -0.01 | -0.05 | 0.00 | -0.04 | 0.00 |
| O3 | 0.02 | -0.03 | 0.01 | 0.01 | 0.01 | 0.01 | 0.11 | -0.01 | 0.00 | 0.00 | -0.01 | 0.00 | -0.03 | -0.02 | 0.02 | 0.02 | 0.03 | 0.03 | 0.00 | -0.02 | 0.00 | 0.00 | -0.02 | -0.01 | -0.03 | -0.01 | 0.03 | 0.02 | -0.01 | 0.02 | 0.03 | 0.02 | 0.02 | 0.01 | 0.00 |
| O1 | 0.00 | 0.00 | 0.02 | -0.01 | 0.01 | -0.02 | 0.10 | -0.01 | 0.00 | 0.00 | 0.00 | 0.01 | -0.02 | -0.01 | 0.01 | -0.02 | -0.01 | -0.02 | 0.00 | 0.01 | 0.01 | 0.00 | 0.00 | -0.01 | 0.00 | 0.00 | 0.00 | 0.01 | 0.00 | -0.01 | -0.02 | -0.01 | 0.01 | -0.01 | -0.02 |
| O2 | 0.04 | 0.00 | -0.03 | -0.03 | 0.00 | -0.01 | 0.17 | 0.01 | 0.01 | 0.04 | 0.03 | 0.04 | 0.04 | 0.01 | -0.03 | -0.03 | 0.02 | 0.07 | 0.02 | 0.04 | 0.01 | 0.03 | -0.04 | -0.01 | 0.00 | 0.01 | 0.02 | 0.04 | -0.03 | -0.01 | 0.01 | -0.03 | 0.03 | -0.03 | 0.00 |

*Table S 16: Mulliken spin population of the [**V**-NO$_3$]$^0$, $M_S$ = $^3/_2$, Functional: TPSSh*

| BS | 1 | 2 | 3 | 3 | 3 | 4 | 4 | 4 | 5 | 5 | 5 | 5 | 5 | 6 | 6 | 6 | 7 | 7 | 7 | 8 | 8 | 8 | 8 | 8 | 9 | 9 | 9 | 10 | 10 | 10 | 10 | 10 | 10 |
|---|---|---|---|---|---|---|---|---|---|---|---|---|---|---|---|---|---|---|---|---|---|---|---|---|---|---|---|---|---|---|---|---|---|
| Flip | 567 | 234 | 123 | 124 | 134 | 257 | 356 | 467 | 256 | 267 | 357 | 367 | 456 | 457 | 156 | 157 | 167 | 235 | 247 | 346 | 236 | 237 | 245 | 246 | 345 | 347 | 126 | 137 | 145 | 125 | 127 | 135 | 136 | 146 | 147 |
| V | 1.75 | -1.74 | -1.81 | -1.69 | -1.69 | 0.04 | 0.57 | 1.58 | 1.76 | 1.58 | 1.73 | 1.57 | 0.34 | 1.78 | 0.16 | -0.17 | 1.39 | -1.58 | 0.40 | -0.02 | 0.31 | -0.08 | -0.18 | 0.88 | -0.40 | 0.81 | 0.15 | -0.20 | -1.56 | -1.55 | -0.72 | -1.50 | 0.16 | 0.92 | 1.34 |
| Fe1 | 1.92 | 3.42 | -2.83 | -2.87 | -2.90 | 3.34 | 3.42 | 2.25 | 2.60 | 2.83 | 2.77 | 2.90 | 3.11 | 1.91 | -3.44 | -3.46 | -3.44 | 3.46 | 2.92 | 2.97 | 3.44 | 3.40 | 3.17 | 2.85 | 3.17 | 3.11 | -3.52 | -3.11 | -3.46 | -2.88 | -3.52 | -2.87 | -3.51 | -3.47 | -3.47 |
| Fe2 | 3.23 | -3.23 | -3.21 | -3.12 | 3.21 | -3.32 | 2.64 | 3.23 | -3.34 | -3.34 | 2.59 | 2.82 | 3.21 | 3.01 | 3.11 | 3.16 | 3.10 | -3.33 | -3.22 | 3.25 | -3.17 | -3.17 | -3.34 | -3.24 | 3.01 | 2.87 | -3.29 | 3.19 | 3.38 | -3.18 | -3.28 | 3.28 | 3.31 | 3.16 | 3.11 |
| Fe3 | 3.32 | -3.33 | -3.30 | 3.24 | -3.21 | 2.79 | -3.36 | 3.27 | 2.75 | 2.90 | -3.32 | -3.34 | 2.82 | 3.28 | 3.16 | 3.36 | 3.29 | -3.40 | 3.27 | -3.30 | -3.28 | -3.19 | 2.92 | 3.09 | -3.32 | -3.30 | 3.32 | -3.04 | 3.43 | 3.34 | 3.38 | -3.22 | -3.32 | 3.19 | 3.22 |
| Fe4 | 3.30 | -3.22 | 3.31 | -3.14 | -3.17 | 3.29 | 3.24 | -3.25 | 3.23 | 3.17 | 3.19 | 3.13 | -3.28 | -3.27 | 3.29 | 3.26 | 3.03 | 3.32 | -3.21 | -3.21 | 3.18 | 3.10 | -3.26 | -3.34 | -3.17 | -3.32 | 3.39 | 3.31 | -3.21 | 3.30 | 3.37 | 3.34 | 3.43 | -3.23 | -3.24 |
| Fe5 | -3.34 | 3.29 | 3.34 | 3.38 | 3.39 | -3.29 | -3.29 | 3.11 | -3.28 | 3.15 | -3.30 | 3.12 | -3.23 | -3.24 | -3.02 | -3.03 | 3.06 | -3.11 | 3.07 | 3.27 | 2.97 | 3.03 | -3.20 | 3.09 | -3.17 | 3.09 | 3.29 | 3.09 | -3.05 | -3.04 | 3.37 | -3.00 | 3.23 | 3.13 | 3.04 |
| Fe6 | -3.29 | 3.28 | 3.27 | 3.24 | 3.09 | 3.20 | -3.28 | -3.27 | -3.20 | -3.16 | 3.19 | -3.15 | -3.24 | 3.26 | -3.15 | 3.11 | -3.21 | 3.28 | 3.13 | -3.17 | -3.25 | 3.10 | 3.20 | -3.27 | 3.01 | 3.03 | -3.15 | 3.07 | 3.31 | 3.06 | 3.30 | 3.10 | -3.19 | -3.25 | 2.99 |
| Fe7 | -3.35 | 3.35 | 3.34 | 3.16 | 3.31 | -3.29 | 3.16 | -3.29 | 3.23 | -3.19 | -3.22 | -3.19 | 3.16 | -3.36 | 3.13 | -3.18 | -3.26 | 3.30 | -3.28 | 3.29 | 3.08 | -3.20 | 3.17 | 3.16 | 3.23 | -3.24 | 3.27 | -3.19 | 3.33 | 3.09 | -3.08 | 3.12 | 3.26 | 3.17 | -3.27 |
| S1A | 0.29 | -0.12 | -0.03 | -0.14 | -0.06 | 0.08 | 0.22 | 0.00 | 0.09 | 0.07 | 0.00 | 0.08 | 0.14 | -0.01 | 0.08 | 0.12 | 0.09 | 0.12 | -0.10 | 0.04 | 0.06 | 0.04 | -0.15 | -0.13 | 0.03 | 0.01 | -0.11 | 0.15 | -0.12 | 0.00 | -0.11 | 0.12 | 0.15 | -0.12 | -0.13 |
| S2A | 0.13 | -0.14 | -0.15 | -0.09 | -0.06 | 0.01 | 0.03 | 0.16 | -0.07 | -0.01 | -0.07 | 0.01 | 0.15 | 0.00 | 0.09 | 0.12 | 0.09 | -0.18 | -0.01 | -0.03 | -0.14 | -0.13 | 0.02 | -0.01 | 0.05 | 0.03 | -0.14 | -0.10 | 0.16 | 0.03 | -0.12 | 0.02 | -0.14 | 0.08 | 0.09 |
| S4A | 0.28 | -0.12 | -0.01 | -0.03 | -0.17 | 0.26 | 0.06 | 0.00 | 0.04 | 0.09 | 0.06 | 0.04 | 0.04 | 0.02 | 0.12 | 0.10 | 0.12 | 0.09 | 0.05 | -0.16 | 0.05 | 0.02 | 0.03 | 0.02 | -0.17 | -0.16 | 0.17 | -0.01 | -0.08 | 0.17 | 0.15 | -0.02 | -0.11 | -0.11 | -0.10 |
| S1B | -0.31 | 0.31 | 0.33 | 0.30 | 0.29 | 0.03 | -0.24 | -0.11 | -0.29 | -0.10 | -0.06 | -0.12 | -0.24 | -0.05 | -0.17 | 0.08 | -0.11 | 0.12 | 0.12 | -0.04 | -0.11 | 0.15 | 0.03 | -0.09 | 0.00 | 0.07 | -0.04 | 0.17 | 0.11 | 0.11 | 0.27 | 0.10 | -0.04 | -0.06 | -0.02 |
| S3B | -0.35 | 0.36 | 0.33 | 0.30 | 0.29 | 0.04 | -0.04 | -0.34 | -0.06 | -0.28 | -0.02 | -0.29 | -0.05 | -0.05 | -0.05 | 0.00 | -0.32 | 0.33 | -0.01 | -0.04 | -0.03 | 0.03 | 0.21 | -0.03 | 0.20 | 0.00 | -0.04 | -0.03 | 0.32 | 0.24 | 0.07 | 0.25 | -0.04 | -0.05 | -0.04 |
| S4B | -0.35 | 0.34 | 0.36 | 0.32 | 0.32 | -0.23 | -0.01 | -0.11 | -0.05 | -0.12 | -0.31 | -0.10 | 0.03 | -0.34 | 0.07 | -0.17 | -0.11 | 0.12 | -0.10 | 0.22 | 0.11 | -0.08 | 0.01 | 0.08 | 0.04 | -0.09 | 0.21 | -0.06 | 0.11 | 0.11 | 0.04 | 0.11 | 0.20 | 0.05 | -0.13 |
| S2B | -0.05 | 0.04 | 0.08 | 0.09 | 0.39 | -0.01 | -0.18 | -0.07 | -0.51 | -0.49 | 0.27 | -0.11 | -0.06 | 0.44 | -0.02 | 0.40 | -0.07 | 0.04 | -0.01 | -0.04 | -0.48 | 0.02 | 0.03 | -0.51 | 0.28 | 0.30 | -0.50 | 0.39 | 0.47 | -0.03 | 0.05 | 0.43 | 0.00 | -0.14 | 0.32 |
| S5A | 0.03 | -0.04 | -0.01 | 0.35 | 0.05 | -0.10 | -0.11 | -0.01 | 0.25 | -0.09 | -0.47 | -0.47 | 0.22 | 0.00 | 0.34 | 0.08 | 0.03 | -0.04 | 0.00 | -0.10 | -0.09 | -0.40 | 0.25 | 0.34 | 0.00 | -0.45 | 0.41 | -0.31 | 0.46 | 0.40 | 0.12 | -0.09 | -0.03 | 0.35 | -0.05 |
| C* | -0.01 | 0.02 | -0.15 | -0.26 | -0.25 | -0.01 | -0.02 | -0.01 | 0.02 | 0.07 | 0.01 | 0.07 | -0.12 | -0.11 | -0.33 | -0.31 | -0.26 | 0.00 | 0.02 | 0.04 | 0.06 | 0.08 | -0.11 | 0.00 | -0.09 | -0.01 | -0.13 | -0.27 | -0.29 | -0.25 | -0.08 | -0.27 | -0.12 | -0.30 | -0.30 |
| N | 0.02 | 0.01 | 0.00 | -0.03 | 0.00 | 0.00 | 0.01 | 0.01 | 0.00 | 0.03 | 0.02 | 0.03 | -0.02 | 0.00 | -0.02 | -0.02 | 0.01 | 0.00 | 0.00 | 0.03 | 0.02 | 0.03 | -0.03 | 0.00 | -0.01 | 0.01 | 0.01 | 0.02 | -0.03 | -0.02 | 0.01 | -0.01 | 0.02 | -0.01 | 0.00 |
| O3 | -0.01 | -0.01 | 0.03 | 0.01 | 0.01 | -0.01 | -0.01 | 0.00 | 0.00 | 0.00 | -0.01 | 0.00 | -0.02 | -0.03 | 0.02 | 0.01 | 0.02 | -0.01 | -0.01 | -0.01 | 0.01 | 0.01 | -0.01 | -0.01 | -0.02 | -0.02 | 0.03 | 0.01 | 0.00 | 0.01 | 0.03 | 0.01 | 0.02 | 0.01 | 0.01 |
| O1 | 0.01 | 0.00 | 0.01 | 0.00 | 0.01 | 0.01 | 0.01 | -0.01 | 0.00 | 0.00 | 0.00 | 0.00 | 0.00 | -0.01 | 0.01 | 0.01 | 0.00 | 0.01 | 0.00 | 0.00 | 0.00 | 0.00 | -0.01 | -0.01 | 0.00 | 0.00 | 0.00 | 0.00 | 0.01 | 0.00 | 0.01 | 0.01 | -0.01 | -0.01 | -0.01 |
| O2 | 0.01 | 0.02 | 0.03 | -0.02 | 0.00 | 0.00 | 0.00 | 0.01 | 0.00 | 0.05 | 0.01 | 0.04 | -0.04 | -0.04 | -0.02 | -0.02 | 0.03 | 0.00 | 0.00 | 0.03 | 0.04 | 0.05 | -0.05 | 0.00 | -0.04 | 0.01 | 0.03 | 0.04 | -0.04 | -0.02 | 0.03 | -0.01 | 0.05 | -0.01 | 0.00 |

*Table S 17: Mulliken spin population of the [**V**-NO$_3$]$^0$, $M_S$ = $^1/_2$, Functional: TPSSh*

| BS | 1 | 2 | 3 | 3 | 3 | 4 | 4 | 4 | 5 | 5 | 5 | 5 | 5 | 6 | 6 | 6 | 7 | 7 | 7 | 8 | 8 | 8 | 8 | 8 | 9 | 9 | 9 | 10 | 10 | 10 | 10 | 10 | 10 |
|---|---|---|---|---|---|---|---|---|---|---|---|---|---|---|---|---|---|---|---|---|---|---|---|---|---|---|---|---|---|---|---|---|---|
| Flip | 567 | 234 | 123 | 124 | 134 | 257 | 356 | 467 | 256 | 267 | 357 | 367 | 456 | 457 | 156 | 157 | 167 | 235 | 247 | 346 | 236 | 237 | 245 | 246 | 345 | 347 | 126 | 137 | 145 | 125 | 127 | 135 | 136 | 146 | 147 |
| V | 1.75 | -1.76 | -1.80 | -1.72 | -1.70 | 0.05 | 0.58 | 1.58 | -0.86 | 1.38 | -0.87 | 1.44 | 0.34 | -0.12 | 0.27 | 0.04 | 0.17 | -1.62 | -1.71 | 0.01 | -0.26 | -1.83 | -1.69 | 0.00 | -1.68 | -0.32 | 0.16 | -0.28 | -1.56 | -1.56 | -1.71 | -1.58 | -0.19 | 0.01 | -0.53 |
| Fe1 | -0.08 | 3.42 | -3.63 | -3.59 | -3.60 | 1.78 | 2.24 | 1.78 | 2.62 | 1.50 | 3.33 | 2.79 | 1.97 | 2.02 | -3.48 | -3.48 | -3.46 | 3.41 | 3.24 | 2.91 | 3.20 | 3.28 | 3.14 | 2.86 | 3.12 | 2.96 | -3.58 | -3.56 | -3.46 | -3.53 | -3.56 | -3.32 | -3.55 | -3.49 | -3.49 |
| Fe2 | 3.22 | -3.34 | -3.36 | -3.35 | 3.16 | -3.34 | 2.93 | 2.99 | -3.34 | -3.34 | 1.33 | 3.02 | 3.05 | 2.77 | 2.50 | 2.70 | 2.93 | -3.36 | -3.36 | 3.18 | -3.39 | -3.33 | -3.37 | -3.22 | 2.99 | 2.87 | -3.43 | 3.16 | 3.10 | -3.38 | -3.39 | 3.13 | 3.16 | 3.12 | 2.98 |
| Fe3 | 3.29 | -3.44 | -3.45 | 3.16 | -3.43 | 3.15 | -3.38 | 2.99 | 2.70 | 3.16 | -3.33 | -3.45 | 2.81 | 3.08 | 3.04 | 3.14 | 3.11 | -3.42 | 3.23 | -3.39 | -3.46 | -3.30 | 2.87 | 2.89 | -3.40 | -3.32 | 3.26 | -3.45 | 3.26 | 3.36 | 3.33 | -3.28 | -3.47 | 3.08 | 3.16 |
| Fe4 | 3.26 | -3.38 | 3.34 | -3.22 | -3.20 | 3.19 | 3.09 | -3.36 | 3.25 | 3.09 | 3.31 | 2.17 | -3.29 | -3.29 | 3.12 | 3.07 | 3.02 | 3.22 | -3.37 | -3.27 | 3.16 | 3.10 | -3.29 | -3.35 | -3.29 | -3.33 | 3.14 | 3.32 | -3.26 | 3.24 | 3.31 | 3.21 | 3.16 | -3.30 | -3.29 |
| Fe5 | -3.32 | 2.98 | 3.37 | 3.40 | 3.41 | -3.28 | -3.29 | 3.02 | -3.14 | 3.05 | -3.10 | 3.03 | -3.23 | -3.16 | -3.24 | -3.30 | 3.13 | -3.15 | 3.09 | 2.78 | 3.03 | 3.18 | -3.24 | 2.98 | -3.22 | 2.95 | 2.98 | 3.07 | -3.10 | -3.06 | 3.36 | -3.11 | 3.10 | 2.88 | 2.98 |
| Fe6 | -3.31 | 3.09 | 3.32 | 3.26 | 3.06 | 3.17 | -3.32 | -3.32 | -3.09 | -3.27 | 3.24 | -3.33 | -3.28 | 3.21 | -3.23 | 2.90 | -3.25 | 2.91 | 3.14 | -3.24 | -3.32 | 3.22 | 3.15 | -3.27 | 2.90 | 2.86 | -3.23 | 2.99 | 3.02 | 3.01 | 3.25 | 2.93 | -3.22 | -3.26 | 3.00 |
| Fe7 | -3.37 | 3.24 | 3.37 | 3.12 | 3.33 | -3.32 | 3.12 | -3.39 | 3.17 | -3.39 | -3.15 | -3.40 | 3.17 | -3.28 | 3.01 | -3.28 | -3.34 | 2.95 | -3.33 | 2.78 | 3.06 | -3.30 | 2.95 | 2.78 | 3.14 | -3.27 | 3.06 | -3.21 | 3.18 | 3.09 | -3.26 | 3.08 | 3.16 | 2.94 | -3.23 |
| S1A | 0.24 | -0.17 | -0.15 | -0.46 | -0.07 | 0.03 | 0.02 | -0.06 | 0.08 | 0.00 | 0.07 | 0.01 | 0.03 | 0.00 | -0.02 | 0.03 | 0.06 | 0.07 | -0.21 | 0.03 | 0.01 | 0.02 | -0.15 | -0.12 | 0.00 | 0.01 | -0.25 | 0.10 | -0.14 | -0.14 | -0.19 | 0.10 | 0.07 | -0.13 | -0.13 |
| S2A | 0.15 | -0.13 | -0.55 | -0.16 | -0.17 | -0.10 | -0.15 | -0.07 | -0.09 | -0.02 | -0.02 | 0.00 | -0.08 | -0.10 | -0.05 | 0.04 | 0.03 | -0.22 | 0.09 | -0.06 | -0.23 | -0.19 | 0.04 | -0.08 | 0.04 | -0.06 | -0.21 | -0.26 | 0.00 | -0.18 | -0.16 | -0.11 | -0.22 | 0.01 | 0.00 |
| S4A | 0.21 | -0.18 | -0.14 | -0.05 | -0.45 | 0.12 | -0.01 | -0.05 | 0.04 | 0.14 | 0.11 | -0.01 | 0.00 | 0.02 | 0.09 | 0.08 | 0.11 | 0.04 | 0.01 | -0.18 | -0.02 | -0.01 | 0.03 | 0.01 | -0.18 | -0.16 | 0.08 | -0.15 | -0.10 | 0.11 | 0.13 | -0.04 | -0.18 | -0.11 | -0.10 |
| S1B | -0.31 | 0.21 | 0.34 | 0.31 | 0.29 | 0.04 | -0.25 | -0.13 | -0.07 | -0.11 | 0.09 | -0.13 | -0.24 | 0.07 | -0.20 | 0.03 | -0.03 | 0.10 | 0.24 | -0.08 | -0.07 | 0.28 | 0.11 | -0.05 | 0.09 | 0.11 | -0.09 | 0.16 | 0.11 | 0.11 | 0.31 | 0.11 | -0.04 | -0.06 | 0.14 |
| S3B | -0.36 | 0.35 | 0.35 | 0.30 | 0.29 | 0.03 | -0.04 | -0.36 | 0.00 | -0.33 | 0.06 | -0.36 | -0.05 | 0.02 | -0.05 | 0.00 | -0.26 | 0.12 | 0.03 | -0.08 | -0.06 | 0.07 | 0.24 | -0.09 | 0.22 | -0.02 | -0.09 | -0.02 | 0.20 | 0.23 | 0.06 | 0.17 | -0.01 | -0.06 | 0.03 |
| S4B | -0.35 | 0.27 | 0.36 | 0.32 | 0.33 | -0.24 | 0.00 | -0.14 | 0.08 | -0.13 | -0.07 | -0.13 | 0.03 | -0.21 | 0.02 | -0.22 | -0.04 | 0.11 | 0.01 | 0.06 | 0.17 | 0.04 | 0.09 | 0.08 | 0.12 | -0.05 | 0.13 | -0.06 | 0.11 | 0.11 | 0.05 | 0.12 | 0.17 | 0.08 | -0.03 |
| S2B | -0.03 | -0.13 | 0.04 | 0.06 | 0.34 | -0.06 | -0.12 | -0.11 | -0.47 | -0.52 | 0.10 | -0.11 | -0.07 | 0.33 | -0.19 | 0.22 | -0.21 | -0.10 | -0.05 | -0.03 | -0.54 | 0.02 | -0.04 | -0.50 | 0.21 | 0.22 | -0.56 | 0.39 | 0.24 | -0.09 | -0.02 | 0.28 | -0.05 | -0.06 | 0.29 |
| S5A | 0.05 | -0.19 | -0.06 | 0.28 | -0.01 | 0.01 | -0.18 | -0.04 | 0.21 | -0.04 | -0.44 | -0.53 | 0.25 | -0.02 | 0.30 | -0.07 | -0.17 | -0.18 | -0.17 | -0.24 | -0.29 | -0.48 | 0.17 | 0.10 | -0.09 | -0.47 | 0.32 | -0.53 | 0.36 | 0.39 | -0.05 | 0.01 | -0.17 | 0.20 | 0.03 |
| C* | -0.03 | -0.14 | -0.10 | -0.21 | -0.21 | -0.03 | -0.04 | -0.14 | 0.00 | 0.01 | 0.05 | 0.00 | -0.12 | -0.10 | -0.33 | -0.38 | -0.36 | -0.09 | -0.09 | -0.07 | -0.04 | 0.04 | -0.10 | -0.02 | -0.11 | -0.06 | -0.23 | -0.26 | -0.36 | -0.26 | -0.10 | -0.35 | -0.27 | -0.39 | -0.39 |
| N | -0.01 | -0.01 | 0.00 | -0.03 | 0.00 | -0.03 | -0.01 | 0.03 | 0.00 | 0.00 | 0.02 | 0.02 | -0.02 | -0.02 | -0.02 | -0.03 | -0.03 | 0.01 | 0.00 | 0.01 | 0.01 | 0.02 | -0.02 | 0.00 | -0.01 | 0.01 | 0.02 | 0.02 | -0.02 | -0.02 | 0.00 | -0.01 | 0.01 | -0.01 | 0.00 |
| O3 | 0.01 | -0.03 | 0.03 | 0.02 | 0.01 | 0.00 | -0.01 | -0.02 | 0.00 | 0.02 | -0.01 | 0.00 | -0.01 | -0.02 | 0.01 | 0.01 | 0.03 | -0.01 | -0.02 | -0.02 | 0.02 | 0.01 | -0.01 | -0.01 | -0.02 | -0.02 | 0.02 | 0.01 | -0.01 | 0.01 | 0.03 | 0.00 | 0.02 | 0.00 | 0.00 |
| O1 | 0.00 | 0.00 | 0.01 | 0.00 | 0.01 | 0.00 | 0.01 | -0.01 | 0.00 | -0.01 | 0.01 | 0.00 | 0.00 | 0.00 | 0.00 | -0.01 | 0.00 | 0.01 | 0.00 | -0.02 | 0.00 | 0.01 | -0.01 | -0.02 | 0.00 | -0.01 | -0.01 | 0.01 | 0.00 | 0.01 | 0.01 | 0.01 | 0.00 | -0.02 | -0.01 |
| O2 | -0.02 | -0.01 | 0.03 | -0.02 | 0.00 | -0.03 | -0.01 | 0.02 | 0.00 | 0.03 | 0.01 | 0.04 | -0.04 | -0.04 | -0.02 | -0.03 | 0.00 | 0.00 | 0.00 | 0.01 | 0.04 | 0.04 | -0.05 | 0.00 | -0.03 | 0.01 | 0.04 | 0.04 | -0.04 | -0.02 | 0.02 | -0.01 | 0.04 | -0.01 | -0.01 |

*Table S 18:* *Mulliken spin populations of the [**V**-$CO_3$]$^{2-}$ model, $M_S$ = 3/2. Functional: TPSSh. The spin of the vanadium ion is flipped from a low spin BS solution for each BS solution.*

| BS | 1 | 2 | 3 | 3 | 3 | 4 | 4 | 4 | 5 | 5 | 5 | 5 | 5 | 5 | 6 | 6 | 6 | 7 | 7 | 7 | 8 | 8 | 8 | 8 | 8 | 8 | 9 | 9 | 9 | 10 | 10 | 10 | 10 | 10 | 10 |
|---|---|---|---|---|---|---|---|---|---|---|---|---|---|---|---|---|---|---|---|---|---|---|---|---|---|---|---|---|---|---|---|---|---|---|---|
| Flip | 567 | 234 | 123 | 124 | 134 | 257 | 356 | 467 | 256 | 267 | 357 | 367 | 456 | 457 | 156 | 157 | 167 | 235 | 247 | 346 | 236 | 237 | 245 | 246 | 345 | 347 | 126 | 137 | 145 | 125 | 127 | 135 | 136 | 146 | 147 |
| V | 2.12 | -2.12 | -2.18 | -2.07 | -2.04 | 0.48 | 1.11 | 1.61 | 0.90 | 1.35 | 0.57 | 1.38 | 0.99 | 0.60 | 0.88 | 0.57 | 1.43 | -1.60 | -1.12 | -0.71 | -0.66 | -1.03 | -1.45 | -0.57 | -1.42 | -0.86 | -0.51 | -0.77 | -1.48 | -1.50 | -1.01 | -1.45 | -0.61 | -0.60 | -0.92 |
| Fe1 | 0.81 | 3.46 | -2.34 | -3.38 | -3.37 | 3.31 | 3.32 | 2.15 | 3.28 | 3.20 | 3.31 | 3.29 | 3.15 | 3.23 | -3.45 | -3.45 | -3.48 | 3.44 | 3.37 | 3.34 | 3.40 | 3.41 | 3.36 | 3.34 | 3.34 | 3.32 | -3.32 | -3.33 | -3.39 | -3.32 | -3.32 | -3.35 | -3.35 | -3.41 | -3.40 |
| Fe2 | 3.27 | -3.03 | -3.27 | -3.00 | 3.41 | -3.36 | 2.21 | 3.22 | -3.34 | -3.36 | 2.46 | 2.38 | 3.31 | 2.42 | 3.12 | 3.04 | 3.09 | -3.22 | -3.25 | 3.32 | -3.28 | -3.35 | -3.31 | -3.24 | 3.36 | 3.31 | -3.30 | 3.27 | 3.34 | -3.28 | -3.29 | 3.37 | 3.29 | 3.30 | 3.37 |
| Fe3 | 3.30 | -3.11 | -3.29 | 3.42 | -3.13 | 3.08 | -3.35 | 3.22 | 2.42 | 2.56 | -3.33 | -3.37 | 2.54 | 3.34 | 3.13 | 3.21 | 3.13 | -3.23 | 3.34 | -3.30 | -3.37 | -3.32 | 3.37 | 3.29 | -3.33 | -3.28 | 3.32 | -3.28 | 3.37 | 3.39 | 3.32 | -3.30 | -3.30 | 3.37 | 3.32 |
| Fe4 | 3.32 | -3.22 | 3.41 | -3.28 | -3.23 | 3.13 | 3.29 | -3.44 | 3.38 | 3.26 | 3.38 | 3.28 | -3.43 | -3.41 | 3.20 | 3.21 | 3.20 | 3.43 | -3.36 | -3.35 | 3.39 | 3.41 | -3.38 | -3.47 | -3.35 | -3.44 | 3.42 | 3.45 | -3.32 | 3.44 | 3.45 | 3.47 | 3.47 | -3.34 | -3.34 |
| Fe5 | -3.27 | 3.45 | 3.51 | 3.54 | 3.56 | -3.44 | -3.31 | 3.15 | -3.39 | 3.17 | -3.38 | 3.17 | -3.36 | -3.32 | -3.33 | -3.29 | 3.18 | -3.18 | 3.27 | 3.26 | 3.29 | 3.33 | -3.18 | 3.34 | -3.18 | 3.36 | 3.33 | 3.37 | -3.06 | -3.06 | 3.42 | -3.02 | 3.39 | 3.36 | 3.38 |
| Fe6 | -3.20 | 3.13 | 3.23 | 3.37 | 3.30 | 3.11 | -3.22 | -3.17 | -3.19 | -3.23 | 3.09 | -3.28 | -3.26 | 3.11 | -3.19 | 3.17 | -3.26 | 3.17 | 3.17 | -3.18 | -3.21 | 3.24 | 3.26 | -3.19 | 3.21 | 3.16 | -3.15 | 3.18 | 3.26 | 3.24 | 3.22 | 3.31 | -3.12 | -3.15 | 3.30 |
| Fe7 | -3.28 | 3.25 | 3.28 | 3.36 | 3.45 | -3.28 | 3.12 | -3.23 | 3.06 | -3.33 | -3.21 | -3.28 | 3.07 | -3.27 | 3.13 | -3.21 | -3.31 | 3.22 | -3.14 | 3.20 | 3.24 | -3.15 | 3.26 | 3.16 | 3.30 | -3.14 | 3.22 | -3.10 | 3.33 | 3.33 | -3.09 | 3.28 | 3.22 | 3.29 | -3.11 |
| S1 | 0.31 | 0.00 | -0.04 | -0.41 | -0.03 | -0.01 | 0.26 | -0.05 | 0.10 | 0.04 | 0.28 | 0.24 | 0.09 | 0.05 | 0.02 | 0.01 | 0.00 | 0.18 | -0.13 | 0.15 | 0.14 | 0.12 | -0.16 | -0.17 | 0.15 | 0.10 | -0.11 | 0.19 | -0.10 | -0.09 | -0.11 | 0.17 | 0.17 | -0.12 | -0.14 |
| S2 | 0.27 | 0.02 | -0.27 | -0.05 | -0.08 | 0.04 | -0.01 | 0.20 | 0.07 | 0.07 | 0.08 | 0.05 | 0.26 | 0.28 | -0.02 | -0.01 | 0.00 | -0.06 | 0.17 | 0.13 | -0.11 | -0.11 | 0.14 | 0.15 | 0.12 | 0.13 | -0.11 | -0.12 | 0.13 | -0.11 | -0.11 | -0.15 | -0.14 | 0.11 | 0.11 |
| S3 | 0.27 | -0.04 | -0.03 | -0.03 | -0.38 | 0.36 | 0.03 | -0.01 | 0.25 | 0.22 | 0.08 | 0.05 | 0.05 | 0.11 | 0.04 | 0.05 | 0.03 | 0.15 | 0.15 | -0.14 | 0.09 | 0.13 | 0.14 | 0.09 | -0.15 | -0.16 | 0.17 | -0.10 | -0.09 | 0.17 | 0.17 | -0.10 | -0.12 | -0.11 | -0.10 |
| S4 | -0.25 | 0.29 | 0.31 | 0.30 | 0.30 | -0.01 | -0.24 | -0.08 | -0.25 | -0.08 | -0.02 | -0.09 | -0.26 | 0.00 | -0.25 | 0.01 | -0.08 | 0.08 | 0.23 | -0.01 | -0.01 | 0.26 | 0.09 | 0.01 | 0.07 | 0.24 | 0.00 | 0.25 | 0.11 | 0.10 | 0.26 | 0.10 | 0.01 | 0.01 | 0.25 |
| S5 | -0.32 | 0.25 | 0.27 | 0.31 | 0.32 | 0.00 | -0.05 | -0.27 | -0.04 | -0.29 | 0.01 | -0.29 | -0.07 | -0.01 | -0.04 | 0.01 | -0.31 | 0.26 | 0.04 | -0.02 | 0.00 | 0.06 | 0.29 | -0.03 | 0.28 | 0.03 | 0.01 | 0.07 | 0.30 | 0.30 | 0.06 | 0.30 | 0.01 | 0.00 | 0.07 |
| S6 | -0.29 | 0.29 | 0.33 | 0.32 | 0.33 | -0.26 | -0.02 | -0.10 | -0.03 | -0.10 | -0.24 | -0.09 | -0.02 | -0.25 | 0.00 | -0.24 | -0.10 | 0.10 | 0.01 | 0.23 | 0.24 | 0.01 | 0.08 | 0.23 | 0.10 | 0.02 | 0.24 | 0.01 | 0.12 | 0.11 | 0.03 | 0.12 | 0.25 | 0.25 | 0.02 |
| S7 | -0.03 | 0.06 | 0.03 | 0.24 | 0.50 | 0.04 | -0.19 | -0.06 | -0.46 | -0.47 | 0.21 | -0.21 | -0.07 | 0.23 | -0.09 | 0.40 | -0.12 | 0.03 | 0.03 | -0.05 | -0.45 | 0.01 | 0.03 | -0.45 | 0.46 | 0.44 | -0.45 | 0.42 | 0.46 | 0.03 | 0.03 | 0.49 | -0.02 | -0.04 | 0.48 |
| S8 | 0.01 | 0.03 | -0.02 | 0.46 | 0.17 | -0.15 | -0.07 | -0.01 | 0.14 | -0.19 | -0.41 | -0.44 | 0.15 | -0.01 | 0.36 | -0.04 | -0.08 | -0.01 | 0.03 | -0.03 | -0.04 | -0.38 | 0.42 | 0.38 | 0.00 | -0.38 | 0.39 | -0.38 | 0.43 | 0.44 | 0.03 | -0.02 | -0.04 | 0.41 | 0.03 |
| C | -0.03 | 0.03 | -0.09 | 0.00 | 0.01 | -0.14 | -0.03 | -0.08 | -0.03 | -0.03 | -0.03 | -0.03 | -0.12 | -0.11 | -0.24 | -0.22 | -0.21 | 0.03 | -0.01 | -0.03 | 0.03 | 0.04 | -0.03 | -0.04 | -0.03 | -0.02 | -0.13 | -0.11 | -0.13 | -0.09 | -0.06 | -0.09 | -0.09 | -0.16 | -0.14 |
| C | 0.00 | 0.00 | 0.01 | 0.00 | 0.00 | 0.00 | 0.00 | 0.00 | 0.00 | 0.01 | 0.00 | 0.01 | -0.01 | -0.01 | 0.00 | 0.00 | 0.01 | 0.00 | 0.00 | 0.00 | 0.01 | 0.01 | -0.01 | 0.00 | -0.01 | 0.00 | 0.01 | 0.01 | -0.01 | 0.00 | 0.01 | 0.00 | 0.01 | 0.00 | 0.00 |
| O | 0.03 | -0.04 | 0.06 | -0.02 | -0.01 | 0.02 | 0.03 | -0.05 | 0.03 | 0.04 | 0.04 | 0.05 | -0.06 | -0.06 | 0.03 | 0.03 | 0.05 | 0.04 | -0.04 | -0.04 | 0.06 | 0.05 | -0.06 | -0.06 | -0.06 | -0.05 | 0.06 | 0.07 | -0.05 | 0.05 | 0.06 | 0.05 | 0.07 | -0.04 | -0.04 |
| O | -0.03 | 0.04 | 0.06 | 0.05 | 0.05 | -0.05 | -0.03 | 0.02 | -0.04 | 0.04 | -0.04 | 0.04 | -0.05 | -0.05 | -0.04 | -0.04 | 0.04 | -0.02 | 0.03 | 0.03 | 0.05 | 0.05 | -0.04 | 0.03 | -0.04 | 0.03 | 0.04 | 0.04 | -0.03 | -0.02 | 0.04 | -0.02 | 0.05 | 0.03 | 0.03 |
| O | 0.00 | 0.00 | 0.03 | 0.00 | 0.01 | -0.01 | 0.00 | 0.00 | 0.00 | 0.02 | 0.00 | 0.02 | -0.03 | -0.02 | 0.00 | -0.01 | 0.02 | 0.00 | 0.00 | 0.00 | 0.02 | 0.02 | -0.02 | 0.00 | -0.02 | 0.00 | 0.02 | 0.02 | -0.02 | 0.00 | 0.02 | 0.00 | 0.03 | 0.00 | 0.00 |

*Table S 19:* *Mulliken spin populations of the [**V**-$CO_3$]$^{2-}$ model, $M_S$ = 3/2. Functional: TPSSh. The spin of the vanadium is flipped along the irons from a high spin solution.*

| BS | 1 | 2 | 3 | 3 | 3 | 4 | 4 | 4 | 5 | 5 | 5 | 5 | 5 | 5 | 6 | 6 | 6 | 7 | 7 | 7 | 8 | 8 | 8 | 8 | 8 | 8 | 9 | 9 | 9 | 10 | 10 | 10 | 10 | 10 | 10 |
|---|---|---|---|---|---|---|---|---|---|---|---|---|---|---|---|---|---|---|---|---|---|---|---|---|---|---|---|---|---|---|---|---|---|---|---|
| Flip | 567 | 234 | 123 | 124 | 134 | 257 | 356 | 467 | 256 | 267 | 357 | 367 | 456 | 457 | 156 | 157 | 167 | 235 | 247 | 346 | 236 | 237 | 245 | 246 | 345 | 347 | 126 | 137 | 145 | 125 | 127 | 135 | 136 | 146 | 147 |
| V | 2.12 | -2.13 | -2.18 | -2.13 | -2.04 | 0.48 | 1.11 | 1.61 | 0.90 | 1.35 | 0.57 | 1.38 | 0.99 | 0.61 | 0.88 | 0.57 | 1.43 | -1.60 | -1.12 | -0.71 | -0.66 | -1.03 | -1.45 | -0.57 | -1.42 | -0.86 | -0.52 | -0.77 | -1.48 | -1.50 | -1.01 | -1.45 | -0.61 | -0.60 | -0.92 |
| Fe1 | 0.81 | 3.46 | -2.34 | -2.54 | -3.37 | 3.31 | 3.32 | 2.15 | 3.28 | 3.20 | 3.31 | 3.29 | 3.15 | 2.34 | -3.45 | -3.45 | -3.48 | 3.44 | 3.37 | 3.34 | 3.40 | 3.41 | 3.36 | 3.34 | 3.34 | 3.32 | -3.32 | -3.33 | -3.39 | -3.32 | -3.32 | -3.35 | -3.35 | -3.41 | -3.40 |
| Fe2 | 3.27 | -3.03 | -3.27 | -3.16 | 3.41 | -3.36 | 2.21 | 3.22 | -3.34 | -3.36 | 2.46 | 2.38 | 3.31 | 3.21 | 3.12 | 3.04 | 3.09 | -3.22 | -3.25 | 3.32 | -3.28 | -3.35 | -3.31 | -3.24 | 3.36 | 3.31 | -3.30 | 3.27 | 3.34 | -3.28 | -3.29 | 3.37 | 3.29 | 3.30 | 3.37 |
| Fe3 | 3.30 | -3.10 | -3.29 | 3.35 | -3.13 | 3.08 | -3.35 | 3.22 | 2.42 | 2.56 | -3.33 | -3.37 | 2.54 | 3.33 | 3.13 | 3.21 | 3.13 | -3.23 | 3.34 | -3.30 | -3.37 | -3.32 | 3.37 | 3.29 | -3.33 | -3.28 | 3.32 | -3.28 | 3.37 | 3.39 | 3.32 | -3.30 | -3.30 | 3.37 | 3.32 |
| Fe4 | 3.32 | -3.21 | 3.41 | -3.31 | -3.23 | 3.13 | 3.29 | -3.44 | 3.38 | 3.26 | 3.38 | 3.28 | -3.43 | -3.37 | 3.20 | 3.21 | 3.20 | 3.43 | -3.36 | -3.35 | 3.39 | 3.41 | -3.38 | -3.47 | -3.35 | -3.44 | 3.42 | 3.45 | -3.32 | 3.44 | 3.45 | 3.47 | 3.47 | -3.34 | -3.34 |
| Fe5 | -3.27 | 3.28 | 3.51 | 3.35 | 3.56 | -3.44 | -3.31 | 3.15 | -3.39 | 3.17 | -3.38 | 3.17 | -3.36 | -3.31 | -3.33 | -3.29 | 3.18 | -3.18 | 3.27 | 3.26 | 3.29 | 3.33 | -3.18 | 3.34 | -3.18 | 3.36 | 3.33 | 3.37 | -3.06 | -3.06 | 3.42 | -3.02 | 3.39 | 3.36 | 3.38 |
| Fe6 | -3.20 | 3.20 | 3.23 | 3.26 | 3.30 | 3.11 | -3.22 | -3.17 | -3.19 | -3.23 | 3.09 | -3.28 | -3.26 | 3.18 | -3.19 | 3.17 | -3.26 | 3.17 | 3.17 | -3.18 | -3.21 | 3.24 | 3.26 | -3.19 | 3.21 | 3.16 | -3.15 | 3.18 | 3.26 | 3.24 | 3.22 | 3.31 | -3.12 | -3.15 | 3.30 |
| Fe7 | -3.28 | 3.30 | 3.28 | 3.33 | 3.45 | -3.28 | 3.12 | -3.23 | 3.06 | -3.33 | -3.21 | -3.28 | 3.07 | -3.28 | 3.13 | -3.21 | -3.31 | 3.22 | -3.14 | 3.20 | 3.24 | -3.15 | 3.26 | 3.16 | 3.30 | -3.14 | 3.22 | -3.10 | 3.33 | 3.33 | -3.09 | 3.28 | 3.22 | 3.29 | -3.11 |
| S1 | 0.31 | -0.01 | -0.04 | -0.22 | -0.03 | -0.01 | 0.26 | -0.05 | 0.10 | 0.04 | 0.28 | 0.24 | 0.09 | 0.03 | 0.02 | 0.01 | 0.00 | 0.18 | -0.13 | 0.15 | 0.14 | 0.12 | -0.16 | -0.17 | 0.15 | 0.10 | -0.11 | 0.19 | -0.10 | -0.09 | -0.11 | 0.17 | 0.17 | -0.12 | -0.14 |
| S2 | 0.27 | 0.03 | -0.27 | -0.03 | -0.08 | 0.05 | -0.01 | 0.20 | 0.07 | 0.07 | 0.08 | 0.05 | 0.26 | 0.24 | -0.02 | -0.01 | 0.00 | -0.06 | 0.17 | 0.13 | -0.11 | -0.11 | 0.14 | 0.15 | 0.12 | 0.13 | -0.11 | -0.12 | 0.13 | -0.11 | -0.11 | -0.15 | -0.14 | 0.11 | 0.11 |
| S3 | 0.27 | -0.03 | -0.03 | -0.04 | -0.38 | 0.36 | 0.03 | -0.01 | 0.25 | 0.22 | 0.08 | 0.05 | 0.05 | 0.06 | 0.04 | 0.05 | 0.03 | 0.15 | 0.15 | -0.14 | 0.09 | 0.13 | 0.14 | 0.09 | -0.15 | -0.16 | 0.17 | -0.10 | -0.09 | 0.17 | 0.17 | -0.10 | -0.12 | -0.11 | -0.10 |
| S4 | -0.25 | 0.24 | 0.31 | 0.26 | 0.30 | -0.01 | -0.24 | -0.08 | -0.25 | -0.08 | -0.02 | -0.09 | -0.26 | 0.00 | -0.25 | 0.01 | -0.08 | 0.08 | 0.23 | -0.01 | -0.01 | 0.26 | 0.09 | 0.01 | 0.07 | 0.24 | 0.00 | 0.25 | 0.11 | 0.10 | 0.26 | 0.10 | 0.01 | 0.01 | 0.25 |
| S5 | -0.32 | 0.32 | 0.27 | 0.32 | 0.32 | 0.00 | -0.05 | -0.27 | -0.04 | -0.29 | 0.01 | -0.29 | -0.07 | -0.01 | -0.04 | 0.01 | -0.31 | 0.26 | 0.04 | -0.02 | 0.00 | 0.06 | 0.29 | -0.03 | 0.28 | 0.03 | 0.01 | 0.07 | 0.30 | 0.30 | 0.06 | 0.30 | 0.01 | 0.00 | 0.07 |
| S6 | -0.29 | 0.27 | 0.33 | 0.30 | 0.33 | -0.26 | -0.02 | -0.10 | -0.03 | -0.10 | -0.24 | -0.09 | -0.02 | -0.25 | 0.00 | -0.24 | -0.10 | 0.10 | 0.01 | 0.23 | 0.24 | 0.01 | 0.08 | 0.23 | 0.10 | 0.02 | 0.24 | 0.01 | 0.12 | 0.11 | 0.03 | 0.12 | 0.25 | 0.25 | 0.02 |
| S7 | -0.03 | 0.07 | 0.03 | 0.02 | 0.50 | 0.04 | -0.19 | -0.06 | -0.46 | -0.47 | 0.21 | -0.21 | -0.07 | 0.41 | -0.09 | 0.40 | -0.12 | 0.03 | 0.03 | -0.05 | -0.45 | 0.01 | 0.03 | -0.45 | 0.46 | 0.44 | -0.45 | 0.42 | 0.46 | 0.03 | 0.03 | 0.49 | -0.02 | -0.04 | 0.48 |
| S8 | 0.01 | 0.05 | -0.02 | 0.44 | 0.17 | -0.15 | -0.07 | -0.01 | 0.14 | -0.19 | -0.41 | -0.44 | 0.15 | 0.01 | 0.36 | -0.04 | -0.08 | -0.01 | 0.03 | -0.03 | -0.04 | -0.38 | 0.42 | 0.38 | 0.00 | -0.38 | 0.39 | -0.38 | 0.43 | 0.44 | 0.03 | -0.02 | -0.04 | 0.41 | 0.03 |
| C | -0.03 | 0.04 | -0.09 | -0.17 | 0.01 | -0.14 | -0.03 | -0.08 | -0.03 | -0.03 | -0.03 | -0.03 | -0.12 | -0.09 | -0.24 | -0.22 | -0.21 | 0.03 | -0.01 | -0.03 | 0.03 | 0.04 | -0.03 | -0.04 | -0.03 | -0.02 | -0.13 | -0.11 | -0.13 | -0.09 | -0.06 | -0.09 | -0.09 | -0.16 | -0.14 |
| C | 0.00 | 0.00 | 0.01 | 0.00 | 0.00 | 0.00 | 0.00 | 0.00 | 0.00 | 0.01 | 0.00 | 0.01 | -0.01 | -0.01 | 0.00 | 0.00 | 0.01 | 0.00 | 0.00 | 0.00 | 0.01 | 0.01 | -0.01 | 0.00 | -0.01 | 0.00 | 0.01 | 0.01 | -0.01 | 0.00 | 0.01 | 0.00 | 0.01 | 0.00 | 0.00 |
| O | 0.03 | -0.03 | 0.06 | -0.03 | -0.01 | 0.02 | 0.03 | -0.05 | 0.03 | 0.04 | 0.04 | 0.05 | -0.06 | -0.06 | 0.03 | 0.03 | 0.05 | 0.04 | -0.04 | -0.04 | 0.06 | 0.05 | -0.06 | -0.06 | -0.06 | -0.05 | 0.06 | 0.07 | -0.05 | 0.05 | 0.06 | 0.05 | 0.07 | -0.04 | -0.04 |
| O | -0.03 | 0.03 | 0.06 | 0.03 | 0.05 | -0.05 | -0.03 | 0.02 | -0.04 | 0.04 | -0.04 | 0.04 | -0.05 | -0.05 | -0.04 | -0.04 | 0.04 | -0.02 | 0.03 | 0.03 | 0.05 | 0.05 | -0.04 | 0.03 | -0.04 | 0.03 | 0.04 | 0.04 | -0.03 | -0.02 | 0.04 | -0.02 | 0.05 | 0.03 | 0.03 |
| O | 0.00 | 0.00 | 0.03 | 0.00 | 0.01 | -0.01 | 0.00 | 0.00 | 0.00 | 0.02 | 0.00 | 0.02 | -0.03 | -0.02 | 0.00 | -0.01 | 0.02 | 0.00 | 0.00 | 0.00 | 0.02 | 0.02 | -0.02 | 0.00 | -0.02 | 0.00 | 0.02 | 0.02 | -0.02 | 0.00 | 0.02 | 0.00 | 0.03 | 0.00 | 0.00 |

## Mayer bond orders for FeMoco and FeVco

*Table S 20: Mayer bond order for metal-metal, metal-sulfide and carbide-metal interaction in QM/MM models of FeMoco and FeVco*

| Cofactor | FeVco | FeMoco | FeVco | FeVco | FeMoco |
|---|---|---|---|---|---|
| Model | X-ray[a] | X-ray[a] | QM/MM | QM/MM | QM/MM |
| QM size | 57 | 57 | 57 | 181 | 247 |
| M-Fe5 | 0.42 | 0.41 | 0.38 | 0.37 | 0.47 |
| M-Fe6 | 0.20 | 0.40 | 0.16 | 0.18 | 0.45 |
| M-Fe7 | 0.28 | 0.42 | 0.27 | 0.30 | 0.49 |
| Fe1-Fe2 | 0.19 | 0.20 | 0.20 | 0.21 | 0.20 |
| Fe1-Fe3 | 0.23 | 0.20 | 0.22 | 0.24 | 0.23 |
| Fe1-Fe4 | 0.44 | 0.38 | 0.42 | 0.43 | 0.41 |
| Fe2-Fe3 | 0.39 | 0.40 | 0.40 | 0.42 | 0.41 |
| Fe2-Fe4 | 0.26 | 0.24 | 0.23 | 0.23 | 0.24 |
| Fe3-Fe4 | 0.27 | 0.23 | 0.23 | 0.24 | 0.29 |
| Fe5-Fe6 | 0.26 | 0.28 | 0.24 | 0.24 | 0.28 |
| Fe5-Fe7 | 0.24 | 0.28 | 0.21 | 0.25 | 0.31 |
| Fe6-Fe7 | 0.40 | 0.45 | 0.40 | 0.42 | 0.47 |
| Fe2-Fe6 | 0.29 | 0.32 | 0.28 | 0.32 | 0.32 |
| Fe3-Fe7 | 0.29 | 0.33 | 0.28 | 0.32 | 0.34 |
| Fe4-Fe5 | 0.27 | 0.29 | 0.29 | 0.33 | 0.30 |
| C-Fe2 | 0.36 | 0.30 | 0.36 | 0.32 | 0.31 |
| C-Fe3 | 0.31 | 0.34 | 0.37 | 0.27 | 0.27 |
| C-Fe4 | 0.43 | 0.40 | 0.48 | 0.36 | 0.35 |
| C-Fe5 | 0.49 | 0.40 | 0.50 | 0.37 | 0.36 |
| C-Fe6 | 0.39 | 0.32 | 0.38 | 0.30 | 0.33 |
| C-Fe7 | 0.35 | 0.34 | 0.33 | 0.29 | 0.35 |
| S1A-Fe1 | 0.68 | 0.64 | 0.68 | 0.69 | 0.68 |
| S1A-Fe2 | 0.91 | 0.77 | 0.88 | 0.85 | 0.86 |
| S1A-Fe4 | 0.82 | 0.80 | 0.82 | 0.77 | 0.82 |
| S2A-Fe1 | 0.90 | 0.87 | 0.96 | 1.00 | 0.88 |
| S2A-Fe2 | 0.79 | 0.76 | 0.80 | 0.80 | 0.77 |
| S2A-Fe3 | 0.78 | 0.81 | 0.80 | 0.78 | 0.76 |
| S4A-Fe1 | 0.65 | 0.67 | 0.65 | 0.73 | 0.70 |
| S4A-Fe3 | 0.95 | 0.85 | 0.82 | 0.85 | 0.93 |
| S4A-Fe4 | 0.77 | 0.81 | 0.74 | 0.76 | 0.90 |
| S1B-V | 0.86 | 1.03 | 0.87 | 0.81 | 1.00 |
| S1B-Fe5 | 0.69 | 0.75 | 0.66 | 0.68 | 0.71 |
| S1B-Fe6 | 0.76 | 0.72 | 0.76 | 0.78 | 0.78 |
| S3B-Fe6 | 0.69 | 1.04 | 0.62 | 0.71 | 0.99 |
| S3B-Fe5 | 0.71 | 0.66 | 0.70 | 0.71 | 0.67 |
| S3B-Fe7 | 0.76 | 0.67 | 0.84 | 0.70 | 0.65 |
| S4B-V | 0.89 | 1.01 | 0.88 | 0.84 | 1.02 |
| S4B-Fe5 | 0.74 | 0.71 | 0.72 | 0.75 | 0.75 |
| S4B-Fe7 | 0.80 | 0.72 | 0.82 | 0.81 | 0.80 |
| S2B-Fe2 | 1.04 | 0.92 | 1.05 | 0.99 | 0.77 |
| S2B-Fe2 | 1.04 | 1.10 | 1.02 | 1.03 | 1.04 |
| S5A-Fe3 | 1.09 | 1.01 | 0.99 | 1.03 | 0.95 |
| S5A-Fe7 | 0.97 | 1.09 | 1.00 | 0.96 | 1.02 |
| S3A-Fe4 | N/A | 0.94 | N/A | N/A | 0.70 |
| S3A-Fe5 | N/A | 0.97 | N/A | N/A | 0.91 |
| Ave. non bridging Fe-S | 0.78 | 0.75 | 0.78 | 0.78 | 0.78 |
| Ave. bridging Fe-S | 1.03 | 1.01 | 1.01 | 1.00 | 0.90 |
| Average M-S | 0.81 | 1.03 | 0.79 | 0.79 | 1.00 |

[a] Single point QM/MM using crystal structure geometry with the protein matrix as pointcharges.

## Localized Orbital Analysis of FeVco

The electronic structure of FeVco in redox states $[V\text{-}CO_3]^{2-/1-/0}$ as interpreted via IAOIBO localized orbital analysis is shown in Figures S21-S23.

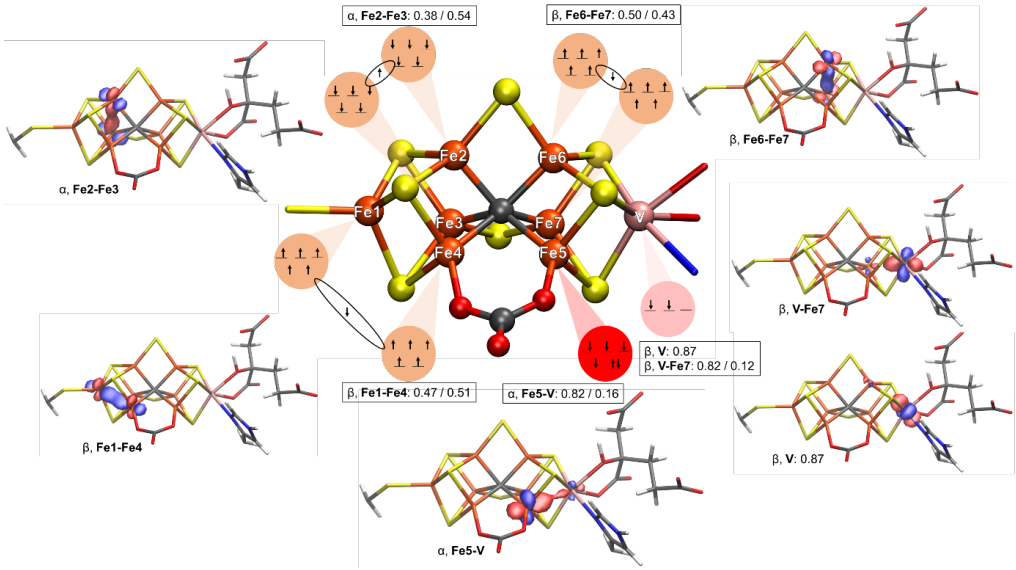


*Figure S 21: Electronic structure of $[V\text{-}CO_3]^{2-}$ with $M_S = {}^3/_2$ as interpreted by IAOIBOs. 181 QM atom QM/MM model. Iso value of 0.1 was used to generate the figures of the orbitals.*

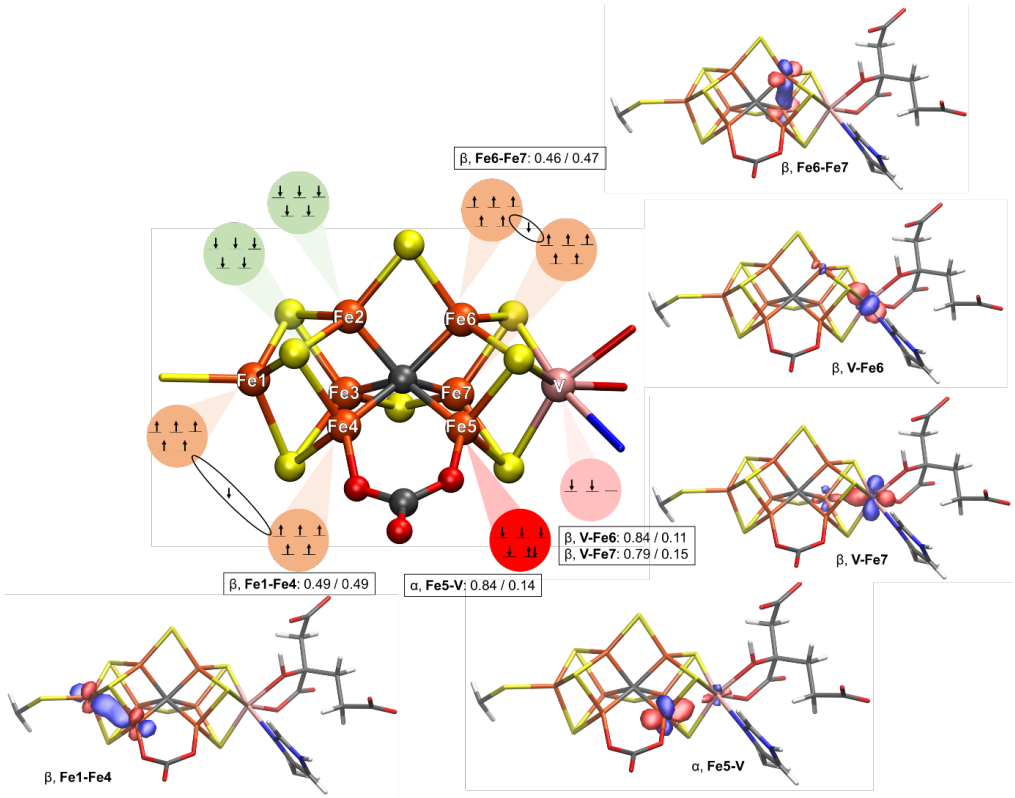


*Figure S 22: The electronic structure of $[V\text{-}CO_3]^{1-}$ $M_S$ = 1 BS7-235 model as interpreted by IAOIBOs. Shown are localized orbitals for the minority-spin electrons and the vanadium electrons and the atomic populations. Using 181 QM atom QM/MM model. Iso value of 0.1 was used to generate the figures of the orbitals.*

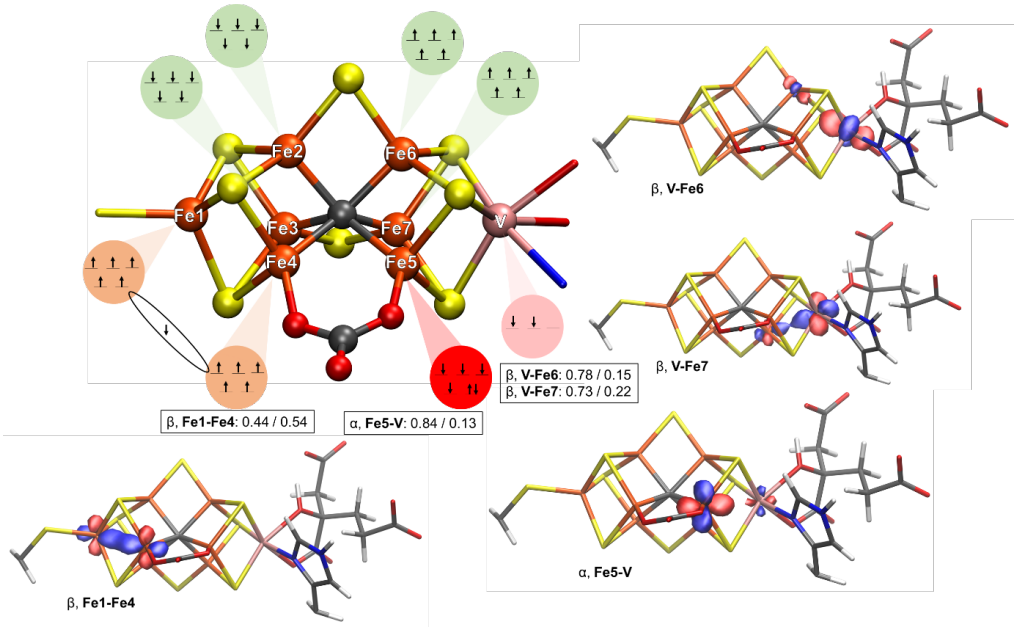


*Figure S 23: The electronic structure of [**V**-$CO_3$]$^0$ $M_S$ = $^3/_2$ BS7-235 model as interpreted by IAOIBOs. Shown are localized orbitals for the minority-spin electrons and the vanadium electrons and the atomic populations. Using 181 QM atom QM/MM model. Iso value of 0.1 was used to generate the figures of the orbitals.*

## The BS7 solutions: FeMoco vs. FeVco

As discussed in the manuscript, for FeVco the BS7-235 solution is considerably lower in energy (by 6 kcal/mol) than the analogous BS7-247 and BS7-346 solutions. For FeMoco the 3 BS7 solutions are all within 1 kcal/mol for FeMoco (Benediktsson, B.; Bjornsson, R. QM/MM Study of the Nitrogenase MoFe Protein Resting State: Broken-Symmetry States, Protonation States, and QM Region Convergence in the FeMoco Active Site. *Inorg. Chem.* **2017**, *56* (21), 13417–13429)

To separate out the effects of carbonate vs. sulfide, V vs. Mo and the different Fe redox state, we carried out calculations where the carbonate of FeVco was substituted by a sulfide, V was substituted by Mo or with both substitutions. When the carbonate ligand in FeVco is exchanged for a sulfide, the difference between the BS7-235 and the other BS7 solutions drops by ~4 kcal/mol (Table S22) and the three BS7 solutions are much more similar in energy. A similar change in energy difference is, however, observed when the vanadium is substituted for molybdenum (and the negative charge is reduced by 1). Simultaneously substituting the vanadium for molybdenum and carbonate for sulfide in FeVco within the VFe protein matrix (essentially substituting FeVco for FeMoco), we see a further drop in the energy difference between the three BS7 solutions which is now less than 1 kcal/mol. Overall this suggests that the preference for BS7-235 in FeVco arises from both the carbonate ligand as well as the presence of V instead of Mo (and the reduced Fe environment).

*Table S 21 The electronic energy of the three BS7 spin isomers of FeVco, FeVco-triS[a], FeVco-Mo[b], FeVco-triS-Mo[c] and FeMoco[d], using a 57 QM atom QM/MM model for FeVco and 54 QM atom QM/MM model for FeMoco.*

| | FeVco | FeVco-triS[a] | FeVco-Mo[b] | FeVco-triS-Mo[c] | FeMoco[d] |
|---|---|---|---|---|---|
| BS7-235 | 0.0 | 0.0 | 0.0 | 0.0 | 0.7 |
| BS7-247 | 6.0 | 2.0 | 2.3 | 0.3 | 1.1 |
| BS7-346 | 6.5 | 1.6 | 1.4 | 0.6 | 0.0 |

[a]FeVco-triS: A 54 QM atom QM/MM optimized model (of the VFe protein) where carbonate has been substituted for a sulfide. $[VFe_7S_9C]^{2-}$ and $M_S = {}^3/_2$
[b]FeVco-Mo: A 57 QM atom QM/MM optimized model (of the VFe protein) where vanadium has been substituted for a molybdenum. $[MoFe_7S_8C(CO_3)]^-$ and $M_S = {}^3/_2$
[c]FeVco-triS-Mo: A 54 QM atom QM/MM optimized model (of the VFe protein) where carbonate has been substituted for sulfide and vanadium has been substituted for molybdenum (essentially FeMoco within the VFe protein matrix). $[MoFe_7S_9C]^-$ and $M_S = {}^3/_2$
[d]FeMoco: A 54 QM atom QM/MM optimized model (of the MoFe protein) as previously described. $[MoFe_7S_9C]^-$ and $M_S = {}^3/_2$.

The energy difference between the BS7 solutions of FeVco is not very sensitive to the QM region size, however, the geometries of all BS7 solutions when optimized are systematically improved with respect to the 5NY6 X-ray structure (Table S20) as the QM region increases. The BS7-235 structure is still in best agreement with the 5N6Y X-ray structure.

*Table S 22: Root-Mean-Square Deviations (in Å) of different QM/MM Optimized Geometries with the Possible FeVco structure compared to the Experimentally Determined Crystal Structure). The RMSD is defined as the deviation of the $[VFe_7S_8C(XO_3)]$ part with respect to both cofactors in the crystal structure.*

| Model | RMSD [Å] | Relative energy difference [kcal/mol] | V-Fe1 distance [Å] (crystal 7.11 Å) |
|---|---|---|---|
| BS7-235-57QM | 0.080 | 0 | 7.11 |
| BS7-247-57QM | 0.101 | 6.00 | 7.15 |
| BS7-346-57QM | 0.096 | 6.53 | 7.10 |
| BS235-83QM | 0.083 | 0 | 7.09 |
| BS7-247-83QM | 0.098 | 5.58 | 7.10 |
| BS7-346-83QM | 0.091 | 5.52 | 7.12 |
| BS7-235-181QM | 0.076 | 0 | 7.05 |
| BS7-247-181QM | 0.088 | 5.27 | 7.11 |
| BS7-346-181QM | 0.089 | 6.13 | 7.09 |

*Table S 23: The effect of geometry optimization on the relative energy difference of BS7 class of broken symmetry solutions.*

| BS | Geometry type | QM region | Relative energy difference [kcal/mol] |
|---|---|---|---|
| BS7-235 | X-ray | 57 | 0 |
| BS7-247 | X-ray | 57 | 7.83 |
| BS7-346 | X-ray | 57 | 8.18 |
| BS7-235 | QM/MM opt | 57 | 0 |
| BS7-247 | QM/MM opt | 57 | 6.00 |
| BS7-346 | QM/MM opt | 57 | 6.53 |
| BS7-235 | QM/MM opt | 83 | 0 |
| BS7-247 | QM/MM opt | 83 | 5.58 |
| BS7-346 | QM/MM opt | 83 | 5.52 |
| BS7-235 | QM/MM opt | 181 | 0 |
| BS7-247 | QM/MM opt | 181 | 5.27 |
| BS7-346 | QM/MM opt | 181 | 6.13 |

## Protonation state of homocitrate

QM/MM calculations of FeVco ([**V**-$CO_3$]$^{2-}$ model) with and without the alcohol group of homocitrate protonated were carried out. A comparison of the computed structures with the X-ray crystal structure (PDB ID: 5N6Y) reveal that the alcohol group is most likely protonated. This is consistent with our previous finding for FeMoco in MoFe protein Benediktsson, B.; Bjornsson, R. QM/MM Study of the Nitrogenase MoFe Protein Resting State: Broken-Symmetry States, Protonation States, and QM Region Convergence in the FeMoco Active Site. *Inorg. Chem.* **2017**, *56* (21), 13417–13429). and another study (Cao, L.; Caldararu, O.; Ryde, U. Protonation States of Homocitrate and Nearby Residues in Nitrogenase Studied by Computational Methods and Quantum Refinement. *J. Phys. Chem. B* **2017**, *121* (35), 8242–8262.)

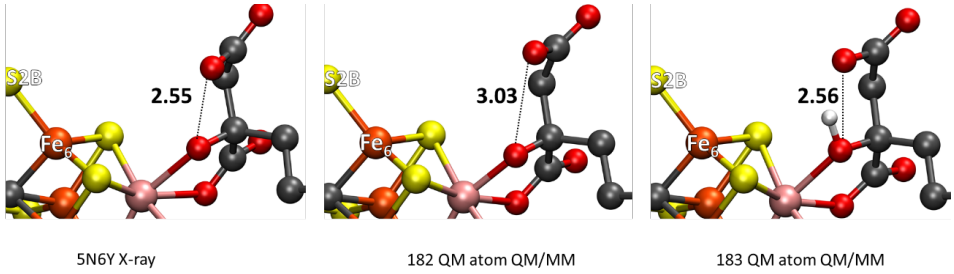


*Figure S 24: Protonation state of the alcohol group of homocitrate of FeVco. Left: Close-up of the alcohol group of homocitrate of FeVco in the 5N6Y X-ray structure with the O-O distance between the alcohol group and the shorter carboxylate arm indicated. Middle: Computed structure with no proton present. Right: Computed structure with alcohol proton present.*

## Protonated FeVco

*Table S 24: Structural parameters comparing the average of the two FeVco cofactors of the X-ray structure to QM/MM calculated structures of protonated forms of the cofactors. HS2B: Sulfide S2B protonated, HS5A: Sulfide S5A protonated, 2XHCA: longer carboxylate arm of FeVco protonated. 58 QM atom QM/MM calculations.*

| | Crystal | HS2B | HS5A | 2XHCA |
|---|---|---|---|---|
| Fe1-Fe2 | 2.71 | 2.69 | 2.69 | 2.72 |
| Fe1-Fe3 | 2.66 | 2.64 | 2.61 | 2.65 |
| Fe1-Fe4 | 2.58 | 2.66 | 2.66 | 2.63 |
| V-Fe5 | 2.70 | 2.71 | 2.69 | 2.70 |
| V-Fe6 | 2.77 | 2.74 | 2.82 | 2.90 |
| V-Fe7 | 2.73 | 2.72 | 2.66 | 2.73 |
| Fe2-Fe3 | 2.63 | 2.56 | 2.59 | 2.60 |
| Fe2-Fe4 | 2.62 | 2.62 | 2.63 | 2.63 |
| Fe3-Fe4 | 2.63 | 2.67 | 2.64 | 2.67 |
| Fe5-Fe6 | 2.60 | 2.62 | 2.66 | 2.67 |
| Fe5-Fe7 | 2.63 | 2.65 | 2.63 | 2.66 |
| Fe6-Fe7 | 2.60 | 2.53 | 2.51 | 2.57 |
| V-Fe1 | 7.11 | 7.12 | 7.10 | 7.15 |
| C-Fe1 | 3.48 | 3.51 | 3.50 | 3.53 |
| C-V | 3.63 | 3.61 | 3.61 | 3.63 |
| Fe2-Fe6 | 2.61 | 2.67 | 2.61 | 2.62 |
| Fe3-Fe7 | 2.60 | 2.59 | 2.64 | 2.60 |
| Fe4-Fe5 | 2.76 | 2.72 | 2.72 | 2.72 |
| C-Fe2 | 1.95 | 2.01 | 2.01 | 2.03 |
| C-Fe3 | 2.04 | 2.02 | 2.01 | 2.04 |
| C-Fe4 | 2.02 | 2.00 | 1.99 | 2.00 |
| C-Fe5 | 2.05 | 2.01 | 2.00 | 1.99 |
| C-Fe6 | 1.98 | 2.02 | 2.02 | 2.02 |
| C-Fe7 | 2.01 | 2.01 | 2.02 | 2.02 |
| Fe4-OX | 1.97 | 1.91 | 1.91 | 1.93 |
| Fe5-Ocarb | 1.93 | 1.91 | 1.91 | 1.92 |
| Fe4-O-O-Fe5 | -11.30 | -2.57 | -2.89 | -5.06 |

| | | | | |
|---|---|---|---|---|
| V-Oalk | 2.20 | 2.12 | 2.11 | 2.16 |
| V-Ocarb | 2.35 | 2.05 | 2.06 | 2.08 |
| V-His | 2.35 | 2.20 | 2.21 | 2.22 |
| Fe1-Scys | 2.16 | 2.26 | 2.26 | 2.29 |
| Fe2-S2B | 2.21 | 2.35 | 2.19 | 2.21 |
| Fe6-S2B | 2.17 | 2.34 | 2.19 | 2.19 |
| Fe3-S5A | 2.23 | 2.20 | 2.34 | 2.22 |
| Fe7-S5A | 2.27 | 2.20 | 2.34 | 2.20 |

Unbound electrons

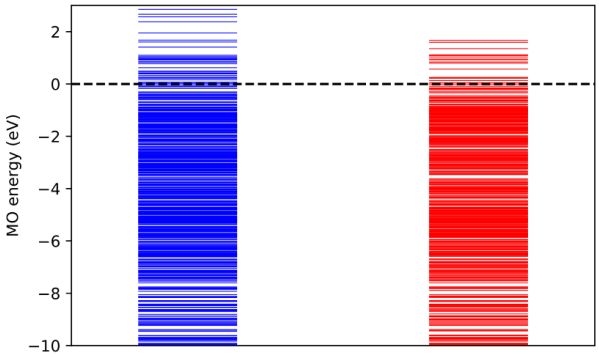


| **Alpha electrons:** | **Beta electrons:** |
|---|---|
| 497α: 0.0064 eV | 496β: 0.0497 eV |
| 498α: 0.0662 eV | 497β: 0.1307 eV |
| 499α: 0.2503 eV | 498β: 0.2392 eV |
| 500α: 0.2547 eV | 499β: 0.2514 eV |
| 501α: 0.3847 eV | 500β: 0.7961 eV |
| 502α: 0.4911 eV | 501β :0.8426 eV |
| 503α: 0.6242 eV | 502β: 0.9262 eV |
| 504α: 0.8518 eV | 503β 1.0820 eV |
| 505α: 0.9152 eV | 504β: 1.1137 eV |
| 506α: 0.9676 eV | 505β :1.3524 eV |
| 507α: 1.0450 eV | 506β: 1.5942 eV |
| 508α: 1.4082 eV | 507β 1.6636 eV |
| 509α: 1.6039 eV | |
| 510α: 1.6793 eV | |

*Figure S 25: MO diagram showing the occupied valence orbitals in the 181 QM atom QM/MM model of [**V**-$CO_3$]$^{2-}$. Orbitals with positive energies correspond to unbound electrons and are listed to the right.*

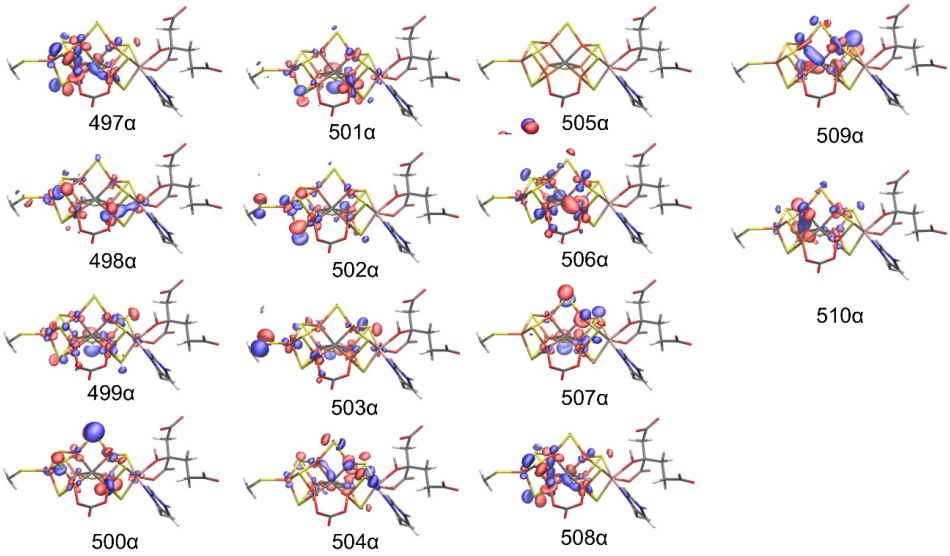


*Figure S 26: Molecular orbitals of α electrons that that have positive orbital energies in a 181 QM atom QM/MM model of the [**V**-$CO_3$]$^{2-}$ model. These high energy orbitals show mainly, but not only, sulfide and iron character*

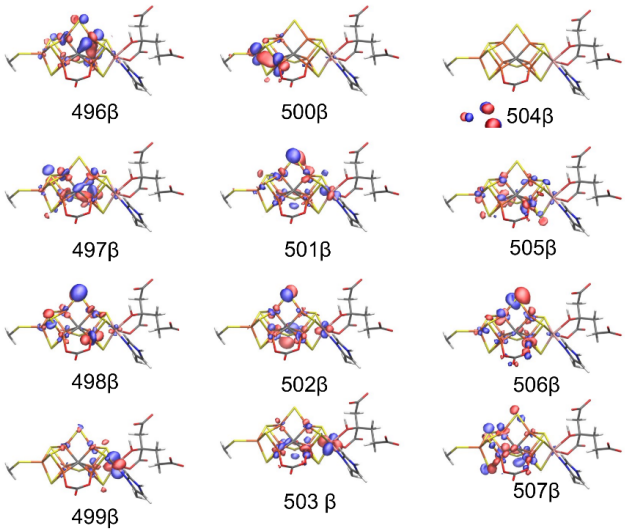


*Figure S 27: Molecular orbitals of β electrons that that have positive orbital energies in a 181 QM atom QM/MM model of the [**V**-$CO_3$]$^{2-}$ model. These high energy orbitals show mainly, but not only, sulfide and iron character*

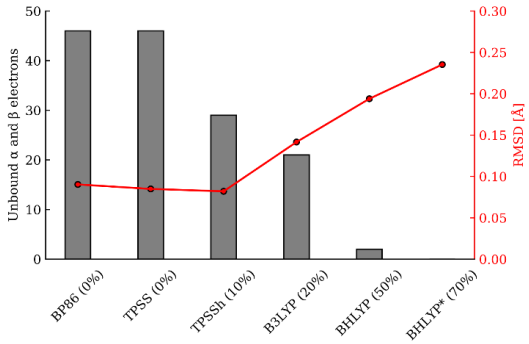


*Figure S 28: The dependence of unbound electrons in the [**V**-$CO_3$]$^{2-}$ resting state model on density functionals with different amount of HF exchange. Also shown (right y-axis) is the RMSD of the optimized cofactor with the respective functional. QM/MM model with a QM region size of 57 atoms. The RMSD is defined as the deviation of the [$VFe_7S_8C(XO_3)$] part with respect to both cofactors in the crystal structure.*

## Alternative QM/MM model of whole protein

The model is prepared similarly as the spherical QM/MM model. The difference between the two models is that instead of a spherical cut from the MD step, the whole protein is included as well as all water molecules within 3 Å of the protein matrix. This new QM/MM model 47 516 atoms in size.

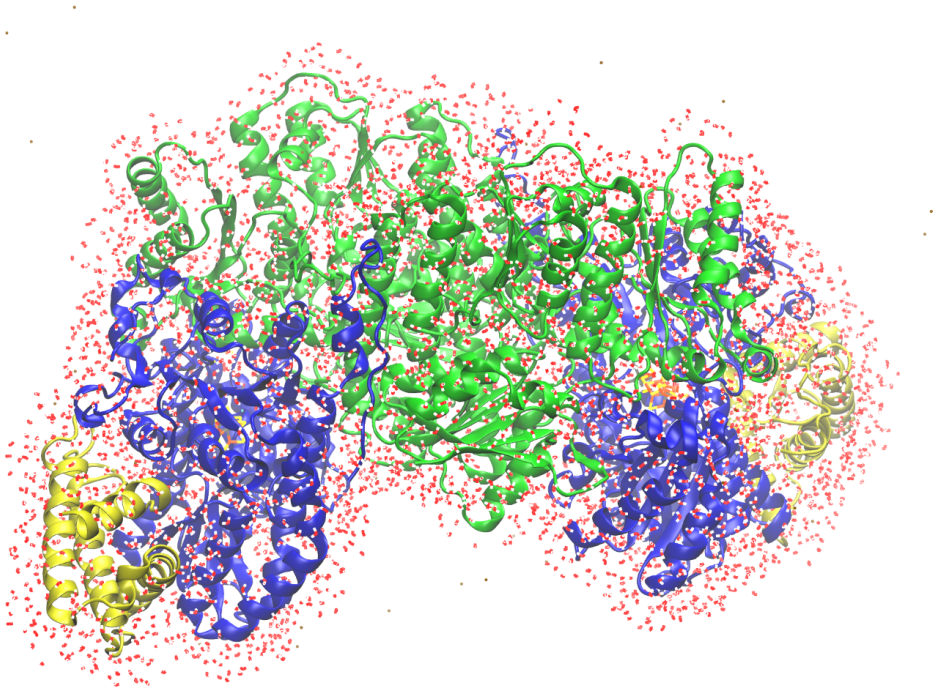

*Figure S 29: The new QM/MM model (47 516 atoms) includes the whole VFe protein as well as sodium ion counterions and 3 Å thick water layer at the edge of the VFe protein.*

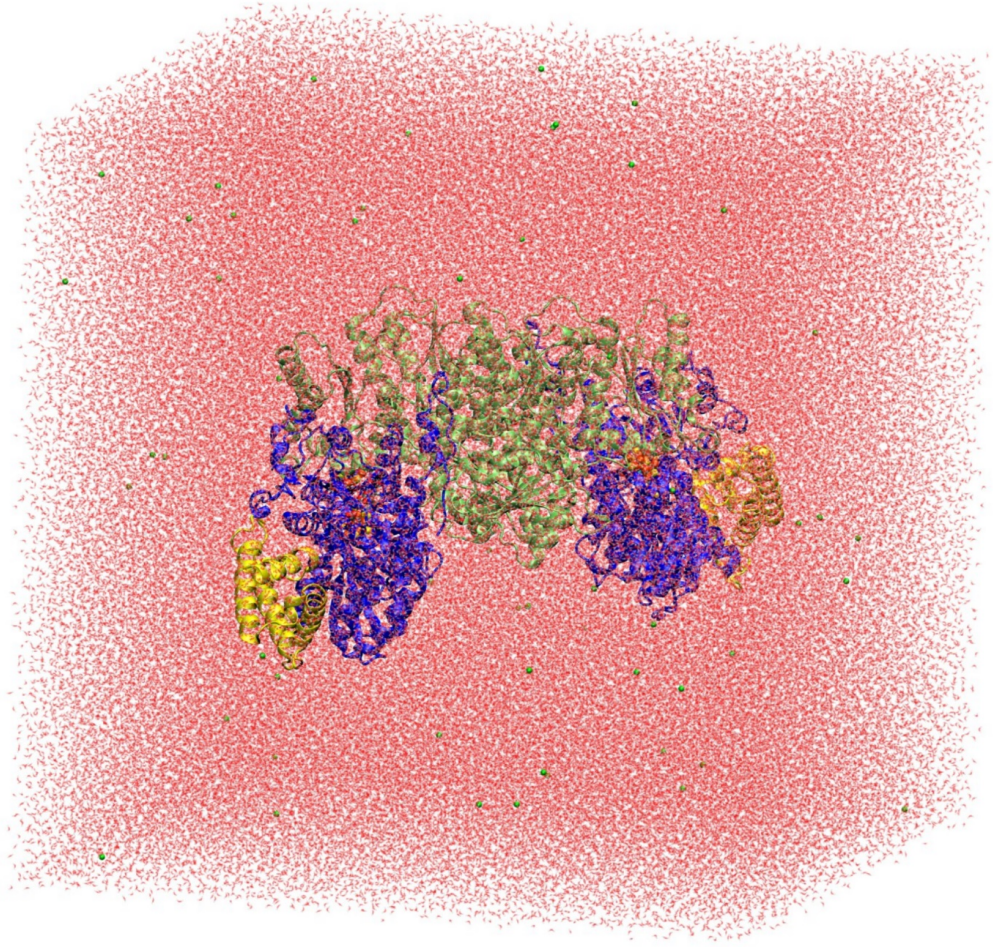

Figure S 30: *The 531 080 atom QM/MM model (full box from the MM setup).*

*Table S 25: Mulliken spin populations of the FeVco $[VFe_7S_8C(CO_3)]^{2-}$ model using 47 516 atom and 531 080 atom QM/MM model setups.*

| QM atoms | 57 | 57 | 181 | 181 |
|---|---|---|---|---|
| QM/MM Model size | 47 516 | 531 080 | 47 516 | 531 080 |
| V | -1.650 | -1.649 | -1.634 | -1.630 |
| Fe1 | 3.477 | 3.479 | 3.459 | 3.462 |
| Fe2 | -3.292 | -3.292 | -3.286 | -3.288 |
| Fe3 | -3.290 | -3.293 | -3.274 | -3.277 |
| Fe4 | 3.428 | 3.427 | 3.387 | 3.388 |
| Fe5 | -3.218 | -3.218 | -3.187 | -3.186 |
| Fe6 | 3.289 | 3.288 | 3.291 | 3.289 |
| Fe7 | 3.221 | 3.222 | 3.210 | 3.208 |
| S1A | 0.183 | 0.182 | 0.200 | 0.199 |
| S2A | -0.014 | -0.019 | -0.013 | -0.018 |
| S4A | 0.164 | 0.161 | 0.169 | 0.167 |
| S1B | 0.084 | 0.084 | 0.079 | 0.079 |
| S3B | 0.273 | 0.270 | 0.279 | 0.275 |
| S4B | 0.106 | 0.105 | 0.099 | 0.098 |
| S2B | 0.012 | 0.015 | 0.009 | 0.013 |
| S5A | 0.014 | 0.019 | -0.008 | -0.004 |
| C* | 0.059 | 0.061 | 0.055 | 0.057 |
| C | -0.001 | 0.000 | -0.005 | -0.005 |
| O3 | 0.041 | 0.043 | 0.026 | 0.027 |
| O1 | -0.020 | -0.022 | -0.008 | -0.009 |
| O2 | -0.001 | -0.001 | 0.000 | 0.000 |

*Table S 26: Comparison of metal-metal distances in different X-ray structures of MoFe: the deviation of metal-metal distances of each FeMoco unit in various X-ray structures to one FeMoco unit in the 1.0 Å resolution crystal structure (PDB ID: 3U7Q).*

| Resolution [Å] | 1.00 | 1.16 | 1.16 | 1.16 | 1.16 | 1.43 | 1.43 | QM/MM |
|---|---|---|---|---|---|---|---|---|
| PDB ID | 3U7Q | 1M1N[b] | 1M1N[b] | 1M1N[b] | 1M1N[b] | 4TKU[c] | 4TKU[c] | 367 QM atoms[d] |
| FeMoco unit number[a] | 2 | 1 | 2 | 3 | 4 | 1 | 2 | |
| Fe1-Fe2 | -0.012 | -0.004 | 0.008 | -0.012 | -0.001 | -0.006 | 0.001 | 0.021 |
| Fe1-Fe3 | 0.005 | -0.004 | 0.010 | -0.001 | -0.002 | -0.003 | -0.001 | 0.034 |
| Fe1-Fe4 | -0.007 | 0.004 | 0.002 | -0.006 | -0.005 | 0.004 | 0.007 | 0.013 |
| Mo-Fe6 | 0.007 | 0.002 | 0.004 | 0.011 | -0.001 | 0.017 | 0.015 | 0.025 |
| Mo-Fe7 | 0.005 | -0.005 | -0.002 | -0.007 | -0.006 | 0.014 | 0.005 | 0.055 |
| Mo-Fe5 | 0.003 | -0.003 | 0.001 | 0.014 | 0.001 | 0.010 | 0.004 | 0.022 |
| Fe2-Fe3 | 0.002 | -0.001 | 0.013 | -0.002 | 0.009 | 0.008 | 0.005 | 0.019 |
| Fe3-Fe4 | -0.002 | -0.003 | -0.002 | 0.000 | -0.009 | 0.005 | -0.002 | 0.028 |
| Fe2-Fe4 | 0.000 | 0.001 | 0.013 | -0.003 | 0.003 | 0.017 | 0.015 | 0.026 |
| Fe6-Fe7 | 0.003 | -0.004 | 0.015 | 0.017 | 0.007 | 0.013 | 0.001 | 0.040 |
| Fe5-Fe6 | 0.001 | -0.006 | 0.002 | 0.018 | 0.000 | 0.001 | -0.007 | -0.002 |
| Fe5-Fe7 | -0.002 | 0.004 | 0.006 | 0.011 | 0.008 | 0.004 | -0.008 | 0.010 |
| Fe2-Fe6 | -0.003 | -0.004 | -0.001 | 0.003 | 0.003 | -0.004 | -0.007 | -0.010 |
| Fe3-Fe7 | -0.001 | 0.026 | 0.028 | 0.031 | 0.032 | 0.035 | 0.032 | 0.003 |
| Fe4-Fe5 | -0.006 | -0.032 | -0.041 | -0.041 | -0.035 | -0.030 | -0.034 | -0.011 |
| Absolute average deviation | 0.004 | 0.007 | 0.010 | 0.012 | 0.008 | 0.011 | 0.010 | 0.021 |

[a] As the MoFe protein is a dimer, there are two units of FeMoco per protein.

[b] In the case of 1M1N, there are two units of the MoFe protein in the X-ray structure and therefore 4 units of FeMoco (Reference: Einsle, O. Nitrogenase MoFe-Protein at 1.16 A Resolution: A Central Ligand in the FeMo-Cofactor. *Science.* **2002**, *297* (5587), 1696–1700. https://doi.org/10.1126/science.1073877.)

[c] As the MoFe protein is a dimer, there are two units of FeMoco per protein (Reference: Spatzal, T.; Perez, K. A.; Einsle, O.; Howard, J. B.; Rees, D. C. Ligand Binding to the FeMo-Cofactor: Structures of Co-Bound and Reactivated Nitrogenase. *Science.* **2014**, *345* (6204), 1620–1623.)

[d] From a previous study by us (Reference: Benediktsson, B.; Bjornsson, R. QM/MM Study of the Nitrogenase MoFe Protein Resting State: Broken-Symmetry States, Protonation States, and QM Region Convergence in the FeMoco Active Site. *Inorg. Chem.* **2017**, *56* (21), 13417–13429)

# Article II

**Analysis of the Geometric and Electronic Structure of Spin-Coupled Iron–Sulfur Dimers with Broken-Symmetry DFT: Implications for FeMoco.**

B. Benediktsson, R. Bjornsson

Journal of Chemical Theory and Computation **18**, 1437-1457, 2022.

JCTC Journal of Chemical Theory and Computation

pubs.acs.org/JCTC Article

# Analysis of the Geometric and Electronic Structure of Spin-Coupled Iron−Sulfur Dimers with Broken-Symmetry DFT: Implications for FeMoco

Bardi Benediktsson and Ragnar Bjornsson*

Cite This: J. Chem. Theory Comput. 2022, 18, 1437−1457 Read Online

ACCESS | Metrics & More | Article Recommendations | Supporting Information



**ABSTRACT:** The open-shell electronic structure of iron−sulfur clusters presents considerable challenges to quantum chemistry, with the complex iron−molybdenum cofactor (FeMoco) of nitrogenase representing perhaps the ultimate challenge for either wavefunction or density functional theory. While broken-symmetry density functional theory has seen some success in describing the electronic structure of such cofactors, there is a large exchange−correlation functional dependence in calculations that is not fully understood. In this work, we present a geometric benchmarking test set, FeMoD11, of synthetic spin-coupled Fe−Fe and Mo−Fe dimers, with relevance to the molecular and electronic structure of the Mo-nitrogenase FeMo cofactor. The reference data consists of high-resolution crystal structures of metal dimer compounds in different oxidation states. Multiple density functionals are tested on their ability to reproduce the local geometry, specifically the Fe−Fe/Mo−Fe distance, for both antiferromagnetically coupled and ferromagnetically coupled dimers via the broken-symmetry approach. The metal−metal distance is revealed not only to be highly sensitive to the amount of exact exchange in the functional but also to the specific exchange and correlation functionals. For the antiferromagnetically coupled dimers, the calculated metal−metal distance correlates well with the covalency of the bridging metal−ligand bonds, as revealed via the corresponding orbital analysis, Hirshfeld S/Fe charges, and Fe−S Mayer bond order. Superexchange via bridging ligands is expected to be the dominant interaction in these dimers, and our results suggest that functionals that predict accurate Fe−Fe and Mo−Fe distances describe the overall metal−ligand covalency more accurately and in turn the superexchange of these systems. The best performing density functionals of the 16 tested for the FeMoD11 test set are revealed to be either the nonhybrid functionals r$^2$SCAN and B97-D3 or hybrid functionals with 10−15% exact exchange: TPSSh and B3LYP*. These same four functionals are furthermore found to reproduce the high-resolution X-ray structure of FeMoco well according to quantum mechanics/molecular mechanics (QM/MM) calculations. Almost all nonhybrid functionals systematically underestimate Fe−Fe and Mo−Fe distances (with r$^2$SCAN and B97-D3 being the sole exceptions), while hybrid functionals with >15% exact exchange (including range-separated hybrid functionals) overestimate them. The results overall suggest r$^2$SCAN, B97-D3, TPSSh, and B3LYP* as accurate density functionals for describing the electronic structure of iron−sulfur clusters in general, including the complex FeMoco cluster of nitrogenase.

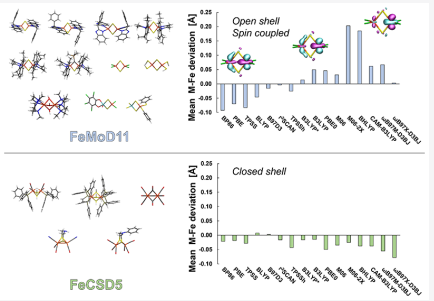


## INTRODUCTION

Nature utilizes complex polynuclear spin-coupled cofactors to carry out complex chemical transformations with the reduction of dinitrogen to ammonia being a prime example. The iron−molybdenum cofactor of the Mo nitrogenase enzyme (FeMoco) features 8 metal ions in Fe(II) and Fe(III) oxidation states, 41 unpaired electrons, spin-polarized covalent Fe−S, Mo−S, and Fe−C metal−ligand bonds; unusual ligand environments (e.g., interstitial carbide); and an unusual spin-coupled Mo(III).[1] The cofactor has been extensively characterized by X-ray crystallography,[2] electron paramagnetic resonance (EPR),[3−6] $^{57}$Fe Mössbauer,[7] X-ray absorption, and X-ray emission spectroscopy,[8−15] yet details still remain to be uncovered about the nature of the electronic structure such as the local Fe oxidation states, spin coupling, and spin delocalization.[6] These complex electronic structure properties are likely behind the unique reactivity of the cluster. While theory has played an important role in unraveling the molecular and electronic structure of FeMoco[9,11,16−23] and similar iron−sulfur clusters[24−27] (and multiple density functional theory (DFT) studies have suggested possible reaction

Received: July 27, 2021
Published: February 15, 2022

mechanisms of dinitrogen reduction),[28−35] much uncertainty remains about how well theory describes the complicated electronic structure that these clusters exhibit.

The simplest spin-coupled systems already pose a challenge to contemporary quantum chemistry. An antiferromagnetically coupled singlet state cannot be fully described by a single-determinant wavefunction. Instead, one must settle for a symmetry-broken spin-contaminated $M_S = 0$ unrestricted Hartree−Fock (HF) state that features unphysical localized spin density present on each spin center ($\alpha$ and $\beta$ spin density, respectively), while the exact $S = 0$ state has zero spin density everywhere in space. This lack of a spin eigenfunction in the reference is an inconvenient starting point for a post-HF approach, and this problem is arguably only satisfactorily dealt with at the multireference wavefunction level where a spin-adapted multiconfigurational reference can be used instead. Alternatively, spin projection of spin-symmetry-broken states via the use of model Hamiltonians (e.g., Heisenberg−Dirac−Van Vleck, HDVV) can be used to correct the energy of the low-spin state, and this strategy has recently been used to correct coupled-cluster calculations utilizing a broken-symmetry UHF reference.[36]

Spin-adapted multireference calculations should allow the most satisfactory treatment of spin-coupled systems. However, there are challenges associated with treating a large enough active space in the complete active space self-consistent field (CASSCF) reference calculation, and even more difficult challenges in the subsequent dynamic correlation treatment. Large active space CASSCF calculations that use approximations to the full configuration interaction (FCI) problem within the active space are beginning to emerge for iron−sulfur systems.[27,37−42] Examples include: calculations based on the density matrix renormalization group, DMRG-CASSCF,[27] and FCI quantum Monte Carlo[42] that have been applied to the simplest [2Fe−2S] dimers as well as [4Fe−4S] clusters. Recently, DMRG-CASSCF calculations of the large $Fe_8S_7$ cluster of the MoFe protein (P-cluster) were performed with active spaces of up to 120 electrons in 77 orbitals, shedding light on the complex dense low-energy spectrum of this complex cluster.[41] CASSCF calculations of FeMoco with active spaces up to 113 electrons in 76 orbitals have recently been achieved.[38] These studies have revealed that spin-coupled iron−sulfur systems feature a large number of low-energy electronic states, more than assumed in effective spin Hamiltonians (HDVV as well as the extended double-exchange version HDE).[27] While it is encouraging that large active space CASSCF calculations are becoming possible for systems as large as the P-cluster and FeMoco, questions remain about the accuracy of these results as dynamic correlation effects are typically unaccounted for in these calculations,[43] yet they would be important for capturing the covalency of the iron−sulfur chemical bonds. Unfortunately, there are theoretical problems with applying multireference perturbation theory to large active space CASSCF references,[44,45] and more robust multireference configuration interaction (MRCI) or coupled-cluster (MRCC) approaches typically remain out of reach.

An alternative to the multireference wavefunction approach comes from unrestricted density functional theory. Kohn−Sham density functional theory (KS-DFT) bypasses the calculation of the wavefunction of the system and assumes instead that a single-determinant description of a non-interacting reference system together with an exchange−correlation energy functional is sufficient to describe the electron density and energy of any system of interest. The single-determinant nature of KS-DFT implies at first glance that it should suffer from the same problem as a single-determinant HF wavefunction with unphysical spin density for an $S = 0$ system.[46] However, the extent of this problem remains unclear since the total spin operator operates on the noninteracting KS reference system instead of the full interacting system, with the spin of the system thus not well defined. KS-DFT is typically considered an exact approach (although this rests on the assumption that the density is always noninteracting $v$-representable),[47−53] which implies that an exact Kohn−Sham density functional calculation should give the exact energy of a system, even though the noninteracting reference system clearly breaks spin symmetry.[54] Approximate spin projection schemes, e.g., based on the Yamaguchi[55,56] or the Noodleman[57−59] equations, are commonly applied to correct for the spin contamination of the low-spin state. This is performed using the energies of the antiferromagnetic broken-symmetry solution and the ferromagnetic solution to parameterize an effective Hamiltonian such as the HDVV. This allows one to derive the energy of the true uncontaminated $S = 0$ spin state. Such spin projection schemes have been reasonably successful in many studies,[60] leading to qualitatively and often semiquantitatively correct results, albeit with a large functional dependence.[61]

The ambiguous nature of the spin-contaminated broken-symmetry state poses a theoretical problem for structural optimizations of spin-coupled systems, with some practitioners preferring to optimize the structure of the less spin-contaminated ferromagnetic state rather than the broken-symmetry state. This approach seems justified in cases of weak spin-coupling where geometries of ferromagnetic and antiferromagnetic states have been found to be very similar, e.g., for Mn−O dimers.[62] This is not the case for Fe−S systems (see, e.g., refs 37 and 69) and is discussed later. A pragmatic alternative is to instead optimize the geometries of spin-coupled systems using the broken-symmetry determinant and assume thereby that the broken-symmetry state is an accurate enough representation of the spin-coupled low-spin state and that all important correlation effects are included via the exchange−correlation functional. This approach has been utilized by us and others in various DFT and DFT/molecular mechanics (MM) studies on the multimetal spin-coupled FeMoco and FeVco (iron−vanadium cofactor of vanadium nitrogenase) clusters where excellent agreement with the high-resolution crystal structure has been obtained.[22,63−65] In fact, the strong correlation between the experimental Fe−Fe and Mo−Fe distances of FeMoco and BS-DFT-calculated Fe−Fe and Mo−Fe distances implies that the BS-DFT states calculated might be considered quite reasonable approximations to the true electronic states. As recently discussed in the literature, however, there is a large functional dependence in BS-DFT calculations on FeMoco, and the functional choice strongly affects both the structure of the cofactor and reaction energies.[28,29,66,67] In previous work,[29] we have argued that hybrid functionals with >20% exact exchange lead to unacceptable structural deviations (systematic overestimations) for FeMoco compared to the high-resolution (1.0 Å) crystal structure.[2] In the case of nonhybrid functionals, these functionals systematically underestimate the Fe−Fe and Mo−Fe distances instead. TPSSh, a 10% exact exchange hybrid functional, was found to give the most satisfactory description of the molecular structure of FeMoco of tested functionals.[29]


https://doi.org/10.1021/acs.jctc.1c00753
J. Chem. Theory Comput. 2022, 18, 1437−1457

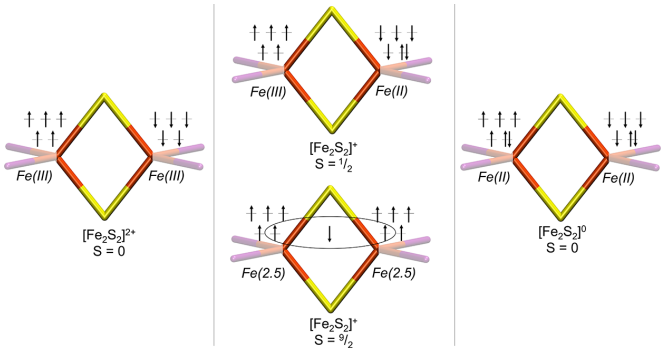


**Figure 1.** Spin-coupled redox states exhibited by the [2Fe−2S] core as representative for the FeMoD11 test set. Orange indicates iron, yellow indicates sulfur, and purple is a terminal ligand.

Finally, we note a recent alternative approach: approximate spin projection correction of gradients via the extended broken-symmetry (EBS) method.[68] The extended broken-symmetry approach employs approximate spin projection to the nuclear gradient, and the method has been applied to structural optimizations and even vibrational frequencies of iron−sulfur systems.[68,69,70,77] This approach assumes the validity of a specific model Hamiltonian (e.g., HDVV), which may present problems if the model Hamiltonian does not give a realistic description of the system, a problem that has been discussed for iron−sulfur systems.[27]

Systematic structural benchmarking studies of metal complexes, such as those by Bühl and co-workers[71−73] using gas-phase electron diffraction and microwave spectroscopy reference data, have been popular in the literature and continue to be used to test different density functional approximations. Importantly, these test sets feature exclusively metal complexes with closed-shell electronic structure and fewer studies include test sets featuring complexes with open-shell electronic structure. Szilagyi and Winslow investigated spin-coupled iron−sulfur complexes and showed that the geometry of a $[Fe_2S_2(SPh)_4]^{2-}$ dimer was sensitive to both basis set and functional choice. Their results indicated that a 5% hybrid functional (B5HFP) gave accurate spin density distributions,[74] and in a later study, Harris and Szilagyi demonstrated that a 5% hybrid functional also gave reasonable Fe−S covalency.[75] Moreover, Noodleman and co-workers demonstrated that accurate geometries of spin-coupled iron−sulfur systems are essential for accurate $^{57}$Fe Mössbauer parameters.[76] Guidoni and co-workers, testing both BS-DFT and EBS-DFT geometry optimizations found, on the other hand, that B3LYP yielded reasonable vibrational frequencies, but geometries optimized with the M06 functional gave structures in best agreement with experiment.[69,77]

In this work, we study the molecular and electronic structure of spin-coupled Fe−S systems (see Figure 1) as described by broken-symmetry DFT structural optimizations, focusing especially on the functional dependence and how the electronic structure of these systems influences the molecular structure. We introduce a test set of 11 complexes, FeMoD11, which includes eight antiferromagnetically spin-coupled Fe−Fe dimers, one ferromagnetically spin-coupled Fe−Fe dimer, and two antiferromagnetically coupled Mo−Fe dimers, inspired by dimeric fragments found in FeMoco. The test set features antiferromagnetic interactions (via bridging ligand super-exchange), as well as double-exchange interactions (via direct d-overlap), both known to be important features in the electronic structure of iron−sulfur clusters such as FeMoco. We show that the spin-coupled systems have completely different functional dependencies compared to closed-shell systems and discuss how the metal−metal distance depends strongly on the covalency of bridging metal−ligand bonds in spin-coupled metal dimers. The implications for the BS-DFT description of FeMoco are discussed, and we extend the functional comparison to a quantum mechanics/molecular mechanics (QM/MM) model of FeMoco.

## COMPUTATIONAL DETAILS

All X-ray crystal structures were downloaded from the Cambridge Crystallographic Data Centre[78] and were used as the starting structure for geometrical optimizations. Where missing, hydrogens were added manually. All calculations were performed with the ORCA quantum chemistry program package version 4.2.1[79] (unless otherwise stated). The self-consistent field (SCF) convergence criteria were set to $10^{-8}$ Eh (energy change), and tight optimization criteria were used (energy change of $10^{-6}$ Eh, root-mean-square (RMS) gradient of $3 \times 10^{-5}$ Eh/au, max gradient of $10^{-4}$ Eh/au, RMS displacement of $6 \times 10^{-4}$, and max displacement of $1 \times 10^{-3}$ au).

The density functionals used were BP86,[80,81] B97-D3[82] (uses D3BJ), TPSS,[83] TPSSh,[83,84] BLYP,[80,85] B3LYP,[80,85,86] B3LYP*,[87,88] PBE,[85] PBE0,[89,90] M06,[91] M06-2X,[91] BHLYP,[92] CAM-B3LYP,[93] ωB97M-D3BJ,[94,95] ωB97X-D3BJ,[94,96] and r$^2$SCAN.[97] As ωB97M-D3BJ and ωB97X-D3BJ are based on their parent ωB97M-V and ωB97X-V functionals but have been reparameterized for the D3BJ correction,[94] we include D3BJ as a label (which also distinguishes the functional from the different ωB97X and ωB97X-D3 functionals[98]). The D3 dispersion correction with Becke−Johnson damping, DFT-D3BJ,[99,100] was used for all functionals except for the Minnesota (M06 and M06-2X) functionals, where the older zero-damping[99] version was used. The scalar relativistic zeroth order regular approximation (ZORA)[101,102] was used in all calculations described in the Density Functional Comparison of the FeMoD11 and FeCSD5 Test Sets, Correlation between Bridging Metal−Ligand Bond Lengths and Metal−Metal Distance in FeMoD11, and Correlation between Fe−S Bond Covalency and Fe−Fe Distance sections. The ZORA calculations utilized the one-center approximation, and a


https://doi.org/10.1021/acs.jctc.1c00753
J. Chem. Theory Comput. 2022, 18, 1437−1457

**Table 1. FeMoD11 Test Set**[a]

| complex | CSD ID | *S* | charge[b] | M ox.[c] | bridging L | terminal L | counterion | temp (K) | R (%)[d] | M–Fe (Å)[e] |
|---|---|---|---|---|---|---|---|---|---|---|
| **1** | UZOHEX | 0 | 2– | 2 × $Fe^{3+}$ | 2 × $S^{2-}$ | 2 × bis(benzimidazolato)$^{2-}$ | 2 × $(NEt_4)^+$ | 133 | 3.21 | 2.702 |
| **2** | UZOHIB | 1/2 | 3– | $Fe^{2+}$, $Fe^{3+}$ | 2 × $S^{2-}$ | 2 × bis(benzimidazolato)$^{2-}$ | 3 × $(NEt_4)^+$[g] | 133 | 5.72 | 2.686 |
| **3** | CEWTIJ | 0 | 4– | 2 × $Fe^{2+}$ | 2 × $S^{2-}$ | 2 × bis(benzimidazolato)$^{2-}$ | 4 × $(NEt_4)^+$ | 100 | 6.55 | 2.748 |
| **4** | MUWQUS | 0 | 0 | 2 × $Fe^{3+}$ | 2 × $S^{2-}$ | 2 × nacnac | N/A | 150 | 3.63 | 2.679 |
| **5** | MUWRED | 1/2 | 1– | $Fe^{2+}$, $Fe^{3+}$ | 2 × $S^{2-}$ | 2 × nacnac | 1 × $(NBut_4)^+$ | 150 | 2.75 | 2.689 |
| **6** | FUQYUO | 0 | 0 | 2 × $Fe^{3+}$ | $S^{2-}$, $CHSi(CH_3)_3^{2-}$ | 2 × nacnac | N/A | 93 | 3.07 | 2.603 |
| **7** | EAFESD | 0 | 2– | 2 × $Fe^{3+}$ | 2 × $S^{2-}$ | 4 × $Cl^-$ | 2 × $(NEt_4)^+$ | 295 | 3.60 | 2.714 |
| **8** | XUQVAI | 0 | 2– | 2 × $Fe^{3+}$ | 2 × $S^{2-}$ | 4 × $SH^-$ | 2 × $(Ph_3P)N_2^+$ | 100 | 4.06 | 2.695 |
| **9** | VADDEJ01 | 9/2 | 2+ | 2 × $Fe^{2.5+}$ | 3 × $OH^-$ | 2 ×tmtacn[f] | $(ClO_4)^-$ | 193 | 10.8 | 2.508 |
| **10** | LAJPAN | 2 | 2– | $Fe^{3+}$, $Mo^{5+}$ | 2 × $S^{2-}$ | $Cl_4cat^{2-}$, $O^{2-}$, 2 × $Cl^-$ | 2 × $(NEt_4)^+$ | 295 | 6.26 | 2.756 |
| **11** | EAPTFM01 | 2 | 2– | $Fe^{3+}$, $Mo^{5+}$ | 2 × $S^{2-}$ | 2 × $SPh^-$, 2 × $S^{2-}$ | 2 × $(NEt_4)^+$ | 295 | 4.9 | 2.765 |

[a]The table includes information on spin, charge, oxidation state, bridging ligands, counterions, as well as crystallographic data: crystallized counterion, X-ray diffraction temperature, *R*-factor, and metal–metal distance. [b]Total charge of the complex. [c]Local oxidation state of the Fe/Mo ions. [d]The conventional residual factor. [e]M = Fe or Mo. [f]1,4,7-Trimethyl-1,4,7-triazononane. [g]Cobaltocene is additionally present in the crystal structure.

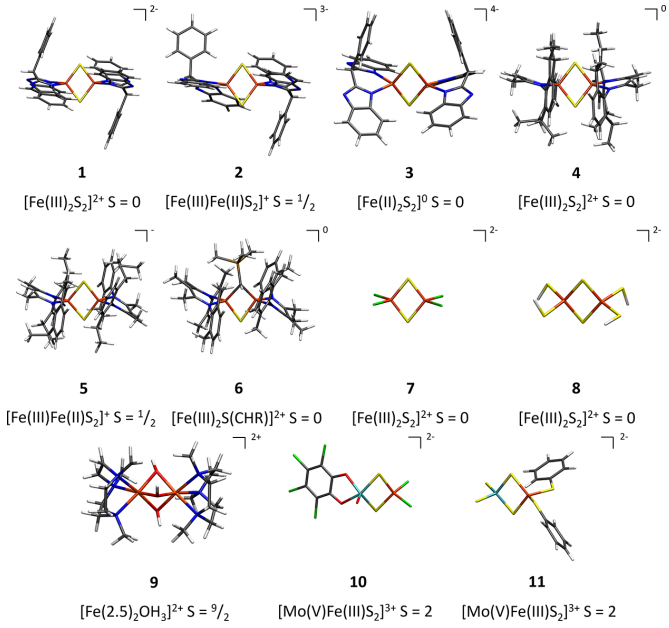


**Figure 2.** FeMoD11 test set of spin-coupled Fe–Fe and Fe–Mo dimers. The local oxidation state of each Fe ion is indicated as well as the charge of the core structure, the total spin, and the total charge of the complex.

relativistically recontracted triple-ζ def2 Ahlrichs basis set[103,104] (ZORA-def2-TZVP keyword in ORCA) was used on all atoms except for Mo, where a ZORA-recontracted all-electron Ahlrichs basis set, TZVPPAlls,[104,105] was used. The Basis Set, Relativistic, and Environmental Effects section describes calculations using other basis sets and relativistic approximations. Fine Lebedev angular integration grids were used for the exchange–correlation integrals (Grid5/Finalgrid6 keywords in ORCA), whereas for M06 and M06-2X, even tighter grids were used (Grid7 for M06 and M06-2X). The Split-RI-J approximation was used for Coulomb integrals in nonhybrid calculations, while the RIJCOSX[106,107] approximation was used for Coulomb and Exchange integrals (GridX7 grid for COSX). Calculations using the r$^2$SCAN functional were performed using ORCA version 5.0.0, using the tight grid settings (defgrid3 keyword) and using the libXC library to define the functional.[108] A decontracted Coulomb auxiliary basis set by Weigend[103] was used (SARC/J keyword) with the RIJ and RIJCOSX approximations. A polarizable continuum model (conductor-like polarizable continuum model (CPCM))[109] including a Gaussian-charge scheme was included in all DFT calculations with a scaled van der Waals surface.[110,111] We used the default vdW radii in ORCA with a 1.2 scaling factor as recommended in the implementation; this corresponds to scaled Bondi radii for the main group elements (C, N, O, P, S, and Cl), a radius of 1.32 Å for H (after scaling), and a radius of 2.4 Å (after scaling) for the heavy elements (here Fe and Mo). An infinite dielectric constant was used, as a


https://doi.org/10.1021/acs.jctc.1c00753
J. Chem. Theory Comput. 2022, 18, 1437–1457

crude mimic of a polar crystal environment and to stabilize the molecular anions that would otherwise have unbound electrons (see the Basis Set, Relativistic, and Environmental Effects section).

Antiferromagnetic broken-symmetry states of each spin-coupled dimer were located via the spin-flipping procedure implemented in ORCA. For the case of the $Fe_A(II)-Fe_B(III)$ mixed-valence compounds in this study, we calculate a single broken-symmetry state with a localized $Fe_A(II)-Fe_B(III)$ on either $Fe_A$ or $Fe_B$. As the complexes are symmetric, an isoenergetic broken-symmetry solution exists with a reversed oxidation state distribution. While these different solutions lead to distinct geometries, the Fe−Fe distance as well as the average bridging Fe−L distances are the same for both.

The FeMoco QM/MM model used here is the same as previously described,[22] but for the reader's convenience, we include the following short summary. QM/MM calculations are performed within Chemshell (version 3.7)[112,113] using ORCA (version 4.2.1 and 5.0.0) for the QM part and DL_POLY[114] for the MM part. The QM/MM model is spherical and contains 36 987 atoms with a QM region of 244 atoms (not counting link atoms terminating the QM−MM border). The QM theory level of the QM/MM calculations of FeMoco is similar to the QM calculations in this work except we use the ZORA-def2-TZVP basis set for Fe, S, Mo, and interstitial carbide, whereas ZORA-def2-SVP was used for all other atoms.

All figures of molecules presented herein are rendered using Visual Molecular Dynamics (VMD).[115]

## RESULTS AND DISCUSSION

We will first introduce the test set of spin-coupled Fe−Fe and Mo−Fe dimers (FeMoD11) along with a test set of five closed-shell dimers (FeCSD5) and discuss the experimental reference data. In the Basis Set, Relativistic, and Environmental Effects section, we discuss the effect of basis sets, scalar relativistic approximation, and the polarizable continuum on the geometry of the spin-coupled $[Fe_2S_2Cl_4]^{2-}$ (**7**) as an example. In the Density Functional Comparison of the FeMoD11 and FeCSD5 Test Sets section, we discuss the results of the functional dependence of the geometry of the complexes of FeMoD11 and FeCSD5. The Correlation between Bridging Metal−Ligand Bond Lengths and Metal−Metal Distance in FeMoD11 section analyzes the correlation between bridging ligand−metal bond length and metal−metal distance for the spin-coupled systems compared to closed-shell systems. Finally, in the Correlation between Fe−S Bond Covalency and Fe−Fe Distance section, we discuss in detail the electronic structure of a representative system (**7**) from FeMoD11 and analyze how the covalency of the bridging ligand−metal bond affects the metal−metal distance.

**FeMoD11 Test Set.** The FeMoD11 test set, defined in Table 1 and Figure 2, contains 11 spin-coupled Fe−Fe or Mo−Fe dimers. Ten of these systems feature an [M−Fe−S−R] (M = Fe, Mo and R = S, C) diamond core structure with different terminal ligands in tetrahedral coordination geometries (except for one five-coordinate Mo geometry in **10**). These dimeric complexes were chosen as their core geometries [2Fe−2S], [2Fe−S−C], and [Mo−Fe−2S] can all be found in FeMoco; hence, both their molecular structure and spin-coupled electronic structure bear some resemblance to the enzyme cofactor of Mo-nitrogenase. Additionally, we include a [2Fe-3OH] complex (**9**) with octahedral iron coordination, which is a rare example of a complex with a mixed-valence spin-delocalized $S = 9/2$ ground state[116−118] (mixed-valence delocalization being also a feature of polynuclear iron−sulfur clusters like FeMoco). Overall, the complexes feature the common Fe oxidation states that are observed for iron−sulfur systems: Fe(II) and Fe(III), with the mixed-valence complexes in the test set featuring either spin-localization (**2** and **5**) or delocalization (**9**). We note in this context the recent discovery of highly unusual mixed-valence Fe(II)−Fe(III) selenium/tellurium bridged dimers with $S = 3/2$ ground states.[119]

Our choice to focus on spin-coupled dimers rather than larger multinuclear clusters is motivated by the simpler electronic structure in dimers than in trimers or tetramers, where a single electronic state (usually the low-spin antiferromagnetic state) should generally be well separated from other states, which is not necessarily the case for multinuclear clusters where complex spin couplings including, e.g., spin-canting effects and double exchange, can lead to a highly complex spin ladder. As will be shown, the molecular and electronic structures of these simple dimer compounds are still highly relevant to the much more complex FeMoco cluster as discussed in the Density Functional Comparison of the FeMoD11 and FeCSD5 Test Sets and Correlation between Bridging Metal−Ligand Bond Lengths and Metal−Metal Distance in FeMoD11 sections.

Complexes **1**−**3**[120,121] are [2Fe−2S] systems from the Meyer group featuring the bis(benzimidazolato) ligand; this was the first set of dimers that was synthesized in all three redox states (2Fe(III), Fe(III)Fe(II), and 2Fe(II)) characterized by X-ray crystallography, Mössbauer spectroscopy, superconducting quantum interference device (SQUID), and cyclic voltammetry. The overall quality of the X-ray structures is good, with complexes **1**, **2**, and **3** having *R*-factors of 3.21, 5.72 (also 7.22), and 6.5%, respectively. Two X-ray structures are available for complex **2**, with different counterions. The structure containing both an $NEt_4^+$ counterion and cobaltocene (CSD code: UZOHIB) with $r$(Fe−Fe) = 2.686 Å was included in our test set as it has a lower *R*-factor (5.72 vs 7.22%) than the other structure with only $NEt_4^+$ counterion (CSD code: CEWTOP ($r$(Fe−Fe) = 2.727 Å)).

Complexes **4** and **5**[122] are [2Fe−2S] complexes from the Driess group, with $\beta$-diketiminato (nacnac) ligands and in two different redox states (2Fe(III) and Fe(III)Fe(II)). The X-ray structures of **4** and **5** are of high quality with *R*-factors of 3.63 and 2.75%, respectively.

Complex **6**[123] has a [2Fe−S−C] core and contains one bridging alkylidene group and one bridging sulfide (instead of two sulfides) with terminal $\beta$-diketiminato ligands on the Fe ions, with Fe(III) oxidation states and an *R*-factor of 3.07%.

Complexes **7**[124] and **8**[125] are comparatively small and without bulky ligands (complex **7** has terminal chloro ligands and complex **8** has terminal thiolate ligands). The X-ray structures are of high quality with *R*-factors of 3.6 and 4.06%, respectively. Both complexes feature the 2Fe(III) redox state.

Complex **9**[117] by Wieghardt and co-workers is different from the previously discussed complexes **1**−**8** as it contains three hydroxo bridging ligands in a [2Fe−3OH] core with octahedral Fe ions. Although not an iron−sulfur system (and lacking a diamond core), it is of interest due to being a rare case of a mixed-valence system with a ground-state spin of $S = 9/2$. The electronic structure of this complex has been thoroughly characterized[116−118] and is interpreted as containing complete delocalization of the minority-spin electron,



https://doi.org/10.1021/acs.jctc.1c00753
J. Chem. Theory Comput. 2022, 18, 1437−1457

**Table 2. FeSCD5 Test Set**[a]

| complex | CSD ID | *S* | charge[b] | Fe ox.[c] | bridging L | terminal L | counterion | temp (K) | *R* (%)[d] | Fe−Fe (Å) |
|---|---|---|---|---|---|---|---|---|---|---|
| **D1** | NOBXUA | 0 | 1+ | 2 × $Fe^{2+}$ | $H^-$, 2 × $SH^-$ | 4 × CO, 2 × $PPh_3$ | 1 × $(BAr^F{}_4)^-$ | 100 | 4.06 | 2.589 |
| **D2** | PEPSFE | 0 | 1+ | 2 × $Fe^{2+}$ | 3 × $SH^-$ | 2 × PPP[e] | $(ClO_4)^-$ | 295 | 3.63 | 3.192 |
| **D3** | FUZGAI | 0 | 0 | 2 × Fe(0) | 3 × CO | 6 × CO | N/A | 295 | 4 | 2.523 |
| **D4** | YOBSEN | 0 | 2− | 2 × $Fe^+$ | $S(CH_2NHCH_2)S^{2-}$ | 2 × $CN^-$, 4 × CO | 2 × $(NEt_4)^+$ | 293 | 2.96 | 2.509 |
| **D5** | YOBVEQ | 0 | 0 | 2 × $Fe^+$ | $S(CH_2N(Ph)CH_2)S^{2-}$ | 6 × CO | N/A | 193 | 2.39 | 2.505 |

[a]The table includes information on spin, charge, oxidation state, bridging and terminal ligands (L), counterions, as well as crystallographic data: crystallized counterion, X-ray diffraction temperature, *R*-factor, and metal−metal distance. [b]Total charge of the complex. [c]Local oxidation state of each of the Fe ions. [d]The conventional *R*-factor. [e]Bis[2-(diphenylphosphino)ethyl]phenylphosphine.

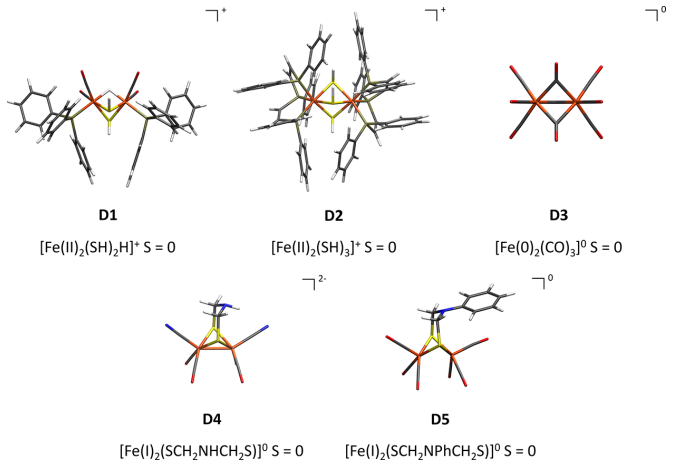


**Figure 3.** FeCSD5 test set of closed-shell Fe−Fe dimers. The local oxidation state of each Fe ion is indicated as well as the charge of the core structure, the total spin, and the total charge of the complex.

resulting in a physical oxidation state description of 2Fe(2.5). The terminal ligands are 1,4,7-trimethyl-1,4,7-triazonane (tmtacn). The X-ray structure has a relatively high *R*-factor of 10.8%. However, as extended X-ray absorption fine structure (EXAFS) measurements indicate an *r*(Fe−Fe) distance of 2.50 ± 0.01 Å, which is in good agreement with the X-ray structure (*r*(Fe−Fe) = 2.508 Å), we consider the X-ray structure nonetheless reliable (at the very least the Fe−Fe distance) and include it in our benchmarking. We note in the context of **9** that another complex from Wieghardt and co-workers with a [2Cr−3OH] core[126] and tmtacn ligands has been the subject of recent discussion in the literature. There is an ongoing debate whether the antiferromagnetism results from the direct overlap of d-orbitals or from superexchange.[127−129]

Complexes **10**[130] and **11**[131] are [MoFe−2S] systems and feature Mo−Fe interactions that resemble Mo−Fe interactions proposed in FeMoco. In both complexes, the molybdenum has been proposed to be in a Mo(V) oxidation state, while iron is in a Fe(III) oxidation state, although $^{57}$Fe Mössbauer experiments suggest complicated spin delocalization effects. While FeMoco features an unusual Mo(III) oxidation state,[9] we note that similar spin delocalization in the Mo−Fe interactions has been proposed for FeMoco. Complexes **10** and **11** have good *R* values, 6.26 and 4.9%, respectively. Complex **10** has two chloro ligands connected to iron, whereas the molybdenum is ligated to tetrachlorocatecolate and an oxo ligand. Complex **11** has two thiophenyl ligands ligated to iron, whereas the molybdenum is ligated to two sulfurs.

For comparison to the spin-coupled dimers in the FeMoD11 test set, we created another test set of five diamagnetic closed-shell complex dimers with local low-spin irons (in oxidation states Fe(II), Fe(I), and Fe(0)) and a diamagnetic ground state of *S* = 0, which we will term here FeCSD5 (Fe closed-shell dimers); see Figure 3. Complexes **D1**[132] and **D2**[133] contain both locally low-spin irons in a Fe(II) oxidation state, whereas the former contains two bridging $SH^-$ ligands and a single bridging hydride and the latter three bridging $SH^-$ ligands. **D1** has two CO and one triphenylphosphine ligands on each of its irons, whereas **D2** is terminally ligated with bis[2-(diphenylphosphino)ethyl]phenylphosphine on each of the irons. Complex **D3**[134] contains irons in a Fe(0) oxidation state and with three bridging carbonyl ligands and three-terminal carbonyl ligands on each iron. Complexes **D4**[135] and **D5**[135] are hydrogenase model complexes with irons in the 2Fe(I) oxidation state and a Fe−Fe σ-bond between the two irons. **D4** has a bridging $S(CH_2NHCH_2)S^{2-}$ ligand, four CO terminal ligands, and two extra CN terminal ligands. **D5** has $S(CH_2N(Ph)CH_2)S^{2-}$ bridging ligand and six CO terminal ligands.

The spin-coupled Fe−Fe dimers in FeMoD11 feature Fe−Fe distances that range from 2.508 to 2.748 Å. The delocalized mixed-valence compound **9** has the shortest Fe−Fe distance (2.508 Å), likely due to both the light bridging ligands (OH) and having a direct d−d interaction. Complex **6** has a short distance of 2.603 Å, due to a bridging carbon ligand in addition to the sulfide. Complexes **1**−**5** and **7**−**8** all feature the same [2Fe−2S] diamond core and the Fe−Fe distances from 2.686


https://doi.org/10.1021/acs.jctc.1c00753
J. Chem. Theory Comput. 2022, 18, 1437−1457

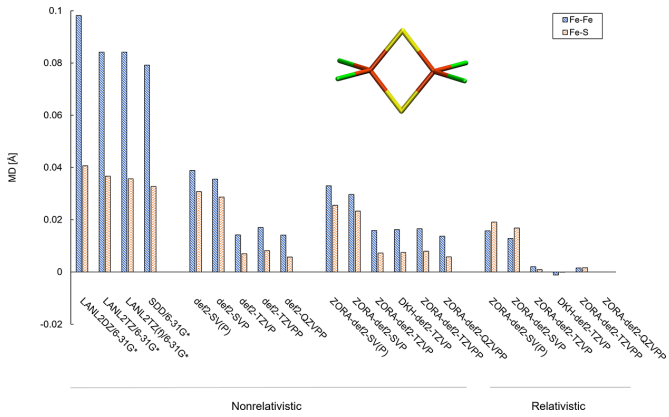


**Figure 4.** Mean deviations (MDs) of Fe−S bond lengths and Fe−Fe distance of complex **7** ($[Fe_2S_2Cl_4]^{2-}$) using ECP-basis combinations (LANL2 or SDD on Fe with 6-31G* on S and Cl) or all-electron basis sets, with and without a scalar relativistic ZORA or Douglas−Kroll−Hess (DKH) Hamiltonian. Deviations are relative to the largest all-electron relativistic ZORA-def2-QZVPP reference ($r$(Fe−Fe) = 2.690 Å and $r_{ave}$(Fe−S) = 2.202 Å). The TPSSh functional was used with a CPCM($\varepsilon = \infty$) continuum model included in all calculations.

to 2.748 Å. These distances seem to vary according to both the bulkiness of the terminal ligands and the metal oxidation states. Complexes **1**−**3** have the same ligand framework (bis-(benzimidazolato) and the Fe−Fe distance changes somewhat nonintuitively from 2.702 Å (all-ferric) via 2.686 Å (mixed-valence) to 2.748 Å (all-ferrous). We note, however, the existence of another X-ray structure for the mixed-valence compound with a 2.727 Å distance (instead of 2.686 Å). Complex **3** is the only all-ferrous complex and has the longest Fe−Fe distance. Complexes **4** and **5** also feature the same ligand framework (nacnac) with different redox states, and a small 0.01 Å increase in Fe−Fe distance is observed upon going from all-ferric to mixed-valence. The nacnac ligand in **4** and **5** is the bulkiest ligand in the test set. Comparing the all-ferric complexes (**1**, **4**, **7**, **8**), we note that **4** has the shortest Fe−Fe distance (2.679 Å) while the least bulky complex **7** has the longest (2.714 Å). This may indicate the presence of a stabilizing dispersion effect between ligands that brings the metal ions closer together. Finally, we also note that the total charge may also be a factor in these comparisons, with complex **4** being neutral, while complexes **1**, **7**, and **8** are dianionic.

To summarize, the Fe−Fe distances in these complexes seem to vary according to the nature of the bridging ligand (largest effect), oxidation state, nature of terminal ligands, and possibly due to differing counterions and total complex charge.

In comparison, the **D1**−**D5** diamagnetic complexes in FeCSD5 in Table 2 and Figure 3 feature mostly shorter Fe−Fe distances (**D1**, **D3**, **D4**, **D5**) except for **D2** with a relatively long Fe−Fe distance of 3.192 Å. The short Fe−Fe distances in **D4** and **D5** are a consequence of a formal Fe−Fe $\sigma$-bond. Complex **D3** features a rather short Fe−Fe distance of 2.523 Å and was originally proposed to feature a Fe−Fe bond, but the short Fe−Fe distance is nowadays interpreted as arising from favorable covalent bridging Fe−CO−Fe interactions.[136] Complex **D1** also features a rather short Fe−Fe distance, most likely due to the covalent bridging Fe−H−Fe bond. In comparison, complex **D2** features a very long Fe−Fe distance, apparently due to the three bridging thiol groups. The test set of **D1**−**D5** was designed to include Fe−Fe dimer complexes that lack a local high-spin electronic structure or spin coupling (no unpaired or spin-coupled electrons), in contrast to FeMoD11.

**Basis Set, Relativistic, and Environmental Effects.** Before discussing the density functional dependency for the FeMoD11 and FeCSD5 test sets, it is important to assess basis set effects as well as scalar relativistic effects that may affect such functional comparisons. The basis set dependency for iron−sulfur systems has previously been discussed by Szilagyi et al.,[74] who found that both the geometry and spin density distribution were quite sensitive to the basis set size. We study here the basis set effects on the geometry of complex **7** as representative of the [2Fe−2S] core that is present in most compounds in FeMoD11. Figure 4 shows the deviation of both the Fe−Fe distance and the average Fe−S bond lengths for various basis sets, using the TPSSh hybrid density functional. The reference values are obtained using the large relativistically recontracted ZORA-def2-QZVPP basis set[103,104] (with the ZORA scalar relativistic Hamiltonian included), which we estimate should be close to the DFT basis set limit. Overall, we find that the basis set errors are highly systematic for Fe−Fe and Fe−S distances, resulting consistently in overestimation with respect to (w.r.t.) the relativistic def2-QZVPP reference. Beginning with the ZORA relativistic results (employing the ZORA scalar relativistic Hamiltonian and the ZORA-recontracted ZORA-def2-XVP basis sets), we see that the results systematically approach the basis set limit. The basis set error is moderate for the double-$\zeta$ basis sets, ZORA-def2-SV(P) and ZORA-def2-SVP (+0.016/+0.013 Å for Fe−Fe and +0.019/+0.013 Å for Fe−S) while practically converged at the triple-$\zeta$ level, ZORA-def2-TZVP and ZORA-def2-TZVPP (+0.002/+0.002 Å for Fe−Fe and +0.001/0.001 Å for Fe−S). These results suggest that geometries of spin-coupled iron−sulfur compounds may generally be converged with a well-polarized triple-$\zeta$ basis set level.

In order to evaluate the effect of using a different scalar relativistic Hamiltonian approximation, we additionally obtained results at the second-order Douglas−Kroll−Hess (DKH) level with DKH-recontracted def2 basis sets.[104] We obtain very similar results for $r$(Fe−Fe) with the DKH-TPSSh/DKH-def2-TZVP and the ZORA-TPSSh/ZORA-def2-TZVP levels of theory, 2.689 and 2.691 Å, respectively. In the


https://doi.org/10.1021/acs.jctc.1c00753
J. Chem. Theory Comput. 2022, 18, 1437−1457

Table 3. Effect of Varying the CPCM Dielectric Constant on the Structural Parameters of 7 at the ZORA-TPSSh/ZORA-def2-TZVP Level[a]

| dielectric constant $\varepsilon$ | 1 | 4 | 10 | 20 | 40 | 80 | ∞ | X-ray |
|---|---|---|---|---|---|---|---|---|
| Fe1−Fe2 (Å) | 2.740 | 2.703 | 2.696 | 2.693 | 2.692 | 2.692 | 2.692 | 2.714 |
| Fe1−Cl1 (Å) | 2.280 | 2.262 | 2.258 | 2.257 | 2.257 | 2.256 | 2.256 | 2.244 |
| Fe1−Cl3 (Å) | 2.280 | 2.262 | 2.258 | 2.257 | 2.256 | 2.256 | 2.255 | 2.256 |
| Fe1−S1 (Å) | 2.211 | 2.205 | 2.204 | 2.203 | 2.203 | 2.203 | 2.203 | 2.201 |
| Fe1−S2 (Å) | 2.211 | 2.204 | 2.203 | 2.202 | 2.202 | 2.202 | 2.202 | 2.198 |
| Fe2−Cl2 (Å) | 2.280 | 2.262 | 2.258 | 2.257 | 2.256 | 2.256 | 2.255 | 2.244 |
| Fe2−Cl4 (Å) | 2.280 | 2.262 | 2.258 | 2.257 | 2.256 | 2.256 | 2.256 | 2.256 |
| Fe2−S1 (Å) | 2.211 | 2.204 | 2.203 | 2.202 | 2.202 | 2.202 | 2.202 | 2.198 |
| Fe2−S2 (Å) | 2.211 | 2.205 | 2.204 | 2.203 | 2.203 | 2.203 | 2.203 | 2.20 |
| average Fe−S (Å) | 2.211 | 2.205 | 2.204 | 2.203 | 2.203 | 2.203 | 2.203 | 2.199 |
| average Fe−Cl (Å) | 2.280 | 2.262 | 2.258 | 2.257 | 2.256 | 2.256 | 2.256 | 2.250 |
| no. of unbound electrons | 8 | 0 | 0 | 0 | 0 | 0 | 0 | |

[a]Also shown is the number of unbound electrons (occupied MOs with positive energies) in each calculation. Structural parameters from the X-ray structure are shown for comparison.

case of $r(\mathrm{Fe-S_{ave}})$, it is 2.203 and 2.202 Å, respectively. These results indicate that the ZORA and DKH approximations account equally well for the scalar relativistic geometric effect on this system.

Looking at the nonrelativistic results, we compare the nonrelativistic all-electron Ahlrichs def2 family[103] with respect to the ZORA/ZORA-def2-QZVPP reference. A systematic decrease in deviations with increased $\zeta$-level of the basis set is evident; however, even at the def2-QZVPP level, an error remains, suggesting that the remaining deviation (+0.014 Å for Fe−Fe and +0.006 Å for Fe−S) arises due to a relativistic effect missing in the nonrelativistic calculations. This is further evidenced by the almost identical behavior of the results employing the relativistically recontracted basis sets (ZORA-def2-XVP) but without the ZORA Hamiltonian. Comparing the nonrelativistic def2-SV(P) basis set that has, for example, been employed in FeMoco research,[137] we find that this results in a combined basis-set-error + lack-of-relativity error that amounts to +0.039 Å for Fe−Fe and +0.031 Å for Fe−S.

There are considerably larger errors associated with using common effective-core-potential/valence-basis protocols such as LANL2DZ/6-31G* or SDD/6-31G*, approximately 2 times larger error than the error from the smallest all-electron basis set (def2-SV(P)). Using the all-electron 6-31G* basis set[138,139] on S and Cl and LANL2DZ, LANL2TZ, or LANL2TZ(f) on Fe (with the associated LANL2 ECP)[140] results in relatively large basis set errors for Fe−Fe distances (0.084−0.098 Å) and Fe−S bond lengths (0.036−0.041 Å). This basis set + ECP combination can thus not be recommended for describing iron−sulfur chemistry, despite its use in mechanistic studies of the nitrogenase iron−molybdenum cofactor in recent studies.[27] Results employing the SDD ECP + basis[141,142] set on Fe and 6-31G* on S and Cl give similarly poor results as well, with errors of +0.079 Å for Fe−Fe and +0.033 Å for Fe−S. These large errors most likely arise due to the effective core potential on Fe, although this was not further investigated. We note that this agrees with previous studies that found considerable errors for 3d transition-metal complexes when ECPs were used.[71,143]

Overall, we find that the basis set effects for complex 7 are not overly large for modern all-electron basis sets (such as the Ahlrichs def2 family) and that the polarized ZORA-def2-TZVP basis set has an acceptably low basis set error. The scalar relativistic effects on the geometry (+0.016 Å for Fe−Fe and +0.007 Å for Fe−S) are small but worth accounting for, as the computational cost associated with the relativistic integrals is very small. The ZORA-def2-TZVP basis including the ZORA Hamiltonian will hence be used throughout this study. We note that the use of a valence-basis + ECP for a 4d transition metal (such as Mo) is likely more justified than for a 3d transition metal (and may account well for scalar relativistic effects); however, the use of ECPs on Mo for the Mo complexes in this work was not investigated and the all-electron ZORA approach was used throughout (using a ZORA-recontracted all-electron triple-$\zeta$ basis set; see the Computational Details section).

Complex 7 is an anion with a charge of 2−. As dianions are typically not stable in the gas phase, a conductor-like polarizable continuum model (CPCM) was used to screen the high negative charge, and this approach has been used in all calculations of the complexes in this study (whether cationic, anionic, or neutral). CPCM acts as an approximation to the polar crystal environment by describing it as a homogeneous polarizable continuum characterized by a global dielectric constant. While this continuum approach cannot account for specific crystal effects such as counterions, hydrogen bonding, intermolecular dispersion within the crystal, it should be generally preferable to calculating charged molecules in the vacuum. Table 3 shows the effect of including the CPCM model with varying dielectric constant on the structure of complex 7. A vacuum calculation ($\varepsilon$ = 1) of 7 gives eight unbound electrons (occupied molecular orbitals (MOs) with positive energies), confirming that the dianion is not stable in the gas phase, and this appears to lead to overestimated Fe−Fe and Fe−L distances compared to the crystal structure. Including the CPCM model with $\varepsilon$ = 4, however, stabilizes the unstable MOs and leads to geometric bond contractions. Further increasing the dielectric constant leads to slight geometric changes that converge at $\varepsilon$ = 10, with further negligible changes up to $\varepsilon$ = ∞. As the dielectric constant cannot easily be determined for different crystals, we chose to use CPCM($\varepsilon$ = ∞) for all DFT calculations in this work.

**Density Functional Comparison of the FeMoD11 and FeCSD5 Test Sets.** We now turn to the results of the functional comparison for both the FeMoD11 and the FeCSD5 test sets. The focus of our comparison is on the Fe−Fe/Mo−Fe distance, both because that distance turns out to be highly sensitive to the theory level and because the



https://doi.org/10.1021/acs.jctc.1c00753
J. Chem. Theory Comput. 2022, 18, 1437−1457

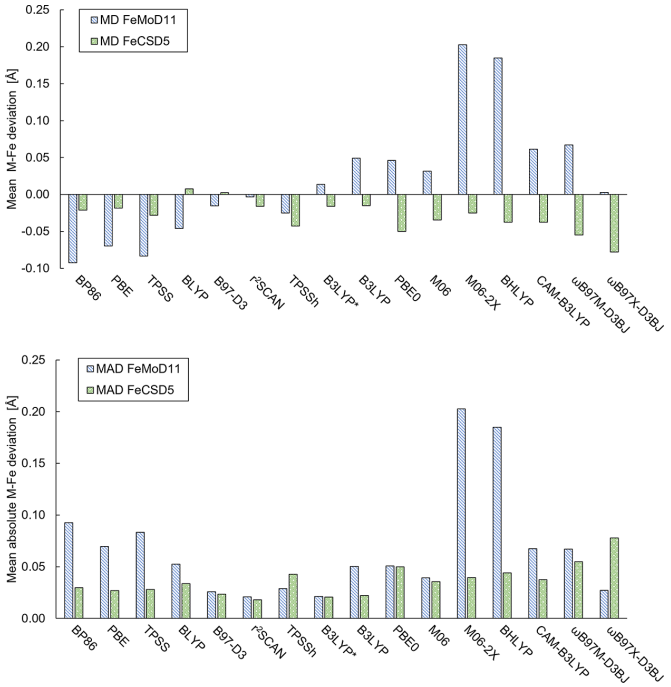


**Figure 5.** Top: mean deviation (MD) of M−Fe (M = Mo, Fe) distances for optimized structures of FeMoD11 and FeCSD5 with different functionals w.r.t. the X-ray structure distances. Bottom: the corresponding mean absolute deviation (MAD). All calculations use a ZORA scalar relativistic Hamiltonian, the relativistically recontracted ZORA-def2-TZVP basis set, a D3BJ (except D3 for M06 and M06-2X) dispersion correction, and CPCM($\varepsilon = \infty$).

positions of the heaviest atoms from an X-ray crystal structure should have lower structural uncertainties than lighter atoms.

Figure 5 shows the mean deviations (MD) and mean absolute deviations (MAD) for both the FeMoD11 and FeCSD5 test sets for all density functionals considered in our study. The first thing to note is the different functional trends for the two test sets. While all density functionals (BLYP and B97-D3 being the exceptions) systematically underestimate the Fe−Fe distance in the FeCSD5 test set (see Figure 5, top) with no clear trend between hybrid and nonhybrid functionals, there is much greater variation in the data for the FeMoD11 test set.

The data clearly shows that the spin-coupled dimers of FeMoD11 are highly sensitive to the amount of exact exchange in the functional. The common nonhybrid functionals, BP86, PBE, and TPSS underestimate the Fe−Fe/Mo−Fe distance on average, giving MDs of −0.093, −0.070, and −0.083 Å (MADs of 0.093, 0.070, and 0.083 Å), respectively. The BLYP functional also underestimates (MD/MAD = −0.046/0.053 Å), although not as much as BP86, PBE, and TPSS. On the other hand, hybrid functionals with a large amount of exact exchange (≥50%) overestimate the Fe−Fe/Mo−Fe distance considerably, with BHLYP (a hybrid generalized gradient approximation (GGA) with 50% exact exchange) and M06-2X (a hybrid meta-GGA with 54% exact exchange) yielding MDs of +0.185 and +0.203 Å (MADs of 0.185 and 0.203 Å), respectively.

TPSSh (a hybrid meta-GGA functional with 10% exact exchange) is the only hybrid functional to underestimate the average Fe−Fe/Mo−Fe distance and gives an MD of −0.023 Å (MAD 0.029 Å). B3LYP* (a hybrid GGA functional with 15% exact exchange, proposed by Reiher and co-workers[87,88]) also yields good Fe−Fe/Mo−Fe distances on average, with MD = +0.014 Å (MAD 0.021 Å) while slightly overestimating the Fe−Fe/Mo−Fe distance. The functionals with 20−28% exact exchange: B3LYP (a hybrid GGA with 20% exact exchange), PBE0 (hybrid GGA with 25% exact exchange), and M06 (a hybrid GGA with 26% exact exchange) give overall similar structures, overestimating the Fe−Fe distance in general and giving MD values of 0.049, 0.046, and 0.032 Å (MAD = 0.050, 0.051, and 0.039 Å), respectively.

The range-separated hybrid functionals, i.e., CAM-B3LYP, ωB97M-D3BJ, and ωB97X-D3BJ, appear not to offer clear advantages over the regular hybrid functionals. For Fe−Fe/Mo−Fe distances, CAM-B3LYP gives worse deviations for both spin-coupled (and diamagnetic complexes) than its parent B3LYP functional with MD = +0.061 Å (MAD 0.067 Å) and the recent ωB97M-D3BJ functional (found to be highly accurate for main group thermochemistry)[94,144] offers no improvement either, with MD of +0.067 Å (MAD = 0.067 Å). The ωB97X-D3BJ functional, however, appears much more promising for treating the spin-coupled systems, with MD = +0.003 Å and MAD = 0.027 Å.

Interestingly, the nonhybrid functionals r$^2$SCAN and B97-D3 break the trend of systematic strong underestimation of the Fe−Fe/Mo−Fe distances with nonhybrid functionals for FeMoD11, being much closer to a mean deviation of 0 and give in fact among the best results for FeMoD11 (along with


https://doi.org/10.1021/acs.jctc.1c00753
J. Chem. Theory Comput. 2022, 18, 1437−1457

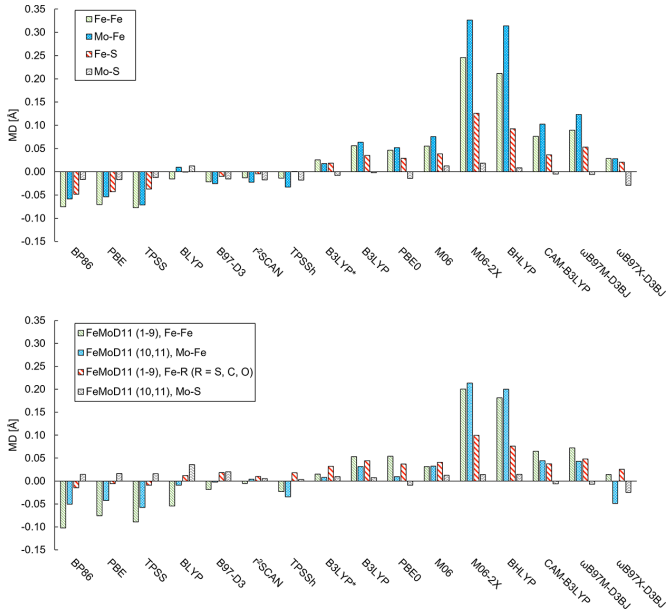


**Figure 6.** Top: mean deviations of Fe−Fe, Mo−Fe, Fe−S, and Mo−S distances from 244 QM-atom QM/MM calculations (deviations relative to the 1.0 Å crystal structure, PDB ID: 3U7Q[2]). Bottom: mean deviations of the Fe−Fe, Mo−Fe, Fe−S, and Mo−S distances in the FeMoD11 test set relative to each respective crystal structure. A plot of the corresponding mean absolute deviations is available in the Supporting Information (SI) as Figure S1.

B3LYP*), according to the mean absolute deviations (MADs of 0.021 and 0.026 Å), respectively. This shows that in addition to the exact exchange component, the exchange and correlation functional components clearly play also a major role in describing these systems.

Within the FeMoD11 test set, there is some variance seen in the behavior of the functionals between the Fe−Fe dimers and Mo−Fe dimers (see Figure S7). PBE0 is considerably better for the Mo−Fe systems than for the Fe−Fe systems, with an MD of +0.010 Å (MAD 0.010 Å) for FeMoD11(**10**,**11**) in comparison to an MD of +0.050 Å (MAD 0.055 Å) for the Fe−Fe systems FeMoD11(**1**−**9**). In contrast, the ωB97X-D3BJ functional yields worse geometries for the Mo−Fe systems than for the Fe−Fe systems, where for the FeMoD11-(**10**,**11**) the functional yields optimized geometries with an MD of −0.049 Å (MAD 0.049 Å) in comparison to the Fe−Fe dimers of FeMoD11(**1**−**9**) with an MD of +0.014 Å (MAD 0.022 Å). Additionally, the nonhybrid functionals, BLYP and B97-D3, do not underestimate the metal−metal distance as much for the Mo−Fe dimers (FeMoD11(**10**,**11**)) with an MD of −0.009 and −0.002 Å (MAD = 0.009 and 0.013 Å), respectively, in comparison to the Fe−Fe dimers (FeMoD11-(**1**−**9**)), where BLYP and B97-D3 underestimate the Fe−Fe distance (not as much as BP86, PBE, and TPSS) with an MD of −0.054 and −0.018 Å (MAD = 0.062 and 0.029 Å) respectively.

In contrast to the FeMoD11 test set, almost all functionals underestimate on average the Fe−Fe distance of the closed-shell complexes in the FeCSD5 test set (BLYP and B97-D3 being curious exceptions), and there is no clear trend observed with an increase in exact exchange with hybrid functionals. The FeMoD11 test set thus clearly features complexes with a more sensitive electronic structure that results in a stronger variation of the resulting molecular geometries. Interestingly though, the range-separated hybrid ωB97X-D3BJ functional, which performed well for the FeMoD11 test set (third lowest MAD), yields the worst geometries of all functionals tested for the FeCSD5 set, with an MD of −0.078 Å (MAD 0.078 Å). All other functionals have MAD values from 0.018 to 0.055 Å. The best performing functional for FeCSD5 is r²SCAN with MAD = 0.018 Å.

The systematic underestimation of Fe−Fe/Mo−Fe distances by nonhybrid functionals BP86, PBE, and TPSS and overestimation of hybrid functionals such as B3LYP and M06-2X for the FeMoD11 test set of spin-coupled Fe−Fe and Fe−Mo dimers are not entirely surprising compared to our previous work on FeMoco of nitrogenase.[29] In that work, density functionals were assessed on their ability to describe the resting-state geometry of the multimetal spin-coupled FeMoco at the QM/MM level by comparison to the high-resolution 1.0 Å X-ray crystal structure.[2] Figure 6 compares the mean deviations for Fe−Fe and Mo−Fe distances in FeMoco (calculated using a QM/MM model) to the analogous distances in the FeMoD11 test set with the same functionals. Despite some differences in the magnitudes of the errors for the FeMoD11 set compared to FeMoco, we clearly see the same trend of the errors for different functional classes, strongly implying that the errors are related to each other (most likely due to a related electronic structure as will be discussed). The data shows that Fe−Fe and Mo−Fe distances are underestimated with the nonhybrid functionals BP86, PBE, and TPSS (while r²SCAN, BLYP, and B97-D3 have MDs closer to zero), for both the FeMoD11 test set and FeMoco while they tend to be overestimated for global hybrid


https://doi.org/10.1021/acs.jctc.1c00753
J. Chem. Theory Comput. 2022, 18, 1437−1457

Table 4. Mean Deviations (MD), Mean Absolute Deviations (MAD), Root-Mean-Square Deviations (RMSD)[a] and Max Deviations (MAX) in Å for Metal−Metal and Metal-Ligand Distances of FeMoD11, FeCSD5, and FeMoco[bcdf]

| | BP86 | PBE | TPSS | B97-D3 | BLYP | r$^2$SCAN | TPSSh | B3LYP* | B3LYP | PBE0 | M06 | M06-2X | BHLYP | CAM-B3LYP | ωB97M-D3BJ | ωB97X-D3BJ |
|---|---|---|---|---|---|---|---|---|---|---|---|---|---|---|---|---|
| FeMoD11 | | | | | | | | | | | | | | | | |
| RMSD[a] | 0.067 | 0.045 | 0.049 | 0.035 | 0.043 | 0.029 | 0.036 | 0.038 | 0.045 | 0.043 | 0.078 | 0.108 | 0.085 | 0.049 | 0.051 | 0.040 |
| MD M−Fe[b] | −0.093 | −0.070 | −0.083 | −0.015 | −0.046 | −0.003 | −0.025 | 0.014 | 0.049 | 0.046 | 0.032 | 0.203 | 0.185 | 0.061 | 0.067 | 0.003 |
| MAD M−Fe[b] | 0.093 | 0.070 | 0.083 | 0.026 | 0.053 | 0.021 | 0.029 | 0.021 | 0.050 | 0.051 | 0.039 | 0.203 | 0.185 | 0.067 | 0.067 | 0.027 |
| MaxD[f] M−Fe[b] | −0.164[2] | −0.119[3] | −0.130[3] | −0.069[1] | −0.103[1] | 0.049[4] | −0.060[1] | 0.084[4] | 0.138[5] | 0.140[5] | 0.122[5] | 0.240[5] | 0.273[5] | 0.176[5] | 0.116[4] | 0.059[4] |
| MD M−R[c] | −0.013 | −0.005 | −0.008 | 0.017 | 0.013 | 0.009 | 0.015 | 0.029 | 0.040 | 0.031 | 0.037 | 0.094 | 0.071 | 0.033 | 0.044 | 0.019 |
| MAD M−R[c] | 0.042 | 0.035 | 0.034 | 0.025 | 0.030 | 0.021 | 0.024 | 0.033 | 0.043 | 0.037 | 0.039 | 0.097 | 0.076 | 0.039 | 0.049 | 0.031 |
| MaxD M−R[c] | 0.134[9] | 0.137[9] | 0.126[9] | 0.135[9] | 0.165[9] | 0.120[9] | 0.116[9] | 0.125[9] | 0.154[5] | 0.137[5] | 0.158[5] | 0.250[9] | 0.229[9] | 0.165[5] | 0.216[9] | 0.155[9] |
| FeCSD5 | | | | | | | | | | | | | | | | |
| RMSD[a] | 0.019 | 0.019 | 0.020 | 0.020 | 0.025 | 0.021 | 0.024 | 0.023 | 0.027 | 0.026 | 0.029 | 0.080 | 0.054 | 0.028 | 0.036 | 0.036 |
| MD Fe−Fe | −0.021 | −0.019 | −0.028 | 0.002 | 0.008 | −0.016 | −0.043 | −0.016 | −0.015 | −0.050 | −0.034 | −0.025 | −0.037 | −0.037 | −0.055 | −0.078 |
| MAD Fe−Fe | 0.030 | 0.027 | 0.028 | 0.023 | 0.034 | 0.018 | 0.043 | 0.021 | 0.022 | 0.050 | 0.036 | 0.039 | 0.044 | 0.037 | 0.055 | 0.078 |
| MaxD[f] Fe−Fe | −0.093[D2] | −0.055[D2] | −0.086[D2] | −0.042[D2] | 0.047[D4] | −0.041[D3] | −0.098[D2] | −0.067[D2] | −0.061[D2] | −0.092[D2] | −0.073[D2] | −0.088[D2] | −0.073[D2] | −0.061[D2] | −0.088[D2] | −0.123[D2] |
| MD Fe−R[d] | −0.010 | −0.010 | −0.009 | 0.008 | 0.020 | −0.008 | −0.014 | 0.007 | 0.013 | −0.020 | 0.003 | 0.069 | 0.036 | −0.001 | −0.001 | −0.028 |
| MAD Fe−R[d] | 0.016 | 0.013 | 0.013 | 0.017 | 0.022 | 0.015 | 0.015 | 0.017 | 0.021 | 0.021 | 0.020 | 0.079 | 0.050 | 0.019 | 0.021 | 0.028 |
| MaxD[f] Fe−R[d] | −0.043[D2] | −0.038[D2] | −0.037[D2] | −0.031[D2] | 0.050[D1] | −0.032[D5] | −0.038[D2] | 0.031[D2] | 0.042[D2] | −0.043[D3] | −0.037[D2] | 0.125[D4] | 0.082[D2] | −0.038[D3] | −0.044[D3] | −0.053[D3] |
| FeMoco | | | | | | | | | | | | | | | | |
| RMSD[a] | 0.088 | 0.079 | 0.079 | 0.046 | 0.048 | 0.040 | 0.042 | 0.050 | 0.071 | 0.068 | 0.076 | 0.241 | 0.212 | 0.085 | 0.107 | 0.062 |
| MD M−Fe[b] | −0.072 | −0.067 | −0.076 | −0.022 | −0.010 | −0.015 | −0.018 | 0.024 | 0.058 | 0.048 | 0.059 | 0.262 | 0.232 | 0.081 | 0.096 | 0.028 |
| MAD M−Fe[b] | 0.072 | 0.067 | 0.076 | 0.024 | 0.024 | 0.017 | 0.020 | 0.026 | 0.058 | 0.048 | 0.059 | 0.262 | 0.232 | 0.081 | 0.096 | 0.028 |
| MaxD M−Fe[b] | −0.114 | −0.110 | −0.118 | −0.045 | 0.062 | −0.044 | −0.059 | 0.048 | 0.088 | 0.083 | 0.099 | 0.401 | 0.375 | 0.143 | 0.165 | 0.069 |
| MD M−Re | −0.046 | −0.042 | −0.038 | −0.012 | −0.002 | −0.007 | −0.003 | 0.016 | 0.032 | 0.025 | 0.037 | 0.124 | 0.093 | 0.037 | 0.049 | 0.015 |
| MAD M−R[e] | 0.046 | 0.042 | 0.038 | 0.017 | 0.015 | 0.014 | 0.014 | 0.022 | 0.036 | 0.031 | 0.038 | 0.128 | 0.099 | 0.044 | 0.054 | 0.028 |
| MaxD M−R[e] | −0.099 | −0.093 | −0.082 | −0.047 | −0.054 | −0.040 | −0.035 | 0.056 | 0.096 | 0.087 | 0.087 | 0.383 | 0.337 | 0.128 | 0.175 | 0.085 |

[a]Root-mean-square deviations (RMSD) of the diamond core of the dimers (or the metal and bridging atoms in the case of **9** and the FeCSD5 complexes) and the [MoFe$_7$S$_9$C] core of FeMoco. [b]M = [Mo, Fe]. [c]M = [Mo, Fe] and R = [S, C, O]. [d]R = [S, C]. [e]M = [Mo, Fe] and R = [S, C]. [f]The label above the values in the MaxDev rows is the label of the complex that has the largest deviation for the given functional (FeMoD11 or FeCSD5).



https://doi.org/10.1021/acs.jctc.1c00753
J. Chem. Theory Comput. 2022, 18, 1437−1457

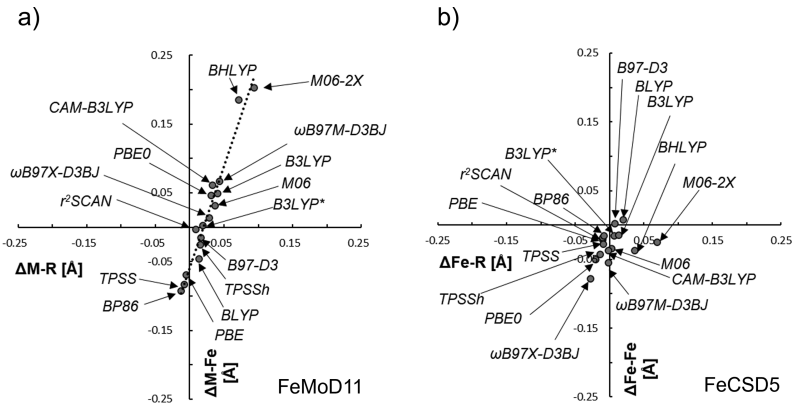


**Figure 7.** Deviation (Å) in the metal−metal distance, ΔM−Fe, vs the mean deviation in the metal−bridging ligand bond length, ΔM−R, for (a) FeMoD11 and for (b) FeCSD5. For (a), M = Fe, Mo and R = C, O, S, whereas for (b), R = C, S. Linear fit parameters for (a) are $y = 2.955x - 0.0585$ with $R^2 = 0.958$.

functionals and range-separated hybrid functionals. Overall, the trends in density functional errors for the FeMoD11 test set correlate well with the behavior to describe the Fe−Fe/Mo−Fe distances in FeMoco: functionals with low MAD values for FeMoD11 give low MAD values for FeMoco (BLYP being an exception).

The nonhybrid functionals that underestimate Fe−Fe/Mo−Fe distances in FeMoD11 (BP86, PBE, TPSS) do the same for FeMoco, while functionals with >20% exact exchange overestimate the distances (dramatically so if >50% exact exchange) for both FeMoD11 and FeMoco. The range-separated hybrids do not offer clear improvements (though ωB97X-D3BJ appears more promising).

Table 4 compares the overall functional statistics for FeMoD11, FeCSD5, and the FeMoco geometry. The best performing functionals for the M−M distances of the FeMoD11 test set (based on MAD values) are r$^2$SCAN (0.021 Å), B3LYP* (0.021 Å), B97-D3 (0.026 Å), ωB97X-D3BJ (0.027 Å), and TPSSh (0.029 Å). For the FeCSD5 set, the best functionals according to MAD values are r$^2$SCAN (0.018 Å), B3LYP* (0.021 Å), B3LYP (0.022 Å), and B97-D3 (0.023 Å). For the FeMoco system, the best performing functionals are r$^2$SCAN (0.017 Å), TPSSh (0.020 Å), B97-D3 (0.024 Å), BLYP (0.024 Å), B3LYP* (0.026 Å), and ωB97X-D3BJ (0.028 Å).

Our focus in this section has been to compare structural parameters for spin-coupled iron−sulfur systems related to FeMoco (with less weight given to the smaller FeCSD5 test set). Based on these results, the functionals that give the best error statistics for FeMoD11 as well as for FeMoco itself based on mean absolute deviations of M−M distances are r$^2$SCAN, TPSSh, B97-D3, B3LYP*, and ωB97X-D3BJ. We note that a comparison based on max M−M deviations as well as metal−ligand distance deviations are also in favor of these functionals. The ωB97X-D3BJ functional, however, shows such poor performance for the closed-shell complexes in FeCSD5 (MAD of 0.078 Å) that its use cannot be fully recommended. As ωB97X-D3BJ is one of only two functionals tested that exhibits the correct long-range behavior (100% self-interaction free in the long-range) and the relatively low errors for FeMoD11 and FeMoco, exploration of a modified form of ωB97X-D3BJ or other range-separated hybrids may be worthy of further future investigations.

Among the functionals r$^2$SCAN, TPSSh, B97-D3, and B3LYP*, we hesitate to further distinguish between them at this stage, though it is noteworthy that r$^2$SCAN is the best performing functional for all three test sets in Table 4. The r$^2$SCAN functional[97] is a revised version of the original SCAN functional,[145] a meta-GGA functional designed to satisfy more exact Kohn−Sham DFT constraints than other functionals. The balanced performance of the functional seen in our comparison (and the lack of expensive exact exchange) and in previous comparisons of both main group and transition-metal test sets[97,146,147] suggests it as a suitable functional for treating iron−sulfur chemistry and perhaps a balanced description of both transition metal and main group chemistry in general. It seems especially suitable for large metal clusters like FeMoco, where evaluating exact exchange becomes an expensive component of the calculation.

Finally, we note that the M−M distance in FeMoD11 and FeCSD5 may not only be sensitive to the local electronic structure but also to crystal packing effects that may depend both on complex total charges and bulkiness of the ligands. The magnitude of such environmental effects for these molecular crystals will be assessed in future work. Clearly, however, our results strongly imply that the molecular structure of spin-coupled iron−sulfur complexes and clusters favors specific functionals that incorporate either zero or a small amount of exact exchange (0−15%) with considerably worse results seen for functionals with >20% exact exchange.

**Correlation between Bridging Metal−Ligand Bond Lengths and Metal−Metal Distance in FeMoD11.** As demonstrated in the previous section, the Fe−Fe/Mo−Fe distances in the FeMoD11 test set are clearly highly sensitive to the exact exchange in the functional (although also to the specific exchange and correlation functionals) with a clear trend with increased exact exchange (going from the underestimation of M−Fe distances to overestimation), while no such trend can be found for the closed-shell test set.

The reason for this different behavior between spin-coupled and closed-shell compounds might be rationalized by recognizing the role that the bridging ligand is known to play in the interactions between open-shell metal ions


https://doi.org/10.1021/acs.jctc.1c00753
J. Chem. Theory Comput. 2022, 18, 1437−1457

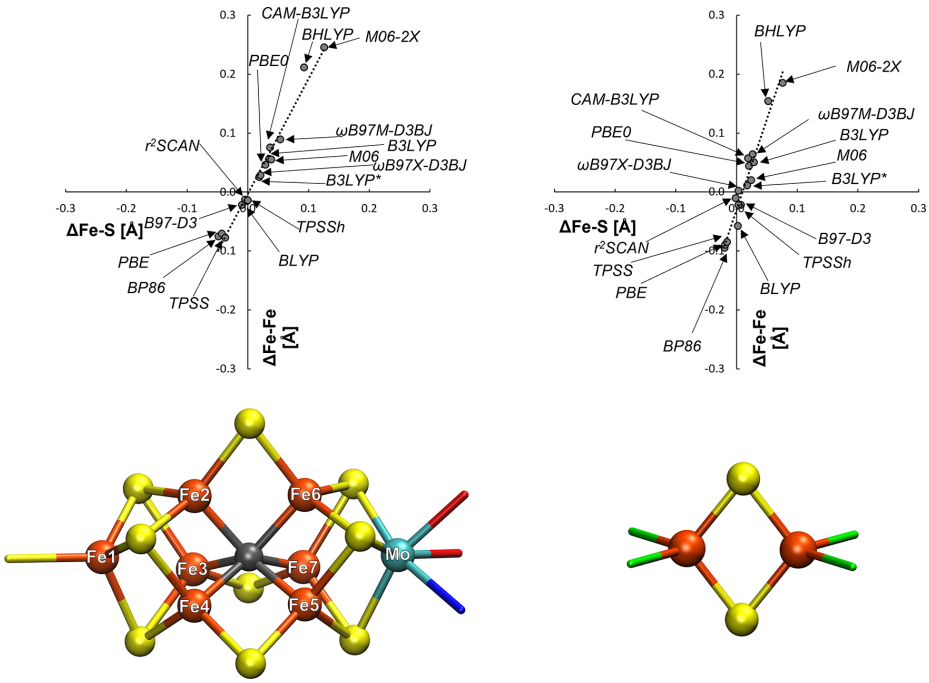


**Figure 8.** Mean deviation in the Fe−Fe distance (ΔFe−Fe) vs mean Fe−S distance (ΔFe−S) of optimized structures in comparison to the X-ray structures (for FeMoco, PDB: 3U7Q, and for **7**, CSD: EAPFTM01) with the functionals tested. Linear fit parameters $y = 1.954x - 0.003$, $R^2 = 0.977$ (FeMoco) and $y = 3.085x - 0.0301$, $R^2 = 0.9509$ (for complex **7**). FeMoco data come from a 244 QM atom QM/MM model (see the Computational Details section).

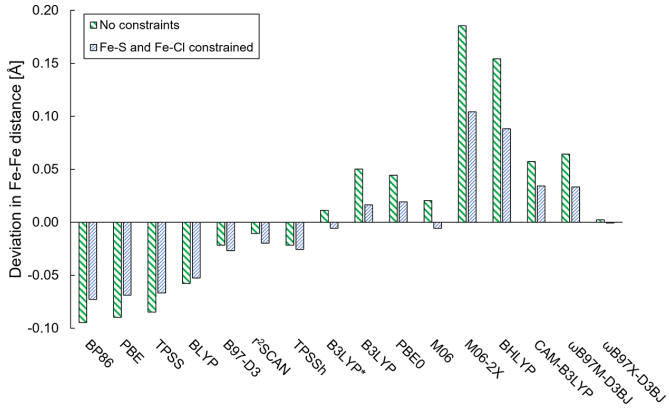


**Figure 9.** Effect of constraining Fe−S/Fe−Cl distances at the X-ray distances, $r$(Fe−S) = 2.201 and 2.198 Å, whereas $r$(Fe−Cl) = 2.244 and 2.256 Å) on the Fe−Fe distance for $[Fe_2S_2Cl_4]^{2-}$ complex **7** with different functionals.

(superexchange and metal−ligand spin polarization) in exchange-coupled dimers.[59] Figure 7 shows the correlation between the deviation of the Fe−Fe/Mo−Fe distance and the deviation for the bridging M−R distances (where R is the bridging ligand atom) for different functionals. The figure is grouped into the spin-coupled M−Fe dimers of FeMoD11 (Figure 7a) and the closed-shell Fe−Fe dimers of FeCSD5 (Figure 7b).

There is an obvious correlation seen for the spin-coupled Fe−Fe and Mo−Fe dimers, suggesting that the errors in Fe−R/Mo−R distances are linked to the errors for the Fe−Fe/Mo−Fe distance. The only exception to this trend is for complex **9** that does not feature a diamond core but instead features three bridging hydroxo groups (see Figure S2 in the SI). Complex **9** is furthermore the only mixed-valence delocalized $S = 9/2$ complex, featuring ferromagnetic coupling (due to double exchange) instead of the antiferromagnetic


https://doi.org/10.1021/acs.jctc.1c00753
J. Chem. Theory Comput. 2022, 18, 1437−1457

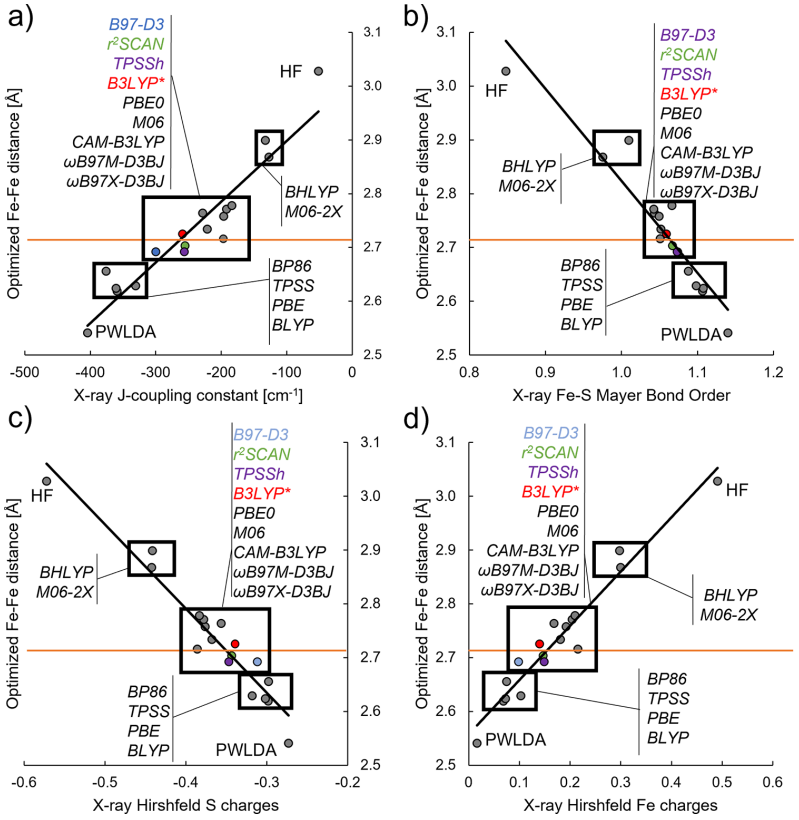


**Figure 10.** Correlation plots of the optimized Fe−Fe distance ($y$-axis) of **7** vs various parameters evaluated on the X-ray structure ($x$-axis): $J$-coupling, Fe−S Mayer bond order, Hirshfeld S charge, or Hirshfeld Fe charge. (a) $J$-coupling constant evaluated in $cm^{-1}$ according to the Yamaguchi equation,[55,56] (b) the calculated Fe−S Mayer bond order, (c) average Hirshfeld charge on sulfides, and (d) average Hirshfeld charge on Fe. The red line indicates the X-ray Fe−Fe distance. Certain functionals are color-coded (the gray dot which the orange line crosses is $\omega$B97X-D3BJ). Values are tabulated in Table S1.

coupling (typically due to superexchange), and would thus be expected to depend more on direct d-orbital overlap between Fe ions rather than via the ligand-based superexchange mechanism. In sharp contrast, the data for the closed-shell complexes in Figure 7b show no visible trend.

Additionally, a highly similar correlation between bridging Fe−S bond length mean errors and Fe−Fe distance mean errors can be seen for FeMoco (Figure 8, left), and this can be compared to the errors for the simplest iron−sulfur dimer in the FeMoD11 test set, complex **7** (Figure 8 right), an Fe(III)−Fe(III) $[Fe_2S_2Cl_4]^{2-}$ complex.

In our opinion, these correlations arise due to one of two possibilities. The first one is that the spin-coupled electronic structure in the FeMoD11 test set is the reason for these trends (implicating bridging ligand-based superexchange). The second is the correlation being related to the specific geometry of the diamond core of the dimers in FeMoD11, i.e., the bridging M−L distances enforcing a specific Fe−Fe distance (a more direct causal relationship). To clarify this, we carried out constrained geometry optimizations for complex **7** (Figure 8) as a representative of the FeMoD11 test set. By constraining the bridging Fe−S bonds as well as the terminal Fe−Cl bonds to the X-ray structure values ($r$(Fe−S) ≈ 2.20 Å, whereas $r$(Fe−Cl) ≈ 2.25 Å) and optimizing the geometry, we obtain the plot in Figure 9 that shows the $r$(Fe−Fe) distance deviations vs functional for both unconstrained and constrained optimizations. The data for unconstrained and constrained optimizations look overall highly similar, with functionals like BP86, PBE, and TPSS underestimating the Fe−Fe distances by a similar amount whether the Fe−S/Fe−Cl bonds are constrained or not. Meanwhile, the hybrid functionals like M06-2X and BHLYP give strongly overestimated distances even when the Fe−S/Fe−Cl bonds are constrained. Overall, these results suggest that the reason for the trends in Fe−Fe distances of the FeMoD11 test set and the correlation with bridging ligand bond lengths cannot primarily be rooted in a geometric effect of the diamond core (otherwise, the Fe−Fe distance would be predicted to be the same for all functionals when the Fe−S bond is constrained) but instead must arise due to some hidden variables, likely the underlying electronic structure. We note though that the plot also reveals more complex behavior for some of the functionals (the hybrid functionals in particular), where constraining the Fe−S/Fe−Cl bonds to the X-ray distance leads to much smaller Fe−Fe distance deviations than without constraints. There is hence also a geometric effect present involving the


https://doi.org/10.1021/acs.jctc.1c00753
J. Chem. Theory Comput. 2022, 18, 1437−1457

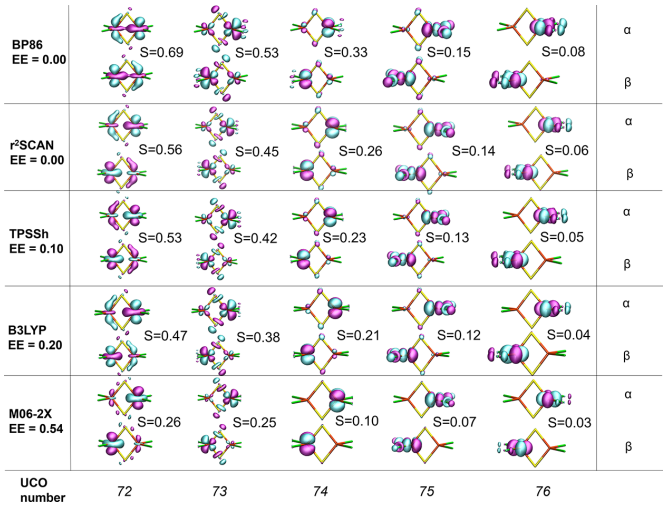


**Figure 11.** Unrestricted corresponding orbitals (UCOs) of **7**. The UCOs are derived from single-point calculations with each respective functional on the X-ray crystal structure geometry. *S* indicates the overlap between the $\alpha$ and $\beta$ orbitals. A contour value of 0.05 was used for the orbital isosurfaces.

diamond core in the calculations, in addition to the electronic structure effect that appears to be responsible for the main method dependency of the results.

The electronic structure effect that should be at play here can be rationalized via a superexchange mechanism that is typically dominant in spin-coupled Fe−S dimers,[59,117] where spin centers interact via spin polarization of the bridging ligand orbitals. The superexchange interaction arises due to the covalency of the metal−ligand bonds, which are known to be quite dependent on the exact exchange in the functional, which in turn should affect metal−ligand distances. More covalent metal−ligand bonds would thus be expected to give a stronger superexchange interaction, which should bring the metal ions closer to each other. This is particularly noticeable for the TPSS and BP86 data in Figures 7a and 8, where the shortest Fe−R ligand bonds are present and in turn give the shortest Fe−Fe distances.

**Correlation between Fe−S Bond Covalency and Fe−Fe Distance.** The correlations in the previous section imply that the treatment of the bridging ligand−metal bond (Fe−S bond in most of the complexes) is important for an overall accurate treatment of the metal−metal interaction. To gain more insight into this correlation, we have analyzed the electronic structure of complex **7** in detail. This structurally simple 2Fe(III) complex features an antiferromagnetically coupled $S = 0$ ground state (described by an $M_S = 0$ determinant with BS-DFT), and the deviations found for different functionals correlate overall quite well for the deviations for the whole test set and even to FeMoco (compare Figures 7 and 8), with BP86 and TPSS underestimating the Fe−Fe distance by 0.08−0.09 Å, r$^2$SCAN ($\Delta$ = −0.01 Å), TPSSh ($\Delta$ = −0.02 Å), B3LYP* ($\Delta$ = +0.015 Å) and $\omega$B97X-D3BJ ($\Delta$ = +0.002 Å) showing smaller deviations and other functionals overestimating the Fe−Fe distance from +0.02 Å (M06) to +0.18 Å (M06-2X). The Fe−Fe distance is highly sensitive to the total spin and thus the nature of the coupling, and we note that if the ferromagnetic $M_S = 5$ state is calculated instead, the distance increases to 2.95 Å at the TPSSh level, in sharp contrast to the 2.70 Å using the antiferromagnetic $M_S = 0$ broken-symmetry state. This both demonstrates that the use of a ferromagnetic state (featuring less spin contamination but the wrong spin state) in geometry optimizations is not a useful approach for iron−sulfur systems and also that the Fe−Fe distance trends discussed must be primarily related to the electronic structure and the specific nature of the spin-coupling.

The Fe−Fe distance for **7** calculated with different functionals correlates well with the calculated exchange coupling constant *J* (Figure 10a) when calculated via the Yamaguchi equation[55,56] via single-point energy evaluation on the X-ray structure. As previously mentioned, the Fe−Fe distance also correlates with the average Fe−S distance errors in the [$Fe_2S_2$] core (see Figure 8). Suspecting Fe−S bond covalency to be the underlying cause behind these correlations, we calculated simple electronic structure parameters with an obvious connection to metal−ligand bond covalency: Hirshfeld charges and Mayer bond orders. Importantly, the Hirshfeld charges and Mayer bond order were evaluated on the X-ray geometry of the complex with each functional rather than an optimized structure. Plotting the calculated Hirshfeld S atomic charge against the optimized Fe−Fe distance for each functional (Figure 10c) results (Figure 10d) in an inverse correlation (more negative S-charge, longer Fe−Fe distance) while the Hirshfeld Fe atomic charge gives a regular correlation (more positive Fe charge, longer Fe−Fe distance). An even better correlation is observed when the Fe−S Mayer bond order is plotted against the Fe−Fe distance (Figure 10b). Adding the local density functional, PWLDA, as well as the HF method to the correlation plots in Figure 10 shows that these correlations hold, even for methods that strongly favor delocalization (PWLDA) or localization (HF). These correlations clearly suggest the covalency of the Fe−S bond to be responsible for the functional dependency of the Fe−Fe distance as the S/Fe atomic charge or Fe−S Mayer bond order changes appreciably when evaluated with each functional (or HF) on the same X-ray structure geometry. Different degree of


https://doi.org/10.1021/acs.jctc.1c00753
J. Chem. Theory Comput. 2022, 18, 1437−1457

covalency of the bridging Fe−S bond would thus result in different magnitude of the superexchange interaction between Fe ions, leading to a different Fe−Fe distance.

A different insight into the superexchange mechanism can be obtained via the corresponding orbital transformation of the broken-symmetry calculation. This offers a convenient valence-bond like the description of the broken-symmetry determinant and leads to a clear distinction of the orbitals of the system into doubly-occupied $\alpha-\beta$ orbital pairs (overlap close to unity), nonorthogonal spin-coupled orbital pairs (overlap <1 and >0), and unpaired uncoupled $\alpha$ orbitals (overlap close to zero). Figure 11 shows isosurfaces of selected corresponding orbitals (having overlap between 0 and 1) of **7**, calculated on the X-ray geometry with five different density functionals. The overlap values for all functionals in this study are present in Table 5.

**Table 5. Overlaps of the Five Unrestricted Corresponding Orbital Pairs with 3d Character (See Figure 11), Evaluated on the X-ray Geometry with Different Functionals**

| | overlap | | | | |
|---|---|---|---|---|---|
| functional | UCO 72 | UCO 73 | UCO 74 | UCO 75 | UCO 76 |
| PWLDA | 0.73 | 0.58 | 0.39 | 0.18 | 0.09 |
| BP86 | 0.69 | 0.54 | 0.35 | 0.17 | 0.08 |
| PBE | 0.69 | 0.54 | 0.35 | 0.16 | 0.07 |
| TPSS | 0.66 | 0.52 | 0.32 | 0.16 | 0.06 |
| BLYP | 0.71 | 0.56 | 0.38 | 0.16 | 0.07 |
| B97-D3 | 0.61 | 0.48 | 0.31 | 0.15 | 0.07 |
| r$^2$SCAN | 0.56 | 0.45 | 0.26 | 0.14 | 0.06 |
| TPSSh | 0.53 | 0.42 | 0.24 | 0.14 | 0.05 |
| B3LYP* | 0.52 | 0.41 | 0.24 | 0.14 | 0.05 |
| B3LYP | 0.47 | 0.38 | 0.21 | 0.12 | 0.04 |
| PBE0 | 0.41 | 0.34 | 0.18 | 0.11 | 0.04 |
| M06 | 0.42 | 0.34 | 0.20 | 0.12 | 0.04 |
| M06-2X | 0.26 | 0.25 | 0.11 | 0.08 | 0.03 |
| BHLYP | 0.27 | 0.25 | 0.11 | 0.08 | 0.02 |
| CAM-B3LYP | 0.40 | 0.34 | 0.18 | 0.11 | 0.03 |
| $\omega$B97M-D3BJ | 0.38 | 0.32 | 0.16 | 0.10 | 0.03 |
| $\omega$B97X-D3BJ | 0.41 | 0.33 | 0.17 | 0.10 | 0.03 |
| HF | 0.12 | 0.11 | 0.05 | 0.03 | 0.01 |

These magnetic orbitals correspond well to the Fe 3d-orbitals of the system, while clearly showing the contribution of bridging sulfide character that is responsible for the superexchange interaction. While the orbitals remain qualitative similar for all five functionals, there is a considerable difference in the overlap itself as well as the bridging sulfide contribution to all unrestricted corresponding orbitals (UCOs); the differing amount of exact exchange likely behind the largest differences. For UCO pairs 74−76, the overlap is fairly small (these orbitals would contribute the least to the spin coupling) and always larger for the nonhybrid functionals compared to the hybrid functionals. UCO pair 72−73 shows the largest differences in terms of overlap and bridging sulfide character and clearly indicates the importance of superexchange in the spin coupling. Intriguingly, the BP86 functional reveals the UCO 72 pairs as having an unusually large overlap ($S = 0.69$) and the shapes of the orbital isosurfaces suggest even some direct overlap of the d-orbital part of the two Fe ions. This would indicate a possible direct-exchange interaction or perhaps even partial metal−metal bonding present in the BP86 calculation, and it is easy to imagine how maximizing this orbital overlap in UCO pair 72 might then lead to a considerable Fe−Fe contraction in this complex. In fact, optimizing the structure at the BP86 level is found to give a Fe−Fe distance shortening of −0.09 Å compared to the X-ray structure. This shortening leads to a change in the overlap of UCO pair 72 from $S = 0.69$ to 0.74. The changes in the overlap upon structure relaxation for the other functionals can be found in Table S2 in the SI, while Figure S5 shows how the individual UCO orbital overlaps for different functionals correlate with Fe−Fe distance.

The rather unusually strong overlap for UCO pair 72 for complex **7** and the general underestimation of Fe−Fe distances seen for **7** and the overall FeMoD11 test set statistics hence indicate that the covalency or delocalization is overestimated in some of the nonhybrid functionals (likely due to the well-known self-interaction and delocalization error that plagues these functionals), leading to an exaggerated Fe−Fe interaction. The problem is reversed in the case of a functional like M06-2X, where the reduced Fe−S covalency leads to reduced favorable superexchange interactions and hence longer Fe−Fe distances. We hypothesize based on these results that the reason for the more favorable geometric statistics of r$^2$SCAN, TPSSh, B97-D3, and B3LYP* for the FeMoD11 test set as well as FeMoco is thus likely to reside in a more accurate treatment of Fe−S bond covalency in these spin-coupled Fe−S systems. As Table 5 shows, these four functionals have UCO overlaps relatively close together.

## CONCLUSIONS

The Fe−Fe and Mo−Fe distances of spin-coupled dimeric systems studied in this work are revealed to be highly sensitive to the density functional employed, specifically to the amount of exact exchange present in the functional definition, and also to the underlying GGA or meta-GGA exchange−correlation components. The results reveal that the common nonhybrid functionals (such as BP86, PBE, and TPSS) systematically underestimate Fe−Fe/Mo−Fe distances, while the common hybrid functionals with >20% exact exchange instead overestimate these distances. Four functionals, r$^2$SCAN, B97-D3, TPSSh, and B3LYP*, with 0−15% exact exchange are found to give the lowest errors for the spin-coupled test set (FeMoD11). r$^2$SCAN gives the lowest errors overall for the FeMoD11 test set, FeMoco itself, and a closed-shell Fe−Fe test set for comparison.

Geometric effects in BS-DFT calculations of spin-coupled systems are not discussed much in the literature, probably as spin coupling is typically thought to be a rather weak interaction. Even more generally, molecular geometries are often assumed not to be very sensitive to the DFT method and a common practice is to use a lower level of theory (e.g., nonhybrid functionals) to optimize geometries while a higher level of theory (e.g., hybrid functionals or wavefunction theory (WFT) methods) used to calculate more accurate reaction energies or spectroscopic properties on the low-level geometry. This common practice (while undoubtedly successful for many systems) is unlikely to be a useful strategy for spin-coupled iron−sulfur complexes, as these systems clearly exhibit a strong functional dependence of the calculated electronic structure that further translates into a strong functional dependence of the molecular structure. It is, e.g., not clear what a single-point energy calculation of an iron−sulfur compound with the M06-2X functional (predicting strong overestimation of Fe−Fe distance) on a BP86-calculated geometry (predicting fairly strong underestimation of the Fe−Fe distance), as an extreme


https://doi.org/10.1021/acs.jctc.1c00753
J. Chem. Theory Comput. 2022, 18, 1437−1457

example, would really describe, seeing as the two functionals predict very different electronic structures and geometries, rendering the energy surface ill-defined.

The effects seen for these spin-coupled systems are large in magnitude, which is very likely due to the strong connection between covalency and superexchange and due to the more flexible metal−ligand bond involving a 3p element (S) than a 2p element (e.g., an oxo bridge). Fe−S covalency as an important metric in DFT calculations of iron−sulfur clusters has been previously discussed by Szilagyi and co-workers.[74,75]

Two caveats regarding our results should be mentioned: (1) We compare DFT-calculated geometries calculated with a polarizable continuum model with X-ray crystal structures. Crystal packing effects have not been considered in the calculations of FeMoD11 and FeCSD5 test sets (though we note that the FeMoco calculations presented include protein environmental effects via QM/MM) and may have non-negligible effects on some of the molecules considered that would slightly affect the error statistics. Based on preliminary data, we expect crystal packing effects to be larger in magnitude for the bulkier complexes while smaller systems such as complex **7** should be less affected. (2) We utilize broken-symmetry determinants in this work that are not eigenfunctions of the total spin operator. This leads to artificial $\alpha$ and $\beta$ spin densities being present in the calculations of the antiferromagnetically coupled singlet states (a real singlet has no spin density). It is unclear what the effects of not preserving spin symmetry are in BS-DFT geometry optimizations, especially since the total spin operator can only be applied to the noninteracting Kohn−Sham wavefunction. Future work may consider the use of spin projection gradients that have recently been utilized by Guidoni and co-workers for iron−sulfur clusters.[69,77,70] However, it remains unclear how appropriate these spin projection schemes (that assume the validity of HDVV spin Hamiltonians) are for the more complex covalent and often delocalized electronic structure exhibited by iron−sulfur clusters.

In this study, we have focused on the usefulness of analyzing geometries of spin-coupled iron−sulfur complexes and shown that a density functional that predicts an accurate geometry (as primarily judged by the distance between the spin-coupled Fe−Fe/Mo−Fe ions) describes a specific electronic structure that primarily relates to the covalency of the bridging iron−sulfur bond. In our view, this strongly implies that a functional that predicts accurate geometries for spin-coupled iron−sulfur systems is describing the electronic structure of these systems more accurately than other methods and should in turn be more suitable to describe the full potential energy surface of these systems. However, the molecular structure can also not reveal the full picture of the accuracy of the electronic structure and for the four functionals that emerged from our comparison: r$^2$SCAN, TPSSh, B97-D3, and B3LYP*, we might not expect identical trends for reaction energies or other properties, as the functional components are rather different (GGA vs meta-GGA, 0% EE vs 10% EE vs 15% EE, etc.). Nonetheless, an accurate treatment of iron−sulfur bond covalency (that as shown affects the molecular structure) should be a prerequisite for obtaining the right result for the right reason with a quantum chemistry method.

For describing energetics related to the complex mechanism of dinitrogen reduction to ammonia by the FeMoco cluster of nitrogenase, errors associated with redox energies, protonation energies, metal hydride bond formation energies, $N_2$ and $H_2$ binding energies, and metal−sulfur bond dissociation energies also need to be evaluated. Some recent studies by Dance and Ryde and co-workers have been devoted to the topic of benchmarking properties related to nitrogenase reactions,[148,149] where density functionals were compared for reactions, structures, and vibrational frequencies involving low-spin, low-valent organometallic compounds with strong-field ligands (primarily CO). We note, however, that FeMoco features high-spin Fe and Mo ions in a weak-field sulfide environment instead and that benchmarking energy errors for high-spin metal ions are likely more relevant than low-spin metal ions.

## ■ ASSOCIATED CONTENT

### Supporting Information

The Supporting Information is available free of charge at https://pubs.acs.org/doi/10.1021/acs.jctc.1c00753.

Plots of data with MAD instead of MD; plots of structure deviations for each functional or each molecule; and all calculated distances and electronic structure parameters (PDF)

*XYZ* coordinates of all compounds (ZIP)

## ■ AUTHOR INFORMATION


### Corresponding Author

**Ragnar Bjornsson** − *Science Institute, University of Iceland, 107 Reykjavik, Iceland; Max-Planck Institute for Chemical Energy Conversion, 45470 Mülheim an der Ruhr, Germany;* Present Address: Univ. Grenoble Alpes, CNRS, CEA, IRIG, Laboratoire de Chimie et Biologie des Métaux, 17 Rue des Martyrs, F-38054 Grenoble Cedex, France; orcid.org/0000-0003-2167-8374; Email: ragnar.bjornsson@cec.mpg.de

### Author

**Bardi Benediktsson** − *Science Institute, University of Iceland, 107 Reykjavik, Iceland*

Complete contact information is available at: https://pubs.acs.org/10.1021/acs.jctc.1c00753


### Author Contributions

The manuscript was written through contributions of all authors.


### Funding

R.B. acknowledges support from the Icelandic Research Fund (grant 162880051) and the Max Planck Society. B.B. acknowledges support from the Teacher Assistant Grant of the University of Iceland. Open access funded by Max Planck Society.


### Notes

The authors declare no competing financial interest.

## ■ ACKNOWLEDGMENTS


The computations were performed on resources provided by the Icelandic High Performance Computing Centre at the University of Iceland. R.B. thanks the Max Planck society for support.


## ■ REFERENCES


(1) Einsle, O.; Rees, D. C. Structural Enzymology of Nitrogenase Enzymes. *Chem. Rev.* **2020**, *120*, 4969−5004.

(2) Spatzal, T.; Aksoyoglu, M.; Zhang, L.; Andrade, S. L.; Schleicher, E.; Weber, S.; Rees, D. C.; Einsle, O. Evidence for Interstitial Carbon in Nitrogenase FeMo Cofactor. *Science* **2011**, *334*, 940.
(3) Lukoyanov, D.; Pelmenschikov, V.; Maeser, N.; Laryukhin, M.; Tran, C. Y.; Noodleman, L.; Dean, D. R.; Case, D. A.; Seefeldt, L. C.; Hoffman, B. M. Testing If the Interstitial Atom, X, of the Nitrogenase Molybdenum-Iron Cofactor Is N or C: ENDOR, ESEEM, and DFT Studies of the S = 3/2 Resting State in Multiple Environments. *Inorg. Chem.* **2007**, *46*, 11437−11449.
(4) Davydov, R.; Khadka, N.; Yang, Z.; Fielding, A. J.; Lukoyanov, D.; Dean, D. R.; Seefeldt, L. C.; Hoffman, B. M. Exploring Electron/Proton Transfer and Conformational Changes in the Nitrogenase MoFe Protein and FeMo-cofactor Through Cryoreduction/EPR Measurements. *Isr. J. Chem.* **2016**, *56*, 841−851.
(5) Hoeke, V.; Tociu, L.; Case, D. A.; Seefeldt, L. C.; Raugei, S.; Hoffman, B. M. High Resolution ENDOR Spectroscopy Combined with Quantum Chemical Calculations Reveals the Structure of the Nitrogenase Janus Intermediate E4(4H). *J. Am. Chem. Soc.* **2019**, *141*, 11984−11996.
(6) Van Stappen, C.; Decamps, L.; Cutsail, G. E.; Bjornsson, R.; Henthorn, J. T.; Birrell, J. A.; DeBeer, S. The Spectroscopy of Nitrogenases. *Chem. Rev.* **2020**, *120*, 5005−5081.
(7) Yoo, S. J.; Angove, H. C.; Papaefthymiou, V.; Burgess, B. K.; Münck, E. Mossbauer Study of the MoFe Protein of Nitrogenase from Azotobacter Vinelandii Using Selective 57Fe Enrichment of the M-Centers. *J. Am. Chem. Soc.* **2000**, *122*, 4926−4936.
(8) Scott, A. D.; Pelmenschikov, V.; Guo, Y.; Yan, L.; Wang, H.; George, S. J.; Dapper, C. H.; Newton, W. E.; Yoda, Y.; Tanaka, Y.; Cramer, S. P. Structural Characterization of CO-Inhibited Mo-Nitrogenase by Combined Application of Nuclear Resonance Vibrational Spectroscopy, Extended X-Ray Absorption Fine Structure, and Density Functional Theory: New Insights into the Effects of CO Binding and The Role of the Interstitial Atom. *J. Am. Chem. Soc.* **2014**, *136*, 15942−15954.
(9) Bjornsson, R.; Lima, F. A.; Spatzal, T.; Weyhermüller, T.; Glatzel, P.; Bill, E.; Einsle, O.; Neese, F.; DeBeer, S. Identification of a Spin-Coupled Mo(iii) in the Nitrogenase Iron−Molybdenum Cofactor. *Chem. Sci.* **2014**, *5*, 3096−3103.
(10) Kowalska, J.; DeBeer, S. The Role of X-Ray Spectroscopy in Understanding the Geometric and Electronic Structure of Nitrogenase. *Biochim. Biophys. Acta, Mol. Cell Res.* **2015**, *1853*, 1406−1415.
(11) Bjornsson, R.; Delgado-Jaime, M. U.; Lima, F. A.; Sippel, D.; Schlesier, J.; Weyhermüller, T.; Einsle, O.; Neese, F.; De Beer, S. Molybdenum L-Edge XAS Spectra of MoFe Nitrogenase. *Z. Anorg. Allg. Chem.* **2015**, *641*, 65−71.
(12) Spatzal, T.; Schlesier, J.; Burger, E.-M.; Sippel, D.; Zhang, L.; Andrade, S. L. A.; Rees, D. C.; Einsle, O. Nitrogenase FeMoco Investigated by Spatially Resolved Anomalous Dispersion Refinement. *Nat. Commun.* **2016**, *7*, No. 10902.
(13) Kowalska, J.; Henthorn, J.; Van Stappen, C.; Trncik, C.; Einsle, O.; Keavney, D.; DeBeer, S. X-Ray Magnetic Circular Dichroism Spectroscopy Applied to Nitrogenase and Related Models: Experimental Evidence for a Spin-Coupled Mo(III). *Angew. Chem., Int. Ed.* **2019**, *58*, 9373−9377.
(14) Henthorn, J. T.; Arias, R. J.; Koroidov, S.; Kroll, T.; Sokaras, D.; Bergmann, U.; Rees, D. C.; DeBeer, S. Localized Electronic Structure of Nitrogenase FeMoco Revealed by Selenium K-Edge High Resolution X-Ray Absorption Spectroscopy. *J. Am. Chem. Soc.* **2019**, *141*, 13676−13688.
(15) Van Stappen, C.; Thorhallsson, A. T.; Decamps, L.; Bjornsson, R.; Debeer, S. Resolving the Structure of the E1 State of Mo Nitrogenase through Mo and Fe K-Edge EXAFS and QM/MM Calculations. *Chem. Sci.* **2019**, *10*, 9807−9821.
(16) Lovell, T.; Li, J.; Liu, T.; Case, D. A.; Noodleman, L. FeMo Cofactor of Nitrogenase: A Density Functional Study of States MN, MOX, MR, and MI. *J. Am. Chem. Soc.* **2001**, *123*, 12392−12410.
(17) Lovell, T.; Torres, R. A.; Han, W. G.; Liu, T.; Case, D. A.; Noodleman, L. Metal Substitution in the Active Site of Nitrogenase MFe7S9 (M = Mo4+, V3+, Fe3+). *Inorg. Chem.* **2002**, *41*, 5744−5753.
(18) Lovell, T.; Li, J.; Case, D. A.; Noodleman, L. FeMo Cofactor of Nitrogenase: Energetics and Local Interactions in the Protein Environment. *JBIC, J. Biol. Inorg. Chem.* **2002**, *7*, 735−749.
(19) Lancaster, K. M.; Roemelt, M.; Ettenhuber, P.; Hu, Y.; Ribbe, M. W.; Neese, F.; Bergmann, U.; DeBeer, S. X-Ray Emission Spectroscopy Evidences a Central Carbon in the Nitrogenase Iron-Molybdenum Cofactor. *Science* **2011**, *334*, 974−977.
(20) Bjornsson, R.; Neese, F.; Schrock, R. R.; Einsle, O.; DeBeer, S. The Discovery of Mo(III) in FeMoco: Reuniting Enzyme and Model Chemistry. *JBIC, J. Biol. Inorg. Chem.* **2015**, *20*, 447−460.
(21) Bjornsson, R.; Neese, F.; DeBeer, S. Revisiting the Mössbauer Isomer Shifts of the FeMoco Cluster of Nitrogenase and the Cofactor Charge. *Inorg. Chem.* **2017**, *56*, 1470−1477.
(22) Benediktsson, B.; Bjornsson, R. QM/MM Study of the Nitrogenase MoFe Protein Resting State: Broken-Symmetry States, Protonation States, and QM Region Convergence in the FeMoco Active Site. *Inorg. Chem.* **2017**, *56*, 13417−13429.
(23) Bergmann, J.; Oksanen, E.; Ryde, U. Critical evaluation of a crystal structure of nitrogenase with bound N2 ligands. *JBIC, J. Biol. Inorg. Chem.* **2021**, *26*, 341−353.
(24) Noodleman, L.; Case, D. A.; Aizman, A. Broken Symmetry Analysis of Spin Coupling in Iron-Sulfur Clusters. *J. Am. Chem. Soc.* **1988**, *110*, 1001−1005.
(25) Noodleman, L.; Peng, C. Y.; Case, D. A.; Mouesca, J. M. Orbital Interactions, Electron Delocalization and Spin Coupling in Iron-Sulfur Clusters. *Coord. Chem. Rev.* **1995**, *144*, 199−244.
(26) Torres, R. A.; Lovell, T.; Noodleman, L.; Case, D. A. Density Functional and Reduction Potential Calculations of Fe 4 S 4 Clusters. *J. Am. Chem. Soc.* **2003**, *125*, 1923−1936.
(27) Sharma, S.; Sivalingam, K.; Neese, F.; Chan, G. K. L. Low-Energy Spectrum of Iron-Sulfur Clusters Directly from Many-Particle Quantum Mechanics. *Nat. Chem.* **2014**, *6*, 927−933.
(28) Siegbahn, P. The Mechanism for Nitrogenase Including All Steps. *Phys. Chem. Chem. Phys.* **2019**, *21*, 15747−15759.
(29) Thorhallsson, A. T.; Benediktsson, B.; Bjornsson, R. A Model for Dinitrogen Binding in the E4 State of Nitrogenase. *Chem. Sci.* **2019**, *10*, 11110−11124.
(30) Cao, L.; Ryde, U. What Is the Structure of the E4 Intermediate in Nitrogenase? *J. Chem. Theory Comput.* **2020**, *16*, 1936−1952.
(31) Cao, L.; Ryde, U. Putative Reaction Mechanism of Nitrogenase after Dissociation of a Sulfide Ligand. *J. Catal.* **2020**, *391*, 247−259.
(32) Dance, I. Mechanism for the Activation of FeMo-Co, the Catalytic Site of Nitrogenase? *Dalton Trans.* **2019**, *48*, 1251−1262.
(33) Raugei, S.; Seefeldt, L. C.; Hoffman, B. M. Critical Computational Analysis Illuminates the Reductive-Elimination Mechanism That Activates Nitrogenase for N2 Reduction [Chemistry]. *Proc. Natl. Acad. Sci. U.S.A.* **2018**, *115*, E10521−E10530.
(34) Cao, L.; Ryde, U. Putative reaction mechanism of nitrogenase after dissociation of a sulfide ligand. *J. Catal.* **2020**, *391*, 247−259.
(35) Jiang, H.; Ryde, U. Thermodynamically favourable states in the reaction of nitrogenase without dissociation of any sulfide ligand. *Chem.—Eur. J.* **2022**, DOI: 10.1002/chem.202103933.
(36) Schurkus, H. F.; Chan, G. K. L.; Chen, D. T.; Cheng, H. P.; Stanton, J. F. Theoretical Prediction of Magnetic Exchange Coupling Constants from Broken-Symmetry Coupled Cluster Calculations. *J. Chem. Phys.* **2020**, *152*, No. 234115.
(37) Nakatani, N.; Guo, S. Density Matrix Renormalization Group (DMRG) Method as a Common Tool for Large Active-Space CASSCF/CASPT2 Calculations. *J. Chem. Phys.* **2017**, *146*, No. 094102.
(38) Li, Z.; Li, J.; Dattani, N. S.; Umrigar, C. J.; Chan, G. K. L. The Electronic Complexity of the Ground-State of the FeMo Cofactor of Nitrogenase as Relevant to Quantum Simulations. *J. Chem. Phys.* **2019**, *150*, No. 024302.
(39) Reiher, M.; Wiebe, N.; Svore, K. M.; Wecker, D.; Troyer, M. Elucidating Reaction Mechanisms on Quantum Computers. *Proc. Natl. Acad. Sci. U.S.A.* **2017**, *114*, 7555−7560.

(40) Montgomery, J. M.; Mazziotti, D. A. Strong Electron Correlation in Nitrogenase Cofactor, FeMoco. *J. Phys. Chem. A* **2018**, *122*, 4988−4996.
(41) Li, Z.; Guo, S.; Sun, Q.; Chan, G. K. L. Electronic Landscape of the P-Cluster of Nitrogenase as Revealed through Many-Electron Quantum Wavefunction Simulations. *Nat. Chem.* **2019**, *11*, 1026−1033.
(42) Li Manni, G.; Dobrautz, W.; Bogdanov, N. A.; Guther, K.; Alavi, A. Resolution of Low-Energy States in Spin-Exchange Transition-Metal Clusters: Case Study of Singlet States in [Fe(III)-4S4] Cubanes. *J. Phys. Chem. A* **2021**, *125*, 4727−4740.
(43) Roemelt, M.; Pantazis, D. A. Multireference Approaches to Spin-State Energetics of Transition Metal Complexes Utilizing the Density Matrix Renormalization Group. *Adv. Theory Simul.* **2019**, *2*, No. 1800201.
(44) Guo, Y.; Sivalingam, K.; Neese, F. Approximations of Density Matrices in N-Electron Valence State Second-Order Perturbation Theory (NEVPT2). I. Revisiting the NEVPT2 Construction. *J. Chem. Phys.* **2021**, *154*, No. 214111.
(45) Guo, Y.; Sivalingam, K.; Kollmar, C.; Neese, F. Approximations of Density Matrices in N-Electron Valence State Second-Order Perturbation Theory (NEVPT2). II. The Full Rank NEVPT2 (FR-NEVPT2) Formulation. *J. Chem. Phys.* **2021**, *154*, No. 214113.
(46) Neese, F. Definition of Corresponding Orbitals and the Diradical Character in Broken Symmetry DFT Calculations on Spin Coupled Systems. *J. Phys. Chem. Solids* **2004**, *65*, 781−785.
(47) Levy, M. Universal variational functionals of electron densities, first-order density matrices, and natural spin-orbitals and solution of the v-representability problem. *Proc. Natl. Acad. Sci. U.S.A.* **1979**, *76*, 6062−6065.
(48) Kohn, W. v-Representability and Density Functional Theory. *Phys. Rev. Lett.* **1983**, *51*, 1596−1598.
(49) Chen, J.; Stott, M. J. v-representability for systems with low degeneracy. *Phys. Rev. A* **1991**, *44*, 2816−2822.
(50) Chen, J.; Stott, M. J. v-representability for noninteracting systems. *Phys. Rev. A* **1993**, *47*, 153−160.
(51) Schindlmayr, A.; Godby, R. W. Density-functional theory and the v-representability problem for model strongly correlated electron systems. *Phys. Rev. B* **1995**, *51*, 10427−10435.
(52) Gonis, A.; Zhang, X.-G.; Däne, M.; Stocks, G. M.; Nicholson, D. M. Reformulation of density functional theory for N-representable densities and the resolution of the v-representability problem. *J. Phys. Chem. Solids* **2016**, *89*, 23−31.
(53) Däne, M.; Gonis, A. On the v-Representabilty Problem in Density Functional Theory: Application to Non-Interacting Systems. *Computation* **2016**, *4*, 2079−3197.
(54) Yu, H. S.; Li, S. L.; Truhlar, D. G. Perspective: Kohn-Sham density functional theory descending a staircase. *J. Chem. Phys.* **2016**, *145*, No. 130901.
(55) Yamaguchi, K.; Takahara, Y.; Fueno, T. *Ab-Initio Molecular Orbital Studies of Structure and Reactivity of Transition Metal-OXO Compounds. In Applied Quantum Chemistry*; Springer: Dordrecht, 1986; Vol. *14*, pp 155−184.
(56) Soda, T.; Kitagawa, Y.; Onishi, T.; Takano, Y.; Shigeta, Y.; Nagao, H.; Yoshioka, Y.; Yamaguchi, K. Ab Initio Computations of Effective Exchange Integrals for H-H, H-He-H and Mn 2 O 2 Complex: Comparison of Broken-Symmetry Approaches. *Chem. Phys. Lett.* **2000**, *319*, 223−230.
(57) Ginsberg, A. P. Magnetic Exchange in Transition Metal Complexes. 12. Calculation of Cluster Exchange Coupling Constants with the X.Alpha.-Scattered Wave Method. *J. Am. Chem. Soc.* **1980**, *102*, 111−117.
(58) Noodleman, L. Valence Bond Description of Antiferromagnetic Coupling in Transition Metal Dimers. *J. Chem. Phys.* **1981**, *74*, 5737−5743.
(59) Noodleman, L.; Davidson, E. R. Ligand Spin Polarization and Antiferromagnetic Coupling in Transition Metal Dimers. *Chem. Phys.* **1986**, *109*, 131−143.
(60) Malrieu, J. P.; Caballol, R.; Calzado, C. J.; De Graaf, C.; Guihéry, N. Magnetic Interactions in Molecules and Highly Correlated Materials: Physical Content, Analytical Derivation, and Rigorous Extraction of Magnetic Hamiltonians. *Chem. Rev.* **2014**, *114*, 429−492.
(61) Illas, F.; Moreira, I. D. P. R.; Bofill, J. M.; Filatov, M. Extent and Limitations of Density-Functional Theory in Describing Magnetic Systems. *Phys. Rev. B: Condens. Matter Mater. Phys.* **2004**, *70*, No. 132414.
(62) Krewald, V.; Neese, F.; Pantazis, D. A. On the Magnetic and Spectroscopic Properties of High-Valent Mn 3CaO4 Cubanes as Structural Units of Natural and Artificial Water-Oxidizing Catalysts. *J. Am. Chem. Soc.* **2013**, *135*, 5726−5739.
(63) Benediktsson, B.; Thorhallsson, A. T.; Bjornsson, R. QM/MM Calculations Reveal a Bridging Hydroxo Group in a Vanadium Nitrogenase Crystal Structure. *Chem. Commun.* **2018**, *54*, 7310−7313.
(64) Benediktsson, B.; Bjornsson, R. Quantum Mechanics/Molecular Mechanics Study of Resting-State Vanadium Nitrogenase: Molecular and Electronic Structure of the Iron−Vanadium Cofactor. *Inorg. Chem.* **2020**, *59*, 11514−11527.
(65) Cao, L.; Caldararu, O.; Ryde, U. Protonation States of Homocitrate and Nearby Residues in Nitrogenase Studied by Computational Methods and Quantum Refinement. *J. Phys. Chem. B* **2017**, *121*, 8242−8262.
(66) Cao, L.; Ryde, U. Extremely Large Differences in DFT Energies for Nitrogenase Models. *Phys. Chem. Chem. Phys.* **2019**, *21*, 2480−2488.
(67) Rao, L.; Xu, X.; Adamo, C. Theoretical Investigation on the Role of the Central Carbon Atom and Close Protein Environment on the Nitrogen Reduction in Mo Nitrogenase. *ACS Catal.* **2016**, *6*, 1567−1577.
(68) Nair, N. N.; Schreiner, E.; Pollet, R.; Staemmler, V.; Marx, D. Magnetostructural Dynamics with the Extended Broken Symmetry Formalism: Antiferromagnetic [2Fe-2S] Complexes. *J. Chem. Theory Comput.* **2008**, *4*, 1174−1188.
(69) Cappelluti, F.; Bencivenni, L.; Guidoni, L. Spin-Symmetrised Structures and Vibrational Frequencies of Iron-Sulfur Clusters. *Phys. Chem. Chem. Phys.* **2020**, *22*, 16655−16664.
(70) Chu, S.; Bovi, D.; Cappelluti, F.; Orellana, A. G.; Martin, H.; Guidoni, L. Effects of Static Correlation between Spin Centers in Multicenter Transition Metal Complexes. *J. Chem. Theory Comput.* **2017**, *13*, 4675−4683.
(71) Bühl, M.; Kabrede, H. Geometries of Transition-Metal Complexes from Density-Functional Theory. *J. Chem. Theory Comput.* **2006**, *2*, 1282−1290.
(72) Bühl, M.; Reimann, C.; Pantazis, D. A.; Bredow, T.; Neese, F. Geometries of Third-Row Transition-Metal Complexes from Density-Functional Theory. *J. Chem. Theory Comput.* **2008**, *4*, 1449−1459.
(73) Waller, M. P.; Braun, H.; Hojdis, N.; Bühl, M. Geometries of Second-Row Transition-Metal Complexes from Density-Functional Theory. *J. Chem. Theory Comput.* **2007**, *3*, 2234−2242.
(74) Szilagyi, R. K.; Winslow, M. A. On the Accuracy of Density Functional Theory for Iron—Sulfur Clusters. *J. Comput. Chem.* **2006**, *27*, 1385−1397.
(75) Harris, T. V.; Szilagyi, R. K. Iron-Sulfur Bond Covalency from Electronic Structure Calculations for Classical Iron-Sulfur Clusters. *J. Comput. Chem.* **2014**, *35*, 540−552.
(76) Sandala, G. M.; Hopmann, K. H.; Ghosh, A.; Noodleman, L. Calibration of DFT Functionals for the Prediction of 57Fe Mössbauer Spectral Parameters in Iron-Nitrosyl and Iron-Sulfur Complexes: Accurate Geometries Prove Essential. *J. Chem. Theory Comput.* **2011**, *7*, 3232−3247.
(77) Bovi, D.; Guidoni, L. Magnetic Coupling Constants and Vibrational Frequencies by Extended Broken Symmetry Approach with Hybrid Functionals. *J. Chem. Phys.* **2012**, *137*, No. 114107.
(78) Groom, C. R.; Bruno, I. J.; Lightfoot, M. P.; Ward, S. C. The Cambridge Structural Database. *Acta Crystallogr., Sect. B: Struct. Sci., Cryst. Eng. Mater.* **2016**, *72*, 171−179.


https://doi.org/10.1021/acs.jctc.1c00753
*J. Chem. Theory Comput.* 2022, 18, 1437−1457

(79) Neese, F. Software Update: The ORCA Program System, version 4.0. *Wiley Interdiscip. Rev.: Comput. Mol. Sci.* **2018**, No. e1327.
(80) Becke, A. D. Density-Functional Exchange-Energy Approximation with Correct Asymptotic Behavior. *Phys. Rev. A* **1988**, *38*, 3098−3100.
(81) Perdew, J. P. Density-Functional Approximation for the Correlation Energy of the Inhomogeneous Electron Gas. *Phys. Rev. B* **1986**, *33*, 8822−8824.
(82) Grimme, S. Semiempirical GGA-Type Density Functional Constructed with a Long-Range Dispersion Correction. *J. Comput. Chem.* **2006**, *27*, 1787−1799.
(83) Tao, J.; Perdew, J. P. Climbing the Density Functional Ladder: Nonempirical Meta − Generalized Gradient Approximation Designed for Molecules and Solids. *Phys. Rev. Lett.* **2003**, *91*, No. 146401.
(84) Staroverov, V. N.; Scuseria, G. E.; Tao, J.; Perdew, J. P. Comparative Assessment of a New Nonempirical Density Functional: Molecules and Hydrogen-Bonded Complexes Comparative Assessment of a New Nonempirical Density Functional: Molecules and Hydrogen-Bonded Complexes. *J. Chem. Phys.* **2003**, 12129.
(85) Lee, C.; Yang, W.; Parr, R. G. Development of the Colle-Salvetti Correlation-Energy Formula into a Functional of the Electron Density. *Phys. Rev. B* **1988**, *37*, 785−789.
(86) Becke, A. D. Density-functional Thermochemistry. III. The Role of Exact Exchange. *J. Chem. Phys.* **1993**, *98*, 5648−5652.
(87) Reiher, M.; Salomon, O.; Artur Hess, B. Reparameterization of Hybrid Functionals Based on Energy Differences of States of Different Multiplicity. *Theor. Chem. Acc.* **2001**, *107*, 48−55.
(88) Salomon, O.; Reiher, M.; Hess, B. A. Assertion and Validation of the Performance of the B3LYP* Functional for the First Transition Metal Row and the G2 Test Set. *J. Chem. Phys.* **2002**, *117*, 4729−4737.
(89) Perdew, J. P.; Burke, K.; Ernzerhof, M. Generalized Gradient Approximation Made Simple. *Phys. Rev. Lett.* **1996**, *77*, 3865−3868.
(90) Perdew, J. P.; Ernzerhof, M.; Burke, K. Rationale for Mixing Exact Exchange with Density Functional Approximations. *J. Chem. Phys.* **1996**, *105*, 9982−9985.
(91) Zhao, Y.; Truhlar, D. G. The M06 Suite of Density Functionals for Main Group Thermochemistry, Thermochemical Kinetics, Noncovalent Interactions, Excited States, and Transition Elements: Two New Functionals and Systematic Testing of Four M06-Class Functionals and 12 Other Functionals. *Theor. Chem. Acc.* **2008**, *120*, 215−241.
(92) Becke, A. D. A New Mixing of Hartree−Fock and Local Density-functional Theories. *J. Chem. Phys.* **1993**, *98*, 1372−1377.
(93) Yanai, T.; Tew, D. P.; Handy, N. C. A New Hybrid Exchange-Correlation Functional Using the Coulomb-Attenuating Method (CAM-B3LYP). *Chem. Phys. Lett.* **2004**, *393*, 51−57.
(94) Najibi, A.; Goerigk, L. The Nonlocal Kernel in van Der Waals Density Functionals as an Additive Correction: An Extensive Analysis with Special Emphasis on the B97M-V and ωb97M-V Approaches. *J. Chem. Theory Comput.* **2018**, *14*, 5725−5738.
(95) Mardirossian, N.; Head-Gordon, M. ωB97M-V: A Combinatorially Optimized, Range-Separated Hybrid, Meta-GGA Density Functional with VV10 Nonlocal Correlation. *J. Chem. Phys.* **2016**, *144*, No. 214110.
(96) Mardirossian, N.; Head-Gordon, M. ωb97X-V: A 10-Parameter, Range-Separated Hybrid, Generalized Gradient Approximation Density Functional with Nonlocal Correlation, Designed by a Survival-of-the-Fittest Strategy. *Phys. Chem. Chem. Phys.* **2014**, *16*, 9904−9924.
(97) Furness, J. W.; Kaplan, A. D.; Ning, J.; Perdew, J. P.; Sun, J. Accurate and Numerically Efficient r2SCAN Meta-Generalized Gradient Approximation. *J. Phys. Chem. Lett.* **2020**, *11*, 8208−8215.
(98) Chai, J.-D.; Head-Gordon, M. Long-Range Corrected Hybrid Density Functionals with Damped Atom−Atom Dispersion Corrections. *Phys. Chem. Chem. Phys.* **2008**, *10*, 6615.
(99) Grimme, S.; Antony, J.; Ehrlich, S.; Krieg, H. A Consistent and Accurate Ab Initio Parametrization of Density Functional Dispersion Correction (DFT-D) for the 94 Elements H-Pu. *J. Chem. Phys.* **2010**, *132*, No. 154104.
(100) Grimme, S.; Ehrlich, S.; Goerigk, L. Effect of the Damping Function in Dispersion Corrected Density Functional Theory. *J. Comput. Chem.* **2011**, *32*, 1456−1465.
(101) van Lenthe, E.; Baerends, E. J.; Snijders, J. G. Relativistic Regular Two-component Hamiltonians. *J. Chem. Phys.* **1993**, *99*, 4597−4610.
(102) van Wüllen, C. Molecular Density Functional Calculations in the Regular Relativistic Approximation: Method, Application to Coinage Metal Diatomics, Hydrides, Fluorides and Chlorides, and Comparison with First-Order Relativistic Calculations. *J. Chem. Phys.* **1998**, *109*, 392−399.
(103) Weigend, F.; Ahlrichs, R. Balanced Basis Sets of Split Valence, Triple Zeta Valence and Quadruple Zeta Valence Quality for H to Rn: Design and Assessment of Accuracy. *Phys. Chem. Chem. Phys.* **2005**, *7*, 3297.
(104) Pantazis, D. A.; Chen, X.-Y.; Landis, C. R.; Neese, F. All-Electron Scalar Relativistic Basis Sets for Third-Row Transition Metal Atoms. *J. Chem. Theory Comput.* **2008**, *4*, 908−919.
(105) Schäfer, A.; Huber, R.; Ahlrichs, J. Fully Optimized Contracted Gaussian Basis Sets of Triple Zeta Valence Quality for Atoms Li to Kr. *J. Chem. Phys.* **1994**, *100*, 5829−5835.
(106) Neese, F.; Wennmohs, F.; Hansen, A.; Becker, U. Efficient, Approximate and Parallel Hartree-Fock and Hybrid DFT Calculations. A "chain-of-Spheres" Algorithm for the Hartree-Fock Exchange. *Chem. Phys.* **2009**, *356*, 98−109.
(107) Izsák, R.; Neese, F. An Overlap Fitted Chain of Spheres Exchange Method. *J. Chem. Phys.* **2011**, *135*, No. 144105.
(108) Lehtola, S.; Steigemann, C.; Oliveira, M. J. T.; Marques, M. A. L. Recent Developments in Libxc — A Comprehensive Library of Functionals for Density Functional Theory. *SoftwareX* **2018**, *7*, 1−5.
(109) Barone, V.; Cossi, M. Conductor Solvent Model. *J. Phys. Chem. A* **1998**, *102*, 1995−2001.
(110) York, D. M.; Karplus, M. A Smooth Solvation Potential Based on the Conductor-like Screening Model. *J. Phys. Chem. A* **1999**, *103*, 11060−11079.
(111) Garcia-Ratés, M.; Neese, F. Effect of the Solute Cavity on the Solvation Energy and Its Derivatives within the Framework of the Gaussian Charge Scheme. *J. Comput. Chem.* **2020**, *41*, 922−939.
(112) Sherwood, P.; De Vries, A. H.; Guest, M. F.; Schreckenbach, G.; Catlow, C. R. A.; French, S. A.; Sokol, A. A.; Bromley, S. T.; Thiel, W.; Turner, A. J.; Billeter, S.; Terstegen, F.; Thiel, S.; Kendrick, J.; Rogers, S. C.; Casci, J.; Watson, M.; King, F.; Karlssen, E.; Sjøvoll, M.; Fahmi, A.; Schäfer, A.; Lennartz, C. QUASI: A General Purpose Implementation of the QM/MM Approach and Its Application to Problems in Catalysis. *J. Mol. Struct.: THEOCHEM* **2003**, *632*, 1−28.
(113) Metz, S.; Kästner, J.; Sokol, A. A.; Keal, T. W.; Sherwood, P. ChemShell-a Modular Software Package for QM/MM Simulations. *Wiley Interdiscip. Rev.: Comput. Mol. Sci.* **2014**, *4*, 101−110.
(114) Smith, W.; Forester, T. R. DL_POLY_2.0: A General-Purpose Parallel Molecular Dynamics Simulation Package. *J. Mol. Graphics* **1996**, *14*, 136−141.
(115) Humphrey, W.; Dalke, A.; Schulten, K. VMD: Visual Molecular Dynamics. *J. Mol. Graphics* **1996**, *14*, 33−38.
(116) Drüeke, S.; Chaudhuri, P.; Pohl, K.; Wieghardt, K.; Ding, X.-Q.; Bill, E.; Sawaryn, A.; Trautwein, A. X.; Winkler, H.; Gurman, S. J. The Novel Mixed-Valence, Exchange-Coupled, Class III Dimer [L 2 Fe 2 (μ-OH) 3] 2+ (L = N,N′,N″-Trimethyl-1,4,7-Triazacyclononane). *J. Chem. Soc., Chem. Commun.* **1989**, *509*, 59−62.
(117) Gamelin, D. R.; Bominaar, E. L.; Kirk, M. L.; Wieghardt, K.; Solomon, E. I. Excited-State Contributions to Ground-State Properties of Mixed-Valence Dimers: Spectral and Electronic-Structural Studies of [Fe2(OH)3(Tmtacn)2]2+ Related to the [Fe2S2]+ Active Sites of Plant-Type Ferredoxins. *J. Am. Chem. Soc.* **1996**, *118*, 8085−8097.
(118) Gamelin, D. R.; Bominaar, E. L.; Mathonière, C.; Kirk, M. L.; Wieghardt, K.; Girerd, J.-J.; Solomon, E. I. Excited-State Distortions and Electron Delocalization in Mixed-Valence Dimers: Vibronic

Analysis of the Near-IR Absorption and Resonance Raman Profiles of [Fe2(OH)3(Tmtacn)2]2+. *Inorg. Chem.* **1996**, *35*, 4323−4335.
(119) Henthorn, J. T.; Cutsail, G. E.; Wyhermüller, T.; DeBeer, S. Stabilization of intermediate spin states in mixed-valent diiron dichalcogenide complexes. *Nat. Chem.* **2022**, DOI: 10.1038/s41557-021-00853-5.
(120) Albers, A.; Demeshko, S.; Dechert, S.; Bill, E.; Bothe, E.; Meyer, F. The Complete Characterization of a Reduced Biomimetic [2Fe-2S] Cluster. *Angew. Chem., Int. Ed.* **2011**, *50*, 9191−9194.
(121) Albers, A.; Demeshko, S.; Pröpper, K.; Dechert, S.; Bill, E.; Meyer, F. A Super-Reduced Diferrous [2Fe−2S] Cluster. *J. Am. Chem. Soc.* **2013**, *135*, 1704−1707.
(122) Yao, S.; Meier, F.; Lindenmaier, N.; Rudolph, R.; Blom, B.; Adelhardt, M.; Sutter, J.; Mebs, S.; Haumann, M.; Meyer, K.; Kaupp, M.; Driess, M. Biomimetic [2Fe-2S] Clusters with Extensively Delocalized Mixed-Valence Iron Centers. *Angew. Chem., Int. Ed.* **2015**, *54*, 12506−12510.
(123) Nagelski, A. L.; Fataftah, M. S.; Bollmeyer, M. M.; McWilliams, S. F.; MacMillan, S. N.; Mercado, B. Q.; Lancaster, K. M.; Holland, P. L. The Influences of Carbon Donor Ligands on Biomimetic Multi-Iron Complexes for N2 Reduction. *Chem. Sci.* **2020**, *11*, 12710−12720.
(124) Bobrik, M. A.; Hodgson, K. O.; Holm, R. H. Inorganic Derivatives of Iron-Sulfide-Thiolate Dimers and Tetramers. Structures of Tetrachloro-$\mu$-Disulfido-Diferrate(III) and Tetrakis(Chloro-$\mu$3-Sulfido-Iron) Dianions. *Inorg. Chem.* **1977**, *16*, 1851−1858.
(125) Tsou, C. C.; Chiu, W. C.; Ke, C. H.; Tsai, J. C.; Wang, Y. M.; Chiang, M. H.; Liaw, W. F. Iron(III) Bound by Hydrosulfide Anion Ligands: NO-Promoted Stabilization of the [FeIII-SH] Motif. *J. Am. Chem. Soc.* **2014**, *136*, 9424−9433.
(126) Bolster, D. E.; Guetlich, P.; Hatfield, W. E.; Kremer, S.; Mueller, E. W.; Wieghardt, K. Exchange Coupling in Tris(.Mu.-Hydroxo)Bis[(1,4,7-Trimethyl-1,4,7-Triazacyclononane)Chromium-(III)] Triperchlorate Trihydrate. *Inorg. Chem.* **1983**, *22*, 1725−1729.
(127) Bennie, S. J.; Collison, D.; McDouall, J. J. W. Electronic and Magnetic Properties of Kremer's Tris-Hydroxo Bridged Chromium Dimer: A Challenge for DFT. *J. Chem. Theory Comput.* **2012**, *8*, 4915−4921.
(128) Pantazis, D. A. Meeting the Challenge of Magnetic Coupling in a Triply-Bridged Chromium Dimer: Complementary Broken-Symmetry Density Functional Theory and Multireference Density Matrix Renormalization Group Perspectives. *J. Chem. Theory Comput.* **2019**, *15*, 938−948.
(129) Sharma, P.; Truhlar, D. G.; Gagliardi, L. Magnetic Coupling in a Tris-Hydroxo-Bridged Chromium Dimer Occurs through Ligand Mediated Superexchange in Conjunction with Through-Space Coupling. *J. Am. Chem. Soc.* **2020**, *142*, 16644−16650.
(130) Coucouvanis, D.; Al-Ahmad, S.; Kim, C. G.; Mosier, P. E.; Kampf, J. W. Oxidative Decoupling of the Molybdenum-Iron-Sulfur MoFe3S4 Clusters and Possible Relevance to the Oxidative Degradation of the Nitrogenase Cofactor. Isolation and Structural Characterization of the [(Cl4cat)Mo(O)($\mu$-S)2FeCl2]2- Anion. *Inorg. Chem.* **1993**, *32*, 1533−1535.
(131) Tieckelmann, R. H.; Silvis, H. C.; Kent, T. A.; Huynh, B. H.; Waszczak, J. V.; Teo, B.-K.; Averill, B. A. Synthetic Molybdenum-Iron-Sulfur Clusters. Preparation, Structures, and Properties of the [S2MoS2Fe(SC6H5)2]2- and [S2MoS2FeCl2]2- Ions. *J. Am. Chem. Soc.* **1980**, *102*, 5550−5559.
(132) Kagalwala, H. N.; Lalaoui, N.; Li, Q. L.; Liu, L.; Woods, T.; Rauchfuss, T. B. Redox and "Antioxidant" Properties of Fe2($\mu$-SH)2(CO)4(PPh3)2. *Inorg. Chem.* **2019**, *58*, 2761−2769.
(133) Di Vaira, M.; Midollini, S.; Sacconi, L. Sulfur Ligand-Transition Metal Complexes. 4. Dinuclear Mercapto Complexes of Iron(II) with the Tridentate Ligand Bis[2-(Diphenylphosphino)-Ethyl]Phenylphosphine: Synthesis and x-Ray Crystal Structure. *Inorg. Chem.* **1979**, *18*, 3466−3469.
(134) Cotton, F. A.; Troup, J. M. Accurate Determination of a Classic Structure in the Metal Carbonyl Field: Nonacarbonyldi-Iron. *J. Chem. Soc., Dalton Trans.* **1974**, 800−802.
(135) Li, H.; Rauchfuss, T. B. Iron Carbonyl Sulfides, Formaldehyde, and Amines Condense to Give the Proposed Azadithiolate Cofactor of the Fe-Only Hydrogenases. *J. Am. Chem. Soc.* **2002**, *124*, 726−727.
(136) Green, J. C.; Green, M. L. H.; Parkin, G. The Occurrence and Representation of Three-Centre Two-Electron Bonds in Covalent Inorganic Compounds. *Chem. Commun.* **2012**, *48*, 11481−11503.
(137) Cao, L.; Ryde, U. Influence of the Protein and DFT Method on the Broken-Symmetry and Spin States in Nitrogenase. *Int. J. Quantum Chem.* **2018**, *118*, No. e25627.
(138) Hehre, W. J.; Ditchfield, K.; Pople, J. A. Self-Consistent Molecular Orbital Methods. XII. Further Extensions of Gaussian-Type Basis Sets for Use in Molecular Orbital Studies of Organic Molecules. *J. Chem. Phys.* **1972**, *56*, 2257−2261.
(139) Francl, M. M.; Pietro, W. J.; Hehre, W. J.; Binkley, J. S.; Gordon, M. S.; DeFrees, D. J.; Pople, J. A. Self-Consistent Molecular Orbital Methods. XXIII. A Polarization-Type Basis Set for Second-Row Elements. *J. Chem. Phys.* **1982**, *77*, 3654−3665.
(140) Hay, P. J.; Wadt, W. R. Ab Initio Effective Core Potentials for Molecular Calculations. Potentials for K to Au Including the Outermost Core Orbitals. *J. Chem. Phys.* **1985**, *82*, 299−310.
(141) Dolg, M.; Wedig, U.; Stoll, H.; Preuss, H. Energy-Adjusted Ab Initio Pseudopotentials for the First Row Transition Elements. *J. Chem. Phys.* **1987**, *86*, 866−872.
(142) Bergner, A.; Dolg, M.; Küchle, W.; Stoll, H.; Preuß, H. Ab Initio Energy-Adjusted Pseudopotentials for Elements of Groups 13−17. *Mol. Phys.* **1993**, *80*, 1431−1441.
(143) Xu, X.; Truhlar, D. G. Performance of Effective Core Potentials for Density Functional Calculations on 3d Transition Metals. *J. Chem. Theory Comput.* **2012**, *8*, 80−90.
(144) Santra, G.; Martin, J. M. L. Some Observations on the Performance of the Most Recent Exchange-Correlation Functionals for the Large and Chemically Diverse GMTKN55 Benchmark. *AIP Conf. Proc.* **2019**, *2186*, No. 030004.
(145) Sun, J.; Ruzsinszky, A.; Perdew, J. P. Strongly Constrained and Appropriately Normed Semilocal Density Functional. *Phys. Rev. Lett.* **2015**, *115*, No. 036402.
(146) Ehlert, S.; Huniar, U.; Ning, J.; Furness, J. W.; Sun, J.; Kaplan, A. D.; Perdew, J. P.; Brandenburg, J. G. R2SCAN-D4: Dispersion Corrected Meta-Generalized Gradient Approximation for General Chemical Applications. *J. Chem. Phys.* **2021**, *154*, No. 061101.
(147) Grimme, S.; Hansen, A.; Ehlert, S.; Mewes, J.-M. r2SCAN-3c: A "Swiss Army Knife" Composite Electronic-Structure Method. *J. Chem. Phys.* **2021**, *154*, No. 064103.
(148) Dance, I. Evaluations of the Accuracies of DMol3 Density Functionals for Calculations of Experimental Binding Enthalpies of N2, CO, H2, C2H2 at Catalytic Metal Sites. *Mol. Simul.* **2018**, *44*, 568−581.
(149) Torbjörnsson, M.; Ryde, U. Comparison of the Accuracy of DFT Methods for Reactions with Relevance to Nitrogenase. *Electron. Struct.* **2021**, *3*, No. 034005.

# Article II: Supplementary information

**Analysis of the Geometric and Electronic Structure of Spin-Coupled Iron–Sulfur Dimers with Broken-Symmetry DFT: Implications for FeMoco.**

B. Benediktsson, R. Bjornsson

Journal of Chemical Theory and Computation **18**, 1437-1457, 2022.

# Supporting Information for:
# Analysis of the geometric and electronic structure of spin-coupled iron-sulfur dimers with broken-symmetry DFT: implications for FeMoco

Bardi Benediktsson[a], Ragnar Bjornsson[a,b]*

[a] Science Institute, University of Iceland, Dunhagi 3, 107 Reykjavik, Iceland.

[b] Max Planck Institute for Chemical Energy Conversion, Stiftstrasse 34-36, 45470 Mülheim an der Ruhr, Germany

* E-mail: ragnar.bjornsson@cec.mpg.de

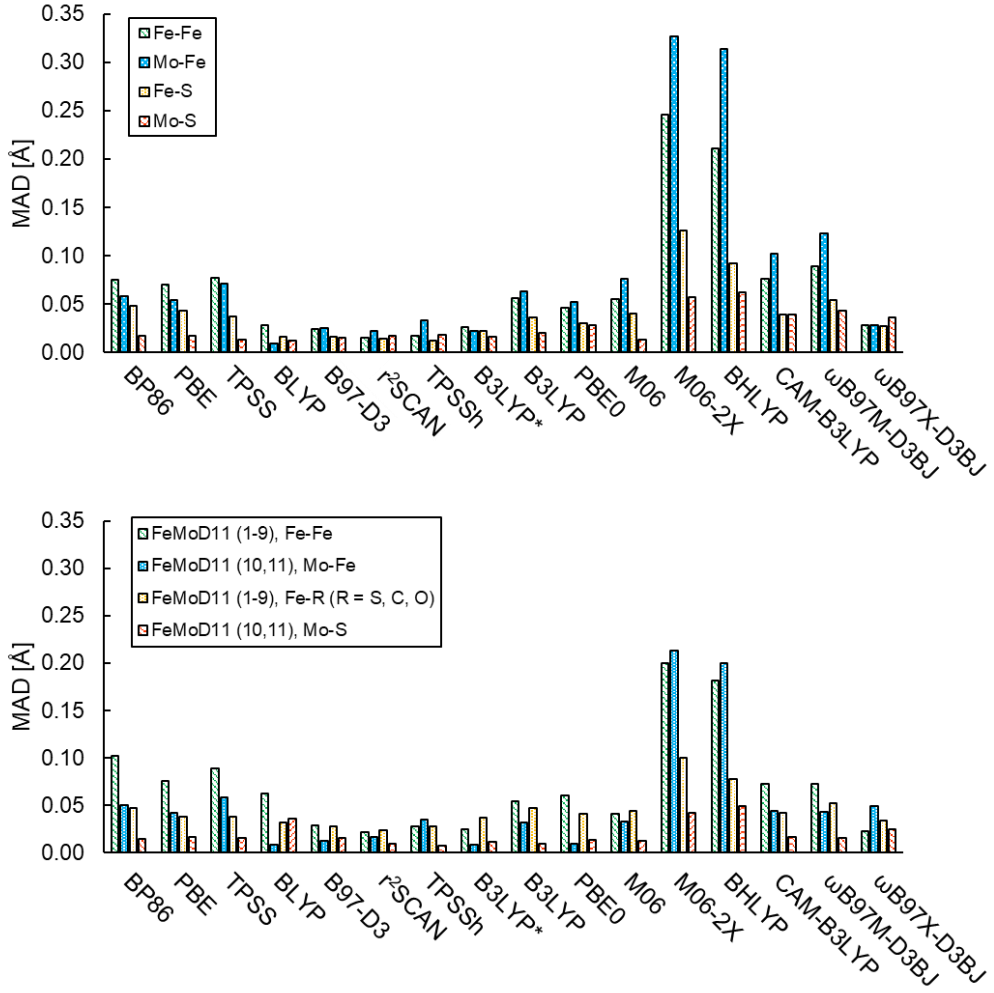


*Figure S1: Top: mean absolute deviations (Å) of calculated Fe-Fe, Mo-Fe, Fe-S, and Mo-S distances of FeMoco (244 QM region QM/MM model) for different functionals, with respect to the X-ray crystal structure. Bottom: mean absolute deviations of calculated Fe-Fe, Mo-Fe, Fe-S, and Mo-S distances in the FeMoD11 test set.*

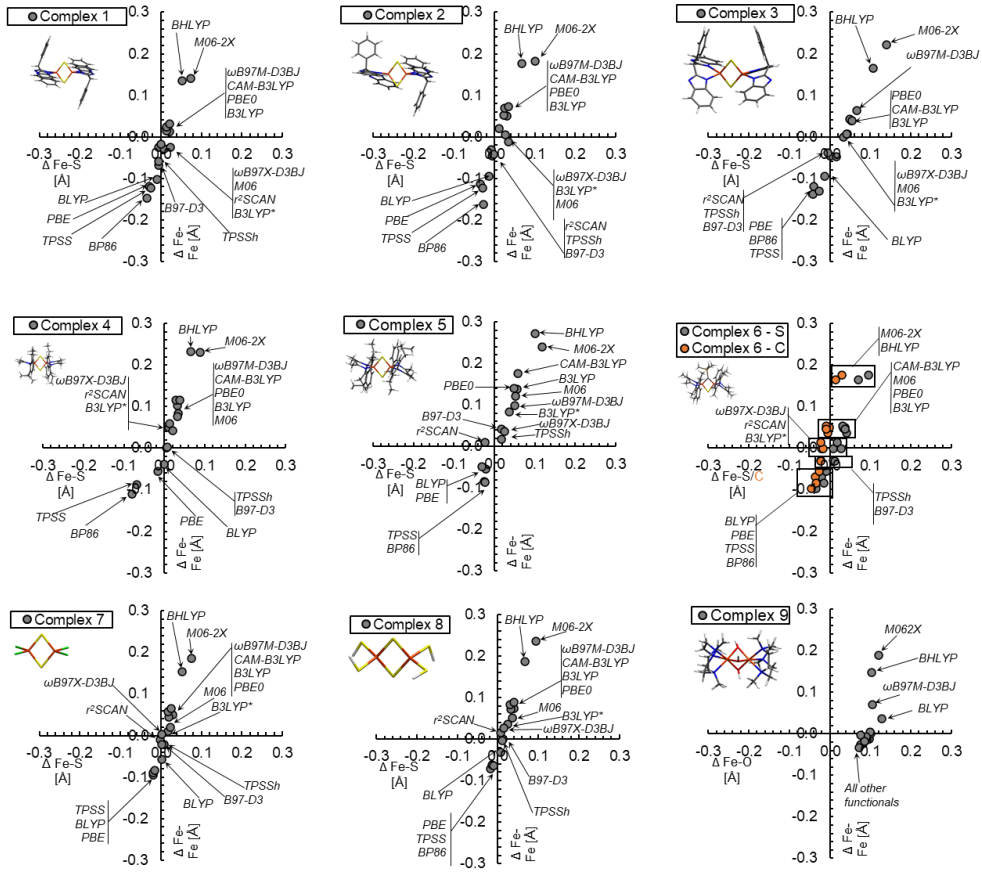


*Figure S2: Deviation of calculated Fe-Fe distance (Å) from the X-ray structure as a function of the mean deviation of the Fe-R bond lengths (Å) for complexes **1**-**9** of FeMoD11 with different functionals (in case of **6**, the grey circles are Fe-C bond lengths).*

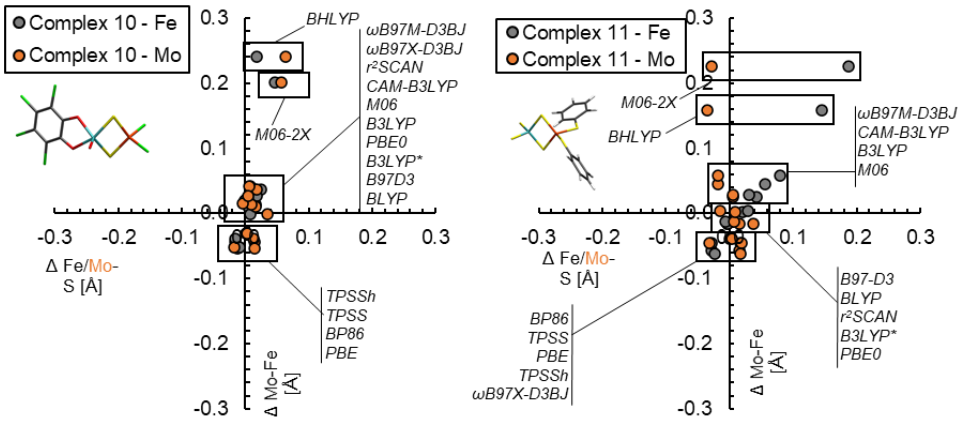


*Figure S3: Deviation of calculated Mo-Fe distance (Å) from the X-ray structure as a function of the mean deviation of the Fe-R bond lengths (Å) for complexes **10** and **11** of FeMoD11 with different functionals (the grey circles are Mo-S bond lengths).*

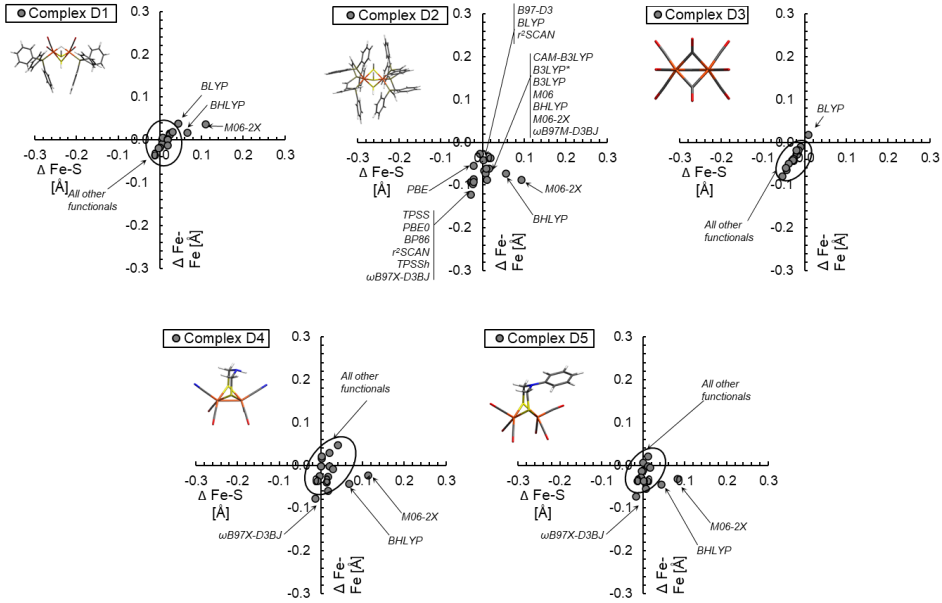


*Figure S4: Deviation of calculated Fe-Fe distance (Å) from the X-ray structure as a function of the mean deviation of the Fe-R bond lengths from the X-ray structure (Å) for complexes **D1**-**D5** of FeCSD5 with different functionals.*

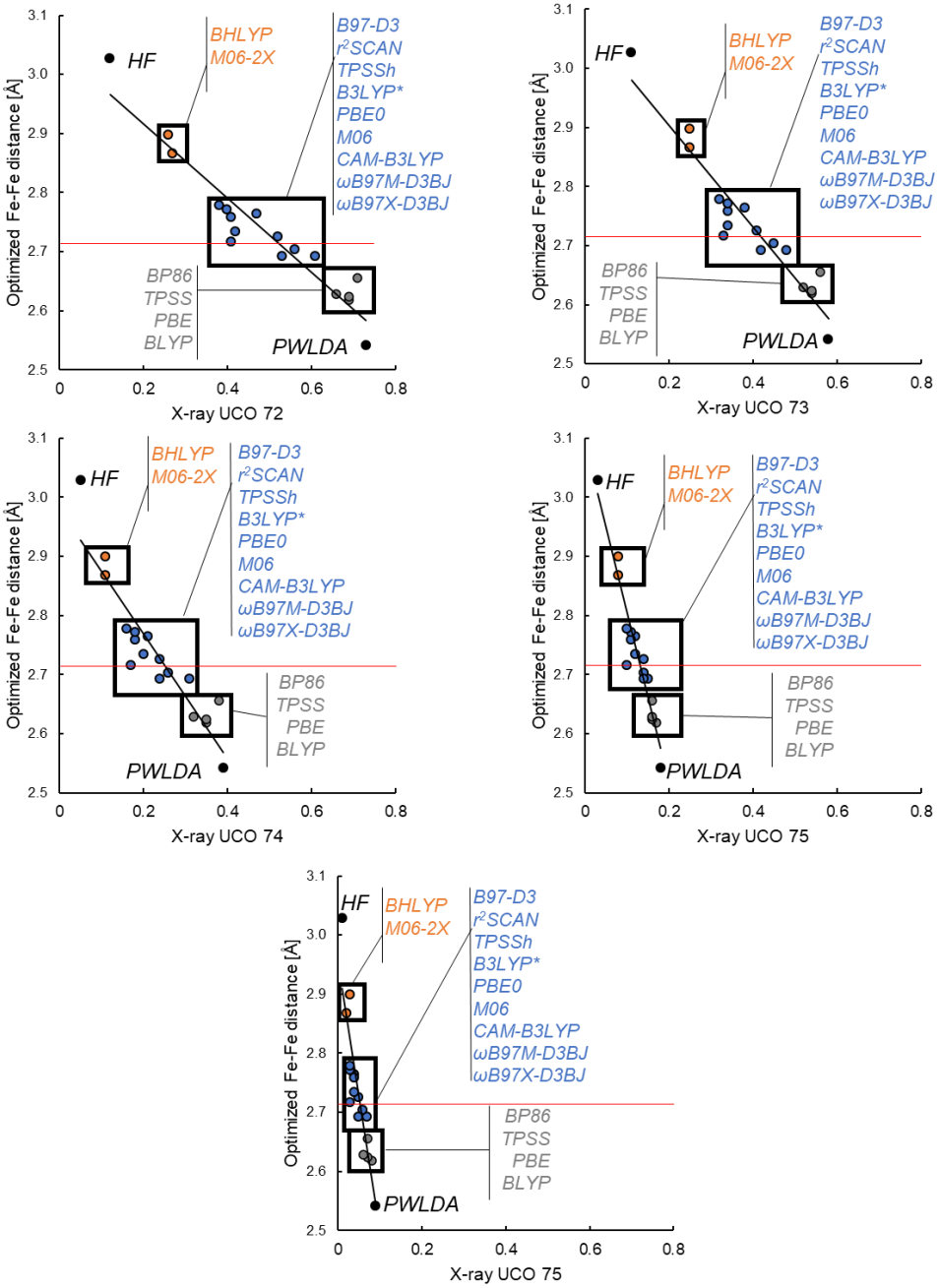


*Figure S5: Optimized Fe-Fe distance (Å) of **7** as a function of different UCO overlaps (see definition of UCO numbers in the main text) from a single point CPCM calculation of the X-ray structure.*

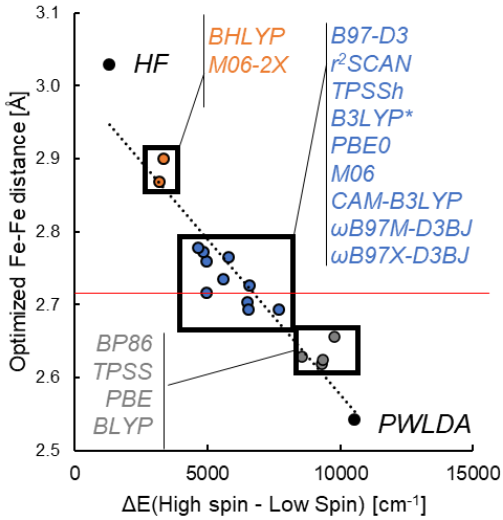


*Figure S6: Optimized Fe-Fe distance (Å) of **7** as a function of high-spin/low-spin energy difference from a single point calculation of the X-ray structure.*

*Table S1: Fe-S Mayer bond orders, Hirshfeld charges on Fe, S and Cl, J-coupling constants ($cm^{-1}$) with different functionals evaluated on the X-ray crystal structure of complex **7**.*

| | BP86 | PBE | TPSS | BLYP | B97-D3 | $r^2$SCAN | TPSSh | B3LYP* | B3LYP | PBE0 | M06 | M062X | BHLYP | CAM-B3LYP | ωB97M-D3BJ | ωB97X-D3BJ |
|---|---|---|---|---|---|---|---|---|---|---|---|---|---|---|---|---|
| Fe-S MBO[a] | 1.11 | 1.11 | 1.10 | 1.09 | 1.07 | 1.07 | 1.08 | 1.06 | 1.04 | 1.05 | 1.05 | 1.01 | 0.98 | 1.04 | 1.07 | 1.05 |
| Ave. Fe HC[b] | 0.07 | 0.07 | 0.10 | 0.07 | 0.10 | 0.14 | 0.15 | 0.14 | 0.17 | 0.19 | 0.18 | 0.30 | 0.30 | 0.20 | 0.21 | 0.22 |
| Ave. S HC[b] | -0.30 | -0.30 | -0.32 | -0.30 | -0.31 | -0.34 | -0.35 | -0.34 | -0.36 | -0.38 | -0.37 | -0.44 | -0.44 | -0.38 | -0.38 | -0.39 |
| Ave. Cl HC[b] | -0.38 | -0.38 | -0.39 | -039 | -0.39 | -0.40 | -0.40 | -0.40 | -0.41 | -0.41 | -0.41 | -0.43 | -0.43 | -0.41 | -0.41 | -0.41 |
| J[c] [$cm^{-1}$] | -359 | -361 | -331 | -376 | -300 | -255 | -256 | -259 | -228 | -196 | -222 | -133 | -127 | -192 | -184 | -197 |
| dE(H-L)[d] [$cm^{-1}$] | 9313 | 9347 | 8547 | 9764 | 7715 | 6537 | 6541 | 6610 | 5805 | 4976 | 5618 | 3343 | 3197 | 4862 | 4643 | 4986 |

[a]Mayer Bond Order
[b]Hirshfeld charge
[c]Yamaguchi J-coupling
[d]Difference in energy between the high spin solution and the low spin broken symmetry solution.

*Table S2: The UCO overlaps with different functionals of the the 5 spin-coupled corresponding orbitals (UCOs: see main text) of complex **7** using the optimized geometry instead of the X-ray geometry.*

| | Overlap | | | | |
|---|---|---|---|---|---|
| Functional | 72 | 73 | 74 | 75 | 76 |
| BP86 | 0.74 | 0.57 | 0.36 | 0.13 | 0.07 |
| PBE | 0.73 | 0.56 | 0.36 | 0.13 | 0.07 |
| TPSS | 0.70 | 0.53 | 0.33 | 0.13 | 0.06 |
| BLYP | 0.72 | 0.56 | 0.39 | 0.14 | 0.07 |
| B97-D3 | 0.61 | 0.48 | 0.31 | 0.15 | 0.07 |
| $r^2$SCAN | 0.56 | 0.45 | 0.26 | 0.14 | 0.06 |
| TPSSh | 0.54 | 0.42 | 0.24 | 0.13 | 0.05 |
| B3LYP* | 0.51 | 0.41 | 0.24 | 0.13 | 0.05 |
| B3LYP | 0.44 | 0.36 | 0.20 | 0.13 | 0.05 |
| PBE0 | 0.39 | 0.33 | 0.17 | 0.11 | 0.04 |
| M06 | 0.41 | 0.33 | 0.19 | 0.11 | 0.04 |
| M06-2X | 0.22 | 0.21 | 0.09 | 0.08 | 0.03 |
| BHLYP | 0.22 | 0.22 | 0.10 | 0.08 | 0.03 |
| CAM-B3LYP | 0.38 | 0.32 | 0.17 | 0.11 | 0.04 |
| ωB97M-D3BJ | 0.34 | 0.31 | 0.15 | 0.10 | 0.03 |
| ωB97x-D3BJ | 0.39 | 0.32 | 0.16 | 0.10 | 0.03 |

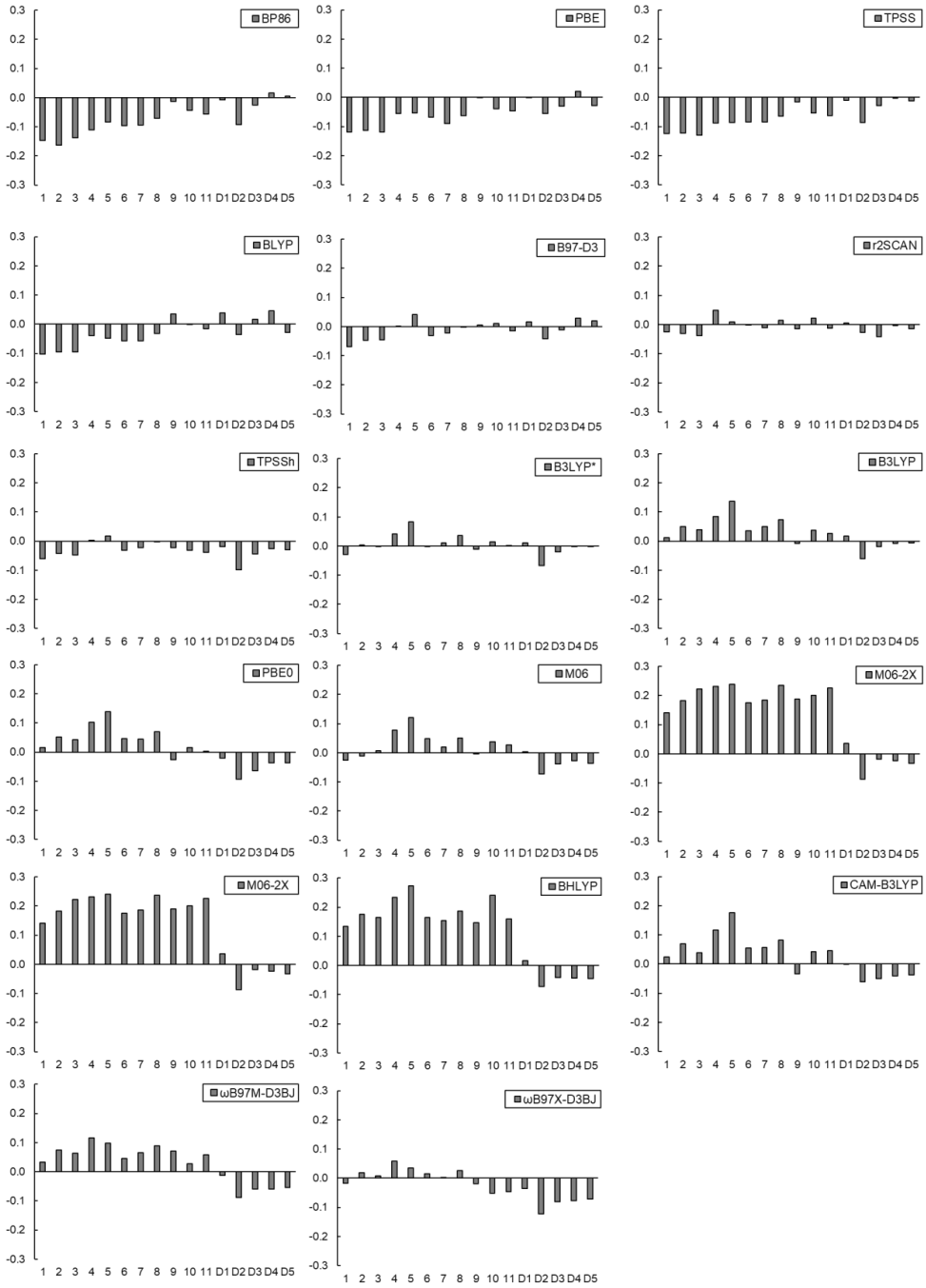


*Figure S7: Fe-Fe distance deviations (Å) for all complexes in FeMoD11 and FeCSD5 for each functional tested.*

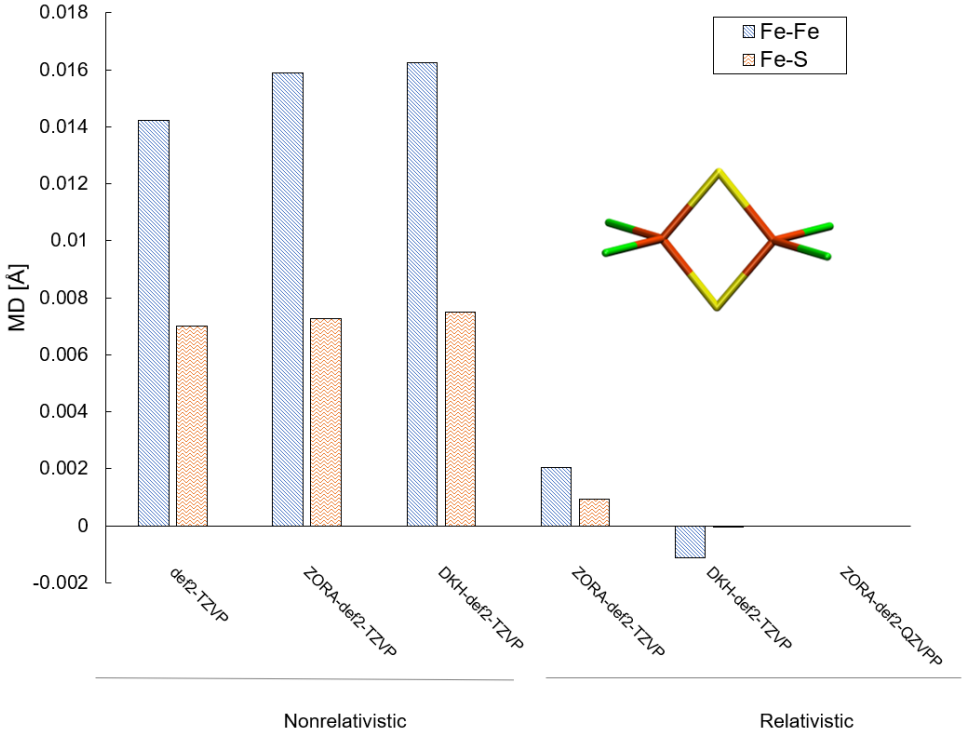


*Figure S8: Mean deviations of Fe-S bond lengths and Fe-Fe distance of complex **7**, $[Fe_2S_2Cl_4]^{2-}$, with and without a scalar relativistic ZORA Hamiltonian or relativistic DKH Hamiltonian with regular Ahlrichs basis set (def2-TZVP) or relativistically reconstracted basis sets for each Hamiltonian (DKH or ZORA). Deviations are relative to the relativistic ZORA-def2-QZVPP reference (r(Fe-Fe) = 2.690 Å and $r_{ave}$(Fe-S) = 2.202 Å). The TPSSh functional was used.*

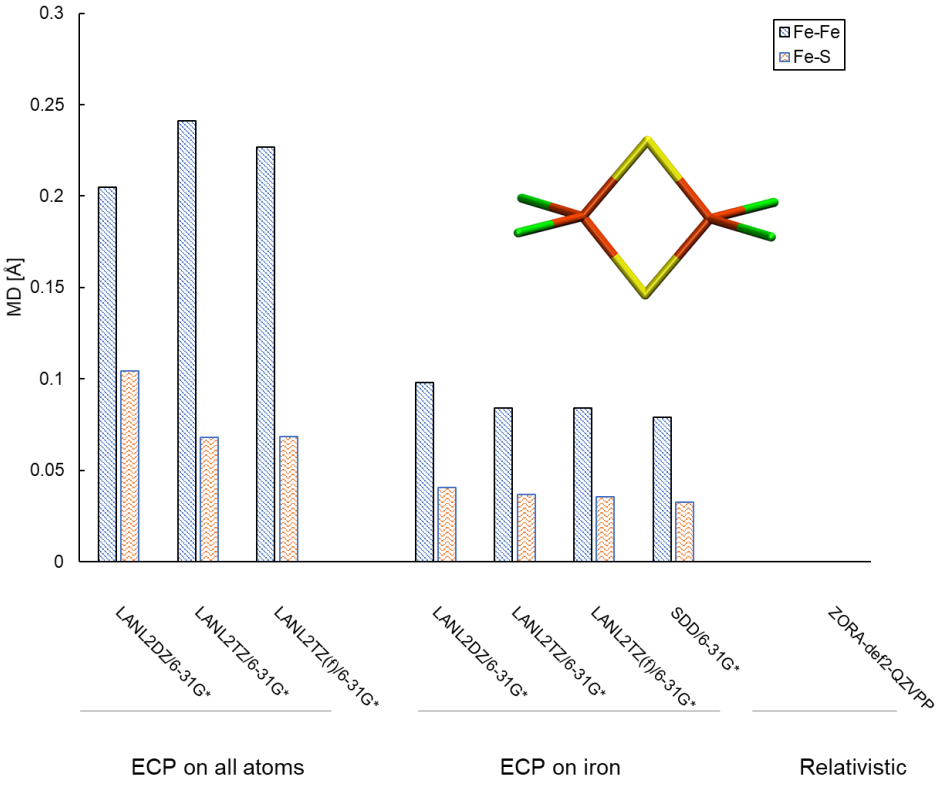


*Figure S9: Mean deviations of Fe-S bond lengths and Fe-Fe distance of complex **7**, $[Fe_2S_2Cl_4]^{2-}$, with or without Hay-Wadt or Stuttgart-Dresden ECPs on all atoms or only on Fe. Deviations are relative to the relativistic ZORA-def2-QZVPP reference (r(Fe-Fe) = 2.690 Å and $r_{ave}$(Fe-S) = 2.202 Å). The TPSSh functional was used.*

*Table S3: Metal-metal distance and metal-ligand bond lengths (Å) for **1**.*

| | Crystal | BP86 | PBE | TPSS | B97D3 | BLYP | r²SCAN | TPSSh | B3LYP* | B3LYP | PBE0 | M06 | M06-2X | BHLYP | CAM-B3LYP | ωB97M-D3BJ | ωB97X-D3BJ |
|---|---|---|---|---|---|---|---|---|---|---|---|---|---|---|---|---|---|
| Fe1-Fe2 | 2.702 | 2.555 | 2.583 | 2.578 | 2.633 | 2.599 | 2.677 | 2.642 | 2.673 | 2.714 | 2.717 | 2.676 | 2.843 | 2.836 | 2.726 | 2.734 | 2.685 |
| Fe1-S1 | 2.208 | 2.174 | 2.180 | 2.183 | 2.205 | 2.199 | 2.195 | 2.204 | 2.218 | 2.231 | 2.223 | 2.242 | 2.282 | 2.258 | 2.224 | 2.230 | 2.209 |
| Fe1-S2 | 2.194 | 2.161 | 2.165 | 2.168 | 2.186 | 2.184 | 2.180 | 2.188 | 2.201 | 2.214 | 2.208 | 2.208 | 2.269 | 2.248 | 2.204 | 2.214 | 2.193 |
| Fe1-N1 | 1.990 | 1.966 | 1.978 | 1.974 | 1.981 | 1.987 | 1.965 | 1.973 | 1.978 | 1.980 | 1.972 | 1.993 | 1.994 | 1.974 | 1.974 | 1.980 | 1.972 |
| Fe1-N2 | 1.978 | 1.967 | 1.978 | 1.974 | 1.981 | 1.987 | 1.965 | 1.973 | 1.978 | 1.980 | 1.971 | 1.961 | 1.990 | 1.973 | 1.974 | 1.980 | 1.971 |
| Fe2-S1 | 2.194 | 2.161 | 2.165 | 2.168 | 2.186 | 2.184 | 2.194 | 2.188 | 2.201 | 2.214 | 2.208 | 2.206 | 2.272 | 2.248 | 2.204 | 2.214 | 2.193 |
| Fe2-S2 | 2.208 | 2.174 | 2.180 | 2.183 | 2.205 | 2.199 | 2.212 | 2.204 | 2.218 | 2.231 | 2.223 | 2.243 | 2.279 | 2.258 | 2.224 | 2.232 | 2.209 |
| Fe2-N3 | 1.990 | 1.966 | 1.978 | 1.974 | 1.981 | 1.987 | 1.982 | 1.973 | 1.978 | 1.981 | 1.972 | 1.961 | 1.989 | 1.974 | 1.974 | 1.981 | 1.972 |
| Fe2-N4 | 1.978 | 1.967 | 1.978 | 1.974 | 1.982 | 1.987 | 1.982 | 1.973 | 1.977 | 1.980 | 1.971 | 1.994 | 1.992 | 1.973 | 1.973 | 1.981 | 1.971 |

*Table S4: Metal-metal distance and metal-ligand bond lengths (Å) for **2**.*

| | Crystal | BP86 | PBE | TPSS | B97D3 | BLYP | r²SCAN | TPSSh | B3LYP* | B3LYP | PBE0 | M06 | M06-2X | BHLYP | CAM-B3LYP | ωB97M-D3BJ | ωB97X-D3BJ |
|---|---|---|---|---|---|---|---|---|---|---|---|---|---|---|---|---|---|
| Fe1-Fe2 | 2.686 | 2.522 | 2.573 | 2.563 | 2.639 | 2.591 | 2.654 | 2.643 | 2.690 | 2.736 | 2.737 | 2.674 | 2.868 | 2.862 | 2.755 | 2.759 | 2.705 |
| Fe1-S1 | 2.220 | 2.201 | 2.192 | 2.202 | 2.234 | 2.213 | 2.226 | 2.253 | 2.219 | 2.303 | 2.302 | 2.321 | 2.439 | 2.372 | 2.310 | 2.322 | 2.294 |
| Fe1-S2 | 2.232 | 2.198 | 2.189 | 2.198 | 2.231 | 2.211 | 2.224 | 2.251 | 2.213 | 2.304 | 2.303 | 2.305 | 2.406 | 2.377 | 2.310 | 2.325 | 2.294 |
| Fe1-N1 | 2.042 | 1.975 | 2.031 | 2.037 | 2.041 | 2.048 | 2.027 | 2.037 | 2.013 | 2.059 | 2.049 | 2.024 | 2.071 | 2.068 | 2.054 | 2.070 | 2.054 |
| Fe1-N2 | 2.053 | 2.053 | 2.048 | 2.037 | 2.053 | 2.060 | 2.041 | 2.045 | 2.012 | 2.051 | 2.041 | 2.092 | 2.119 | 2.059 | 2.047 | 2.062 | 2.047 |
| Fe2-S1 | 2.232 | 2.186 | 2.185 | 2.189 | 2.203 | 2.206 | 2.203 | 2.200 | 2.279 | 2.219 | 2.209 | 2.215 | 2.248 | 2.234 | 2.205 | 2.212 | 2.194 |
| Fe2-S2 | 2.220 | 2.202 | 2.193 | 2.194 | 2.213 | 2.214 | 2.215 | 2.206 | 2.273 | 2.225 | 2.215 | 2.228 | 2.268 | 2.240 | 2.213 | 2.220 | 2.202 |
| Fe2-N3 | 2.042 | 2.022 | 2.023 | 2.015 | 2.028 | 2.033 | 2.023 | 2.015 | 2.052 | 2.022 | 2.011 | 2.026 | 2.043 | 2.009 | 2.015 | 2.022 | 2.012 |
| Fe2-N4 | 2.053 | 1.999 | 2.019 | 2.015 | 2.024 | 2.029 | 2.019 | 2.013 | 2.062 | 2.025 | 2.015 | 2.001 | 2.022 | 2.014 | 2.018 | 2.025 | 2.016 |

*Table S5: Metal-metal distance and metal-ligand bond lengths (Å) for **3**.*

| | Crystal | BP86 | PBE | TPSS | B97D3 | BLYP | r²SCAN | TPSSh | B3LYP* | B3LYP | PBE0 | M06 | M06-2X | BHLYP | CAM-B3LYP | ωB97M-D3BJ | ωB97X-D3BJ |
|---|---|---|---|---|---|---|---|---|---|---|---|---|---|---|---|---|---|
| Fe1-Fe2 | 2.748 | 2.611 | 2.629 | 2.618 | 2.703 | 2.654 | 2.711 | 2.701 | 2.747 | 2.788 | 2.791 | 2.755 | 2.971 | 2.913 | 2.788 | 2.811 | 2.756 |
| Fe1-S1 | 2.267 | 2.222 | 2.225 | 2.237 | 2.266 | 2.252 | 2.248 | 2.282 | 2.299 | 2.320 | 2.314 | 2.307 | 2.405 | 2.375 | 2.321 | 2.333 | 2.308 |
| Fe1-S2 | 2.257 | 2.221 | 2.222 | 2.236 | 2.259 | 2.246 | 2.246 | 2.275 | 2.292 | 2.312 | 2.308 | 2.306 | 2.398 | 2.363 | 2.313 | 2.324 | 2.301 |
| Fe1-N1 | 2.114 | 2.079 | 2.097 | 2.095 | 2.113 | 2.116 | 2.087 | 2.105 | 2.108 | 2.116 | 2.104 | 2.119 | 2.141 | 2.122 | 2.116 | 2.128 | 2.108 |
| Fe1-N2 | 2.115 | 2.081 | 2.102 | 2.095 | 2.112 | 2.118 | 2.093 | 2.098 | 2.112 | 2.121 | 2.109 | 2.111 | 2.146 | 2.122 | 2.121 | 2.132 | 2.117 |
| Fe2-S1 | 2.267 | 2.222 | 2.225 | 2.238 | 2.267 | 2.253 | 2.269 | 2.282 | 2.299 | 2.320 | 2.314 | 2.307 | 2.405 | 2.375 | 2.321 | 2.333 | 2.309 |
| Fe2-S2 | 2.257 | 2.221 | 2.222 | 2.236 | 2.259 | 2.246 | 2.270 | 2.275 | 2.292 | 2.312 | 2.308 | 2.306 | 2.398 | 2.363 | 2.312 | 2.324 | 2.301 |
| Fe2-N3 | 2.114 | 2.079 | 2.097 | 2.095 | 2.113 | 2.116 | 2.121 | 2.105 | 2.108 | 2.116 | 2.104 | 2.119 | 2.140 | 2.122 | 2.116 | 2.129 | 2.108 |
| Fe2-N4 | 2.115 | 2.081 | 2.102 | 2.094 | 2.112 | 2.118 | 2.104 | 2.098 | 2.112 | 2.121 | 2.109 | 2.111 | 2.146 | 2.122 | 2.121 | 2.132 | 2.117 |

*Table S6: Metal-metal distance and metal-ligand bond lengths (Å) for **4.***

| | Crystal | BP86 | PBE | TPSS | B97D3 | BLYP | r²SCAN | TPSSh | B3LYP* | B3LYP | PBE0 | M06 | M06-2X | BHLYP | CAM-B3LYP | ωB97M-D3BJ | ωB97X-D3BJ |
|---|---|---|---|---|---|---|---|---|---|---|---|---|---|---|---|---|---|
| Fe1-Fe2 | 2.679 | 2.569 | 2.624 | 2.591 | 2.680 | 2.641 | 2.728 | 2.682 | 2.721 | 2.763 | 2.781 | 2.756 | 2.910 | 2.912 | 2.795 | 2.795 | 2.738 |
| Fe1-S1 | 2.206 | 2.117 | 2.186 | 2.122 | 2.209 | 2.204 | 2.199 | 2.207 | 2.220 | 2.233 | 2.227 | 2.229 | 2.280 | 2.260 | 2.227 | 2.232 | 2.211 |
| Fe1-S2 | 2.181 | 2.108 | 2.168 | 2.128 | 2.188 | 2.181 | 2.195 | 2.196 | 2.207 | 2.221 | 2.224 | 2.221 | 2.286 | 2.260 | 2.218 | 2.231 | 2.202 |
| Fe1-N1 | 1.996 | 1.907 | 2.010 | 1.920 | 2.011 | 2.017 | 1.991 | 1.994 | 2.000 | 2.003 | 1.994 | 1.999 | 2.008 | 1.993 | 1.997 | 1.999 | 1.988 |
| Fe1-N2 | 2.012 | 1.905 | 1.997 | 1.921 | 2.001 | 2.006 | 1.980 | 1.986 | 1.993 | 1.994 | 1.983 | 1.991 | 1.997 | 1.981 | 1.984 | 1.982 | 1.977 |
| Fe2-S1 | 2.181 | 2.110 | 2.187 | 2.122 | 2.212 | 2.205 | 2.217 | 2.208 | 2.223 | 2.234 | 2.227 | 2.232 | 2.280 | 2.259 | 2.226 | 2.233 | 2.212 |
| Fe2-S2 | 2.206 | 2.120 | 2.167 | 2.128 | 2.187 | 2.180 | 2.207 | 2.194 | 2.204 | 2.222 | 2.222 | 2.219 | 2.281 | 2.259 | 2.218 | 2.229 | 2.200 |
| Fe2-N3 | 1.996 | 1.905 | 2.010 | 1.920 | 2.013 | 2.019 | 2.008 | 1.995 | 2.002 | 2.005 | 1.994 | 2.001 | 2.009 | 1.993 | 1.997 | 1.999 | 1.989 |
| Fe2-N4 | 2.012 | 1.909 | 1.998 | 1.921 | 2.000 | 2.007 | 1.995 | 1.985 | 1.992 | 1.993 | 1.981 | 1.990 | 1.996 | 1.980 | 1.984 | 1.984 | 1.976 |

*Table S7: Metal-metal distance and metal-ligand bond lengths (Å) for **5.***

| | Crystal | BP86 | PBE | TPSS | B97D3 | BLYP | r²SCAN | TPSSh | B3LYP* | B3LYP | PBE0 | M06 | M06-2X | BHLYP | CAM-B3LYP | ωB97M-D3BJ | ωB97X-D3BJ |
|---|---|---|---|---|---|---|---|---|---|---|---|---|---|---|---|---|---|
| Fe1-Fe2 | 2.689 | 2.605 | 2.635 | 2.603 | 2.731 | 2.641 | 2.699 | 2.707 | 2.773 | 2.827 | 2.829 | 2.811 | 2.929 | 2.962 | 2.865 | 2.787 | 2.725 |
| Fe1-S1 | 2.215 | 2.238 | 2.224 | 2.216 | 2.303 | 2.204 | 2.200 | 2.300 | 2.337 | 2.369 | 2.352 | 2.373 | 2.437 | 2.435 | 2.380 | 2.340 | 2.303 |
| Fe1-S2 | 2.233 | 2.207 | 2.217 | 2.221 | 2.264 | 2.181 | 2.182 | 2.275 | 2.296 | 2.324 | 2.325 | 2.313 | 2.413 | 2.397 | 2.343 | 2.329 | 2.298 |
| Fe1-N1 | 2.035 | 1.972 | 2.017 | 2.031 | 1.996 | 2.017 | 1.981 | 2.019 | 2.024 | 2.037 | 2.035 | 2.027 | 2.086 | 2.063 | 2.044 | 2.080 | 2.059 |
| Fe1-N2 | 2.049 | 1.977 | 2.020 | 2.023 | 2.005 | 2.006 | 1.983 | 2.022 | 2.027 | 2.040 | 2.037 | 2.024 | 2.086 | 2.062 | 2.042 | 2.079 | 2.058 |
| Fe2-S1 | 2.227 | 2.158 | 2.171 | 2.174 | 2.182 | 2.205 | 2.197 | 2.183 | 2.192 | 2.201 | 2.194 | 2.190 | 2.252 | 2.220 | 2.192 | 2.209 | 2.190 |
| Fe2-S2 | 2.216 | 2.189 | 2.192 | 2.188 | 2.212 | 2.180 | 2.219 | 2.205 | 2.217 | 2.225 | 2.215 | 2.228 | 2.262 | 2.239 | 2.211 | 2.217 | 2.200 |
| Fe2-N3 | 2.042 | 2.002 | 2.022 | 2.016 | 2.027 | 2.019 | 1.996 | 2.010 | 2.021 | 2.025 | 2.018 | 2.026 | 2.022 | 2.015 | 2.020 | 2.015 | 2.005 |
| Fe2-N4 | 2.045 | 2.004 | 2.029 | 2.018 | 2.033 | 2.007 | 1.998 | 2.014 | 2.027 | 2.031 | 2.022 | 2.022 | 2.028 | 2.016 | 2.023 | 2.017 | 2.010 |

*Table S8: Metal-metal distance and metal-ligand bond lengths for **6.***

| | Crystal | BP86 | PBE | TPSS | B97D3 | BLYP | r²SCAN | TPSSh | B3LYP* | B3LYP | PBE0 | M06 | M06-2X | BHLYP | CAM-B3LYP | ωB97M-D3BJ | ωB97X-D3BJ |
|---|---|---|---|---|---|---|---|---|---|---|---|---|---|---|---|---|---|
| Fe1-Fe2 | 2.603 | 2.506 | 2.534 | 2.518 | 2.573 | 2.546 | 2.602 | 2.571 | 2.601 | 2.639 | 2.650 | 2.652 | 2.778 | 2.768 | 2.657 | 2.648 | 2.617 |
| Fe1-C1 | 2.004 | 1.952 | 1.965 | 1.969 | 1.984 | 1.974 | 1.976 | 1.985 | 1.992 | 2.004 | 1.999 | 2.010 | 2.030 | 2.025 | 2.001 | 2.003 | 1.987 |
| Fe1-S1 | 2.199 | 2.173 | 2.185 | 2.189 | 2.207 | 2.197 | 2.203 | 2.212 | 2.223 | 2.236 | 2.232 | 2.236 | 2.305 | 2.270 | 2.227 | 2.234 | 2.217 |
| Fe1-N1 | 2.007 | 1.981 | 2.005 | 1.995 | 2.011 | 2.010 | 1.988 | 1.994 | 2.001 | 2.003 | 1.993 | 2.002 | 2.006 | 1.993 | 1.996 | 1.992 | 1.986 |
| Fe1-N2 | 1.994 | 1.976 | 1.995 | 1.987 | 1.998 | 2.000 | 1.984 | 1.989 | 1.995 | 1.999 | 1.991 | 1.995 | 2.012 | 1.990 | 1.991 | 1.989 | 1.984 |
| Fe2-C1 | 1.984 | 1.945 | 1.952 | 1.951 | 1.960 | 1.964 | 1.972 | 1.959 | 1.965 | 1.974 | 1.970 | 1.978 | 2.017 | 1.994 | 1.968 | 1.968 | 1.956 |
| Fe2-S1 | 2.235 | 2.193 | 2.208 | 2.217 | 2.244 | 2.220 | 2.248 | 2.248 | 2.265 | 2.280 | 2.269 | 2.272 | 2.321 | 2.306 | 2.271 | 2.276 | 2.254 |
| Fe2-N3 | 2.004 | 1.982 | 2.001 | 1.992 | 2.003 | 2.008 | 2.001 | 1.991 | 1.998 | 2.001 | 1.990 | 2.000 | 2.007 | 1.994 | 1.993 | 1.991 | 1.985 |
| Fe2-N4 | 2.003 | 1.981 | 2.005 | 1.996 | 2.010 | 2.008 | 2.010 | 1.998 | 2.003 | 2.007 | 1.998 | 2.003 | 2.016 | 1.998 | 1.999 | 2.001 | 1.994 |

*Table S9: Metal-metal distance and metal-ligand bond lengths (Å) for **7**.*

| | Crystal | BP86 | PBE | TPSS | B97D3 | BLYP | r²SCAN | TPSSh | B3LYP* | B3LYP | PBE0 | M06 | M06-2X | BHLYP | CAM-B3LYP | ωB97M-D3BJ | ωB97X-D3BJ |
|---|---|---|---|---|---|---|---|---|---|---|---|---|---|---|---|---|---|
| Fe1-Fe2 | 2.714 | 2.619 | 2.624 | 2.629 | 2.692 | 2.656 | 2.703 | 2.692 | 2.725 | 2.764 | 2.758 | 2.734 | 2.899 | 2.868 | 2.771 | 2.778 | 2.716 |
| Fe1-Cl1 | 2.244 | 2.259 | 2.260 | 2.260 | 2.276 | 2.286 | 2.237 | 2.256 | 2.267 | 2.269 | 2.249 | 2.250 | 2.273 | 2.261 | 2.255 | 2.260 | 2.249 |
| Fe1-Cl3 | 2.256 | 2.258 | 2.260 | 2.259 | 2.275 | 2.285 | 2.236 | 2.255 | 2.266 | 2.269 | 2.249 | 2.250 | 2.273 | 2.261 | 2.255 | 2.260 | 2.249 |
| Fe1-S1 | 2.201 | 2.180 | 2.181 | 2.184 | 2.207 | 2.202 | 2.192 | 2.203 | 2.217 | 2.229 | 2.220 | 2.224 | 2.276 | 2.252 | 2.219 | 2.226 | 2.203 |
| Fe1-S2 | 2.198 | 2.179 | 2.180 | 2.183 | 2.206 | 2.201 | 2.191 | 2.202 | 2.216 | 2.227 | 2.219 | 2.223 | 2.274 | 2.251 | 2.217 | 2.224 | 2.202 |
| Fe2-Cl2 | 2.244 | 2.258 | 2.260 | 2.259 | 2.275 | 2.286 | 2.262 | 2.255 | 2.266 | 2.269 | 2.249 | 2.249 | 2.273 | 2.261 | 2.255 | 2.263 | 2.248 |
| Fe2-Cl4 | 2.256 | 2.258 | 2.260 | 2.259 | 2.275 | 2.285 | 2.261 | 2.256 | 2.266 | 2.269 | 2.250 | 2.250 | 2.273 | 2.261 | 2.255 | 2.263 | 2.249 |
| Fe2-S1 | 2.198 | 2.179 | 2.180 | 2.183 | 2.206 | 2.201 | 2.204 | 2.202 | 2.216 | 2.227 | 2.219 | 2.223 | 2.274 | 2.251 | 2.217 | 2.226 | 2.202 |
| Fe2-N4 | 2.201 | 2.180 | 2.181 | 2.184 | 2.207 | 2.202 | 2.205 | 2.203 | 2.217 | 2.229 | 2.220 | 2.224 | 2.276 | 2.252 | 2.219 | 2.227 | 2.203 |

*Table S10: Metal-metal distance and metal-ligand bond lengths (Å) for **8**.*

| | Crystal | BP86 | PBE | TPSS | B97D3 | BLYP | r²SCAN | TPSSh | B3LYP* | B3LYP | PBE0 | M06 | M06-2X | BHLYP | CAM-B3LYP | ωB97M-D3BJ | ωB97X-D3BJ |
|---|---|---|---|---|---|---|---|---|---|---|---|---|---|---|---|---|---|
| Fe1-Fe2 | 2.695 | 2.624 | 2.633 | 2.631 | 2.695 | 2.663 | 2.710 | 2.692 | 2.731 | 2.769 | 2.766 | 2.745 | 2.931 | 2.881 | 2.778 | 2.784 | 2.721 |
| Fe1-Ster | 2.315 | 2.296 | 2.300 | 2.300 | 2.319 | 2.323 | 2.282 | 2.304 | 2.313 | 2.320 | 2.304 | 2.310 | 2.345 | 2.327 | 2.310 | 2.314 | 2.297 |
| Fe1-Ster | 2.316 | 2.315 | 2.320 | 2.322 | 2.343 | 2.348 | 2.309 | 2.323 | 2.336 | 2.339 | 2.321 | 2.336 | 2.351 | 2.335 | 2.323 | 2.324 | 2.308 |
| Fe1-Sbr | 2.203 | 2.188 | 2.189 | 2.193 | 2.216 | 2.211 | 2.204 | 2.212 | 2.227 | 2.240 | 2.232 | 2.243 | 2.290 | 2.268 | 2.230 | 2.237 | 2.214 |
| Fe1-Sbr | 2.196 | 2.184 | 2.187 | 2.191 | 2.215 | 2.208 | 2.198 | 2.213 | 2.228 | 2.242 | 2.234 | 2.235 | 2.296 | 2.269 | 2.233 | 2.242 | 2.218 |
| Fe2-Ster | 2.316 | 2.307 | 2.312 | 2.313 | 2.334 | 2.338 | 2.327 | 2.315 | 2.328 | 2.333 | 2.315 | 2.332 | 2.345 | 2.330 | 2.319 | 2.325 | 2.305 |
| Fe2-Ster | 2.315 | 2.309 | 2.314 | 2.314 | 2.332 | 2.337 | 2.317 | 2.314 | 2.322 | 2.328 | 2.310 | 2.317 | 2.351 | 2.327 | 2.316 | 2.324 | 2.303 |
| Fe2-Sbr | 2.196 | 2.179 | 2.182 | 2.186 | 2.209 | 2.203 | 2.210 | 2.209 | 2.223 | 2.237 | 2.230 | 2.231 | 2.296 | 2.266 | 2.230 | 2.240 | 2.214 |
| Fe2-Sbr | 2.203 | 2.177 | 2.179 | 2.183 | 2.206 | 2.201 | 2.211 | 2.205 | 2.220 | 2.234 | 2.227 | 2.235 | 2.290 | 2.264 | 2.225 | 2.234 | 2.209 |

*Table S11: Metal-metal distance and metal-ligand bond lengths (Å) for **9**.*

| | Crystal | BP86 | PBE | TPSS | B97D3 | BLYP | r²SCAN | TPSSh | B3LYP* | B3LYP | PBE0 | M06 | M06-2X | BHLYP | CAM-B3LYP | ωB97M-D3BJ | ωB97X-D3BJ |
|---|---|---|---|---|---|---|---|---|---|---|---|---|---|---|---|---|---|
| Fe1-Fe2 | 2.508 | 2.495 | 2.508 | 2.493 | 2.513 | 2.544 | 2.493 | 2.485 | 2.498 | 2.501 | 2.482 | 2.504 | 2.697 | 2.655 | 2.474 | 2.579 | 2.489 |
| Fe1-O1 | 1.983 | 2.042 | 2.046 | 2.035 | 2.043 | 2.072 | 2.030 | 2.027 | 2.034 | 2.033 | 2.022 | 2.020 | 1.969 | 2.139 | 2.020 | 2.125 | 2.065 |
| Fe1-O2 | 1.915 | 2.042 | 2.045 | 2.034 | 2.044 | 2.073 | 2.029 | 2.027 | 2.035 | 2.036 | 2.024 | 2.022 | 1.970 | 2.144 | 2.022 | 2.131 | 2.070 |
| Fe1-O3 | 1.933 | 2.041 | 2.044 | 2.034 | 2.041 | 2.070 | 2.029 | 2.025 | 2.033 | 2.032 | 2.019 | 2.018 | 1.970 | 2.140 | 2.018 | 2.127 | 2.066 |
| Fe1-N1 | 2.195 | 2.220 | 2.232 | 2.212 | 2.240 | 2.258 | 2.214 | 2.208 | 2.225 | 2.229 | 2.215 | 2.219 | 2.215 | 2.206 | 2.220 | 2.210 | 2.202 |
| Fe1-N2 | 2.224 | 2.221 | 2.232 | 2.212 | 2.241 | 2.258 | 2.215 | 2.208 | 2.223 | 2.227 | 2.211 | 2.219 | 2.214 | 2.204 | 2.217 | 2.211 | 2.199 |
| Fe1-N3 | 2.216 | 2.221 | 2.233 | 2.214 | 2.242 | 2.260 | 2.216 | 2.209 | 2.225 | 2.228 | 2.214 | 2.219 | 2.216 | 2.205 | 2.218 | 2.211 | 2.202 |
| Fe2-O1 | 1.933 | 2.039 | 2.042 | 2.032 | 2.042 | 2.072 | 2.025 | 2.022 | 2.031 | 2.030 | 2.014 | 2.017 | 2.156 | 1.949 | 2.008 | 1.969 | 1.986 |
| Fe2-O2 | 1.909 | 2.043 | 2.046 | 2.035 | 2.044 | 2.074 | 2.028 | 2.025 | 2.034 | 2.033 | 2.017 | 2.020 | 2.159 | 1.950 | 2.012 | 1.970 | 1.989 |
| Fe2-O3 | 1.983 | 2.038 | 2.042 | 2.032 | 2.040 | 2.068 | 2.026 | 2.022 | 2.030 | 2.029 | 2.014 | 2.017 | 2.152 | 1.948 | 2.008 | 1.969 | 1.989 |
| Fe2-N4 | 2.195 | 2.218 | 2.231 | 2.211 | 2.238 | 2.260 | 2.214 | 2.206 | 2.222 | 2.225 | 2.211 | 2.220 | 2.227 | 2.200 | 2.216 | 2.214 | 2.206 |
| Fe2-N5 | 2.224 | 2.218 | 2.230 | 2.211 | 2.238 | 2.260 | 2.214 | 2.207 | 2.222 | 2.226 | 2.211 | 2.220 | 2.229 | 2.202 | 2.217 | 2.213 | 2.207 |
| Fe2-N6 | 2.216 | 2.218 | 2.229 | 2.209 | 2.237 | 2.258 | 2.212 | 2.205 | 2.221 | 2.224 | 2.209 | 2.217 | 2.227 | 2.201 | 2.215 | 2.211 | 2.205 |

*Table S12: Metal-metal distance and metal-ligand bond lengths (Å) for **10.***

| | Crystal | BP86 | PBE | TPSS | B97D3 | BLYP | r²SCAN | TPSSh | B3LYP* | B3LYP | PBE0 | M06 | M06-2X | BHLYP | CAM-B3LYP | ωB97M-D3BJ | ωB97X-D3BJ |
|---|---|---|---|---|---|---|---|---|---|---|---|---|---|---|---|---|---|
| Mo1-Fe1 | 2.765 | 2.721 | 2.726 | 2.711 | 2.775 | 2.763 | 2.786 | 2.734 | 2.779 | 2.802 | 2.780 | 2.802 | 2.966 | 3.006 | 2.807 | 2.792 | 2.713 |
| Mo1-O1 | 1.677 | 1.707 | 1.705 | 1.706 | 1.699 | 1.719 | 1.693 | 1.693 | 1.696 | 1.692 | 1.675 | 1.676 | 1.662 | 1.661 | 1.674 | 1.667 | 1.665 |
| Mo1-S1 | 2.292 | 2.315 | 2.315 | 2.315 | 2.317 | 2.335 | 2.309 | 2.305 | 2.315 | 2.316 | 2.301 | 2.323 | 2.358 | 2.370 | 2.312 | 2.310 | 2.283 |
| Mo1-S2 | 2.312 | 2.318 | 2.316 | 2.317 | 2.319 | 2.337 | 2.303 | 2.304 | 2.308 | 2.308 | 2.294 | 2.318 | 2.358 | 2.361 | 2.303 | 2.303 | 2.285 |
| Mo1-O2 | 2.044 | 2.068 | 2.070 | 2.062 | 2.074 | 2.087 | 2.061 | 2.055 | 2.070 | 2.068 | 2.048 | 2.053 | 2.042 | 2.028 | 2.048 | 2.056 | 2.047 |
| Mo1-O3 | 2.073 | 2.073 | 2.074 | 2.067 | 2.077 | 2.090 | 2.055 | 2.055 | 2.061 | 2.058 | 2.039 | 2.052 | 2.041 | 2.020 | 2.039 | 2.048 | 2.051 |
| Fe1-Cl1 | 2.250 | 2.257 | 2.259 | 2.261 | 2.274 | 2.282 | 2.255 | 2.259 | 2.266 | 2.271 | 2.255 | 2.256 | 2.281 | 2.261 | 2.260 | 2.273 | 2.259 |
| Fe1-Cl2 | 2.236 | 2.246 | 2.248 | 2.250 | 2.267 | 2.273 | 2.258 | 2.252 | 2.260 | 2.265 | 2.247 | 2.241 | 2.256 | 2.251 | 2.252 | 2.261 | 2.252 |
| Fe1-S1 | 2.225 | 2.209 | 2.210 | 2.213 | 2.229 | 2.233 | 2.222 | 2.226 | 2.238 | 2.247 | 2.232 | 2.239 | 2.272 | 2.239 | 2.230 | 2.240 | 2.217 |
| Fe1-S2 | 2.224 | 2.208 | 2.209 | 2.211 | 2.228 | 2.232 | 2.225 | 2.226 | 2.243 | 2.253 | 2.237 | 2.240 | 2.271 | 2.247 | 2.237 | 2.246 | 2.214 |

*Table S13: Metal-metal distance and metal-ligand bond lengths (Å) for **11.***

| | Crystal | BP86 | PBE | TPSS | B97D3 | BLYP | r²SCAN | TPSSh | B3LYP* | B3LYP | PBE0 | M06 | M06-2X | BHLYP | CAM-B3LYP | ωB97M-D3BJ | ωB97X-D3BJ |
|---|---|---|---|---|---|---|---|---|---|---|---|---|---|---|---|---|---|
| Fe1-Mo1 | 2.756 | 2.699 | 2.710 | 2.694 | 2.741 | 2.740 | 2.743 | 2.718 | 2.758 | 2.782 | 2.760 | 2.784 | 2.982 | 2.915 | 2.802 | 2.815 | 2.710 |
| Fe1-S3 | 2.261 | 2.237 | 2.238 | 2.244 | 2.266 | 2.267 | 2.258 | 2.270 | 2.290 | 2.312 | 2.297 | 2.296 | 2.449 | 2.414 | 2.322 | 2.347 | 2.286 |
| Fe1-S4 | 2.267 | 2.233 | 2.234 | 2.236 | 2.256 | 2.256 | 2.257 | 2.258 | 2.279 | 2.301 | 2.288 | 2.295 | 2.452 | 2.406 | 2.318 | 2.339 | 2.277 |
| Fe1-S5 | 2.299 | 2.268 | 2.274 | 2.278 | 2.296 | 2.296 | 2.297 | 2.294 | 2.303 | 2.315 | 2.308 | 2.317 | 2.387 | 2.352 | 2.315 | 2.330 | 2.302 |
| Fe1-S6 | 2.316 | 2.277 | 2.287 | 2.288 | 2.306 | 2.307 | 2.305 | 2.298 | 2.308 | 2.319 | 2.312 | 2.314 | 2.393 | 2.353 | 2.313 | 2.331 | 2.306 |
| Mo1-S1 | 2.148 | 2.180 | 2.181 | 2.179 | 2.177 | 2.197 | 2.168 | 2.167 | 2.172 | 2.169 | 2.151 | 2.162 | 2.145 | 2.139 | 2.147 | 2.142 | 2.134 |
| Mo1-S2 | 2.156 | 2.182 | 2.178 | 2.176 | 2.176 | 2.195 | 2.170 | 2.165 | 2.171 | 2.168 | 2.150 | 2.166 | 2.141 | 2.144 | 2.150 | 2.141 | 2.133 |
| Mo1-S3 | 2.252 | 2.271 | 2.274 | 2.273 | 2.271 | 2.293 | 2.261 | 2.260 | 2.265 | 2.260 | 2.241 | 2.259 | 2.225 | 2.221 | 2.237 | 2.236 | 2.224 |
| Mo1-S4 | 2.255 | 2.266 | 2.271 | 2.269 | 2.268 | 2.289 | 2.260 | 2.255 | 2.261 | 2.257 | 2.238 | 2.261 | 2.226 | 2.217 | 2.234 | 2.234 | 2.220 |

*Table S14: Metal-metal distance and metal-ligand bond lengths for (Å) **D1.***

| | Crystal | BP86 | PBE | TPSS | B97D3 | BLYP | r²SCAN | TPSSh | B3LYP* | B3LYP | PBE0 | M06 | M06-2X | BHLYP | CAM-B3LYP | ωB97M-D3BJ | ωB97X-D3BJ |
|---|---|---|---|---|---|---|---|---|---|---|---|---|---|---|---|---|---|
| Fe1-Fe2 | 2.589 | 2.581 | 2.589 | 2.579 | 2.605 | 2.628 | 2.594 | 2.571 | 2.601 | 2.607 | 2.569 | 2.592 | 2.625 | 2.606 | 2.589 | 2.577 | 2.554 |
| Fe1-H1 | 1.670 | 1.663 | 1.668 | 1.660 | 1.658 | 1.670 | 1.656 | 1.652 | 1.653 | 1.652 | 1.646 | 1.657 | 1.676 | 1.651 | 1.641 | 1.648 | 1.643 |
| Fe1-P1 | 2.272 | 2.236 | 2.251 | 2.246 | 2.257 | 2.279 | 2.254 | 2.244 | 2.263 | 2.274 | 2.245 | 2.281 | 2.375 | 2.345 | 2.281 | 2.262 | 2.230 |
| Fe1-C17 | 1.781 | 1.753 | 1.753 | 1.764 | 1.751 | 1.770 | 1.749 | 1.767 | 1.770 | 1.779 | 1.764 | 1.783 | 1.888 | 1.859 | 1.787 | 1.801 | 1.784 |
| Fe1-C18 | 1.784 | 1.756 | 1.755 | 1.766 | 1.754 | 1.774 | 1.752 | 1.770 | 1.773 | 1.784 | 1.767 | 1.785 | 1.891 | 1.862 | 1.790 | 1.806 | 1.789 |
| Fe1-S1 | 2.278 | 2.289 | 2.288 | 2.287 | 2.307 | 2.328 | 2.285 | 2.283 | 2.308 | 2.315 | 2.278 | 2.296 | 2.389 | 2.344 | 2.298 | 2.301 | 2.270 |
| Fe1-S2 | 2.268 | 2.283 | 2.282 | 2.281 | 2.298 | 2.318 | 2.286 | 2.276 | 2.299 | 2.306 | 2.272 | 2.300 | 2.386 | 2.344 | 2.298 | 2.295 | 2.265 |
| Fe2-H1 | 1.763 | 1.663 | 1.668 | 1.660 | 1.657 | 1.670 | 1.655 | 1.651 | 1.653 | 1.651 | 1.645 | 1.657 | 1.673 | 1.649 | 1.640 | 1.648 | 1.643 |
| Fe2-S1 | 2.286 | 2.290 | 2.289 | 2.288 | 2.309 | 2.330 | 2.287 | 2.284 | 2.309 | 2.316 | 2.279 | 2.296 | 2.395 | 2.346 | 2.300 | 2.302 | 2.270 |
| Fe2-S2 | 2.283 | 2.281 | 2.281 | 2.280 | 2.297 | 2.317 | 2.285 | 2.275 | 2.298 | 2.304 | 2.271 | 2.301 | 2.382 | 2.344 | 2.297 | 2.293 | 2.264 |
| Fe2-P2 | 2.259 | 2.236 | 2.250 | 2.245 | 2.257 | 2.278 | 2.254 | 2.243 | 2.263 | 2.274 | 2.244 | 2.279 | 2.368 | 2.340 | 2.279 | 2.262 | 2.230 |
| Fe2-C39 | 1.791 | 1.753 | 1.753 | 1.763 | 1.750 | 1.770 | 1.749 | 1.767 | 1.769 | 1.779 | 1.764 | 1.782 | 1.885 | 1.857 | 1.786 | 1.801 | 1.784 |
| Fe2-C40 | 1.793 | 1.756 | 1.755 | 1.766 | 1.754 | 1.773 | 1.752 | 1.770 | 1.773 | 1.783 | 1.767 | 1.785 | 1.892 | 1.863 | 1.791 | 1.805 | 1.789 |

*Table S15: Metal-metal distance and metal-ligand bond lengths (Å) for **D2.***

| | Crystal | BP86 | PBE | TPSS | B97D3 | BLYP | r²SCAN | TPSSh | B3LYP* | B3LYP | PBE0 | M06 | M06-2X | BHLYP | CAM-B3LYP | ωB97M-D3BJ | ωB97X-D3BJ |
|---|---|---|---|---|---|---|---|---|---|---|---|---|---|---|---|---|---|
| Fe1-Fe1 | 3.192 | 3.099 | 3.137 | 3.106 | 3.150 | 3.156 | 3.165 | 3.094 | 3.125 | 3.131 | 3.100 | 3.119 | 3.104 | 3.119 | 3.131 | 3.104 | 3.069 |
| Fe1-S1 | 2.342 | 2.316 | 2.314 | 2.319 | 2.344 | 2.360 | 2.322 | 2.316 | 2.344 | 2.353 | 2.312 | 2.327 | 2.439 | 2.387 | 2.342 | 2.345 | 2.304 |
| Fe1-S2 | 2.332 | 2.329 | 2.334 | 2.334 | 2.363 | 2.376 | 2.352 | 2.333 | 2.361 | 2.374 | 2.335 | 2.369 | 2.442 | 2.414 | 2.367 | 2.369 | 2.329 |
| Fe1-S3 | 2.325 | 2.292 | 2.306 | 2.302 | 2.320 | 2.339 | 2.323 | 2.301 | 2.327 | 2.338 | 2.304 | 2.340 | 2.413 | 2.374 | 2.337 | 2.336 | 2.297 |
| Fe1-P4 | 2.253 | 2.190 | 2.214 | 2.203 | 2.210 | 2.232 | 2.231 | 2.212 | 2.238 | 2.260 | 2.237 | 2.275 | 2.402 | 2.377 | 2.283 | 2.274 | 2.225 |
| Fe1-P5 | 2.230 | 2.147 | 2.161 | 2.155 | 2.156 | 2.180 | 2.168 | 2.159 | 2.179 | 2.193 | 2.173 | 2.196 | 2.394 | 2.272 | 2.200 | 2.199 | 2.161 |
| Fe1-P6 | 2.236 | 2.171 | 2.186 | 2.178 | 2.184 | 2.208 | 2.196 | 2.185 | 2.211 | 2.228 | 2.204 | 2.238 | 2.307 | 2.325 | 2.241 | 2.236 | 2.194 |
| Fe2-S1 | 2.362 | 2.319 | 2.324 | 2.325 | 2.351 | 2.364 | 2.337 | 2.324 | 2.350 | 2.361 | 2.323 | 2.342 | 2.450 | 2.400 | 2.353 | 2.358 | 2.317 |
| Fe2-S2 | 2.345 | 2.327 | 2.328 | 2.330 | 2.357 | 2.373 | 2.340 | 2.327 | 2.356 | 2.367 | 2.326 | 2.358 | 2.436 | 2.399 | 2.356 | 2.355 | 2.316 |
| Fe2-S3 | 2.335 | 2.294 | 2.310 | 2.305 | 2.323 | 2.340 | 2.333 | 2.305 | 2.330 | 2.342 | 2.311 | 2.354 | 2.427 | 2.401 | 2.345 | 2.348 | 2.306 |
| Fe2-P1 | 2.231 | 2.178 | 2.194 | 2.186 | 2.192 | 2.215 | 2.209 | 2.193 | 2.219 | 2.237 | 2.214 | 2.269 | 2.379 | 2.347 | 2.254 | 2.247 | 2.204 |
| Fe2-P2 | 2.204 | 2.150 | 2.163 | 2.158 | 2.159 | 2.184 | 2.170 | 2.162 | 2.182 | 2.196 | 2.175 | 2.203 | 2.299 | 2.274 | 2.203 | 2.201 | 2.163 |
| Fe2-P3 | 2.235 | 2.194 | 2.213 | 2.205 | 2.211 | 2.234 | 2.229 | 2.214 | 2.241 | 2.263 | 2.239 | 2.276 | 2.433 | 2.386 | 2.286 | 2.278 | 2.229 |

*Table S16: Metal-metal distance and metal-ligand bond lengths (Å) for **D3.***

| | Crystal | BP86 | PBE | TPSS | B97D3 | BLYP | r²SCAN | TPSSh | B3LYP* | B3LYP | PBE0 | M06 | M06-2X | BHLYP | CAM-B3LYP | ωB97M-D3BJ | ωB97X-D3BJ |
|---|---|---|---|---|---|---|---|---|---|---|---|---|---|---|---|---|---|
| Fe1-Fe2 | 2.523 | 2.497 | 2.494 | 2.495 | 2.513 | 2.541 | 2.482 | 2.480 | 2.504 | 2.505 | 2.459 | 2.485 | 2.505 | 2.482 | 2.474 | 2.463 | 2.443 |
| Fe1-C1 | 2.013 | 1.995 | 1.993 | 1.996 | 2.004 | 2.022 | 1.983 | 1.987 | 1.997 | 1.999 | 1.971 | 1.987 | 1.994 | 1.987 | 1.975 | 1.969 | 1.960 |
| Fe1-C2 | 1.836 | 1.806 | 1.804 | 1.812 | 1.812 | 1.827 | 1.796 | 1.808 | 1.813 | 1.816 | 1.795 | 1.817 | 1.829 | 1.826 | 1.812 | 1.817 | 1.810 |
| Fe1-C3 | 2.013 | 1.995 | 1.993 | 1.996 | 2.004 | 2.022 | 1.983 | 1.987 | 1.997 | 1.998 | 1.971 | 1.986 | 1.994 | 1.986 | 1.975 | 1.969 | 1.960 |
| Fe1-C4 | 2.013 | 1.995 | 1.994 | 1.996 | 2.003 | 2.022 | 1.984 | 1.986 | 1.997 | 1.998 | 1.970 | 1.985 | 1.993 | 1.985 | 1.975 | 1.969 | 1.960 |
| Fe1-C5 | 1.836 | 1.806 | 1.804 | 1.812 | 1.812 | 1.827 | 1.796 | 1.808 | 1.813 | 1.816 | 1.794 | 1.816 | 1.828 | 1.826 | 1.812 | 1.817 | 1.810 |
| Fe1-C6 | 1.835 | 1.805 | 1.803 | 1.812 | 1.811 | 1.826 | 1.795 | 1.807 | 1.812 | 1.815 | 1.793 | 1.815 | 1.826 | 1.823 | 1.811 | 1.815 | 1.808 |
| Fe2-C1 | 2.013 | 1.995 | 1.994 | 1.996 | 2.004 | 2.022 | 1.983 | 1.987 | 1.997 | 1.999 | 1.971 | 1.987 | 1.994 | 1.986 | 1.975 | 1.969 | 1.960 |
| Fe2-C3 | 2.013 | 1.995 | 1.993 | 1.996 | 2.004 | 2.022 | 1.984 | 1.987 | 1.997 | 1.998 | 1.971 | 1.986 | 1.994 | 1.986 | 1.975 | 1.969 | 1.960 |
| Fe2-C4 | 2.013 | 1.995 | 1.994 | 1.996 | 2.003 | 2.022 | 1.983 | 1.986 | 1.997 | 1.998 | 1.970 | 1.985 | 1.993 | 1.984 | 1.975 | 1.969 | 1.960 |
| Fe2-C7 | 1.836 | 1.806 | 1.804 | 1.812 | 1.812 | 1.827 | 1.796 | 1.808 | 1.813 | 1.816 | 1.795 | 1.817 | 1.829 | 1.826 | 1.812 | 1.817 | 1.810 |
| Fe2-C8 | 1.836 | 1.806 | 1.804 | 1.812 | 1.812 | 1.827 | 1.796 | 1.808 | 1.813 | 1.816 | 1.794 | 1.816 | 1.828 | 1.826 | 1.812 | 1.817 | 1.810 |
| Fe2-C9 | 1.835 | 1.805 | 1.803 | 1.812 | 1.811 | 1.826 | 1.795 | 1.807 | 1.812 | 1.815 | 1.793 | 1.815 | 1.826 | 1.823 | 1.811 | 1.815 | 1.808 |

*Table S17: Metal-metal distance and metal-ligand bond lengths (Å) for **D4.***

| | Crystal | BP86 | PBE | TPSS | B97D3 | BLYP | r²SCAN | TPSSh | B3LYP* | B3LYP | PBE0 | M06 | M06-2X | BHLYP | CAM-B3LYP | ωB97M-D3BJ | ωB97X-D3BJ |
|---|---|---|---|---|---|---|---|---|---|---|---|---|---|---|---|---|---|
| Fe1-Fe2 | 2.509 | 2.525 | 2.530 | 2.506 | 2.538 | 2.556 | 2.506 | 2.484 | 2.507 | 2.501 | 2.473 | 2.482 | 2.486 | 2.465 | 2.469 | 2.450 | 2.431 |
| Fe1-C1 | 1.945 | 1.889 | 1.889 | 1.900 | 1.901 | 1.918 | 1.884 | 1.897 | 1.905 | 1.912 | 1.885 | 1.916 | 1.973 | 1.938 | 1.914 | 1.922 | 1.912 |
| Fe1-C2 | 1.755 | 1.736 | 1.736 | 1.743 | 1.733 | 1.752 | 1.728 | 1.742 | 1.745 | 1.751 | 1.735 | 1.751 | 1.812 | 1.798 | 1.748 | 1.760 | 1.747 |
| Fe1-C3 | 1.741 | 1.736 | 1.735 | 1.743 | 1.733 | 1.752 | 1.728 | 1.741 | 1.745 | 1.750 | 1.735 | 1.751 | 1.813 | 1.798 | 1.748 | 1.759 | 1.746 |
| Fe1-S1 | 2.288 | 2.288 | 2.287 | 2.286 | 2.307 | 2.327 | 2.288 | 2.283 | 2.308 | 2.317 | 2.279 | 2.304 | 2.403 | 2.357 | 2.301 | 2.305 | 2.275 |
| Fe1-S2 | 2.278 | 2.288 | 2.287 | 2.286 | 2.307 | 2.327 | 2.287 | 2.282 | 2.308 | 2.317 | 2.279 | 2.303 | 2.403 | 2.356 | 2.302 | 2.305 | 2.274 |
| Fe2-C4 | 1.743 | 1.739 | 1.738 | 1.745 | 1.736 | 1.755 | 1.731 | 1.744 | 1.747 | 1.753 | 1.738 | 1.753 | 1.818 | 1.800 | 1.750 | 1.762 | 1.748 |
| Fe2-C5 | 1.939 | 1.886 | 1.887 | 1.897 | 1.898 | 1.915 | 1.881 | 1.895 | 1.903 | 1.910 | 1.883 | 1.913 | 1.969 | 1.936 | 1.911 | 1.919 | 1.910 |
| Fe2-C6 | 1.745 | 1.739 | 1.738 | 1.745 | 1.736 | 1.754 | 1.731 | 1.744 | 1.747 | 1.752 | 1.737 | 1.753 | 1.818 | 1.800 | 1.750 | 1.761 | 1.748 |
| Fe2-S1 | 2.290 | 2.282 | 2.282 | 2.281 | 2.301 | 2.321 | 2.280 | 2.276 | 2.301 | 2.308 | 2.271 | 2.296 | 2.388 | 2.343 | 2.292 | 2.294 | 2.265 |
| Fe2-S2 | 2.277 | 2.282 | 2.281 | 2.281 | 2.301 | 2.321 | 2.281 | 2.276 | 2.300 | 2.308 | 2.270 | 2.296 | 2.390 | 2.346 | 2.292 | 2.294 | 2.265 |

*Table S18: Metal-metal distance and metal-ligand bond lengths (Å) for **D5.***

| | Crystal | BP86 | PBE | TPSS | B97D3 | BLYP | r²SCAN | TPSSh | B3LYP* | B3LYP | PBE0 | M06 | M06-2X | BHLYP | CAM-B3LYP | ωB97M-D3BJ | ωB97X-D3BJ |
|---|---|---|---|---|---|---|---|---|---|---|---|---|---|---|---|---|---|
| Fe-Fe | 2.505 | 2.510 | 2.476 | 2.492 | 2.525 | 2.476 | 2.491 | 2.476 | 2.502 | 2.499 | 2.468 | 2.468 | 2.472 | 2.459 | 2.468 | 2.450 | 2.432 |
| Fe1-CO | 1.804 | 1.768 | 1.773 | 1.776 | 1.772 | 1.773 | 1.760 | 1.773 | 1.778 | 1.783 | 1.762 | 1.785 | 1.829 | 1.814 | 1.782 | 1.790 | 1.780 |
| Fe1-CO | 1.793 | 1.771 | 1.779 | 1.780 | 1.773 | 1.779 | 1.764 | 1.779 | 1.783 | 1.789 | 1.772 | 1.787 | 1.844 | 1.827 | 1.788 | 1.797 | 1.786 |
| Fe1-CO | 1.802 | 1.772 | 1.779 | 1.780 | 1.773 | 1.779 | 1.764 | 1.779 | 1.783 | 1.789 | 1.771 | 1.788 | 1.842 | 1.825 | 1.787 | 1.796 | 1.785 |
| Fe1-S | 2.266 | 2.275 | 2.265 | 2.272 | 2.289 | 2.265 | 2.271 | 2.265 | 2.287 | 2.292 | 2.255 | 2.283 | 2.357 | 2.313 | 2.272 | 2.273 | 2.246 |
| Fe1-S | 2.266 | 2.276 | 2.265 | 2.273 | 2.289 | 2.265 | 2.270 | 2.265 | 2.286 | 2.290 | 2.255 | 2.281 | 2.358 | 2.310 | 2.269 | 2.271 | 2.245 |
| Fe2-CO | 1.824 | 1.774 | 1.780 | 1.782 | 1.778 | 1.780 | 1.767 | 1.780 | 1.785 | 1.790 | 1.769 | 1.793 | 1.849 | 1.826 | 1.789 | 1.800 | 1.789 |
| Fe2-CO | 1.797 | 1.767 | 1.776 | 1.776 | 1.769 | 1.776 | 1.761 | 1.776 | 1.780 | 1.786 | 1.768 | 1.783 | 1.840 | 1.827 | 1.785 | 1.795 | 1.783 |
| Fe2-S | 2.255 | 2.269 | 2.260 | 2.266 | 2.281 | 2.260 | 2.266 | 2.260 | 2.282 | 2.287 | 2.253 | 2.283 | 2.376 | 2.316 | 2.270 | 2.272 | 2.245 |
| Fe2-S | 2.277 | 2.284 | 2.274 | 2.280 | 2.299 | 2.274 | 2.282 | 2.274 | 2.297 | 2.303 | 2.267 | 2.294 | 2.381 | 2.330 | 2.284 | 2.289 | 2.260 |
| Fe2-CO | 1.789 | 1.765 | 1.772 | 1.773 | 1.765 | 1.772 | 1.757 | 1.772 | 1.776 | 1.782 | 1.764 | 1.780 | 1.834 | 1.820 | 1.781 | 1.789 | 1.777 |

*Table S19: Metal-metal distance and metal-ligand bond lengths (Å) for the 244 QM atom QM/MM model of FeMoco.*

| | X-ray | X-ray | Ave X Ray | BP86 | PBE | TPSS | B97D3 | BLYP | r²SCAN | TPSSh | B3LYP* | B3LYP | PBE0 | M06 | M06-2X | BHLYP | CAM-B3LYP | ωB97M-D3BJ | ωB97X-D3BJ |
|---|---|---|---|---|---|---|---|---|---|---|---|---|---|---|---|---|---|---|---|
| Mo_C | 3.530 | 3.550 | 3.540 | 3.466 | 3.476 | 3.459 | 3.507 | 3.553 | 3.516 | 3.496 | 3.545 | 3.594 | 3.587 | 3.614 | 3.872 | 3.854 | 3.631 | 3.659 | 3.562 |
| C_Fe1 | 3.467 | 3.448 | 3.458 | 3.373 | 3.385 | 3.365 | 3.434 | 3.462 | 3.454 | 3.451 | 3.496 | 3.539 | 3.534 | 3.529 | 3.764 | 3.748 | 3.594 | 3.603 | 3.529 |
| Mo_Fe1 | 6.996 | 6.997 | 6.997 | 6.836 | 6.858 | 6.822 | 6.938 | 7.012 | 6.969 | 6.946 | 7.040 | 7.132 | 7.121 | 7.141 | 7.635 | 7.600 | 7.224 | 7.261 | 7.089 |
| Fe1_Fe2 | 2.668 | 2.669 | 2.668 | 2.554 | 2.558 | 2.551 | 2.626 | 2.615 | 2.649 | 2.655 | 2.708 | 2.756 | 2.747 | 2.749 | 2.981 | 2.977 | 2.802 | 2.803 | 2.737 |
| Fe1_Fe3 | 2.663 | 2.668 | 2.665 | 2.553 | 2.561 | 2.548 | 2.623 | 2.633 | 2.644 | 2.633 | 2.683 | 2.723 | 2.711 | 2.698 | 2.885 | 2.877 | 2.766 | 2.762 | 2.698 |
| Fe1_Fe4 | 2.662 | 2.655 | 2.658 | 2.650 | 2.654 | 2.622 | 2.672 | 2.721 | 2.663 | 2.643 | 2.681 | 2.701 | 2.689 | 2.685 | 2.903 | 2.908 | 2.758 | 2.764 | 2.694 |
| Fe2_Fe3 | 2.667 | 2.672 | 2.669 | 2.575 | 2.573 | 2.580 | 2.665 | 2.639 | 2.659 | 2.659 | 2.717 | 2.757 | 2.726 | 2.745 | 2.985 | 2.986 | 2.770 | 2.805 | 2.702 |
| Fe2_Fe4 | 2.654 | 2.654 | 2.654 | 2.565 | 2.567 | 2.561 | 2.622 | 2.620 | 2.633 | 2.635 | 2.682 | 2.715 | 2.705 | 2.720 | 2.869 | 2.834 | 2.729 | 2.732 | 2.679 |
| Fe3_Fe4 | 2.644 | 2.641 | 2.642 | 2.552 | 2.556 | 2.550 | 2.605 | 2.609 | 2.614 | 2.612 | 2.651 | 2.686 | 2.679 | 2.681 | 2.913 | 2.851 | 2.717 | 2.735 | 2.667 |
| Fe2_Fe6 | 2.580 | 2.576 | 2.578 | 2.517 | 2.524 | 2.527 | 2.562 | 2.568 | 2.580 | 2.587 | 2.599 | 2.609 | 2.609 | 2.630 | 2.756 | 2.737 | 2.597 | 2.625 | 2.585 |
| Fe4_Fe5 | 2.612 | 2.612 | 2.612 | 2.551 | 2.550 | 2.563 | 2.583 | 2.599 | 2.597 | 2.594 | 2.606 | 2.633 | 2.645 | 2.649 | 2.757 | 2.690 | 2.645 | 2.668 | 2.636 |
| Fe3_Fe7 | 2.589 | 2.583 | 2.586 | 2.537 | 2.563 | 2.551 | 2.584 | 2.600 | 2.597 | 2.597 | 2.614 | 2.633 | 2.634 | 2.636 | 2.746 | 2.688 | 2.629 | 2.650 | 2.619 |
| Fe5_Fe6 | 2.630 | 2.632 | 2.631 | 2.548 | 2.553 | 2.544 | 2.607 | 2.616 | 2.619 | 2.627 | 2.678 | 2.712 | 2.700 | 2.710 | 2.993 | 2.915 | 2.724 | 2.736 | 2.665 |
| Fe5_Fe7 | 2.631 | 2.627 | 2.629 | 2.564 | 2.563 | 2.551 | 2.606 | 2.614 | 2.609 | 2.616 | 2.660 | 2.688 | 2.676 | 2.695 | 2.855 | 2.755 | 2.691 | 2.693 | 2.645 |
| Fe6_Fe7 | 2.595 | 2.601 | 2.598 | 2.522 | 2.523 | 2.513 | 2.575 | 2.574 | 2.574 | 2.568 | 2.618 | 2.652 | 2.629 | 2.658 | 2.896 | 2.907 | 2.673 | 2.691 | 2.604 |
| Mo_Fe6 | 2.667 | 2.674 | 2.671 | 2.618 | 2.620 | 2.605 | 2.640 | 2.672 | 2.651 | 2.646 | 2.696 | 2.755 | 2.753 | 2.769 | 3.022 | 3.036 | 2.814 | 2.835 | 2.735 |
| Mo_Fe7 | 2.676 | 2.681 | 2.679 | 2.606 | 2.615 | 2.592 | 2.634 | 2.680 | 2.635 | 2.620 | 2.671 | 2.724 | 2.713 | 2.727 | 3.080 | 3.054 | 2.781 | 2.813 | 2.697 |
| Mo_Fe5 | 2.725 | 2.727 | 2.726 | 2.677 | 2.679 | 2.664 | 2.725 | 2.753 | 2.722 | 2.710 | 2.761 | 2.786 | 2.764 | 2.807 | 2.952 | 2.927 | 2.788 | 2.797 | 2.728 |
| Fe1_S1 | 2.306 | 2.295 | 2.300 | 2.259 | 2.260 | 2.272 | 2.300 | 2.305 | 2.300 | 2.308 | 2.325 | 2.347 | 2.343 | 2.336 | 2.483 | 2.472 | 2.394 | 2.414 | 2.367 |
| Fe1_S2 | 2.270 | 2.266 | 2.268 | 2.188 | 2.190 | 2.201 | 2.222 | 2.222 | 2.234 | 2.237 | 2.252 | 2.271 | 2.274 | 2.283 | 2.386 | 2.353 | 2.283 | 2.295 | 2.265 |
| Fe1_S3 | 2.289 | 2.287 | 2.288 | 2.256 | 2.258 | 2.265 | 2.298 | 2.309 | 2.298 | 2.301 | 2.324 | 2.341 | 2.329 | 2.328 | 2.482 | 2.435 | 2.368 | 2.385 | 2.340 |
| Fe2_S1 | 2.263 | 2.261 | 2.262 | 2.164 | 2.169 | 2.180 | 2.215 | 2.208 | 2.227 | 2.247 | 2.268 | 2.295 | 2.294 | 2.302 | 2.381 | 2.348 | 2.295 | 2.309 | 2.283 |
| Fe2_S2 | 2.246 | 2.254 | 2.250 | 2.186 | 2.192 | 2.202 | 2.239 | 2.245 | 2.246 | 2.258 | 2.275 | 2.283 | 2.271 | 2.294 | 2.318 | 2.300 | 2.263 | 2.276 | 2.254 |
| Fe2_S7 | 2.198 | 2.206 | 2.202 | 2.152 | 2.157 | 2.159 | 2.180 | 2.184 | 2.181 | 2.192 | 2.207 | 2.220 | 2.214 | 2.234 | 2.265 | 2.231 | 2.206 | 2.217 | 2.200 |
| Fe3_S2 | 2.267 | 2.275 | 2.271 | 2.226 | 2.230 | 2.243 | 2.288 | 2.280 | 2.292 | 2.301 | 2.328 | 2.356 | 2.343 | 2.342 | 2.480 | 2.423 | 2.375 | 2.405 | 2.346 |
| Fe3_S3 | 2.251 | 2.254 | 2.253 | 2.175 | 2.181 | 2.191 | 2.221 | 2.227 | 2.231 | 2.247 | 2.266 | 2.291 | 2.296 | 2.300 | 2.397 | 2.360 | 2.305 | 2.313 | 2.288 |
| Fe3_S9 | 2.229 | 2.221 | 2.225 | 2.183 | 2.189 | 2.192 | 2.211 | 2.227 | 2.212 | 2.221 | 2.233 | 2.250 | 2.251 | 2.253 | 2.342 | 2.302 | 2.251 | 2.271 | 2.248 |
| Fe4_S1 | 2.286 | 2.286 | 2.286 | 2.257 | 2.264 | 2.266 | 2.296 | 2.314 | 2.298 | 2.285 | 2.300 | 2.300 | 2.286 | 2.318 | 2.321 | 2.300 | 2.270 | 2.277 | 2.255 |
| Fe4_S3 | 2.286 | 2.287 | 2.286 | 2.261 | 2.271 | 2.273 | 2.305 | 2.320 | 2.303 | 2.295 | 2.311 | 2.316 | 2.301 | 2.318 | 2.336 | 2.311 | 2.289 | 2.302 | 2.275 |
| Fe4_S8 | 2.240 | 2.240 | 2.240 | 2.196 | 2.209 | 2.215 | 2.240 | 2.251 | 2.248 | 2.244 | 2.258 | 2.271 | 2.266 | 2.280 | 2.303 | 2.270 | 2.255 | 2.260 | 2.246 |
| Fe5_S4 | 2.261 | 2.268 | 2.264 | 2.216 | 2.220 | 2.224 | 2.257 | 2.263 | 2.261 | 2.265 | 2.292 | 2.311 | 2.297 | 2.312 | 2.453 | 2.422 | 2.322 | 2.350 | 2.291 |
| Fe5_S6 | 2.256 | 2.250 | 2.253 | 2.207 | 2.216 | 2.221 | 2.253 | 2.263 | 2.253 | 2.264 | 2.291 | 2.310 | 2.297 | 2.309 | 2.468 | 2.425 | 2.311 | 2.339 | 2.290 |
| Fe5_S8 | 2.261 | 2.261 | 2.261 | 2.192 | 2.204 | 2.206 | 2.225 | 2.242 | 2.221 | 2.226 | 2.239 | 2.252 | 2.248 | 2.248 | 2.344 | 2.311 | 2.249 | 2.268 | 2.242 |
| Fe6_S4 | 2.237 | 2.234 | 2.236 | 2.189 | 2.192 | 2.193 | 2.216 | 2.234 | 2.232 | 2.234 | 2.257 | 2.284 | 2.284 | 2.293 | 2.398 | 2.366 | 2.294 | 2.313 | 2.269 |
| Fe6_S5 | 2.220 | 2.219 | 2.220 | 2.175 | 2.179 | 2.187 | 2.209 | 2.224 | 2.222 | 2.226 | 2.242 | 2.260 | 2.252 | 2.260 | 2.383 | 2.353 | 2.267 | 2.292 | 2.244 |
| Fe6_S7 | 2.178 | 2.173 | 2.175 | 2.147 | 2.153 | 2.157 | 2.171 | 2.188 | 2.184 | 2.186 | 2.194 | 2.206 | 2.208 | 2.212 | 2.287 | 2.254 | 2.206 | 2.220 | 2.200 |
| Fe7_S5 | 2.253 | 2.246 | 2.250 | 2.231 | 2.232 | 2.239 | 2.265 | 2.272 | 2.271 | 2.278 | 2.304 | 2.320 | 2.309 | 2.322 | 2.377 | 2.338 | 2.308 | 2.323 | 2.296 |
| Fe7_S6 | 2.221 | 2.220 | 2.220 | 2.180 | 2.183 | 2.185 | 2.208 | 2.218 | 2.213 | 2.210 | 2.233 | 2.255 | 2.248 | 2.259 | 2.404 | 2.359 | 2.266 | 2.287 | 2.240 |
| Fe7_S9 | 2.213 | 2.210 | 2.212 | 2.167 | 2.174 | 2.175 | 2.195 | 2.208 | 2.202 | 2.200 | 2.214 | 2.224 | 2.218 | 2.230 | 2.255 | 2.233 | 2.214 | 2.222 | 2.213 |
| Mo_S4 | 2.358 | 2.348 | 2.353 | 2.329 | 2.329 | 2.333 | 2.328 | 2.358 | 2.327 | 2.328 | 2.334 | 2.333 | 2.318 | 2.352 | 2.331 | 2.319 | 2.316 | 2.314 | 2.302 |
| Mo_S5 | 2.371 | 2.367 | 2.369 | 2.367 | 2.362 | 2.369 | 2.367 | 2.391 | 2.366 | 2.368 | 2.381 | 2.397 | 2.390 | 2.406 | 2.482 | 2.475 | 2.420 | 2.425 | 2.380 |
| Mo_S6 | 2.354 | 2.354 | 2.354 | 2.330 | 2.333 | 2.336 | 2.335 | 2.364 | 2.330 | 2.327 | 2.337 | 2.340 | 2.325 | 2.356 | 2.318 | 2.307 | 2.324 | 2.319 | 2.307 |
| C_Fe2 | 2.014 | 1.997 | 2.005 | 1.926 | 1.931 | 1.931 | 1.979 | 1.974 | 1.983 | 1.991 | 2.019 | 2.034 | 2.025 | 2.050 | 2.069 | 2.056 | 2.024 | 2.023 | 1.996 |
| C_Fe3 | 1.990 | 1.984 | 1.987 | 1.943 | 1.945 | 1.945 | 1.991 | 1.984 | 1.995 | 2.010 | 2.042 | 2.083 | 2.074 | 2.074 | 2.370 | 2.324 | 2.115 | 2.162 | 2.072 |
| C_Fe4 | 2.003 | 1.991 | 1.997 | 1.952 | 1.958 | 1.957 | 1.980 | 1.992 | 1.992 | 1.983 | 2.001 | 2.016 | 2.018 | 2.019 | 2.092 | 2.060 | 2.115 | 2.036 | 2.009 |
| C_Fe5 | 2.006 | 2.008 | 2.007 | 1.960 | 1.963 | 1.958 | 1.980 | 1.999 | 1.969 | 1.972 | 1.990 | 2.001 | 2.001 | 2.004 | 2.153 | 2.064 | 2.004 | 2.012 | 1.986 |
| C_Fe6 | 2.008 | 2.018 | 2.013 | 1.941 | 1.944 | 1.944 | 1.988 | 1.986 | 2.009 | 2.004 | 2.035 | 2.058 | 2.047 | 2.060 | 2.328 | 2.331 | 2.065 | 2.093 | 2.023 |
| C_Fe7 | 1.979 | 1.997 | 1.988 | 1.946 | 1.951 | 1.946 | 1.986 | 1.990 | 1.998 | 1.992 | 2.019 | 2.040 | 2.034 | 2.051 | 2.022 | 1.991 | 2.039 | 2.028 | 2.015 |

# Article III

**Environmental effects in theoretical calculations of $^{57}$Fe nuclear resonance vibrational spectra: from molecular complexes to complex metalloproteins.**

B. Benediktsson, R. Bjornsson

Manuscript in preparation

# Computing Nuclear Resonance Vibrational Spectra of Fe-S systems


## Abstract

Nuclear resonance vibrational spectroscopy (NRVS) is a spectroscopy method that offers high specificity to study vibrational modes of the metal center of metalloproteins that include a Mössbauer active isotope such as $^{57}$Fe. Iron-sulfur proteins such as nitrogenase have been experimentally characterized with NRVS but it is not clear how well the NRVS spectra of iron-sulfur clusters in proteins can be calculated. It has previously been demonstrated that the geometries and energetics of iron-sulfur clusters are sensitive both to the choice of density functional and whether the protein environment is described explicitly or implicitly. Here, we demonstrate that in order to accurately compute NRVS spectra for iron-sulfur clusters, one must consider the density functional choice, the model size, and the number of atoms included in the calculation of the Hessian. For a qualitative picture of a NRVS spectrum a relatively small model is needed but for a quantitative picture more details need to be considered.


## 1. Introduction

Iron-sulfur systems are present in many proteins where they are essential to the normal function of living organisms. Vibrational spectroscopy can give a great insight into molecular properties of such proteins but usual vibrational spectroscopy methods, infrared (IR) and resonance Raman (RR) lack specificity. Nuclear resonance vibrational spectroscopy (NRVS) is a rather recent spectroscopy technique which is based on the Mössbauer phenomenon and requires synchrotron as a radiation source.[1] A Mössbauer-active nuclei (e.g. $^{57}$Fe) that is hit by a gamma ray undergoes nuclear spin excitation and as it relaxes, emits a photon. If one knows the energy required, then the additional energy is equivalent of a transition between vibrational states. Only vibrational modes that include contribution from the Mössbauer active nuclei will be observed and the intensity of the signal is in direct proportion with the displacement of the Mössbauer-active nuclei.[2]

Since $^{57}$Fe NRVS development, it has been utilized on various iron-sulfur systems, ranging from molecular crystals of iron complexes,[3,4,5] to large iron-sulfur proteins.[6–9] It is particularly useful since the obtained vibrational spectra will only contain the vibrational modes that include iron. This allows one to get insights into the molecular and electronic structure of iron containing cofactors.

How well computational chemistry, and in particular DFT, can describe these modes and reproduce experimental spectra is not as clear. To the authors knowledge, only a single study has focused on what is needed to accurately calculate the NRVS spectra of Rubredoxin, one of the simplest iron-sulfur systems in biology.[10] From an electronic structure viewpoint, the spin-coupled iron-sulfur clusters should be sensitive to the electronic structure method choice as we and others have demonstrated before.[11–14] However, the protein should affect the cluster and lead to complex

vibrational modes that involve both the cluster and protein. The dependence of calculated NRVS spectra on computational protocol has not been explored thoroughly for these systems and to our knowledge, only one group has previously performed a QM/MM study of Rubredoxin, where they found the computed NRVS spectra to be sensitive to QM region size. [10]

We will start with discussing the computational protocols and the methods used to describe these systems. Then we will discuss calculated NRVS spectra for $FeCl_4^-$ and $Fe_2S_2Cl_4^{2-}$ within a molecular crystal. For the iron-sulfur proteins, discussion will start with Rubredoxin ($Fe^{3+/2+}$), and how well different functionals describe this system as well as the number of atoms that should be present in the QM region and in the hessian region. Then the same will be explored for Ferredoxin ([2Fe-2S]). After that, the cluster of the iron protein of Mo-nitrogenase ([4Fe-4S]), and finally the iron-molybdenum cofactor (FeMoco) of Mo-nitrogenase.

# 2. Computational details

## 2.1 MM model preparation

The Rubredoxin protein of *Pyrococcus furiousus* was based on the 0.59 Å resolution X-ray structure (PDB ID: 5NW3), the Ferredoxin protein of *Aquifex* was based on the 1.5 Å resolution X-ray structure (PDB ID: 1M2A), and the MoFe protein of *A. vinelandii* was based on the 1.0 Å resolution X-ray structure (PDB ID: 3U7Q).[15]

The model preparation of the MoFe protein has been described elsewhere.[16] All models of the proteins included only residues present in the X-ray structure and the protonation state of titrable residues was inspected visually through hydrogen bond networks. The proteins were simulated with molecular dynamics classically within the canonical ensemble (NVT) for one to five nanoseconds and the system allowed to heat up from 50 K to 300 K over the course of 500 ps. This is to equilibrate the water, counterions, and protons of the amino acid residues whereas heavy atoms were frozen in their X-ray geometry. The program GROMACS[17,18] was used to do these calculations using the CHARMM36 protein force field.[19]

At a semi-random timepoint after 500 ps, a snapshot was taken of the system which will be used to generate the QM/MM model. The Rubredoxin and Ferredoxin models are both cubical in shape whereas the Fe-protein is spherical (see Figure 1).

## 2.2 QM/MM model preparation

Chemshell version 3.7[20,21] was used for all QM/MM calculations, where the ORCA program[22,23] was used for the QM part and DL_POLY[24] for the MM part. Link atoms were introduced to cut the QM-MM border and the charge on the amino acid residues were distributed through charge-shift. The CHARMM36 forcefield was used to describe the protein and TIP3P the water molecules. The relativistically recontracted def2 Ahlrichs basis set family was used with triple-ζ was used on Mo, Fe, S, and the central carbide of FeMoco whereas double-ζ was used for other atoms.[25,26] The D3BJ dispersion correction was used for dispersion[27,28] (the older D3 was used for Minnesota functionals) and ZORA Hamiltonian for relativistic correction.[29,30] The RIJCOSX approximation was used to speed up calculation of the Coulomb and exchange integrals.[31,32] The functionals used

were BP86,[33,34] B97-D3,[35] BLYP,[33,36] B3LYP,[33,36,37] B3LYP*,[38,39] BHLYP,[40] CAM-B3LYP,[41] PBE,[42] PBE0,[42,43] TPSS,[44] TPSSh,[44,45] r$^2$SCAN,[46] M06,[47] M06-2X,[47] ωB97X-D3BJ,[48,49] and ωB97M-D3BJ.[48,50]

The NRVS spectra were computed by tightly optimizing the geometry with Chemshell (convergence criteria $10^{-6}$ Hartree) and then the Hessian was computed numerically within the harmonic oscillator approximation. The NRVS spectra themselves were computed by importing the Chemshell type hessian file into ORCA type hessian and a NRVS spectra calculated via the orca_vib and orca_mapspc modules available in ORCA,[22,23] using a gaussian linewidth of 12 $cm^{-1}$ and the isotope mass of iron 57.000 a.m.u.

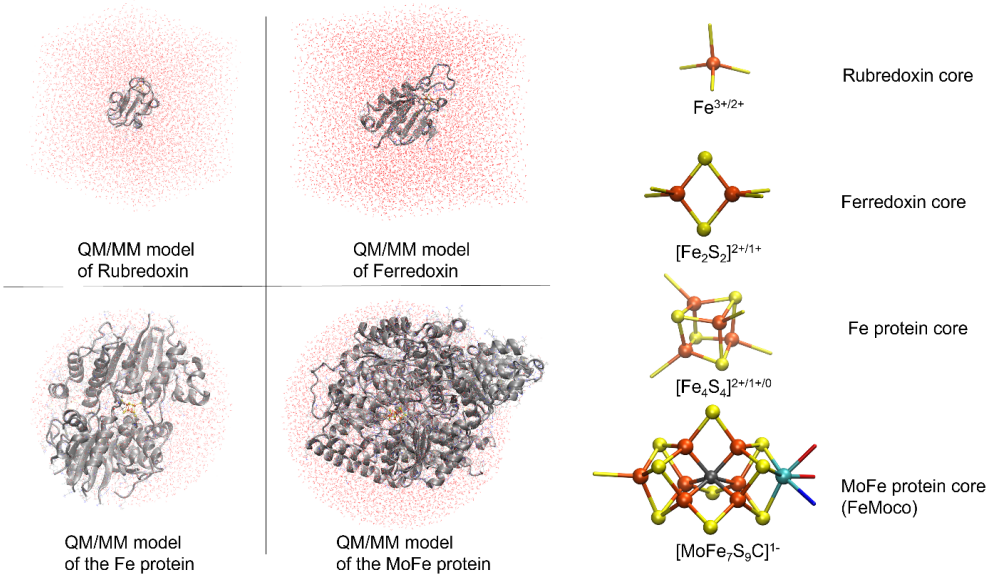


*Figure 1: The QM/MM models of the proteins and the cofactors studied. Not to scale and the relative size is approximate*

# 3. Results and discussion

We will start our discussion with how well we reproduce the NRVS spectra of simpler $FeCl_4$ and $Fe_2S_2Cl_4$ model systems within a molecular crystal. Then, we will move onto proteins and start with the mononuclear Rubredoxin system [Fe] where we will discuss technical aspects of calculating NRVS spectra, functional sensitivity, and model size. Then, we will move onto polynuclear cofactors, starting with ferredoxin [2Fe-2S], and finally FeMoco [Mo-Fe7-S9-C].

## 3.0 Molecular crystals

### 3.0.1 $[FeCl_4][NEt_4]$ and $[FeCl_4][P(C_6H_5)_4]$

The experimental NRVS spectra for $[FeCl_4][Net_4]$ and $[FeCl_4][P(C_6H_5)_4]$ are of a high quality and are an excellent opportunity to investigate the environmental effect on calculated NRVS spectra.[4]

This is due to the two complexes being exactly the same and the molecular crystals only differing with respect to the counterion. The experimental spectra (digitized from the original research article) can be seen along with the calculated spectra in Figure 2. In the measured NRVS spectra of these complexes, a large peak is observed at ~380 $cm^{-1}$ but for $[FeCl_4][NEt_4]$ there is one peak observed at ~150 $cm^{-1}$ , whereas this peak is split into two for $[FeCl_4][P(C_6H_5)_4]$ at 142 $cm^{-1}$ and 128 $cm^{-1}$.

A simple NRVS calculation of $FeCl_4^-$ in a vacuum yields two peaks, one comprised of three near-degenerate $t_2$ vibrational modes at 367 $cm^{-1}$ (average) and another peak comprised of three near-degenerate $t_2$ vibrational modes at 124 $cm^{-1}$ (average). A similar shape is observed for a calculated NRVS spectrum of $FeCl_4^-$ within a continuum (here CPCM[51] is used with a dielectric constant of infinity and Gaussian-charge scheme with a scaled vdW surface),[52,53] with the larger peak appearing now at 354 $cm^{-1}$ (average) and the smaller one at 117 $cm^{-1}$ (average). These calculations do not capture the band structure observed at lower energies for $[FeCl_4][P(C_6H_5)_4]$, which implies that $P(C_6H_5)_4^+$ needs to be accounted for explicitly in order to capture this details correctly in a calculation.

Three NRVS QM/MM calculations were performed for each molecular crystal (with the TPSSh DF) to probe the effect of the crystal environment polarization on the NRVS spectrum calculated as well as the effect of including the counterion only in the QM region or both in the QM region and the Hessian region.

As can be seen in Figure 2, then accounting for the crystal environment through pointcharges, the values of vibrational frequencies are shifted to higher energies and the near-degenerate $t_2$ vibrational modes become less symmetric. For $[FeCl_4][NEt_4]$, then a near perfect fit is obtained with the experimental spectrum for the peak at ~380 $cm^{-1}$ and a good fit at lower energies. Similarly for $[FeCl_4][P(C_6H_5)_4]$, then the computed spectrum fits nicely with experiment, and it can be seen that the splitting of the peak at lower energies is only captured at QM/MM level.

Including the counterion in the QM calculation (but not including it in the calculation of the Hessian), causes some minor shifts and improvements. A larger difference is observed when the counterion is also included in the calculation of the Hessian and with the biggest difference being the low-lying in energy vibrational modes appearing. These are lattice modes which fit surprisingly well with the experiment. It is though worth noting that in order to model lattice model properly, a periodic model would be needed. For other vibrational modes, then in the case of $[FeCl_4][Net_4]$ a near perfect fit between experiment is obtained at ~380 $cm^{-1}$. Although NRVS is not sensitive enough to discern between the three vibrational modes that constitute this peak, Raman data exists for these vibrational modes for these complexes with the $^{57}Fe$ isotope. The Raman energies are 394, 377, and 372 $cm^{-1}$ whereas the calculated NRVS energies are 386, 380, and 369 $cm^{-1}$, which is in a good agreement with experiment. In the case of $[FeCl_4][P(C_6H_5)_4]$, then the three

vibrational modes are discernable with NRVS and are 391, 384, and 369 $cm^{-1}$, whereas the calculated values are 397, 385, and 371 $cm^{-1}$, which is again in a good agreement.

At lower energies (0-200 $cm^{-1}$), a good fit is obtained but there are larger discrepancies between the calculated NRVS spectra and experimental NRVS spectra. Three instead of two peaks are observed for $[FeCl_4][P(C_6H_5)_4]$ and the peak for $[FECl_4][Net_4]$ is too broad.

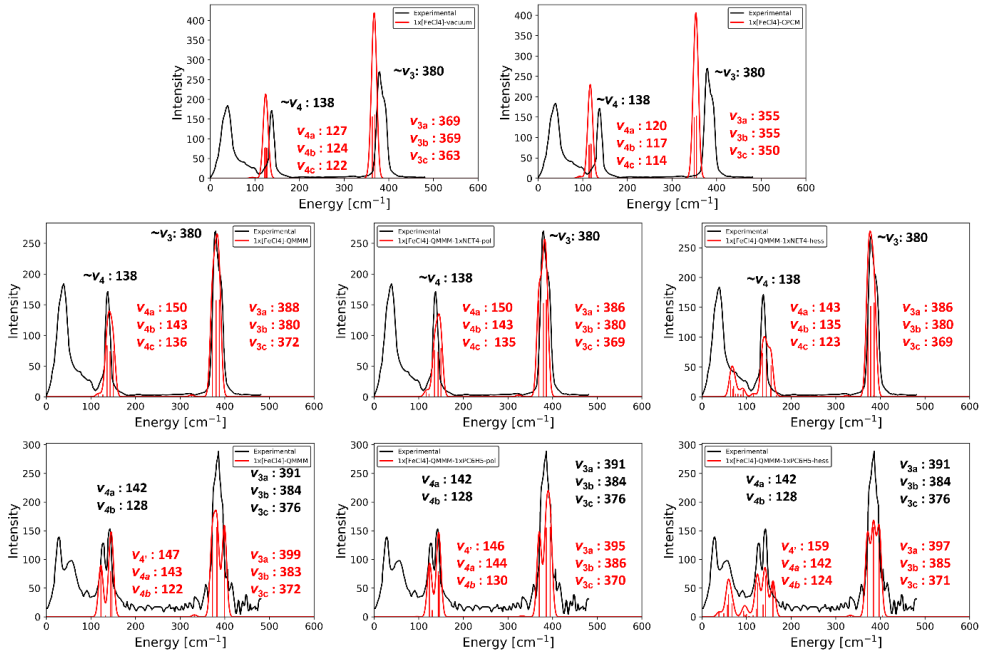


*Figure 2: A comparison of calculated and experimental NRVS spectra. Top: Experimental (black) NRVS spectrum of $[FeCl_4][NEt_4]$ compared to a computed spectrum of $FeCl_4^-$ (red) in either vacuum (to the left) or CPCM (to the right). Middle: Experimental spectrum of $[FeCl_4][NEt_4]$ (black) compared to calculated NRVS spectrum (red) using QM/MM with only $FeCl_4^-$ in the QM region and hessian region (to the left), then with a single $NEt_4^+$ included in the QM region (in the middle), then with a single $NEt_4^+$ included in the QM and Hessian region (to the right). Bottom: Experimental spectrum of $[FeCl_4][PC_6H_5]$ (black) compared to calculated NRVS spectrum (red) using QM/MM with only $FeCl_4^-$ in the QM region and hessian region (to the left), then with a single $PC_6H_5^+$ in the QM region (in the middle), then with a single $PC_6H_5^+$ in the QM region and Hessian region (in the middle). The DF used was TPSSh.*

### 3.0.2 $[Fe_2S_2Cl_4][NEt_4]_2$

The experimental NRVS spectrum of $[Fe_2S_2Cl_4][NEt_4]_2$ is shown in Figure 3 along with calculated NRVS spectra. Already at either vacuum or CPCM level of theory, the calculated spectra fit well with the experimental spectrum. Focusing on the vibrational modes at higher energies than 250 $cm^{-1}$ and starting with the two vibrational modes with the highest vibrational

energy. Adding a dielectric continuum shifts the vibrational energies to higher values whereas when the crystal environment is introduced an even better fit is observed.

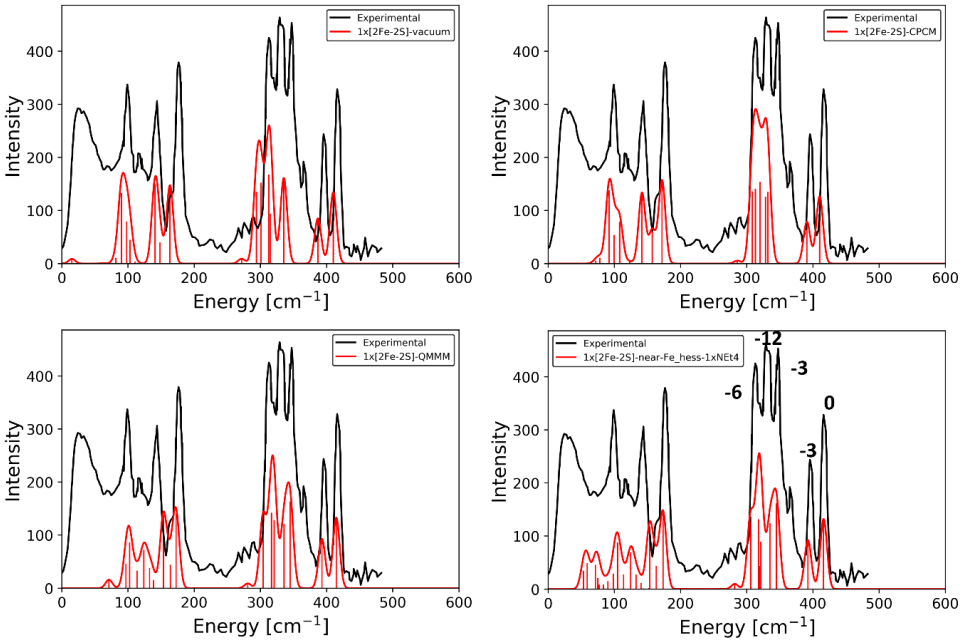


*Figure 3: Comparison of experimental NRVS spectrum of $[Fe_2S_2Cl_4]^{2-}$ (black) to various calculated NRVS spectra (red). Top left: Experimental spectrum compared to a calculated spectrum of $[Fe_2S_2Cl_4]^{2-}$ in vacuum. Top right: Experimental spectrum compared to a calculated spectrum of $[Fe_2S_2Cl_4]^{2-}$ with CPCM. Bottom left: Experimental spectrum compared to a calculated spectrum of $[Fe_2S_2Cl_4]^{2-}$ within QM/MM. Bottom right: Experimental spectrum compared to a calculated spectrum of $[Fe_2S_2Cl_4]^{2-}$ within QM/MM where a single $Net_4^+$ is included both in the QM region and Hessian region.*

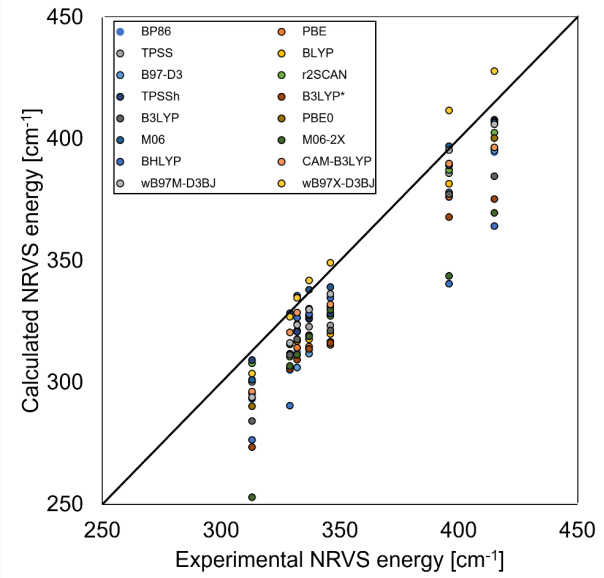


*Figure 4: Correlation plot where computed NRVS vibrational energies are a function of experimentally measured vibrational energies for vibrational modes with higher energy than 250 $cm^{-1}$.*

A functional comparison at CPCM level of theory shows that most functionals underestimate the vibrational energy on average with ωB97X-D3BJ being the sole exception (see Figure 4 and Table 1).

*Table 1: Functional comparison for the vibrational modes of $[Fe_2S_2Cl_4]^{2-}$ with higher vibrational energies than 250 $cm^{-1}$ within a continuum solvation model (CPCM)*

| Functional | MD | MAD |
|---|---|---|
| BP86 | -22.5 | 22.5 |
| PBE | -21.7 | 21.7 |
| TPSS | -13.6 | 13.6 |
| BLYP | -17.4 | 17.4 |
| B97-D3 | -22.7 | 22.7 |
| r2SCAN | -12.6 | 12.6 |
| TPSSh | -10.7 | 10.7 |
| B3LYP* | -29.5 | 29.5 |
| B3LYP | -21.7 | 21.7 |
| PBE0 | -12.7 | 12.7 |
| M06 | -3.1 | 4.7 |
| M06-2X | -33.5 | 33.5 |
| BHLYP | -29.5 | 29.5 |
| CAM-B3LYP | -10.5 | 10.5 |
| ωB97M-D3BJ | -9.5 | 9.5 |
| ωB97X-D3BJ | 4.0 | 7.3 |

## 3.1 Proteins

### 3.1.1 [Fe]-Rubredoxin

Functional dependence

Previously we and others have reported the sensitivity of the geometry of iron-sulfur systems to method of choice.[12,54,55] In order to evaluate the functional effect on vibrational frequencies, we tested 16 different functionals.

There should be four vibrational modes between 300 $cm^{-1}$ and 400 $cm^{-1}$ if perfect tetrahedral symmetry ($T_d$) is assumed. One is a symmetric Fe-S stretch ($A_1$) whereas there are three degenerate Fe-S stretches ($T_2$). In reality, the coordination of the iron at the core of Rubredoxin does not have a perfect tetrahedral symmetry and the $T_2$ Fe-S stretches are no longer symmetric. Therefore, three asymmetric Fe-S stretches are observed experimentally and have also been found from computational studies of Rubredoxin.

In order to distinguish between these three asymmetric Fe-S stretching modes, we label them with an apostrophe. The first asymmetric stretch we observe will be labelled $T_2$', the second $T_2$'', and the third $T_2$'''.

*Table 2: Calculated vibrational frequency of the four vibrational modes assuming $T_d$ symmetry. The values within the brackets is the deviation of calculated values from resonance Raman values, since the vibrational frequency of the $A_1$ mode is not reported.*

| | Vibrational mode (assuming perfect $T_d$ symmetry) | | | | Absolute Average dev |
|---|---|---|---|---|---|
| | $A_1$ | $T_2$' | $T_2$'' | $T_2$''' | $A_1$ and $T_2$ |
| BP86 | 328 (+5) | 362 (+15) | 371 (+11) | 377 (+2) | 8 |
| PBE | 326 (+3) | 360 (+13) | 369 (+9) | 375 (+0) | 6 |
| TPSS | 329 (+6) | 362 (+15) | 373 (+13) | 380 (+5) | 10 |
| BLYP | 324 (+1) | 353 (+6) | 363 (+3) | 370 (-5) | 4 |
| B97-D3 | 324 (+1) | 356 (+9) | 368 (+8) | 373 (-2) | 5 |
| r2SCAN | 333 (+10) | 366 (+19) | 379 (+19) | 387 (+12) | 15 |
| TPSSh | 334 (+11) | 368 (+21) | 380 (+20) | 388 (+13) | 16 |
| B3LYP* | 334 (+11) | 366 (+19) | 376 (+16) | 387 (+12) | 14 |
| B3LYP | 335 (+12) | 367 (+20) | 378 (+18) | 390 (+15) | 16 |
| PBE0 | 340 (+17) | 373 (+26) | 386 (+26) | 399 (+24) | 24 |
| M06 | 342 (+19) | 374 (+27) | 385 (+25) | 399 (+24) | 24 |
| M06-2X | 349 (+26) | 375 (+28) | 389 (+29) | 408 (+33) | 29 |
| BHLYP | 351 (+28) | 381 (+34) | 395 (+35) | 414 (+39) | 34 |
| CAM-B3LYP | 345 (+22) | 377 (+30) | 389 (+29) | 400 (+25) | 27 |
| wB97M-D3BJ | 344 (+21) | 377 (+30) | 388 (+28) | 404 (+29) | 27 |
| wB97X-D3BJ | 352 (+29) | 391 (+44) | 399 (+39) | 413 (+38) | 38 |
| | | | | | |
| Exp. NRVS | | 350 | 358 | 375 | |
| Exp. Raman | 323 | 347 | 360 | 375 | |

The relative NRVS intensity of these modes as we calculate them is as follows: The most intense is the $T_2$' vibrational mode, then $T_2$'' and $T_2$''' are approximately 70-80% of the intensity of $T_2$' whereas the symmetric mode $A_1$' is only approximately 15% of the intensity. Therefore, it is not entirely unexpected that $A_1$' is not observed in the experimental NRVS.

The non-hybrid functionals perform best (excluding r$^2$SCAN) with the mean absolute deviation (MAD) being somewhere between 4 to 10 cm$^{-1}$. Functionals with exact exchange equal to or less than 20% and r$^2$SCAN have a MAD at ~15 cm$^{-1}$. Functionals that have an exact exchange component greater or equal to 25% or are range separated, have a MAD greater than 24 cm$^{-1}$.

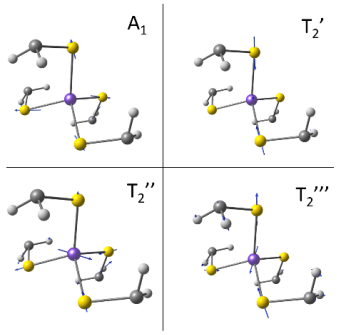


*Figure 5: The four stretching Fe-S vibrational modes for the iron center of Rubredoxin, assuming a perfect tetrahedral symmetry.*

## Sensitivity to the size of the QM region and Hessian region

We turn next to the quality of the model. Since the protein ensemble is responsible for breaking the tetrahedral symmetry around the iron center, it is important to evaluate how large the model needs to be to calculate the NRVS active vibrational frequencies accurately. We introduce three region sizes, one region with 17 atoms, another one with 41 atoms, and a third one with 120 atoms.

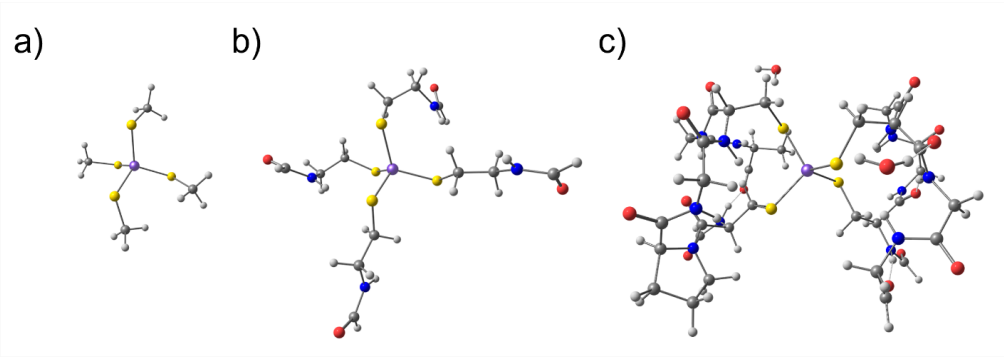


*Figure 6: Three Rubredoxin model sizes tested where a) is 17 atoms, b) is 41 atoms, and c) is 120 atoms (not countin the link atoms that terminate the QM region border).*

Starting with a discussion of the effect of increasing the Hessian region. Immediately for the smallest model size, where there are only 17QM atoms and 17 Hessian atoms, we see that the calculated spectrum captures the overall trend seen in the measured spectrum. Furthermore, there are a lot fewer transitions at 300 to 400 $cm^{-1}$ when compared to larger models that contain more atoms in the Hessian, the vibrational modes can easily be assigned if one assumes $T_d$ symmetry, similarly as was done in Table X. Here, we observe that there are four transitions, one at 334 $cm^{-1}$ which corresponds to symmetric Fe-S stretch, whereas the transitions at 368, 380, and 386 $cm^{-1}$ correspond to asymmetric Fe-S stretches. and the computed peak splits in two, which is not something that is observed experimentally.

Increasing the Hessian region incrementally, starting with 41 atoms, then the splitting of the main peak at ~380 $cm^{-1}$ is no longer observed and a lot of relatively untense transitions can now be observed between 200 and 300 $cm^{-1}$. Increasing the Hessian region even further to 120 atoms, a lot more transitions are observed around 100 $cm^{-1}$ as well as there is an increase in the band at ~420 $cm^{-1}$. The main calculated band falls right into the experimental band.

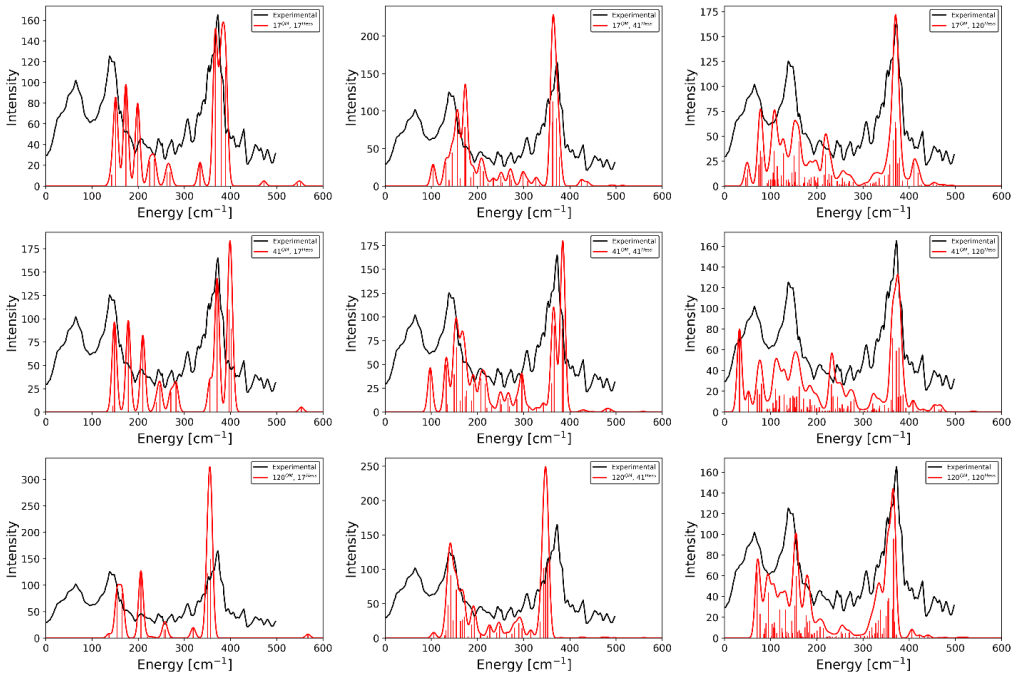


*Figure 7: Computed (red) NRVS spectra for different sizes of QM region and size of the Hessian compared to experimental (black) spectrum. The experimental spectrum is from Cramer and coworkers and has been digitized.*

Furthermore, more vibrational modes are observed as the number of atoms in the calculation of the Hessian are increased. Albeit that it can be seen in Figure 4 that this does in fact improve the fit to experimentally measured spectrum, it makes analysis of the vibrational modes more difficult.

Redox shift

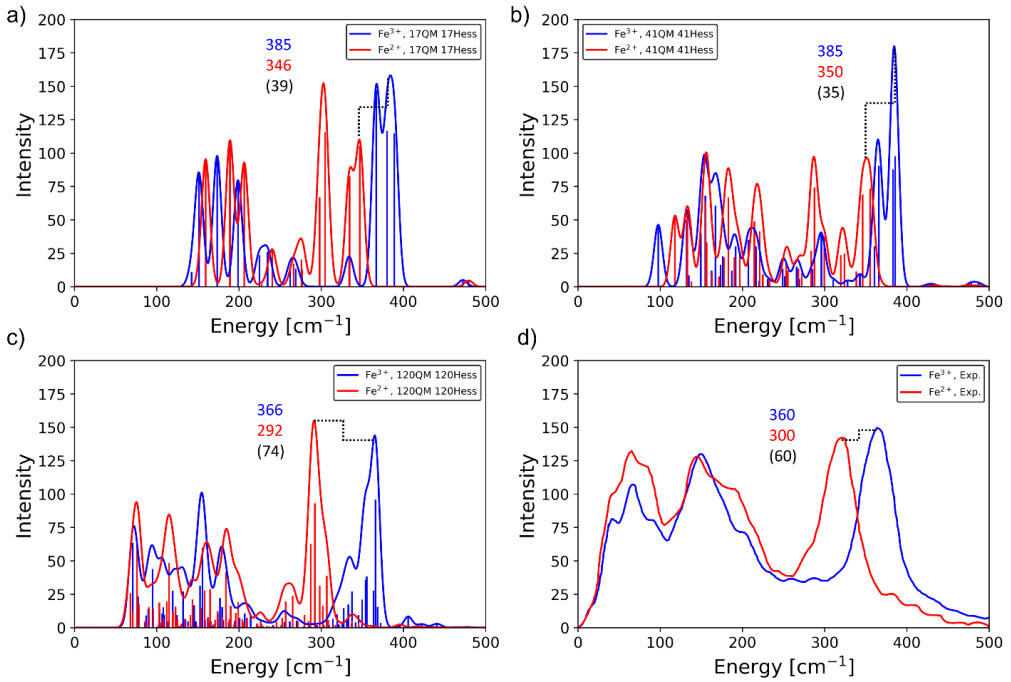


*Figure 8: The redox shift observed for calculated Rubredoxin NRVS spectra when the iron center is oxidized for a) minimal model, b) medium sized model, c) large model, and d) experimental spectra (digitized from ref.[7])*

When Rubredoxin is oxidized, it is observed experimentally in an NRVS spectra that the peak at 360 $cm^{-1}$ is shifted approximately by 60 $cm^{-1}$ to 300 $cm^{-1}$. For the smallest and medium sized models, this shift is not captured exactly, with the shift of the peak in the smallest model being 39 $cm^{-1}$ and the shift for the medium sized model 35 $cm^{-1}$. For the largest model, a shift of 74 $cm^{-1}$ is observed.

### 3.2.2 $[Fe_2S_2]$-Ferredoxin

Functional dependence

We saw that the calculated vibrational modes for the iron center of Rubredoxin are dependent on the choice of functional. The non-hybrid functionals fared on average better than their hybrid counterparts. In the case for the $[Fe_2S_2]$ cluster of ferredoxin, then this observed trend is reversed. The best functional on average are the 10 – 27 HF% hybrids, with MAD ranging from 7 – 10 $cm^{-1}$ whereas the non-hybrid functionals have a MADs of 14 – 30 $cm^{-1}$.

This difference between accuracy of functionals for these two systems can possibly be explained by the nature of the ligand environment of the irons. In Rubredoxin, the iron is only covalently ligated to organic sulfurs and does not interact with any other metal. In ferredoxin, the two

bridging inorganic sulfur ligands are responsible for the superexchange between the two iron ions. As has been demonstrated before, these interactions are heavily sensitive to the amount of HF% present in a hybrid functional and will affect the computed geometry.

*Table 3: Calculated vibrational frequency of vibrational modes above 288 cm⁻1. The values within the brackets is the deviation of calculated values from resonance Raman values, since the vibrational frequency of the $A_1$ mode is not reported.*

| | Vibrational mode | | | | | | | | MAD |
|---|---|---|---|---|---|---|---|---|---|
| | 1 | 2 | 3 | 4 | 5 | 6 | 7 | 8 | |
| BP86 | 370 (-49) | 358 (-35) | 351 | 328 (-24) | 321 (-19) | 301 (-32) | 284 (-35) | 272 (-16) | 30 |
| PBE | 371 (-48) | 359 (-34) | 351 | 329 (-23) | 321 (-19) | 301 (-32) | 285 (-34) | 272 (-16) | 29 |
| TPSS | 378 (-41) | 365 (-28) | 356 | 336 (-16) | 327 (-13) | 307 (-26) | 289 (-30) | 277 (-11) | 24 |
| BLYP | 445 (+26) | 430 (+37) | 399 | 388 (+36) | 375 (+35) | 348 (15) | 332 (+13) | 316 (+28) | 27 |
| B97-D3 | 389 (-30) | 375 (-18) | 354 | 336 (-16) | 330 (-10) | 304 (-29) | 297 (-4) | 284 (-4) | 18 |
| r2SCAN | 392 (-27) | 378 (-15) | 364 | 345 (-7) | 337 (-3) | 313 (-20) | 296 (+2) | 290 (+2) | 14 |
| TPSSh | 416 (-3) | 399 (+6) | 374 | 359 (+7) | 349 (-9) | 324 (-9) | 314 (-5) | 298 (+10) | 7 |
| B3LYP* | 407 (-12) | 393 (0) | 371 | 354 (+2) | 345 (+5) | 320 (-13) | 303 (-16) | 296 (+8) | 8 |
| B3LYP | 407 (-12) | 394 (+1) | 375 | 357 (+5) | 348 (+8) | 324 (-9) | 303 (-16) | 296 (+8) | 8 |
| PBE0 | 419 (0) | 405 (+12) | 385 | 369 (+17) | 356 (+16) | 333 (0) | 311 (-8) | 303 (+15) | 10 |
| M06 | 422 (+3) | 406 (+13) | 385 | 368 (+16) | 355 (+15) | 336 (+3) | 309 (-10) | 281 (-7) | 10 |
| M06-2X | | | | | | | | | |
| BHLYP | 426 (+7) | 412 (+19) | 397 | 381 (+29) | 368 (+28) | 346 (+13) | 327 (+8) | 298 (+10) | 16 |
| CAM-B3LYP | 416 (-3) | 401 (+8) | 379 | 364 (+12) | 356 (+15) | 329 (-4) | 312 (-7) | 290 (+2) | 7 |
| wB97M-D3BJ | 424 (+5) | 407 (+14) | 388 | 371 (+19) | 360 (+20) | 335 (+2) | 316 (-3) | 295 (+7) | 10 |
| wB97X-D3BJ | 428 (+9) | 408 (+15) | 385 | 372 (+20) | 362 (+22) | 335 (+2) | 316 (-3) | 296 (+8) | 11 |
| Exp. NRVS | 419 | 393 | N/A | 352 | 340 | 333 | 319 | 288 | |

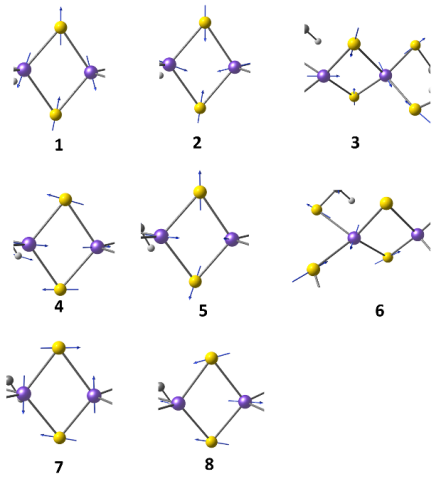


*Figure 9: The eight vibrational modes observed between 280 cm-1 and 420 cm-1 in calculation of the hessian of Ferredoxin.*

Model size

We saw previously for Rubredoxin that the computed vibrational frequencies were sensitive to the number of atoms included both in the QM region and the number of atoms included in the calculation of the hessian. The largest model captured best the overall trend of the whole spectrum.

In the case of ferredoxin, the two highest in energy vibrational modes are already well described for both oxidation states that ferredoxin can be in. The modes at ~400 $cm^{-1}$ seem to be insensitive to the QM region size and the number of atoms in the Hessian. On the other hand, the lower energy end of the spectra is better described by including more atoms in the Hessian.

The reason for this is that the vibrational modes at ~400 $cm^{-1}$ are the Fe-S stretches of inorganic sulfides that bridge the two iron centers. These vibrational modes interact minimally with the protein environment when compared to the organic sulfides and are therefore relatively insensitive to the model size. The vibrational modes at the lower energy end of the spectra on the other hand belong partially to vibrational modes of organic sulfur and in order to model them correctly, the protein matrix needs to be accounted for.

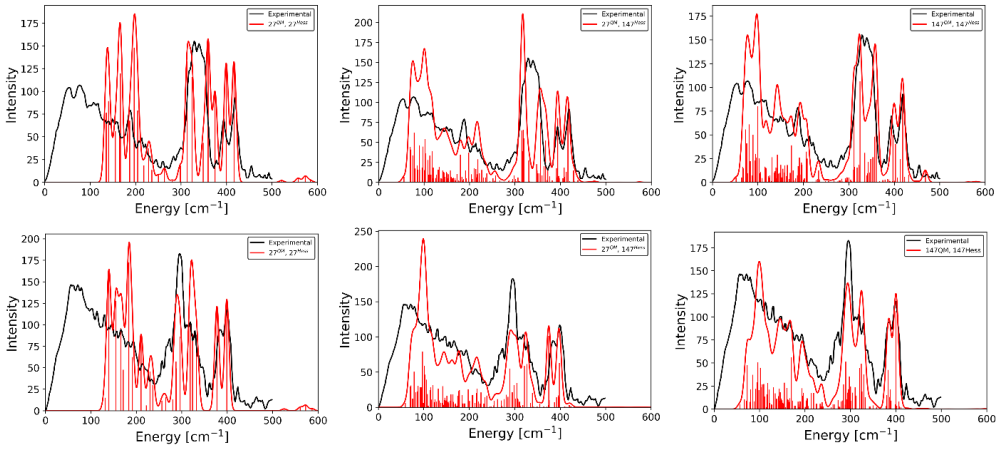


*Figure 10: Convergence of the computed NRVS spectra w.r.t. model size. The upper spectra are for differic Ferredoxin whereas the lower spectra is mixed valence Ferredoxin.*

A topic that hasn't been discussed so far is the interpretation of the computed vibrational modes. Figure 7 compares the computed NRVS spectra for the smallest model and the largest model in the ~400 $cm^{-1}$ region of ferredoxin in the oxidized state. Both models capture relatively well the experimentally measured vibrational frequencies of 419 $cm^{-1}$ (small model 417 $cm^{-1}$, large model 416 $cm^{-1}$) and 393 $cm^{-1}$ (small model 399 $cm^{-1}$, large model 400 $cm^{-1}$). On the other hand, the small model predicts that there is only one vibrational mode responsible for each peak whereas the larger model predicts that there is at least two modes.

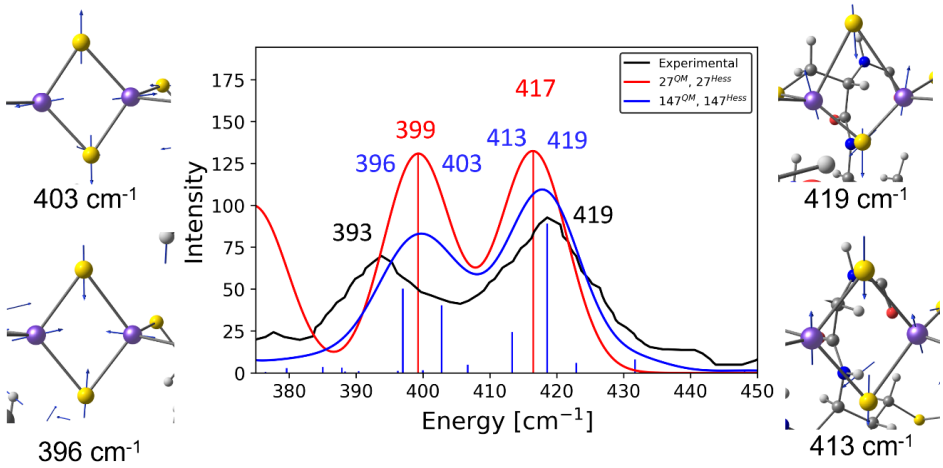


*Figure 11: Increasing the number of atoms that are included in the calculation of the Hessian can complicate the interpretation of the computed NRVS spectra. Here, a single vibrational mode is split into two with the increased number of atoms in the calculation of the numerical Hessian.*

### Redox shift

When Ferredoxin is reduced, experimentally a shift is observed similarly as for Rubredoxin in the NRVS spectra. As can be seen in Figure 12 d), the two peaks at the highest energy values are shifted to lower energies by 21 $cm^{-1}$ and 10 $cm^{-1}$. For a small QM and Hessian region, the peaks are shifted by 17 $cm^{-1}$ and 22 $cm^{-1}$. With a larger Hessian region, a minor improvement is observed with the shift now being 19 $cm^{-1}$ and 20 $cm^{-1}$. When both the QM region and Hessian region are increased to include 147 atoms, the shift is moderately improved to 18 $cm^{-1}$ and 16 $cm^{-1}$.

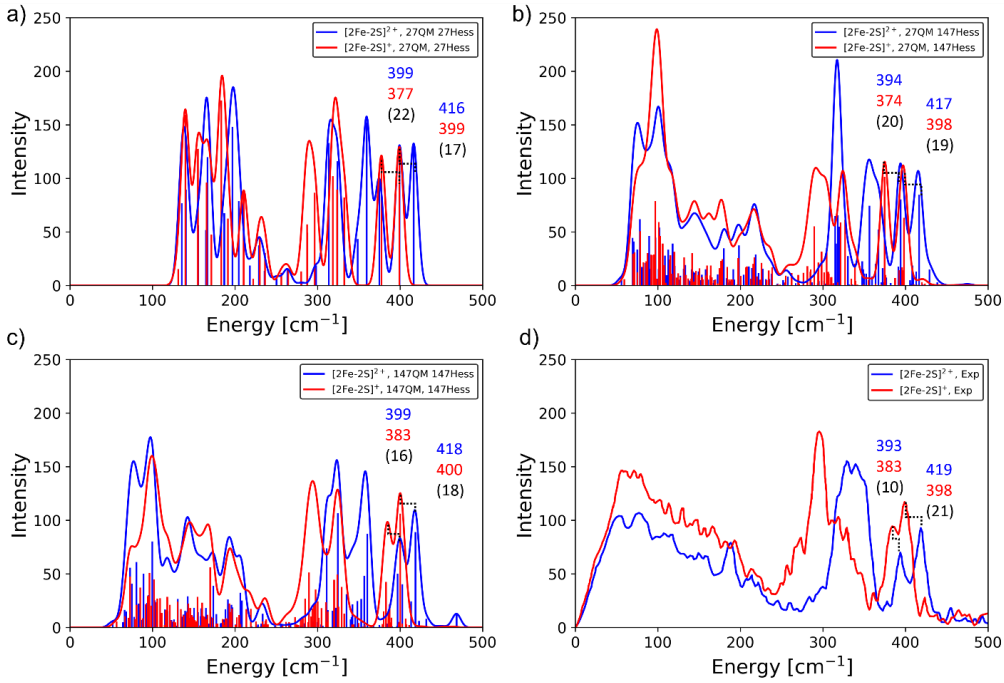


*Figure 12: The redox shift observed for calculated Ferredoxin NRVS spectra when one iron center is reduced for a) small QM region and small Hessian region, b) small QM region and large Hessian region, c) large QM region and large Hessian region, and d) experimental spectra (digitized from ref.[8]). Exp. indicates experiment.*

### 3.2.4 [$MoFe_7S_9C$]: FeMoco of the Molybdenum-Iron protein of the Mo-nitrogenase

Model size convergence

Two NRVS studies have been performed on Mo-nitrogenase,[6,56] with the first study correctly suggesting a carbide as the most likely central atom in FeMoco (which was not known in 2006) due to the calculated NRVS spectrum giving the best fit with the experimental NRVS spectrum. Although this was not enough to eliminate other options such as nitride or oxide but nonetheless demonstrated the possibilities of NRVS experiments.

In previous sections, we have seen that the vibrational modes of Rubredoxin and Ferredoxin are sensitive to both the model size and the functional used. In the case of Rubredoxin, model size is important due to the iron being ligated to the protein matrix whereas this was a less of an issue for Ferredoxin.

Figure 11 shows computed NRVS spectra for FeMoco. The spectra at the top are obtained by having 54 QM atoms whereas the number of atoms in the hessian region are increased systematically (refer to Figure 11 for system size information). The spectra are overall similar with respect to system size except for the vibrational modes at ~420 cm$^{-1}$ with the peak being split into two smaller peaks as the hessian region increases. The vibrational mode corresponding to this

vibrational frequency is the Fe-S stretch of the bridging sulfides (sulfides that are ligated to two irons). The cause of this is that there are vibrational modes in the protein matrix that couple with the Fe-S stretch. This is most likely artificial since this is not observed for other larger models.

Another option is to increase the number of QM atoms while keeping the size of the hessian region a constant. The calculated spectra are presented in the middle of Figure 10. The computed spectra are highly similar with some exceptions. The Fe-S stretches observed at ~420 $cm^{-1}$ shift somewhat as the QM region is increased and the vibrational modes at ~350 $cm^{-1}$ increase in intensity.

When both the QM region and hessian region are systematically increased at the same time, as can be seen in Figure 10 at the bottom, the overall shape of the bands in the spectra is conserved. There are though some noticeable changes, such as shift of the Fe-S stretches at ~420 $cm^{-1}$ to lower values as the model size increases. The peak at ~370 $cm^{-1}$ vanishes, but it is the Fe1-S-cysteine stretch. Furthermore, the small peak at ~350 $cm^{-1}$ becomes more pronounced, but these are few vibrational modes that corresponds to bridging sulfide modes.

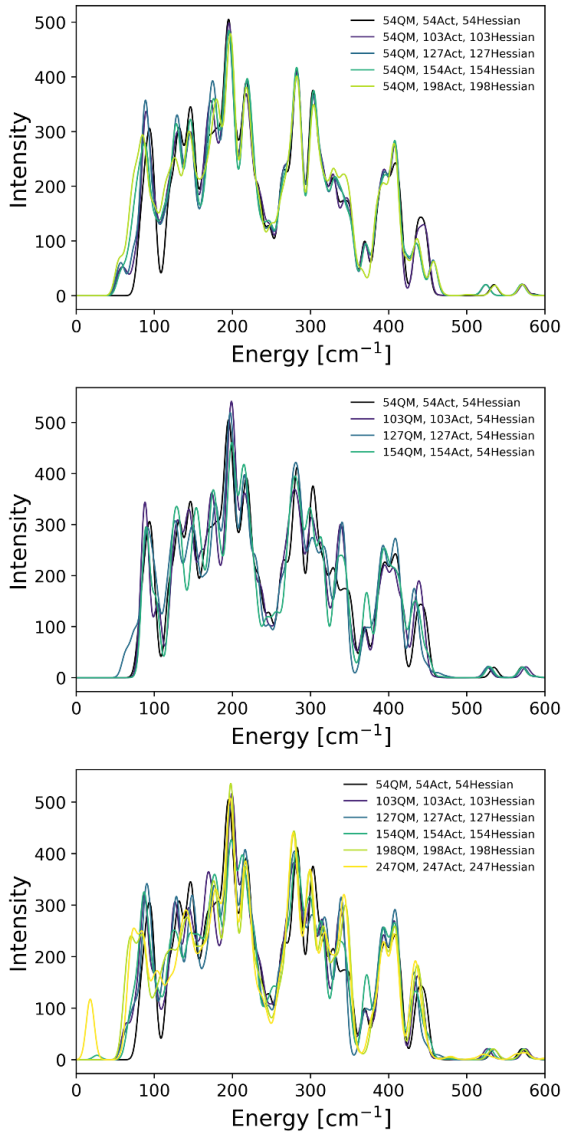


*Figure 13: Convergence for NRVS calculations. Top: Convergence w.r.t. constant number of QM atoms but varying number of atoms in the hessian region. Middle: Convergence w.r.t. number of QM atoms optimized but the number of atoms in the hessian is constant. Bottom: The convergence w.r.t. increasing the number of QM atoms and hessina atoms at the same time.*

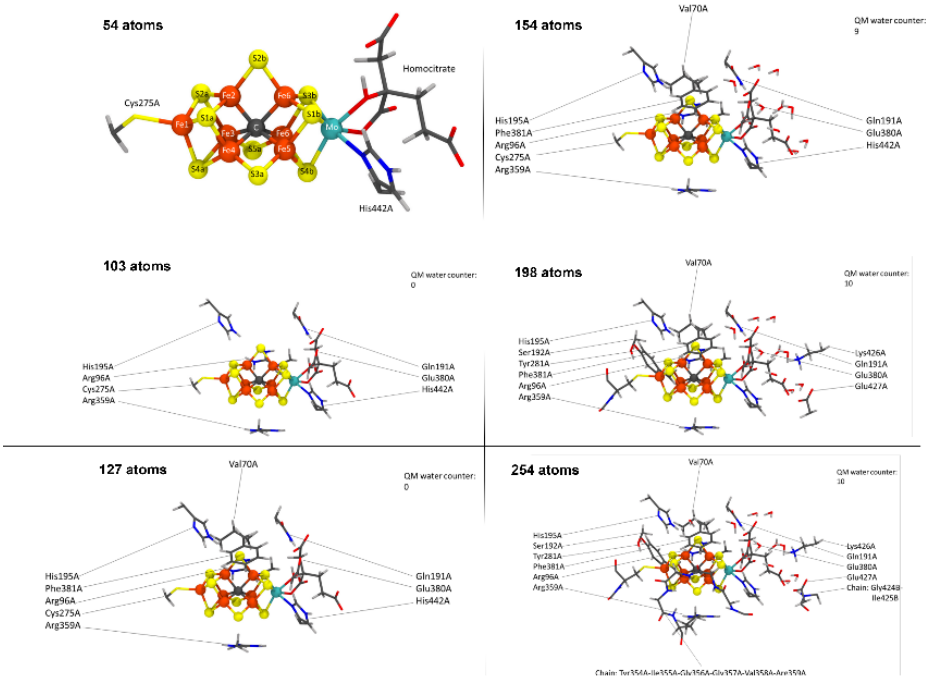


Figure 14: The six model sizes considered here.

Overall, it seems like a justified choice to model FeMoco with a small QM region as well as a small hessian region. This is in line with the results from Ferredoxin and the Fe-protein. Vibrational modes of atoms that are not directly linked to the protein matrix seem to be somewhat unaffected by the model size.

### Comparison of FeMoco and the P-cluster

FeMoco is not the only cluster in the MoFe protein. The P-cluster is a [8Fe-7S] cluster located a dozen Angstroms away from FeMoco. Since it an iron-sulfur cluster, its vibrational modes will also be observed in a measured NRVS experiment. It is of interest to find a region, if any, in a NRVS spectrum of the MoFe protein that only includes signal from FeMoco.

Figure 12 shows a computed NRVS spectra of FeMoco and the P-cluster where the intensities have been normalized, meaning that the intensity from the P-cluster was divided by 8 (contains 8 iron ions) and the intensity from FeMoco was divided by 7 (FeMoco contains 7 iron ions). The regions labelled 1), 2), and 3) all have it in common that the vibrational modes that correspond to these peaks arise from an iron bridging sulfide mode.

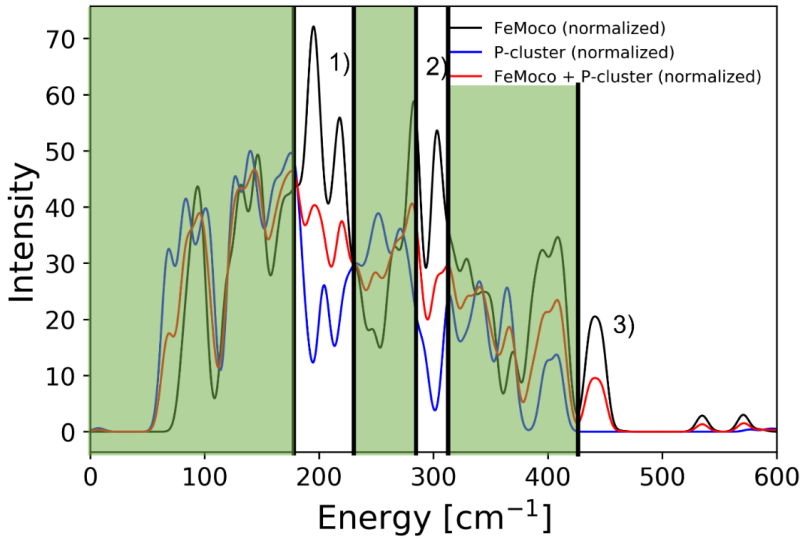


*Figure 15:Calculated NRVS spectra for FeMoco and the P-cluster. The intensity is normalized. The regions labelled with 1), 2), and 3) are dominated by modes that stem from the bridging sulfides of FeMoco.*

### Single protonation and reduction of FeMoco

During the catalytic cycle of FeMoco, the cofactor accepts electrons and protons.[57] The electrons are stored by reducing the present ferric irons into ferrous ions and protons are stored on sulfides as thiols (albeit that this has never been directly measured with vibrational spectroscopy), and hydrides are formed at one point in the catalytic cycle. Where the protons and/or hydrides end up being localized on the cofactor is not clear and it is a current a debate in the literature. A NRVS experiment should be able to shed a light on this issue.

As can be seen in Figure 13, when FeMoco is protonated on its S2B sulfide, the vibrational mode of Fe-S2B stretch at 420 cm$^{-1}$ shifts to a lower energy by approximately 10 cm$^{-1}$, as well as some other subtle differences are seen in the overall spectrum. When the cofactor is reduced instead, the overall computed spectrum seems to shift leftwards. When reduction and protonation is combined (the $E_1$ state of FeMoco during the catalytic cycle) a combination of both effects is observed. The spectrum is slightly shifted leftwards and the vibrational modes that include a protonated bridging sulfide is also slightly shifted to lower energies.

If a NRVS experiment is performed on FeMoco in the $E_1$ state of the catalytic cycle, it should be possible to characterize the state through modelling. In some computational studies, protonation of the S2B sulfide is suggested to be the first step in the catalytic cycle.[58,59] Furthermore, some studies have suggested that the S2B sulfide dissociates from the cofactor.[60–62]f This should be discernable in with an NRVS experiment and computational modelling.

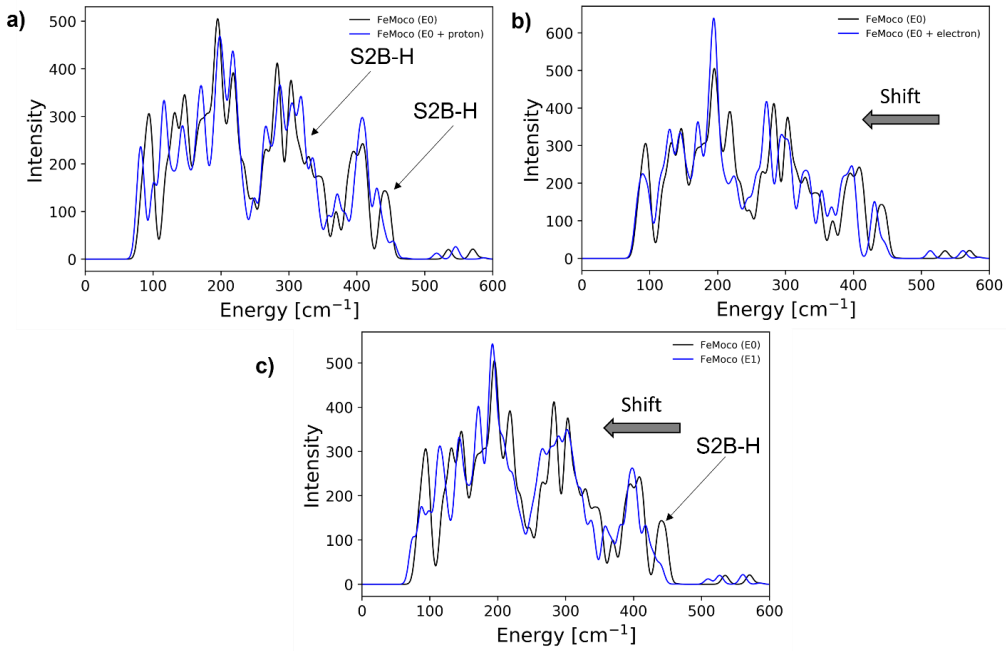


*Figure 16: The effect of a) protonating FeMoco, b) reducing FeMoco by one electron ($M_S$ = 1 and BS7-235), and c) both reducing and protonating FeMoco.*

# 4. Conclusion

We have shown that through accurate modelling of iron-sulfur proteins by QM/MM, it is possible to calculate NRVS spectra to quite considerable accuracy. Vibrational modes of ligands that are not directly connected to the protein matrix are comparably insensitive to the number of atoms included either in the QM region or in the hessian region. The vibrational modes of ligands, such as organic sulfides, are affected a lot more to the model size.

With respect to density functionals, the calculated vibrational frequencies including the iron core in Rubredoxin show a different trend when compared to the [2Fe-2S] core of Ferredoxin. This is most likely caused by the complex interactions, such as superexchange and antiferromagnetic coupling, between the two metal centres. Similarly, the geometry has previously been found to be very sensitive to the functional used.

For FeMoco, the work here importantly demonstrates that a small QM/MM model should give a qualitatively correct NRVS spectrum. Furthermore, it is demonstrated that there are specific energy regions where the vibrational modes should be FeMoco specific and contain minimum number of vibrational modes from the P-cluster. Then the highest energy vibrational modes are the Fe-S bond stretching which are sensitive to both protonation and to reduction.

# 5. References


1. Wang, H., Braun, A., Cramer, S. P. & Gee, L. B. Nuclear Resonance Vibrational Spectroscopy : A Modern Tool to Pinpoint Site-Specific Cooperative Processes. (2021).

2. Zeng, W., Silvernail, N. J., Scheidt, W. R. & Sage, J. T. Nuclear Resonance Vibrational Spectroscopy (NRVS). in *Encyclopedia of Inorganic Chemistry* 1–21 (John Wiley & Sons, Ltd, 2008). doi:10.1002/0470862106.ia321

3. Xiao, Y. *et al.* Dynamics of an [Fe4S4(SPh)4]2-cluster explored via IR, Raman, and nuclear resonance vibrational spectroscopy (NRVS)-analysis using36S substitution, DFT calculations, and empirical force fields. *Dalt. Trans.* 4, 2192–2201 (2006).

4. Smith, M. C. *et al.* Normal-Mode Analysis of FeCl 4 - and Fe 2 S 2 Cl 4 2 - via Vibrational Mössbauer, Resonance Raman, and FT-IR Spectroscopies. *Inorg. Chem.* 44, 5562–5570 (2005).

5. Cramer, S. P., Xiao, Y., Wang, H., Guo, Y. & Smith, M. C. Nuclear resonance vibrational spectroscopy (NRVS) of Fe-S model compounds, Fe-S proteins, and nitrogenase. *Hyperfine Interact.* 170, 47–54 (2006).

6. Xiao, Y. *et al.* How nitrogenase shakes - Initial information about P-cluster and FeMo-cofactor normal modes from nuclear resonance vibrational spectroscopy (NRVS). *J. Am. Chem. Soc.* 128, 7608–7612 (2006).

7. Xiao, Y. *et al.* Normal Mode Analysis of Pyrococcus furiosus Rubredoxin via Nuclear Resonance Vibrational Spectroscopy (NRVS) and Resonance Raman Spectroscopy. *J. Am. Chem. Soc.* 127, 14596–14606 (2005).

8. Xiao, Y. *et al.* Dynamics of Rhodobacter capsulatus [2Fe-2S] frredoxin VI and Aquifex aeolicus frredoxin 5 via nuclear resonance vibrational spectroscopy (NRVS) and resonance raman spectroscopy. *Biochemistry* 47, 6612–6627 (2008).

9. Mitra, D. *et al.* Characterization of [4Fe-4S] cluster vibrations and structure in nitrogenase Fe protein at three oxidation levels via combined NRVS, EXAFS, and DFT analyses. *J. Am. Chem. Soc.* 135, 2530–2543 (2013).

10. Paulsen, H. *et al.* Interpretation of nuclear resonant vibrational spectra of rubredoxin using a combined quantum mechanics and molecular mechanics approach. *ChemPhysChem* 12, 3434–3441 (2011).

11. Thorhallsson, A. T., Benediktsson, B. & Bjornsson, R. A model for dinitrogen binding in the E 4 state of nitrogenase. *Chem. Sci.* 10, 11110–11124 (2019).

12. Benediktsson, B. & Bjornsson, R. Analysis of the Geometric and Electronic Structure of Spin-Coupled Iron–Sulfur Dimers with Broken-Symmetry DFT: Implications for FeMoco. *J. Chem. Theory Comput.* 18, 1437–1457 (2022).

13. Szilagyi, R. K. & Winslow, M. A. On the accuracy of density functional theory for iron—sulfur clusters. *J. Comput. Chem.* 27, 1385–1397 (2006).

14. Cao, L. & Ryde, U. Extremely large differences in DFT energies for nitrogenase models. *Phys. Chem. Chem. Phys.* 21, 2480–2488 (2019).

15. Spatzal, T. *et al.* Evidence for interstitial carbon in nitrogenase FeMo cofactor. *Science (80-. ).* 334, 940 (2011).

16. Benediktsson, B. & Bjornsson, R. QM/MM Study of the Nitrogenase MoFe Protein Resting State: Broken-Symmetry States, Protonation States, and QM Region Convergence in the FeMoco Active Site. *Inorg. Chem.* 56, 13417–13429 (2017).

17. Hess, B., Kutzner, C., Van Der Spoel, D. & Lindahl, E. GROMACS 4: Algorithms for highly efficient, load-balanced, and scalable molecular simulation. *J. Chem. Theory Comput.* 4, 435–447 (2008).

18. Abraham, M. J. *et al.* GROMACS: High performance molecular simulations through multi-level parallelism from laptops to supercomputers. *SoftwareX* 1–2, 19–25 (2015).

19. Best, R. B. *et al.* Optimization of the Additive CHARMM All-Atom Protein Force Field Targeting Improved Sampling of the Backbone phi, psi and Side-Chain chi(1) and chi(2) Dihedral Angles. *J. Chem. Theory Comput.* 8, 3257–3273 (2012).

20. Sherwood, P. *et al.* QUASI: A general purpose implementation of the QM/MM approach and its application to problems in catalysis. *J. Mol. Struct. THEOCHEM* 632, 1–28 (2003).

21. Metz, S., Kästner, J., Sokol, A. A., Keal, T. W. & Sherwood, P. ChemShell-a modular software package for QM/MM simulations. *Wiley Interdiscip. Rev. Comput. Mol. Sci.* 4, 101–110 (2014).

22. Neese, F. The ORCA program system. *Wiley Interdiscip. Rev. Mol. Sci.* 2, 73–78 (2012).

23. Neese, F. Software update: the ORCA program system, version 4.0. *Wiley Interdiscip. Rev. Comput. Mol. Sci.* 8, 4–9 (2018).

24. Smith, W. & Forester, T. R. DL_POLY_2.0: A general-purpose parallel molecular dynamics simulation package. *J. Mol. Graph.* 14, 136–141 (1996).

25. Weigend, F. & Ahlrichs, R. Balanced basis sets of split valence, triple zeta valence and quadruple zeta valence quality for H to Rn: Design and assessment of accuracy. *Phys. Chem. Chem. Phys.* 7, 3297 (2005).

26. Pantazis, D. A., Chen, X.-Y., Landis, C. R. & Neese, F. All-Electron Scalar Relativistic Basis Sets for Third-Row Transition Metal Atoms. *J. Chem. Theory Comput.* 4, 908–919

(2008).

27. Grimme, S., Antony, J., Ehrlich, S. & Krieg, H. A consistent and accurate ab initio parametrization of density functional dispersion correction (DFT-D) for the 94 elements H-Pu. *J. Chem. Phys.* 132, 154104 (2010).

28. Grimme, S., Ehrlich, S. & Goerigk, L. Effect of the damping function in dispersion corrected density functional theory. *J. Comput. Chem.* 32, 1456–1465 (2011).

29. Lenthe, E. van, Baerends, E. J. & Snijders, J. G. Relativistic regular two-component Hamiltonians. *J. Chem. Phys.* 99, 4597–4610 (1993).

30. van Wüllen, C. Molecular density functional calculations in the regular relativistic approximation: Method, application to coinage metal diatomics, hydrides, fluorides and chlorides, and comparison with first-order relativistic calculations. *J. Chem. Phys.* 109, 392–399 (1998).

31. Neese, F., Wennmohs, F., Hansen, A. & Becker, U. Efficient, approximate and parallel Hartree-Fock and hybrid DFT calculations. A 'chain-of-spheres' algorithm for the Hartree-Fock exchange. *Chem. Phys.* 356, 98–109 (2009).

32. Izsák, R. & Neese, F. An overlap fitted chain of spheres exchange method. *J. Chem. Phys.* 135, 144105 (2011).

33. Becke, A. D. Density-functional exchange-energy approximation with correct asymptotic behavior. *Phys. Rev. A* 38, 3098–3100 (1988).

34. Perdew, J. P. Density-functional approximation for the correlation energy of the inhomogeneous electron gas. *Phys. Rev. B* 33, 8822–8824 (1986).

35. Grimme, S. Semiempirical GGA-type density functional constructed with a long-range dispersion correction. *J. Comput. Chem.* 27, 1787–1799 (2006).

36. Lee, C., Yang, W. & Parr, R. G. Development of the Colle-Salvetti correlation-energy formula into a functional of the electron density. *Phys. Rev. B* 37, 785–789 (1988).

37. Becke, A. D. Density-functional thermochemistry. III. The role of exact exchange. *J. Chem. Phys.* 98, 5648–5652 (1993).

38. Reiher, M., Salomon, O. & Artur Hess, B. Reparameterization of hybrid functionals based on energy differences of states of different multiplicity. *Theor. Chem. Accounts Theory, Comput. Model. (Theoretica Chim. Acta)* 107, 48–55 (2001).

39. Salomon, O., Reiher, M. & Hess, B. A. Assertion and validation of the performance of the B3LYP⋆ functional for the first transition metal row and the G2 test set. *J. Chem. Phys.* 117, 4729–4737 (2002).

40. Becke, A. D. A new mixing of Hartree–Fock and local density-functional theories. *J. Chem. Phys.* 98, 1372–1377 (1993).

41. Yanai, T., Tew, D. P. & Handy, N. C. A new hybrid exchange-correlation functional

using the Coulomb-attenuating method (CAM-B3LYP). *Chem. Phys. Lett.* 393, 51–57 (2004).

42. Perdew, J. P., Burke, K. & Ernzerhof, M. Generalized Gradient Approximation Made Simple. *Phys. Rev. Lett.* 77, 3865–3868 (1996).

43. Perdew, J. P., Ernzerhof, M. & Burke, K. Rationale for mixing exact exchange with density functional approximations. *J. Chem. Phys.* 105, 9982–9985 (1996).

44. Tao, J. & Perdew, J. P. Climbing the Density Functional Ladder : Nonempirical Meta – Generalized Gradient Approximation Designed for Molecules and Solids. 3–6 (2003). doi:10.1103/PhysRevLett.91.146401

45. Staroverov, V. N. *et al.* Comparative assessment of a new nonempirical density functional : Molecules and hydrogen-bonded complexes Comparative assessment of a new nonempirical density functional : Molecules and hydrogen-bonded complexes. 12129, (2003).

46. Furness, J. W., Kaplan, A. D., Ning, J., Perdew, J. P. & Sun, J. Accurate and Numerically Efficient r2SCAN Meta-Generalized Gradient Approximation. *J. Phys. Chem. Lett.* 11, 8208–8215 (2020).

47. Zhao, Y. & Truhlar, D. G. The M06 suite of density functionals for main group thermochemistry, thermochemical kinetics, noncovalent interactions, excited states, and transition elements: Two new functionals and systematic testing of four M06-class functionals and 12 other function. *Theor. Chem. Acc.* 120, 215–241 (2008).

48. Najibi, A. & Goerigk, L. The Nonlocal Kernel in van der Waals Density Functionals as an Additive Correction: An Extensive Analysis with Special Emphasis on the B97M-V and ωb97M-V Approaches. *J. Chem. Theory Comput.* 14, 5725–5738 (2018).

49. Mardirossian, N. & Head-Gordon, M. ωb97X-V: A 10-parameter, range-separated hybrid, generalized gradient approximation density functional with nonlocal correlation, designed by a survival-of-the-fittest strategy. *Phys. Chem. Chem. Phys.* 16, 9904–9924 (2014).

50. Mardirossian, N. & Head-Gordon, M. ω B97M-V: A combinatorially optimized, range-separated hybrid, meta-GGA density functional with VV10 nonlocal correlation. *J. Chem. Phys.* 144, 214110 (2016).

51. Barone, V. & Cossi, M. Conductor Solvent Model. *J. Phys. Chem. A* 102, 1995–2001 (1998).

52. York, D. M. A smooth solvation potential based on the conductor-like screening model. *J. Phys. Chem. A* 103, 11040–11044 (1999).

53. Garcia-Ratés, M. & Neese, F. Effect of the Solute Cavity on the Solvation Energy and its Derivatives within the Framework of the Gaussian Charge Scheme. *J. Comput. Chem.* 41, 922–939 (2020).

54. Sandala, G. M., Hopmann, K. H., Ghosh, A. & Noodleman, L. Calibration of DFT

functionals for the prediction of 57Fe mössbauer spectral parameters in iron-nitrosyl and iron-sulfur complexes: Accurate geometries prove essential. *J. Chem. Theory Comput.* 7, 3232–3247 (2011).

55. Thorhallsson, A. T., Benediktsson, B. & Bjornsson, R. A model for dinitrogen binding in the E<inf>4</inf> state of nitrogenase. *Chem. Sci.* 10, (2019).

56. Guo, Y. *et al.* Nuclear resonance vibrational spectroscopy (NRVS) of rubredoxin and MoFe protein crystals. *Hyperfine Interact.* 222, 77–90 (2013).

57. Einsle, O. & Rees, D. C. Structural Enzymology of Nitrogenase Enzymes. *Chem. Rev.* 120, 4969–5004 (2020).

58. Van Stappen, C., Thorhallsson, A. T., Decamps, L., Bjornsson, R. & Debeer, S. Resolving the structure of the E1 state of Mo nitrogenase through Mo and Fe K-edge EXAFS and QM/MM calculations. *Chem. Sci.* 10, 9807–9821 (2019).

59. Cao, L. & Ryde, U. Protonation and reduction of the nitrogenase active site. *J. Chem. Theory Comput.* submitted (2018). doi:10.1021/acs.jctc.8b00778

60. Skubi, K. L. & Holland, P. L. So Close, yet Sulfur Away: Opening the Nitrogenase Cofactor Structure Creates a Binding Site. *Biochemistry* (2018). doi:10.1021/acs.biochem.8b00529

61. Sippel, D. *et al.* A bound reaction intermediate sheds light on the mechanism of nitrogenase. *Science (80-. ).* 359, 1484–1489 (2018).

62. Cao, L. & Ryde, U. Putative reaction mechanism of nitrogenase after dissociation of a sulfide ligand Lili Cao and Ulf Ryde *. *J. Catal.* (2020). doi:10.1016/j.jcat.2020.08.028

# 9 Appendix A - VFe protein QM/MM model

The details of how the QM/MM model of the VFe protein is prepared has already been published and details are available in the SI of the article [28]. However, here is included the same details with additional dialogue.

This section is organized in such a way that the first subsection describes the model preparation from the initial X-ray structure, the second subsection explains how the VFe protein model is equilibrated *via* molecular dynamics (MD) simulation, the third section deals with the creation of the QM/MM model, and the fourth subchapter describes the computational details for the QM/MM calculations.

## 9.1 Model preparation

The starting point of the QM/MM model of the VFe protein is the 1.35 Å resolution X-ray structure (PDB ID: 5N6Y) from Sippel and Einsle [42]. As protons are not resolved at this resolution, they are not present in the PDB file and must therefore be generated. This is a straightforward process for polar and non-polar neutral amino acids since it is easy to guess proton placement for these residues. Taking alanine as an example with its methyl group, any person with an organic chemistry background would be able to make a reasonable guess to proton placement on the methyl group. This, on the other hand, is not as straightforward for titrable residues that have sidechains that are alkaline or acidic. These residues are glutamate, aspartate, lysine, arginine and histidine. Taking glutamate as an example, depending on its protein environment the carboxyl group on its sidechain can either be protonated or deprotonated.

For the QM/MM model of the VFe protein, the protonation state of titrable residues was deduced from visual inspection of hydrogen bonds. As the VFe protein is a $\alpha_2\beta_2\gamma_2$ heterohexamer, made up from two units of $\alpha\beta\gamma$ trimers, only protonation state of residues in one of the trimers was investigated. No arginine or lysine was deemed deprotonated and no glutamate was protonated. Only the follwing aspartate residues were designated as protonated: $\alpha - 9^{Asp}$, $\beta - 30^{Asp}$, and $\beta - 73^{Asp}$.

Histidine on the other hand is more tricky as there are two titrable sites on each residue, the $\delta$ or the $\epsilon$ nitrogen. The following histidines were protonated on the $\delta$ nitrogen: $\alpha-364^{His}$, $\alpha-448^{His}$, $\beta-80^{His}$, $\beta-177^{His}$, $\beta-334^{His}$, $\gamma-5^{His}$, and $\gamma-110^{His}$. The following histinde residues were protonated on the $\epsilon$ nitrogen: $\alpha-18^{His}$, $\alpha-70^{His}$, $\alpha-81^{His}$, $\alpha-91^{His}$, $\alpha-106^{His}$, $\alpha-120^{His}$, $\alpha-180^{His}$, $\alpha-181^{His}$, $\alpha-234^{His}$, $\alpha-248^{His}$, $\alpha-342^{His}$, $\alpha-416^{His}$, $\alpha-423^{His}$, $\alpha-426^{His}$, $\alpha-453^{His}$, $\beta-51^{His}$, $\beta-51^{His}$, $\beta-67^{His}$, $\beta-158^{His}$, $\beta-234^{His}$, $\beta-321^{His}$, $\beta-379^{His}$, $\beta-409^{His}$, $\beta-461^{His}$, and $\gamma-111^{His}$. It is also possible that both nitrogens are either deprotonated or protonated but only $\beta-150^{His}$ is found to be doubly protonated and no histidine residue is found to be doubly deprotonated.

Furthermore, cysteine residues ligated to metals were modeled as cysteinate residues (with a deprotonated sulfide). These are the residues $\alpha-49^{Cys}$, $\alpha-75^{Cys}$, $\alpha-138^{Cys}$, $\alpha-257^{Cys}$, $\beta-31^{Cys}$, $\beta-56^{Cys}$, and $\beta-115^{Cys}$.

In addition to protonation states of some residues, it may be difficult to distuingish between N and O atoms or C and N atoms in X-ray structures at lower resolutions (higher value in Å), as the electron density of these atoms are quite similar. This is generally not an issue for most residues, since if one knows the molecular structure of an amino acid, it is easy to assign whether a given electron density corresponds to a nitrogen or an oxygen. This is not the case for residues such as glutamine, histidine and asparagine. The orientation of the side chain can have significant effect on the hydrogen bonding network so one has to take care that the orientatin of these residues are correct. Generally speaking this is not an issue as crystallographers take a great care in resolving the X-ray structures, but one may still disagree with their interpretation of the electron density and take an independent decision from an analysis of hydrogen bond networks.

The following residues had their functional group flipped: $\alpha-120^{His}$, $\alpha-249^{Gln}$, $\alpha-426^{His}$, $\beta-243^{His}$, $\beta-260^{Asn}$, $\beta-267^{Gln}$, $\beta-361^{Gln}$, $\gamma-3^{Gln}$, and $\gamma-46^{Gln}$.

## 9.2 Equilibration by molecular dynamics

In order to have an equilibrated starting point, an MM model of the VFe protein in solution is created and simulated *via* MD. To do so, the program GROMACS version 5.1.4 was used [167] with the CHARMM36 forcefield [168] for the protein, TIP3P for water [169], and modified forcefield paramaters of citrate for homocitrate [170]. There are no forcefield

parameters available for FeVco and the P-cluster, but the SM atom type was used for Lennard-Jones parameters on sulfides but for charges on irons, sulfides, carbonate, and carbide are derived from Hirshfeld population analysis of X-ray geometry of FeVco assuming that the overall structure and charge of FeVco is $[VFe_7S_8(CO_3)C]^{2-}$.

The computational details for the Hirshfeld analysis are as follows. For the electronic structure, ORCA version 3.0.3 was used with the density functional TPSSh, a relativistically recontracted triple-$\zeta$ basis set on iron, vanadium, sulfide, carbonate, and carbide whereas other atoms had a double-$\zeta$ basis set. A relativistic ZORA hamiltonian was employed to include relativistic effects, RIJCOSX to speed up calculations, and finally the protein matrix was approximated using the conductor like screening model (COSMO) [171] using the value for the dielectric constant of $\epsilon = 4$. The model includes the $[VFe_7S_8(CO_3)C]^{2-}$ part, homocitrate, side chain of the histinde and cysteine residues connected to FeVco. The Carboxylate groups on homocitrate were protonated and proton placement optimized.

Here, the preparation of the QM/MM model is split up into seven steps.

1. Entries in the topology file and parameters file were made for FeVco, where the atom type SM was used for sulfides but pointcharges for all atoms in the cofactor were derived from a Hirshfeld charge analysis. Then the original PDB file is processed and protons generated.

2. A cubic system with periodic boundary conditions is defined with the requirement that the edge of the system is at least 10 Å away from the VFe protein everywhere. The volume of the cubic simulation box is 5356.17 $nm^3$ with all sides of the same length (174.97 Å).

3. Water molecules are generated at random positions, mainly outside of the protein matrix. After solvation, the density of the system is 1006 g/l.

4. The VFe protein has an overall negative charge of -62 and the overall charge was neutralized by replacing random water molecules with sodium ions.

5. Water molecules, sodium ions, and protons of the protein are relaxed using the steepest descent algorithm.

6. A restricted molecular dynamics simulation is performed using the velocity-Verlet algorithm [172, 173] with cons, where only water, sodium ions, and protons are allowed to move, for 5 ns within the canonical ensemble. The velocities of atoms are generated from a

Boltzmann distribution at 50 K and the system is slowly heated from 50 K to 300 K over a time period of 500 ps and kept at 300 K using a four-chain Nosé-Hover thermostat [174, 175]. A snapshot of the MD simulation was taken at 1100 ps to be used in the generation of the QM/MM model.

## 9.3 Construction of the QM/MM model

The afforementioned snapshot at 1100 ps is used to generate the QM/MM model. The coordinates are loaded into VMD [176] and a spherical model of 32 562 atoms is created. This spherical model includes all water molecules and residues within 42 Å of the central carbide of FeVco in addition to residues numbered 12 to 19, 194 to 209, and 282 to 440 from chain D (as labelled in the X-ray structure). The overall charge of the model is -35 so 35 sodium ions were included in total.

This spherical model was then saved as a PDB file and processed with in-house script made by Dr. Bjornsson.

## 9.4 QM/MM computational details

Chemshell version 3.7 [24, 177] was used to perform the QM/MM calculations, whereas ORCA version 4.1.0 [20, 178] was used to do the QM part and DL_POLY [179] (as implemented in Chemshell) with the CHARMM36 forcefield [168] for the MM part. For geometry optimizations, DL-FIND [180] was used and link atoms, as implemented in Chemshell, were used to terminate the QM-MM border with a charge shift scheme [24].

The electronic structure calculations were performed with the hybrid meta-GGA functional TPSSh [181, 182], using a relativistically recontracted def2 Ahlrichs basis set [113, 183] with a triple-$\zeta$ basis set (ORCA keyword ZORA-def2-TZVP) on Fe, V, S, $XO_3$, and carbide whereas a smaller double-$\zeta$ basis set (ORCA keyword ZORA-def2-SVP) was used on all other atoms. In order to speed up the Coulomb and exchange integrals, the RIJCOSX approximation was used [184, 185] with the default grid and an auxiliary basis set (SARC/J keyword in ORCA) [186]. In order to correct for dispersion effects, the D3BJ dispersion correction [187, 188] was used and to account for relativistic effects, the zeroth order regular approximation (ZORA) Hamiltonian [119, 120] was used.

It is rather impractical to do an optimization of 32 562 atoms and therefore the most of the molecules in the QM/MM model are frozen. Therefore, an active region of 1 038 atoms was chosen, *i.e.* atoms that are

allowed to move during geometrical optimizations. Most of these 1 038 atoms are described *via* a forcefield but at the center of active region is the QM region which is described by DFT. Three QM region sizes were chosen:

1. A 57 QM atom QM-region which only includes FeVco, $\alpha - 257^{Cys}$, and $\alpha - 423^{His}$.

2. A 83 QM atom QM-region which includes FeVco, $\alpha - 257^{Cys}$, $\alpha - 423^{His}$, $\alpha - 83^{Lys}$, $\alpha - 339^{Arg}$, and $\alpha - 361^{Lys}$

3. A 83 QM atom QM-region which includes FeVco, $\alpha - 52^{Cys}$, $\alpha - 83^{Lys}$, $\alpha - 176^{Gln}$, $\alpha - 180^{His}$, $\alpha - 257^{Cys}$, $\alpha - 260^{Ser}$, $\alpha - 335^{Thr}$, $\alpha - 336^{Gly}$, $\alpha - 337^{Gly}$, $\alpha - 338^{Pro}$, $\alpha - 339^{Arg}$, $\alpha - 361^{Lys}$, and $\alpha - 423^{His}$

# 10 Bibliography

# Bibliography


1. Johnson, M. K. & Smith, A. D. in *Encyclopedia of Inorganic and Bioinorganic Chemistry* (John Wiley and Sons Ltd, 2011). ISBN: 9781119951438. eprint: `https://onlinelibrary.wiley.com/doi/pdf/10.1002/9781119951438.eibc0109`.
2. Dixon, R. & Kahn, D. Genetic regulation of biological nitrogen fixation. *Nature Reviews Microbiology* **2,** 621–631 (2004).
3. Einsle, O. & Rees, D. C. Structural enzymology of nitrogenase enzymes. *Chemical reviews* **120,** 4969–5004 (2020).
4. Seefeldt, L. C. *et al.* Reduction of substrates by nitrogenases. *Chemical reviews* **120,** 5082–5106 (2020).
5. Nørskov, J., Chen, J., Miranda, R., Fitzsimmons, T. & Stack, R. *Sustainable Ammonia Synthesis–Exploring the scientific challenges associated with discovering alternative, sustainable processes for ammonia production* tech. rep. (US DOE Office of Science, 2016).
6. Noodleman, L., Peng, C., Case, D. & Mouesca, J.-M. Orbital interactions, electron delocalization and spin coupling in iron-sulfur clusters. *Coordination Chemistry Reviews* **144,** 199–244 (1995).
7. Chilkuri, V. G., DeBeer, S. & Neese, F. Ligand Field Theory and Angular Overlap Model Based Analysis of the Electronic Structure of Homovalent Iron–Sulfur Dimers. *Inorganic chemistry* **59,** 984–995 (2019).
8. Schrödinger, E. An undulatory theory of the mechanics of atoms and molecules. *Physical review* **28,** 1049 (1926).
9. Jensen, F. in *Introduction to Computational Chemistry, 3rd Edition* n (Wiley, 2017). ISBN: 978-1-118-82599-0.
10. Born, M. & Oppenheimer, R. Zur quantentheorie der molekeln. *Annalen der physik* **389,** 457–484 (1927).
11. Sommerfeld, T. Lorentz trial function for the hydrogen atom: a simple, elegant exercise. *Journal of Chemical Education* **88,** 1521–1524 (2011).

12. Hohenberg, P. & Kohn, W. Inhomogeneous electron gas. *Physical review* **136,** B864 (1964).

13. Kohn, W. & Sham, L. J. Self-consistent equations including exchange and correlation effects. *Physical review* **140,** A1133 (1965).

14. Fermi, E. Statistical method to determine some properties of atoms. *Rend. Accad. Naz. Lincei* **6,** 5 (1927).

15. Thomas, L. H. *The calculation of atomic fields* in *Mathematical proceedings of the Cambridge philosophical society* **23** (1927), 542–548.

16. Becke, A. D. Density-functional exchange-energy approximation with correct asymptotic behavior. *Physical review A* **38,** 3098 (1988).

17. Perdew, J. P. Density-functional approximation for the correlation energy of the inhomogeneous electron gas. *Physical Review B* **33,** 8822 (1986).

18. Becke, A. D. Density-functional thermochemistry. III. The role of exact exchange. *The Journal of Chemical Physics* **98,** 5648–5652 (1993).

19. Sharma, S., Sivalingam, K., Neese, F. & Chan, G. K. Low-energy spectrum of iron–sulfur clusters directly from many-particle quantum mechanics. *Nature chemistry* **6,** 927–933 (2014).

20. Neese, F. Software update: the ORCA program system, version 4.0. *Wiley Interdisciplinary Reviews: Computational Molecular Science* **8,** e1327 (2018).

21. Jorgensen, W. L., Chandrasekhar, J., Madura, J. D., Impey, R. W. & Klein, M. L. Comparison of simple potential functions for simulating liquid water. *The Journal of chemical physics* **79,** 926–935 (1983).

22. Senn, H. M. & Thiel, W. QM/MM methods for biological systems. *Atomistic approaches in modern biology,* 173–290 (2006).

23. Vennelakanti, V., Nazemi, A., Mehmood, R., Steeves, A. H. & Kulik, H. J. Harder, better, faster, stronger: large-scale QM and QM/MM for predictive modeling in enzymes and proteins. *Current opinion in structural biology* **72,** 9–17 (2022).

24. Sherwood, P. *et al.* QUASI: A general purpose implementation of the QM/MM approach and its application to problems in catalysis. *Journal of Molecular Structure: THEOCHEM* **632,** 1–28 (2003).

25. Mulliken, R. S. Electronic population analysis on LCAO–MO molecular wave functions. I. *The Journal of Chemical Physics* **23,** 1833–1840 (1955).

26. Hirshfeld, F. L. Bonded-atom fragments for describing molecular charge densities. *Theoretica chimica acta* **44,** 129–138 (1977).

27. Mayer, I. Charge, bond order and valence in the AB initio SCF theory. *Chemical Physics Letters* **97,** 270–274 (1983).

28. Benediktsson, B. & Bjornsson, R. Quantum Mechanics/Molecular Mechanics Study of Resting-State Vanadium Nitrogenase: Molecular and Electronic Structure of the Iron-Vanadium Cofactor. *Inorganic Chemistry* **59,** 11514–11527 (2020).

29. McRose, D. L., Zhang, X., Kraepiel, A. M. & Morel, F. M. Diversity and activity of alternative nitrogenases in sequenced genomes and coastal environments. *Frontiers in microbiology* **8,** 267 (2017).

30. Bishop, P. E. & Joerger, R. D. Genetics and molecular biology of alternative nitrogen fixation systems. *Annual review of plant biology* **41,** 109–125 (1990).

31. Jasniewski, A. J., Lee, C. C., Ribbe, M. W. & Hu, Y. Reactivity, mechanism, and assembly of the alternative nitrogenases. *Chemical reviews* **120,** 5107–5157 (2020).

32. Rebelein, J. G., Lee, C. C., Hu, Y. & Ribbe, M. W. The in vivo hydrocarbon formation by vanadium nitrogenase follows a secondary metabolic pathway. *Nature communications* **7,** 1–6 (2016).

33. Bulen, W. & LeComte, J. The nitrogenase system from Azotobacter: two-enzyme requirement for N2 reduction, ATP-dependent H2 evolution, and ATP hydrolysis. *Proceedings of the National Academy of Sciences of the United States of America* **56,** 979 (1966).

34. Silverstein, R. & Bulen, W. A. Kinetic studies of the nitrogenase-catalyzed hydrogen evolution and nitrogen reduction reactions. *Biochemistry* **9,** 3809–3815 (1970).

35. Lukoyanov, D. *et al.* Reductive Elimination of H2 Activates Nitrogenase to Reduce the N N Triple Bond: Characterization of the E4 (4H) Janus Intermediate in Wild-Type Enzyme. *Journal of the American Chemical Society* **138,** 10674–10683 (2016).

36. Harris, D. F. *et al.* Mechanism of N2 reduction catalyzed by Fe-nitrogenase involves reductive elimination of H2. *Biochemistry* **57,** 701–710 (2018).

37. Harris, D. F. *et al.* Mo-, V-, and Fe-nitrogenases use a universal eight-electron reductive-elimination mechanism to achieve N2 reduction. *Biochemistry* **58,** 3293–3301 (2019).

38. Eady, R. R. Structure- function relationships of alternative nitrogenases. *Chemical reviews* **96,** 3013–3030 (1996).

39. Lancaster, K. M. *et al.* X-ray emission spectroscopy evidences a central carbon in the nitrogenase iron-molybdenum cofactor. *Science* **334,** 974–977 (2011).

40. Spatzal, T. *et al.* Evidence for interstitial carbon in nitrogenase FeMo cofactor. *Science* **334,** 940–940 (2011).

41. Harris, T. V. & Szilagyi, R. K. Comparative assessment of the composition and charge state of nitrogenase FeMo-cofactor. *Inorganic chemistry* **50,** 4811–4824 (2011).

42. Sippel, D. & Einsle, O. The structure of vanadium nitrogenase reveals an unusual bridging ligand. *Nature Chemical Biology* **13,** 956–960 (2017).

43. Burgess, B. K. The iron-molybdenum cofactor of nitrogenase. *Chemical Reviews* **90,** 1377–1406 (1990).

44. Bjornsson, R., Neese, F. & DeBeer, S. Revisiting the Mössbauer Isomer Shifts of the FeMoco Cluster of Nitrogenase and the Cofactor Charge. *Inorganic chemistry* **56,** 1470–1477 (2017).

45. Spatzal, T. *et al.* Nitrogenase FeMoco investigated by spatially resolved anomalous dispersion refinement. *Nature communications* **7,** 1–7 (2016).

46. Benediktsson, B. & Bjornsson, R. QM/MM study of the nitrogenase MoFe protein resting state: Broken-symmetry states, protonation states, and QM region convergence in the FeMoco active site. *Inorganic Chemistry* **56,** 13417–13429 (2017).

47. Bjornsson, R. *et al.* Identification of a spin-coupled Mo (III) in the nitrogenase iron–molybdenum cofactor. *Chemical Science* **5,** 3096–3103 (2014).

48. Kowalska, J. K. *et al.* X-ray Magnetic Circular Dichroism Spectroscopy Applied to Nitrogenase and Related Models: Experimental Evidence for a Spin-Coupled Molybdenum (III) Center. *Angewandte Chemie International Edition* **58,** 9373–9377 (2019).

49. Eady, R. R. Current status of structure function relationships of vanadium nitrogenase. *Coordination Chemistry Reviews* **237,** 23–30 (2003).

50. Yang, Z.-Y. *et al.* The electronic structure of FeV-cofactor in vanadium-dependent nitrogenase. *Chemical science* **12,** 6913–6922 (2021).

51. Rees, J. A. *et al.* Comparative electronic structures of nitrogenase FeMoco and FeVco. *Dalton Transactions* **46,** 2445–2455 (2017).

52. George, G., Coyle, C., Hales, B. & Cramer, S. P. X-ray absorption of Azotobacter vinelandii vanadium nitrogenase. *Journal of the American Chemical Society* **110,** 4057–4059 (1988).

53. Arber, J. M. *et al.* Vanadium K-edge X-ray absorption spectrum of the VFe protein of the vanadium nitrogenase of Azotobacter chroococcum. *Nature* **325,** 372–374 (1987).

54. Thorneley, R. N. & Lowe, D. J. Kinetics and mechanism of the nitrogenase enzyme system. *Molybdenum enzymes* **7,** 89–116 (1985).

55. Burgess, B. K. & Lowe, D. J. Mechanism of molybdenum nitrogenase. *Chemical reviews* **96,** 2983–3012 (1996).

56. Thorneley, R. N. & Lowe, D. Nitrogenase of Klebsiella pneumoniae. Kinetics of the dissociation of oxidized iron protein from molybdenum-iron protein: identification of the rate-limiting step for substrate reduction. *Biochemical Journal* **215,** 393–403 (1983).

57. Lee, C. C., Hu, Y. & Ribbe, M. W. Vanadium nitrogenase reduces CO. *Science* **329,** 642–642 (2010).

58. Sickerman, N. S., Hu, Y. & Ribbe, M. W. Activation of CO2 by vanadium nitrogenase. *Chemistry–An Asian Journal* **12,** 1985–1996 (2017).

59. Oehlmann, N. N. & Rebelein, J. G. The Conversion of Carbon Monoxide and Carbon Dioxide by Nitrogenases. *ChemBioChem* (2021).

60. Sippel, D. *et al.* A bound reaction intermediate sheds light on the mechanism of nitrogenase. *Science* **359,** 1484–1489 (2018).

61. Benediktsson, B., Thorhallsson, A. T. & Bjornsson, R. QM/MM calculations reveal a bridging hydroxo group in a vanadium nitrogenase crystal structure. *Chemical Communications* **54,** 7310–7313 (2018).

62. Cao, L., Caldararu, O. & Ryde, U. Does the crystal structure of vanadium nitrogenase contain a reaction intermediate? Evidence from quantum refinement. *JBIC Journal of Biological Inorganic Chemistry* **25,** 847–861 (2020).

63. Lovell, T. *et al.* Metal substitution in the active site of nitrogenase MFe7S9 (M= Mo4+, V3+, Fe3+). *Inorganic chemistry* **41,** 5744–5753 (2002).

64. Dance, I. How does vanadium nitrogenase reduce CO to hydrocarbons? *Dalton Transactions* **40,** 5516–5527 (2011).

65. Varley, J. B. & Nørskov, J. K. First-Principles Calculations of Fischer–Tropsch Processes Catalyzed by Nitrogenase Enzymes. *ChemCatChem* **5,** 732–736 (2013).

66. Rees, J. A. *et al.* The Fe–V cofactor of vanadium nitrogenase contains an Interstitial carbon atom. *Angewandte Chemie International Edition* **54,** 13249–13252 (2015).

67. Cao, L., Caldararu, O. & Ryde, U. Does the crystal structure of vanadium nitrogenase contain a reaction intermediate? Evidence from quantum refinement. *JBIC Journal of Biological Inorganic Chemistry* **25,** 847–861 (2020).

68. Bergmann, J., Oksanen, E. & Ryde, U. Quantum-refinement studies of the bidentate ligand of V-nitrogenase and the protonation state of CO-inhibited Mo-nitrogenase. *Journal of Inorganic Biochemistry* **219,** 111426 (2021).

69. Lovell, T., Li, J., Case, D. A. & Noodleman, L. FeMo cofactor of nitrogenase: energetics and local interactions in the protein environment. *JBIC Journal of Biological Inorganic Chemistry* **7,** 735–749 (2002).

70. Cao, L. & Ryde, U. Influence of the protein and DFT method on the broken-symmetry and spin states in nitrogenase. *International Journal of Quantum Chemistry* **118,** e25627 (2018).

71. Cao, L. & Ryde, U. Extremely large differences in DFT energies for nitrogenase models. *Physical Chemistry Chemical Physics* **21,** 2480–2488 (2019).

72. Benediktsson, B. & Bjornsson, R. Analysis of the Geometric and Electronic Structure of Spin-Coupled Iron–Sulfur Dimers with Broken-Symmetry DFT: Implications for FeMoco. *Journal of chemical theory and computation* **18,** 1437–1457 (2022).

73. Chandra, A. & Gerson, A. R. The mechanisms of pyrite oxidation and leaching: A fundamental perspective. *Surface Science Reports* **65,** 293–315 (2010).

74. Fontecave, M. Iron-sulfur clusters: ever-expanding roles. *Nature chemical biology* **2,** 171–174 (2006).

75. Cammack, R. in *Advances in inorganic chemistry* 281–322 (Elsevier, 1992).

76. Stephens, P., Jollie, D. & Warshel, A. Protein control of redox potentials of iron- sulfur proteins. *Chemical Reviews* **96,** 2491–2514 (1996).

77. Venkateswara Rao, P. & Holm, R. Synthetic analogues of the active sites of iron- sulfur proteins. *Chemical reviews* **104,** 527–560 (2004).

78. Yamaguchi, K., Takahara, Y. & Fueno, T. in *Applied quantum chemistry* 155–184 (Springer, 1986).

79. Soda, T. *et al.* Ab initio computations of effective exchange integrals for H–H, H–He–H and Mn2O2 complex: comparison of broken-symmetry approaches. *Chemical Physics Letters* **319,** 223–230 (2000).

80. Ginsberg, A. Magnetic exchange in transition metal complexes. 12. Calculation of cluster exchange coupling constants with the X. alpha.-scattered wave method. *Journal of the American Chemical Society* **102,** 111–117 (1980).

81. Noodleman, L. Valence bond description of antiferromagnetic coupling in transition metal dimers. *The Journal of Chemical Physics* **74,** 5737–5743 (1981).

82. Noodleman, L. & Davidson, E. R. Ligand spin polarization and antiferromagnetic coupling in transition metal dimers. *Chemical physics* **109,** 131–143 (1986).

83. Illas, F., de PR Moreira, I., Bofill, J. & Filatov, M. Extent and limitations of density-functional theory in describing magnetic systems. *Physical Review B* **70,** 132414 (2004).

84. Pantazis, D. A., Krewald, V., Orio, M. & Neese, F. Theoretical magnetochemistry of dinuclear manganese complexes: broken symmetry density functional theory investigation on the influence of bridging motifs on structure and magnetism. *Dalton Transactions* **39,** 4959–4967 (2010).

85. Blachly, P. G. *et al.* Broken-Symmetry DFT computations for the reaction pathway of IspH, an iron–sulfur enzyme in pathogenic bacteria. *Inorganic chemistry* **54,** 6439–6461 (2015).

86. Donnan, P. H. & Mansoorabadi, S. O. Broken-Symmetry Density Functional Theory Analysis of the Ω Intermediate in Radical S-Adenosyl-l-methionine Enzymes: Evidence for a Near-Attack Conformer over an Organometallic Species. *Journal of the American Chemical Society* (2022).

87. Goerigk, L. *et al.* A look at the density functional theory zoo with the advanced GMTKN55 database for general main group thermochemistry, kinetics and noncovalent interactions. *Physical Chemistry Chemical Physics* **19,** 32184–32215 (2017).

88. Kozuch, S., Gruzman, D. & Martin, J. M. DSD-BLYP: A general purpose double hybrid density functional including spin component scaling and dispersion correction. *The Journal of Physical Chemistry C* **114,** 20801–20808 (2010).

89. Chai, J.-D. & Head-Gordon, M. Long-range corrected hybrid density functionals with damped atom–atom dispersion corrections. *Physical Chemistry Chemical Physics* **10,** 6615–6620 (2008).

90. Lin, Y.-S., Li, G.-D., Mao, S.-P. & Chai, J.-D. Long-range corrected hybrid density functionals with improved dispersion corrections. *Journal of Chemical Theory and Computation* **9,** 263–272 (2013).

91. Zhao, Y. & Truhlar, D. G. Design of density functionals that are broadly accurate for thermochemistry, thermochemical kinetics, and nonbonded interactions. *The Journal of Physical Chemistry A* **109,** 5656–5667 (2005).

92. Sun, J., Ruzsinszky, A. & Perdew, J. P. Strongly constrained and appropriately normed semilocal density functional. *Physical review letters* **115,** 036402 (2015).

93. Zhang, Y. & Yang, W. Comment on "Generalized gradient approximation made simple". *Physical Review Letters* **80,** 890 (1998).

94. Grimme, S. Semiempirical GGA-type density functional constructed with a long-range dispersion correction. *Journal of computational chemistry* **27,** 1787–1799 (2006).

95. Bühl, M. & Kabrede, H. Geometries of transition-metal complexes from density-functional theory. *Journal of Chemical Theory and Computation* **2,** 1282–1290 (2006).

96. Waller, M. P., Braun, H., Hojdis, N. & Bühl, M. Geometries of second-row transition-metal complexes from density-functional theory. *Journal of chemical theory and computation* **3,** 2234–2242 (2007).

97. Buhl, M., Reimann, C., Pantazis, D. A., Bredow, T. & Neese, F. Geometries of third-row transition-metal complexes from density-functional theory. *Journal of chemical theory and computation* **4,** 1449–1459 (2008).

98. Dohm, S., Hansen, A., Steinmetz, M., Grimme, S. & Checinski, M. P. Comprehensive thermochemical benchmark set of realistic closed-shell metal organic reactions. *Journal of chemical theory and computation* **14,** 2596–2608 (2018).

99. Maurer, L. R., Bursch, M., Grimme, S. & Hansen, A. Assessing Density Functional Theory for Chemically Relevant Open-Shell Transition Metal Reactions. *Journal of Chemical Theory and Computation* **17,** 6134–6151 (2021).

100. Szilagyi, R. K. & Winslow, M. A. On the accuracy of density functional theory for iron—sulfur clusters. *Journal of computational chemistry* **27,** 1385–1397 (2006).

101. Harris, T. V. & Szilagyi, R. K. Iron–sulfur bond covalency from electronic structure calculations for classical iron–sulfur clusters. *Journal of computational chemistry* **35,** 540–552 (2014).

102. Sandala, G. M., Hopmann, K. H., Ghosh, A. & Noodleman, L. Calibration of DFT Functionals for the Prediction of 57Fe Mössbauer Spectral Parameters in Iron–Nitrosyl and Iron–Sulfur Complexes: Accurate Geometries Prove Essential. *Journal of chemical theory and computation* **7,** 3232–3247 (2011).

103. Jafari, S., Tavares Santos, Y. A., Bergmann, J., Irani, M. & Ryde, U. Benchmark Study of Redox Potential Calculations for Iron–Sulfur Clusters in Proteins. *Inorganic chemistry* (2022).

104. Dance, I. Computational investigations of the chemical mechanism of the enzyme nitrogenase. *ChemBioChem* **21,** 1671–1709 (2020).

105. Thorhallsson, A. T., Benediktsson, B. & Bjornsson, R. A model for dinitrogen binding in the E 4 state of nitrogenase. *Chemical science* **10,** 11110–11124 (2019).

106. Cao, L. & Ryde, U. Putative reaction mechanism of nitrogenase after dissociation of a sulfide ligand. *Journal of Catalysis* **391,** 247–259 (2020).

107. Wei, W.-J. & Siegbahn, P. E. The active E4 structure of nitrogenase studied with different DFT functionals. *Journal of computational chemistry* **42,** 81–85 (2021).

108. Raugei, S., Seefeldt, L. C. & Hoffman, B. M. Critical computational analysis illuminates the reductive-elimination mechanism that activates nitrogenase for N2 reduction. *Proceedings of the National Academy of Sciences* **115,** E10521–E10530 (2018).

109. Dance, I. How feasible is the reversible S-dissociation mechanism for the activation of FeMo-co, the catalytic site of nitrogenase? *Dalton Transactions* **48,** 1251–1262 (2019).

110. Rao, L., Xu, X. & Adamo, C. Theoretical investigation on the role of the central carbon atom and close protein environment on the nitrogen reduction in Mo nitrogenase. *ACS Catalysis* **6,** 1567–1577 (2016).

111. Mejuto-Zaera, C. *et al.* The Effect of Geometry, Spin, and Orbital Optimization in Achieving Accurate, Correlated Results for Iron–Sulfur Cubanes. *Journal of Chemical Theory and Computation* (2022).

112. Drüeke, S. *et al.* The novel mixed-valence, exchange-coupled, class III dimer [L 2 Fe 2 ($\mu$-OH) 3] 2+(L= N, N, N -trimethyl-1, 4, 7-triazacyclononane). *Journal of the Chemical Society, Chemical Communications,* 59–62 (1989).

113. Weigend, F. & Ahlrichs, R. Balanced basis sets of split valence, triple zeta valence and quadruple zeta valence quality for H to Rn: Design and assessment of accuracy. *Physical Chemistry Chemical Physics* **7,** 3297–3305 (2005).

114. Hay, P. J. & Wadt, W. R. Ab initio effective core potentials for molecular calculations. Potentials for K to Au including the outermost core orbitals. *The Journal of chemical physics* **82,** 299–310 (1985).

115. Hehre, W. J., Ditchfield, R. & Pople, J. A. Self—consistent molecular orbital methods. XII. Further extensions of Gaussian—type basis sets for use in molecular orbital studies of organic molecules. *The Journal of Chemical Physics* **56,** 2257–2261 (1972).

116. Francl, M. M. *et al.* Self-consistent molecular orbital methods. XXIII. A polarization-type basis set for second-row elements. *The Journal of Chemical Physics* **77,** 3654–3665 (1982).

117. Dolg, M., Wedig, U., Stoll, H. & Preuss, H. Energy-adjusted abinitio pseudopotentials for the first row transition elements. *The Journal of chemical physics* **86,** 866–872 (1987).

118. Bergner, A., Dolg, M., Küchle, W., Stoll, H. & Preuß, H. Ab initio energy-adjusted pseudopotentials for elements of groups 13–17. *Molecular Physics* **80,** 1431–1441 (1993).

119. Lenthe, E. v., Baerends, E.-J. & Snijders, J. G. Relativistic regular two-component Hamiltonians. *The Journal of chemical physics* **99,** 4597–4610 (1993).

120. Van Wüllen, C. Molecular density functional calculations in the regular relativistic approximation: Method, application to coinage metal diatomics, hydrides, fluorides and chlorides, and comparison with first-order relativistic calculations. *The Journal of chemical physics* **109,** 392–399 (1998).

121. Perdew, J. P., Burke, K. & Ernzerhof, M. Generalized gradient approximation made simple. *Physical review letters* **77,** 3865 (1996).

122. Perdew, J. P., Ernzerhof, M. & Burke, K. Rationale for mixing exact exchange with density functional approximations. *The Journal of chemical physics* **105,** 9982–9985 (1996).

123. Tao, J., Perdew, J. P., Staroverov, V. N. & Scuseria, G. E. Climbing the density functional ladder: Nonempirical meta–generalized gradient approximation designed for molecules and solids. *Physical Review Letters* **91,** 146401 (2003).

124. Staroverov, V. N., Scuseria, G. E., Tao, J. & Perdew, J. P. Comparative assessment of a new nonempirical density functional: Molecules and hydrogen-bonded complexes. *The Journal of chemical physics* **119,** 12129–12137 (2003).

125. Lee, C., Yang, W. & Parr, R. G. Development of the Colle-Salvetti correlation-energy formula into a functional of the electron density. *Physical review B* **37,** 785 (1988).

126. Salomon, O., Reiher, M. & Hess, B. A. Assertion and validation of the performance of the B3LYP functional for the first transition metal row and the G2 test set. *The Journal of chemical physics* **117,** 4729–4737 (2002).

127. Reiher, M., Salomon, O. & Artur Hess, B. Reparameterization of hybrid functionals based on energy differences of states of different multiplicity. *Theoretical Chemistry Accounts* **107,** 48–55 (2001).

128. Becke, A. D. A new mixing of Hartree–Fock and local density-functional theories. *The Journal of chemical physics* **98,** 1372–1377 (1993).

129. Furness, J. W., Kaplan, A. D., Ning, J., Perdew, J. P. & Sun, J. Accurate and numerically efficient r2SCAN meta-generalized gradient approximation. *The journal of physical chemistry letters* **11,** 8208–8215 (2020).

130. Zhao, Y. & Truhlar, D. G. The M06 suite of density functionals for main group thermochemistry, thermochemical kinetics, noncovalent interactions, excited states, and transition elements: two new functionals and systematic testing of four M06-class functionals and 12 other functionals. *Theoretical chemistry accounts* **120,** 215–241 (2008).

131. Yanai, T., Tew, D. P. & Handy, N. C. A new hybrid exchange–correlation functional using the Coulomb-attenuating method (CAM-B3LYP). *Chemical physics letters* **393,** 51–57 (2004).

132. Mardirossian, N. & Head-Gordon, M. $\omega$ B97M-V: A combinatorially optimized, range-separated hybrid, meta-GGA density functional with VV10 nonlocal correlation. *The Journal of chemical physics* **144,** 214110 (2016).

133. Najibi, A. & Goerigk, L. The nonlocal kernel in van der Waals density functionals as an additive correction: An extensive analysis with special emphasis on the B97M-V and $\omega$B97M-V approaches. *Journal of Chemical Theory and Computation* **14,** 5725–5738 (2018).

134. Mardirossian, N. & Head-Gordon, M. $\omega$B97X-V: A 10-parameter, range-separated hybrid, generalized gradient approximation density functional with nonlocal correlation, designed by a survival-of-the-fittest strategy. *Physical Chemistry Chemical Physics* **16,** 9904–9924 (2014).

135. Baiz, C. R. *et al.* Vibrational spectroscopic map, vibrational spectroscopy, and intermolecular interaction. *Chemical reviews* **120,** 7152–7218 (2020).

136. Scheidt, W. R., Durbin, S. M. & Sage, J. T. Nuclear resonance vibrational spectroscopy–NRVS. *Journal of inorganic biochemistry* **99,** 60–71 (2005).

137. Gerber, R., Brauer, B., Gregurick, S. & Chaban, G. Calculation of anharmonic vibrational spectroscopy of small biological molecules. *PhysChemComm* **5,** 142–150 (2002).

138. Petrenko, T., Sturhahn, W. & Neese, F. First-principles calculation of nuclear resonance vibrational spectra. *Hyperfine interactions* **175,** 165–174 (2007).

139. Sage, J. *et al.* Nuclear resonance vibrational spectroscopy of a protein active-site mimic. *Journal of Physics: Condensed Matter* **13,** 7707 (2001).

140. Leu, B. M. *et al.* Quantitative vibrational dynamics of iron in carbonyl porphyrins. *Biophysical journal* **92,** 3764–3783 (2007).

141. Scheidt, W. R., Barabanschikov, A., Pavlik, J. W., Silvernail, N. J. & Sage, J. T. Electronic structure and dynamics of nitrosyl porphyrins. *Inorganic chemistry* **49,** 6240–6252 (2010).

142. Tonzetich, Z. J. *et al.* Identification of protein-bound dinitrosyl iron complexes by nuclear resonance vibrational spectroscopy. *Journal of the American Chemical Society* **132,** 6914–6916 (2010).

143. Linder, D. P. *et al.* The diagnostic vibrational signature of penta-coordination in heme carbonyls. *Journal of the American Chemical Society* **136,** 9818–9821 (2014).

144. Scheidt, W. R., Li, J. & Sage, J. T. What can be learned from nuclear resonance vibrational spectroscopy: vibrational dynamics and hemes. *Chemical reviews* **117,** 12532–12563 (2017).

145. Kneebone, J. L. *et al.* A combined probe-molecule, Mossbauer, nuclear resonance vibrational spectroscopy, and density functional theory approach for evaluation of potential iron active sites in an oxygen reduction reaction catalyst. *The Journal of Physical Chemistry C* **121,** 16283–16290 (2017).

146. Ogata, H. *et al.* Hydride bridge in [NiFe]-hydrogenase observed by nuclear resonance vibrational spectroscopy. *Nature communications* **6,** 1–8 (2015).

147. Smith, M. C. *et al.* Normal-mode analysis of FeCl4-and Fe2S2Cl42-via vibrational mössbauer, resonance Raman, and FT-IR spectroscopies. *Inorganic Chemistry* **44,** 5562–5570 (2005).

148. Xiao, Y. *et al.* Normal mode analysis of Pyrococcus furiosus rubredoxin via nuclear resonance vibrational spectroscopy (NRVS) and resonance Raman spectroscopy. *Journal of the American Chemical Society* **127,** 14596–14606 (2005).

149. Xiao, Y. *et al.* Dynamics of Rhodobacter capsulatus [2Fe-2S] ferredoxin VI and Aquifex aeolicus ferredoxin 5 via nuclear resonance vibrational spectroscopy (NRVS) and resonance Raman spectroscopy. *Biochemistry* **47,** 6612–6627 (2008).

150. Mitra, D. *et al.* Characterization of [4Fe-4S] cluster vibrations and structure in nitrogenase Fe protein at three oxidation levels via combined NRVS, EXAFS, and DFT analyses. *Journal of the American Chemical Society* **135,** 2530–2543 (2013).

151. Xiao, Y. *et al.* How Nitrogenase Shakes- Initial Information about P-Cluster and FeMo-cofactor Normal Modes from Nuclear Resonance Vibrational Spectroscopy (NRVS). *Journal of the American Chemical Society* **128,** 7608–7612 (2006).

152. George, S. J. *et al.* EXAFS and NRVS reveal a conformational distortion of the FeMo-cofactor in the MoFe nitrogenase propargyl alcohol complex. *Journal of inorganic biochemistry* **112,** 85–92 (2012).

153. Reijerse, E. J. *et al.* Direct observation of an iron-bound terminal hydride in [FeFe]-hydrogenase by nuclear resonance vibrational spectroscopy. *Journal of the American Chemical Society* **139,** 4306–4309 (2017).

154. Rodrıguez-Maciá, P. *et al.* Caught in the Hinact: Crystal Structure and Spectroscopy Reveal a Sulfur Bound to the Active Site of an O2-stable State of [FeFe] Hydrogenase. *Angewandte Chemie International Edition* **59,** 16786–16794 (2020).

155. Paulsen, H. *et al.* Interpretation of nuclear resonant vibrational spectra of rubredoxin using a combined quantum mechanics and molecular mechanics approach. *ChemPhysChem* **12,** 3434–3441 (2011).

156. Yeh, A. P. *et al.* High resolution crystal structures of the wild type and Cys-55→ Ser and Cys-59→ Ser variants of the thioredoxin-like [2Fe-2S] ferredoxin from Aquifex aeolicus. *Journal of Biological Chemistry* **277,** 34499–34507 (2002).

157. Wenke, B. B., Spatzal, T. & Rees, D. C. Site-Specific Oxidation State Assignments of the Iron Atoms in the [4Fe: 4S] 2+/1+/0 States of the Nitrogenase Fe-Protein. *Angewandte Chemie* **131,** 3934–3937 (2019).

158. Bjornsson, R. & Bühl, M. Modeling molecular crystals by QM/MM: self-consistent electrostatic embedding for geometry optimizations and molecular property calculations in the solid. *Journal of Chemical Theory and Computation* **8,** 498–508 (2012).

159. Breneman, C. M. & Wiberg, K. B. Determining atom-centered monopoles from molecular electrostatic potentials. The need for high sampling density in formamide conformational analysis. *Journal of Computational Chemistry* **11,** 361–373 (1990).

160. Rappé, A. K., Casewit, C. J., Colwell, K., Goddard III, W. A. & Skiff, W. M. UFF, a full periodic table force field for molecular mechanics and molecular dynamics simulations. *Journal of the American chemical society* **114,** 10024–10035 (1992).

161. Bobrik, M., Hodgson, K. O. & Holm, R. Inorganic derivatives of iron-sulfide-thiolate dimers and tetramers. Structures of tetrachloro-. mu.-disulfido-diferrate (III) and tetrakis (chloro-. mu. 3-sulfido-iron) dianions. *Inorganic Chemistry* **16,** 1851–1858 (1977).

162. Lutz, M., Huang, Y., Moret, M.-E. & Klein Gebbink, R. J. Phase transitions and twinned low-temperature structures of tetraethylammonium tetrachloridoferrate (III). *Acta Crystallographica Section C: Structural Chemistry* **70,** 470–476 (2014).

163. Kovalevsky, A. Y. & Coppens, P. *CSD Communication* (2001).

164. Cappelluti, F., Bencivenni, L. & Guidoni, L. Spin-symmetrised structures and vibrational frequencies of iron–sulfur clusters. *Physical Chemistry Chemical Physics* **22,** 16655–16664 (2020).

165. Varley, J., Wang, Y., Chan, K., Studt, F. & Nørskov, J. Mechanistic insights into nitrogen fixation by nitrogenase enzymes. *Physical Chemistry Chemical Physics* **17,** 29541–29547 (2015).

166. Siegbahn, P. E. The mechanism for nitrogenase including all steps. *Physical Chemistry Chemical Physics* **21,** 15747–15759 (2019).

167. Abraham, M. J. *et al.* GROMACS: High performance molecular simulations through multi-level parallelism from laptops to supercomputers. *SoftwareX* **1-2,** 19–25. ISSN: 2352-7110 (2015).

168. Best Robert, B. *et al.* Optimization of the Additive CHARMM All-Atom Protein Force Field Targeting Improved Sampling of the Backbone $\phi$, $\psi$ and Side-Chain $\chi 1$ and $\chi 2$ Dihedral Angles. *Journal of Chemical Theory and Computation* **8,** 3257–3273 (2012).

169. Jorgensen, W. L., Chandrasekhar, J., Madura, J. D., Impey, R. W. & Klein, M. L. Comparison of simple potential functions for simulating liquid water. *The Journal of chemical physics* **79,** 926–935 (1983).

170. Wright, L. B., Rodger, P. M. & Walsh, T. R. Aqueous citrate: a first-principles and force-field molecular dynamics study. *RSC advances* **3,** 16399–16409 (2013).

171. Klamt, A. & Schüürmann, G. COSMO: a new approach to dielectric screening in solvents with explicit expressions for the screening energy and its gradient. *Journal of the Chemical Society, Perkin Transactions 2,* 799–805 (1993).

172. Verlet, L. Computer" experiments" on classical fluids. I. Thermodynamical properties of Lennard-Jones molecules. *Physical review* **159,** 98 (1967).

173. Swope, W. C., Andersen, H. C., Berens, P. H. & Wilson, K. R. A computer simulation method for the calculation of equilibrium constants for the formation of physical clusters of molecules: Application to small water clusters. *The Journal of chemical physics* **76,** 637–649 (1982).

174. Nosé, S. A molecular dynamics method for simulations in the canonical ensemble. *Molecular Physics* **52,** 255–268 (1984).

175. Nosé, S. A unified formulation of the constant temperature molecular dynamics methods. *The Journal of Chemical Physics* **81,** 511–519 (1984).

176. Humphrey, W., Dalke, A. & Schulten, K. VMD: Visual molecular dynamics. *Journal of Molecular Graphics* **14,** 33–38. ISSN: 0263-7855 (1996).

177. Metz, S., Kästner, J., Sokol, A. A., Keal, T. W. & Sherwood, P. ChemShell—a modular software package for QM/MM simulations. *WIREs Computational Molecular Science* **4,** 101–110. eprint: `https://wires.onlinelibrary.wiley.com/doi/pdf/10.1002/wcms.1163` (2014).

178. Neese, F. The ORCA program system. *Wiley Interdisciplinary Reviews: Computational Molecular Science* **2,** 73–78 (2012).

179. Smith, W. & Forester, T. DL_POLY_2. 0: A general-purpose parallel molecular dynamics simulation package. *Journal of molecular graphics* **14,** 136–141 (1996).

180. Kästner, J. *et al.* DL-FIND: an open-source geometry optimizer for atomistic simulations. *The journal of physical chemistry A* **113,** 11856–11865 (2009).

181. Tao, J., Perdew, J. P., Staroverov, V. N. & Scuseria, G. E. Climbing the density functional ladder: Nonempirical meta–generalized gradient approximation designed for molecules and solids. *Physical Review Letters* **91,** 146401 (2003).

182. Staroverov, V. N., Scuseria, G. E., Tao, J. & Perdew, J. P. Comparative assessment of a new nonempirical density functional: Molecules and hydrogen-bonded complexes. *The Journal of Chemical Physics* **119,** 12129–12137 (2003).

183. Pantazis, D. A., Chen, X.-Y., Landis, C. R. & Neese, F. All-electron scalar relativistic basis sets for third-row transition metal atoms. *Journal of chemical theory and computation* **4,** 908–919 (2008).

184. Neese, F., Wennmohs, F., Hansen, A. & Becker, U. Efficient, approximate and parallel Hartree–Fock and hybrid DFT calculations. A 'chain-of-spheres' algorithm for the Hartree–Fock exchange. *Chemical Physics* **356,** 98–109 (2009).

185. Izsák, R. & Neese, F. An overlap fitted chain of spheres exchange method. *The Journal of chemical physics* **135,** 144105 (2011).

186. Weigend, F. & Ahlrichs, R. Balanced basis sets of split valence, triple zeta valence and quadruple zeta valence quality for H to Rn: Design and assessment of accuracy. *Physical Chemistry Chemical Physics* **7,** 3297–3305 (2005).

187. Grimme, S., Antony, J., Ehrlich, S. & Krieg, H. A consistent and accurate ab initio parametrization of density functional dispersion correction (DFT-D) for the 94 elements H-Pu. *The Journal of chemical physics* **132,** 154104 (2010).

188. Grimme, S., Ehrlich, S. & Goerigk, L. Effect of the damping function in dispersion corrected density functional theory. *Journal of computational chemistry* **32,** 1456–1465 (2011).